SCHOLARLY PUBLICATIONS

A CURRENT AWARENESS BULLETIN
OF RESEARCH OUTPUT

@DTU

(33rd Edition)

SEPTEMBER 2015

BY: CENTRAL LIBRARY

DELHI TECHNOLOGICAL UNIVERSITY
(FORMERLY *DELHI COLLEGE OF ENGINEERING)*
GOVT. OF N.C.T. OF DELHI
SHAHBAD DAULATPUR, MAIN BAWANA ROAD
DELHI 110042

PREFACE

This is the **Thirty Three** Issue of Current Awareness Bulletin started by Delhi Technological University, Central Library. The aim of the bulletin is to compile, preserve and disseminate information published by the faculty, students and alumni for mutual benefits. The bulletin also aims to propagate the intellectual contribution of Delhi Technological University (DTU) as a whole to the academia.

The bulletin contains information resources available in the internet in the form of articles, reports, presentations published in international journals, websites, etc. by the faculty and students of DTU. The publications of faculty and student which are not covered in this bulletin may be because of the reason that the full text either was not accessible or could not be searched by the search engine used by the library for this purpose.

The learned faculty and students are requested to provide their uncovered publications to the library either through email or in CD, etc to make the bulletin more comprehensive.

This issue contains the information published during **September 2015**. The arrangement of the contents is alphabetical. The full text of the article which is either subscribed by the university or available in the web is provided in this bulletin.

Central Library

CONTENTS

10. Design and Development of hybrid electrochemical and centrifugal force assisted abrasive flow machining, Rahul Vaishya, ***3.R.S. Walia*** And P. Kalra, Mechanical Engineering, DTU

11. Design and Simulation of "I" shaped Split Ring Resonator metamaterial at optical communication window around 1.55 μm, ***3.Kamal Kishor***, ***3.Monu Nath Baitha*** and ***3.R. K. Sinha***, Applied Physics, DTU

12. News - Energy Section Far & Near in Water & Energy, ***8.Shri Tapan Kumar Barai*** And Dr. Somit Dasgupta, Electrical Engineeering, DTU

13. Jeans made out of plastics, ***3.Navendu Sharma***, ***3.Amish***, ***3.Manisha Meena*** And ***3.Saurabh Agrawal***, Production and Industrial Engineering, DTU

14. Label-Free Piezoelectric Immunosensor Decorated With Gold Nanoparticles: Kinetic Analysis and Biosensing Application, Ruchika Chauhan, ***3.Jay Singh*** Applied Chemistry & Polymer Technology, Pratima R. Solanki, T. Manaka, M. Iwamoto, T. Basu And ***3.B.D. Malhotra***, Biotechnology, DTU

15. Nanostructured SnO2 encapsulated guar-gum hybrid nanocomposites for electrocatalytic determination of hydrazine, ***3.Priya Malik***, Manish Srivastava, Ranjana Verma, ***3.Manish Kumar***, ***3.D. Kumar*** And ***3.Jay Singh***, ACPT, DTU

16. ON -LICT SIGNED GRAPHS Lc(S) AND -LINE SIGNED GRAPHS L(S) Mukti Acharaya, ***3.Rashmi Jain*** And ***3.Sangita Kansal***, Applied Mathematics, DTU

17. Opposition and dimensional based modified firefly algorithm, ***3.Om Prakash Verma***, ***3.Deepti Aggarwal*** And ***3.Tejna Patodi***, Information Technology, DTU

18. Production of Biodiesel from Crude Neem Oil Feedstock and the Effects of Various Parameters on the Yield of Biodiesel, ***7.Anand Prakash Mall***, Thermal Engineering, DTU

19. Role of oxygen anion diffusion in improved electrochemical performance of layered perovskite LnBa1 – ySryCo2 – xFexO5 + δ (Ln = Pr, Nd, Gd) electrodes, Uzma Anjuma, ***3.Saumye Vashishtha***, Nishant Sinha And M. Ali Haider, ACPT, DTU

20. Scuffing behaviour of EN31 steel under dry sliding condition using pin-on-disc machine, ***3.Paras Kumar***, Harish Hirani And ***3.Atul Agrawal***, Mechanical Engineering, DTU

21. Selection of locations of collection centers for reverse logistics using GTMA, ***3.Sana Malik***, ***3.Aradhana Kumari*** And ***3.Saurabh Agrawal***, DTU

22. Sol Freeze Dry Nd:YAG Nanopowder Synthesis and Sinterability Studies, ***6.1.Rekha Mann***, Kiranmala Laishram Sheikh Ashfaq Ahmed, Khavangkhui Zimik, and Neelam Malhan, Applied Chemistry, DTU

23. TCAD Analysis of Small Signal Parameters and RF Performance of Heterogeneous Gate Dielectric- Gate All Around Tunnel FET, ***3.J. Madan***, R.S. Gupta and ***3.R. Chaujar***, DTU

24. White Light Emission and Color Tunability of Dysprosium doped Barium Silicate Glasses, ***3.Lokesh Mishra***,***3. Anchal Sharma***, ***3.Amit K. Vishwakarma***, ***3.Kaushal Jha***, ***3.M. Jayasimhadri***, B.V. Ratnam, Kiwan Jang,***3. A.S. Rao*** And ***3.R.K. Sinha***, Department of Applied Physics, DTU

1. Vice Chancellor	***1.1. Ex Vice Chancellor***
2. Pro Vice Chancellor	***2.1. Ex Pro Vice Chancellor***
3. Faculty	***3.1. Ex Faculty***
4. Teaching-cum-Research Fellow	
5. Alumni	
6. Research Scholar	***6.1. Ex Research Scholar***
7. PG Scholar	***7.1. Ex PG Scholar***
8. Undergraduate Student	***8.1. Ex Undergraduate Student***

A Web Metric Collection and Reporting System

Ruchika Malhotra
Delhi Technological University
Delhi, India
ruchikamalhotra2004@yahoo.com

Anjali Sharma
CSIR-National Physical Laboratory
New Delhi, India
anjali@nplindia.org

ABSTRACT

The web genre classification distinguishes between pages by means of their features such as style, presentation layout, etc rather than on the topic; improving search results returned to the user by providing genre class of a web page apart from topic. Hence, if a user is able to specify the genre of search like Help, FAQ, Wikipedia etc, chances of getting results in accordance to his interest are high. The classification of web pages into genre is a challenging task as the information is semi-structured, heterogeneous and dynamic. Therefore it is required to find appropriate features which describes web page in the context of genre to increase the genre classification and accuracy of the search result.

In this paper we propose a Metric Collection and Reporting System (MCRS) for Web Application, an automated tool designed to collect 126 significant attributes of web pages for genre identification. MCRS collects and reports important style, presentation layout, form, linguistic, lexical and meta-content features of web page. It collects 88 HTML tags metrics clustered in five groups namely Text formatting tags, Document Structure Tags, External object tags, instruction tags and Navigation Tags. MCRS also reports thirty-eight text metrics including punctuation metrics to describe the lexical attributes of the web page. The NLP module has also been integrated into the system to identify linguistic properties of the web content. The MRCS can be used in parallel with topic search to increase the quality of information retrieval through web genre identification.

Keywords

Web Page, Web Page Metrics, HTML tags, NLP, genre, web genre, information retrieval

1. INTRODUCTION

Genre in broad term refers to any work that share certain characteristics defined by its style, content and form. A good example for knowing genre is through genres of books like Fiction, Folk tale, Poetry, Non-fiction, Biography, etc. If we tag a book with the genre then we can find the books with that genre easily. Similarly, if we add genre to retrieve information from the web, it will be easy for the user to find desired information effectively. For e.g. - If we search for the word "mockingbird" in a search engine, the result is returned depending upon the keyword or topic search in the database. Hence the topic based serach result returns web pages in various genres categories like Article, Wikipedia, Video, News etc. It is difficult for the user to identify the relevant style content of the web page by simple keyword search and have to go through the list of irrelevant content on various pages to retrieve document of a particular genre appropriate to his query. Hence, if a user is able to specify the genre of search which depends on content style like 'TV' or 'Social Network Site' or 'News Scholar Material & Articles' or 'Videos & Images' or 'Help FAQ & Wikipedia' or 'e-Commerce' or 'Blogs Discussion forums', he will get more specific results in accordance to his interest as it will filter out the unwanted information by eliminating noise and extracting main content blocks from web page effectively [1, 2]. This will also increase the speed of classification and accuracy of the search result.

The web genre classification distinguishes between pages by means of their features such as style, presentation layout, form and meta-content rather than on the topic. Therefore a web page genre adds another dimension to the classification of web pages apart from topic and improves the search results returned to the user by providing genre class of a web page. The classification of web pages into genre is a challenging task as the information is semi-structured, heterogeneous and dynamic. Therefore it is important to find appropriate features that describe web page in the context of genre.

In this paper we propose a web Metric Collection and Reporting System (here onwards, referred as MCRS) for Web Applications. The system is designed to collect 126 attributes covering style, presentation layout, form and meta-content features of web pages that are important to describe web page in context of genre as per the research literature [1, 2, 3, 4, 5, 9, 10]. MCRS is capable of collecting total 88 HTML tags metrics clustered in five groups namely Text formatting tags, Document Structure Tags, External object tags, instruction tags and Navigation Tags. A total of 38 text metrics are acquired by the system to describe lexical properties of the web content. The NLP (Natural Language Processing) module is also built in the system to identify interesting and informative phrases in the web content. The MCRS will provide a comprehensive report of 126

WCI '15, August 10 - 13, 2015, Kochi, India

DOI: http://dx.doi.org/10.1145/2791405.2791561

quantitative attributes in the context of web genre as well as provide frequency count of n-grams generation from the web page. Therefore this system is useful in collecting the significant attributes of web pages useful for distinguishing them according to genre. The MRCS can be used in parallel with query search to assist in reporting the genre of a web page and to increase the quality of the information retrieved from the web. This paper is organized as follows: Design and scope of the system is described in Section II; Section III describes the overall working mechanism and architecture of the system. The results of MCRS demonstration are described in Section IV. Section V talks about the application of the tool and concludes the paper along with future directions for research.

2. RELATED WORK

To discriminate the genres and to assign a correct genre to a web page, various studies [1, 2, 9, 10] focused on to extract a set of features useful in classifying web pages according to genres. The web pages are represented with these genre specific features which consist of various HTML tag metrics, text metrics, n-grams and Part-of-Speech (POS) tags. Various tools like [11, 12, 13, 14] are available from industries and research institutes that are capable of performing some NLP operations or collect web and text metrics in bits and pieces. However none of these tools provide the integrated environment for collecting and reporting metrics useful in identifying genre of web page. Our work fills this gap by providing a Python based tool capable of collecting 126 significant attributes of web pages covering style, presentation layout, form, linguistic, lexical, meta-content and NLP features for genre identification.

3. DESIGN OF THE SYSTEM

MCRS is a 3-layer system influenced by the Model-View-Controller (MVC) architecture. The motive behind using this framework is to have separation of concerns so that the business logic logic is independent of the presentation layer. The Model is responsible for all the logic to collect various metrics and is independent of the various views presented to the user. The Controller module acts as an interface between view and model. It intercepts all the requests from view as well as model and provide response accordingly. For example a request from user through View module is received by the Controller and necessary command is transferred to Model for generation of required data. The Model provides the updated data to the Controller, which in turn which can push this data to multiple views as desired by the user. The benefit of this approach is that we are able to design different presentation formats like graph or table to the user without changing the metric collection code embedded in Model. This separation has provided us with code modularity and easy debugging.

MCRS is developed to collect and report web metrics for improving information retrieval of a web page using genre classification. The salient features for genre classification are presentation and lexical properties of the document. However only textual properties are not distinctive for classification of web pages as it is a composite of HTML tags, links, navigational buttons, menus, ads, search boxes, text, images and multimedia, URL, scripts etc. Therefore the MCRS system is designed and developed to retrieve not only lexical properties of the web content but also HTML attributes in form of metrics collected for document structured tags, navigation tags, instruction tags, external object tags and text formatting tags. The NLP contributes to improving web genre retrieval performance in several ways (Lewis & Sparck-Jones, 1996). So, MCRS also retrieves the n-grams metrics by removing stop words, tokenizing the web page content and by performing Part of Speech (POS) tagging. Therefore the system is designed to perform the functions as shown in figure 2 and described below:

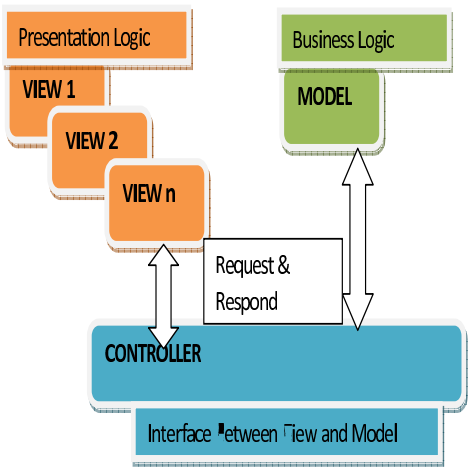

Figure 1: Design framework

First, the system will obtain a URL or a list of URLs from the user to crawl the website and search the html documents using python programming language.

It will perform the computation of text metrics like total number of words, characters, punctuation marks, sentences, paragraphs of the given URL. In addition to it the system will be able to count the number of links and various tags like text formatting tags, document structure tags, navigational tags and many more.

Using nltk, a Natural Language Toolkit the system developed is capable of doing tokenization and POS tagging the text. The bigrams and trigrams frequency is also calculated.

The metrics obtained will be saved as files on the hard disk drive of the user computer.

We have used Python programming language to develop this tool. Apart from being simple, extensible, scalable and easy to learn, Python has a large and comprehensive set of standard libraries like Scrapy, BeautifulSoup, Urllib2 and nltk for web scraping, HTML parsing and natural language processing respectively. Canopy has been used as an Integarted Development Environment for coding.

4. ARCHITECTURE & WORKING

The architecture of the MRCS system is shown in Figure 3. The User Interface Module (UIM) takes a URL or a file consisting of a list of URL as input. The URL entered is displayed on the screen and if a file is uploaded to extract a list of URLs, then the path of the directory in which the file is stored is displayed. Next, this directory path is given as input to the Controller which sends this URL list to the web crawler to crawl the website. The web crawler send crawled web pages output to the controller. The con-

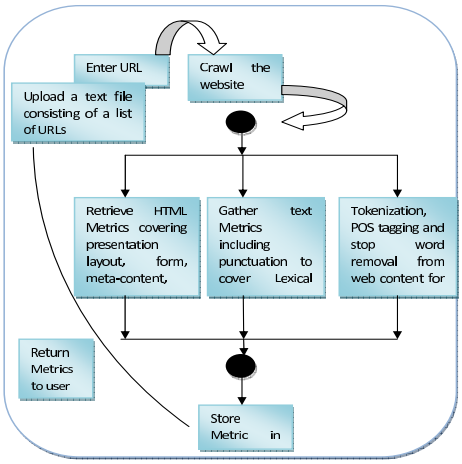

Figure 2: Workflow of MCRS

troller transfers these web pages to the Model which consists of three independent modules namely, HTML Metric Collector, NLP Module and Text Metric Collector. These independent modules collect metrics and saves them in the database through File Handler Module. The NLP module performs tokenization, stop word removal and POS tagging to retrieve NLP metrics of the web page. The updated data from these Model modules is pushed to the controller which hands it over to the UIM. The UIM presents these metrics in the desired format like tabular or graphical to the user. The working of all the modules depicted in Figure 3 is explained in detail below:

4.1 User Interface Module

The User Interface Module (UIM) of MRCS is a part of View, and allows users to interact with the system easily and efficiently. The GUI part of UIM is shown in Figure 4, using which end user can provide a URL or can upload a text file consisting of list of URLs for any or all metric suites. The output is a collection web metrics which is presented to the user in desired tabular or graphical format.

4.2 Web Crawler

The User Interface Module (UIM) of MRCS is a part of View, and allows users to interact with the system easily and efficiently. The GUI part of UIM is shown in Figure 4, using which end user can provide a URL or can upload a text file consisting of list of URLs for any or all metric suites. The output is a collection web metrics which is presented to the user in desired tabular or graphical format.

4.3 Controller

The MRCS controller serves as an interface between the user interface module and three metric collector modules, HTML Metric Collector, NLP module and Text Metric Collector. The controller is invoked when a user enters a URL or uploads a file consisting of list of URLs or user clicks on a control to collect any of the metrics. It is also responsible for providing the desired output to the UIM by invoking respective metric collection modules.

4.4 HTML Metric Collector

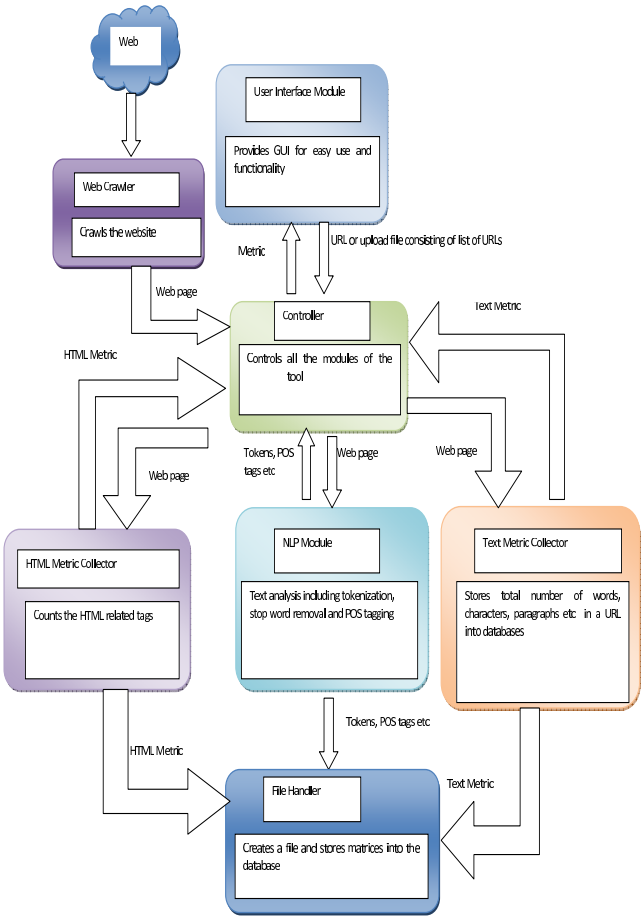

Figure 3: Architecture of MCRS

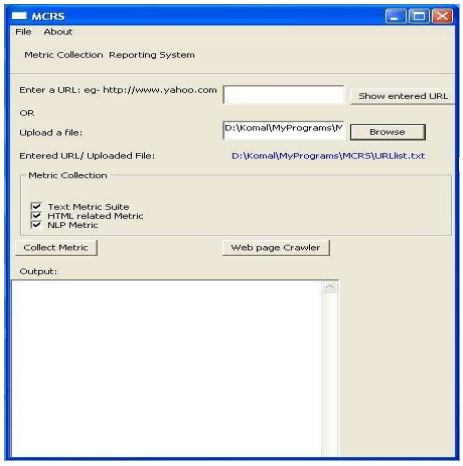

Figure 4: MRCS GUI, snapshot

HTML Metric Collector is capable of collecting total 88 HTML tags metrics clustered in five groups namely Text formatting tags, Document Structure Tags, External object tags, instruction tags and Navigation Tags for the list of URLs provided by the user. This module takes web page as input from controller module and parses it to count HTML tag metrics which are stored in the database and a handler is returned back to Controller. Classification distinguishes between pages by means of their features such as style, presentation layout, form and meta-content rather than on the topic. Therefore a web page genre adds another dimension to the classification of web pages apart from topic and improves the search results returned to the user by providing genre class of a web page. Hence, if a user is able to specify the genre of search which depends on content style like 'News Scholar Material & Articles' or 'Videos & Images' or 'Help FAQ & Wikipedia' etc, he will get more specific results in accordance to his interest as it will filter out the unwanted information by eliminating noise and extracting main content blocks from web page effectively [1, 2]. The classification of web pages into genre is a challenging task as the information is semi-structured, heterogeneous and dynamic. Therefore it is important to find appropriate features which describes web page in the context of genre and increase the speed of classification and accuracy of the search result. In this paper we propose a Metric Collection and Reporting System (MCRS) for Web Application which is an automated tool designed to collect significant attributes of web pages for genre identification and to increase the quality of retrieved information from web. MCRS collects 126 web metrics providing holistic view of the attributes covering style, presentation layout, form, linguistic, lexical and meta-content features of web page. The web metrics collected by the system include 88 HTML tags metrics clustered in five groups namely Text formatting tags, Document Structure Tags, External object tags, instruction tags and Navigation Tags. Apart from HTML tag metrics, MCRS also reports thirty-eight text metrics including punctuation metrics to describe the lexical attributes of the web page. The NLP module has also been integrated into the system to identify interesting and informative phrases in the web content. In addition to the overall functioning of the proposed system, we have described the importance of the web metrics collected by our tool. The MRCS can be used in parallel with query search to assist in reporting the genre of a web page and to increase the quality of the information retrieved from the web. Table 1 present the set of HTML metrics collected and reported by our system in a principled and consistent way for various URLs provided by the user.

Table 1: HTML metrics

HTML Tag Metrics	Tags included
Text Formatting Tags	<abbr>, <acronym>, <address>, <b>, <basefont>, <vdo>, <big>, <blackquote>, , <cite>, <code>, <del>, <dfn>, , <font>, <h1>, <h2>, <h3>, <h4>, <h5>, <h6>, <i>, <ins>, <kbd>, <per>, <q>, <s>, <samp>, <small>, <string>, , <style>, <sub>, <sup>, <tt>, <u>, <var>
Document Structure Tags	 , <caption>, <col>, <colgroup>, <dd>, <dir>, , <dl>, <dt>, <frame>, <hr>, <iframe>, , <menu>, <noframes>, , <p>, , <table>, <tbody>, <td>, <tfoot>, <th>, <thread>, <tr>,
External Object Tags	<applet>, <img>, <object>, <param>, <script>, <noframes>
Instruction Tags	<button>, <field-set>, <forms>, <input>, <isindex>, <label>, <legend>, <opt-group>, <option>, <select>, <textarea>
Navigation Tags	<a>, <area>, <link>, and <base>

4.5 NLP Module

The NLP module takes web page as input and outputs NLP metrics like bigram and trigram frequency of the web content. The web content is retrieved from the web page after striping off all the HTML tags. Then the stop words are removed from this web content. The list of stopwords are taken from a text file and user is allowed to modify this file. Stopwords are the most frequently used words in English such as- the, of, and, to you, yourself and many more. The reduced content is tokenized to perform POS tagging. POS tagging is the task of assigning an appropriate part of speech (e.g. Noun, Verb, Adjective, etc.) to each word in a sentence extracted from a web page. On the POS tagged text we apply n-grams to count the frequency count of bigrams and trigrams. In addition the system also applies stemming of web page content with the help of Porter Stemmer algorithm to find out the root/stem of a word. For example- for the words like engineering, engineered, engineer; the word 'engineer' is a stem. Finally these NLP metrics collected by the module are sent to the File Handler for saving into the database. The Controller is also notified with the updated data.

We have used nltk Python library for processing textual data extracted from web page as it provides some of the common NLP tasks like tokenization, stop word removal, part-of-speech(POS) tagging and many more. The NLP code snippets depicting steps followed to extract NLP metrics are shown below.

```
//1. Stop Word Removal
def strip_stopwords(self,text,stopword):
        print '\n Text after removing all stopwords is –'
        words = text.split()
        text = [ ]
        for word in words:
            if word.lower() not in stopword:
                text.append(word)
return text
```

```
//2. Tokenization
def tokenize(self,text):
        tokens = nltk.word_tokenize(str(text))
        print tokens
return tokens

//3. POS Tagging
def tagging(self,tokens):
        tagged_tokens = nltk.pos_tag(tokens)
        print tagged_tokens
return tagged_tokens

//4. Bigrams def bigrams(self,tags):
        print '\n Bigrams...'
        text_bigram = list(nltk.bigrams(tags))
        for text in text_bigram:
            fdist_bigram = FreqDist(text_bigram)
            bigram_items = fdist_bigram.items()
return bigram_items

//5. Trigrams
def trigrams(self,tags):
        print '\n Trigrams...'
        text_trigram = list(nltk.trigrams(tags))
        for text in text_trigram:
            fdist_trigram = FreqDist(text_trigram)
            trigram_items = fdist_trigram.items()
return trigram_items

//6. Porter Stemming
def stemming(self,text):
        print '\n Stemming text...'
        stem_text = [ ]
        for item in text:
            stem_text.append(stemmer.stem(item))
return stem_text
```

4.6 Text Metric Collector

Text Metric Controller is used to count different punctuation marks and total number of words, sentences, and paragraphs of the web page. The module takes web page as input from controller module and a total of 38 text metrics are acquired by this module to describe lexical properties of the web content. The metrics are stored into database usinf File Handler module. Table 2 present the set of text metrics collected and reported by this module for various web pages provided to it by the controller

Table 2: Text Metrics

Text Metric	Included Metrics
Counts	Letters, words, sentences, paragraphs
Punctuation Marks	!, ", #, $, %, &, (,), -, ., /, :, ;, <, =, >, ?, @, [,\,], ^, _, ', {, |, }, ~

4.7 File Handler

The File Handler module works with the Metric Collector modules to store the various metrics collected by these modules. The files are named dynamically by appending current date and time to the URL name. The module is capable of creating, reading, writing and appending a file. The files are compatible to be used with Excel or any other Word Processor.

5. RESULTS

In this section we present our demonstration of the MCRS by operating on 135 URLs and then discuss the results obtained for the same.

5.1 Data Sets

For the demonstration of MCRS we collected the metrics for five website categories. The five categories included in the collection are - e-commerce, news, travel, entertainment and social media. For 148 URLs we gathered various web metrics like HTML tag metric, text metrics and NLP metrics. The number of web pages included for analyzing the data for each genre is presented in Table 3.

Table 3: Web page count for each Website Category

Categories	Number of Web Pages
E-Commerce	28
News	26
Travel	38
Entertainment	20
Social media	36

5.2 Result Analysis

We have operated the MCRS on various categories of website depicted in Table 3. Figure 5 gives the MCRS distribution percentage report of HTML tags metrics used by the web pages . The HTML metrics were categorized under five metrics namely- Text Formatting metrics, document structure metrics, external object metrics, instruction tags metrics and navigation tag metric.

5.3 Experimentation Setup & Accuracy

MRCS is controlled by a GUI that helps the user to enter a URL or to upload a file consisting of list of URLs. On click of the Collect Metric button, a crawler is instructed to crawl the web page and save the available hyperlinks. The respective metric collection modules are then invoked and results are presented to the user in desired format. For the demonstration of MCRS we collected the metrics for five web genres i.e. News, e-Commerce,Travel, Entertainment and Social media. For 148 URLs we gathered 126 web attributes including HTML, text and NLP metrics. The accuracy of the results reported by the tool has been verified manually by two independent MTech scholars. Some of the URLs were picked randomly to verify the results. The HTML tag and text metrics have been validated by parsing View Page Source of the web pages. The NLP n-gram results have been verified using [15]. The results reported from tool matched exactly with the findings of the MTech scholars.

Figure 6 gives the distribution percentage report of text metrics which gives the count of letters, words, sentences, paragraphs and punctuation marks.

Figure 7 presents the file data reporting view of the results provided by MCRS.

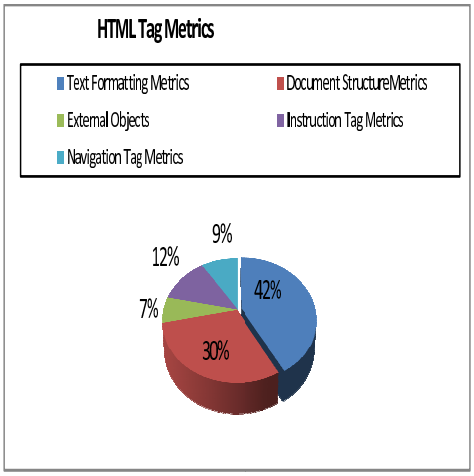

Figure 5: Graphical view of HTML metrics

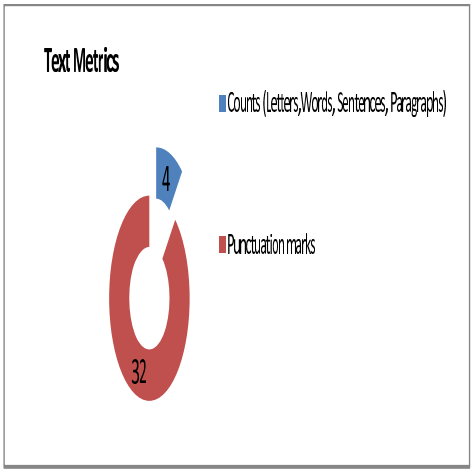

Figure 6: Graphical view of text metrics

6. APPLICATION

The Web Metric Collection and Reporting System has been developed for acquiring and analyzing web metrics with minimal human effort. The metrics collected from MCRS can be utilized for the following studies:

6.1 Website Genre Classification Studies

Web Genre classification distinguishes between pages by means of their presentation, lexical and style attributes rather than on the topic. Therefore a web page genre add another dimension to the classification of web pages apart from topic and improves the search results returned to the user by providing genre class of a web page. The classification of web pages into genre is a challenging task as the information is semi-structured, heterogeneous and dynamic. Therefore it is important to find appropriate features that describe web page in the context of genre. Various studies have also been carried out in the past for predicting and classification of web genres [1, 2, 3, 4, 5, 9, 10].

The metrics collected through MCRS can be used in Website Genre Classification studies and therefore for website genre prediction studies as well.

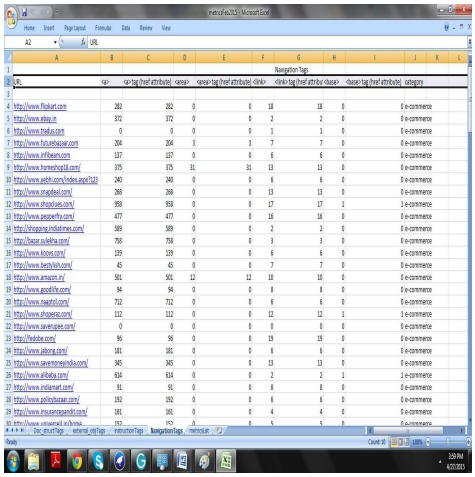

Figure 7: Tabular view of text metrics

6.2 Website Quality Prediction Studies

In order to control the quality of the website, web metrics are considered to be the important source of decision and are useful for estimating as well as predicting the quality of web engineering product [8]. Therefore it is important to measure the web metrics that can be utilized for quality assessment of websites. The research studies condicted [6, 7, 8] have applied the HTML tag metrics for quality prediction. Therefore the metrics generated through MCRS can also be used for quality predction studies of websites.

7. CONCLUSION

The tool has been developed using MVC framework. In case required, the logic to include other metrics useful for website genre classification or quality prediction can be easily integrated into the system. We have plans to develop the next version of the system to include integration of website quality prediction and genre classification logic into the system.

8. REFERENCES

[1] A. Kennedy and M. Shepherd, "Cybergenre: Automatic Identification of Home Pages on the Web" Journal of Web Engineering, Vol 3(4), pp. 236-251, 2004.

[2] M. Santini, "Characterizing Genres of Web Pages: Genre Hybridism and Individualization," Proceedings of 40th Annual Hawaii International Conference System Science, pp. 71-71, 2007.

[3] B. Stein and S. Eissen, "Retrieval models for genre classification" Scand. Journal of Information Systems, Vol. 20, No. 1, 2008.

[4] V. Vidulin, M. Lustrek, and M. Gams, "Multi-Label Approaches to Web Genre Identification" JLCL, Vol. 24, No. 1, pp. 97-114, 2009.

[5] C. Jebari and M. A. Wani, "A Multi-label and Adaptive Genre Classification of Web Pages" Proceedings of 11th International Conference on

Machine Learning and Applications, pp. 578-581, Dec. 2012.

[6] M.Y. Ivory, R. Sinha, M.A. Hearst, "Preliminary findings on quantitative measures for distinguishing highly rated information-centric web pages" Proceedings of the 6th Conference on Human Factors and the Web, 2000.

[7] M.Y. Ivory, R.Sinha, M.A. Hearst, "Empirically Validated Web Page Design Metrics" Proceedings of the SIGCHI conference on Human factors in computing systems, p.53-60, Seattle, Washington, United States, 2001.

[8] Malhotra, R.; Sharma, A., "A neuro-fuzzy classifier for website quality prediction" Proceedings of the International Conference on Advances in Computing, Communications and Informatics (ICACCI),pp.1274-1279, 2013.

[9] Y.B. Lee, S.H. Myaeng, "Text Genre Classification with Genre-revealing and Subject-revealing Features" Proceedings of the 25th ACM SIGIR Conf. on Research and Development in Information Retrieval, pp. 145-150, 2002.

[10] C.S. Lim, K.J. Lee, G.C. Kim, "Multiple Sets of Features for Automatic Genre Classification of Web Documents" Information Processing and Management, 41(5),pp. 1263-1276, 2005.

[11] http://opennlp.apache.org/

[12] http://nlp.stanford.edu/software/tagger.shtml

[13] http://redwriteblue.com/tags/htmlcount.html

[14] http://www.8nog.com/counter/?hl=en

[15] http://www.kwicfinder.com/kfNgram/kfNgramHelp.html

Electrical Power and Energy Systems 75 (2016) 127–138

Contents lists available at ScienceDirect

Electrical Power and Energy Systems

journal homepage: www.elsevier.com/locate/ijepes

AGC of a multi-area multi-source hydrothermal power system interconnected via AC/DC parallel links under deregulated environment

Yogendra Arya [a,*], Narendra Kumar [b]

[a] Department of Electrical & Electronics Engineering, Maharaja Surajmal Institute of Technology, Janakpuri, New Delhi, India
[b] Department of Electrical Engineering, Delhi Technological University, Delhi, India

ARTICLE INFO

Article history:
Received 24 May 2014
Received in revised form 15 August 2015
Accepted 21 August 2015

Keywords:
Automatic generation control
Dynamic system performance
Optimal PI regulators
AC/DC parallel links
Generation rate constraint
Governor dead-band nonlinearity

ABSTRACT

This paper proposes the automatic generation control (AGC) of an interconnected multi-area multi-source hydrothermal power system under deregulated environment. The two equal control areas with hydro and thermal generating power sources are interconnected via AC/DC parallel links. The optimal proportional integral (PI) regulators are designed for the proposed power system to simulate all power market transactions which are possible in a restructured power system. The concept of DISCO participation matrix (DPM) is harnessed to simulate the transactions. Eigenvalue study is conducted to assess the effect of AC/DC parallel links on system performance. The study is also conducted, considering appropriate generation rate constraints (GRCs) for thermal and hydro generating sources. Further, the dynamic responses of the proposed multi-source hydrothermal power system are compared with single-source thermal–thermal power system and it has been ascertained that the responses of proposed power system are sluggish with large overshoots and settling times. Finally, the study is extended to frame and implement optimal PI regulators for the first time for the AGC of a conventional two-area non-reheat thermal power system with governor dead-band nonlinearity. The superiority of the optimal PI regulators has been established by comparing the results with recently published best claimed craziness based particle swarm optimization (CRAZYPSO) and hybrid bacterial foraging optimization algorithm-particle swarm optimization (hBFOA-PSO) algorithms based PI controller tuned for the same interconnected power system.

Introduction

Automatic generation control (AGC) has greater currency in power system operation and control to supply sufficient, efficient, reliable and quality electrical power to the consumers. A critical up-to-date literature review explaining all aspects of AGC is reported in [1–3]. A power system can be considered as being divided into control areas interconnected by the tie-lines. For satisfactory operation of a power system the frequency should remain nearly constant under fluctuating load demands. AGC system adjusts the generator set point by changing speed changer settings automatically to compensate the mismatch between total generation and total load demand plus associated system losses. The AGC system sustains the scheduled system frequency and established interchange with other control areas within predetermined limits during normal/abnormal operating conditions [4]. Various aspects of AGC of conventional interconnected power systems are discussed in [4–28]. Several control strategies, like optimal control [4,5,8–12], variable structure control [11,12], continuous–discrete mode control [13], sliding mode [14], beta wavelet artificial neural networks [15], differential evolution [16], non-dominated sorting genetic algorithm-II [17], bacteria foraging [18,19], hybrid bacterial foraging-particle swarm optimization [19], craziness based particle swarm optimization [20], teaching–learning technique [14,21], fuzzy logic control [21–25], bat algorithm [23], big bang-big crunch [24], quasi-oppositional harmony search [25], cuckoo search algorithm [26,27] and firefly algorithm [28] are applied to design various AGC controllers for different single and multi-area interconnected conventional electrical power systems.

Due to spiraling power demands, interconnected electric power systems are becoming more and more complicated. Federal energy regulatory commission (FERC) of USA encourages an open market system for price based operation [29]. Under the premise of deregulated environment, the planning and operation of the power system have to be reformulated. However, the common AGC goals like restoring the frequency and the net tie-line exchanges to their

* Corresponding author. Tel.: +91 9891484801.
E-mail addresses: mr.y.arya@gmail.com (Y. Arya), dnk_1963@yahoo.com (N. Kumar).

http://dx.doi.org/10.1016/j.ijepes.2015.08.015
0142-0615/

desired values for each control area still thrive in this new restructured scenario. In the deregulated environment, the vertically integrated utilities (VIUs) no longer survive. In the deregulated structure, several independent entities like distribution companies (DISCOs), generation companies (GENCOs), transmission companies (TRANSCOs) and independent system operator (ISO) have been introduced [5,6,29–46]. ISO is independent, disassociated agent for market participants who perform various ancillary services and among them is the AGC [30]. In open market scenario consumers have a choice to choose among DISCOs in their area, while DISCOs of an area have the freedom to have power contracts for transaction of power with GENCOs of the same or other area. A decentralized AGC scheme for competitive electricity market comprising 39-bus New England and 75-bus Indian power system has been ruminated upon [31]. The decentralized load frequency control (LFC) schemes for two-area [32,38], three-area [33,35,37,43] and four-area [34,43] restructured power systems, are also reported in the literature. Various AGC issues in power system control and operation after deregulation, are touched in [30,36,37]. In deregulated market the effective application of load following controllers is discussed in [38–40]. Compliance with North American electric reliability council (NERC) control performance standards (CPS) for AGC under deregulated environment, are discussed in [31,41]. Recently various control strategies are reported in the literature for AGC of restructured power systems such as trajectory sensitivities using gradient Newton algorithm [30], eigenstructure assignment technique [31], H_2/H_∞ control [32], neural networks [33], firefly algorithm [34], hybrid neuro fuzzy [35], genetic algorithm [34,37,38], bacteria foraging [41,42], non-integer controller [42], active disturbance rejection [43], fuzzy logic controller [34,44,45], particle swarm optimization [45] and optimal control [31,45,46].

Recent advances in power electronic devices led to the development of fast acting flexible alternating current transmission system (FACTS) devices to improve the stability of the interconnected modern power systems. FACTS devices provide more flexibility in power system operation and control to maintain a constant system voltage and frequency profiles. FACTS devices such as thyristor controlled series compensator [38], interline power flow controller (IPFC) [41] and thyristor controlled phase shifter (TCPS) [44] are employed in series with AC tie-line to stabilize the system frequency and tie-power oscillations. Further, advancements in power electronics industry have helped to produce high voltage direct current (HVDC) transmission to transmit bulk power over distant places with lower capital costs and power losses than high voltage alternating current (HVAC) transmission system. Some important advantages of HVDC transmission include controlled huge power transmission between unsynchronized AC distribution systems, no limitation of distance for power transfer, requires less number of conductors, hence it reduces the line cost and can carry more power per conductor than HVAC system. On the other hand, many problems plague the power systems interconnected via long AC tie-lines, like frequent tripping due to power oscillations, large fault current level and reduction in system dynamic performance due to transmission of disturbances among systems [47]. Hence, in order to enhance controllability, one important application of HVDC transmission line is, operating in parallel with an existing AC transmission line acting as AC/DC parallel links interconnecting any two control areas. In literature, AGC of a two-area power system interconnected via AC/DC parallel links, is carried out by using optimal AGC regulators in deregulated mode [45,46]. In addition, AC/DC parallel links in conventional power systems are found in the literature employing sliding mode control [14], optimal control [10,47–49], sub-optimal control [50,51] and differential evolution [52] based control techniques.

Recently some researchers have investigated the AGC of conventional power systems with diverse sources such as hydro, thermal, gas, and nuclear, operating in each control area [14,18,47,52–56]. Optimal AGC regulators are designed and implemented effectively on a two-area power system with hydro-thermal–gas generating units in each area [47]. The study is also performed using differential evolution [52] and particle swarm optimization [53] techniques for AGC of multi-source single/multi-area power systems. Optimal full state feedback and output feedback controllers are proposed for a realistic single-area multi-source system [54]. An optimal output feedback controller is proposed for two-area system with hydro-thermal–gas diverse sources in each area under deregulated power environment [55]. Recently, a hybrid soft computing technique is proposed for a two-area diverse-source hydrothermal system [56]. To the best of authors' knowledge, till date, no attempt has been made to design optimal PI or any other controller for AGC of two-area power system with hydrothermal multi-sources in each area under deregulated environment and interconnected via AC/DC parallel links. In view of the above developments seen in the literature, following are the important objectives of the present work:

(a) To design state space model for AGC study of a two-area power system containing hydrothermal generating source in each control area interconnected via AC/DC parallel links under deregulated environment.
(b) To develop optimal proportional integral (PI) regulators for AGC study of the proposed power system.
(c) To optimize gains of the optimal PI regulators using full state feedback control strategy and hence to study the dynamic performance of the proposed power system and to authenticate these responses by comparing with desired values.
(d) To check the performance of the optimal PI regulators during contract violation in deregulated environment.
(e) To study the effectiveness of the optimal PI regulators and AC/DC parallel links with and without considering generation rate constraints (GRCs).
(f) To validate the sluggish response effect of the proposed multi-source hydrothermal power system by comparing with the same single-source two-area restructured power system containing thermal–thermal sources in each area and interconnected via AC/DC parallel links.
(g) To propose optimal PI regulators for the first time for AGC study of a two-area non reheat thermal power system with governor dead-band nonlinearity and to establish the superiority of the optimal PI regulators in comparison to recently published craziness based particle swarm optimization (CRAZYPSO) and hybrid bacterial foraging optimization algorithm-particle swarm optimization (hBFOA-PSO) algorithms based PI controllers for the same system.

Description of the power system model under deregulated environment

In deregulated environment, the generation companies (GENCOs) sell power they generate to different distribution companies (DISCOs) in open market at competitive prices. The entity which wheels this power between GENCOs and DISCOs is termed as transmission company (TRANSCO). In the new structure, a DISCO can have contracts individually with GENCOs to buy the power and these transactions are done under the supervision of the ISO [30]. DISCOs of any area have freedom to establish contracts for transaction of power with the GENCOs of different areas, usually christened as bilateral transactions [30,31]. Another is poolco based transactions in which GENCOs of an area for AGC have contracts only with the DISCOs of their own area [30,31]. The AGC of interconnected restructured power systems is discussed in details in [5,6,29–46,55]. The AGC study under deregulated environment

should be designed to accommodate all power contracts possible like poolco based, bilateral and a combination of these two transactions. A GENCO in contract changes its power output till it does not exceed the contracted value, while a DISCO is responsible for monitoring its load demand to meet load following requirements as per contractual agreement [31]. To carry out different transactions and to provide information about the participation of a DISCO in contract with a GENCO, a DISCO participation matrix (DPM) has been proposed [30]. The number of rows in DPM corresponds to the number of GENCOs and the number of columns has to be equal to the number of DISCOs in the power system under study. Each entry in DPM is defined as contract participation factor (cpf) and corresponds to a contracted load by a DISCO demanded from the corresponding GENCO. Sum of the entries of a column of DPM is $\sum_i^{\mathrm{NGENCO}} \mathrm{cpf}_{ij} = 1$, $j = 1, 2, \ldots,$ NDISCO, where NGENCO is number of GENCOs and NDISCO is number of DISCOs [40]. In the proposed two-area power system model, each control area has two DISCOs and two GENCOs. Let GENCO_1, GENCO_2, DISCO_1 and DISCO_2 be in control area-1 while GENCO_3, GENCO_4, DISCO_3 and DISCO_4 be in control area-2. In control area-1, one generating source is single reheat thermal power plant (GENCO_1) and other is mechanical governor based hydro power plant (GENCO_2). Similarly GENCO_3 is thermal and GENCO_4 is hydro source of the same configuration. The two-area power system with each area capacity of 2000 MW interconnected via AC/DC parallel links, as shown in Fig. 1, is considered to demonstrate the effectiveness of the optimal PI regulators based on full state feedback control strategy. The detailed transfer function model of the power system under study is depicted in Fig. 2. To make the realization of contracts simpler a DISCO participation matrix (DPM) is usually used [6,30,34,37,38,40–42,44–46,55] and for the system under investigation is given as

$$\mathrm{DPM} = \begin{bmatrix} \mathrm{cpf}_{11} & \mathrm{cpf}_{12} & \mathrm{cpf}_{13} & \mathrm{cpf}_{14} \\ \mathrm{cpf}_{21} & \mathrm{cpf}_{22} & \mathrm{cpf}_{23} & \mathrm{cpf}_{24} \\ \mathrm{cpf}_{31} & \mathrm{cpf}_{32} & \mathrm{cpf}_{33} & \mathrm{cpf}_{34} \\ \mathrm{cpf}_{41} & \mathrm{cpf}_{42} & \mathrm{cpf}_{43} & \mathrm{cpf}_{44} \end{bmatrix}. \tag{1}$$

The actual steady state tie-line power flows for a two-area power system interconnected via AC link is given as [30]

$$\Delta P\mathrm{tie}_{\mathrm{actual}} = \frac{2\pi T_{12}}{s}[\Delta F_1 - \Delta F_2]. \tag{2}$$

The DC link is assumed to be operated in constant current control mode [47]. The incremental power flow through DC link ($\Delta P\mathrm{tie}_{\mathrm{dc}}$) is modeled with incremental change in frequency at rectifier end [47]. The representation of transfer function model of DC link is taken from [45–52] as shown in Fig. 2. For small perturbation the DC tie-line flow can be given as

$$\Delta P\mathrm{tie}_{\mathrm{dc}} = \frac{K_{\mathrm{dc}}}{1 + sT_{\mathrm{dc}}}[\Delta F_1 - \Delta F_2]. \tag{3}$$

For small load change, the actual tie-line power flow, as given by Eq. (2) for the system interconnected via AC link, is modified due to the presence of a DC link in parallel with the existing AC link as

$$\Delta P\mathrm{tie}_{\mathrm{mactual}} = \Delta P\mathrm{tie}_{\mathrm{actual}} + \Delta P\mathrm{tie}_{\mathrm{dc}}. \tag{4}$$

The scheduled steady state power flow on the tie-line is given as [6,30,37,40–42,46,55]

$$\Delta P\mathrm{tie}_{\mathrm{scheduled}} = \sum_{i=1}^{2}\sum_{j=3}^{4} \mathrm{cpf}_{ij}\Delta P_{Lj} - \sum_{i=3}^{4}\sum_{j=1}^{2} \mathrm{cpf}_{ij}\Delta P_{Lj},$$
$$\Delta P\mathrm{tie}_{\mathrm{scheduled}} = [P_{\mathrm{exp1}}] - [P_{\mathrm{imp1}}]. \tag{5}$$

where $[P_{\mathrm{exp1}}]$ is the total power exported from area-1 and equal to the demand of DISCOs in area-2 from GENCOs in area-1, while $[P_{\mathrm{imp1}}]$ is the total power imported in area-1 and equal to the demand of DISCOs in area-1 from the GENCOs in area-2 [55]. The tie-line power flow error is stated as

$$\Delta P\mathrm{tie}_{\mathrm{error}} = \Delta P\mathrm{tie}_{\mathrm{mactual}} - \Delta P\mathrm{tie}_{\mathrm{scheduled}}. \tag{6}$$

In steady state $\Delta P\mathrm{tie}_{\mathrm{error}}$ vanishes as $\Delta P\mathrm{tie}_{\mathrm{mactual}}$ attains $\Delta P\mathrm{tie}_{\mathrm{scheduled}}$ tie-line power flows. In new scenario the area control error (ACE) is modified due to the presence of AC/DC parallel links and may be defined as

$$\mathrm{ACE}_{m1} = \beta_1 \Delta f_1 + \Delta P\mathrm{tie}_{\mathrm{error}}, \tag{7}$$

$$\mathrm{ACE}_{m2} = \beta_2 \Delta f_2 + \alpha_{12}\Delta P\mathrm{tie}_{\mathrm{error}}. \tag{8}$$

where α_{12} is area size ratio and β_1, β_2 are frequency bias constants of the respective area. Since there are usually more than one GENCO in each area, so modified area control error (ACE_m) signal must be shared by these GENCOs in proportion to their contributions in AGC. The factors which denote this sharing, are called ACE participation factors (apfs) and it is assumed that all GENCOs participate in the AGC depending on their corresponding apfs. It should be noted that in all the current simulations, apfs are kept at the same values, i.e., $\mathrm{apf}_{t1} = 0.5$, $\mathrm{apf}_{h1} = 1 - \mathrm{apf}_{t1}$, $\mathrm{apf}_{t2} = 0.5$, and $\mathrm{apf}_{h2} = 1 - \mathrm{apf}_{t2}$. The expressions for steady state generated power of GENCOs in contract with DISCOs are given as

$$\Delta P_{Gti} = \mathrm{cpf}_{i1}\ \Delta P_{L1} + \mathrm{cpf}_{i2}\ \Delta P_{L2} + \mathrm{cpf}_{i3}\ \Delta P_{L3} + \mathrm{cpf}_{i4}\ \Delta P_{L4}, \quad i = 1, 3, \tag{9}$$

$$\Delta P_{Ghi} = \mathrm{cpf}_{i1}\ \Delta P_{L1} + \mathrm{cpf}_{i2}\ \Delta P_{L2} + \mathrm{cpf}_{i3}\ \Delta P_{L3} + \mathrm{cpf}_{i4}\ \Delta P_{L4}, \quad i = 2, 4. \tag{10}$$

In Fig. 2 the market disturbance signal $\Delta P_{L1,LOC}$ $(= \Delta P_{L1} + \Delta P_{L2})$ can be defined as the total local demand in area-1 while $\Delta P_{L2,LOC}$ $(= \Delta P_{L3} + \Delta P_{L4})$ is the total local load demand in area-2. ΔP_{Li} denotes the power demanded by DISCO_i. The disturbance signals ΔP_{UC1} and ΔP_{UC2} are the uncontracted power demanded by DISCOs in area-1 and area-2 respectively. The market signals ΔP_{UC1} and ΔP_{UC2} will be equal to zero, when uncontracted power demand of DISCOs are absent.

State space model of the power system under investigation

The power system model under investigation shown in Fig. 2, is a linear continuous-time system which can be represented by the following standard state space equations

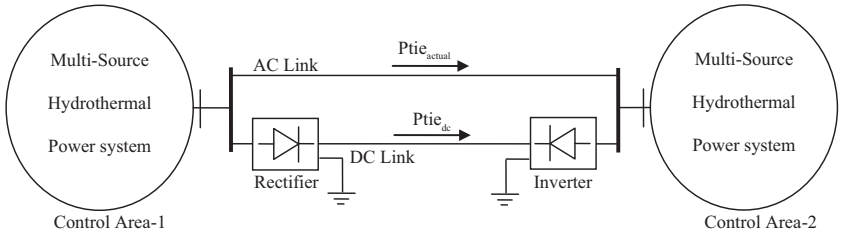

Fig. 1. Two-area multi-source power system interconnected via AC/DC parallel links [46–49].

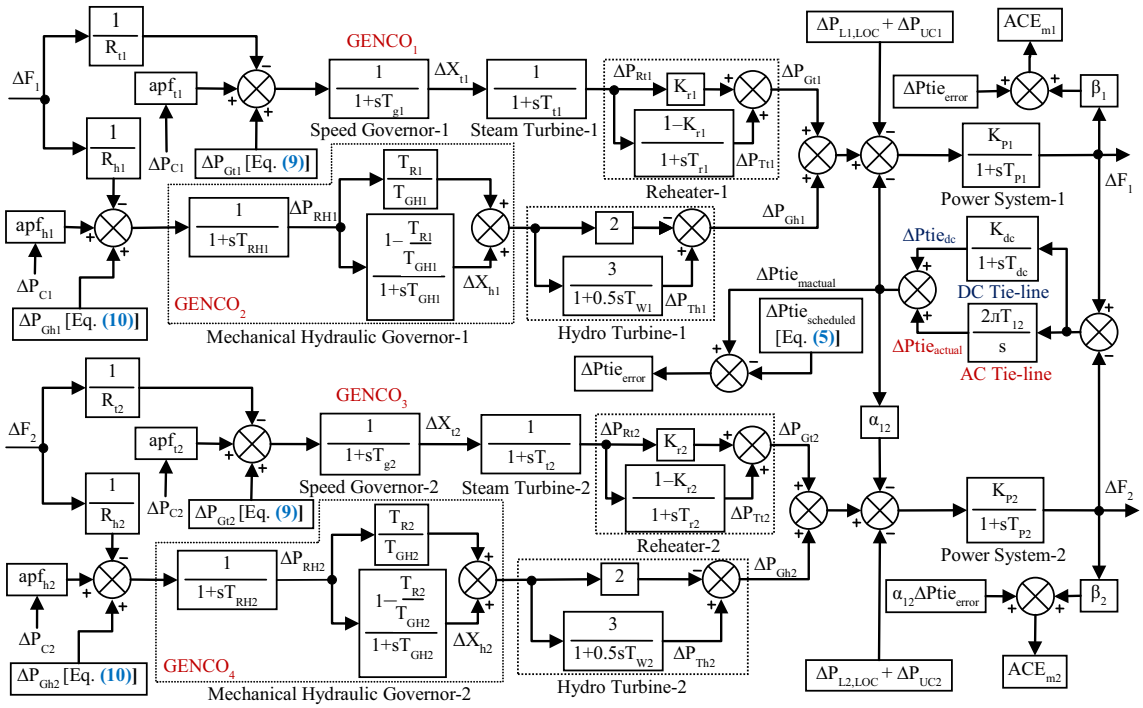

Fig. 2. Transfer function model of two-area multi-source power system under deregulated environment.

$$\frac{d}{dt}\underline{X} = A\underline{X} + B\underline{U} + \Gamma\underline{P_d}, \quad \underline{X(0)} = 0 \tag{11}$$

$$\underline{Y} = C\underline{X} \tag{12}$$

where $\underline{X}$ is system state vector of the dimension $n \times 1$, n is number of state variables = 18, $\underline{U}$ is control input vector of the dimension $m \times 1$, m is number of control variables = 2, $\underline{P_d}$ is disturbance vector of the dimension $p \times 1$, p is number of disturbance variables = 6, $\underline{Y}$ is output vector of the dimension $q \times 1$, q is number of measured output variables = 18. A, B, C, and Γ are system, control, output and disturbance matrices having dimensions of $n \times n$, $n \times m$, $q \times n$, and $n \times p$ respectively, and are given in Appendix A. In optimal control theory application, the term $\underline{P_d}$ in Eq. (11) is eliminated in steady state occurring after a disturbance. So the Eq. (11) can be rephrased in a convenient form as

$$\frac{d}{dt}\underline{X} = A\underline{X} + B\underline{U}, \quad \underline{X(0)} = -X_{ss} \tag{13}$$

where new state vector is equal to the old state vector minus its steady state value X_{ss}[11,12].

State, control and disturbance vectors selected for the power system under study are given as follows:

- State vector:

$$\underline{X} = [\Delta F_1\ \Delta P\text{tie}_{\text{actual}}\ \Delta F_2\ \Delta P_{Tt1}\ \Delta P_{Th1}\ \Delta P_{Tt2}\ \Delta P_{Th2}\ \Delta P_{Rt1}\ \Delta X_{h1}\ \Delta P_{Rt2}\ \Delta X_{h2}\ \Delta X_{t1}\ \Delta P_{RH1}\ \Delta X_{t2}\ \Delta P_{RH2}\ \int \text{ACE}_{m1}dt\ \int \text{ACE}_{m2}dt\ \Delta P\text{tie}_{\text{dc}}]^T \tag{14}$$

- Control vector:

$$\underline{U} = [\Delta P_{C1}\Delta P_{C2}]^T \tag{15}$$

- Disturbance vector:

$$\underline{P_d} = [\Delta P_{L1}\ \Delta P_{L2}\Delta P_{L3}\ \Delta P_{L4}\ \Delta P_{UC1}\ \Delta P_{UC2}]^T \tag{16}$$

The states stated above are selected as the deviations of frequency in area-1 (ΔF_1) and area-2 (ΔF_2), the deviations in the intermediate power outputs of GENCOs in area-1 (ΔP_{Tt1}; ΔP_{Th1}) and area-2 (ΔP_{Tt2}; ΔP_{Th2}), the deviations in thermal turbine outputs in area-1 (ΔP_{Rt1}) and area-2 (ΔP_{Rt2}), the deviations in thermal governor outputs in area-1 (ΔX_{t1}) and area-2 (ΔX_{t2}), the deviations in intermediate outputs of hydro governor in area-1 (ΔP_{RH1}; ΔX_{h1}) and area-2 (ΔP_{RH2}; ΔX_{h2}), the deviation in speed changer position of area-1 (ΔP_{C1}) and area-2 (ΔP_{C2}), the deviation in actual tie-line power ($\Delta P\text{tie}_{\text{actual}}$), the deviation in DC link power output ($\Delta P\text{tie}_{\text{dc}}$) and integral of modified area control error in area-1 ($\int \text{ACE}_{m1}dt$) and area-2 ($\int \text{ACE}_{m2}dt$).

Design of optimal PI regulators

The design of optimal PI regulators has been reported in the literature [4,5,8–12,45–50]. This section is devoted to derive optimal feedback gains (K^*) of optimal PI regulators. The continuous time dynamic model of power system in the state variable form is given by Eqs. (11) and (12). The control vector $\underline{U}$ defines the performance criterion to minimize the functional or performance index J given by

$$J = \int_0^\infty \frac{1}{2}\left[\underline{X}^T Q\underline{X} + \underline{U}^T R\underline{U}\right]dt \tag{17}$$

where Q is a positive semi-definite symmetric state cost weighting matrix and R is a positive definite symmetric control cost weighting matrix as given in Appendix A. The optimal control law is given [8,9] as

$$\underline{U}^* = -K^*\underline{X} \tag{18}$$

where

$$K^* = R^{-1}B^T P \tag{19}$$

and P is the solution of algebraic matrix Riccati equation

$$PA + A^T P - PBR^{-1}B^T P + Q = 0. \tag{20}$$

Simulation and discussion of results

The state space model of a multi-area power system shown in Fig. 2 with multi-source power generation under deregulated environment is simulated with the optimum regulator gains using workspace of MATLAB software version 7.5.0(R2007b). The system data are given in Appendix B. The corresponding nomenclature is explained in [9,13,47,49,55,57,58]. The following case studies are investigated in the present study:

Multi-area multi-source restructured power system with different transactions

The optimal PI regulators are designed by using the state space model written in MATLAB (.mfile) for the power system model under study, to simulate all types of possible power transaction like poolco based, bilateral and a combination of the two transactions taking place in a deregulated environment. The system data are given in Appendix B_1. The optimal gains of optimal PI regulators are obtained for power system model considering (i) AC link and (ii) AC/DC parallel links along with the minimum performance index values J^* as given in Table 1. The open-loop and closed-loop system eigenvalues for both the power system models are given in Table 2. The study of Table 1 reveals that system performance cost index J^* is reduced when AC/DC parallel links ($J^* = 2.9347e^{+3}$) are used as area interconnection than that obtained with only AC link ($J^* = 3.6800e^{+3}$). Further, the investigations of the power system eigenvalues given in Table 2 indicate that open-loop eigenvalues of both systems corresponding to 1st two states lie on the $j\omega$-axis in s-plane, while all other values lie in the left half of s-plane. Therefore system is marginally stable in open-loop interconnected via AC and AC/DC parallel links. On the other hand all close-loop eigenvalues are with negative real parts which ensure system stability with good stability margins for both cases i.e., AC link and AC/DC parallel links. Additionally, the magnitudes of imaginary parts of closed-loop eigenvalues of some states are less as compared with those of open-loop eigenvalues, which may improve the system dynamic responses. Some eigenvalues have more negative real parts in case of AC/DC parallel links which improve the stability margins of the power system. The cases for different transactions are:

Case-A: Poolco based transactions

In poolco based transactions GENCOs participate in AGC of their own control area, here area-1 only i.e., power is demanded only by $DISCO_1$ and $DISCO_2$ [6,30,33–35,41]. Let the load demanded by each DISCO be 10%, i.e., $\Delta P_{L1,LOC} = 0.2$ puMW and $\Delta P_{L2,LOC} = 0$ puMW. Both DISCOs demand equally from two GENCOs of area-1, i.e., $apf_{t1} = apf_{h1} = 0.5$. The DPM for this case is given as

$$\mathrm{DPM} = \begin{bmatrix} 0.5 & 0.5 & 0 & 0 \\ 0.5 & 0.5 & 0 & 0 \\ 0 & 0 & 0 & 0 \\ 0 & 0 & 0 & 0 \end{bmatrix}.$$

$DISCO_3$ and $DISCO_4$ do not demand power from any GENCO, therefore the corresponding cpfs are taken zero. Generation of a GENCO in the steady state must match the demand of the DISCOs in contract with it. From Eqs. (9) and (10), in steady state the theoretical values of generations of $\Delta P_{Gt1} = 0.1$ puMW, $\Delta P_{Gh1} = 0.1$ puMW, $\Delta P_{Gt2} = 0$ puMW and $\Delta P_{Gh2} = 0$ puMW. Also the scheduled power flow on the tie-line can be calculated by Eq. (5), i.e., $\Delta P\mathrm{tie}_{\mathrm{scheduled}} = 0$ puMW. The Simulation results for the power system interconnected via AC/DC parallel links are shown in Fig. 3. For Case-A, it is observed that in the steady state the deviations in frequency of each area settle to zero under a step power demand change of $DISCO_1$ and $DISCO_2$, hence AGC requirement is fulfilled. The scheduled steady state tie-line power flows are equal to the actual tie-line power flows, i.e., $\Delta P\mathrm{tie}_{\mathrm{scheduled}} = \Delta P\mathrm{tie}_{\mathrm{actual}} = \Delta P\mathrm{tie}_{\mathrm{mactual}} = 0$ puMW. Therefore, $\Delta P\mathrm{tie}_{\mathrm{error}} = 0$ puMW. The actual generated powers of the all GENCOs reach the theoretically calculated (desired) values in the steady state as shown in Figs. 3e–h. As GENCOs situated in area-2 do not transact the power, $\Delta P_{Gt2} = \Delta P_{Gh2} = 0$ puMW in steady state. It is also observed that the system responses belonging to area of power demand/disturbance, i.e., area-1, experience more deviations as compared to other control area having zero power demand/disturbance, i.e., area-2. Therefore, it is concluded that the effect of disturbance has local dominance but it also affects the dynamic performances of other control area due to the presence of frail tie-line used to connect the two control areas.

Case-B: Combination of poolco and bilateral transactions

In this case, DISCOs have the freedom to have a power contract with any GENCOs situated in its own or other control areas [6,30,33–35,41,55]. For this scenario the contracts between available DISCOs and GENCOs is simulated on the basis of the DPM given as

$$\mathrm{DPM} = \begin{bmatrix} 0.1 & 0.1 & 0.1 & 0.1 \\ 0.1 & 0.1 & 0.1 & 0.3 \\ 0.5 & 0.2 & 0.5 & 0.3 \\ 0.3 & 0.6 & 0.3 & 0.3 \end{bmatrix}.$$

Let each DISCO demand 6% power from GENCOs as per the pattern of cpfs shown in the DPM, i.e., $\Delta P_{L1,LOC} = \Delta P_{L2,LOC} = 1.2$ puMW. Using Eq. (5), the scheduled tie-line power flows will be, $\Delta P\mathrm{tie}_{\mathrm{scheduled}} = \{(0.1+0.1+0.1+0.3)-(0.5+0.3+0.2+0.6)\}0.06 = -0.06$ puMW. For Case-B, the simulation results for the power system interconnected via AC/DC parallel links are also shown in Fig. 3. In steady state the deviation in frequencies of both control areas settle to zero. The actual tie-line power flows shown in Fig. 3c and d settles to desired value of −0.06 puMW, which is the scheduled tie-line power flow in the steady state. Therefore, tie-line power error is equal to zero puMW. The steady state desired values of generations are $\Delta P_{Gt1} = 0.024$ puMW, $\Delta P_{Gh1} = 0.036$ puMW, $\Delta P_{Gt2} = 0.09$ puMW, and $\Delta P_{Gh2} = 0.09$ puMW. These are verified in Fig. 3e–h.

Table 1
Optimal gain matrices of the optimal PI regulators for two-area multi-source restructured power system.

Type of area interconnections	Optimal feedback gain matrix (K^*)									J^*
AC link only	[0.6377	−1.5684	0.0974	5.1642	2.0584	0.4118	0.1356	0.8880	−0.2779	$3.6800e^{+3}$
	0.0196	0.5464	0.4448	−2.3890	0.0016	4.3984	1.0000	−0.0000;		
	0.0974	1.5684	0.6377	0.4118	0.1356	5.1642	2.0584	0.0196	0.5464	
	0.8880	−0.2779	0.0016	4.3984	0.4448	−2.3890	0.0000	1.0000]		
AC/DC links	[0.4060	−0.1332	0.3290	4.4167	1.3850	1.1592	0.8089	0.6380	0.3429	$2.9347e^{+3}$
	0.2696	−0.0744	0.3846	4.2529	0.0618	−2.2435	1.0000	0.0000	−0.0174;	
	0.3290	0.1332	0.4060	1.1592	0.8089	4.4167	1.3850	0.2696	−0.0744	
	0.6380	0.3429	0.0618	−2.2435	0.3846	4.2529	0.0000	1.0000	0.0174]	

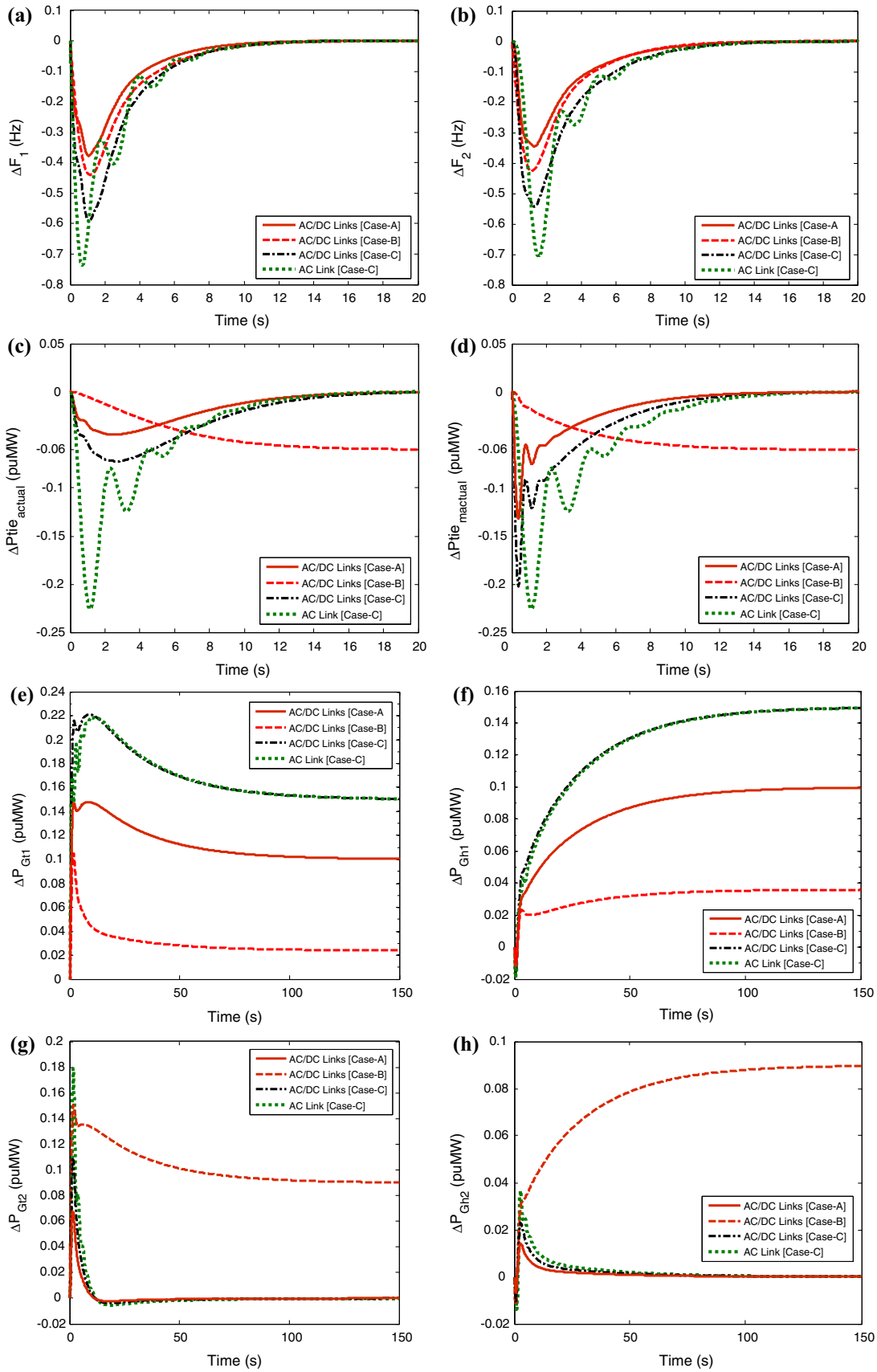

Fig. 3. Dynamic performance of two-area multi-source power system (a) ΔF_1 (Hz) vs. time (s), (b) ΔF_2 (Hz) vs. time (s), (c) $\Delta P\text{tie}_{\text{actual}}$ (puMW) vs. time (s), (d) $\Delta P\text{tie}_{\text{mactual}}$ (puMW) vs. time, (e) ΔP_{Gt1} (puMW) vs. time, (f) ΔP_{Gh1} (puMW) vs. time, (g) ΔP_{Gt2} (puMW) vs. time and (h) ΔP_{Gh2} (puMW) vs. time.

Table 2
Pattern of open-loop and closed-loop eigenvalues for two-area multi-source restructured power system.

S. no.	State variables	Eigenvalues with AC link		Eigenvalues with AC/DC links	
		Open-loop	Closed-loop	Open-loop	Closed-loop
1.	ΔF_1	−0.0000	−14.2205	−0.0000	−14.2205
2.	$\Delta P\text{tie}_{\text{actual}}$	−0.0000	−14.2105	−0.0000	−14.1122
3.	ΔF_2	−12.9224	−0.5128 + 2.8721i	−12.9224	−2.1258 + 7.8182i
4.	ΔP_{Tt1}	−12.9074	−0.5128 − 2.8721i	−12.7630	−2.1258 − 7.8182i
5.	ΔP_{Th1}	−0.1628 + 2.9641i	−2.8032 + 0.8295i	−2.0752 + 7.8229i	−3.7737
6.	ΔP_{Tt2}	−0.1628 − 2.9641i	−2.8032 − 0.8295i	−2.0752 − 7.8229i	−2.8032 + 0.8295i
7.	ΔP_{Th2}	−2.6410 + 0.8493i	−2.7959 + 0.4668i	−3.4881	−2.8032 − 0.8295i
8.	ΔP_{Rt1}	−2.6410 − 0.8493i	−2.7959 − 0.4668i	−2.6410 + 0.8493i	−1.1848 + 1.2818i
9.	ΔX_{h1}	−2.6553 + 0.6186i	−1.1848 + 1.2818i	−2.6410 −0.8493i	−1.1848 − 1.2818i
10.	ΔP_{Rt2}	−2.6553 − 0.6186i	−1.1848 − 1.2818i	−0.7514 + 1.3220i	−1.9882 + 0.3470i
11.	ΔX_{h2}	−0.7514 + 1.3220i	−1.3861	−0.7514 − 1.3220i	−1.9882 − 0.3470i
12.	ΔX_{t1}	−0.7514 − 1.3220i	−0.3352	−1.9876 + 0.3891i	−0.4896
13.	ΔP_{RH1}	−1.2913	−0.2026 + 0.0778i	−1.9876 − 0.3891i	−0.3352
14.	ΔX_{t2}	−0.2113	−0.2026 − 0.0778i	−0.4585	−0.1996 + 0.0755i
15.	ΔP_{RH2}	−0.0980	−0.1974	−0.2113	−0.1996 − 0.0755i
16.	$\int \text{ACE}_{m1}dt$	−0.0347	−0.0347	−0.0976	−0.1974
17.	$\int \text{ACE}_{m2}dt$	−0.0204	−0.0344	−0.0347	−0.0347
18.	$\Delta P\text{tie}_{\text{dc}}$			−0.0204	−0.0344

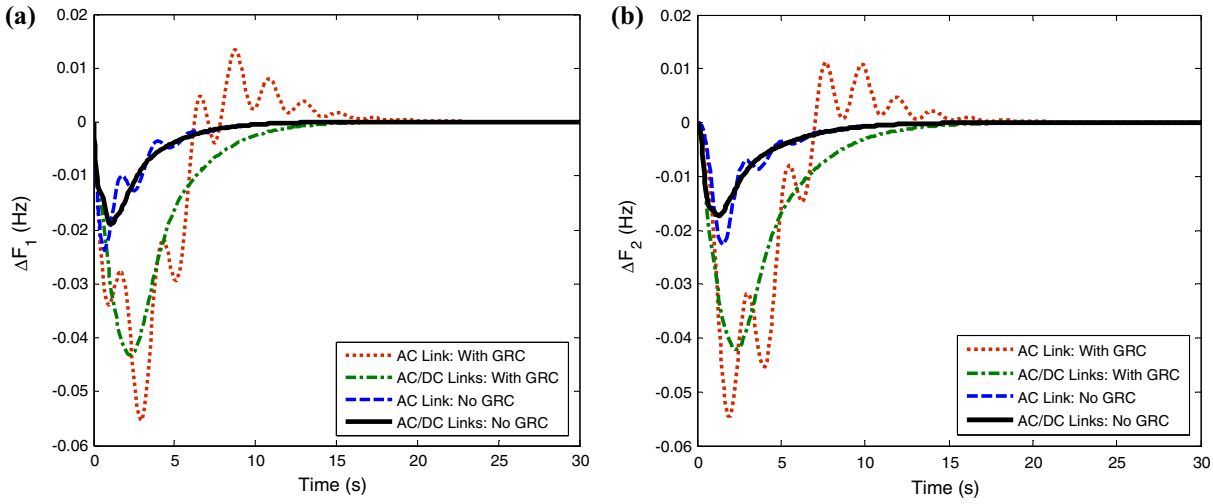

Fig. 4. Dynamic performance of two-area multi-source power system with and without considering GRC (a) ΔF_1 (Hz) vs. time (s) and (b) ΔF_2 (Hz) vs. time (s).

Case-C: Contract violation

It may happen that a DISCO may violate a contract by demanding more power than that specified in the contract. This excess power is not contracted to any GENCOs and it must be supplied by the GENCOs situated in the same control area as the DISCO [6,30,32–35,38,40–46]. Therefore, it must be reflected as a local load of the concerned control area but not as the contract demand. Consider Case-A again with a modification that DISCO_1 demands excess power of 0.1 puMW. So, the total load demand in area-1 $= \Delta P_{L1} + \Delta P_{UC1} + \Delta P_{L2} = 0.1 + 0.1 + 0.1 = 0.3$ puMW. The total load demand in area-2 will be same, as was in Case-A, i.e., 0 puMW. In the steady state, ACE participation factors (apfs) of area-1 decide the distribution of excess load power demand. Therefore, the steady state desired values of generations are $\Delta P_{Gt1} = \Delta P_{Gt1} + (\text{apf}_{t1} \times \Delta P_{UC1}) = 0.1 + (0.5 \times 0.1) = 0.15$ puMW, $\Delta P_{Gh1} = \Delta P_{Gh1} + (\text{apf}_{h1} \times \Delta P_{UC1}) = 0.1 + (0.5 \times 0.1) = 0.15$ puMW and verified in Fig. 3e–h for Case-C. Regarding the system interconnected via AC/DC parallel links for Case-C from Fig. 3, it can be observed that the oscillations in area frequencies and tie-line power deviations have been damped to a considerable extent as compared to those of the system interconnected via AC link only. Therefore, it is observed that the system interconnected via AC/DC parallel links effectively suppress the oscillations with reduced settling times and peak overshoots for the frequency, tie-line power and generation deviations. The frequency deviations vanish in the steady state as shown in Fig. 3a and b. The actual tie-line powers are same as were in Case-A in the steady state as verified in Fig. 3c and d. In the steady state, the generations of GENCO_3 and GENCO_4 are not affected by the excess load demand of DISCO_1, i.e., $\Delta P_{Gt2} = \Delta P_{Gh2} = 0$ puMW as shown in Fig. 3g and h. Therefore, optimal PI regulators work efficiently to fulfill AGC goals in restructured power system.

Multi-area multi-source restructured power system with generation rate constraints

In most of the studies with multi-source generations, the effect of restriction on the rate of change of power generation is not considered [18,47,52,55]. But in practice, generation of a power system incorporating steam/hydro plants can change only at a specified maximum rate. Therefore, there exist constraints on the rate of change of power generation called generation rate constraints (GRCs) [6,12,14,16,32,33,43,53,54]. Appropriate controllers should be used in the presence of GRC to avoid system instability

Table 3
Optimal gain matrices of the optimal PI regulators for multi-source restructured power system while comparing with single-source restructured power system.

Type of area interconnections	Optimal feedback gain matrix (K^*)									J^*
AC link only	[0.5732	−2.1986	0.2294	5.7910	2.3543	0.9526	0.2429	0.7772	0.4333	4.5654e^{+3}
	0.0671	0.5850	0.4199	4.3255	0.0109	4.9256	1.0000	−0.0000;	0.2294	
	2.1986	0.5732	0.9526	0.2429	5.7910	2.3543	0.0671	0.5850	0.7772	
	0.4333	0.0109	4.9256	0.4199	4.3255	−0.0000	1.0000]			
AC/DC links	[0.4219	1.4145	0.3807	4.6428	1.5300	2.1008	1.0671	0.5892	0.7510	3.0556e^{+3}
	0.2551	0.2674	0.3725	8.3368	0.0582	0.9143	1.0000	−0.0000	−0.1575;	
	0.3807	−1.4145	0.4219	2.1008	1.0671	4.6428	1.5300	0.2551	0.2674	
	0.5892	0.7510	0.0582	0.9143	0.3725	8.3368	0.0000	1.0000	0.1575]	

[11,12,56]. Additionally, GRC must be incorporated for practical study of the power systems [35,53,54]. To explore this aspect and further testing the effectiveness of the optimal PI regulators, in the extant study, a GRC of 10%/min (±0.00167 pu/s) is considered for reheat thermal source [12,13,40,53,54] and GRC for hydro power source of 270%/min (+0.045 pu/s) for raising generation and 360%/min (−0.06 pu/s) for lowering generation [13,14,19,34,35,44,53,54,56] has been considered. The power system is simulated for Case-A including the effect of GRC limits as given above. In the presence of GRC the individual load demand of $DISCO_1$ and $DISCO_2$ is taken equal to 0.005 puMW [12]. The dynamic frequency responses of area-1 and area-2 are shown in Fig. 4. From the responses of ΔF_1 (Fig. 4a) and ΔF_2 (Fig. 4b), it is observed that (i) the proposed optimal PI regulators work satisfactorily in the presence of GRC and (ii) the dynamic performance of the power system with GRC deteriorates and show larger overshoots and longer setting times in comparison to the power system without GRC. Only two dynamic responses are shown for justification of the statement.

Comparison of multi-area multi-source system with multi-area single-source power system

In this section a comparison is made between the proposed two-area multi-source hydrothermal (HT) power system and a two-area single-source thermal–thermal (TT) power system interconnected via AC/DC parallel links under deregulated power environment [46]. The system data are given in Appendix B_2. The DPM is taken from [46] as

$$\mathrm{DPM} = \begin{bmatrix} 0.5 & 0.0 & 0.5 & 0.1 \\ 0.0 & 0.5 & 0.0 & 0.4 \\ 0.5 & 0.5 & 0.5 & 0.0 \\ 0.0 & 0.0 & 0.0 & 0.5 \end{bmatrix}.$$

Consider case 4 of [46] in which the power demanded by $DISCO_1$, $DISCO_2$, $DISCO_3$ and $DISCO_4$ is 0%, 0%, 1% and 1% respectively. In addition, $DISCO_3$ demands excess power of 1% puMW. So the total load demand in area-2 = 0.03 puMW. Therefore, the steady state theoretical values of generations are $\Delta P_{Gt1} = 0.06$ puMW, $\Delta P_{Gh1} = 0.04$ puMW, $\Delta P_{Gt2} = 0.01$ puMW and $\Delta P_{Gh2} = 0.01$ puMW and $\Delta P\mathrm{tie}_{\mathrm{scheduled}} = 0.01$ puMW. The optimal feedback gains and optimal performance index values obtained for the optimal PI regulators for the proposed power system, as per state vector given in Eq. (14), are given in Table 3 and for the single-source system are given in Table 2 of [46]. Table 3 reveals that the systems' optimal performance cost index reduces with AC/DC parallel links ($J^* = 3.0556e^{+3}$) in comparison to AC link ($J^* = 4.5654e^{+3}$). It can also be noted that these values are larger than the corresponding values i.e., 48.8422 and 42.3037 respectively, given in Table 2 of [46]. Due to space limitations, the simulation results of four states only are shown in Fig. 5. Fig. 5b–d validates the desired values of tie-line power flows and different generations. It is observed and established that all the results of the proposed power system shown in Fig. 5 get deteriorated and sluggish in the presence of hydro generation as one of the multi-source in each area participating in the AGC as compared to those obtained when thermal–thermal sources in each area are contributing to AGC of the power system.

Extension to nonlinear multi-area conventional power system

The study is further extended to a two-area non reheat thermal power system with governor dead-band (GDB) nonlinearity. The detailed design and analysis of AGC of interconnected power systems considering the effects of GDB, is explained in the pioneer work of Tripathy et al. [57,58]. The AGC study of interconnected power systems with GDB has been widely reported recently in the literature [16,17,19,20,34,53,56]. The power system transfer function block diagram is shown in Fig. 6. The nominal parameters of system under study with governor dead-band nonlinearity are given in Appendix B_3. GDB is the total amount of a sustained speed change within which there is no change in valve position [16,17,19,20,34,53,56–58]. The limiting value of dead-band is specified as 0.06% [57,58]. GDB nonlinearity has to be considered to carry out more practical analysis [16]. The speed-governor dead-band turns the system oscillatory [16,17]. A describing function approach is used to include the GDB nonlinearity. The transfer function of speed governor shown in Fig. 2, is modified using Fourier expansion of the nonlinear function describing GDB nonlinearity and neglecting the fourth and higher order terms [16,17,19,20,57,58], as given below and shown in split form in Fig. 6.

$$G_{gi} = \frac{N_1 + s\frac{N_2}{\omega_o}}{1 + sT_{gi}} \tag{21}$$

The state vector used to develop the state space model of Eqs. (11) and (12) is as follows:

$$\underline{X} = \left[\Delta P\mathrm{tie}_{12}\ \Delta F_1\ \Delta P_{g1}\ \Delta X_{g1}\ \textstyle\int \mathrm{ACE}_1 dt\ \Delta F_2\ \Delta P_{g2}\ \Delta X_{g2}\ \int \mathrm{ACE}_2 dt\right]^T. \tag{22}$$

A program is written and run in workspace of MATLAB to access the dynamic performance of the optimal PI regulators under application of a step load perturbation of 1% at $t = 0$ s in area-1. The state space structure of system matrices is not reported due to brevity, however the optimal feedback gain matrix, using optimal PI regulators, is given in Table 4 and the system dynamic responses are shown in Fig. 7. To make a comparison, the simulation results of PI controller optimized by best claimed craziness based particle swarm optimization (CRAZYPSO) and hybrid bacteria foraging optimization algorithm-particle swarm optimization (hBFOA-PSO) algorithms are also shown in Fig. 7. Critical analysis of the dynamic responses of ΔF_1, ΔF_2, $\Delta P\mathrm{tie}_{12}$ and ΔP_{g2} clearly indicates that dynamic performance of the system is more or less the same

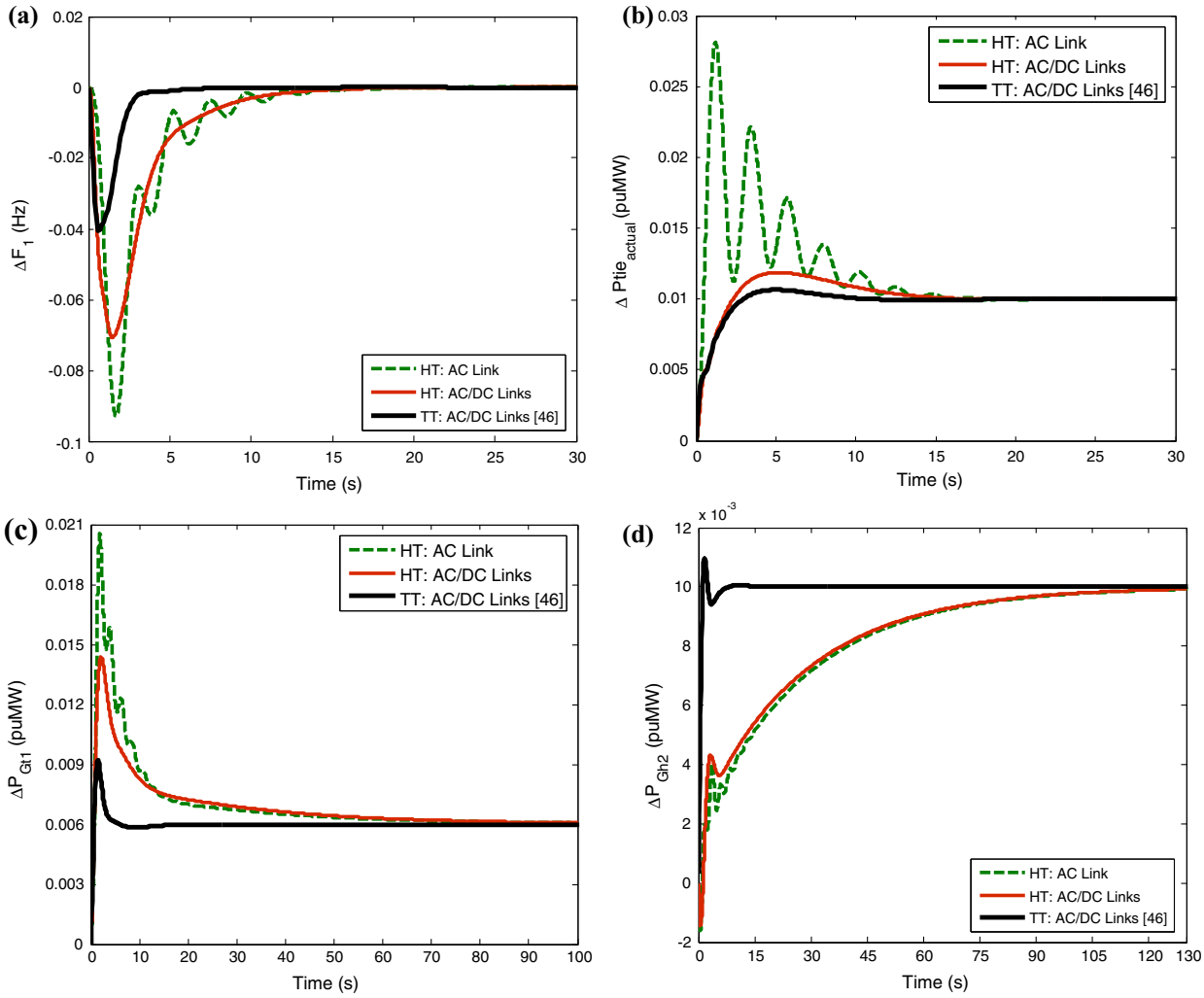

Fig. 5. Comparison of dynamic performance of two-area multi-source and single-source restructured power systems (a) ΔF_1 (Hz) vs. time (s), (b) $\Delta P\text{tie}_{\text{actual}}$ (puMW) vs. time (s), (c) ΔP_{Gt1} (puMW) vs. time (s) and (d) ΔP_{Gh2} (puMW) vs. time (s).

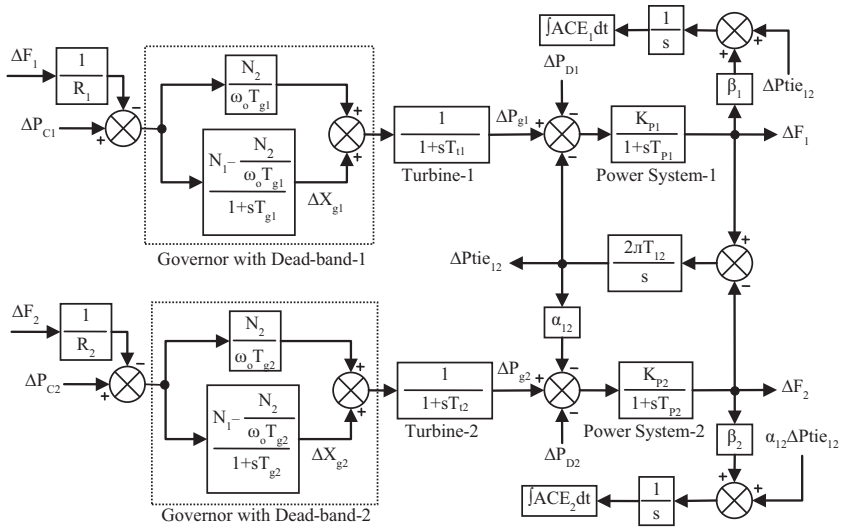

Fig. 6. Transfer function model of two-area thermal power system with governor dead-band nonlinearity.

Table 4
Optimal gain matrix of the optimal PI regulators for power system with governor dead-band nonlinearity.

Type of area interconnections	Optimal feedback gain matrix [K*]								
AC link	[−1.8991	0.8098	1.6921	1.2522	1.0000	0.0976	0.0135	−0.0043	0.0000
	1.8991	0.0976	0.0135	−0.0043	0.0000	0.8098	1.6921	1.2522	1.0000]

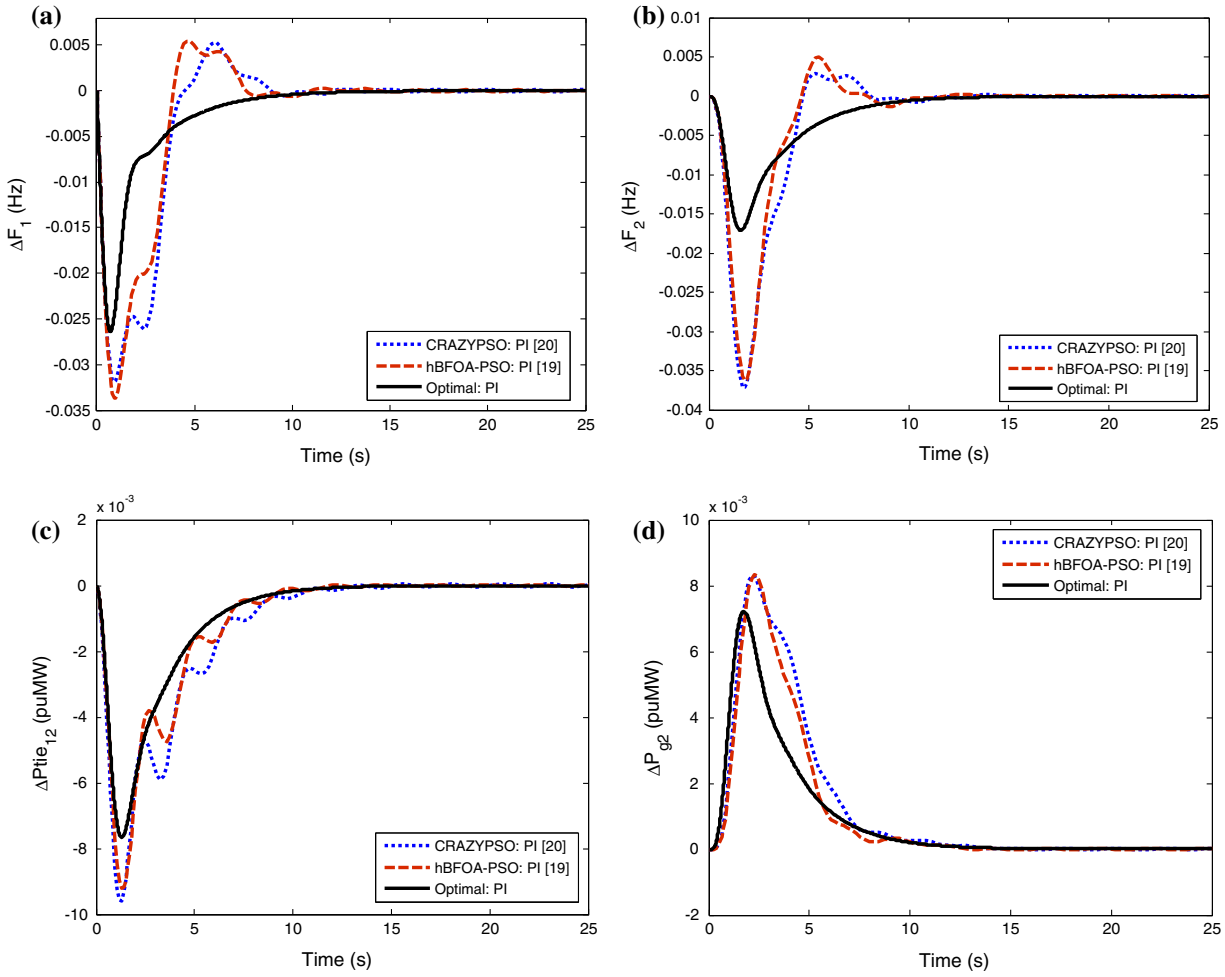

Fig. 7. Dynamic performance of conventional two-area power system with governor dead-band nonlinearity for 1% step load demand increase in area-1 at $t = 0$ s (a) ΔF_1 (Hz) vs. time (s), (b) ΔF_2 (Hz) vs. time (s), (c) $\Delta P\text{tie}_{12}$ (puMW) vs. time (s) and (d) ΔP_{g2} (puMW) vs. time (s).

with CRAZYPSO and hBFOA-PSO based PI controllers, while the dynamic performance of the power system under study is significantly improved with optimal PI regulators.

Conclusions

In this paper, the optimal AGC of a two-area multi-source power system under deregulated environment has been investigated. The equal two-area power system equipped with hydro and single reheat thermal units in each area is interconnected via AC/DC parallel links. The optimal proportional integral (PI) regulators are designed using full state feedback vector control strategy to incorporate all market contracts possible between GENCOs and DISCOs in a restructured power scenario. A critical analysis has been performed for proposed AGC scheme under poolco, bilateral and a combination of these two transactions. The MATLAB simulation results with optimal PI regulators for different generations and tie-line power exchanges of GENCOs are validated with the desired values. It has been observed that with both AC link and AC/DC parallel links the power system is marginally stable in open-loop and stable with good stability margins in closed-loop modes. In addition, dynamic stability margins appreciably improve further with AC/DC parallel links. It has also been observed that the system performance cost index has been reduced and overall dynamic performance of the power system has improved remarkably, as characterized by reduced settling times, peak overshoots/undershoots and oscillations with AC/DC parallel links in comparison with AC link. Further, published results of a two-area single-source restructured power system with two thermal units in each area with optimal PI regulators are compared with the results of the proposed multi-source restructured power system with hydro as one of the two units in each area and it is established that the results of the latter power system are sluggish/inferior. Additionally, it is observed that the performance of the proposed power system interconnected via AC link degrades with GRC, while with GRC, the dynamic performance is better enough with good stability margins in case of AC/DC parallel links. Finally, the superiority of

the optimal PI regulators is proved by comparing the results with recently published modern heuristic optimization approaches such as craziness based particle swarm optimization (CRAZYPSO) and hybrid bacteria foraging optimization algorithm-particle swarm optimization (hBFOA-PSO) algorithms based PI controllers for the same interconnected power system.

State space model matrices

For the two-area multi-source hydrothermal restructured power system model interconnected via AC/DC links, the system matrix A is of the order of 18 × 18 and its non-zero (a_{ij}) elements are given as:

$$a_{1,1}=-\frac{1}{T_{P1}},\quad a_{1,2}=-\frac{K_{P1}}{T_{P1}},\quad a_{1,4}=\frac{K_{P1}}{T_{P1}},\quad a_{1,5}=\frac{K_{P1}}{T_{P1}},$$
$$a_{1,8}=\frac{K_{r1}K_{P1}}{T_{P1}},\quad a_{1,9}=-\frac{2K_{P1}}{T_{P1}},\quad a_{1,13}=-\frac{2T_{R1}K_{P1}}{T_{GH1}T_{P1}},$$

$$a_{1,18}=-\frac{K_{P1}}{T_{P1}},\quad a_{2,1}=2\pi T_{12},\quad a_{2,3}=-2\pi T_{12},\quad a_{3,2}=-\frac{\alpha_{12}K_{P2}}{T_{P2}},$$
$$a_{3,3}=-\frac{1}{T_{P2}},\quad a_{3,6}=\frac{K_{P2}}{T_{P2}},\quad a_{3,7}=\frac{K_{P2}}{T_{P2}},$$

$$a_{3,10}=\frac{K_{r2}K_{P2}}{T_{P2}},\quad a_{3,11}=-\frac{2K_{P2}}{T_{P2}},\quad a_{3,15}=-\frac{2T_{R2}K_{P2}}{T_{GH2}T_{P2}},$$
$$a_{3,18}=-\frac{\alpha_{12}K_{P2}}{T_{P2}},\quad a_{4,4}=-\frac{1}{T_{r1}},a_{4,8}=\frac{1-K_{r1}}{T_{r1}},$$

$$a_{5,5}=-\frac{2}{T_{W1}},\quad a_{5,9}=\frac{6}{T_{W1}},\quad a_{5,13}=\frac{6T_{R1}}{T_{GH1}T_{W1}},\quad a_{6,6}$$
$$=-\frac{1}{T_{r2}},\quad a_{6,10}=\frac{1-K_{r2}}{T_{r2}},\quad a_{7,7}=-\frac{2}{T_{W2}},\quad a_{7,11}=\frac{6}{T_{W2}},$$

$$a_{7,15}=\frac{6T_{R2}}{T_{GH2}T_{W2}},\quad a_{8,8}=-\frac{1}{T_{t1}},\quad a_{8,12}=\frac{1}{T_{t1}},\quad a_{9,9}=-\frac{1}{T_{GH1}},$$
$$a_{9,13}=\frac{T_{GH1}-T_{R1}}{T_{GH1}^2},\quad a_{10,10}=-\frac{1}{T_{t2}},\quad a_{10,14}=\frac{1}{T_{t2}},$$

$$a_{11,11}=-\frac{1}{T_{GH2}},\quad a_{11,15}=\frac{T_{GH2}-T_{R2}}{T_{GH2}^2},\quad a_{12,1}=-\frac{1}{R_{t1}T_{g1}},$$
$$a_{12,12}=-\frac{1}{T_{g1}},\quad a_{13,1}=-\frac{1}{R_{h1}T_{RH1}},\quad a_{13,13}=-\frac{1}{T_{RH1}},$$

$$a_{14,3}=-\frac{1}{R_{t2}T_{g2}},\quad a_{14,14}=-\frac{1}{T_{g2}},\quad a_{15,3}=-\frac{1}{R_{h2}T_{RH2}},$$
$$a_{15,15}=-\frac{1}{T_{RH2}},\quad a_{16,1}=\beta_1,\quad a_{16,2}=1,\quad a_{16,18}=1,$$

$$a_{17,2}=\alpha_{12},\quad a_{17,3}=\beta_2,\quad a_{17,18}=\alpha_{12},\quad a_{18,1}=\frac{K_{dc}}{T_{dc}},$$
$$a_{18,3}=-\frac{K_{dc}}{T_{dc}},\quad a_{18,18}=-\frac{1}{T_{dc}}.$$

The control matrix B is of the order of 18 × 2 and its non-zero elements (b_{ij}) are given as:

$$b_{12,1}=\frac{\mathrm{apf}_{t1}}{T_{g1}},\quad b_{13,1}=\frac{\mathrm{apf}_{h1}}{T_{RH1}},\quad b_{14,2}=\frac{\mathrm{apf}_{t2}}{T_{g2}},\quad b_{15,2}=\frac{\mathrm{apf}_{h2}}{T_{TRH2}}.$$

The disturbance matrix Γ is of the order of 18 × 6 and its non-zero elements (d_{ij}) are given as:

$$d_{1,1}=-\frac{K_{P1}}{T_{P1}},\quad d_{1,2}=-\frac{K_{P1}}{T_{P1}},\quad d_{1,5}=-\frac{K_{P1}}{T_{P1}},\quad d_{3,3}=-\frac{K_{P2}}{T_{P2}},$$
$$d_{3,4}=-\frac{K_{P2}}{T_{P2}},\quad d_{3,6}=-\frac{K_{P2}}{T_{P2}},\quad d_{12,1}=\frac{\mathrm{cpf}_{11}}{T_{g1}},$$

$$d_{12,2}=\frac{\mathrm{cpf}_{12}}{T_{g1}},\quad d_{12,3}=\frac{\mathrm{cpf}_{13}}{T_{g1}},\quad d_{12,4}=\frac{\mathrm{cpf}_{14}}{T_{g1}},\quad d_{13,1}=\frac{\mathrm{cpf}_{21}}{T_{RH1}},$$
$$d_{13,2}=\frac{\mathrm{cpf}_{22}}{T_{RH1}},\quad d_{13,3}=\frac{\mathrm{cpf}_{23}}{T_{RH1}},\quad d_{13,4}=\frac{\mathrm{cpf}_{24}}{T_{RH1}},$$

$$d_{14,1}=\frac{\mathrm{cpf}_{31}}{T_{g2}},\quad d_{14,2}=\frac{\mathrm{cpf}_{32}}{T_{g2}},\quad d_{14,3}=\frac{\mathrm{cpf}_{33}}{T_{g2}},\quad d_{14,4}=\frac{\mathrm{cpf}_{34}}{T_{g2}},$$
$$d_{15,1}=\frac{\mathrm{cpf}_{41}}{T_{RH2}},\quad d_{15,2}=\frac{\mathrm{cpf}_{42}}{T_{RH2}},\quad d_{15,3}=\frac{\mathrm{cpf}_{43}}{T_{RH2}},$$

$$d_{15,4}=\frac{\mathrm{cpf}_{44}}{T_{RH2}},\quad d_{16,1}=\mathrm{cpf}_{31}+\mathrm{cpf}_{41},\quad d_{16,2}=\mathrm{cpf}_{32}+\mathrm{cpf}_{42},$$
$$d_{16,3}=-(\mathrm{cpf}_{13}+\mathrm{cpf}_{23}),\quad d_{16,4}=-(\mathrm{cpf}_{14}+\mathrm{cpf}_{24}),$$

$$d_{17,1}=\alpha_{12}(\mathrm{cpf}_{31}+\mathrm{cpf}_{41}),\quad d_{17,2}=\alpha_{12}(\mathrm{cpf}_{32}+\mathrm{cpf}_{42}),$$
$$d_{17,3}=-\alpha_{12}(\mathrm{cpf}_{13}+\mathrm{cpf}_{23}),\quad d_{17,4}=-\alpha_{12}(\mathrm{cpf}_{14}+\mathrm{cpf}_{24}).$$

The output matrix C, the state cost weighting matrix Q and the control cost weighting matrix R are taken identity matrices of 18 × 18, 18 × 18, and 2 × 2 dimensions respectively.

System data

B_1 – Nominal parameters for multi-area multi-source power system [4,7,9,13]

$P_{r1}=P_{r2}=2000$ MW, $\mathrm{Ptie}_{\max}=200$ MW, Base power = 2000 MVA, $\Delta P_{Di}^0=1000$ MW, $F^0=60$ Hz, $\alpha_{12}=(-P_{r1}/P_{r2})=-1$, $D_i=(\partial\Delta P_{Di}^0/\partial f P_{ri})=8.33\times10^{-3}$ puMW/Hz, $H_i=5$ MWs/MVA, $T_{gi}=0.08$ s, $T_{ti}=0.3$ s, $K_{ri}=0.5$, $T_{ri}=10$ s, $R_{ti}=R_{hi}=2.4$ Hz/puMW, $K_{Pi}=(1/D_i)=120$ Hz/puMW, $T_{Pi}=(2H_i/F^0D_i)=20$ s, $B_i=(\beta_i=D_i+1/R_{ti})=0.425$ puMW/Hz, $\delta=0.31$ pu, $\sigma=(R_{hi}=F^0\sigma)=0.04$ pu, $T_{Ri}=5$ s, $T_{Gi}=0.2$ s, $T_{RHi}=([T_G+T_R(\sigma+\delta)]/\sigma)=48.7$ s, $T_{GHi}=(T_RT_G/[T_G+T_R(\sigma+\delta)])=0.513$ s, $T_{Wi}=1$ s, $\delta_{12}=(\delta_1-\delta_2)=30^\circ$, $T_{12}=0.1\cos\delta_{12}$ puMW/rad, $2\pi T_{12}=0.545$ puMW/Hz, $K_{dc}=1$, $T_{dc}=(L_{dc}/R_{dc})=0.2$ s.

B_2 – Nominal parameters for multi-area multi/single-source power systems [4,7,9,13,46]

$P_{r1}=P_{r2}=2000\,MW$, $\mathrm{Ptie}_{\max}=200$ MW, Base power = 2000 MVA, $\Delta P_{Di}^0=1000$ MW, $F^0=60$ Hz, $\alpha_{12}=-1$, $D_i=8.33\times10^{-3}$ puMW/Hz, $H_i=5$ MWs/MVA, $T_{gi}=0.08$ s, $T_{ti}=0.3$ s, $K_{ri}=0.3$, $T_{ri}=5$ s, $R_i=R_{ti}=R_{hi}=2.4$ Hz/puMW, $K_{Pi}=120$ Hz/puMW, $T_{Pi}=20$ s, $\beta_i=0.4249$ puMW/Hz, $T_{12}=0.0867$ puMW/rad, $T_{RHi}=48.7$ s, $T_{GHi}=0.513$ s, $T_{Ri}=5$ s, $T_{Wi}=1$ s, $T_{Gi}=0.2$ s, $\sigma=0.04$, $\delta=0.31$, $\delta_{12}=30^\circ$, $K_{dc}=1$, $T_{dc}=0.2$ s.

B_3 – Nominal parameters for power system with governor dead-band nonlinearity [16,17,19,20,57,58]

$P_{r1}=P_{r2}=2000$ MW, $\mathrm{Ptie}_{\max}=200$ MW, Base power = 2000 MVA, $\Delta P_{Di}^0=1000$ MW, $F^0=60$ Hz, $\alpha_{12}=-1$, $D_i=8.33\times10^{-3}$ puMW/Hz, $H_i=5$ MWs/MVA, $\beta_i=0.425$ puMW/Hz, $R_i=2.4$ Hz/puMW, $T_{gi}=0.2$ s, $T_{ti}=0.3$ s, $\delta_{12}=45^\circ$, $T_{12}=0.0707$ puMW/rad, $\omega_o=\pi$, $N_1=0.8$, $N_2=-0.2$.

References

[1] Ibraheem, Kumar P, Kothari DP. Recent philosophies of automatic generation control strategies in power systems. IEEE Trans Power Syst 2005;20(1):346–57.
[2] Shayeghi H, Shayanfar HA, Jalili A. Load frequency control strategies: a state-of-the-art survey for the researcher. Energy Convers Manage 2009;50(2):344–53.
[3] Pandey SK, Mohanty SR, Kishor N. A literature survey on load–frequency control for conventional and distribution generation power systems. Renewab Sustainab Energy Rev 2013;25:318–34.
[4] Elgerd OI. Electric energy systems theory: an introduction. 2nd ed. New Delhi: Tata McGraw-Hill; 2014 [42th reprint].
[5] Gupta SK. Power system engineering. 2nd ed. New Delhi: Umesh Publications; 2013.
[6] Das D. Electrical power systems. 1st ed. Delhi: New Age International Publications; 2010.
[7] Elgerd OI, Fosha CE. Optimum megawatt-frequency control of multiarea electric energy systems. IEEE Trans Power App Syst 1970;PAS-89(4):556–63.
[8] Fosha CE, Elgerd OI. The megawatt-frequency control problem: a new approach via optimal control theory. IEEE Trans Power App Syst 1970;PAS-89(4):563–77.
[9] Kothari ML, Nanda J. Application of optimal control strategy to automatic generation control of a hydrothermal system. IEE Proc Control Theory Appl 1988;135(D4):268–74.
[10] Ibraheem, Niazi KR, Sharma G. Study on dynamic participation of wind turbines in automatic generation control of power systems. Elect Power Compon Syst 2015;43(1):44–55.
[11] Chan W-C, Hsu Y-Y. Automatic generation control of interconnected power systems using variable-structure controllers. IEE Proc Gener Transm Distrib 1981;128(C5):269–79.
[12] Chan W-C, Hsu Y-Y. Optimal control of electric power generation using variable structure controllers. Elect Power Syst Res 1983;6(4):269–78.
[13] Nanda J, Kothari ML, Satsangi PS. Automatic generation control of an interconnected hydrothermal system in continuous and discrete modes considering generation rate constraints. IEE Proc Control Theory Appl 1983;130(D1):17–27.
[14] Mohanty B. TLBO optimized sliding mode controller for multi-area multi-source nonlinear interconnected AGC system. Int J Electr Power Energy Syst 2015;73:872–81.
[15] Francis R, Chidambaram IA. Optimized PI+ load–frequency controller using BWNN approach for an interconnected reheat power system with RFB and hydrogen electrolyser units. Int J Electr Power Energy Syst 2015;67:381–92.
[16] Sahu RK, Panda S, Rout UK. DE optimized parallel 2-DOF PID controller for load frequency control of power system with governor dead-band nonlinearity. Int J Electr Power Energy Syst 2013;49:19–33.
[17] Panda S, Yegireddy NK. Automatic generation control of multi-area power system using multi-objective non-dominated sorting genetic algorithm-II. Int J Electr Power Energy Syst 2013;53:54–63.
[18] Nasiruddin I, Bhatti TS, Hakimuddin N. Automatic generation control in an interconnected power system incorporating diverse source power plants using bacteria foraging optimization technique. Elect Power Compon Syst 2015;43(2):189–99.
[19] Panda S, Mohanty B, Hota PK. Hybrid BFOA-PSO algorithm for automatic generation control of linear and nonlinear interconnected power systems. Appl Soft Comput 2013;13(12):4718–30.
[20] Gozde H, Taplamacioglu MC. Automatic generation control application with craziness based particle swarm optimization in a thermal power system. Int J Electr Power Energy Syst 2011;33(1):8–16.
[21] Sahu BK, Pati S, Panda S. Teaching-learning based optimization algorithm based fuzzy-PID controller for automatic generation control of multi-area power system. Appl Soft Comput 2015;27:240–9.
[22] Yousef H. Adaptive fuzzy logic load frequency control of multi-area power system. Int J Electr Power Energy Syst 2015;68:384–95.
[23] Khooban MH, Niknam T. A new intelligent online fuzzy tuning approach for multi-area load frequency control: self adaptive modified bat algorithm. Int J Electr Power Energy Syst 2015;71:254–61.
[24] Yesil E. Interval type-2 fuzzy PID load frequency controller using big bang-big crunch optimization. Appl Soft Comput 2014;15:100–12.
[25] Tarkeshwar, Mukherjee V. A novel quasi-oppositional harmony search algorithm and fuzzy logic controller for frequency stabilization of an isolated hybrid power system. Int J Electr Power Energy Syst 2015;66:247–61.
[26] Dash P, Saikia LC, Sinha N. Comparison of performances of several cuckoo search algorithm based 2DOF controllers in AGC of multi-area thermal system. Int J Electr Power Energy Syst 2014;55:429–36.
[27] Chaine S, Tripathy M. Design of an optimal SMES for automatic generation control of two-area thermal power system using cuckoo search algorithm. J Electr Syst Inform Tech 2015;2(1):1–13.
[28] Debbarma S, Saikia LC, Sinha N. Automatic generation control using two degree of freedom fractional order PID controller. Int J Electr Power Energy Syst 2014;58:120–9.
[29] Kumar J, Ng K-H, Sheble G. AGC simulator for price based operation: part II-case study results. IEEE Trans Power Syst 1997;12(2):533–8.
[30] Donde V, Pai MA, Hiskens IA. Simulation and optimization in an AGC system after deregulation. IEEE Trans Power Syst 2001;16(3):481–9.
[31] Tyagi B, Srivastava SC. A decentralized automatic generation control scheme for competitive electricity markets. IEEE Trans Power Syst 2006;21(1):312–20.
[32] Shayeghi H. A robust decentralized power system load frequency control. J Electr Eng 2008;59(6):281–93.
[33] Shayeghi H, Shayanfar HA, Malik OP. Robust decentralized neural networks based LFC in a deregulated power system. Elect Power Syst Res 2007;77(3–4):241–51.
[34] Sekhar GTC, Sahu RK, Baliarsingh AK, Panda S. Load frequency control of power system under deregulated environment using optimal firefly algorithm. Int J Electr Power Energy Syst 2016;74:195–211.
[35] Shree SB, Kamaraj N. Hybrid neuro fuzzy approach for automatic generation control in restructured power system. Int J Electr Power Energy Syst 2016;74:274–85.
[36] Christie RD, Bose A. Load frequency control issues in power system operations after deregulation. IEEE Trans Power Syst 1996;11(3):1191–200.
[37] Demiroren A, Zeynelgil HL. GA application to optimization of AGC in three-area power system after deregulation. Int J Electr Power Energy Syst 2007;29(3):230–40.
[38] Deepak M, Abraham RJ. Load following in a deregulated power system with thyristor controlled series compensator. Int J Electr Power Energy Syst 2015;65:136–45.
[39] De Tuglie E, Torelli F. Load following control schemes for deregulated energy markets. IEEE Trans Power Syst 2006;21(4):1691–8.
[40] Abraham RJ, Das D, Patra A. Load following in a bilateral market with local controllers. Int J Electr Power Energy Syst 2011;33(10):1648–57.
[41] Chidambaram IA, Paramasivam B. Optimized load–frequency simulation in restructured power system with redox flow batteries and interline power flow controller. Int J Electr Power Energy Syst 2013;50:9–24.
[42] Debbarma S, Saikia LC, Sinha N. AGC of a multi-area thermal system under deregulated environment using a non-integer controller. Elect Power Syst Res 2013;95:175–83.
[43] Tan W, Hao Y, Li D. Load frequency control in deregulated environments via active disturbance rejection. Int J Electr Power Energy Syst 2015;66:166–77.
[44] Rao CS, Nagaraju SS, Raju PS. Automatic generation control of TCPS based hydrothermal system under open market scenario: a fuzzy logic approach. Int J Electr Power Energy Syst 2009;31(7–8):315–22.
[45] Sinha S, Patel R, Prasad R. Application of AI supported optimal controller for automatic generation control of a restructured power system with parallel AC–DC tie lines. Euro Trans Electr Power 2012;22(5):645–61.
[46] Ibraheem, Kumar P, Hasan N, Singh Y. Optimal automatic generation control of interconnected power system with asynchronous tie-lines under deregulated environment. Elect Power Comp Syst 2012;40(10):1208–28.
[47] Ibraheem, Nizamuddin, Bhatti TS. AGC of two area power system interconnected by AC/DC links with diverse sources in each area. Int J Electr Power Energy Syst 2014;55:297–304.
[48] Ibraheem, Kumar P. Current status of the Indian power system and dynamic performance enhancement of hydro power systems with asynchronous tie lines. Elect Power Comp Syst 2003;31(7):605–26.
[49] Hasan N, Ibraheem, Kumar P. Optimal automatic generation control of interconnected power system considering new structures of matrix Q. Elect Power Comp Syst 2013;41(2):136–56.
[50] Sharma G, Nasiruddin I, Niazi KR. Optimal automatic generation control of asynchronous power systems using output feedback control strategy with dynamic participation of wind turbines. Elect Power Comp Syst 2015;43(4):384–98.
[51] Hasan N, Ibraheem, Kumar P, Nizamuddin. Sub-optimal automatic generation control of interconnected power system using constrained feedback control strategy. Int J Electr Power Energy Syst 2012;43(1):295–303.
[52] Mohanty B, Panda S, Hota PK. Controller parameters tuning of differential evolution algorithm and its application to load frequency control of multi-source power system. Int J Electr Power Energy Syst 2014;54:77–85.
[53] Zare K, Hagh MT, Morsali J. Effective oscillation damping of an interconnected multi-source power system with automatic generation control and TCSC. Int J Electr Power Energy Syst 2015;65:220–30.
[54] Parmar KPS, Majhi S, Kothari DP. Load frequency control of a realistic power system with multi-source power generation. Int J Electr Power Energy Syst 2012;42(1):426–33.
[55] Parmar KPS, Majhi S, Kothari DP. LFC of an interconnected power system with multi-source power generation in deregulated power environment. Int J Electr Power Energy Syst 2014;57:277–86.
[56] Sahu RK, Panda S, Padhan S. A hybrid firefly algorithm and pattern search technique for automatic generation control of multi area power systems. Int J Electr Power Energy Syst 2015;64:9–23.
[57] Tripathy SC, Bhatti TS, Jha CS, Malik OP, Hope GS. Sampled data automatic generation control analysis with reheat steam turbines and governor dead-band effects. IEEE Trans Power App Syst 1984;PAS-103(5):1045–51.
[58] Tripathy SC, Hope GS, Malik OP. Optimisation of load–frequency control parameters for power systems with reheat steam turbines and governor deadband nonlinearity. IEE Proc Gener Transm Distrib 1982;129(C1):10–6.

Wireless Netw
DOI 10.1007/s11276-015-1054-5

Betweenness centrality based connectivity aware routing algorithm for prolonging network lifetime in wireless sensor networks

Aarti Jain[1]

Abstract Network lifetime is the key design parameter for wireless sensor network protocols. In recent years, based on energy efficient routing techniques numerous methods have been proposed for enhancing network lifetime. These methods have mainly considered residual energy, number of hops and communication cost as route selection metrics. This paper introduces a method for further improvement in the network lifetime by considering network connectivity along with energy efficiency for the selection of data transmission routes. The network lifetime is enhanced by preserving highly connected nodes at initial rounds of data communication to ensure network connectivity during later rounds. Bassed on the above mentioned concept, a connectivity aware routing algorithm: CARA has been proposed. In the proposed algorithm, connectivity factor of a node is calculated on the basis of Betweenness centrality of a node and energy efficient routes are found by using fuzzy logic and ant colony optimization. The simulation results show that the proposed algorithm CARA performs better than other related state-of-the-art energy efficient routing algorithms viz. FML, EEABR and FACOR in terms of network lifetime, connectivity, energy dissipation, load balancing and packet delivery ratio.

Keywords Energy efficiency · Connectivity measure · Betweenness centrality · Ant colony optimization · Fuzzy logic · Wireless sensor networks

✉ Aarti Jain
aartijain@aiactr.ac.in

[1] Department of ECE, Ambedkar Institute of Advanced Communication Technologies and Research, Delhi, India

1 Introduction

A wireless sensor network (WSN) is a collection of distributed sensor nodes with limited energy, processing and communicating capabilities. These sensor nodes are densely and randomly deployed in a particular region with a basic aim to efficiently sense, collect and communicate the information [1–4]. Since sensor nodes are small in size and have low distance communication capabilities, the information is communicated by multi-hop communication mode. Moreover, sensor nodes in WSN are battery powered and in most of the cases, it is neither possible to recharge them nor to change their batteries. All these characteristics bring in very special requirements that are required to be met while designing routing protocol for WSNs [5, 6].

In WSNs, enhancement in network lifetime i.e. the time period during which there are nodes which are able to collect and transmit the information along with Quality of service (*QoS*) parameters viz. minimum latency and maximum capacity is one of the key performance metric. The design of network layer protocol i.e. routing protocols plays an important role in improving network lifetime of the WSN and addressing various *QoS* parameters in WSNs. In literature, various routing protocols have been proposed for ensuring *QoS* and energy efficiency leading to improvement in the network's lifetime. These protocols are mainly[1] unicast routing protocols and use residual energy, number of hops (distance), latency and communication cost as path selection metrics [7, 8]. Another way of increasing network lifetime is by adopting a sleep-awake scheduling methodology in which sensor nodes can switch between

[1] In unicast routing, each forwarding node select one of its neighbouring nodes as its next-hop relaying node.

Published online: 01 September 2015

active and sleep state. In these methodologies, a sensor node can anytime switch-on its transceiver to transmit its own data packet, but can receive an information packet only when it is in active state [9, 10]. When linked with network layer protocols, the sleep-awake method requires global and local synchronisation between active time of neighbouring nodes, otherwise it leads to increase in latency and decrease in maximum channel utilization [11].[2] The objective of this paper is to find efficient route so as to improve the network lifetime.

In wireless sensor networks due to random deployment, there are certain nodes which are connected to comparatively higher number of nodes and are members of large number of network paths. Early energy depletion of these nodes may lead to network partitioning and reduce overall effective network lifetime. In this paper, it has been proposed that the network lifetime of the WSN can be further enhanced by conserving the energy of these highly connected nodes. Among the various energy efficient paths, the first priority is given to paths which have lesser number of these highly connected nodes. This in turn ensures that highly connected nodes are preserved leading to deferment of the partition of network.

The above mentioned concept has been implemented using graph connectivity measures for designing the routing algorithm. Graph connectivity measures have been extensively studied in field of social network analysis (SNA) [12] and are popular choice among researchers to find the importance of node in a network. In SNA, to locate the individuals which are most central or are most connected is very important. Also, the relation of individuals with each other is one of the fundamental problems in the analysis. In order to address these issues in social networks, certain measures like centrality and connectivity have been proposed, which allow characterization of the structures and properties of large networks and make predictions about their behavior [13, 14]. In the proposed work, Betweenness centrality measure has been used to find the connectivity share of a node in the network. Betweenness centrality of a vertex (node) is defined as the number of the shortest paths from all vertices to all other vertices that pass through it in a graph or network [15]. Further, depending upon the value of Betweenness centrality, each node is classified into θ (*low*), Ω (*moderate*) and η (*high*) connectivity domains. At the time of route selection, energy efficient routes of nodes falling under low connectivity domain are preferred, which in turn ensures that the connectivity of the network is prolonged with the presence of highly connected nodes in later rounds.

[2] In future, the proposed routing method can be extended in the field of sleep awake scheduling with cross layer interaction of network layer and MAC layer.

In WSNs, energy efficiency and *QoS* of a route is ensured by considering parameters such as remaining energy of node, communication distance between nodes and total path length. The complexity involved in implementation and consideration of these multiple objectives has motivated researchers to use the heuristic techniques viz. Swarm intelligence, evolutionary algorithms, reinforcement learning for finding efficient routing paths in WSNs. However, due to complex interactions and interdependency among various parameters, the basis of use of heuristic based methods is uncertain. However, this uncertainty can be effectively handled by modelling the different objectives by using fuzzy set theory [16].

In this paper, to find energy efficient routes, the network has been modeled as a Fuzzy vertex and edge Graph [17]. For modeling of wireless sensor network as fuzzy graph, nodes of the network are modeled as member of a fuzzy set corresponding to their residual energy and communication link between two nodes is modeled as member of a another fuzzy set corresponding to optimal link length. By using fuzzy set corresponding to vertices and edges, a combined fuzzy cost metric that captures the interplay of both sets is computed and has been assigned as final edge weight of fuzzy graph. The energy efficient and short paths are identified by applying ant colony optimization (ACO) [18–20]. In literature various fuzzy based [32–35], ACO based [43–48] and joint fuzzy and ACO based [54–57] routing methods have been proposed to find the energy efficient routes. In these methods, all nodes are treated equally and the route formation is mainly dependant on the residual energy, transmission cost function and delay. Hence, some nodes which are very vital for maintaining connectivity of the network are also treated as normal nodes and failure of these nodes will lead to network partition. This may lead to a situation when no communication is feasible even though there are certain nodes with sufficient energy. In the proposed method, this has been addressed by preserving the highly connected nodes during the initial rounds. Further, the energy efficiency is ensured by duly considering the residual energy, transmission cost and delay of the member nodes by using fuzzy logic in combination with ACO. The salient feature of the proposed routing method CARA is that it provides all the benefits offered by energy efficient routing protocols while enhancing the network lifetime by avoiding early partition of the network.

The proposed method has been simulated under various network scenarios. The simulation results show that CARA performs better in terms of energy efficiency, load balancing and effective network lifetime as compared to other state-of-the-art energy efficient routing algorithms viz. FML [32], EEABR [43] and FACOR [57] routing algorithm. Where, FML represents fuzzy logic based energy efficient routing algorithms. EEABR represents ACO

based energy efficient routing algorithm and FACOR represents joint fuzzy and ACO based family of energy efficient routing algorithms.

This paper has been organized as follows. The paper begins with the related work in Sect. 2. Section 3 covers the preliminaries through which basic definitions are presented. Section 4 presents the proposed method in detail. The effectiveness of the proposed method is evaluated through simulations in Sect. 5. The paper concludes with brief discussion of the method along with future considerations in Sect. 6.

2 Related work

The selection of routing protocol is important for efficient transmission of information packet to its destination. In WSNs, the routing protocol is required to be energy efficient and should ensure optimum and maximal use of available resources. During recent years, several energy efficient routing protocols have been proposed with an objective to enhance network lifetime of WSNs. Chang and Tassiulas [21] have proposed a maximum lifetime routing protocol for wireless sensor networks. In this method, the routing problem is formulated as Integer Linear Program (ILP) to find the shortest path. The main idea behind this algorithm is to find a path with nodes having maximum residual energy. In [22] Kemal Akkaya and Mohamed Younis have proposed a routing protocol which calculates the cost function for each link by using nodes residual energy, cost of transmission, error rate. The protocol finds multiple candidate routes by using K least cost path algorithm. The route which satisfies the constraints and provides maximum throughput is selected for communication. Akkaya et al. [23] proposed an energy efficient routing protocol which selects a least-cost and delay-constrained path for real-time packets in wireless sensor networks. However, in this protocol it is assumed that every node knows the position of all other nodes and also the cost of transmission among nodes in WSNs, which may not be possible in real time applications. EARQ [24] is one of the energy efficient routing protocols which while selecting between different available paths considers energy cost, delay and reliability of a path to the sink node. The method delivers reliable delivery of information packet. In EARQ, a node is required to estimate the transmission cost, delay and reliability of a path, based on collected information from neighboring nodes. Finally, to achieve real-time delivery, only paths that may deliver a packet within the pre-specified time are considered. Moreover, in order to achieve reliability redundant data packets are sent via an alternate path. The said method has very high control overhead and hence is not suitable for energy constrained WSNs. In EAODV method [25], the selection of path is based upon the transmission energy required for communication between two nodes. In this method the cost of transmission is calculated by dimidiate search arithmetic. Multiple routes between source and sink are found on demand using AODV protocol [26] and finally cost effective route is selected using accumulative summing method. In this method, the delay associated with finding of route is high as final path selection is based on iterative dimidiate search arithmetic and accumulative power is required for transmission. In [27], Park and Sahni have proposed an online maximum lifetime (OML) heuristic based routing algorithm. OML is basically the extension of CMAX algorithm [28]. In OML, firstly the edges with low remaining energy are removed from the graph. After the removal, the remaining edges are assigned weights according to the remaining energy of connecting nodes. Finally, the OML algorithm uses Dijkstra's algorithm to find the paths with higher energy and low communication cost. In the said algorithm, due to removal of certain edges, connectivity of the network decreases, which may lead to delays in data transmission and overall throughput of the network. In [29], a cross layer protocol has been proposed for increasing routing energy efficiency of WSN. In the proposed method energy efficiency is achieved by avoiding new route formation in DSR in case of packet delivery failure. In [30], a backpressure approach based routing method has been proposed for delay tolerant networks. This method results in energy efficiency but results in low packet delivery ratio. In [31] a spatial reusability based routing protocols viz. spatial reusability-aware single-path routing and any-path routing protocols have been proposed for multi-hop wireless networks. The simulation results for these routing protocols show that the use of spatial reusability results in tremendous improvement in the end-to-end throughput.

In [32], two reactive (online) fuzzy based routing algorithms are proposed. The First algorithm FML (Fuzzy Maximum Lifetime routing) efforts to maximize the WSN network life time while the second algorithm FMO (fuzzy Multi Objective routing) attempts to optimize both network lifetime and energy. In this method, the edge weights are formulated as fuzzy weights and OWA (ordered weighted average) operator has been used to find the weighted sum of the edges. The method has also considered the residual energy for route discovery. But unlike methods discussed above the edge weights are formulated as fuzzy weights for effectively expressing the metrics involved in the finding of route. However, the algorithm has high overhead and considers only residual energy for path selection while ignoring communication cost and transmission delay. Similarly, in REAR [33] Time, Hop Count and Energy are taken as selection parameters with priorities in the

respective order. In [34], A-star algorithm and fuzzy logic based routing method has been proposed. In this method, the path is determined by using residual energy of nodes, number of hops between source and destination and current traffic load on nodes. FEAR [35] protocol is a fuzzy based energy efficient reactive protocol. FEAR consumes lesser bandwidth and has lesser control overhead as compared to proactive protocols. However, the delay in determining the route is substantial. Routing decisions in FEAR are based on the fuzzy distance to the Base station in terms of hops as well as remaining energy of nodes on the path towards the base station.

In literature, a few bio inspired computational intelligence based routing methods [36–42] have also been proposed for wireless networks and wireless sensor networks. The key idea of these methods is to find energy efficient paths while using residual energy, communication cost and distance as optimization parameters. In [43], EEABR-an energy efficient ACO based routing method, has been proposed. In this method, each node periodically sends a number of artificial ants to search the paths between the sensor nodes and a sink node. The ants select a path on the basis of the length of route and energy efficiency. In EEABR protocol several iterations are executed to build a routing tree with optimized energy branches. However, proactive nature and route maintenance by all nodes results in high overhead. In [44], AntChain, which is a centralized chain-based routing protocol, has been proposed. In this method, the ants are transmitted by the base station to finds the routes of all the sensor nodes. The base station collects the information through ants and then based on the collected information calculates the optimal path for each node. After calculating the routes, this information is communicated to the respective sensor nodes. Due very high overhead and being a centralized approach, this method is not suitable for large scale WSNs. Moreover, in this method, the selection of routing paths is based on energy metric only. Thus, the method results in high end-to-end delays. In [45], a method ("E&D ANTS") which has used ACO has been proposed. The main objective of this method is to minimize the delay in communication of a fixed number of information packets. In order to optimize both energy and delay, the reinforcement learning (RL) algorithm based training method has been adopted. The main idea of E&D ANT's method is pheromones updation by ants while using both energy and delay in wireless communication network. In [46], a method based on deflection angle is proposed while using ACO as the optimization method. In this algorithm, the energy, distance, and deflection angle between nodes are utilized for the selection of final routing path. A reinforcement learning based scheme is proposed in [47], which reduces the energy consumption and shortens the time delay. The algorithm, however, uses only the distance as metric, so it cannot protect the minimum energy node which may in turn shorten the network lifetime. In [48], Ren et al. proposed a multipath routing based on ant colony system, which extends the network lifetime. Although the algorithm balances the energy consumption among nodes by multipath, it does not take into consideration the influence of the minimum energy node on multiple paths. In Refs. [49, 50] a centralized method which is Tabu search based and a distributed ant-colony gossiping based method is given to find routes which are both delay and cost sensitive. The method has used compressive sensing technique [51–53] to reduce the generated amount of traffic in the network.

Energy efficient routing methods that have used fuzzy logic and ACO have also been proposed in literature to enhance the network lifetime. Amiri et al. [54] have proposed a fuzzy ACO based routing protocol (FACOR) to enhance the network lifetime of WSNs. In this method, ACO is used to find the energy efficient routes from nodes to the base station, while next hop selection by an ant is dependent upon the fuzzy amounts possessed by the neighbor nodes. In [55], Zhang et al. have proposed a clustering based routing method CRT2FLACO. In this method type 2 Mamdani rule based inference system has been used to select cluster heads. Residual energy, number of neighbor nodes and distance from base station are taken as input variables. For data transmission from CH to base station, route is founded by using ACO. Similar to [55], Gajjar et al. [56], have presented a cross layer MAC/routing protocol (FAMACRO) that have used fuzzy logic and ACO. In this method, fuzzy rule based inference system (FIS) [63] is used for cluster head selection and ACO technique is used to find energy efficient route from cluster head to base station. The FIS has used residual energy, number of neighbors and communication link quality as input variables and ACO has used residual energy, distance from cluster head, distance from master station and rate of packet reception as path selection metrics. Similarly, in [57] fuzzy rule based system is used to select cluster head, while residual energy and distance from BS have been taken as input variables. Further ACO has been used to find energy efficient path from node to CH and then CH to BS.

In literature a few contributions exist in which fuzzy logic is combined with ACO to solve various optimization problems [58–61]. In these contributions, the basic aim is to obtain fuzzy controllers by using ACO. In these methods, membership function of linguistic variables is constructed and optimized by using ACO. However, in the proposed method, fuzzy membership functions are utilized in ACO to select multiple paths between sources to sink. The salient feature of the proposed routing method CARA is that it provides all the benefits offered by energy efficient routing protocols while enhancing the network lifetime by preventing early partition of the network.

3 Preliminaries

In this section, the basic concepts used in the proposed work are presented.

3.1 Fuzzy set and set membership value

Fuzzy logic delivers mathematical tools to carry out approximate reasoning for the systems having inexact, uncertain or incomplete information. For wireless sensor networks for which most of the network related information is collected from a dynamic topology, these features of fuzzy logic add on more flexibility, competency and are computationally inexpensive for modeling. Moreover, Fuzzy logic has the characteristics of delivering multiple performance criterions even when these are even conflicting in nature. These capabilities of fuzzy logic has led to its successful application in the field of communications and networking [16]. The mathematical frame work of Fuzzy logic [62] was established by Lofti-Zadeh (Zadeh, 1994) in the mid of 1960s. Accordingly, For a crisp set X, which is set of objects denoted by x, the derived fuzzy set $\widetilde{X}$ of X is a set of ordered pairs (Fig. 1): $\widetilde{X} = \{(x, \mu_{\widetilde{X}}(x))|x \in X\}$. Where $\mu_{\widetilde{X}}(x)$ is called the membership function of x in $\widetilde{X}$. The membership function $\mu_{\widetilde{X}}(x)$ maps the crisp set X to the membership space M. The range of the membership function is a subset of the non-negative real numbers whose supremum is finite. The membership function is not limited to values between 0 and 1 but if $sup_x(\mu_{\widetilde{X}}(x)) = 1$, the fuzzy set $\widetilde{X}$ is called normal i.e. $\mu_{\widetilde{X}} : X \rightarrow [0, 1]$.

Fuzzy sets allow an object to be a partial member of a set and provide a mapping of objects in continuous membership domain value in the interval [0, 1]. When $(\mu_X(x) \rightarrow 1)$, it means that input x belongs to the set $\widetilde{X}$ with high degree and is approaching towards full membership, while small membership values $(\mu_X(x) \rightarrow 0)$, indicate that input x is approaching towards no membership a [63]. Accordingly remaining energy of nodes and communication link between them are modeled as fuzzy sets and their partial belongingness to the best possible solution leads to efficient route formation without increasing the computational complexity.

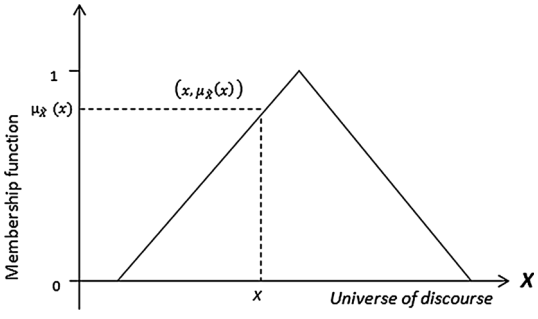

Fig. 1 Membership function of element x a fuzzy set $\widetilde{X}$

3.2 Betweenness centrality

Centrality is related to structural position of vertices (nodes) in a network and helps in determining their relative importance in the network. Betweenness centrality introduced by Freeman [13], is one of the most prominent measures of centrality and is defined as the number of the shortest paths from all vertices to all other vertices that pass through it in a graph or network. A node with higher Betweenness Centrality [14] score represents a higher degree of connectedness of a node in a network and removal of it may affect the communication between many pairs of nodes. For a given network modeled as graph $G(V,E)$, where V represents the set of nodes and E represents the set of edges. The shortest path between two vertices $u, v \in V$ is defined as the path having minimum number of edges among all the available paths. For $x, y \in V$ if $\sigma_{x,y}$ represents the number of shortest paths originating from node x and ending at node y and $\sigma_{x,y}(v)$ represents the cardinality of subset of shortest paths between x and y that passes through node v, then Betweenness Centrality of node v is given by Eq. (1) as:

$$C_B(v) = \sum_{x \neq y \neq v \in V} \frac{\sigma_{x,y}(v)}{\sigma_{x,y}} \tag{1}$$

In literature, several algorithms are proposed for computing Betweenness centrality [64–67]. For the algorithms, that are based on computing single source shortest paths from every node, are computationally complex and required computations are at least quadratic to the number of nodes, making these algorithms unsuitable for large networks. Accordingly, a computationally efficient algorithm that has been proposed in [65] for computing approximate Betweenness centrality has been used for the present work. In this algorithm the centrality score is estimated from a limited set of single source shortest path computations. The algorithm is based on selecting k vertices and computing dependency scores and Betweenness centrality of other vertices in respect of selected vertices. The dependency score of a vertex $x \in V$ on a vertex $v \in V \backslash \{s\}$, is defined as

$$\delta_{x\cdot}(v) = \sum_{y \in V \backslash \{v,x\}} \frac{\sigma_{xy}(v)}{\sigma_{xy}} \tag{2}$$

and Betweenness centrality of v in respect to x is given by:

$$C_B(v) = \sum_{x \in V \backslash \{v\}} \delta_{s\cdot}(v) \tag{3}$$

The computation time complexity for computing Betweenness Centrality by this algorithm is equal to $O(n)$, where n is number of source nodes [65]. In WSNs, nodes have limited computing capabilities and therefore, it is undesirable for these nodes to compute computationally expensive centrality metrics. For wireless sensor networks where data transfer is from sensor nodes to sink i.e. destination is fixed, the computation complexity gets further reduced. Moreover, in the proposed method Betweenness centrality is computed only once i.e. at the time of network initialization making it an optimum choice for the present work.

3.3 Ant colony optimization

Ant inspired intelligent algorithms which works on cooperative behavior of ants with one another are popular choice among researchers for solving multi-objective optimization related problems [45–48]. In ACO artificial ants find the best path from source node to destination for a given problem graph by imitating as real ants. The artificial ants communicate with each other by laying pheromone trials on the edges. The amount of pheromone deposits indicates the quality of the solution. For finding path, at each iteration, a number of artificial ants n_a, start from a source node u and move through neighbour nodes v, until they reach at the final destination (sink node in the present case). Whenever, a connection is required to be established between two nodes, launching of ants is performed for finding the various paths between source and destination. After an ant is launched, the selection of the next relay node is based upon probabilistic decision rule as given by Eq. (4).

$$P_k(u,v) = \begin{cases} \dfrac{\left[[\tau(u,v)]^{\alpha}[\lambda(u,v)]^{\beta}\right]}{\sum_{v\in N_v}\left[[\tau(u,v)]^{\alpha}[\lambda(u,v)]^{\beta}\right]} & \text{if } v \notin M_k \\ 0 & \text{otherwise} \end{cases} \quad (4)$$

where, $\tau(u,v)$ is the pheromone value, $\lambda(u,v)$ is the value of the heuristic parameter related to the performance metric under consideration. In the proposed method $\lambda(u,v)$ is made equal to fuzzy weight assigned to edges (refer Sect. 4). M_k is memory of node that contains the list of identifiers of received data packets previously. α and β are the control parameters related to the weight of pheromone and heuristic value.

Ants use reinforcement learning to discover the best paths. In reinforcement learning [47], the intelligent system is just given a goal to reach. The system then adopts the goal by a trial and error interaction with the environment. For the interaction that takes the system close to the target, a positive reward is received and while going away from the target, a negative reward is assigned. All this is done by an artificial system by introducing the concept called pheromone update. The pheromone update policy depicted as follows in Eq. 5 and 6.

$$\tau_t(u,v) \leftarrow \Delta\tau(u,v) + \rho \times \tau_{t-1}(u,v) \quad (5)$$

$$\Delta\tau_s(u,v) = \begin{cases} \dfrac{1}{L_s} & \text{if } route\_found \\ 0 & \text{otherwise} \end{cases} \quad (6)$$

Here, L_s length of tour, is covered by ant s at any iteration t. ρ is pheromone decay parameter (with value between 0 to 1) which shows the evaporation rate since the last time $\tau(u,v)$ was updated. This decay parameter ensures the balanced use of resources.

In literature, Dijkstra algorithm has been extensively used to find shortest path computation in networks. For smaller networks, Dijkstra algorithm is efficient for computing shortest paths. However for large networks, where the numbers of computations are required to repeated, this algorithm is not suitable. In such situations bio inspired computational methods are used to find near optimal solutions. In the family of bio inspired computational methods, ACO is one of the established branch for finding shortest path between a pair of nodes. The basic of this algorithm is to evaluate the performance of some randomly selected paths and finding the optimal solution. The actual proof of computational complexity and time complexity is difficult to achieve, but the real time experimental results show low run time complexity for ACO in finding optimal shortest paths.

4 Proposed method

We have modeled the WSN as directed Fuzzy vertex and edge graph [17] $\widetilde{G}(V,E,\mu_{\widetilde{V}},\mu_{\widetilde{E}})$. Where V represents the set of n sensor nodes and $E \subseteq V \times V$ denotes the set of m edges representing direct communication capability between sensor nodes. The proposed fuzzy vertex and edge graph $\widetilde{G}(V,E,\mu_{\widetilde{V}},\mu_{\widetilde{E}})$ is derived from the geometric graph, $G(V,E)$ and is defined as follows:

Definition 1 [17] (*Fuzzy Vertex and Edge Graph*). The graph $\widetilde{G}(V,E,\mu_{\widetilde{V}},\mu_{\widetilde{E}})$ is called a fuzzy vertex and edge graph on vertex set V and edge set E where, $\mu_{\widetilde{V}} : V \rightarrow [0,1]$ represents membership level of each node $v \in V$ and $\mu_{\widetilde{E}} : E \rightarrow [0,1]$ stands for the membership level of each link $e \in E$ between the nodes. The final edge weight) i.e. μ_e between nodes is derived from $\mu_{\widetilde{V}}$, $\mu_{\widetilde{E}}$ by using fuzzy relationship *T-norms* [63].

In the proposed work, the membership degree attached to each node (vertex) and membership degree attached to

each edge are adopted in a way so as to approximate the capacity of the nodes to stay alive in network and required transmission power respectively [68]. In the next subsections, fuzzy membership values assigned to nodes and edges has been discussed separately.

4.1 Fuzzy membership function of node $\mu_{\widetilde{V}}(v)$

In this paper, for each node $v \in V$, a linguistic variable *Residual Energy* and a fuzzy set *High Lifetime* $(\widetilde{V})$ are defined. A fuzzy membership function is designed to map the value of the residual energy of a node to its corresponding Fuzzy Lifetime membership degree $\mu_{\widetilde{V}}(v)$ (Fig. 2) in the fuzzy set *High Lifetime*. A high membership value is assigned to a node having a large amount of residual energy. At the time of network initialization, the residual energy $re(v)$ of all the nodes is high and is near to σ. Hence the membership function value 1 is assigned to these nodes till their residual energy decreases to a level say z. After level z, the membership value is first made to fall at a low rate. Subsequently, when the residual energy level decreases below another threshold point $\mho \times \sigma$ (where $\mho \in [0,1]$ is an algorithmic parameter) [32], the corresponding membership is decreased at a sharper rate.

This behavior of the membership function is selected to strongly discourage the selection of nodes that have depleted their energy beyond a certain threshold value for special responsibilities. The threshold point may be altered by adjusting the value of $\mho$. The characteristic Equations showing the membership degree assigned to a node v are depicted in Eq. 7.
Here,

$$\mu_{\widetilde{V}}(v) = \begin{cases} 1 & \text{if } z < re(v) \le \sigma \\ 1 - \left(\dfrac{1-\gamma}{1-\mho}\right) * \left(1 - \dfrac{re(v)}{\sigma}\right) & \text{if } \mho * \sigma < re(v) \le z \\ \dfrac{\gamma}{\mho * \sigma - E_{tr}(m,d)} * (re(v) - E_{tr}(m,d)) & \text{if } E_{tr}(m,d) < re(v) \le \mho * \sigma \\ 0 & \text{if } re(v) \le E_{tr}(m,d) \end{cases} \tag{7}$$

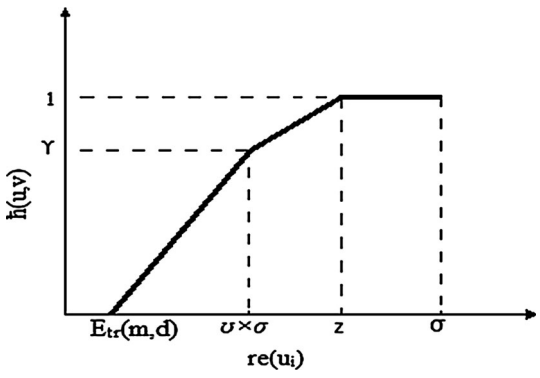

Fig. 2 Membership function for node set with high energy

$$re(v) = ce(v) - E_{tr}(m,d) \tag{8}$$

where $ce(v)$ denote current energy and $re(v)$ denotes predicted residual energy after one unit of data transmission by node v respectively, and $\gamma \in [0,1]$ is another algorithmic parameter [32]. $E_{tr}(m,d)$ is the average energy consumed in one unit of data transmission [69].

4.2 Fuzzy membership function of edge $\mu_{\widetilde{E}}(e)$

In order to incorporate minimum transmission cost for a node, another linguistic variable *low distance* for an edge $e(i,j)$, and a corresponding fuzzy set *Low Energy Consumption* $(\widetilde{E})$ are defined. In WSNs, distance between nodes provides an approximation to minimum requisite transmission power for establishing communication link between them. The low value of requisite transmission power indicates better proximity between communicating nodes and thus results in energy efficient and reliable connection. In the given WSN modeled as fuzzy graph, the defined fuzzy set *Low Energy Consumption* $(\widetilde{E})$ in E is a set of ordered pairs: $\widetilde{E} = \left\{ \left(e(i,j), \mu_{\widetilde{E}}(e) \right) | e(i,j) \in E \right\}$. $\mu_{\widetilde{E}}(e)$ is called the membership function of edge $e(i,j)$ in $\widetilde{E}$ and is given by following equations.:
where, MAX_D is the maximum possible communication

$$\mu_{\widetilde{E}}(e) = \begin{cases} 0 & for\ R < MIN_D \\ (MAX_D - D)/(MAX_D - MIN_D) & for\ MIN_D \leq R \leq MAX_D \\ 0 & for\ R > MAX_D \end{cases} \quad \forall e(i,j) \in E \tag{9}$$

radius defined on the basis of receiver's sensitivity, MIN_D is the minimum possible communication distance [70] and D is the actual distance between nodes. For a sensor node, the maximum value of communication distance depends on the transmitter capability, which may differ as per the specifications given by the manufacturers.

4.2.1 Resulting degree of edge μ_e

The final weight for edges of fuzzy graph has been obtained by using fuzzy relationship *min* Triangular norms (T-norm). Fuzzy relationship T-norms are monotone, commutative and associative functions $[0, 1] \times [0, 1] \rightarrow [0, 1]$ and are eligible for fuzzy set intersection [63]. In this work, *Min* T-norm has been preferred as during initial rounds of data transmission each node possess sufficient and equal energy and communication cost is the sole deciding factor for energy efficient routing. However, due to uneven energy consumption of member nodes in later communication rounds, the residual energy also become another key factor so as to ensure to balanced energy consumption. Thus, the modeling by fuzzy graph takes into consideration the dynamic nature of the network. Mathematically, for the given fuzzy graph $\widetilde{G}$, the final resulting degree of edge i.e. μ_e is represented as:

$$\mu_e = \underset{u,v \in E}{\forall} \min(\mu_{\widetilde{V}}, \mu_{\widetilde{E}}) \tag{10}$$

4.3 The proposed algorithm

The proposed algorithm optimizes the energy consumption and maximizes lifetime using fuzzy logic, degree of connectedness and ACO. Fuzzy logic has been used to assign the residual energy and communication link distance dependent fuzzy weight to all the connected edges in the network. Betweenness Centrality has been used to find the degree of connectedness among various nodes and then to categorize nodes into different types of connectivity domains viz. Ω, θ and η. The short energy aware paths between nodes and sink are identified using ACO. The flow diagram of the proposed method has been presented in Fig. 3 and pseudo code of the algorithm is given by Algorithm 1. The details of the proposed algorithm are as follows:

(A) Network initialization (lines 1–4 of Algorithm 1)

At the time of network initialization (line 1–4) each node is assumed to have equal energy E_{max}. The network is modeled as a fuzzy vertex and edge graph $\widetilde{G}(V, E, \mu_{\widetilde{V}}, \mu_{\widetilde{E}})$ where V is the set of n number of nodes; E is the set of m connected edges. $\mu_{\widetilde{V}}(v)$ is membership function representing lifetime of a node corresponding to its residual energy and $\mu_{\widetilde{E}}(e)$ is called the membership function of edge corresponding to distance between two connecting nodes. On the resulted fuzzy graph, modified brands' algorithm [58] has been applied to find Betweenness centrality of each node. The resulted value of Betweenness centrality of a node by executing Brand's algorithm varies between 0 and 1. High value of Betweenness centrality i.e. near to 1 represents higher connectivity of node. After calculating the Betweenness centrality, the resulted range i.e. [0,1] is divided into three sub-ranges and on the basis of that the nodes are classified into θ, Ω and η nodes, where η nodes are highly connected nodes, Ω are moderately connected and θ nodes have low connectivity. In other words, a node v in fuzzy graph is classified as θ connected when $C_B(v) \in$ low. These θ nodes have low share in maintaining network connectivity. So, the failure of nodes in this range does not have any much impact on the degree of connectivity of the overall network. A node v in fuzzy graph is classified as Ω node if $C_B(v) \in$ moderate. These nodes have more network connectivity than θ range. Thus, the probability of affecting the network connectivity in case of failure of these nodes is comparatively higher. Finally a node v in fuzzy graph is called η node if $C_B(v) \in high$. These nodes are highly connected nodes. The classification of nodes in these ranges helps in prolonging the network lifetime by avoiding early depletion of these highly connected nodes i.e. η nodes.

(B) Fuzzy graph updation (line 5–9)

In the proposed method, each node after the transmission of data, updates its current residual energy and correspondingly its membership function $\mu_{\widetilde{V}}(v)$(using Eq. 7). Then on

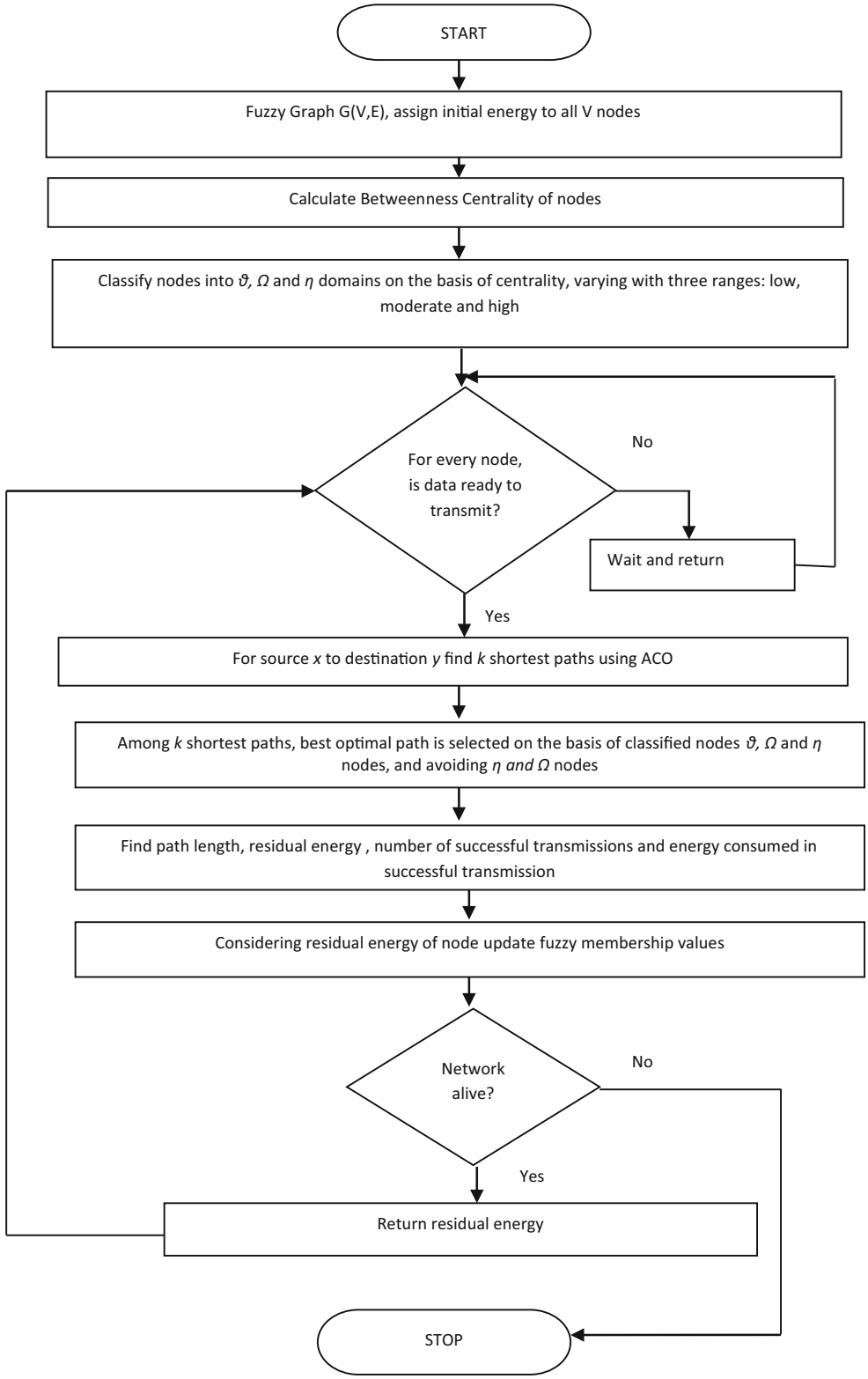

Fig. 3 Flow chart of the CARA Algorithm

the basis of both $\mu_{\tilde{V}}(v)$ and edge membership function $\mu_{\tilde{E}}(e)$ (Eq. 9) the weight assigned to the edges μ_e is updated.

(C) Route discovery (lines 10–36 of Algorithm 1)

In the proposed method, ACO has been used to find shortest path between source to destination for any source

node. In this paper, the probabilistic rule for selection of next relay node in ACO has been formulated as:

$$P_k(u,v) = \begin{cases} \dfrac{\left[[\tau(u,v)]^{\alpha}\left[\dfrac{1}{\mu_e(u,v)}\right]^{\beta}\right]}{\sum_{v\in N_v}\left[[\tau(u,v)]^{\alpha}\left[\dfrac{1}{\mu_e(u,v)}\right]^{\beta}\right]} & if\ v \notin M_k \\ 0 & otherwise \end{cases} \quad (11)$$

where, resultant fuzzy edge membership value of node $\mu_e(u,v)$ is assigned as a heuristic weight $\lambda(u,v)$ (in Eq. 4) to find k shortest paths from source node x to sink node y. The pheromone value $\tau(u,v)$ depends on the path length and is computed as per Eqs. (5) and (6). Among all the k paths, the final path is selected on the basis of θ, Ω and η nodes. The first preference is given to routes having least number of highly connected nodes i.e. η nodes. Among the routes having similar number of highly connected nodes, the preference is given to routes with lower number of Ω nodes. The objective is to preserve the energy of highly and moderately connected nodes so that network connectivity is prolonged.

The parameter k i.e. number of candidate paths plays an important role in the effectiveness of the proposed routing method. A high value of k will increase the number of candidate routes and thus can lead to the selection of route which is not energy efficient. A low value of k will lead to decrease in the importance of connectedness of graph.

In order to calculate the optimum value of k, the average energy consumption per communication round by sensor node, network lifetime and percentage of isolated nodes metric have been used as performance metrics to measure the efficiency of network operation. The effect of k on the network performance has been analyzed through simulations by fixing network topology and then varying k between 1 and 10. The average total energy consumption per round by sensor nodes is normalized by maximum energy cost and is denoted by E_s. Each result is averaged on all possible communication rounds and further for 100 different random network topologies. Network lifetime [71] is normalized by maximum number of rounds for random topologies. It has been observed from results obtained from simulation (Fig. 4) that there exists a maximum network lifetime value corresponding to an optimal value of k. At this k_{opt} both energy cost incurred by sensor nodes (E_s) and number of isolated nodes are minimum. Thus, the optimum point for network performance ranges between $5 \leq k_{opt} \leq 7$.

Algorithm 1

```
// Network initialization
∀ edges E_i ∈ G(V,E)
assign initial energy to each node;
apply Betweenness centrality( );
classify nodes ();        //nodes classification as θ, Ω and η nodes

// Fuzzy Graph updation

    update re(u_i) →V ;
    Assign membership value to each node μ_V(v)        ∀ v∈V
    Assign membership value to each edge μ_E(u,v)      ∀ e∈E
    Compute resultant edge weight μ_e(u,v)             ∀ e∈E
end
Route Discovery
∀source x
    best-path = ∞
    while(n_a = no. of ants )
    set ant ( start );
    while (goal not reached y)
            apply probability rule ( );
            move to choose vertex ,
    end
    if length (ants journey )< length (best path )
            best path = ants journey ;
    end
    update pheromone;
    end
end
return best possible k paths;
for all selected k paths
pathηinfo[i] <- no. of η nodes;
    pathΩinfo[i] <- no. of Ω nodes;
sortassending(pathηinfo);
sortassending(pathΩinfo);
if(pathηinfo[0] != pathηinfo[1])
select path corresponding pathηinfo[0]
break;
else if (pathΩinfo[0] != pathΩinfo[1])
select path corresponding pathΩinfo[0]
break;
find pathlength ;
return pathlength ;
calculate energy consumed ;
return re(u_i);
go to step 6;
```

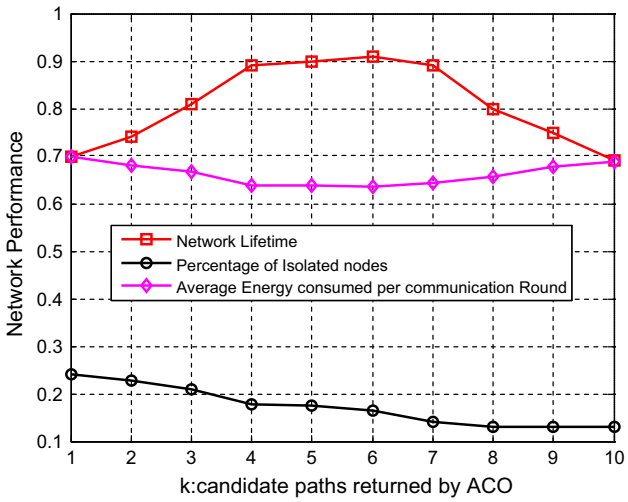

Fig. 4 Selection of candidate routes returned by ACO

5 Performance evaluation

In this section, the performance of the proposed method has been evaluated with MATLAB simulations. In Sect. 5.1, the simulation environment and performance metrics are discussed. In Sect. 5.2 the results of the simulations have been evaluated.

5.1 Simulation environment and metrics

For simulations, n randomly deployed nodes in an area of 1000×1000 m^2 have been considered. All these nodes have been assigned an equal initial energy σ i.e. 1 J. The weight of edges has been calculated by using Fuzzy membership function of μ_e as discussed in Sect. 4.1. As contention free MAC layer has been assumed, a constant factor of energy loss has been considered for re-transmissions. For the experiment no predefined traffic flow has been considered. The data packet sizes are kept equal to 64 bytes. The other parameters considered for simulation and their values are given in Table 1.

For maximum lifetime, the best range of values for algorithmic parameters υ and γ (Eq. 7) is defined as $\upsilon \in [0.1, 0.9]$ and $\gamma \in [0.1, 0.9]$ [32]. On the basis of same and the simulation results $\gamma = 0.9$, and $\upsilon = 0.2$ have been used for the simulations. In the present work, θ (low) ranges between $[0 \leq \theta < 0.4]$, Ω (moderate) ranges between $[0.4 \leq \Omega < 0.8]$ and η (high) ranges between $[0.8 \leq \eta \leq 1]$. These ranges are dependent upon the type of network and the path loss model used for data communication [53]. On the basis of network performance as shown in Fig. 4, the maximum value of k i.e. number of candidate paths have been kept equal to 5.

The performance analysis of the proposed method vis-a-vis FML [32], EEABR [43] and FACOR [54] has been undertaken while considering the average of the respective simulation results. The average of the individual simulation results for 100 randomly generated networks have been considered for the performance analysis. In this paper, the energy dissipation model as adopted in [69] has been considered. According to this model, transmission and receiving costs are defined as follows:

$$E_{Tx}(l,d) = \begin{cases} l \times E_{elec}^{tx} + l \times \varepsilon_{fs} \times d^2, & d < d_0 \\ l \times E_{elec}^{tx} + l \times \varepsilon_{amp} \times d^4, & d \geq d_0 \end{cases} \quad (12)$$

$$E_{Rx}(l) = l \times E_{elec}^{Rx} \quad (13)$$

where, l represents the number of bits per packet, d is the distance between sender and receiver node; E_{elec} represents the energy dissipation per bit in transmitter or receiver circuitry. ε_{fs} and ε_{amp} represents the respective energy expenditure factor of amplification for free space and multipath radio models. The energy cost $E(\psi)$ of any route ψ is computed by the following equation.

$$E(\psi) = \sum_{m \in \psi} \left(E_{Tx}^{m} + E_{Rx}^{m} \right) \quad (14)$$

Thus the final energy calculations are based on both transmission and reception energy incurred by node m on the route ψ. For the present simulations, the values 50 nJ/bit, 10 pJ/bit/m^2 and .0013 pJ/bit/m^4 are assigned to E_{elec}, ε_{fs} and ε_{amp} respectively as given by Table 1.

Performance of the proposed method has evaluated in terms of (A) network lifetime and energy efficiency: network lifetime is defined as the maximum number of communication rounds during which the collected information can be effectively delivered to the base station. Thus the network lifetime indicates the communication rounds during which the network is operational. Energy

Table 1 A list of values used for various simulation parameters

E_{elec} (energy used in electronic circuit)	100 nJ/bit
E_{amp} (energy used in amplification of signal, multipath)	50 pJ/bit/m^4
ε_{fs} (energy used in amplification of signal, freespace)	10 pJ/bit/m^2
M (ant memory)	8 bytes
Number of nodes (N)	[100, 200, 300, 400, 500]
n_a (number of ants)	100
r_t (maximum transmission radius)	[50 m, 80 m]

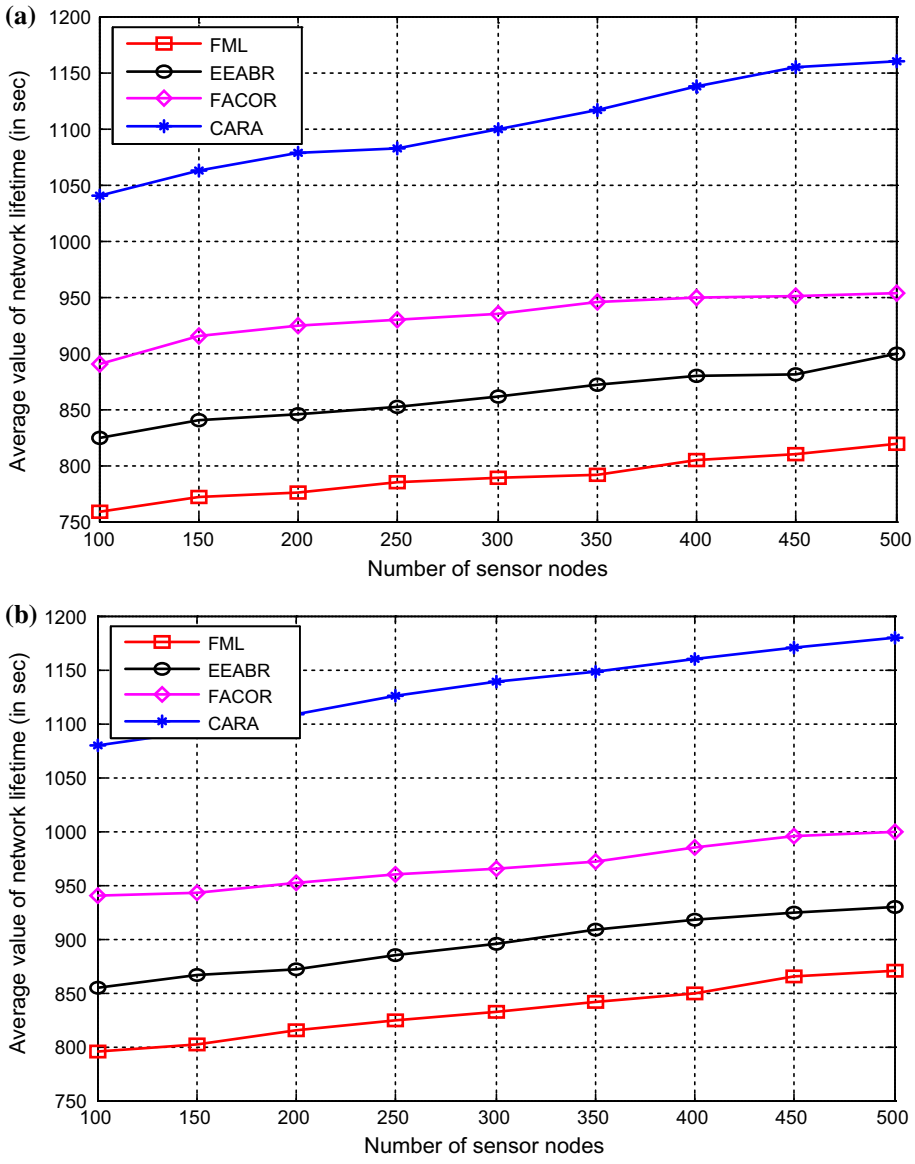

Fig. 5 Lifetime comparison between CARA, FML, EEABR and FACOR routing algorithms for Transmission ranges, **a** r_t is 50 m, **b** r_t is 80 m

Table 2 Comparative analysis of network lifetime

Routing methods	Maximum transmission range (r_t)	Number of nodes		Percentage increase
		100	500	
Average network lifetime				
FML	50	759	819	.07905
	80	795	870	.09433
EEABR	50	825	900	.09090
	80	855	925	.0818
FACOR	50	890	953	.0707
	80	940	1000	.06382
CARA	50	1040	1160	.10526
	80	1076	1187	.10315

efficiency is measured in terms of aggregate energy consumed by member nodes per communication round. (B) Connectivity percentage: It is defined as the percentage of alive nodes which can transmit the information to the base station either directly or indirectly (multihop). (C) Packet delivery ratio: it is the ratio of number of successful packet transmitted to the total number of packets transmitted in a communication round. (D) Load distribution: it is defined as the standard deviation in the residual energy of nodes after every 100 communication rounds.

The performance of the proposed method has been compared with FML, EEABR and FACOR. The protocol FML [32] represents the energy efficient routing methods which have used fuzzy logic to represent residual energy of

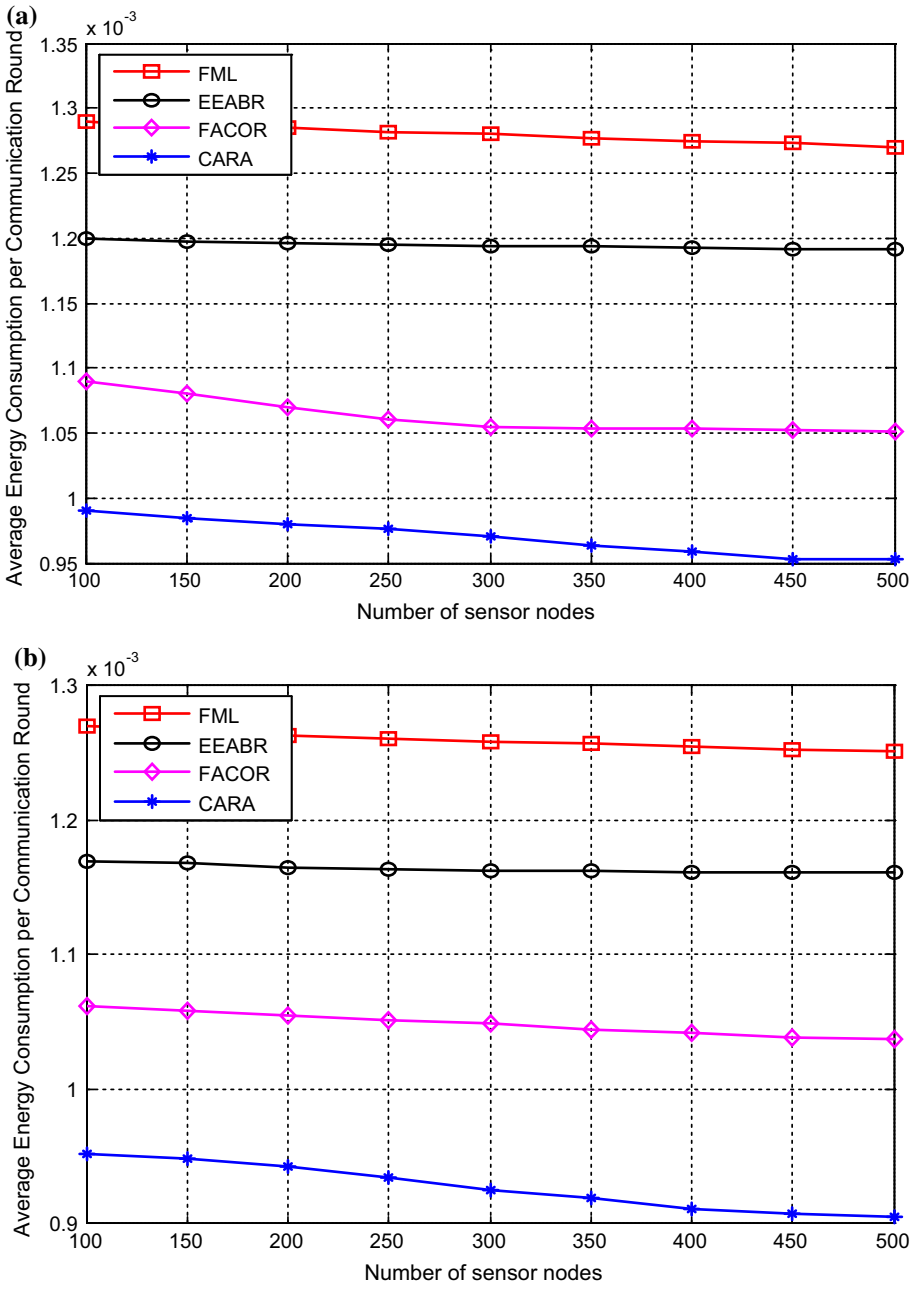

Fig. 6 Aggregate energy consumption per communication round by CARA, FACOR and FML and EEABR routing algorithms when transmission range, **a** $r_t = 50$ m, **b** $r_t = 80$ m

nodes and execute the shortest path algorithm to find the routes from source nodes to base station. To apply fuzzy logic a fuzzy set "high lifetime" and corresponding fuzzy lifetime membership function has been defined for edges. The fuzzy lifetime membership function assigns a higher membership value to an edge with higher residual energy start node. Finally shortest path algorithm is executed to find minimum weight path from the source node to destination node.

EEABR [43] i.e. energy efficient ant based routing algorithm, represents the methods, which have used ACO to discover the paths on the basis of residual energy and distance between source and base station. The EEABR method has used a colony of forward and backward artificial ants to find short and energy efficient paths.

FACOR [54] represents the methods which have used fuzzy logic in combination with ACO. In this method, ACO is used to find the energy efficient routs from respective nodes to Base station. However, next hop selection by an ant is dependent upon the fuzzy amounts possessed by its neighbor nodes. Fuzzy rule based system with inputs residual energy, distance between nodes, connectivity degree and pheromone concentration amount are used to find fuzzy amounts possessed by nodes. Finally,

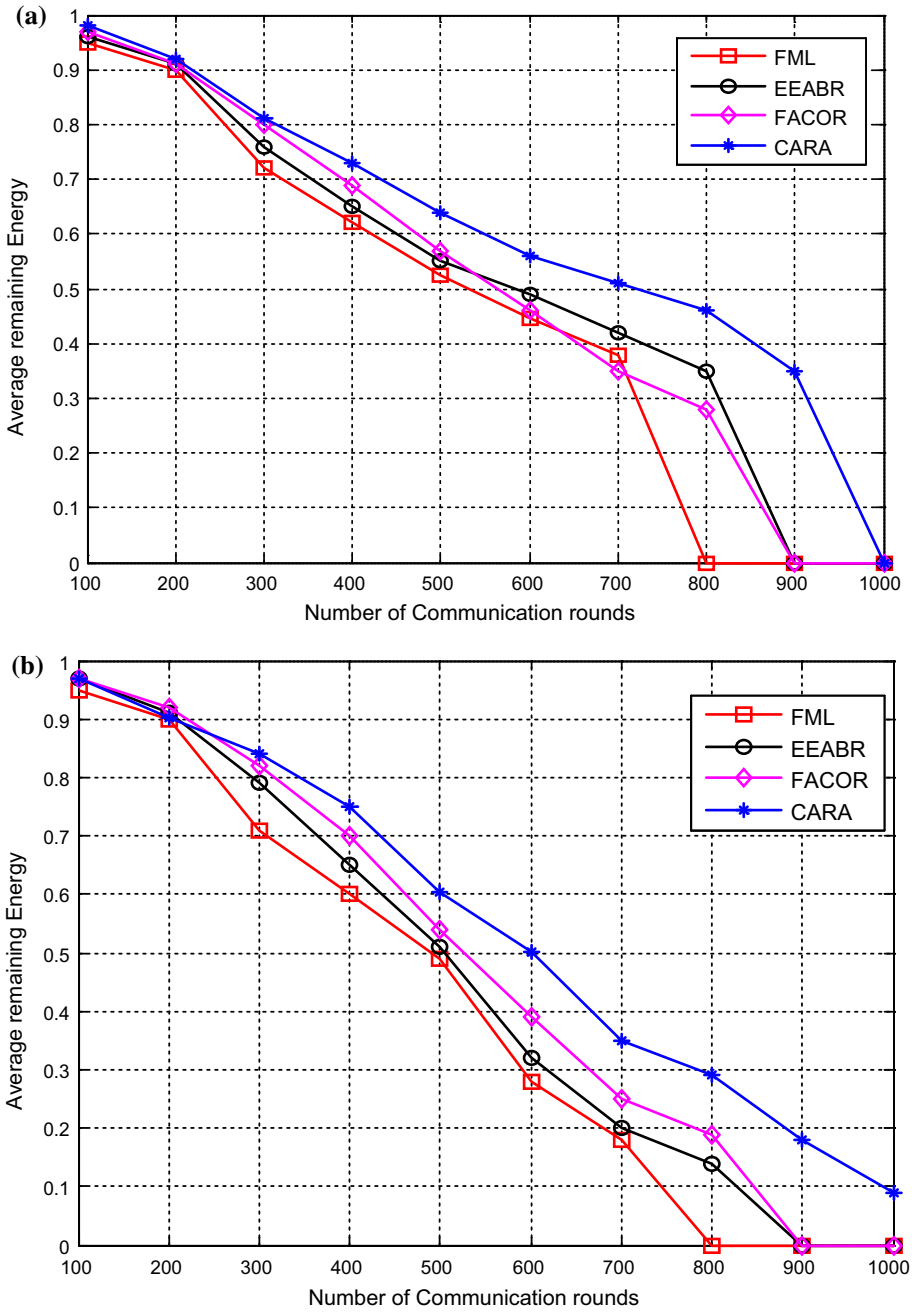

Fig. 7 Average remaining energy after every 100 communication rounds. Number of nodes = 200, **a** r_t = 50 m, **b** r_t = 80 m

ACO method is used to find the optimal path between source and sink node.

5.2 Performance evaluation

In this section, the performance of the proposed method is evaluated and compared in terms of defined performance parameters.

(A) Network lifetime and energy efficiency

For the simulations, number of nodes have been varied from 100 to 500 to evaluate the impact of node density on network lifetime. The evaluation has also been done for different maximum transmission ranges of nodes of r_t = 50 m and r_t = 80 m, so as to examine the effect of transmission range on the network performance.

The results obtained are shown in Fig. 5(a, b). The results indicate that for both values of r_t i.e. 50 and 80 m; CARA has higher lifetime values. Moreover, with the rising node density, CARA shows a consistent increase in the lifetime irrespective of the transmission radius used. FML, EEABR and FACOR routing algorithm do not indicate an increasing trend at higher transmission radii and this performance lag is more evident at r_t = 80. Table 2 provides

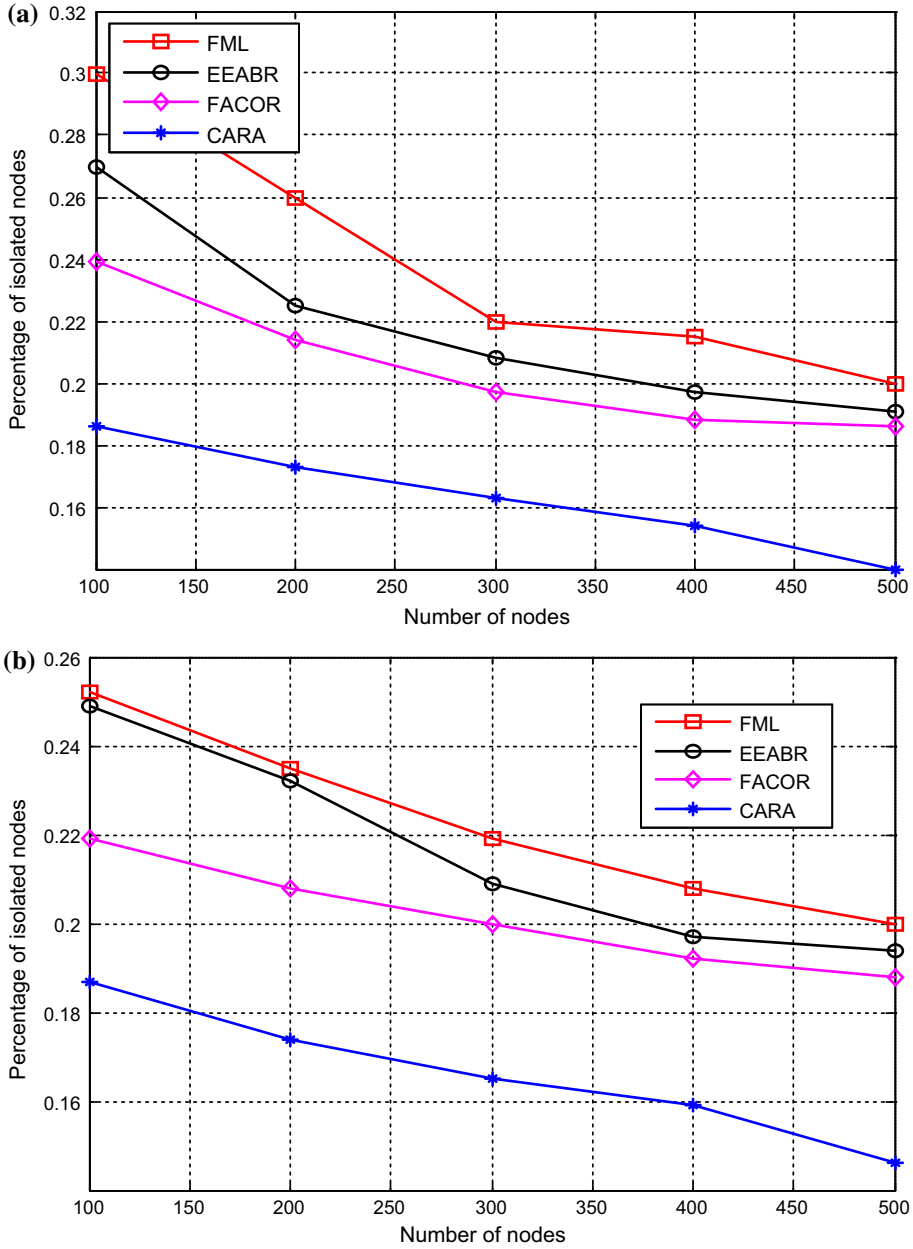

Fig. 8 Percentage of alive nodes with no connectivity to base station, **a** $r_t = 50$ m, **b** $r_t = 80$ m

the comparative analysis of rise in network lifetime with increase in network density and transmission radii.

The reasons for improvement in the performance of each method can be attributed to the fact that with the increase in r_t, each node has more number of neighbouring nodes leading to higher network connectivity which in turn offers more routing choices at each node. The CARA performs better as in addition to residual energy; it takes into account the importance of individual nodes in maintaining the network connectivity. Thus, by conserving the energy of highly connected nodes, CARA achieves improvement in the network lifetime.

The simulation results of energy consumption are shown in Fig. 6(a, b). It can be observed that with increase in transmission radius, there is increase in per node energy consumption. The same is due to the fact that increase in transmission radius makes it possible to transmit directly to relatively distant neighbour. However, with increase in transmission radius there is decrease in the overall energy consumption due to decrease in number of intermediate forwarding nodes (relay nodes).

The results indicate that in similar environment the routes identified by CARA consume considerably lesser energy than those found by FML, EEABR and FACOR routing algorithms. The performance of CARA is better as it identifies the route on the basis of fuzzy logic based defined edge-weight and application of ACO.

The simulations have also been done to find average remaining energy of nodes after every 100 communication

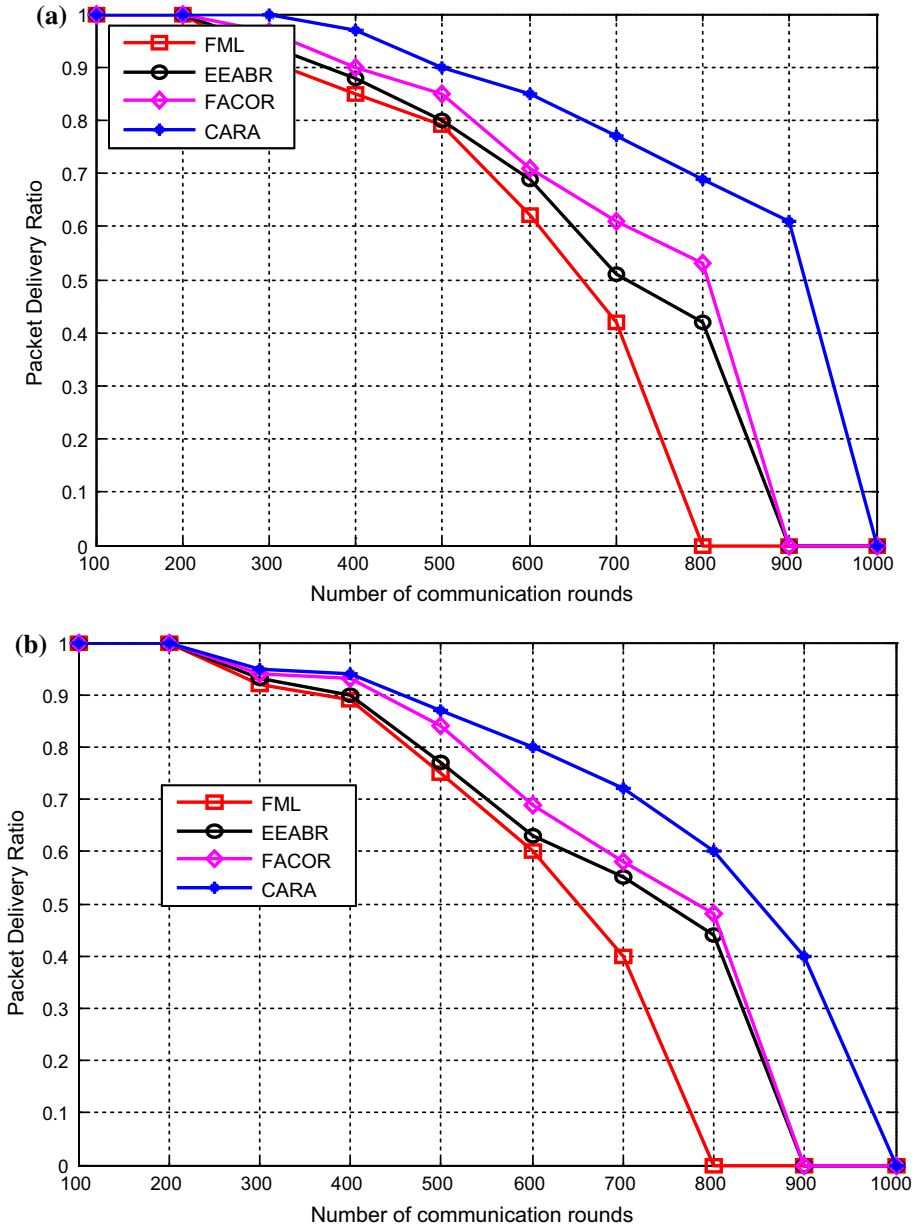

Fig. 9 Successful packet transmission with respect to communication rounds. Number of nodes = 200, **a** r_t = 50 m, **b** r_t = 80 m

rounds. Figure 7(a, b) shows the results of these simulations. From the simulation results it has been observed that during initial rounds the average energy of nodes resulted by EEABR and the proposed method is comparable. However, as the number of communication rounds increase, the proposed method outperforms in respect of average remaining energy in comparison to FML, EEABR and FACOR respectively.

(B) Connectivity percentage

This metric has been applied to compute the percentage of nodes which have sufficient energy but are not able to communicate with base station due to non-availability of intermediate nodes (relay nodes) in their transmission range. This metric provides indication regarding the efficiency of network in maintaining overall connectivity by keeping the energy consumption as uniform as possible. From the simulation results as indicated in Fig. 8(a, b) it can be observed that the proposed method has lower number of isolated nodes with sufficient energy and thus performs better as compared to other methods. The same is due to the fact that the proposed method preserves the energy of highly connected nodes so that the network connectivity can be maintained for a longer period.

Table 3 Standard deviation in remaining energy of nodes with respect to communication rounds

Number of communication rounds	FML	EEABR	FACOR	CARA
Standard deviation in remaining energy of nodes after each 100 communication rounds				
Maximum transmission radius (50 m)				
100	.0184	.0183	.0183	.0183
200	.0183	.0183	.0180	.0180
300	.0182	.0180	.0175	.0179
400	.0179	.0175	.0172	.0179
500	.0180	.0177	.0177	.0179
600	.0185	.0179	.0178	.0181
700	.0189	.0187	.0184	.0182
Maximum transmission radius (80 m)				
100	.0181	.0182	.0181	.0182
200	.0180	.0182	.0180	.0178
300	.0174	.0181	.0174	.0178
400	.0176	.0176	.0171	.0178
500	.0179	.0174	.0178	.0179
600	.0181	.0178	.0179	.0180
700	.0185	.0185	.0182	.0182

(C) Packet delivery ratio

This metric examines the efficiency of the proposed method in terms of number of packets transmitted successfully with respect to communication rounds. As the communication rounds progress, there is depletion of energy of nodes. The failure of certain nodes due to this energy depletion affects the network connectivity and subsequently affects the number of transmissions in subsequent rounds.

In Fig. 9, the ratio of number of successfully transmitted packets to the total number of generated packets has been depicted in respect to communication rounds. CARA performs better as compared to FML, EEABR and FACOR in respect of this metric. The same has been due to the fact that while FML, EEABR and FACOR consider residual energy as the sole parameter for path selection, CARA tries to prolong the overall network connectivity.

(D) Load distribution

Load distribution calculations are done on the basis of standard deviation in remaining energy of nodes after every 100 communication rounds. Table 3 presents the standard deviation of the remaining energy at the end of every 100 communication rounds. As indicated in the results the proposed method results in steady energy consumption by the sensor nodes.

On the basis of the simulation results as discussed in this section, it may conclude that the proposed algorithm, CARA outperforms FML, EEABR and FACOR routing algorithms in terms of network lifetime, energy efficiency, connectivity percentage, packet delivery ratio and load distribution.

6 Conclusion

The real-life deployment of WSNs requires energy efficiency and longer lifetime without human intervention. However, due to non-uniform energy consumption there is always a possibility of early partition of the whole network which substantially decreases the overall useful lifespan of the network despite the presence of nodes with sufficient energy. To address these inherent constraints of the WSNs, a new algorithm has been proposed which is based on the Fuzzy logic, Betweenness centrality and ACO. The proposed method enhances the overall network lifetime by prolonging the lifespan of highly connected nodes. The same is achieved by giving higher priority to routes having nodes with lesser connectivity than the routes having highly connected nodes, while selecting the data transmission route amongst the various energy efficient routes. The performance of the proposed method has been evaluated and compared with FML, EEABR and FACOR routing algorithm under the same set of conditions and environment. Simulation results demonstrate the effectiveness of the new approach with regards to enhancement of the lifetime and optimization of average energy consumption of wireless sensor networks with randomly scattered nodes. In future the same concept can be applied

for congestion control, route formation in wireless ad-hoc and mesh networks.

References

1. Akyildiz, I. F., Su, W., Sankarasubramaniam, Y., & Cayirci, E. (2002). A survey on sensor networks. *IEEE Communications Magazine, 40*(8), 102–114.
2. Xiao, Y., Peng, M., Gibson, J., Xie, G. G., Du, D. Z., & Vasilakos, A. V. (2012). Tight performance bounds of multihop fair access for MAC protocols in wireless sensor networks and underwater sensor networks. *IEEE Transactions onMobile Computing, 11*(10), 1538–1554.
3. Wang, X., Vasilakos, A. V., Chen, M., Liu, Y., & Kwon, T. T. (2012). A survey of green mobile networks: Opportunities and challenges. *Mobile Networks and Applications, 17*(1), 4–20.
4. Li, M., Li, Z., & Vasilakos, A. V. (2013). A survey on topology control in wireless sensor networks: Taxonomy, comparative study, and open issues. *Proceedings of the IEEE, 101*(12), 2538–2557.
5. Manap, Z., Ali, B. M., Ng, C. K., Noordin, N. K., & Sali, A. (2013). A review on hierarchical routing protocols for wireless sensor networks. *Wireless Personal Communications, 72*(2), 1077–1104.
6. Sheng, Z., Yang, S., Yu, Y., Vasilakos, A., Mccann, J., & Leung, K. (2013). A survey on the IETF protocol suite for the internet of things: Standards, challenges, and opportunities. *IEEE Wireless Communications, 20*(6), 91–98.
7. Vasilakos, A. V., Zhang, Y., & Spyropoulos, T. (Eds.). (2011). *Delay tolerant networks: Protocols and applications*. Boca Raton: CRC Press.
8. Chen, M., Wan, J., González, S., Liao, X., & Leung, V. (2014). A survey of recent developments in home M2M networks. *IEEE Communications Surveys and Tutorials, 16*(1), 98–114.
9. Han, K., Luo, J., Liu, Y., & Vasilakos, A. V. (2013). Algorithm design for data communications in duty-cycled wireless sensor networks: A survey. *IEEE Communications Magazine, 51*(7), 107–113.
10. Shen, Z., Luo, J., Zimmermann, R., & Vasilakos, A. V. (2011). Peer-to-peer media streaming: Insights and new developments. *Proceedings of the IEEE, 99*(12), 2089–2109.
11. Zeng, Y., Xiang, K., Li, D., & Vasilakos, A. V. (2013). Directional routing and scheduling for green vehicular delay tolerant networks. *Wireless Networks, 19*(2), 161–173.
12. Wasserman, S. (1994). *Social network analysis: Methods and applications* (Vol. 8). Cambridge: Cambridge University Press.
13. Freeman, L. C. (1978). Centrality in social networks: Conceptual clarification. *Social Networks, 1*, 215–239.
14. Bonacich, P. (1987). Power and centrality: A family of measures. *American Journal of Sociology, 92*, 1170–1182.
15. Aarti J., Reddy, B. V. R. (2013). Node centrality in wireless sensor networks: Importance, applications and advances. In *Proceedings of 3rd IEEE international advanced computing conference (IACC-2013)* (pp. 126–130).
16. Marwaha, S., Srinivasan, D., Tham, C. K., & Vasilakos, A. (2004). Evolutionary fuzzy multi-objective routing for wireless mobile ad hoc networks. In *Congress on evolutionary computation, 2004. CEC2004* (Vol. 2, pp. 1964–1971).
17. Koczy, L. T. (1992). Fuzzy graphs in the evaluation and optimization of networks. *Fuzzy Sets and Systems, 46*, 307–319.
18. Dorigo, M. (Ed.). (2006). Ant colony optimization and swarm intelligence. In *Proceedings of 5th international workshop, ANTS 2006* (Vol. 4150), Brussels, Belgium, September 4–7, 2006. Springer.
19. Lin, Ying, et al. (2012). An ant colony optimization approach for maximizing the lifetime of heterogeneous wireless sensor networks. *IEEE Transactions on Systems, Man, and Cybernetics, Part C: Applications and Reviews, 42*(3), 408–420.
20. Chandra Mohan, B., & Baskaran, R. (2012). A survey: Ant Colony Optimization based recent research and implementation on several engineering domain. *Expert Systems with Applications, 39*(4), 4618–4627.
21. Chang, J. H., & Tassiulas, L. (2004). Maximum lifetime routing in wireless sensor networks. *IEEE/ACM Transactions on Networking (TON), 12*(4), 609–619.
22. Akkaya, K., & Younis, M. (2003). An energy-aware QoS routing protocol for wireless sensor networks. In *Proceedings of 23rd IEEE international conference on distributed computing systems workshops, 2003*.
23. Akkaya, Kemal, & Younis, Mohamed. (2004). Energy-aware delay-constrained routing in wireless sensor networks. *International Journal of Communication Systems, 17*(6), 663–687.
24. Heo, J., Jiman, H., & Yookun, C. (2009). EARQ: Energy aware routing for real-time and reliable communication in wireless industrial sensor networks. *IEEE Transactions on Industrial Informatics, 5*(1), 3–11.
25. Li, W., Chen, M., & Li, M. M. (2009). An enhanced aodv route protocol applying in the wireless sensor networks. In *Fuzzy information and engineering* (Vol. 2, pp. 1591–1600). Berlin: Springer.
26. Perkins, C. E., & Royer, E. M. (1999). Ad hoc on-demand distance vector routing. In *Proceedings of the second IEEE workshop on mobile computing systems and applications, 1999, WMCSA'99* (pp. 90–100).
27. Park, Joongseok, & Sahni, Sartaj. (2006). An online heuristic for maximum lifetime routing in wireless sensor networks. *IEEE Transactions on Computers, 55*(8), 1048–1056.
28. Kar, K., Kodialam, M., Lakshman, T., & Tassiulas, L. (2003). Routing for network capacity maximization in energy-constrained ad-hoc networks. In *Proceedings of IEEE INFOCOM, 2003*.
29. Chilamkurti, N., Zeadally, S., Vasilakos, A., & Sharma, V. (2009). Cross-layer support for energy efficient routing in wireless sensor networks. *Journal of Sensors*. doi:10.1155/2009/134165.
30. Dvir, A., & Vasilakos, A. V. (2011). Backpressure-based routing protocol for DTNs. *ACM SIGCOMM Computer Communication Review, 41*(4), 405–406.
31. Meng, T., Wu, F., Yang, Z., Chen, G., & Vasilakos, A. (2015). Spatial reusability-aware routing in multi-hop wireless networks. *IEEE TMC*. doi:10.1109/TC.2015.2417543.
32. Minhas, M. R., Gopalakrishnan, S., & Leung, V. C. M. (2008). Fuzzy algorithms for maximum lifetime routing in wireless sensor networks. In *Global telecommunications conference, 2008. IEEE GLOBECOM 2008.*
33. Jabbar, S., Minhas, A. A., Akhtar, R. A., & Aziz, M. Z. (2009). REAR: Real-time energy aware routing for wireless adhoc micro sensors network. In *Eighth IEEE international conference on dependable, autonomic and secure computing, 2009. DASC'09* (pp. 825–830).
34. AlShawi, I. S., Yan, L., Pan, W., & Luo, B. (2012). Lifetime enhancement in wireless sensor networks using fuzzy approach and A-star algorithm. *IEEE Sensors Journal, 12*(10), 3010–3018.
35. ALMomani, I. M., & Saadeh, M. K. (2011). FEAR: Fuzzy-based energy aware routing protocol for wireless sensor networks. *International Journal of Communications, Network and System Sciences, 4*(06), 403.
36. Cheng, H., Xiong, N., Vasilakos, A. V., Yang, L. T., Chen, G., & Zhuang, X. (2012). Nodes organization for channel assignment

with topology preservation in multi-radio wireless mesh networks. *Ad Hoc Networks, 10*(5), 760–773.
37. Sengupta, S., Das, S., Nasir, M., Vasilakos, A. V., & Pedrycz, W. (2012). An evolutionary multiobjective sleep-scheduling scheme for differentiated coverage in wireless sensor networks. *IEEE Transactions on Systems, Man, and Cybernetics, Part C: Applications and Reviews, 42*(6), 1093–1102.
38. Wei, G., Ling, Y., Guo, B., Xiao, B., & Vasilakos, A. V. (2011). Prediction-based data aggregation in wireless sensor networks: Combining grey model and Kalman filter. *Computer Communications, 34*(6), 793–802.
39. Song, Y., Liu, L., Ma, H., & Vasilakos, A. V. (2014). A biology-based algorithm to minimal exposure problem of wireless sensor networks. *IEEE Transactions on Network and Service Management, 11*(3), 417–430.
40. Yen, Y. S., Chao, H. C., Chang, R. S., & Vasilakos, A. (2011). Flooding-limited and multi-constrained QoS multicast routing based on the genetic algorithm for MANETs. *Mathematical and Computer Modelling, 53*(11), 2238–2250.
41. Kassotakis, I. E., Markaki, M. E., & Vasilakos, A. V. (2000). A hybrid genetic approach for channel reuse in multiple access telecommunication networks. *IEEE Journal on Selected Areas in Communications, 18*(2), 234–243.
42. Vasilakos, A., Saltouros, M. P., Atlassis, A. F., & Pedrycz, W. (2003). Optimizing QoS routing in hierarchical ATM networks using computational intelligence techniques. *IEEE Transactions on Systems, Man, and Cybernetics, Part C: Applications and Reviews, 33*(3), 297–312.
43. Camilo, T., Carreto, C., Silva, J. S., & Boavida, F. (2006). An energy-efficient ant-based routing algorithm for wireless sensor networks. In *Ant colony optimization and swarm intelligence* (pp. 49–59). Berlin: Springer.
44. Ding, N., & Liu, P. X. (2005). A centralized approach to energy-efficient protocols for wireless sensor networks. In *2005 IEEE international conference mechatronics and automation* (Vol. 3, pp. 1636–1641).
45. Wen, Y. F., Chen, Y. Q., & Pan, M. (2008). Adaptive ant-based routing in wireless sensor networks using Energy* Delay metrics. *Journal of Zhejiang University Science A, 9*(4), 531–538.
46. Liu, Y., Zhu, H., Xu, K., & Jia, Y. (2007). A routing strategy based on ant algorithm for WSN. In *Third international conference on natural computation, 2007. ICNC 2007* (Vol. 5, pp. 685–689).
47. GhasemAghaei, Reza, et al. (2007). Ant colony-based reinforcement learning algorithm for routing in wireless sensor networks. In *Instrumentation and measurement technology conference proceedings. IMTC 2007*.
48. Xiu-li, Ren, Liang Hong-wei, and Wang Yu. (2008). Multipath routing based on ant colony system in wireless sensor networks. In *2008 International conference on computer science and software engineering* (Vol. 3).
49. Yao, Y., Cao, Q., & Vasilakos, A. V. (2013). EDAL: An energy-efficient, delay-aware, and lifetime-balancing data collection protocol for wireless sensor networks. In *2013 IEEE 10th international conference on Mobile ad-hoc and sensor systems (MASS)* (pp. 182–190).
50. Yao, Y., Cao, Q., & Vasilakos, A. V. (2015). EDAL: An energy-efficient, delay-aware, and lifetime-balancing data collection protocol for heterogeneous wireless sensor networks. In *IEEE transactions on networking* (Vol. 23, No. 3).
51. Xiang, L., Luo, J., & Vasilakos, A. (2011). Compressed data aggregation for energy efficient wireless sensor networks. In *2011 8th annual IEEE communications society conference on sensor, mesh and ad hoc communications and networks (SECON)* (pp. 46–54).
52. Liu, X. Y., Zhu, Y., Kong, L., Liu, C., Gu, Y., Vasilakos, A. V., & Wu, M. Y. (2014). CDC: Compressive data collection for wireless sensor networks. *IEEE Transactions on Parallel and Distributed Systems*. doi:10.1109/TPDS.2014.2345257.
53. Xu, X., Ansari, R., Khokhar, A., & Vasilakos, A. V. (2015). Hierarchical data aggregation using compressive sensing (HDACS) in WSNs. *ACM Transactions on Sensor Networks (TOSN), 11*(3), 45.
54. Amiri, E., Keshavarz, H., Alizadeh, M., Zamani, M., & Khodadadi, T. (2014). Energy efficient routing in wireless sensor networks based on fuzzy ant colony optimization. *International Journal of Distributed Sensor Networks*. doi:10.1155/2014/768936.
55. Zhang, Q. Y., Sun, Z. M., & Zhang, F. (2014). A clustering routing protocol for wireless sensor networks based on type-2 fuzzy logic and ACO. In *2014 IEEE international conference on fuzzy systems (FUZZ-IEEE)* (pp. 1060–1067).
56. Gajjar, S., Sarkar, M., & Dasgupta, K. (2015). FAMACRO: Fuzzy and ant colony optimization based MAC/routing cross-layer protocol for wireless sensor networks. *Procedia Computer Science, 46*, 1014–1021.
57. Tomar, G. S., Sharma, T., & Kumar, B. (2015). Fuzzy based ant colony optimization approach for wireless sensor network. *Wireless Personal Communications*, *84*(1), 361–375.
58. Khalouli, S., Ghedjati, F., & Hamzaoui, A. (2008). Hybrid approach using ant colony optimization and fuzzy logic to solve multi-criteria hybrid flow shop scheduling problem. In *Proceedings of the 5th international conference on Soft computing as transdisciplinary science and technology (ACM)* (pp. 44–50).
59. Van Ast, J., Babuska, R., & De Schutter, B. (2009). Fuzzy ant colony optimization for optimal control. In *American control conference, 2009. ACC'09* (pp. 1003–1008).
60. Alsawy, A. A., & Hefny, H. A. (2010). Fuzzy-based ant colony optimization algorithm. In *2nd international conference on computer technology and development (ICCTD), 2010* (pp. 530–534).
61. Ginidi, A. R. G., Kamel, A. M., & Dorrah, H. T. (2010). Development of new fuzzy logic-based ant colony optimization algorithm for combinatorial problems. In *Proceedings of the 14th international middle east power systems conference*, Cairo University, Egypt.
62. Zadeh, L. A. (1965). Fuzzy sets. *Information and Control, 8*(3), 338–353.
63. Ross, T. (2004). *Fuzzy logic with engineering applications* (2nd ed.). Chichester: Wiley.
64. Baglioni, M., Geraci, F., Pellegrini, M., & Lastres, E. (2012). Fast exact computation of betweenness centrality in social networks. In *Proceedings of the 2012 international conference on advances in social networks analysis and mining (ASONAM 2012) (IEEE Computer Society)* (pp. 450–456).
65. Brandes, U., & Pich, C. (2007). Centrality estimation in large networks. *International Journal of Bifurcation and Chaos, 17*(07), 2303–2318.
66. Brandes, U. (2001). A faster algorithm for betweenness centrality. *Journal of Mathematical Sociology, 25*, 163–177.
67. Brandes, U. (2008). On variants of shortest-path betweenness centrality and their generic computation. *Social Networks, 30*(2), 136–145.
68. Jain, A., & Reddy, B. R. (2015). A Novel method of modeling wireless sensor network using fuzzy graph and energy efficient fuzzy based k-hop clustering algorithm. *Wireless Personal Communications*, *82*(1), 157–181.
69. Heinzelman, W. R., Chandrakasan, A., & Balakrishnan, H. (2002). An application-specific protocol architecture for wireless microsensor networks. *IEEE Transactions on Wireless Communications, 1*, 660–670.

70. Narayanaswamy, S., Kawadia, V., Sreenivas, R. S., & Kumar, P. (2002). Power control in ad-hoc networks: Theory, architecture, algorithm and implementation of the COMPOW protocol. In *European wireless conference*.
71. Handy, M. J., Haase, M., & Timmermann, D. (2002). Low energy adaptive clustering hierarchy with deterministic cluster-head selection. In *Proceedings of international workshop mobile wireless communication networks* (pp. 368–372).

Aarti Jain graduated with a B.Tech degree in Electronics and Communication Engineering from Beant Govt. Engineering College, Punjab, India in June 2002. Then she obtained her M.E. degree in Electronics and Communication from Delhi College of Engineering, University of Delhi, India in 2009. Currently, she is working as Asst. Prof. at the Department of Electronics and Communication Engineering, Ambedkar Institute of Advanced Communication Technologies and Research. She has submitted her Ph.D. thesis to Guru Gobind Singh Indraprastha University, Delhi in the field of wireless sensor networks. She has contributed more than 15 research articles in the field of wireless sensor networks. Her current research interests are in Energy and quality management for wireless sensor networks, bio inspired computing and its application, localization.

Available online at www.sciencedirect.com

ScienceDirect

materialstoday: PROCEEDINGS

Materials Today: Proceedings 2 (2015) 2886 – 2895

4th International Conference on Materials Processing and Characterization

CNT reinforced Aluminium matrix Composite-a review

Devanshu Singla[a] , Kaza Amulya[a] ,Qasim Murtaza[a]*

[a]Delhi Technological University, Shahbad Daulatpur, Bawana Road, Delhi-110042, India.

Abstract

This paper summarises the research work carried out in the field of carbon nanotube (CNT) aluminium matrix composites which are being investigated for their use in automobile and aerospace industries because of their low density and high specific strength .This paper addresses a brief description on fabrication techniques particularly ball milling which aims to achieve homogeneous distribution of CNT in the matrix. Also, the effect of ball milling parameters on CNT dispersion and the effect of CNT reinforcement on mechanical properties-toughness and hardness and friction and wear behaviour has been critically reviewed as well. The analysis presented here would be instrumental in the future design of high strength CNT/Al matrix composites.

Selection and peer-review under responsibility of the conference committee members of the 4th International conference on Materials Processing and Characterization.

Keywords: Carbon nanotubes(CNT); Aluminium; Ball milling;Mechanical properties; Friction and Wear behaviour.

1. Introduction:

In the past few decades, the research in material science has become focused on composite materials as they can be developed into light weight, environment friendly, and high performance appliances. At least two chemically distinct materials that are separated by a clear interface constitute a composite. As compared to conventional materials, composites have high stiffness and strength [1]. In the past few decades, ongoing research in CNTs as

* Corresponding author. Tel.:9654364948
E-mail address: qasimmurtaza@dce.ac.in

Selection and peer-review under responsibility of the conference committee members of the 4th International conference on Materials Processing and Characterization.
doi:10.1016/j.matpr.2015.07.248

reinforcements in composite materials has not focused much on CNT reinforced Metal matrix composites [2].

Today, most of the structural materials used being metals, CNT reinforced metal matrix composites has the potential to revolutionize aerospace ,automotive and sports industries where light weight combined with high stiffness and strength is desired [3].Aluminium is known for its low density making it ideal for aerospace and automotive industries; however, it is severely limited by its low strength. The carbon nanotubes have a Young's modulus of 1TPa and exceptional chemical stability due to their seamless cylindrical graphite structure makes it an ideal candidate for the reinforcement in aluminium matrix [4].Currently CNT/Al composites are in research phase with no viable commercial applications. These composites find potential application in automobile and aerospace industries for the manufacturing of brake shoes, cylinder liners and aircraft landing gears due to its low density, high strength and good wear resistance. In sports industry, light weight bicycles, tennis and badminton rackets can be manufactured utilizing its high elastic modulus. Thus, CNT/Al composites can be utilized in real life applications by overcoming the challenges in processing and achieving improved mechanical properties.

Thus, this paper will provide a detailed study on the research done with CNTs as reinforcement in aluminium metal matrix composites. Also, it focusses on high energy ball milling as processing technique and its effect on mechanical properties.

In 1960, graphite whiskers possessing flexibility and tensile strength up to 20 GPa was demonstrated by Roger Bacon. [2]. Large scale production of these fibres was achieved by carbonization of Rayon, Poly-Acrylonitrile (PAN), or pitch. By 1970, high strength of carbon fibres made it the best choice for manufacture of advanced composites for use in rocket nozzle exit cones, missile nose tips, re-entry heat shields, packaging and thermal management [5]. However, it was only after 1991 when Iijima discovered that CNTs were tubes made by rolling a graphene sheet onto itself, its true potential in the coming years was realised [6]. Thus, it was established with further research that CNTs are the strongest fibres known yet with stiffness up to 1000 GPa, strength of the order of 100 GPa and thermal conductivity of up to 6000 W m^{-1} K^{-1}[5]. The various methods for CNT synthesis have been illustrated with figure 1 below:

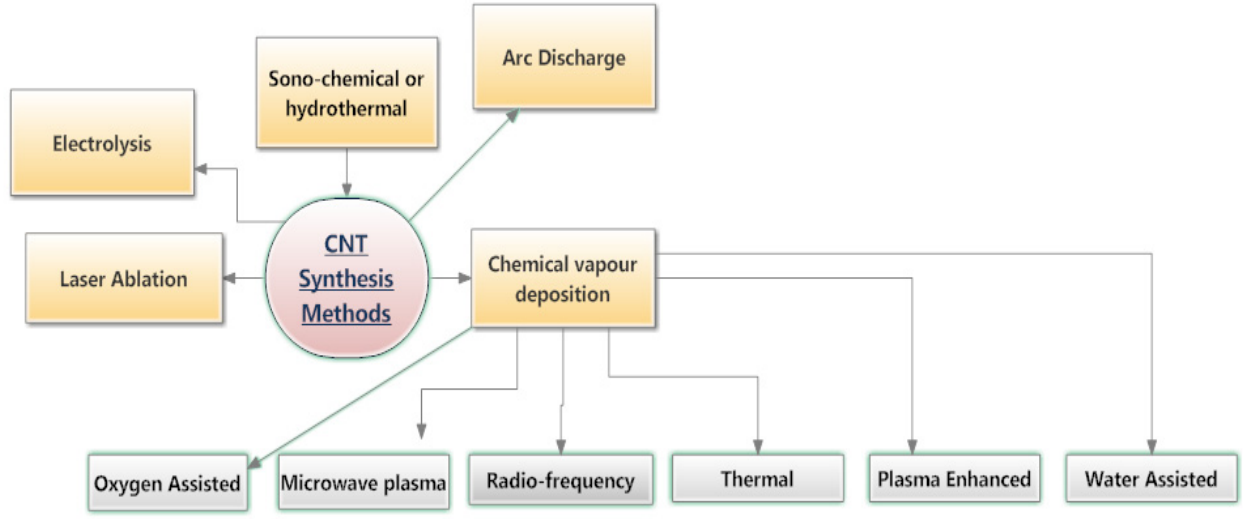

Fig1. Various method of CNT synthesis [adapted from 24]

2. Composite Fabrication Techniques:

Aluminium has been reinforced with CNT by various processing techniques such as ball milling, friction stir processing and spark plasma sintering in order to improve its strength and stiffness while maintaining its light-weightedness. The homogeneous mixture is then hot extruded, standard test samples are machined and tests are

performed to observe improvement of mechanical properties [3].The various processes have been briefly discussed as follows:

2.1 friction stir processing:

This method uses a non-consumable rotating tool inserted into the workpiece. This tool then travels along the region of interest, thus heating it due to friction produced by the tool rubbing on the workpiece. This heat results in plastic deformation and the material being soft starts to flow around the tool from its front to its back. This process leads to a severely deformed and well dispersed material, keeping it in solid state, thus eliminating deformities produced during solidification [7]. Johannes et al. [8] and Morisada et al. [9] reported an increase in HV hardness using friction stir processing.

2.2 spark plasma sintering:

The sintering method leads to densification in 1 vol. % CNT upto 96.8% relative density to Al powder. Enhancements in tensile strength are attributed to reduction in movements of dislocations. It is this resistance to plastic deformation when stressed that resulted in control of boundary layer [10].

2.3 spread dispersion method:

In this method, several sheets are layed, pressed and rolled thus bonding them into one layer. The tensile strength was reported to be increased by 66%and grain structure refined to 20 nm. The improvement in the properties can be attributed to uniform dispersion of CNTs without clusters or CNT- free zones, no porosity, improved bonding between Al/CNT and retention of graphite properties [11].

2.4 *stir casting:*

In this process, aluminium ingot is melted in a muffle furnace followed by addition of a purified sample of Multi Walled Carbon Nanotubes (MWCNT) powder. The mixture is then mixed with a stirring bar. The resulting mixture is poured into a die and solidified. There has been use of ultrasound energy to continuously stir the melt followed by the particles being injected into it [28]. However, using stir casting, reduction in tensile strength in 2wt% MWCNT was reported as compared to lower CNT content [25].It is a low cost process but also the reinforcement phase is not uniform throughout the matrix phase. This problem arises due to irregular flow of melt at the time of pouring of melt in the mould and at the time of solidification, stirring in the mould almost becomes impossible [28].

2.5 ball milling:

In high energy ball milling, materials are grinded into extremely fine powder by the action of high pressure generated locally due to the collision between the tiny and rigid balls [12]. The grinding action results in effective dispersion of CNTs in aluminium matrix by breaking up the entangled CNTs but it can also lead to structural and morphological damage to CNTs [12].

In hot extrusion process, the milled powder is initially placed in a passive atmosphere to avoid oxidation/burning. Then, it is placed in a high temperature steel mould in an inert atmosphere followed by the mould being heated at the desired extrusion temperature for a suitable time. Finally, it is extruded at a particular extrusion ratio and rate [27].

In order to achieve an optimum mechanical performance, the CNTs need to be uniformly dispersed in the Al matrix .The uniform dispersion also results in good interfacial bonding between CNTs and aluminium matrix which is very important for load transfer from matrix to CNTs. However, van der waal forces of attraction between the CNTs makes them vulnerable to agglomeration which is one of the prime challenges faced [13]. Due to low cost and availability of catalytic MWCNTs, these have been primarily used by researchers [14] .Use of high energy ball milling has been reported to be an effective processing technique in dispersing CNTs in the aluminium matrix as it produces a homogeneous composite with a fine microstructure and a good distribution of dispersed particles [13, 14, 26]. A mixture of aluminium and CNTs when ball milled were reported to be well dispersed over the surface of the deformed aluminium powders. Subsequently, CNTs are embedded in the matrix with cold welding of the deformed powders also protecting it from the harsh milling conditions [15].

However, it was recently reported that the CNTs are mostly damaged when milled with aluminium powders [14].

Therefore, the process of ball milling has been critically studied in this review as it is a promising processing technique to efficiently control agglomeration of CNTs [26].

3. Ball Milling Methodology:

In this process, a powder mixture is placed in the ball mill which is subjected to high-energy collision from the balls. The ball milling process or mechanical alloying is carried out using planetary mill or a horizontal ball mill. This process leads to cold welding and fracturing and for successful alloying these two processes must be balanced. Planetary ball milling is suitable for research purpose as a very small amount of powder is required. The ball milling apparatus consists of one (turntable) that rotates in one direction and two or four bowls which rotate in the opposite direction. The powder mixture is fractured and cold welded due to the centrifugal forces leading to high energy impact. Microstructurally, the mechanical alloying process can be divided into four stages: (a) initial stage, (b) intermediate stage, (c) final stage, and (d) completion stage.

(a) Initially, compressive forces due to collision of the balls flatten the powder particles. Micro-forging changes the shapes of individual particles or cluster of particles due to repeated impact by the milling balls possessing high kinetic energy with no net change in mass.

(b) Micro forging is followed by cold welding where the intimate mixture of the powder constituents reduces the diffusion distance to the micrometer range. Fracturing and cold welding are the dominant milling processes at this stage.

(c)The microstructure of the particle becomes more homogenous in microscopic scale due to particle refinement as compared to earlier stages. True alloys may have already been formed.

(d) At the completion stage of the mechanical alloying process, the powder particles possess an extremely deformed metastable structure. At this stage, the lamellae are no longer resolvable by optical microscopy.

The following parameters were found to be of critical importance during our review:

3.1 *milling time:*

With the increase in milling time, the aluminium powders changed to flaky morphology increasing the surface area, thus increasing the formation of Al_2O_3 which reduces the ductility and increases the hardness [16].

With a milling time of 30 minutes and 2% wt. content of CNT in aluminium MMC, A.M.K Esawi et al. reported a 50% increase in strengthening and 23% increase in Young's modulus [3] whereas the results concluded by Z.Y. Liu et al. for a progressively increasing milling time of 2, 4, 6,8,12 hrs showed that the Al powders got thinner as ball milling time increased. The high surface area and flat morphology of powders provided more sites for CNT dispersion and thus were beneficial to the uniform distribution of CNTs [12]. Another work by M.Raviathul Basariya et al. inferred that with an increase in milling time from 10-50 hrs, nano-hardness and elastic modulus values doubled as compared to that of pure aluminium, with a hardness value of 0.7 GPa and elastic modulus of 76 GPa [16] as shown in figure 2. Yoshida et al. reported a 285% increase in mechanical performance with a milling time of 20hrs [13].

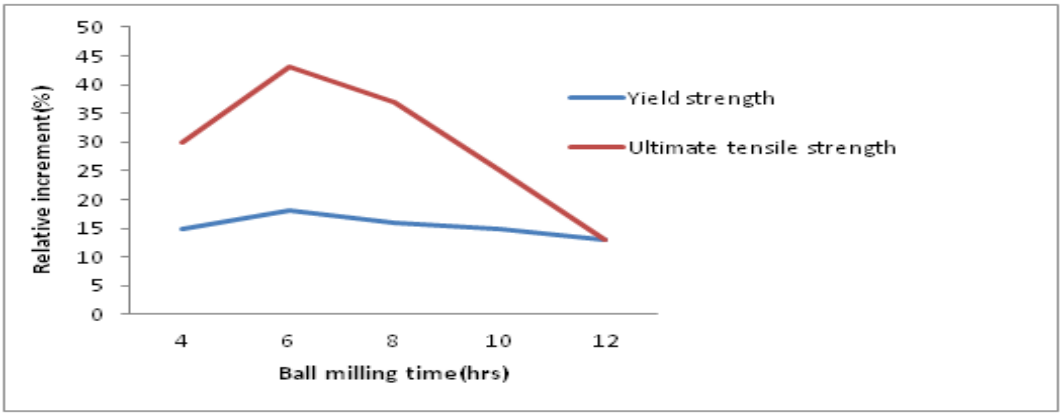

Fig2.Relative increments of Ultimate Tensile Strength and Yield Strength of CNT/Al composites relative to Al matrix [adapted from 12]

The CNTs were gradually dispersed into the Al matrix as ball-milling time increased and achieved a uniform dispersion after 6 hrs ball-milling. Further, increasing the ball-milling time to 8–12 hrs resulted in serious damage to the CNTs. The tensile tests showed that as the ball-milling time increased, the tensile and yield strengths of the composites increased, while the elongation increased first and then decreased. The strengthening of CNTs increased significantly as the ball-milling time increased to 6 hrs, but then decreased with further increasing the ball-milling time. The yield strength of the composite with 6 hrs of ball-milling increased by 42.3% compared with the unreinforced matrix [12]. Therefore, it can be concluded from the earlier research publications as cited above, the milling time plays a significant role in the enhancement of the mechanical properties. But it's not the only parameter as the results concluded by various researchers showed no convergence. The reason behind this is the effect of the following parameters – type of CNT (Multi-walled/Single walled), CNT aspect ratio, CNT + Aluminium powder composition by particle size, experimental procedure used for CNT synthesis, and specifications of ball milling setup.

3.2 *CNT content:*

The CNT content by weight in Aluminium metal matrix directly affects the strengthening and Young's modulus of elasticity. Previous works by A.M.K. Esawi et al. has reported that addition of 2 wt.% CNT provides the most significant strengthening (50% increase) and Young's modulus (23% increase) but saturates at 5 wt.% CNT [12].

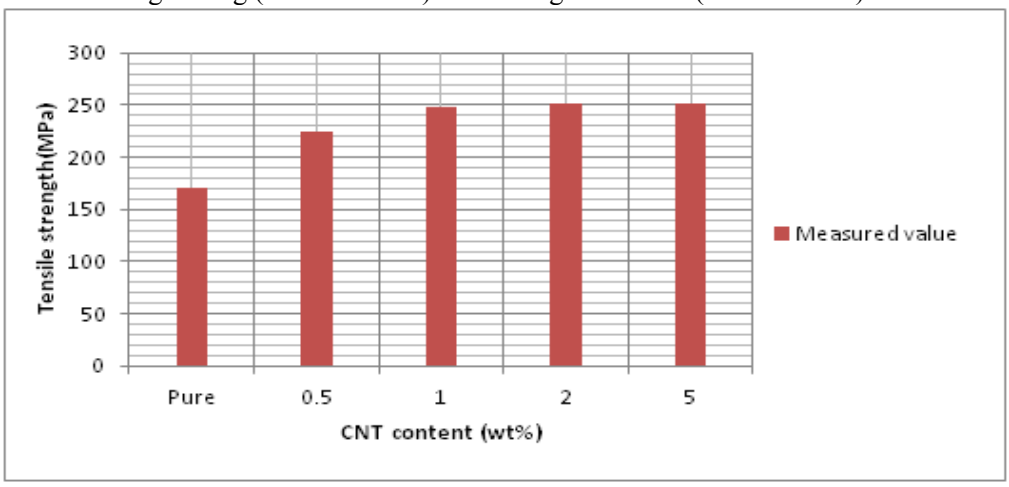

Fig3. The effect of CNT content on the tensile strengths of the investigated composites [adapted from 3]

3.3 diameters of CNTs:

The diameter of CNTs affects the dispersion of CNTs in aluminium matrix significantly. The larger diameter (140nm) CNTs disperse easily in the aluminium matrix than the smaller diameter (40nm) ones which had a stronger tendency to agglomerate [14]. CNTs with 140 ± 30 nm outer diameters, 4-8 nm internal diameters have been previously employed during composite fabrication [17].

3.4 process controlling reagents:

A variety of Process Controlling reagents such as Toluene[16], methanol[3 , 14], 1 wt.% stearic acid [12] ,1 wt.% ethanol and stearic acid [18] have been used previously to achieve the following characteristics:

1. Minimises cold welding of the Al particles and prevents powder sticking to the balls and the jar walls [3, 14].
2. Promotes the refinement of Al particles but may also increase the damage of CNT during the ball milling process [18].

3.5 inert gas atmosphere and ball to powder ratio:

All the milling experiments are carried out in an inert gas atmosphere such as argon in order to prevent decomposition of CNTs at high temperature. Usually, ball to powder weight ratio – 10: 1 [16], 8: 1 [12], 5: 1 [14] is employed.

4. Effect on Mechanical properties:

4.1 hardness:

The Incorporation of CNTs, particularly functionalized ones substantially improve the hardness. Even with an addition of a small quantity of CNT, the Vickers hardness number can increase by three times as compared to pure aluminium [19].The increase in hardness is attributed to the combination of various strengthening mechanism such as:

(1) The ball milling introduces a large amount of deformation leading to high dislocation density in powder particles. This increases the lattice strain.

(2) Interruption of dislocation movement.

(3) Thermal mismatch between MWCNT and Al-alloy (MWCNTs with thermal expansion coefficient of 10^{-6} K^{-1} and Al-alloy with thermal expansion coefficient of $24*10^{-6}$ K^{-1}) leads to mechanical adhesion of the MWCNTs to the matrix due to volume contraction of Al after milling [16].

The other reasons which can be put forward for the increase in the composite particle hardness are (a) the work-hardening effect due to plastic deformation during milling (b) Solution hardening as a result of higher solubility of alloying elements in nanostructured matrix and (c) reduced probability of large scale of cluster formation [16].

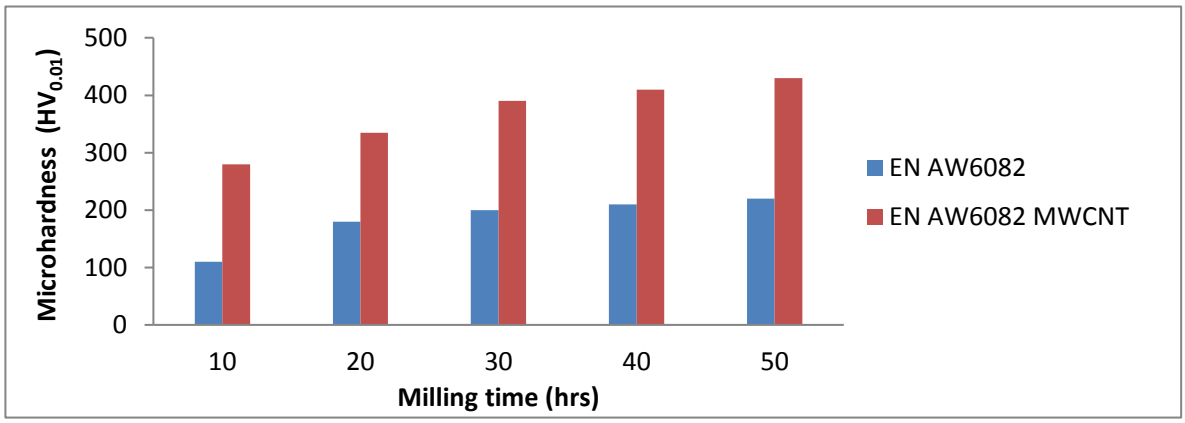

Fig4. Effect on hardness of unreinforced EN AW6082 and composite powders with increasing milling time [adapted from 16].

M. Raviathul Basariya et al. [16] investigated the effect of milling time on micro-hardness of CNT reinforced aluminium composite. It was found that the hardness value of both the unreinforced EN AW6082 and reinforced nano-composite powder increased with milling time as shown in figure 4. The deformed structure due to high energy milling was the primary reason for improve in hardness of unreinforced alloy. It was observed that the hardness of both the composite and unreinforced alloy increased significantly during earlier stages of milling. Due to the completion of alloying and the occurrence of dynamic recovery as a result of high work hardening effect of the deformed matrix, the hardness increased slowly at longer milling time. The MWCNTs added as reinforcement in Al alloy interacts with the dislocations, generating high dislocation density thus leading to further grain refinement. The hardness value increasing with the milling time attained a maximum value of 436 HV after 50 hrs of milling whereas 10 h of milling resulted in a hardness value of less than 300 HV. Perez-Bustamante et al. [20, 21] proposed that the mechanical properties increase due to uniform distribution of MWCNTs in the matrix which effectively inhibits matrix deformation, thereby producing a strengthening effect.

4.2 toughness:

Fig.5 shows the effect of CNT addition on the ratio of the failure strain of Al/CNT composite to that of un-reinforced Al sample. All the previous studies have reported a reduction in the ductility of the composite with CNT addition as also depicted in the fig. 5 and 6. This trend is obtained from the tensile data on the samples prepared by Esawi et al. [17]. Poor dispersion and poor CNT-matrix bonding lead to low strengthening and decrease in ductility. A poor CNT–matrix bonding can be susceptible to cracking nucleation under tension. Due to the small size of the CNTs, the cracks may be smaller and below the critical flaw size to create any damage. However overlapping of CNTs leading to interconnected cracks can cause premature failure of the composite. The second trend is obtained from data from Choi et al. [21]. It depicts that strengthening is achieved at the expense of ductility. This is

commonly observed in fibre reinforced composites because of smaller ductility of the fibre. So there is an adjustment that needs to be made between strength and ductility.

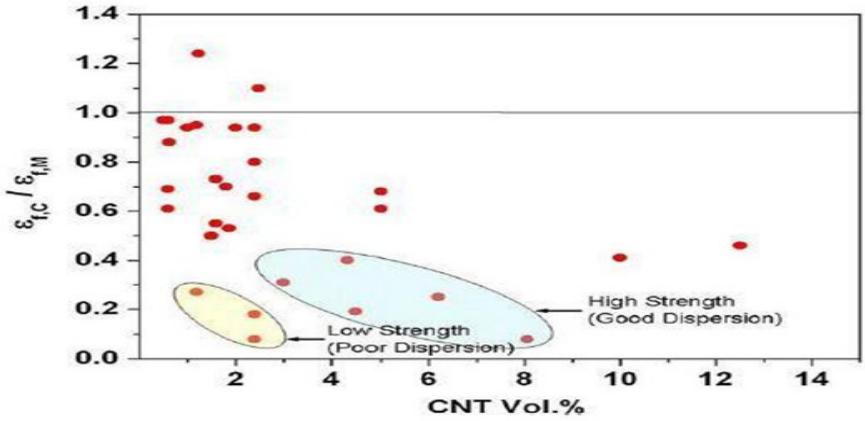

Fig5. Effect of CNT content on the ratio of failure strain of Al/CNT composite to un-reinforced Al sample [22].

Fig.6 shows the percentage change in the toughness of Al/CNT composites over Al sample prepared by the same route. It is observed that there is a lot of variation in the data. Poor CNT dispersion leads to decrease in toughness as shown by the data by Esawi et al. [17]. Toughness of the composite decreases when the CNT concentration increases above 5%. The effect of the increase in the strength resulting from good dispersion is suppressed by the decrease in ductility.

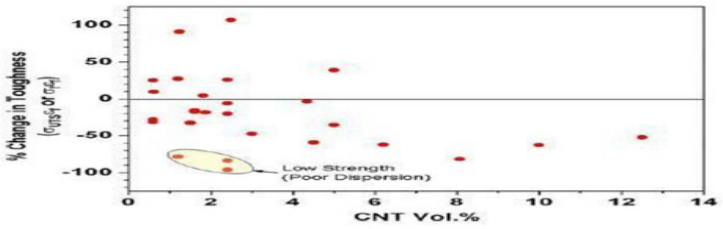

Fig6. Effect of CNT content on change in the toughness of Al/CNT composites over Al sample [22].

4.3 friction and wear behaviour of CNT-Al composites:

Esawi et al. [23] experimented by varying the CNT content from 0 wt.% up to 5 wt.% and these samples were tested at different sliding speeds and acted upon by different loads. The results showed a significant increase in the hardness and the wear resistance, as well as a decrease in the coefficient of friction and the wear rate. The coefficient of friction was observed to decrease with increase in sliding speed; the wear rate increased while the coefficient of friction decreased on increasing the applied load.

The SEM observations by Esawi et al. showed the presence of a carbon film formed due to crushed or worn out CNTs which acted as a solid lubricant and thus was instrumental in reducing the wear rate and coefficient of friction. The non-embedded CNTs in the matrix reduced the wear of the surface directly in contact with the rubbing surface, thereby improving the wear characteristics.

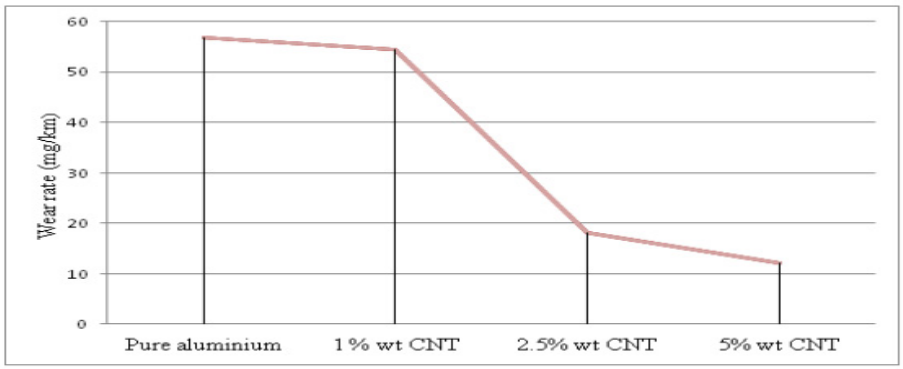

Fig7.Wear rate versus CNT wt. % [adapted from 23]

5. Conclusion:

In this paper, the improvement of mechanical properties such as toughness, micro-hardness and friction and wear behaviour in carbon nanotube reinforced aluminium composites has been carefully analysed. It is evident that the milling time plays a very significant role in the enhancement of mechanical properties especially Young's modulus of elasticity. Also, the effect of CNT content, process controlling reagents, diameter of CNTs and inert gas atmosphere on CNT/Al composite is examined. Using data from various experiments conducted with ball milling technique, it is concluded that CNT dispersion is very critical in obtaining high strengthening of composite.

Thus, the ball milling conditions need to be optimized to achieve the best combination of CNT dispersion, improved CNT/metal interface, reduced cold working of the metal matrix and minimum damage to the CNTs. Further challenges include achieving uniform dispersion of CNTs at high concentration, dispersion of CNTs at micro-level if bulk manufacturing techniques are utilised, effect of alignment of CNTs, bridging the gap between nano-scale and bulk properties and developing innovative methods keeping these aspects in mind.

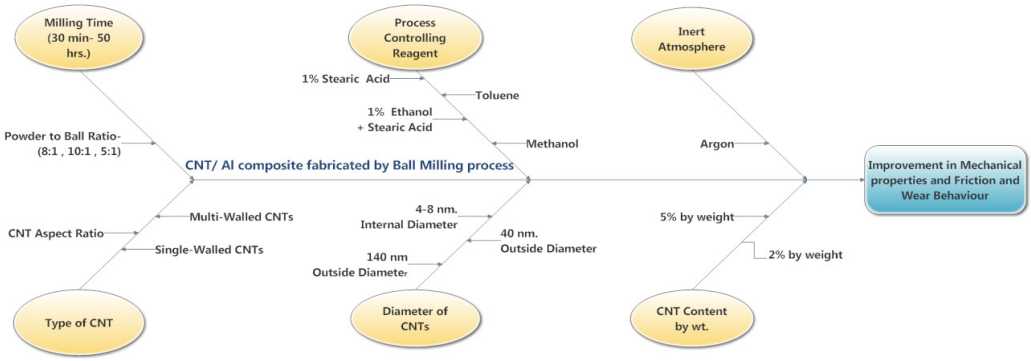

Fig. 8 Fish-Bone diagram illustrating the parameters that improve the mechanical properties and friction and wear behaviour of Aluminium matrix composite

6. References:

[1] Kim H.H.; J.S.S Babu., C.G. Kang; Fabrication ofA356aluminum alloy matrix composite with CNTs/Al2O3 hybrid reinforcements; *Materials Science & Engineering*, 2013, A573, 92–99.

[2] R. Bacon; *Appl. Phys*., 1960, 31, (2), 283–290.

[3] Esawi A.M.K.; K. Morsi, A. Sayed, M. Taher, S. Lanka; Effect of carbon nanotube (CNT) content on The mechanical properties of CNT-reinforced aluminium composites; *Composites Science and Technology,* 2010, 70, 2237–2241.

[4] Shadakshari R; K. Mahesha, H.B. Niranjan; Carbon Nanotube Reinforced Aluminium Matrix Composites – A Review; *International Journal of Innovative Research in Science, Engineering and Technology*, 2012, Vol.1, issue 2.

[5] Bakshi S. R.; D. Lahiri, A. Agarwal; Carbon nanotube reinforced metal matrix composites – a review; *International Materials Reviews*, 2010, Vol. 55, 41-64.

[6] IIjima S.; *Nature*, 1991, 354, 56–58.

[7] Liu Z.Y. ; B.L. Xiao, W.G. Wang, Z.Y. Ma; Singly dispersed carbon nanotube/aluminum composites fabricated by powder metallurgy combined with friction stir processing; *Carbon* , 2012, 50, 1843-1852.

[8] Johannes LB; L.L. Yowell, E. Sosa, S. Arepalli, R.S. Mishra; Survivability of single-walled carbon nanotubes during friction stir processing; *Nanotechnology*, 2006; 17 (12), 30814.

[9] Morisada Y; H. Fujii, T. Nagaoka, M. Fukusumi; MWCNTs/AZ31 surface composites fabricated by friction stir processing; *Mater Sci Eng A*, 2006, 419(1–2), 344–8.

[10] Kwon H.; D.H. Park, J.F. Silvain, A. Kawasaki; Investigation of carbon nanotube reinforced aluminum matrix composite materials; *Composites Science and Technology, 70,* 2010, 546–550.

[11] Lao J.; M.J Tan.;A simple approach to prepare Al/CNT composite: Spread–Dispersion (SD) method; *Materials Letters*,2011, Vol.65, Issues 17-18,2742-2744.

[12] Liu Z.Y. ; S.J. Xu, B.L. Xiao, P. Xue, W.G. Wang, Z.Y. Ma ; Effect of ball-milling time on mechanical properties of carbon nanotubes reinforced aluminum matrix composites ; *Composites*, 2012, PartA43, 2161-2168

[13] Bustamante R.P; I..E. Guela, L.L. Jiménezc, M.M Yoshidaa, R. M Sáncheza ; Effect of milling time and CNT concentration on hardness of CNT/Al_{2024} composites produced by mechanical alloying ; *Material characterization,* 2013, 75, 13-19.

[14] Esawi A.M.K. ; K. Morsi , A. Sayed , M. Taher , S. Lanka ; The influence of carbon nanotube (CNT) morphology and diameter on the processing and properties of CNT-reinforced aluminium composites ; *Composites*, 2011, PartA42, 234-243.

[15] Choi H.J ; G.B. Kwon, G.Y. Lee ,D.H. Bae ; Reinforcement with carbon nanotubes in aluminum matrix composites; *Scripta Materialia ;* 2008, 59, 360-363.

[16] Basariya M. Raviathul ; V.C. Srivastava , N.K. Mukhopadhyay ; Microstructural characteristics and mechanical properties of carbon nanotube reinforced aluminum alloy composites produced by ball milling ; *Materials and Design,*2014, 64, 542-549.

[17] Esawi A.M.K ; K. Morsi, A. Sayed, A. Gawad, P. Borah ; Fabrication and properties of dispersed carbon nanotube–aluminum composites; *Materials Science and Engineering*, 2009, A508, 167-173.

[18] Peng T; I. Chang ; Mechanical alloying of multi-walled carbon nanotubes reinforced aluminum composite powder ; *Powder Technology*, 2014, 266, 7-15.

[19] Silvestre N; State-of-the-art Review on Carbon Nanotube Reinforced Metal Matrix Composites; *International Journal of Composite Materials; 2013, 3(6A), 28-44.*

[20] Bustamante R.P.; M.J.G. Ibarra, J.G. Cantú, I.E. Guel, J.M.H Ramírez, M.M. Yoshida, R.M. Sánchez; AA2024–CNTs composites by milling process after T6-temper condition; *Journal of Alloys and Compounds*, 2012, 536S, S17-S20.

[21] Bustamante P.R.; G.C.D Esparza, I.E. Guel, M.M. Yoshida, L.L Jiménez; P.L.A. García; Microstructural and mechanical characterization of Al-MWCNT composites produced by mechanical milling; *Mater Sci Eng A,* 2009,502,159–63.

[22] Bakshi S.R.; A. Agarwal; An analysis of the factors affecting strengthening in carbon nanotube reinforced aluminum composites; *Carbon*, 2011, 49, 533-544.

[23] Bastwros Mina M.H ; Amal M.K. Esawi , Abdalla Wifi; Friction and wear behaviour of Al–CNT composites; *Wear*, 2013, 307, 164-173.

[24] Prasek J., J. Drbohlavova, J. Chomoucka, J. Hubalek, O. Jasek, V. Adamc, R. Kizek; Methods for carbon nanotubes synthesis—review; *Journals of Materials Chemistry*, 2011, 21, 15872.

[25] Girisha L.; G. Raji; Study on Properties of Multi Walled Carbon Nanotube Reinforced Aluminum Matrix Composite through Casting Technique; *International Journal of Engineering Research & Technology (IJERT),* 2014, Vol. 3 Issue 4.

[26] Esawi AMK; K. Morsi; Dispersion of carbon nanotubes (CNT) in aluminium powder; *Composites*, 2007, Part A 38, 646-650.

[27] Kwon H.; M. Leparoux; Hot extruded carbon nanotube reinforced aluminum matrix composite materials; *Nanotechnology, 2012*, 23, 415701.

[28] Ghauri K.M.; L. Ali., A. Ahmad, R. Ahmad, K.M. Din, I.A. Chaudhary, R. A. Karim; Synthesis and Characterization of Al/SiC Composite Made by Stir Casting Method; *Pak. J. Engg. & Appl. Sci*., 2013, Vol. 12, 102-110.

Accepted Manuscript

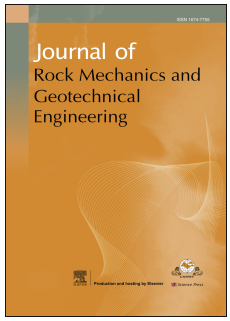

Computing in-situ strength of rock masses based upon RQD and modified joint factor: Using pressure and damage sensitive constitutive relationship

Ashutosh Trivedi

PII: S1674-7755(15)00088-8

DOI: 10.1016/j.jrmge.2015.05.005

Reference: JRMGE 185

To appear in: *Journal of Rock Mechanics and Geotechnical Engineering*

Received Date: 8 February 2015

Revised Date: 15 May 2015

Accepted Date: 28 May 2015

Please cite this article as: Trivedi A, Computing in-situ strength of rock masses based upon RQD and modified joint factor: Using pressure and damage sensitive constitutive relationship, *Journal of Rock Mechanics and Geotechnical Engineering* (2015), doi: 10.1016/j.jrmge.2015.05.005.

Computing in-situ strength of rock masses based upon RQD and modified joint factor: Using pressure and damage sensitive constitutive relationship

Ashutosh Trivedi*

Department of Civil Engineering, Delhi Technological University, Delhi, India

Received 8 February 2015; received in revised form 15 May 2015; accepted 28 May 2015

Abstract: In this study, a new model was presented for computing strength of rock masses based upon in-situ observations of RQD popularly known as rock quality designation. This model links up the rock mass parameters from in-situ investigations with the strength parameters of jointed rocks obtained from laboratory scale experimental observations. Using the constitutive relation, the author derived a pressure and damage sensitive plastic parameter to determine strength of rock masses for varied extents of discontinuity and pressure induced damage. The test results show that plasticity characterized by hardening and softening inclusive of damage invariably depends upon mean pressure and extent of deformations already experienced by rock masses. The present work explores the test data that reveal the dependence of in-situ strength on incremental joint parameters obtained from the joint number, joint orientation, joint roughness, gouge parameters and water pressure. Substituting the relationship between the RQD and modified joint factor with that between modulus ratio and strength ratio, the model shows successfully that using damage inclusive plastic parameter and RQD provides a relationship for estimating the strength of rock masses. One of the main objectives of this work is to illustrate that the present model is sensitive to plasticity and damage together in estimating in-situ strength of rock masses in foundations, underground excavation and tunnels.

Key words: strength ratio; rock mass; plastic parameter; joint parameters; damage; rock quality designation (RQD)

1. Introduction

Mechanical properties of rock mass interpreted by engineers in field differ significantly due to the micro-disconformities of strength. The failure theories indicate that the strength is a thermodynamic state depending upon isotropic pressure, which is insignificant at the opening of the discontinuity and reaches a peak at a location of stress concentration. The peak pressure seeks adjustment due to localization of deformation. This process of adjustment, accompanied by plastic deformations, proceeds through a path-specific initial condition to a state often referred to as failure. In the course of compression, rock masses show varied levels of hardening and softening together in relation to the tension, isotropic pressure and peak uniaxial compressive strength of relatively intact rocks. The initial confinement for varied joint conditions sets a path-dependent guided deformation up to failure stress. The plastic theories of failure propose the path- dependent guided deformation incorporating stress invariants (I_1, J_2, J_3) (Yu, 2006) where the confining pressure, the magnitude of shear stresses and their directions control the failure behavior. The critical state model (Roscoe et al., 1958) suggests a robust model to explain shear deformation of soft homogeneous granular material which confirms that critical state line shifts downward as grading broadens (Li et al., 2015), as that happens in case of increasing the number of joints in rock masses. The behaviors of mass materials, consisting of inherent and induced discontinuities, anisotropy, and non-homogeneities, namely, rock masses, require considerations of cumulative plastic strains in a relatively intact and fully adjusted state, which can be explained realistically by the disturbed state concept (DSC) (Desai, 2015a, b).

During deformation, all the mass materials show conservative and dissipative work components. With the progress of plastic deformation, there is a zone of plastic flow. As a result, a component of work dissipates as a scatter of thermal output, often ignored in rock engineering practices. The limited plastic flow, carried forward at varied strength ratios, is the cumulative irrecoverable strain, which finally develops into continuous joint. The strength ratio (σ_{mr}) is a ratio of the strength (σ_m) of rock mass containing a network of joints to unixial compressive strength of intact rocks (σ_i) where the network of joints is microscopic. With the progress of loading, a flow rule depending upon a plastic potential function captures the plastic flow. The deformation of fractured rock mass undergoes hardening and/or softening, which makes it hard or soft on yield relative to its reference state. In other words, the hardening mode sets a condition for contraction, while the softening assumptions permit gradual dissociation of grains at micromechanical level (Fig. 1). Such microscopic dissociations, frequently bring conflicting deformation in rock masses at macro-mechanical level, are often mapped by jointing patterns visible on scan line survey as captured by the rock quality designation (RQD) (Table 1). The RQD is one of the most popular rock investigation techniques. It uses directly the in-situ core recovery data of rock mass and is defined as percent recovery of intact pieces of rock core larger than 10 cm to the total length of drilled core (usually 100 cm) as proposed by Deere et al. (1967). Therefore, the present work proposes a relationship between strength ratio and RQD incorporating nonlinearity owing to rock mass mapping and intrinsic joint characteristics. The mean confining pressure (p_i) induces a progressive hardening or softening through strain energy storage, respectively, up to a value related to uniaxial compressive strength of intact rock (σ_i). This strain energy dissipates at a rate depending upon a pressure sensitive dissipation process.

*Corresponding author. Tel: +91 1127871027; E-mail: atrivedi@dce.ac.in

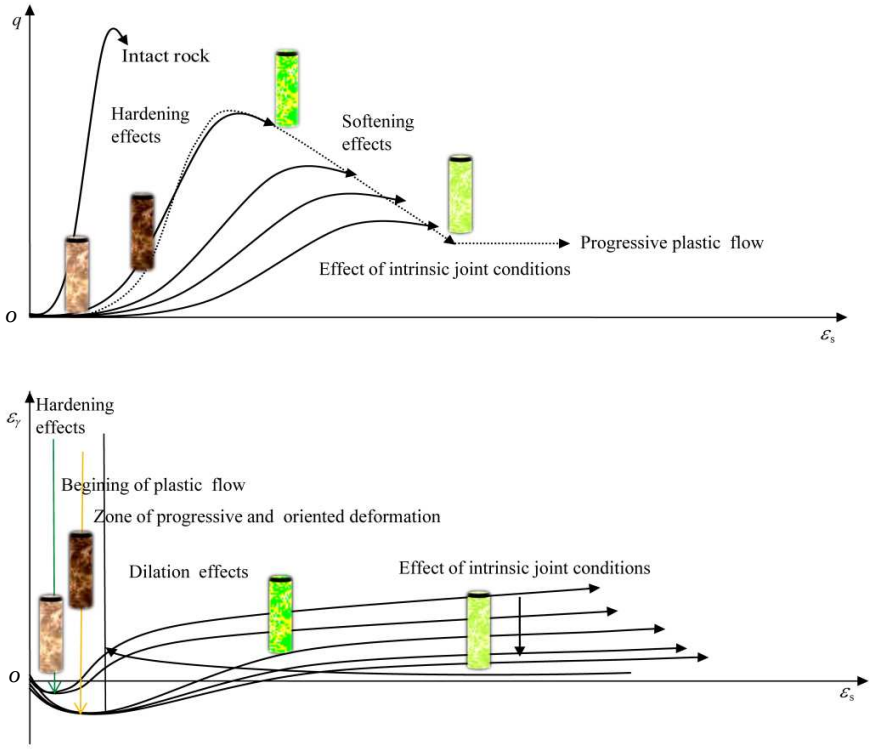

Fig. 1. Shear-volume change characteristics of rock masses under mechanical loading.

1.1. Evolution of pressure and damage sensitive plastic parameters

Drucker and Prager (1952) and Drucker (1959) described in their seminal work that the mass materials may experience isotropic and kinematic hardening (Shield and Ziegler, 1958) and softening. The temporal softening process invokes a plastic flow as postulated by several investigators (Roscoe et al., 1958; Hirai and Satake, 1982; Spitzig and Richmond, 1984). Based upon these concepts, the author considered a transition of yield surface due to a progressive plastic flow for the rock mass, which transforms in the stress space. The yield surface may expand, contract, change its shape or translate upon loading and yield characterized by a pressure to set a plastic flow. Then a flow rule governs the evolution, both in the magnitude and in the direction of the plastic strain rate with the stress and stress increment. Additionally, a hardening or softening rule accompanying damage provides scope for modified yield conditions during plastic flow. Based upon this concept, at an ambient temperature and initial isotropic pressure (p_y/σ_t), the joint hardening or softening occurs at a nonlinear rate. Therefore, this study recognized a pressure dependent and a pressure-temperature coupled nonlinear plastic parameter ($<C_{hs}>$) at granular level for unit changes in joint damage parameter ($<\eta_{hs}>$). $<C_{hs}>$ is piece-wise continuous in hardening or softening range, within the limits of $\ddot{I}$ and $\hat{I}$, such that they correspond to $\ddot{I} > <C_{hs}> > \hat{I}$. If $\ddot{I} \rightarrow 0$, the work is conserved, and the deformation is independent of joint contraction or dilation. The joint damage parameter is a ratio of modified joint factor (J_{fg}) in hardening and softening ranges. For an initial value of the plastic parameter, $\ddot{I} > <C_{hs}> > \hat{I}$, the rock masses undergo deformations with the effects of confinement, shape and size. The modified joint factor is physically estimated from joint and in-situ rock mass characterization, namely, RQD, with consideration of cumulative plastic strains. Although there are several variants of dilatancy dependent plastic parameter in the contemporary engineering literature (Taylor, 1948; Rowe, 1962, 1969; de Jong, 1976; Bolton, 1986; Yuan and Harrison, 2004) which consider cumulative plastic strains, one of the most popular definitions consists of the percent volume change following plastic deformation divided by the magnitude of the shear strain. If the ratio of shear stress to isotropic pressure is such that volume increases, then the specimens are strong at yield and hence dilate (Schofield and Wroth, 1968).

The force interaction at varied scales and plastic dilatancy experienced by various mass materials, namely, metals, soils, and rocks, vary in a widely significant range as reported in Tables 1 and 2, respectively. The author envisaged a relationship for volume change characteristics with the damage sensitive plastic parameters which varies between $\ddot{I}$ and $\hat{I}$ covered by the range of hardening and softening parameters affected by the applied pressure. It relates the strength of rock mass to the joint parameters with plastic parameters in selected range of observed values (Table 3).

Several early investigators such as Bieniawski (1978) and Serafim and Pereira (1983) affirmed that varied in-situ states, conditions and boundary settings may produce different deformations. The loading and boundary settings indirectly refer to the path sensitive deformations as duly considered in this work. This work conceives a consistent model for rock masses which connects the strength with a pressure sensitive plastic parameter including progressive failure (Trivedi and Sud, 2005) using constitutive relationship from the laboratory test data to in-situ testing, namely, RQD.

Table 1. Scan line survey for multi-grain, multi-block, block-grain interaction in mass materials and engineering solutions.

Scanning size (mm)	Example	Force interaction	Dominant activity and uses	Solutions
10^{-7}–10^{-6}	Electron cloud, ions [a]	Quantum mechanical interactions, no free parameters, few 100 s of atoms [b, c, d]	Determine crystal structure and defects	

10^{-6}–10^{-5}	Dilute granular interaction [e], Brownian motion, precipitation, sub-grain boundaries, micro- porous zeolite and clay formations [b, c, d], origin of micro-porous rocks [f]	Effective interaction potential, few million of atoms, molecular dynamics [e], sedimentation-consolidation processes [f]	Evolution of self-similar, self- assembled structures involving several so-called interacting defects	Initial value problem to boundary value
10^{-4}	Dislocations, meso-porous silicate formations [b, c, d]	Discrete material dislocation, elasticity-based modeling of large ensembles of defects	Aims to predict mechanical properties	
10^{-3}	Sub-grain-slip-band	Meso-friction, plasticity multi-mode interactions: macroscopic-friction, plasticity, dislocations, bifurcations, separations, disturbance, and damage; interaction of several thousand of bundle of blocks at micro-, meso- and macro- mechanical levels	Plane strain problem	
10^{-2}	Grain inclusions, voids		Plane strain to plane stress problem, forced interactions, damage sensitivities, aims to predict engineering behavior of mass materials	Boundary value problem to initial value
10^{-1}	Large plastic strains			
10^{0}	Elasto-plastic field			
10^{1}	Continued elasto-plastic assumption and observations, rebound-indentation			
10^{2}	Intact-sample-test-size such as core diameter in triaxial cell			
10^{3}	RQD-core scan line, rock-masses, multi-scale: multi-block interaction[g]			
$>10^{3}$	Massive structures			

Note: [a] McClintock and Irwin (1965) , [b] Förster and Plantenberg (2002), [c] Sen et al. (2003), [d] Innocenzi et al. (2013), [e] Luding (2009), [f]Trivedi et al. (2015), [g]Trivedi (2010, 2013a).

Table 2. Observed plastic dilatancy for various mass materials.

Material		Observed maximum plastic dilatancy	Material		Observed maximum plastic dilatancy
Aluminum	1100 aluminum[a]	0.0005	Rocks	Natural calcarenite [c]	~0.5
Steel	Maraging steel (unaged)[a, b]	0.001		Cemented soft rock [g]	1.5
	HY80 steel [a, b]	0.002		Soft rocks [h, i]	~3
	4310 steel [a, b]	0.004		Jointed rocks [j]	0.6 at high confinement 3 at low confinement
	4330 steel [a, b]	0.004		Vosges sandstone [k, l]	~0.6 at confinement of 30 MPa ~8 at confinement of 0.5 MPa
	Maraging steel (aged) [a, b]	0.007		Gebdykes dolomite [m, l]	~0.06 at confinement of 90 MPa ~8 at confinement of 5 MPa
Clay	Marl clay [c]	~0.5		Rock masses [n]	~1–5 (for ζ=1–5) inclusive of associated damages
	Leda clay [c]	~0.64			
Sand	Mersey river quartz sand [d, e]	1			
	17 different sands [f]	1.25			

Note: [a] Spitzig and Richmond (1984), [b] Stoughton and Yoon (2004), [c] Vatsala et al. (2001), [d] Horne (1965), [e] Rowe (1969), [f] Bolton (1986), [g] Castellanza and Nova (2004), [h] Hirai and Satake (1982), [i] Akai et al. (1978), [j] Trivedi (2010), [k] Besuelle et al. (2000), [l] Yuan and Harrison (2004), [m] Santarelli (1987), [n] Present work.

Table 3. Estimates of the maximum ($\ddot{I}$) and minimum ($\hat{I}$) values of α_p.

Material	$\ddot{I}$ (maximum)	$\hat{I}$ (minimum)	Data gradient	Selected data points	Determination coefficient
Gypsum [a]	–0.0053	–0.011	$e^{-0.0006 J_1}$	6	$r^2 = 0.0518$
Gypsum [b]	–0.0032	–0.015	$e^{-0.0008 J_1}$	4	$r^2 = 0.1056$
Concrete blocks [c]	–0.001	–0.011	$e^{-0.0006 J_1}$	10	$r^2 = 0.0168$
Plaster of Paris, Kota sandstone, granite [d]	–0.0017	–0.085	$e^{-0.0084 J_1}$	26	$r^2 = 0.3447$
Jamrani sandstone, Agra sandstone [e]	–0.0001	–0.019	$e^{-0.0002 J_1}$	30	$r^2 = 0.0023$
Kota sandstone [f]	–0.0054	–0.031	$e^{-0.0003 J_{1g}}$	17	$r^2 = 0.0012$
Plaster of Paris [g]	–0.0016	–0.012	$e^{-0.0005 J_1}$	50	$r^2 = 0.0396$
Cement blocks [h]	–0.002	–0.015	$e^{-0.0006 J_{1g}}$	14	$r^2 = 0.0168$

Note: [a] Brown (1970), [b] Brown and Trollope (1970), [c] Einstein and Hirschfeld (1973), [d] Yaji (1984), [e] Arora (1987), [f]Trivedi (1990), [g] Roy (1993), [h] Jain (2011).

Historically, varied rock mass classification systems, namely, rock mass rating (RMR) by Bieniawski (1978) and Nicholson and Bieniawski (1990), and geological strength index (GSI) by Hoek and Brown (1980), Hoek (1983), Hoek and Diederichs (2006), and Hoek and Martin (2014) using their prolific experiences, considered a set of field observations to propose compressive strength of rock mass. Hoek and Brown (1980) derived their strength criterion on the basis of a vast amount of data and knowledge gathered from the deformation of concrete which in fact has a strength comparable to intact rocks, both consisting of micro-disconformities. Kalamaras and Bieniawski (1995) used RMR, which included the joint spacing, and RQD to predict strength of rock mass. Martin et al. (1999) considered tunnel instability and brittle failure as functions of RMR and the ratio of the maximum far-field stress to the unconfined compressive strength. Villeneuve et al. (2012) considered the effect of grain scale heterogeneity on rock strength and the chipping process which is conceived as fragmentation of joints in several studies. As per Terzaghi (1946), the joints are among the most important causes of overbreak and of troubles induced by water, and they always deserve careful consideration. Additionally, RMR and GSI present a measure of qualitative assessment of jointed rock masses. The Q-system (Barton, 1986, 2013) considered six parameters including RQD, joint number, roughness, effect of gouge, conditions of joints, groundwater condition and stress reduction factor. McLamore and Gray (1967) pointed out the significant effect of the joint inclination on the strength of jointed rocks at low confinement. Ramamurthy and Arora (1994) and Trivedi (2010) considered joint parameters consisting of joint number, orientation, roughness

and block to propose the strength of jointed rock mass based on statistical and numerical analysis, respectively. Priest and Hudson (1976) and Sen (1984) proposed a relationship between discontinuity spacing and RQD to capture in-situ state of rock quality designated on a broad scale.

The deformation obtained from joint number, vertical and horizontal stiffnesses (Zhang and Einstein, 2004; Zhang, 2010; Trivedi, 2013a, b) provided a correlation with RQD obtained from different sources. The relationship between joint stiffness characteristics and rock mass deformation (Zhang, 2009) leaves a scope to consider a pressure and damage sensitive plastic parameter dependent on joint characteristics in order to predict strength of rock mass from RQD.

The equivalent continuum model (ECM) considers the rock mass as a continuum that reflects the deformations of both the intact rocks and discontinuities (Zhang, 2010). The ECM uses some of the strength properties of intact rocks and discontinuities from the laboratory as well in-situ tests as compared in Tables 4 and 5, where UCS is the unconfined compressive strength.

1.2. Scope of study

The early studies left a scope for estimation of pressure and damage sensitive parameters of rock masses as one of the unsolved issues. The strength of jointed rock mass was yet to relate a readily obtained plasticity unifying hardening, softening and damage sensitivities with experimentally estimated quantities obtained through measurements such as joint parameters and RQD.

Based upon the observations, the key features of the present study are presented as follows:

(1) The rock masses have characteristics of inherent and induced discontinuities, micro-structural dissociations, fractures, and massive non-homogeneities, namely, gouge. The inherent discontinuities normally present in the rock mass. The induced discontinuities are produced due to the presence of pressure.
(2) The rock masses consist of elastic and damage coupled plastic deformations.
(3) The stress invariants conveniently express the behavior of rock masses.
(4) The empirical data including JC-criterion (Johnston and Chiu, 1984; Johnston, 1985) provide a basis for obtaining yield functions.
(5) A pressure sensitive plastic parameter relates the initial to final conditions of joint and plastic yield.
(6) The experimental database provides a relationship between the rock mass strength and J_{fg} using a softening parameter. Similarly, there exists a relationship characterized by a hardening parameter between modulus ratio and J_{fg} in the hardening range.
(7) The in-situ exploration of rock mass provides a relationship between J_{fg} and RQD.
(8) Using the concept of joint damage, hardening and softening, a pressure sensitive plastic parameter is evolved.
(9) A pressure and damage sensitive plastic parameter connects strength of rock mass with RQD, which allows considering the effects of cumulative plastic strains and damage together.

The present study proposes that rock mass strength parameters should be re-examined to have potential for capturing extent of damage and plasticity, unifying effects of anisotropy, joint orientation, discontinuity frequency, presence of gouge, water pressure and especially plasticity due to the confinement and direction of shear stresses from initial to final conditions of failure in relation to the in-situ tests. A modified joint factor (J_{fg}), observed during rock explorations, considers intrinsic rock mass characteristics, i.e. discontinuity frequency such as joint number found from scan line, roughness from friction parameter, joint inclination using orientation parameter (Table 6), joint and gouge conditions, density of gouge, groundwater and stress conditions, to be incorporated in strength (Tables 4–6).

In this paper, the plastic parameter was obtained numerically for input of isotropic pressure ratio (p_i/σ_r), which was set into rock mass as per JC-criterion. The rock mass tends to reach failure upon loading. It was conceived in strength ratio (σ_{mr}). The strength ratio is obtained from laboratory tests on intact rock and jointed rock samples. It is influenced by the direction of joints, which in turn influences direction of shear stresses (J_3). The strength ratio (σ_{mr}) has been captured as a function of joint parameters, namely, modified joint factor (J_{fg}), and plastic parameter (C_{hs}). The strength loss as an effect of jointing pattern used in the present work has similar effects on DSC proposed by Desai (2015a, b), which recognizes a relatively intact strength and fully adjusted state where the effect of damage inclusive cumulative plastic strain may decrease strength values to be lower than the values predicted by the critical state model.

Table 4. Strength ratio from rock mass characterizations systems (RMR, GSI, RQD and Q-system).

Rock mass characterization system (scale)	RQD	Joints spacing (m)	UCS (MPa)	Joint water pressure ($J_w=u/\sigma_1$)	Inflow (J_k) (L/min)	Gouge thickness parameter (t/t_a) (J_a) (mm)	Roughness parameter (J_r)	Orientation parameter (n_{β}) (^{0})	SRF	Application
RMR	100–0 (R_1=25–0)	0.01–10 (R_2=25–0)	300–0 (R_3=16–0)	0–0.6 (R_4=16–0)	1–1000 For 10 m tunnel (R_4=16–0)	0-6 (R_5=35–0)	-	0 - 90 (R_6=–30–0)	-	Tunnels deformations
(0-100)	$RMR=R_1+R_2+R_3+R_4+R_5+R_6$; [a] σ_{mr}= [exp{(RMR–100)/9}]$^{0.5}$ and [b] σ_{mr}= exp[(RMR–100)/24]									
Q	100–0	0.5–20	-	-	1–0.05	0.75–20	0.5–4	-	10–1	Tunnels deformations
(0.001-1000)	$Q=[(RQD/J_n)\,(J_r/J_a)(J_w/SRF)]$; [c] $\sigma_m = 5\gamma(Q\sigma_r/100)^{1/3}$, γ is the unit weight in g/cm^3									
GSI	100–0	0.01–10	300–0 MPa	0-0.6	-	-	-	-	-	Characterization of deformations
(0-100)	$GSI=9\log_{10}[(RQD/J_n)\,(J_r/J_a)]+44$ (J_r/J_a from Q-system) $GSI=10+R_1+R_2+R_3+R_4$ (from RMR) ; [a] σ_{mr}= [exp{(GSI–100)/9}]$^{0.5}$ for GSI>25									
RQD[d, e]	-	$J_n=f_2(R_2)$	$\sigma_r=f_3(R_3)$	$J_w=f_4(R_4)$		$c_g=f_5(R_5)$	$r=f(\sigma_m)$	$n_{\beta}=f_6(R_6)$	$\alpha_p=\lambda/C$	
(0-100)	$J_{fg}=a[\exp(b\,RQD)]$; $\sigma_{mr}=E_{mr}\exp[a\,C_{hs}\exp(bRQD)]$; a and b depend upon the relationship between J_{fg} and RQD; C_{hs} is a pressure and damage sensitive plastic parameter									in-situ applications

Note: [a] Hoek and Brown (1980), [b] Kalamaras and Bieniawski (1995), [c] Barton (2002), [d] Trivedi (2013a); [e] Present work.

Table 5. Strength ratio from laboratory and in-situ characterization systems (RAC, J_{fg}, and RQD).

Rock mass characterization system (scale)	RQD	Number of joints (m^{-1})	UCS (σ_i)	Joint water pressure ($J_w=u/\sigma_1$)	Inflow (J_k)	Gouge thickness parameter (t/t_a) (J_a)	Roughness parameter (J_r)	Orientation parameter (n_β)	Dilatancy	Application
RAC [a]	-	13 – 500	σ_{mr}	-	-	-	$r=\tan\phi$	0.1–1	-	Strength characteristics
(J_f=0–500)	$\sigma_{mr}=\exp(\alpha_p J_f)$; $J_f=J_w/(n_\beta r)$; α_p=–0.008									
Modified joint factor [b, c]	-	$f(J_n)$	σ_{mr}	As per the depth of water table relative to the joint		$f(t/t_a)$	$r=f(\sigma_m)$	0.1–1	$\alpha_p=\lambda/C$	Strength characteristics, deformations
(J_{fg}=0–1000)	$\sigma_{mr}=E_{mr}\exp(C_{hs}J_{fg})$; $\sigma_{mr}=\exp(\alpha_p J_{fg}^{p})$; α_p=–0.001 to –0.1									
RQD [c, d] (0–100)	$J_{fg}=a\exp(bRQD)$; $\sigma_{mr}=E_{mr}\exp[aC_{hs}\exp(bRQD)]$; a and b depend upon the relationship between J_{fg} and RQD									In-situ strength and deformation

Note: [a] Ramamurthy and Arora (1994); [b] Trivedi (2010); [c] Trivedi (2013a); [d] Present work.

Table 6. Orientation parameters for different joint inclinations of blank and gouged joints.

Joint inclination angle, β (°)	[a] Orientation parameter, n_β	[b] Orientation parameter with clay gouge, $n_{\beta r}$
0	0.82	-
10	0.46	-
20	0.11	-
30	0.05	-
40	0.09	-
50	0.30	-
55	0.39	0.054
60	0.475	0.195
70	0.644	0.445
75	0.729	0.557
80	0.814	0.661
85	0.9	0.76
90	0.95	0.853
Intact rock	1	1

Note: [a] Arora (1987), [b] Trivedi (1990).

2. Preliminary definitions

2.1. Strength ratio

The strength of rock masses (σ_m) is evaluated in terms of strength ratio (σ_{mr}) which is a ratio of strength of rock mass (σ_m) to that of intact rock sample (σ_r) of the same size and shape. One of the main aims of finding strength ratio in terms of significant joint parameters, namely, modified joint factor, is to get readily the strength of rock mass by conducting uniaxial compression test on the intact rock. If σ_{1m}, σ_{2m} and σ_{3m} are the principal stresses in the rock mass and σ_r is the compressive strength of intact rock sample in uniaxial test, then in the triaxial case, the ratio at failure is expressed as

$$p=(\sigma_{1m}+\sigma_{2m}+\sigma_{3m})/3 \quad (1)$$

In axisymmetrical case, we have

$$p=(\sigma_{1m}+2\sigma_{3m})/3 \quad (2)$$

$$q=\sigma_{1m}-\sigma_{3m} \quad (3)$$

$$\sigma_{mr}=[(\sigma_{1m}+\sigma_{2m}+\sigma_{3m})/3]/(\sigma_r/3) \quad (4)$$

According to Eqs. (1) and (4), we have

$$\sigma_{mr}=p/(\sigma_r/3) \quad (5)$$

Under uniaxial condition, σ_{mr} can be calculated as

$$\sigma_{mr}=\sigma_m/\sigma_r \quad (6)$$

The mean confining pressure ratio and shear stress ratio in axisymmetrical case are respectively defined as

$$p_{mr}=[(\sigma_{1m}+2\sigma_{3m})/3]/\sigma_r \quad (7)$$

$$q_{mr}=(\sigma_{1m}-\sigma_{3m})/\sigma_r \quad (8)$$

Under triaxial condition, the modulus ratio is represented as

$$E_{mr}=E_m/E_r \quad (9)$$

where E_r and E_m are the deformation moduli defined as stress and strain ratio of intact rock and rock mass, respectively, at varied strain levels in a selected range of pressure.

2.2. Intrinsic joint characteristics: Joint number, joint factor and modified joint factor

The strength of rock masses depends on the presence of a number of joints. The joint number (J_n) is defined as joints number per unit length of a scan line. The assigned joint number is an equivalent directional parameter based upon the occurrence of the joints. The orientation of the joint shows its tendency of slipping and shearing in a selected direction. It may obstruct or facilitate the joints to contract or dilate at different rates once stress is applied. The joint set per unit volume considers equivalent joint frequency, its orientation, and quantity of frictional granular fill. According to Arora (1987) and Ramamurthy and Arora (1994), the joint set is multiplicatively equivalent to joint factor (J_f). According to Trivedi (2010), a modified joint factor (J_{fg}) was proposed to capture the multiplicative equivalence of all the rock and gouge parameters and their transition as the loading proceeds. Arora (1987) and Trivedi (1990) obtained the orientation parameter for the blank and gouged joints as shown in Table 6.

The modified joint factor relates the joint number (J_n) and the modified joint factor (J_f) to joint and gouge parameters, presented in dimensionless form as

$$\left.\begin{aligned} J_{fg}&=c_g J_f=c'_g J_n \\ J_f&=(L_{na}/n_\beta r)J_n \\ c'_g&=c_g(L_{na}/n_\beta r)\end{aligned}\right\} \quad (10)$$

where n_β is the orientation parameter related to the angle between joints orientation and the direction of loading (β) or to the friction parameter (r). The reference value of friction parameter r=1, and the reference value of length parameter L_a=1 m.

Based upon the experimental results of several investigators (Yaji, 1984; Arora, 1987; Trivedi, 1990; Arora and Trivedi, 1992; Trivedi and Arora, 2007; Trivedi, 2010, 2013a, b), the author considered varied engineering parameters of rock masses from laboratory tests in relation to field investigations to define c_g as

$$c_g=J_{dj}J_t/(g_d J_w) \quad (11)$$

where J_{dj} is the modified coefficient for joint depth (joint stress parameter); J_t is the modified coefficient for thickness of gouge (gouge thickness parameter); g_d

is the modified coefficient for the compactness of joint walls and relative density of granular fill, namely, gouge, which equals 1 for fully compacted joints; J_w is the modified coefficient for groundwater conditions.

Accordingly, the gouge is a hydro-thermal deposit in rock masses which may allow the flow of water through the joints measurable in terms of permeability (Singh et al., 2014). The consolidated and unconsolidated gouge in rock masses (Trivedi et al., 2014, 2015) may increase or decrease the strength. The grains in the discontinuity tend to consolidate or dilate during loading. J_{fg}^{h} and J_{fg}^{p} refer to the instantaneous values of modified joint factor (J_{fg}) in the hardening and softening range, respectively, separated by a saddle pressure at a maximum value of damage-sensitive plastic parameter characterised by $\ddot{I}$. The effect of pressure sensitive plasticity on rock mass parameters, stress condition (plane stress and plane strain) and E_{mr} is listed in Tables 7 – 9, respectively. The progressive compression and dilation of infill influence the strength and deformation characteristics of rock masses. In the water pressure induced field condition, J_w may be considered as a linear function of excess pore pressure parameter (in a range of 1 – 0.05) (similar to the Q-system by Barton (2013)). Similarly, J_w is indirectly estimated from the groundwater parameter R_4 of RMR system (as R_4 in Tables 4 and 5).

Since in the hardening range, $J_{fg} \rightarrow J_{fg}^{h}$, while in the softening range, $J_{fg} \rightarrow J_{fg}^{p}$, strength ratio at failure is

$$\sigma_{mr} = \exp(\alpha_p J_{fg}^{p}) \quad (12)$$

where α_p is a fitting parameter. The values of α_p appear in a wide range, as shown in Table 3.

Alternatively, Eq. (12) can be rewritten as

$$\alpha_p = \ln \sigma_{mr} / J_{fg}^{p}$$

(13) Similarly, we have

$$E_{mr} = \exp(C_h J_{fg}^{h})$$

(14)

$$C_h = \ln E_{mr} / J_{fg}^{h} \quad (15)$$

where C_h is a pressure and joint dependent hardening parameter.

Table 7. Trial parameters for yield surfaces (Johnston, 1985).

Group	Rock type	UCS (MPa)	*B*	*M*	χ_b	χ	χ_m
A	Limestone [a]	96	0.481	7.43			0.170
B	Mudstone [b]	1.3	0.750	6.16			0.231
C	Sandstone [c]	68	0.444	11.4	0.0172	2.065	0.270
E	Granite [d]	230	0.538	15.6			0.659
All types [b]							0.276

Note: [a]Brook (1979), [b]Johnston (1985), [c]Aldrich (1969), [d]Swanson and Brown (1971).

Table 8. Plastic parameter α_p for rock mass from numerical trials.

End conditions	A_b [a]	C [b]	$\alpha_p = \lambda/C$	λ	A_b/C [b]
Triaxial (min)	3	–1	–0.025	0.025	–3
		–2.75	–0.009		–1.09
		–5	–0.005		–0.6
		–10	–0.0025		–0.3
Triaxial (max)		–1	–0.038	0.0383	–3
		–2.75	–0.0139		–1.09
		–5	–0.0076		–0.6
		–10	–0.0038		–0.3
Plane strain (min)	5	–1	–0.0275	0.0275	–5
		–2.75	–0.01		–1.81
		–5	–0.0055		–1
		–10	–0.00275		–0.5
Plane strain (max)		–1	–0.0415	0.0416	–5
		–2.75	–0.0151		–1.81
		–5	–0.0083		–1
		–10	–0.00415		–0.5

Note: [a] Bolton (1986), [b] Trivedi (2010).

Table 9. Relationship between UCS and modulus ratio.

Material	UCS (MPa)	Best fit d_{mr}	d, d_m	Selected data points and determination coefficient
Concrete	80	-	3[a]	Wide range
	41	-	2[b]	Wide range
Intact rocks and rock masses	10–250	2.02[c]	-	55; r^2=0.96
	5–120	1.4[d]	-	52; r^2=0.95
	10–320	0.80[e]	-	35; r^2=0.57
	-	-	1–0.4[d]	-
	-	0.7[f]	1–0.5[f]	-
	2-200	1.08[g]	-	12; r^2=0.76
	0.1 – 20	0.726[g]	-	30; r^2=0.91
	3–20	0.628[g]	-	14; r^2=0.86
	0.1–20	0.595[g]	-	12; r^2=0.79

Note: [a] CEB-FIP Model Code (1990), [b] ACI committee 318 (1995), [c] Chun et al. (2009), [d] Sonmez et al. (2004), [e] Lama and Vutukuri (1978), [f] Zhang (2009), [g] Arora (1987), [g] Singh (1997), [g] Ramamurthy (2004), [g] Singh and Rao (2005).

Fig. 2 shows compiled experimental data of strength ratio and modified joint factor obtained by various investigators including the data obtained from in-situ observations of GSI and RMR system. The upper bound values correspond to the laboratory controlled studies while the lower bound values are obtained from in-situ observations.

Table 3 shows low values of determination coefficient and maximum and minimum values of α_p based upon joint factor and modified joint factor in the past studies. It is important to note that not all these studies necessarily capture the plastic and damage induced volume change during deformation.

2.3. Joint strains, volume changes and yield function

According to elastoplastic theory, the total strain increment consists of elastic and plastic strain increments as an effect of pressure, temperature and resultant shear. The global change of strain is adjusted primarily among joints and later it transforms joints by means of irrecoverable strains (ε^p). The irrecoverable strains consist of volumetric ($\delta\varepsilon_v^{ps}$), shear and damage components ($\delta\varepsilon_s^{ps}$ and $\delta\varepsilon_s^{pd}$) which are distinctively related to volumetric and shear stresses, respectively. The volumetric stresses produce joint closure and separation leading to a volume change. As an effect, damage-inclusive plastic shear strain and joint shear stresses are induced. Therefore, potential of initial isotropic stresses and joint strain relative to plastic volumetric strain and joint shear stresses respectively is always present in rock masses. The notions of stress and strain are interlinked to the joints. At the fundamental level they are related by mechanical power, and the rate of work per unit current volume of the rock mass material, but the effect is measured in terms of joints. Therefore, due to the applied stresses, the effect of joint is measured instead of that of strain.

Therefore, the total strain is presented as

$$\delta\varepsilon = \delta\varepsilon^{e} + \delta\varepsilon^{p}$$

(16)

The plastic strain can be formulated as

$$\delta\varepsilon^{p} = \delta\varepsilon_v^{p} + \delta\varepsilon_s^{p}$$

(1 7)

where $\delta\varepsilon_v^{p}$ and $\delta\varepsilon_s^{p}$ are the changes in damage-inclusive plastic volumetric strain and plastic shear strain, respectively.

The plastic shear and damage strains are considered as

$$\left.\begin{aligned} \delta\varepsilon_s^{p} &= \delta\varepsilon_s^{ps} + \delta\varepsilon_s^{pd} \\ \delta\varepsilon_m^{p} &= \delta\varepsilon_r^{ps} + \delta\varepsilon_j^{ps} + \delta\varepsilon_g^{ps} + \delta\varepsilon_r^{pd} + \delta\varepsilon_j^{pd} + \delta\varepsilon_g^{pd} \end{aligned}\right\} \quad (18)$$

where $\delta\varepsilon_r^{ps}$, $\delta\varepsilon_j^{ps}$ and $\delta\varepsilon_g^{ps}$ are the changes in plastic shear strain in intact rock, rock mass, and rock joints and gouge, respectively; $\delta\varepsilon_r^{pd}$, $\delta\varepsilon_j^{pd}$ and $\delta\varepsilon_g^{pd}$ are the changes in plastic damage strain in intact rock, rock mass, and rock joints and gouge, respectively.

For rock masses without gouge, joints are orthogonal to loads and reference friction parameter, $c'_g = 1$, and $J_{fg} = J_n$, thus we have $\delta\varepsilon_m^{p} = \delta\varepsilon_r^{ps} + \delta\varepsilon_j^{ps} + \delta\varepsilon_r^{pd} + \delta\varepsilon_j^{pd}$.

For conditions without damage and insignificant presence of joint, $\delta\varepsilon_{\mathrm{j}}^{\mathrm{ps}} \to 0$ and $\delta\varepsilon_{\mathrm{j}}^{\mathrm{pd}} \to 0$, thus $\delta\varepsilon_{\mathrm{m}}^{\mathrm{p}} = \delta\varepsilon_{\mathrm{r}}^{\mathrm{p}}$.

The relationship of cumulative plastic strain, amid the anisotropic potential of plastic strain in pressure-joint regime (*ij*) in rock masses, may be represented in terms of commonly used notations in continuum mechanics as

$$\left.\begin{aligned} \delta\boldsymbol{\varepsilon}_{ij}^{\mathrm{p}} &= \sum \delta\boldsymbol{\varepsilon}_{kl}^{\mathrm{p}} \\ \boldsymbol{\varepsilon}_{kl}^{\mathrm{p}} &= \begin{bmatrix} \varepsilon_{11} & \varepsilon_{12} & \varepsilon_{13} \\ \varepsilon_{21} & \varepsilon_{22} & \varepsilon_{23} \\ \varepsilon_{31} & \varepsilon_{32} & \varepsilon_{33} \end{bmatrix} \end{aligned}\right\} \tag{19}$$

where $\boldsymbol{\varepsilon}_{kl}^{\mathrm{p}}$ is the plastic strain in three-dimensional (3D) symmetric tensor space; the subscripts *k*, *l* = 1, 2, 3 are used for tensorial representation. If *k*=*l*, $\varepsilon_{\mathrm{v}}^{\mathrm{p}} = f(\varepsilon_{kk}^{\mathrm{p}})$; and if *k*≠*l*, then $\varepsilon_{\mathrm{s}}^{\mathrm{p}} = f(\varepsilon_{kl}^{\mathrm{p}})$.

Similarly, the stress tensor ($\boldsymbol{\sigma}_{mn}$) is related to a strain tensor (ε_{kl}) using a compliance matrix ($\boldsymbol{C}_{klmn}$) as

$$\boldsymbol{\sigma}_{mn} = \sum_{kl} \boldsymbol{C}_{klmn} \boldsymbol{\varepsilon}_{kl} \tag{20}$$

where the subscripts *k*, *l*, *m*, *n* = 1, 2, 3 are used for tensorial representation.

The scalar modulus of stress in pressure-joint regime (*ij*) may be represented as $\sigma_{ij} = (\sigma_{mn})_{1,2,3}$ which is resolved into (p, q, C_{hs}) space, such that, if *m*=*n*, $\sigma_{nn}=\sigma_{ij}=f(p)$; and if *m*≠*n*, then $\sigma_{mn}=\sigma_{ij}=f(q)$. Moreover, if $|j|\to+\infty$, $|\sigma_{ij}|\to 0$.

However, the use of tensorial indices has been omitted in the following arguments for simplicity. The application of full tensorial form can be quite complex to handle numerically in presence of non-coaxial plasticity and damage. Fortunately, most of the implicit features of fractured material (namely, rock masses) behavior (p, q, C_{hs}) can be described using scalar models in deformation fields (Herrmann et al., 1989; Herrmann and Roux, 1990; Zapperi et al., 1997).

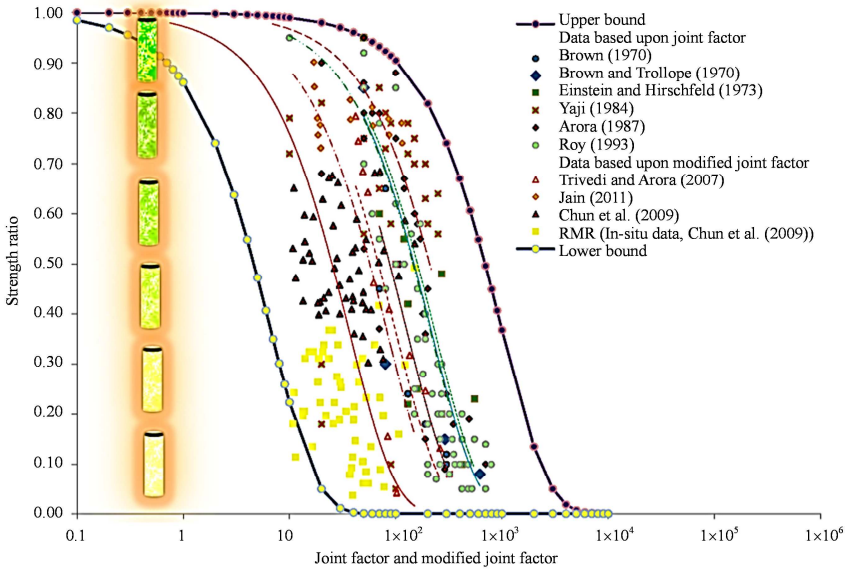

Fig. 2. Strength ratio vs. joint factor and modified joint factor.

In the pressure-joint regime, the size of yield surface is assumed to be affected by softening of cemented bonds as per the observations in experiments (Horpibulsuk et al., 2004). The effect of hardening and softening due to pressure-temperature coupling and joints may be considered together for the plastic yield. Thus, the yield function for rock mass is defined as

$$f(p, q, C_{\mathrm{hs}}) = 0 \tag{21}$$

where C_{hs} is the plastic parameter depending on hardening and softening evaluated in a potential pressure-joint regime (*ij*).

Theoretically, the incidental value of modified joint factor (J_{fg}) has an effect of time history in terms of already experienced dilatancy and damages of rock joints:

$$J_{\mathrm{fg}} = J(\varepsilon_{\mathrm{v}}^{\mathrm{p}}, \varepsilon_{\mathrm{s}}^{\mathrm{p}}) \tag{22}$$

$$J_{\mathrm{fg}} = J'(D^{\mathrm{p}}) \tag{23}$$

where D^{p} is the damage-inclusive plastic dilatancy, which considers change in volume and is associated with shear distortion and damage. It is a function of plastic volumetric strain, plastic shear and damage in intact rock, rock mass and gouge material.

2.4. Direct measurement of rock mass characteristics and damage through RQD

In-situ rock masses consist of discontinuity, inclusions and weaknesses. The weak formations are relatively more vulnerable to damage upon loading and unloading. Therefore, the weakness reappears prominently within a continuous deposit subjected to a combination of stresses due to the drilling associated process. The drilling process recovers a core of rock mass while joints appear as discontinuities at unequal intervals. Normally the average joints number is counted in the unit length of the scan line. Figs. 3–5 shows idealized rock joint parameters in the rock core as functions of modified joint factor and RQD. Fig. 6 shows the gradual closure of joint pattern due to pressure-induced hardening while Fig. 7 shows gradual impairment of rock mass as an effect of pressure-induced softening.

Field investigations to obtain RQD consist of the orientation of the joints relative to the direction of the scan line to obtain orientation parameter. The core recovery log should be specified additionally to get record of orientation on the data sheet of bore log. The geotechnical applications consider RQD as a percentage of scan line consisting of intact samples greater than 100 mm, which is presented as

$$RQD = \sum L^{\mathrm{i}} / L^{\mathrm{n}} \times 100\% \tag{24}$$

where L^{i} is the length of intact piece of core in a scan line having size equal to or greater than 100 mm, and L^{n} is the total length of drill length for core recovery.

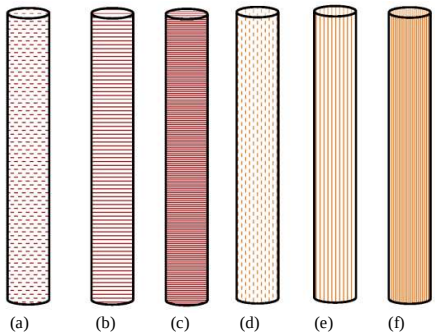

Fig. 3. Evolution of horizontal and vertical joints. β is the inclination of joints to the direction of loading. (a) J_n=30, β=90°; (b) J_n=60, β=90°; (c) J_n=120, β=90°; (d) J_n=30, β=0°; (e) J_n=60, β=0°; (f) J_n=120, β=0°.

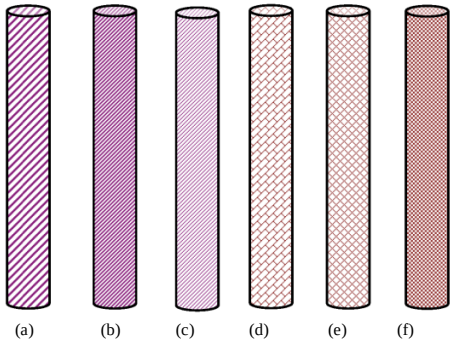

Fig. 4. Evolution of inclined joints. (a) J_n=30, β=45°; (b) J_n=60, β=45°; (c) J_n=120, β=45°; (d) J_n=150, β=45°; (e) J_n=240, β=45°; (f) J_n=480, β=45°.

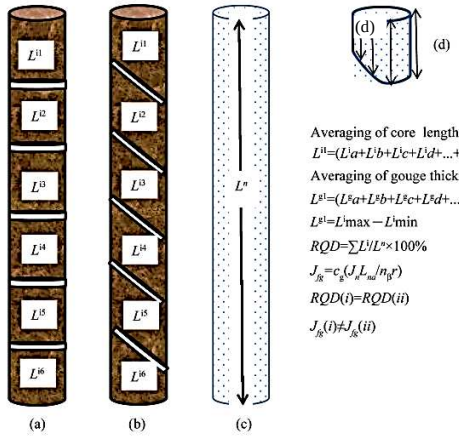

Fig. 5. Consideration of horizontal and inclined joints in RQD and modified joint factor. L^{i1} is the length of the first core segment, and L^{g1} is the thickness of the first gouge segment. (a) J_n=5, β=90°; (b) J_n=5, β=45°; (c) Intact core with length of L^n=1 m; (d) Core segment, β=45°.

Fig. 6. The evolution of hardening and damage in six stages as an effect of accumulated plastic strains in hardening range to increase strength at all possible values of modified joint factor at selected RQDs.

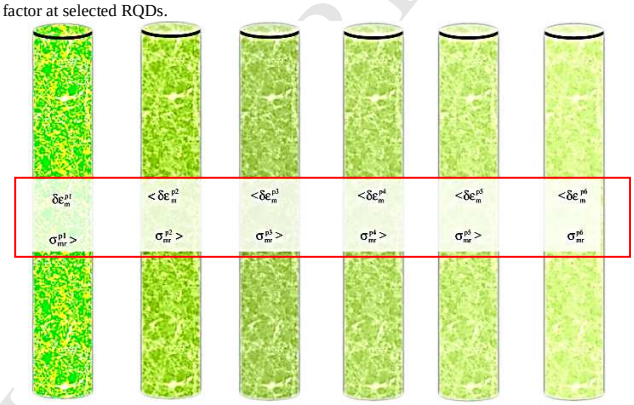

Fig. 7. The evolution of softening and damage in six stages as an effect of accumulated plastic strains in softening range to decrease strength at all possible values of modified joint factor at selected RQDs.

The RQD appears to be a qualitative parameter in rock mechanics that has a lot of challenging questions. There is a quantitative evaluation system available to supplement RQD (such as the parameters considered in calculation of modified joint factor) based upon field geotechnical investigation and a pressure and damage sensitive plastic parameter obtained from constitutive relationships. The RQD (as considered by Deere and Deere (1988)) can yet be supported and improved by a set of reflective parameters (as parameterized in modified joint factor J_{fg}). In a similar attempt, several researchers introduced other parameters to describe quality of the rock mass, such as Q-system, *GSI*, and *RMR*.

Priest and Hudson (1976) proposed that the estimate of *RQD* should be related to joint spacing measurement of the core as

$$RQD = 100(1+0.1J_n)e^{-0.1J_n} \quad (2.5)$$

They also suggested a modification for the joint number ranging from 6 to 16 per meter represented in parametric form as

$$RQD = RQD_{fn} - n_l J_n \quad (2.6)$$

where RQD_{fn} is a value of RQD that is not necessarily observed in the *RQD* scale but appears in empirical relationship due to linearization. Here in Eq. (26), RQD_{fn} = 110.4, n_l = 3.68.

Palmstrom (1996) considered block volume V_b (related to joint frequency), and joint condition (j_C) including roughness of joints to propose the rock mass strength:

$$\sigma_{mr} = 0.2 j_c^{0.5} V_b^D \quad (2.7)$$

where $D = 0.37 j_c^{-0.2}$.

Based upon the observations of Palmstrom (1996) and Grenon and Hadjigeorgiou (2003) that neglected volumetric joint count and thus would estimate erroneously the discontinuity pattern in rock masses, Palmstrom (2005) proposed the joint number per unit volume ($n_v J_v = n_l J_n$) instead of J_n, which may be represented as

$$RQD = RQD_{fv} - n_v J_v = RQD_{fn} - n_l J_n \quad (28)$$

There are inherent similarities between Eqs. (26) and (28). As per Palmstrom (2005), RQD_{fv} is equal to 115, the value of n_v may be 3.3 and n_l / n_v =1–6, therefore the range of n_l may be as high as 1–20.

Eq. (28) is applicable if the volumetric joint count (J_v) is 4.5–35. The relationship between RQD and volumetric joint characteristics (Eqs. (26)–(28)) provides a scope for further analysis of intrinsic joint characteristics. The minimum value of joint volume in Eq. (28) for intact rocks nearly equals 4.5%, which is not necessarily consistent with the in-situ observations as shown in Fig. 8 where the effects of accumulated plastic strains and scale effects are considered (up to b=–0.05). In fact, the observation of RQD for rock masses (Eqs. (25)–(28)) is essentially exclusionary in nature, which offsets the influence of drill mass sizes less than 10 cm. In order to fracture initiation at micro- to meso-scale and accumulated plastic strain, the author proposed to relate RQD with intrinsic joint characteristics (b=–1 to 0.01).

2.5. Relationship between RQD and intrinsic joint characteristics

Sen and Eissa (1991) examined the use of lognormal and negative exponential relationships between RQD and joint volume. They showed that decreasing RQD value with increasing difference in length of block side or joint spacing, the changes in block size tend to adjust the stress intensity at discontinuities. These observations call for modification of the relationship between RQD and joint and gouge parameters, namely, extent of joints, volume of gouge, friction, material of gouge, and water pressure. The scan line as well as the volumetric joint count has an exponential relation with RQD as the block size changes with increasing infill magnitude. At RQD=0, the recovered rock core sizes are less than 10 cm (relatively fragmented state), the rock mass strength characterization should ideally be captured using parameters considered in the calculation of modified joint factor, J_{fg}. Other than RQD and modified joint factor, there are more parameters, namely, total core recovery (TCR), solid core recovery (SCR) and core recovered from the following run (CRF), which can also be used to map the rock mass classification at RQD=0. Based on limited data available, it may be stated that TCR, SCR and CRF similar to RQD (Eid, 2007; Valentine and Norbury, 2011, 2012; Nicholls, 2012) do have inverse relationships with J_{fg}.

On the basis of previous studies (Sen, 1984; Sen and Eissa, 1991; Grenon and Hadjigeorgiou, 2003; Palmstrom, 2005; Trivedi, 2013a, b), an exponential relationship between modified joint factor and RQD is proposed as

$$J_{fg} = a \exp(bRQD) \quad (29)$$

$$J_f = (a/c_g) \exp(bRQD) \quad (30)$$

$$J_n = (a/c'_g) \exp(bRQD) \quad (31)$$

where a and b are the fitting parameters determined according to the minimum size of fragmented rock and characteristics of joints in relation to RQD. The minimum size at grain boundaries, where fracture begins, relative to the drilling length, may have a modified joint factor higher than 1000. However, the significant measurement of fragmented rock grain relative to the drilling length tends to the value of modified joint factor, a, which is conveniently considered as 1000. Similarly, as per the characteristics of joints and friction in relation to RQD, the value of b may vary between –1 and –0.01. With reference to a set of data points from Chun et al. (2009), b takes a value close to –0.2. The physical meaning associated with b relates convexity in the relationship between J_{fg} and RQD, which in fact is a function of accumulated plastic strain. In hardening and softening ranges, the modified joint factor is transformed to J_{fg}^{h} and J_{fg}^{p} due to the transition of b between –1 and –0.01. In the present data sets, lower values of b are associated largely with in-situ observation while higher values are from controlled laboratory tests.

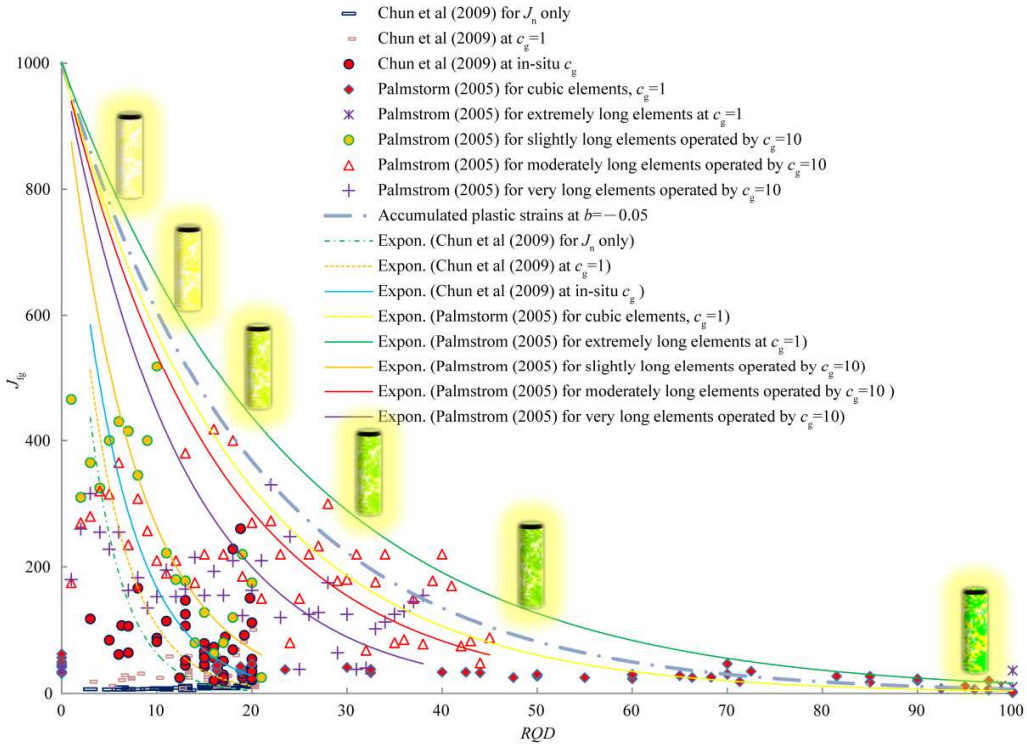

Fig. 8. Variation of modified joint factor with RQD at c_g=1 for lower bound and c_g=10 for upper bound of the maximum accumulated plastic strain.

Thus, the transition of modified joint factor (J_{fg}) considers the volumetric effect on strength and deformation characteristics through the spacing, orientation, friction, volume of gouge material, groundwater and internal pressure. The scan line data from core drilling of the rock mass provide a scope for evaluation of the fitting parameters *a* and *b*.

Fig. 6 shows the variation of J_{fg} (modified joint factor) with RQD, as well as the field data of selected fitting parameters *a* and *b* along with a range of anticipated values of *b* with and without consideration of the effect of gouge and joint parameters (namely, c_g *and* c_g'), respectively.

The experimental data indicate that the value of modified joint factor (J_{fg}) changes between 1000 and 0 for RQD varying from 0 to 100. For RQD of about 100, J_{fg} would be in excess as per the linear equivalent obtained by Eqs. (26) and (28) , the number of joints is greater than 16, therefore, the mass materials may be classified as heavily jointed rock masses. Accordingly, even for higher values of RQD, J_{fg} vs. RQD relationship may continue to affect *b* values due to the presence of gouge. However, as RQD tends to a reduced value, J_{fg} vs. RQD relationship becomes progressively sensitive to multi-size, multi-scale and localized interactions of gouge amid accumulated plastic strains.

3. Experimental input and numerical formulation

The present work considers the generalized theoretical framework of a flow rule and experimental outputs of Johnston and Chiu (1984), Johnston (1985), Arora (1987), and Trivedi (1990) for empirical relation between strength and modulus ratio based on significant joint characteristics, and of Chun et al. (2009) and Zhang (2010) for experimental data relating modulus ratio to RQD.

3.1. Strength criterion in relation to the intrinsic joint characteristics and volume changes

The JC-criterion proposes a relationship in normalized form for intact rocks based upon the observations of Brook (1979), Johnston (1985), Aldrich (1969), and Swanson and Brown (1971) which cover a range of strength variation well from the tensile to compressive strength. The review and observation of test results from several reports published on triaxial testing on concrete, rocks and rock-like materials (Bortolotti, 1991, 1994; Setunge et al., 1993; Yapı Merkezi Inc., 1996; Arioglu et al., 2006; Trivedi, 2010, 2013a, b) strongly support the suitability of JC-criterion for a wide range of materials. The JC-criterion can be expressed as

$$\left.\begin{aligned}\sigma_{1N}&=[(M/B)\sigma_{3N}+1]^B\\ \sigma_{1N}&=\sigma_1/\sigma_r \quad \sigma_{3N}=\sigma_3/\sigma_r\end{aligned}\right\} \tag{32}$$

where σ_1 and σ_3 are the principal stresses; *M* and *B* are empirical rock parameters related to compressive and tensile strength, respectively, derived from compressive strength as per the JC-criterion.

Upon simplification of Eq. (32) we get

$$\sigma_r/\sigma_t=-M/B \tag{33}$$

where σ_t is the tensile strength of rock sample.

The Mohr-Coulomb criterion (MC-criterion), one of the most popular strength criteria for geo-materials, is applied reasonably and well to the rock masses when σ_r/σ_t >10 (Labuz and Zang, 2012). Interestingly, once *B*=1, Eq. (32) is reduced to MC-criterion as $\sigma_{1N}=M\,\sigma_{3N}+1$, where $M=(1+\sin\phi)/(1-\sin\phi)$, in which ϕ is the angle of internal friction of joint material.

The JC-criterion takes an advantage of inclusion of a ratio of compressive to tensile strength as per Eq. (33) and a ratio of principal stresses (Eq. (32)) in the dimensionless form. It considers the ratio of tensile to compressive strength as a material constant which can be readily estimated by standard laboratory techniques. The frictional forces in the micro-joints and micro-crack network modify the ratio as per Eq. (33). The modification of empirical rock constants, consequently on the changes in initial isotropic condition and joint conditions, is related to the modified joint factor. The range of uniaxial compressive and tensile strengths of rocks and rock-like materials varies significantly upon the intrinsic factors (Carpinteri et al., 2005), which are well considered by modified joint characteristics. The concentration of stresses tends to extend the failure surface, which in turn changes the stress and volume varying pattern. With the progressive failure, the joint damage occurs which transforms the mean effective confining pressure on the elements under consideration.

Based upon the JC-criterion, a relationship for rock masses is considered as

$$B=1-\chi_b[\log_{10}(\sigma_m/\sigma_a)]^2 \tag{34}$$

$$M=\chi+\chi_m[\log_{10}(\sigma_m/\sigma_a)]^2 \tag{35}$$

where σ_a is the reference stress taken as 1 kPa. The values of the empirical constants in Eqs. (32)–(35) are compiled in Table 7. χ, χ_b, χ_m are empirical rock constants in JC-criterion. For rock masses having negligible χ_m, the value of *M* tends to χ (=2) as per the JC-criterion. The values of χ_b and χ_m refer to the gradient in the fitting linear relationship of *B* and *M* with square of logarithmic normalized rock mass strength as shown in Fig. 9a and b.

A wide-ranging experimental ratio of compressive to tensile strength obtained by Palchik and Hatzor (2004) on cemented porous chalk and other rocks and rock-like materials (Lama and Vutukuri, 1978; Johnston, 1985) supports the proposition of linearity of *M*/*B* with square of logarithmic normalized rock mass strength as shown in Fig. 9c. There is an observed linearity of compressive to tensile strength ratio with crack initiation strength (Perras and Diederichs, 2014; Zhao et al., 2015). However, increasing deformation after crack initiation tends to be log-normalized with compressive strength. The parameters of JC-criterion are shown in Fig. 9a–c in generalized form.

A great number of empirical data are available for validation of strength theories of rock masses in relation to widely popular Hoek– Brown criterion (HB-criterion) (Hoek and Brown, 1980, 1997). The empirical constants associated with HB-criterion for rock masses may be related to the constants used by JC-criterion.

The generalized HB-criterion (Hoek and Brown, 1997) for evaluating rock mass strength is represented as

$$\sigma_{1N}=\sigma_{3N}+(m_b\sigma_{3N}+s)^{a_{HB}} \tag{36}$$

where a_{HB}, m_b and *s* are the empirical rock constants as per the generalized HB-criterion for rock masses. The constants of HB-criterion (a_{HB}, m_b and *s*) are related to the constants of JC-criterion (*M* and *B*) as

$$M/B=m_b s^{a_{HB}-1} \tag{37}$$

Normally the development of strength criterion is based upon a relationship between stress and strain invariants, but under field conditions it is inherently difficult to measure actual stress-deformation fields. Therefore, a plastic parameter based upon preliminary observations of dilatancy from different investigators (Table 2) is related to joint characteristics of rock mass as observed in laboratory and field tests.

3.2. Pressure and damage sensitive plastic parameter in relation to the dilatancy

The volume change of rock masses is normally localized due to joints having lower values of joint parameters, namely, modified joint factor. For higher values of modified joint factor, the volume changes are well distributed over a larger segment of rock masses. In these circumstances, the average value of volume change is inherently interpretive. Moreover, the joint friction factor does

not remain constant during shear. During shear the rock mass may contract or dilate to transform joint parameters as a compressed function of state, namely, magnitude of pressure, compactness of joints, damage or impairment, and material characteristics of gouge, which are difficult to be measured in practice but easier to be interpreted if the concept of pressure sensitive damage and dilatancy is applied to the rock masses.

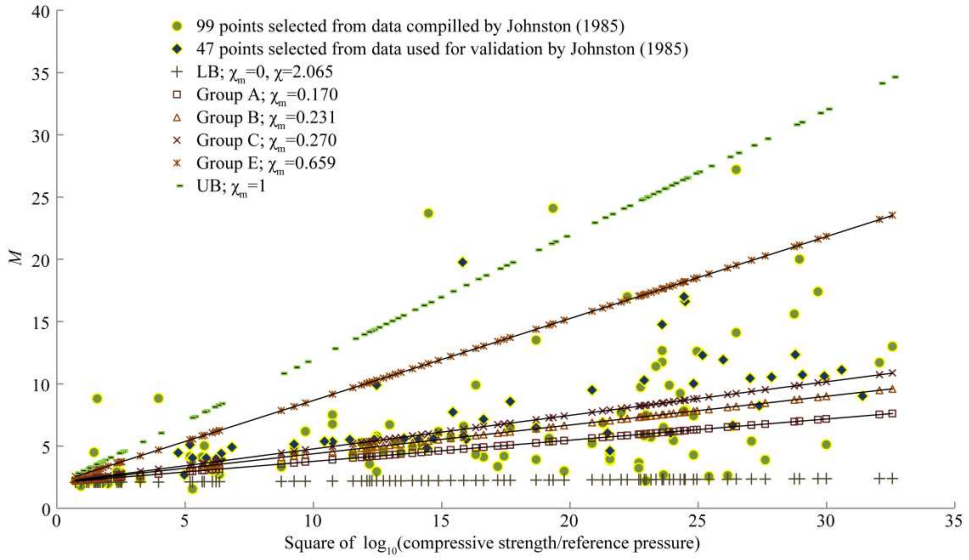

(a) χ and χ_m.

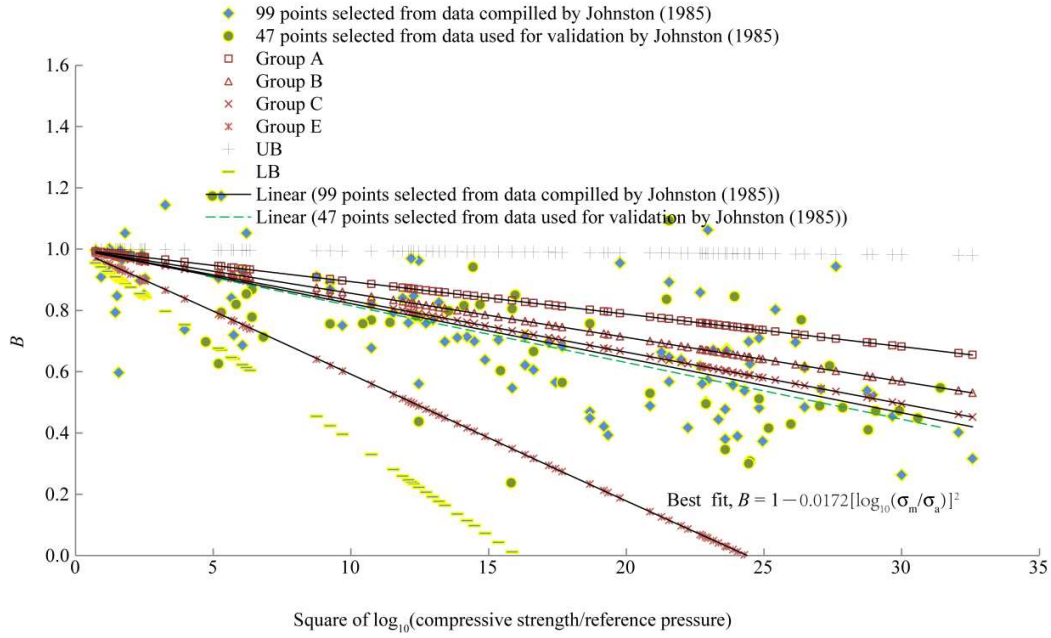

(b) χ_b and χ_m.

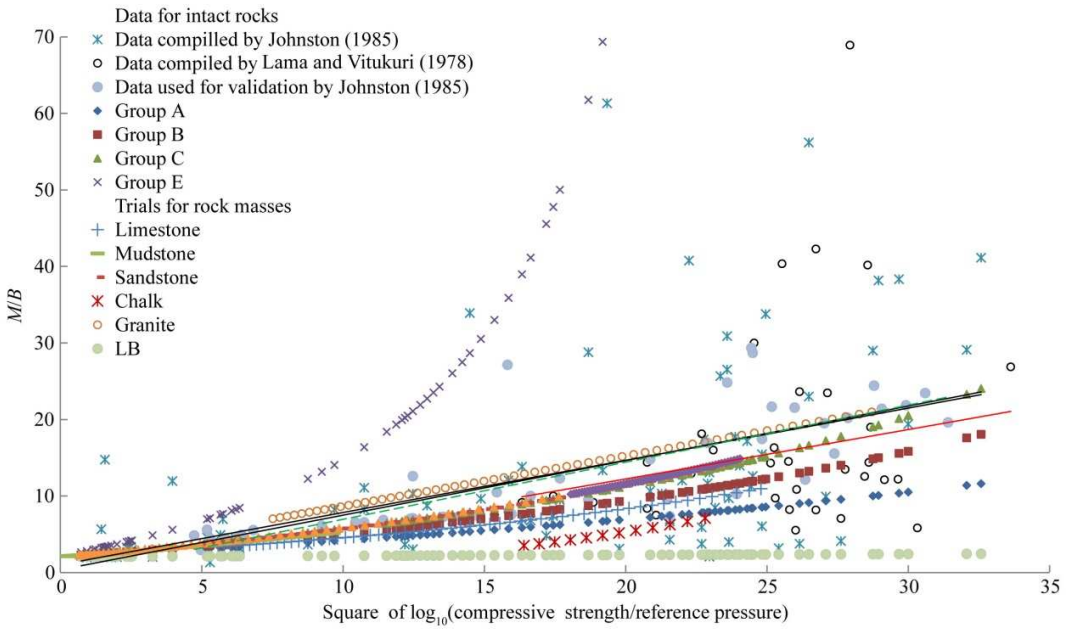

(c) χ, χ_b and χ_m.

Fig. 9. Variation of intact and rock mass parameters.

Based upon the work of Taylor (1948), Rowe (1962), Vesic and Clough (1968), Billam (1972), and de Jong (1976), Bolton (1986) reviewed the stress-dilatancy relation for 17 different sands and proposed an empirical relation for dilatancy of soils, where the angle of dilation is $\psi_{max} = A_b I_r$, in which A_b is an empirical constant and has a value of 3 for axisymmetrical and 5 for plane strain conditions. Such that the dilation angle ($\psi=\phi_p-\phi_c$) is defined as a difference of peak (ϕ_p) and critical friction angle (ϕ_c) in degree. Accordingly, relative dilatancy is $I_r = 10(-d\varepsilon_v/d\varepsilon_s)/3$ where $d\varepsilon_v$ is the change in volumetric strain in the zone of shear and $d\varepsilon_s$ is the change in shear strain. Ojha and Trivedi (2013) and Xiao et al. (2014) extended this relationship to the volume change characteristics of compacted silty soils and compacted rockfill materials, respectively. Walton and Diederichs (2015), based upon the observations of Vermeer and de Borst (1984), related the dilation angle with the ratios of plastic volumetric strain and shear strains to confining pressure for intact rocks. Since J_{fg} is a function of plastic volume change (Eqs. (20) and (21)), it is advanced for plasticity and damage of rock masses in relation to empirical fitting parameter (ξ_{pd}) as

$$\sigma_{mr} = \exp[\xi_{pd}(-d\varepsilon_v / d\varepsilon_s)] \quad (38)$$

Based upon the observations of several investigators (Horne, 1965; Rowe, 1969; Akai et al., 1978; Hirai and Sitake, 1982; Spitzig and Richmond, 1984; Bolton, 1986; Santarelli, 1987; Besuelle et al., 2000; Vatsala et al., 2001; de Buhan et al., 2002; Stoughton and Yoon, 2004; Yuan and Harrison, 2004; Castellanza and Nova, 2004; Trivedi, 2010, 2013a; Noorian-Bidgoli, 2014; Perras and Diederichs, 2014; Li et al., 2015; Walton and Diederichs, 2015) on mass materials, the author extended inputs from JC-criterion, and formulated related strength ratio with dilatancy of rock masses, in a simple form as

$$\sigma_{mr} = \exp(\alpha_p J_{fg}^{pd}) \quad (39)$$

where $\alpha_p=\lambda/C$, and J_{fg}^{pd} is the modified joint factor for plasticity and damage. Eqs. (12) and (39) are similar in appearance but differ significantly in magnitude due to damage.

Similarly, the strength ratio is related to relative dilatancy inclusive of damage as

$$\sigma_{mr} = \exp(\xi I_r) \quad (40)$$

where $\xi = A_b/C$.

Ideally, the strength depends upon the number of joints if $c_g' = 1$ and upon joint factor alone if $c_g = 1$. Table 8 provides selected values of coefficient of modified joint factor and dilatancy index with varied end conditions and initial confining pressure. Most often the strain does not remain exactly in plane strain or triaxial condition, but the end conditions allow for in-between values of α_p. The values of α_p and ξ depend upon volume change characteristics of rock masses. Interestingly the ranges of their values overlap the zone of plastic dilatancy of selected mass materials as also shown in Table 2 and supported by Eqs. (38)–(40).

3.3. Numerical formulation

Consequent to the loading, the volumetric strains of rock masses are set, accompanied by the joint damage due to the changes in the magnitude of cracks, micro-cracks and fracture network which can be modeled for fracturing process in rock masses (Lisjak and Grasselli, 2014). The stress redistribution continues till the deformation develops. The infinitesimal changes in isotropic pressure (δp) produces irrecoverable volume changes ($\delta\varepsilon_v^p$) which may be due to plasticity and damage. Hence there is an induced potential isotropic pressure ($\delta i = \delta p / \delta\varepsilon_v^p$). Therefore, the changes in plastic shear strain ($\delta\varepsilon_s^p$) and shear stresses (δq) are connected with changes in the induced potential of isotropic pressure (δi). The plastic shear strain is due to the potential of changes in significant joint parameters ($\delta j = \delta\varepsilon_s^p / \delta q$). The variables with subscript '*ij*' in Eqs. (41)–(52) have dependence on the instantaneous values of potential of isotropic pressure and joint parameters. The superscripts of the variables are used to formulate iterative steps for incremental damage and plasticity of rock masses. The strain variables, namely, ε_v^p and ε_s^p, with subscripts representing volumetric and shear components while superscripts showing range of plastic behavior can be formulated as

$$i_n = \delta i + i_{n-1} \quad (41)$$

$$j_n = \delta\varphi + j_{n-1} \quad (42)$$

where i_n and j_n arrive through a hardening and softening process characterized by a plastic parameter. In the process, the rock mass has a maximum conservative component of the input energy corresponding to the critical value of pressure. The final state of plasticity and damage does have a scope to capture the initial conditions in steps by trial.

It was observed that the incremental potential of isotropic pressure (δi) and incremental potential of joint parameter (δj) influence the contraction-expansion, translation and shift in *p*-*q* space, which can be represented as

$$f(q,\ p,\ C_{\mathrm{hs}}) = q - (C_{ij}p^2 + C'_{ij}p + C''_{ij}) \tag{43}$$

where C_{ij}, C'_{ij} and C''_{ij} belong to a set of plastic parameters depending upon the incremental potential of isotropic pressure (δi) and incremental potential of joint parameter (δj). For rock masses, the values of hardening-softening parameters C_{hs} and $<C_{\mathrm{hs}}>$ can be related to the set of plastic parameters identified in Eq. (43).

There is one to one mapping of C_{hs} corresponding to the value of $<C_{\mathrm{hs}}>$ at micro-mechanical and granular level due to unit changes in the joint damage parameter. The value of C_{hs} for rock masses is obtained by estimating strength with varying effective confining pressure for different isotropic ratios (p_i/σ_r).

It was observed that increasing the pressure ratio up to the critical one (associated with $\varepsilon^{\mathrm{h}}_{\mathrm{mr}}$) tends to increase the plastic parameter, while beyond this limit, the plastic parameter tends to decrease. A critical pressure ratio is a ratio of pressure at peak softening characterized by α_{p} to that at peak hardening characterized by the peak value of C_{hs}. It permits numerical separation of dominant hardening from that of softening regimes. It is explicitly difficult to know at which pressure either of the hardening or softening offsets each other without using the proposed technique. The solution to Eq. (43) implies an increasing or decreasing intercept on *q*-axis with increasing confinement. An increasing value of C''_{ij} conserves energy so that rock masses appear stronger on yield which is a characteristic of dense granular material (Schofield and Wroth, 1968). The effect of C'_{ij} is translational in the *p*-*q* space to actuate softening process. The shape and size of *p*-*q* plot in Eq. (43) is modified by the parameter C_{ij} and represented as

$$\delta q/\delta p = 2C_{ij}p + C'_{ij} \tag{44}$$

$$\delta(\delta q/\delta p)/\delta p = \delta^2 q/\delta p^2 = 2C_{ij} \tag{45}$$

The shear stress in Eq. (44) is presented in a simplified form as

$$\delta q = (\delta q/\delta\varepsilon^{\mathrm{p}}_{\mathrm{s}})(\delta\varepsilon^{\mathrm{p}}_{\mathrm{s}}/\delta\varepsilon^{\mathrm{p}}_{\mathrm{v}})(\delta\varepsilon^{\mathrm{p}}_{\mathrm{v}}/\delta p)\delta p \tag{46}$$

$$\delta q = (\delta q/\delta\varepsilon^{\mathrm{p}}_{\mathrm{s}})F(\delta\varepsilon^{\mathrm{p}}_{\mathrm{v}}/\delta p)\delta p \tag{47}$$

where F is a function of $\delta\varepsilon^{\mathrm{p}}_{\mathrm{s}}/\delta\varepsilon^{\mathrm{p}}_{\mathrm{v}}$ which is opposite to dilatancy. Thus we have

$$\delta q/\delta p = F(\delta q/\delta\varepsilon^{\mathrm{p}}_{\mathrm{s}})(\delta\varepsilon^{\mathrm{p}}_{\mathrm{v}}/\delta p) \tag{48}$$

If $\delta p/\delta\varepsilon^{\mathrm{p}}_{\mathrm{v}} \to \Lambda_i$, $\delta\varepsilon^{\mathrm{p}}_{\mathrm{s}}/\delta q \to \Lambda_j$, then we have

$$\Lambda_i\Lambda_j(\delta^2 q/\delta p^2) = \delta F/\delta p \tag{49}$$

From Eqs. (45) and (49), we have

$$(\Lambda_i\Lambda_j 2C_{ij})\delta p = \delta F \tag{50}$$

Eq. (50) gives a pressure-sensitive directional frictional flow with consideration of effects of damage and joint parameters. If there is a continued gain or decay in strength due to deformations, either hardening or softening is set into the process, therefore, solutions to Eq. (43) which considers plasticity and yielding amid joints for an assumed frictional flow of rock mass can be represented as

$$C_{\mathrm{hs}} = f(\delta j,\ \delta i,\ \delta A) \tag{51}$$

where δA represents a parameter associated with changes in Helmholtz free energy density due to frictional flow and joint damage at an ambient temperature normally ignored in the rock mechanics practices. Based on Eqs. (41) – (51), the pressure and damage sensitive plastic parameter, C_{hs}, is expressed as

$$C_{\mathrm{hs}} = f(p_i/\sigma_{\mathrm{r}},\ \alpha_{\mathrm{p}},\ <\eta_{\mathrm{hs}}>) \tag{52}$$

where $<\eta_{\mathrm{hs}}>$ is the joint damage parameter. If $J_{\mathrm{fg}}{}^{\mathrm{p}} > J_{\mathrm{fg}}{}^{\mathrm{h}}$, then $<\eta_{\mathrm{hs}}> <1$; if $J_{\mathrm{fg}}{}^{\mathrm{p}} = J_{\mathrm{fg}}{}^{\mathrm{h}}$, then $<\eta_{\mathrm{hs}}> =1$; and if $J_{\mathrm{fg}}{}^{\mathrm{p}} < J_{\mathrm{fg}}{}^{\mathrm{h}}$, then $<\eta_{\mathrm{hs}}> >1$. In the initial hardening range, $C_{\mathrm{hs}} \to C_{\mathrm{h}}$, then $C_{\mathrm{hs}} = f(p_i/\sigma_{\mathrm{r}},\ \alpha_{\mathrm{p}})$, which can be expressed as a power function:

$$C_h = \kappa(p_i/\sigma_{\mathrm{r}})^{\eta} \tag{53}$$

The limit values of hardening and softening parameters are listed in Table 10, and the values of constants κ and η used in Eq. (53) are shown in Table 11.

Table 10. Limit values of hardening and softening parameters.

Rock mass classification	Rock type	C_{h}	R^2	α_p
Intact rock	Westerly granite[a]	–0.0024	0.963	-
Intact rock	KTB amphibolite[a]	–0.002	0.9066	-
Intact rock	Dunhum dolomite[a]	–0.002	0.897	-
Intact rock	Solenhofem limestone[a]	–0.00016	0.7059	-
Intact rock	Muzeho trachyte[a]	–0.0038	0.8874	-
Intact rock	Shrihama sandstone[a]	–0.01	0.8391	-
Intact rock	Dense marble[a]	–0.0004	0.9801	-
Intact rock	Yuubari shale[a]	–0.0018	0.7039	-
Jointed rock	Splitting mode[b]	–0.02	-	–0.0123
Jointed rock	Shearing mode[b]	–0.02	-	–0.0123
Jointed rock	Rotation mode[b]	–0.05	-	–0.025
Jointed rock	Sliding mode[b]	–0.035	-	–0.018
Jointed rock	All types[c]	–0.0115	-	–0.008
Rock masses	All types (based upon in-situ J_{fg})[f]	–0.024[d]	-	–0.012[e]
Rock masses	All types(based upon RMR)[f]	–0.035[d]	-	–0.028[e]
Rock masses	All types[d, e]	–0.0001 to –1	-	–0.0001 to –0.1

Note: Using best fitting results from published data of [a] Al-Ajmi and Zimmerman (2005), [b] Singh and Rao (2005), [c] Arora (1987), [d] Trivedi (2013a, b), [e] Present work, [f] Interpreted from the data of Chun et al. (2009).

3.4. Discussion of results

As a consequence of these observations, it is understood that softening of resistance to loading and volumetric dilation control the relationship of σ_{mr} and E_{mr}.

The strength of intact cemented and jointed material specimens is plotted (Fig. 10) from the published data sets (Lama and Vutukuri, 1978; Arora, 1987; ACI-318, 1995; Ramamurthy, 2004; Sonmez et al., 2004; Singh and Rao, 2005; Chun et al., 2009) for modulus of deformation as

Table 11. Constants used for calculation of plastic parameter C_{h} in hardening range.

End conditions, α_{p}	Values of κ and η for evaluation of plastic parameter C_{h} in hardening range					
	κ[a]	η[a]	Initial convexity[b]	κ[b]	η[b]	Final convexity[b]
–0.005	–0.04	–1	$\pi/80$	–0.040015	–1.011	$\pi/628$
–0.006	-	-	$\pi/92$	–0.034129	–1.028	$\pi/524$
–0.007	-	-	$\pi/110$	–0.028446	–1.08	$\pi/448$
–0.008	–0.022	–1.23	$\pi/136$	–0.022967	–1.167	$\pi/392$
–0.009	–0.02	–1.25	$\pi/178$	–0.017691	–1.288	$\pi/350$
–0.01	–0.011	–1.42	$\pi/248$	–0.012619	–1.444	$\pi/314$
–0.011	-	-	$\pi/406$	–0.00775	–1.636	$\pi/286$
–0.0125	–0.001	–2	$\pi/3800$	–0.000828	–1.988	$\pi/250$

Note: [a]Trivedi (2013a), [b] Interpreted values.

$$\sigma_{\mathrm{r}} = a_{\gamma} E_{\mathrm{r}}^{d} \quad (54)$$

$$\sigma_{\mathrm{m}} = a_{\gamma \mathrm{m}} E_{\mathrm{m}}^{d_{\mathrm{m}}} \quad (55)$$

where a_{γ} and $a_{\gamma \mathrm{m}}$ are constants of proportionality showing effects of unit weight and strain level on rock masses, respectively; d and d_{m} are the fitting exponents which depend upon softening due to the dilation of intact rock and rock masses from the passage of initial tangency to an eventual failure:

$$\sigma_{\mathrm{mr}} = a_{\mathrm{mr}} E_{\mathrm{mr}}^{d_{\mathrm{mr}}} \quad (56)$$

where d_{mr} is a fitting exponent which varies according to the relative dilation of rock mass compared to that of intact rock. If $a_{\gamma \mathrm{m}} = a_{\gamma}$, then $\sigma_{\mathrm{mr}} = E_{\mathrm{mr}}^{d_{\mathrm{mr}}}$. Table 9 shows values of d_{mr} computed from the available data sets of several investigators along with the determination coefficients.

As per the empirical estimates shown in Table 9, d_{mr} normally takes a value from 1 to 0.4.

In fact, Eq. (56) provides an empirical estimate for the relationship between strength and modulus ratio without consideration of joint contraction and dilation (Fig. 10).

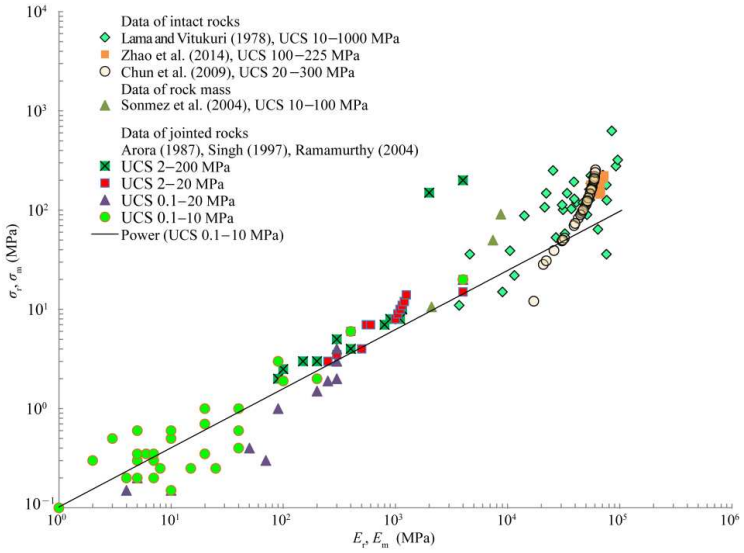

Fig. 10. Variation of compressive strength and modulus at varied strength levels.

3.5. A relationship of σ_{mr} vs. E_{mr} based upon pressure and damage sensitive plastic parameter, joint parameters and RQD

The typical shear-volume change characteristics of jointed rocks under mechanical loading are shown in Fig. 1. The observations of the volumetric response of rock masses are summarized (Table 2) as follows: (1) The mass materials can be characterized in a relatively intact (strong) and a fully mobilized (weak) state where the strength can be lower than that obtained at the critical state, as postulated in DSC. (2) Irrespective of the magnitude of the confining pressure and joint conditions, there exists an initial phase of linear contraction which is characterized by "hardening" effects. (3) The bigger grains and intact block show crack initiation and damage. (4) Hardening begins initially and continues to offset damage and softening up to a critical (saddle) pressure. (5) Further increasing pressures lead to dilation and damage occurring after contraction effects. (6) The higher the confining stress applied is, the less the degree of dilation and damage that occurs in the hardening regime is. (7) As the peak load is reached, deformation becomes localized along oriented paths, and disintegrates progressively to collapse. (8) The "softening and damage" produce a path specific drop in resistance and cause the resistance of surrounding rock following a pressure gradient.

As Eqs. (12) and (13) and Eqs. (14) and (15) provide a relationship by σ_{mr} vs. $J_{\mathrm{fg}}^{\mathrm{p}}$ and E_{mr} vs. $J_{\mathrm{fg}}^{\mathrm{h}}$, respectively, Eqs. (29) – (31) connect modified joint factor, joint factor and joint number with RQD, respectively. As a result, the strength ratio is shown to depend upon RQD.

There are two ways to validate such a relationship indirectly. As most of the available data of in-situ testing are captured, not necessarily, at the arrival of failure, σ_{mr} vs. RQD relationship is validated using the available data set of E_{mr} vs. RQD and by evaluating σ_{mr} using empirical relationship of σ_{mr} vs. E_{mr} (Eqs. (56) and (60)). Secondly, utilizing the final value of σ_{mr} from RQD, corresponding to the end values of α_{p} (Eqs. (12) and (13)) using empirical fitting coefficients a and b for modified joint factor and RQD relationship (Eq. (29)).

However, since the sensitivity to damage is not considered in Eqs. (12), (13), (19) and (56), a parameter, ζ, is adopted for inclusion of damage.

The strength ratio (σ_{mr}) and modulus ratio (E_{mr}) in hardening range are associated with the amplification factor ($\eta_{\mathrm{m}}^{\mathrm{h}} = \sigma_{\mathrm{m}}^{\mathrm{p}} / \sigma_{\mathrm{m}}^{\mathrm{h}}$, $\eta_{\mathrm{r}}^{\mathrm{h}} = \sigma_{\mathrm{r}}^{\mathrm{p}} / \sigma_{\mathrm{r}}^{\mathrm{h}}$) applied on peak hardening strain of rock mass and intact rock ($\varepsilon_{\mathrm{m}}^{\mathrm{h}}$ and $\varepsilon_{\mathrm{r}}^{\mathrm{h}}$), respectively, to provide a plastic strain ratio ($\varepsilon_{\mathrm{mr}}^{\mathrm{p}}$) relative to the hardening strain ($\varepsilon_{\mathrm{mr}}^{\mathrm{h}}$) for the rock masses as

$$\sigma_{\mathrm{mr}} / E_{\mathrm{mr}} = (\sigma_{\mathrm{m}} / E_{\mathrm{m}}) / (\sigma_{\mathrm{r}} / E_{\mathrm{r}})$$

$$[(\sigma_{\mathrm{m}}^{\mathrm{p}} / \sigma_{\mathrm{m}}^{\mathrm{h}}) \varepsilon_{\mathrm{m}}^{\mathrm{h}}] / [(\sigma_{\mathrm{r}}^{\mathrm{p}} / \sigma_{\mathrm{r}}^{\mathrm{h}}) \varepsilon_{\mathrm{r}}^{\mathrm{h}}] = (\eta_{\mathrm{m}}^{\mathrm{h}} / \varepsilon_{\mathrm{m}}^{\mathrm{h}}) / (\eta_{\mathrm{r}}^{\mathrm{h}} / \varepsilon_{\mathrm{r}}^{\mathrm{h}}) = \eta_{\mathrm{mr}}^{\mathrm{h}} \varepsilon_{\mathrm{mr}}^{\mathrm{h}} = \varepsilon_{\mathrm{mr}}^{\mathrm{p}} \quad (58)$$

The modulus ratio is related to observations of modified joint factor in hardening range, similar to the relationship between strength ratio and modified joint factor in softening range. Therefore, it is convenient to propose a relationship between strength ratio and modulus ratio incorporating a pressure-dependant plastic parameter. Hence, we have

$$\sigma_{\mathrm{mr}} = E_{\mathrm{mr}} \exp(\alpha_{\mathrm{p}} J_{\mathrm{fg}}^{\mathrm{p}} - C_{\mathrm{h}} J_{\mathrm{fg}}^{\mathrm{h}}) \quad (59)$$

The experimentally observed values of hardening parameter C_{h} of intact and jointed rock masses are shown in Table 10. Table 11 shows the range of

observed and computed values of C_h. As the change in modified joint factor is significant during hardening and softening processes, Eq. (59) becomes

$$\sigma_{mr} = E_{mr} \exp\{\alpha_p |[1-(C_h/\alpha_p)<\eta_{hs}>]<\eta>| J_{fg}^{p}\} \quad (60)$$

$$C_{hs} = \alpha_p |[1-(C_h/\alpha_p)<\eta_{hs}>]<\eta>| \quad (61)$$

where $|[1-(C_h/\alpha_p)<\eta_{hs}>]<\eta>| = \zeta$ is a pressure and damage sensitive plastic multiplier, which takes only positive values, otherwise it violates the laws of thermodynamics. A critical pressure ratio at a saddle pressure is a ratio of pressure at peak softening to that at peak hardening. It allows numerical separation of dominant hardening from that of softening regimes with the help of two more plastic parameters, namely, $<\eta_{hs}>$ and $<\eta>$. $<\eta_{hs}>$ and $<\eta>$ are also plasticity and damage sensitive parameters such that they allow a transition between J_{fg}^{h} and J_{fg}^{p}. The nature of parameter $<\eta>$ is the signum function undefined at zero. It is a function of applied pressure and takes a value of ±1 while changing its sign as the state of stress is greater than the saddle pressure. Furthermore, $<\eta>$ differentiates sensitivity of this parameter such that $<\eta> = \pm 1$, as either hardening or softening takes place. Since $<\eta> \neq 0$, it implies that the work done is essentially non-conservative. Similarly ζ implies that there is a functional relation between the plastic multiplier and damage parameter. The effect of variation of plastic parameter C_{hs} (at values of $<\eta_{hs}>=0.1$, 1, 10, 100 and 1000) with increasing pressure ratio is shown in Fig. 11.

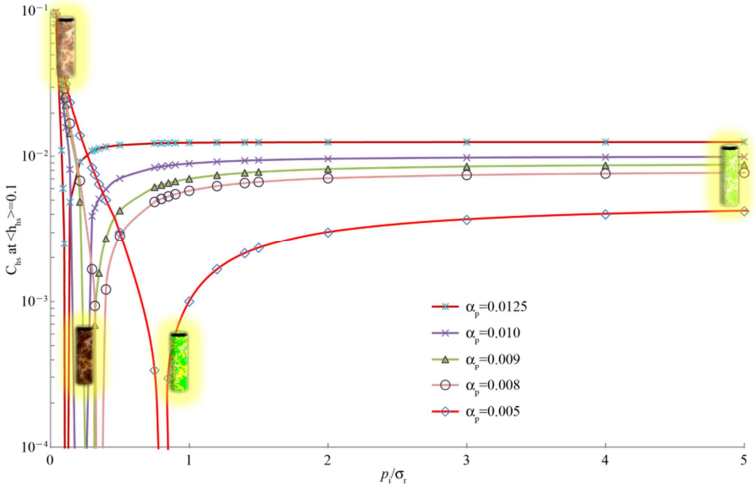

(a) $<\eta_{hs}>=0.1$.

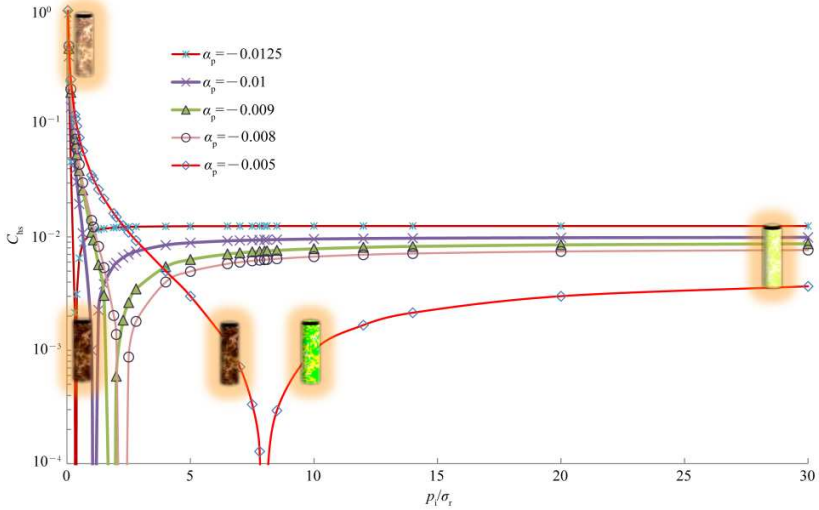

(b) $<\eta_{hs}>=1$.

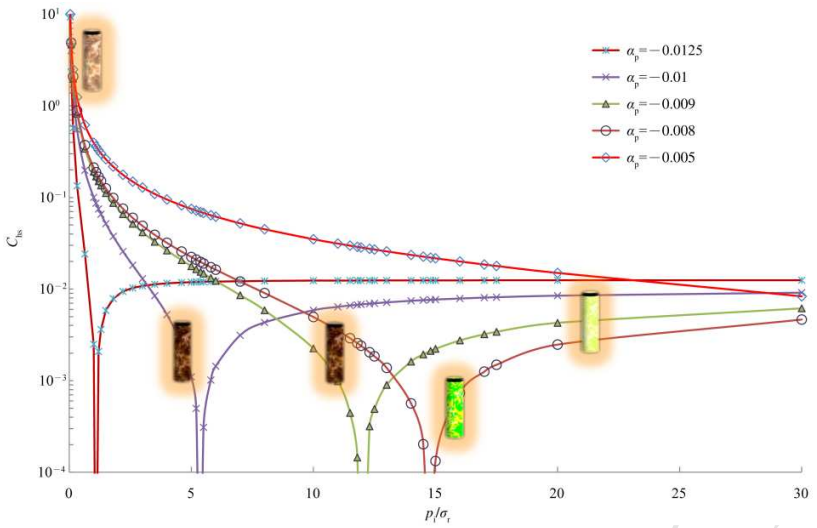

(c) $<\eta_{hs}>$=10.

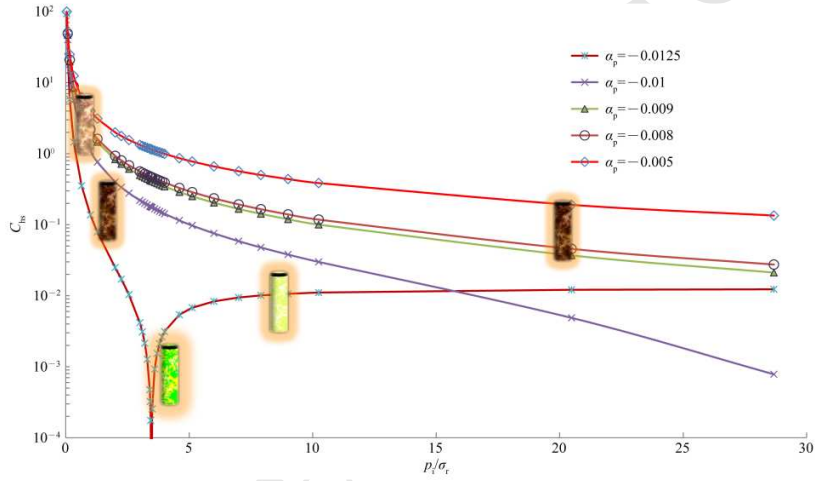

(d) $<\eta_{hs}>$=100.

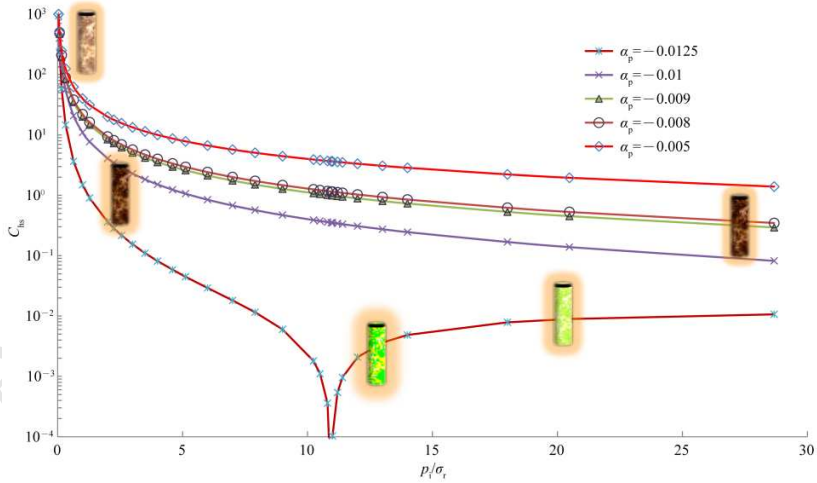

(e) $<\eta_{hs}>$=1000.

Fig. 11. Variation of plastic parameter with confining pressure ratio at different values of $<\eta_{hs}>$.

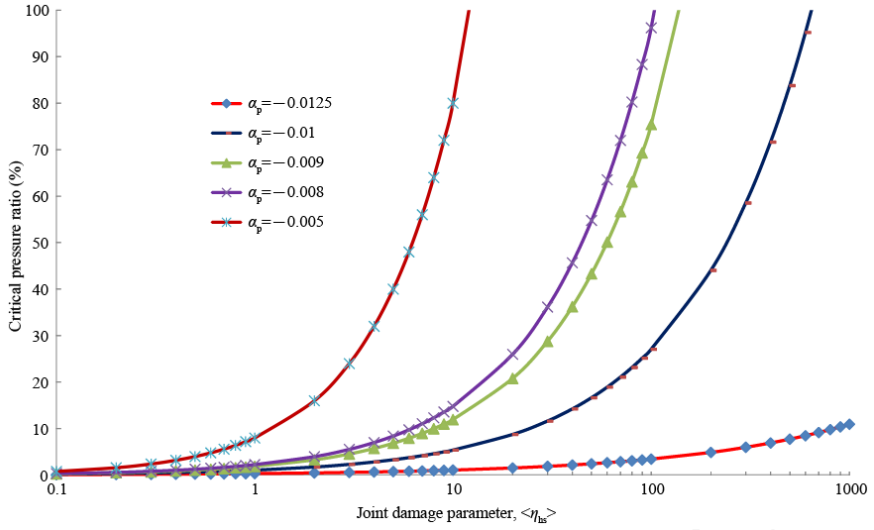

Fig. 12. Variation of critical pressure ratio with joint damage parameter.

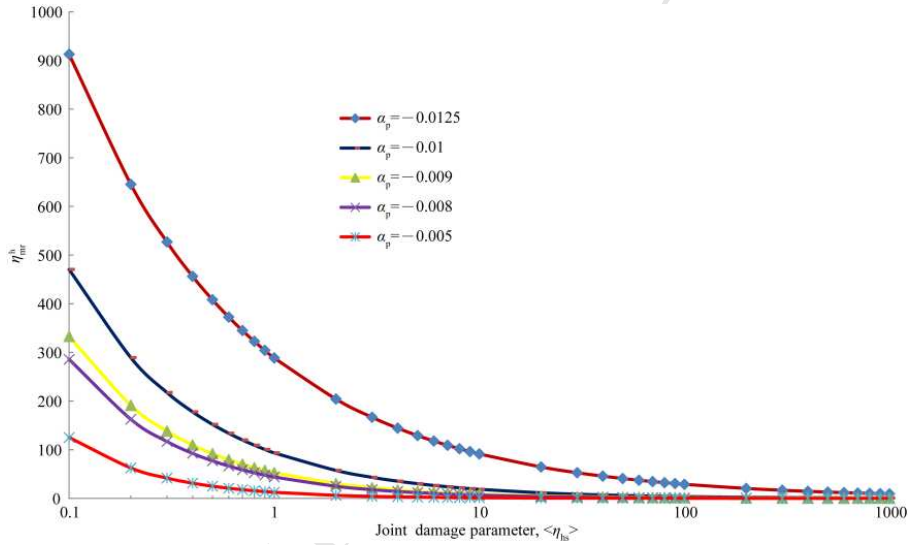

Fig. 13. Variation of amplification parameter η^h_{mr} with joint damage parameter.

Fig. 11 shows that the saddle pressure increases sharply if the joint damage parameter <η_{hs}>>>0.1, as summarized in Fig. 12. Fig. 13 shows the variation of amplification factor with joint damage parameter. An important outcome of the study is to find a pressure at which softening starts dominating the hardening process. The peak hardening pressure is obtained from the pressure of peak hardening shown in Fig. 11, and presented in Figs. 12 and 13.

Corresponding to the plastic parameter, per unit changes in the joint damage parameter C_{hs}, a variant of plastic parameter <C_{hs}>, are defined as

$$<C_{hs}>=C_{hs}/<\eta_{hs}> \quad (62)$$

The minimum value of <C_{hs}> would attain a non-zero value ($\hat{I}$ <0), while the maximum value would correspond to the peak hardening.

From Eq. (57)–(62), we have

$$\sigma_{mr}=E_{mr}\exp(<C_{hs}><\eta_{hs}>J^p_{fg}) \quad (63)$$

The joint damage parameter (<η_{hs}>) implies deterioration of the rock mass condition ever since the pressure increases beyond the peak hardening pressure, while <C_{hs}> is a variant of plastic parameter per unit change in the joint damage parameter. Fig. 14 demonstrates the variation of <C_{hs}> with pressure ratio for varied end conditions and joint damage parameters. Fig. 14 shows the intermediate stages in the evolution of the parameter C_{hs} with incremental damage as per the increasing values of the damage parameter, <η_{hs}> at the arrival of shear flow.

Fig. 15 shows indirect interpretation of σ_{mr} vs. RQD relation using the empirical relationship of σ_{mr} vs. E_{mr} at d_{mr}= 0.5 and 1, respectively. The effect of plasticity and damage on RQD has been considered through a parameter C_{hs} (at values of ζ=0.5, 1, 2, and 5) as shown in Fig. 16. Fig. 16 shows indirect validation from in-situ data. It provides a relation to obtain σ_{mr} vs. RQD with consideration of softening and damage.

It would be appropriate to define the similarity between the two ways of indirect validation. Both the methods estimate the value of strength ratio, but the estimate shown in Fig. 15 is obtained by the crude empirical technique based upon power law while that shown in Fig. 15 is supported by in-situ empirical data. One of the strong supports for this validation is the data fitting corresponding to the empirical observation in Fig. 15a which closely follows one of the observations plotted in Fig. 16a.

The data of σ_{mr} plotted in Fig. 16a and b do not necessarily represent the peak strength. From the small scale testing and in-situ measurements, they relate the deformation and strength of rock mass as ideally shown in Eqs. (38)–(40) through the use of damage sensitive plastic parameter.

Therefore, utilizing the relationship of joint mapping through damage and pressure sensitive characteristics in hardening and softening ranges (Eq. (59)), the strength ratio is expressed as

$$\sigma_{mr} = E_{mr} \exp(C_{hs} J_{fg}^{p}) \quad (64)$$

By applying and utilizing Eq. (29), the rock mass strength ratio is expressed in terms of the plastic parameter and RQD as

$$\sigma_{mr} = E_{mr} \exp[aC_{hs} \exp(bRQD)] \quad (65)$$

where a=1000 and b=–1 to –0.01, depending upon joint characteristics.

Eqs. (64) and (65) provide a relationship to obtain the strength based upon pressure dependent softening and damage. The values of E_{mr} and σ_{mr} evaluated from in-situ observations are presented in Tables 12 and 13.

Therefore, using Figs. 15 and 16, the strength ratio may be expressed as an exclusive function of RQD:

$$\sigma_{mr} = m \log_{10} RQD + n \quad (66)$$

where m and n depend upon the pressure and damage sensitivities of rock masses. The damage and pressure sensitivities as per the selected data set are shown in Tables 14 and 15, which show varied levels of initial plasticity quantified through n. If the block obtained from a core recovery sample is less than 10 cm in length, the RQD value sets to zero. As RQD=0, $\log_{10}RQD$ reaches singularity, it cannot be defined. Therefore, the strength ratio can be evaluated by obtaining the modified joint factor. To evaluate the strength ratio at RQD=1, since $\log_{10}RQD$ =0, σ_{mr}=n in Eq. (66). In fact, n can be fine adjusted as a function of modified joint factor.

As RQD→0, Eq. (66) has constants (m and n) and the strength may be obtained by statistical extrapolation. For evaluating the strength corresponding to RQD→0, there are a wide-ranging values of J_{fg} associated with varied site stress condition, plasticity and damage at specific pressure conditions as shown in Fig. 6.

The relationship proposed in Eq. (66) is further supported by the back calculated data of RQD shown in Fig. 17 which deterministically quantify the initial plasticity and damage through rock mass parameters considered in the modified joint factor vs. RQD relation.

Fig. 17 provides a validation for the theoretical relationship of RQD and strength ratio in a generalized form, taking plasticity and damage into consideration (α_p and ζ) at varied levels of accumulated plastic strains characterized by the rock mass parameter b. Fig. 17d shows indirect validation of the theoretical relationship shown in Fig. 17a–c using calculated data of RQD and mobilized strength ratio in the hardening range obtained from in-situ data. Fig. 17e shows direct validation of the theoretical relationship shown in Fig. 17a–c using back calculated data of RQD and mobilized strength ratio in the softening-damage range obtained from laboratory tests.

Based upon the in-situ observations of strength (σ_m^{obs}) corresponding to a RQD value in two most probable states of strength, namely, the minimum (σ_m^{min}) and maximum (σ_m^{max}) strength ratios, an index of progressive failure (I_m) is defined as

$$I_m = (\sigma_m^{obs} - \sigma_m^{min}) / (\sigma_m^{max} - \sigma_m^{min}) \quad (67)$$

$$I_m = M_{rqd} RQD \quad (68)$$

where M_{rqd} is the slope of linear fitting obtained from I_m vs. RQD observation.

The index of progressive failure (I_m) is obtained from the values of the minimum (σ_m^{min}) and maximum (σ_m^{max}) strengths from plasticity and damage sensitivities of rock masses. An example of the index of progressive failure observed in the laboratory and in-situ test is shown in Fig. 18. The value of M_{rqd} depends upon the nature and extent of inherent and induced discontinuities in the rock mass. Therefore, for each data set, M_{rqd} can be statistically obtained, and $M_{rqd}^{obs} = I_m / RQD$ is calculated. The value of $I_{mr} = M_{rqd}^{obs} / M_{rqd}$ shows proximity of individual data point to the anticipated progressive failure of the data set. This indicates that full mobilization of strength exists while it is negligible when the index tends to zero. It can be observed that the maximum strength is mobilized for RQD as low as 20% for the selected in-situ test data.

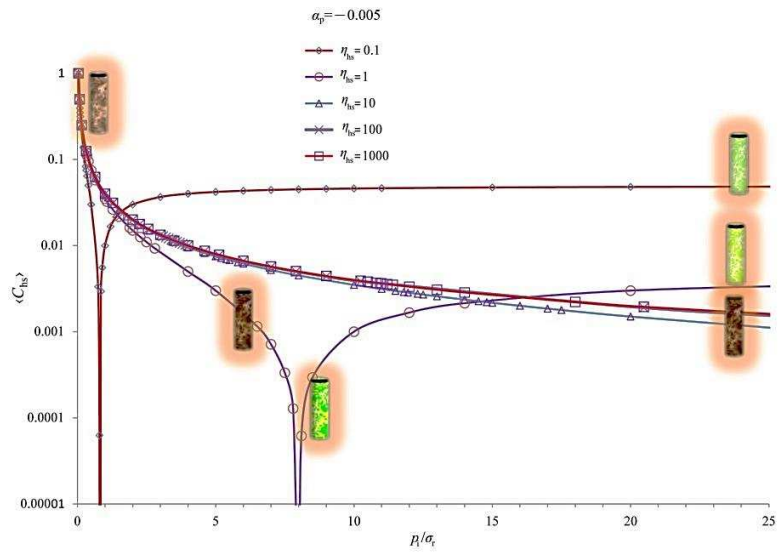

(a) α_p=–0.005.

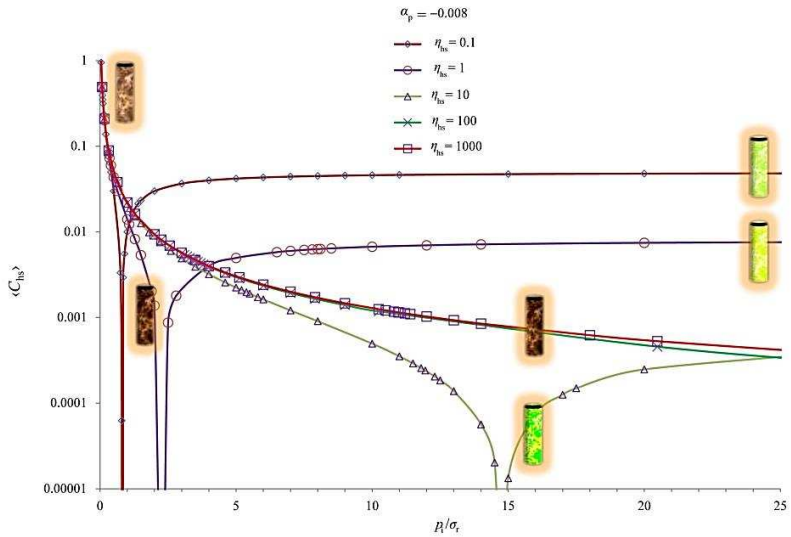

(b) α_p=–0.008.

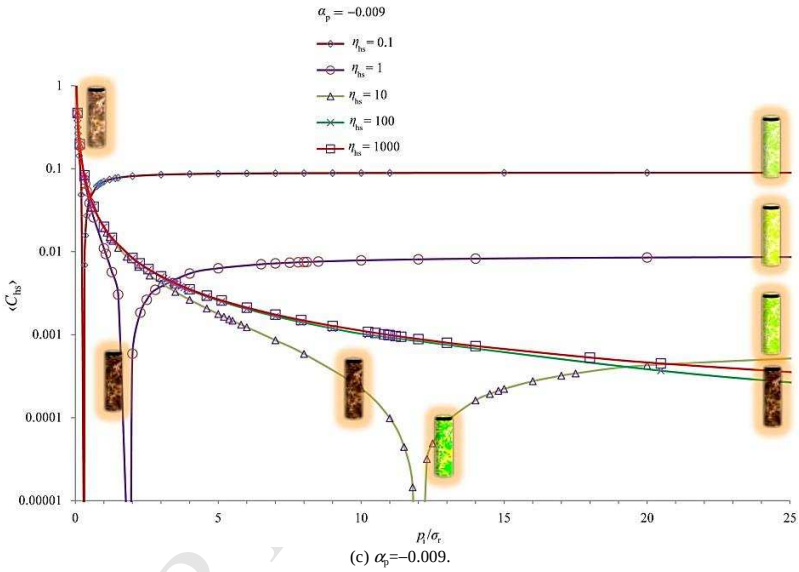

(c) α_p=–0.009.

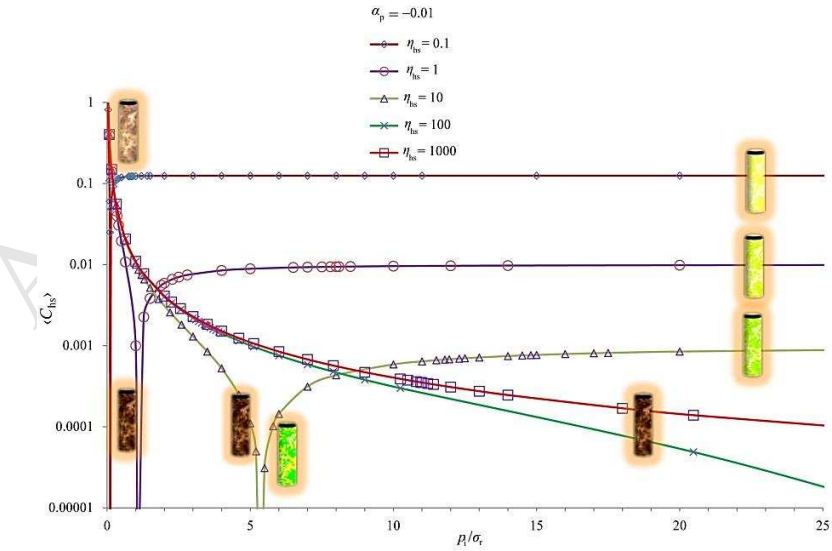

(d) α_p=–0.010.

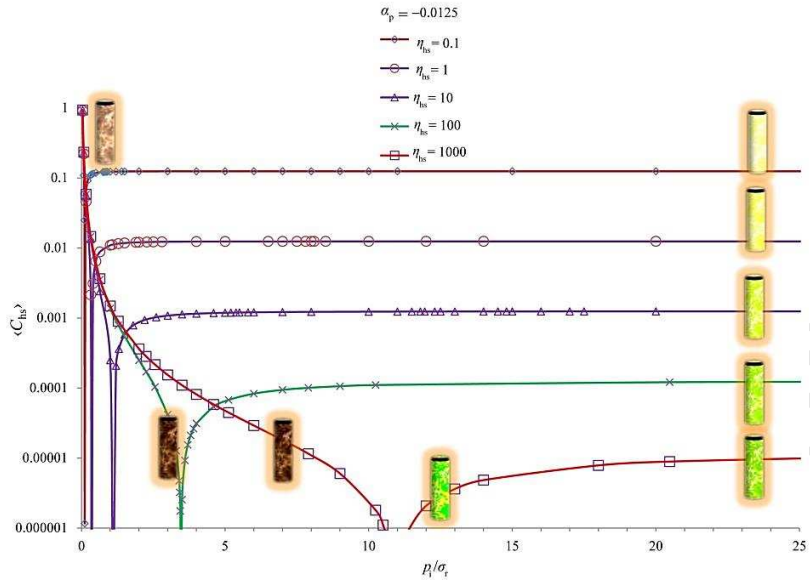

(e) α_p=−0.0125.

Fig. 14. Variation of plastic parameter with confining pressure ratio for varied joint damage parameters at different end conditions.

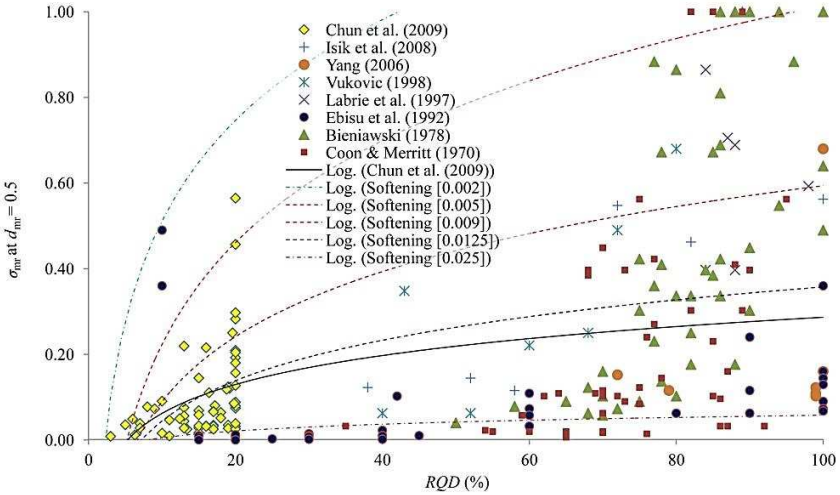

(a) d_{mr}=0.5.

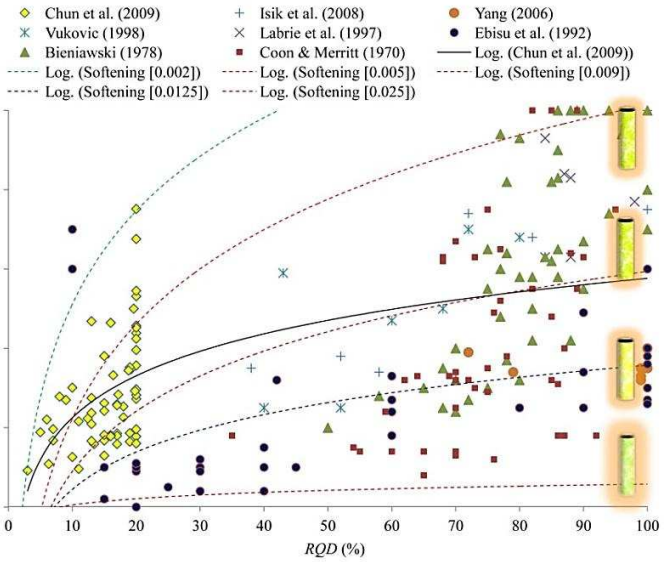

(b) d_{mr}=1.

Fig. 15. Indirect validation of relationship of σ_{mr} vs. RQD. Data points are obtained by $J_{fg}^{p}C_{hs} \rightarrow 0$ in Eq. (9) and different values of d_{mr}; dotted lines are obtained by α_p=−0.002 to −0.025 with reference to the best fit with the power law.

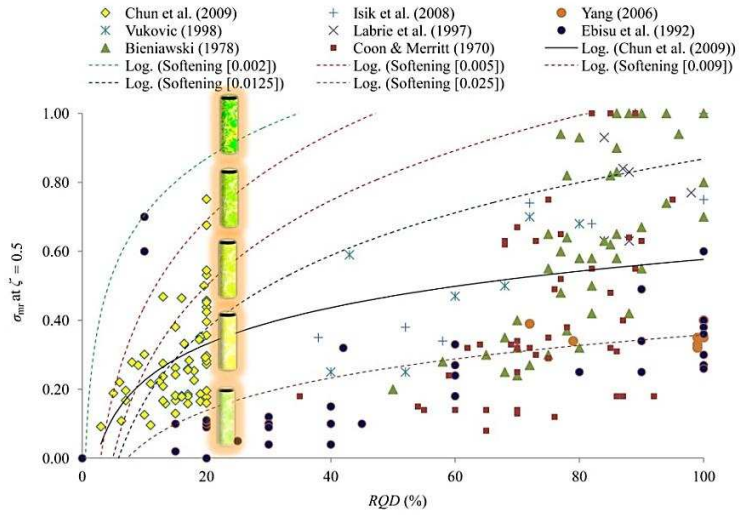

(a) ζ=0.5.

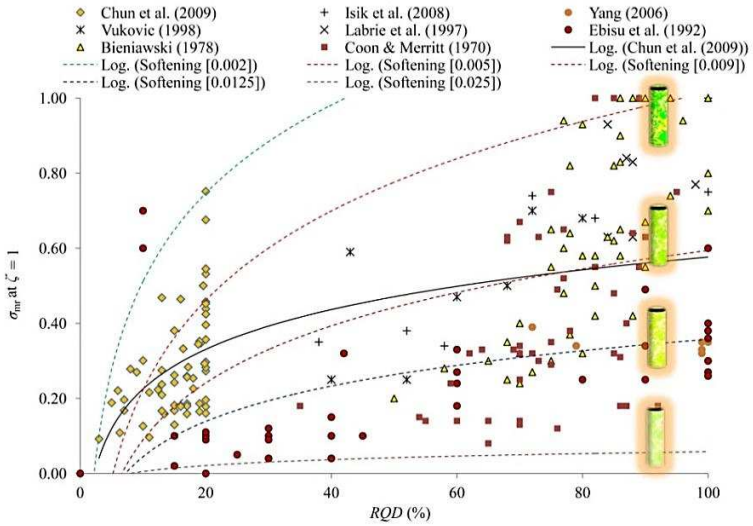

(b) ζ=1.

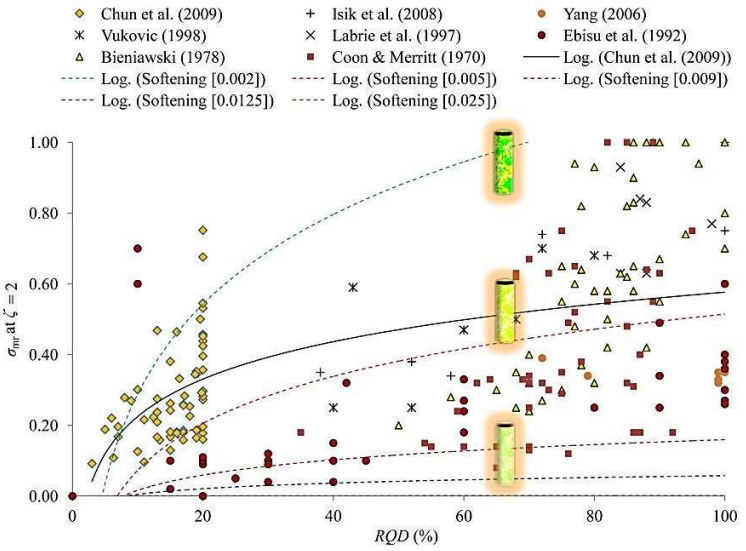

(c) ζ=2.

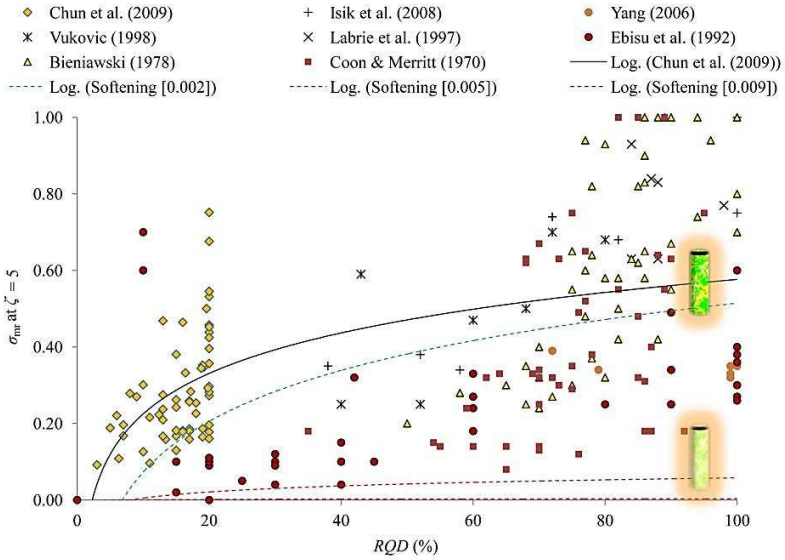

(d) ζ=5.

Fig. 16. Indirect validation of relationship of σ_{mr} vs. RQD. Data points are obtained by $J_{fg}^{p}C_{hs} \rightarrow 0$ in Eq. (64) and different values of ζ; dotted lines are obtained for α_p=–0.002 to –0.025 with reference to the best fit.

Table 12. In-situ modulus ratio of rock masses evaluated from published data set.

Published data set[a]							Interpreted E_{mr} using published work[b] at a=1000, b=–0.1 and ζ=1			
Depth (m)	UCS (MPa)	Observed *RQD*	Discontinuity condition	Groundwater condition	Discontinuity orientation adjustment	*RMR*	E_{mr}	α_p= 0.005	α_p= 0.008	α_p= 0.0125
5	28.4	5	9	7	–10	21	0.19	0	0.005	0.87
8.5	148.9	3	10	7	–5	33	0.09	0.013	0.195	0.982
9.5	12.1	8	12	7	–5	30	0.28	0	0	0.137
20.4	82.9	17	24	10	–5	62	0.19	0.008	0.088	0.922
8.5	109.9	6.3	12	10	–5	42	0.11	0.014	0.181	0.976
17.5	70	17.2	20	7	–5	54	0.28	0.008	0.088	0.921
31	119.9	19.2	27	7	–5	71	0.35	0.017	0.126	0.931
8.5	213.9	16.4	17	10	–10	59	0.33	0.459	0.76	0.998
17	219.9	20	27	7	–10	76	0.46	0.34	0.648	0.994
24	159.9	20	25	7	–15	62	0.36	0.118	0.375	0.978

Note: Using published data set of ten observations from [a]Chun et al. (2009) and [b]Trivedi (2013a).

Table 13. In-situ strength of rock masses evaluated from published data set.

Published data set[a]			Using a=1000, b=–0.1 and ζ=1[b]								σ_{mr} at different values of α_p[b]			
Depth (m)	UCS (MPa)	Observed *RQD*	Vertical stress (MPa)	*RMR*	*r*	J_n	g_d	J_w	*n*	J_{fg}	α_p =0.002	α_p =0.005	α_p =0.009	α_p =0.0125
5	28.4	5	0.14	21	0.76	6	0.3	0.47	0.67	84	0.297	0.048	0.004	0.001
8.5	148.9	3	0.23	33	1.05	6.4	0.33	0.47	0.33	118	0.227	0.025	0.001	0
9.5	12.1	8	0.26	30	0.62	6.4	0.4	0.47	0.33	166	0.407	0.106	0.018	0.004
20.4	82.9	17	0.55	62	0.95	8.6	0.8	0.67	0.33	51	0.694	0.401	0.193	0.102
8.5	109.9	6.3	0.23	42	1	9.5	0.4	0.67	0.33	107	0.345	0.07	0.008	0.001
17.5	70	17.2	0.47	54	0.92	8.5	0.67	0.47	0.33	89	0.699	0.408	0.2	0.107
31	119.9	19.2	0.84	71	1.01	13	0.9	0.47	0.33	92	0.746	0.48	0.267	0.16
8.5	213.9	16.4	0.23	59	1.11	10.8	0.57	0.67	0.67	39	0.678	0.379	0.175	0.089
17	219.9	20	0.46	76	1.11	16.9	0.9	0.47	0.67	54	0.763	0.508	0.296	0.184
24	159.9	20	0.65	62	1.06	12.2	0.83	0.47	1	30	0.763	0.508	0.296	0.184

Note: [a] Using published data set of ten observations from Chun et al. (2009) and [b] Interpreted values using present work.

Table 14. Evaluation of in-situ strength of rock masses from *RQD* in Eq. (66) using σ_{mr}-E_{mr} power law relationship.

Rock mass characteristic parameters				Reference figure
d_m	α_p	*m*	*n*	
0.5	-0.002	0.3392	-0.1697	Fig. 15a
	-0.005	0.3438	-0.5689	
	-0.009	0.2191	-0.4152	
	-0.012	0.0975	-0.1625	Best fit
	-0.0125	0.316	-0.2688	
	-0.025	0.0229	-0.0477	
1.0	-0.002	0.3392	-0.2697	Fig. 15b
	-0.005	0.3438	-0.5689	
	-0.009	0.2191	-0.4152	
	-0.012	0.1527	-0.1266	Best fit
	-0.0125	0.136	-0.2688	
	-0.025	0.0229	-0.0477	

Table 15. Evaluation of in-situ strength of rock masses from *RQD* using Eq. (66) using parameter ζ

Rock mass characteristic parameters				Reference figure
ζ	α_p	*m*	*n*	
0.5	-0.002	0.2367	+0.1602	Fig. 16a
	-0.005	0.3614	-0.3924	
	-0.009	0.3565	-0.5679	

	-0.012	0.1527	-0.1266	Best fit
	-0.0125	0.3054	-0.5388	
	-0.025	0.136	-0.2688	
1	-0.002	0.3392	-0.2697	Fig. 16b
	-0.005	0.3438	-0.5689	
	-0.009	0.2191	-0.4152	
	-0.012	0.1527	-0.1266	Best fit
	-0.0125	0.136	-0.2688	
	-0.025	0.0229	-0.0477	
2	-0.002	0.3663	-0.5551	Fig. 16c
	-0.005	0.1919	-0.3692	
	-0.009	0.0626	-0.1271	
	-0.012	0.1527	-0.1266	Best fit
	-0.0125	0.0229	-0.0477	
	-0.025	0.0007	-0.0015	
5	-0.002	0.1919	-0.3692	Fig. 16d
	-0.005	0.0229	-0.0477	
	-0.009	0.0014	-0.0029	
	-0.012	0.1527	-0.1266	Best fit
	-0.0125	0.0001	-0.0003	

Table 16. Index of progressive failure of rock masses from *RQD* in Eqs. (67) and (68) using $I_m = M_{rqd}\, RQD$.

Rock mass characteristic parameters				Reference figure
Broad description	M_{rqd}	R^2	J_{fg}	
In-situ data based upon RMR	0.0273	0.56	10-150	
In-situ data based upon GSI	0.0232	0.486	10-150	
Without fill	0.0119	0.484	10-320	Fig. 18
Without fill, inclined joints	0.0106	0.718	10-720	
Clayey fill	0.0108	0.461	40-260	
Cemented fill	0.0056	0.12	18-114	

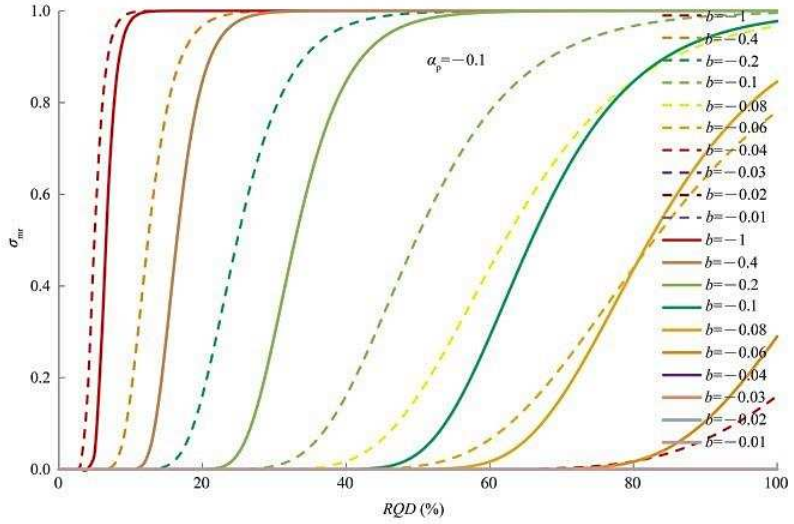

(a) α_p=–0.1.

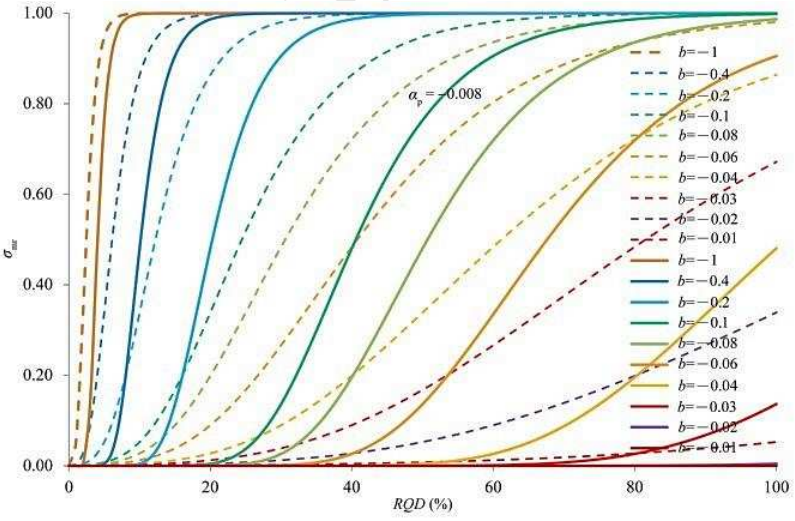

(b) α_p=–0.008.

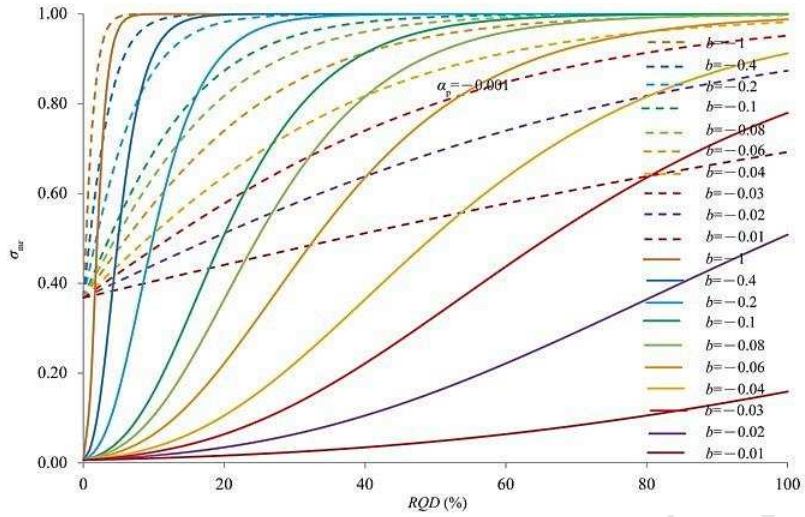

(c) α_p=−0.001.

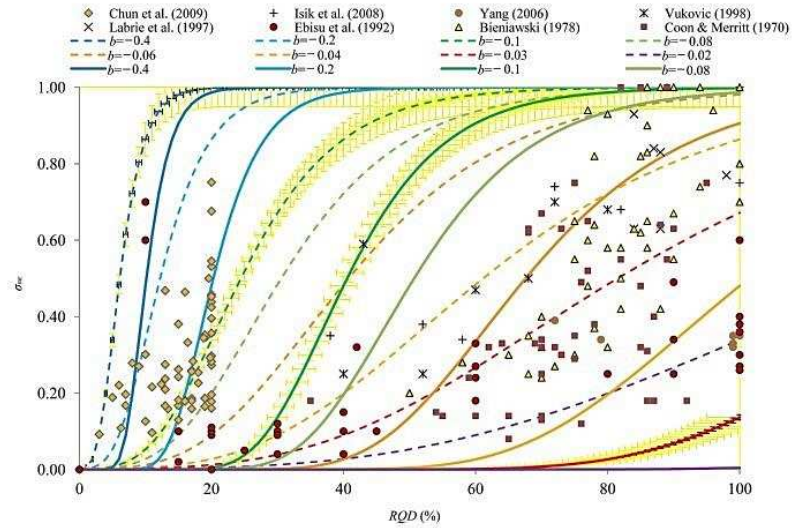

(d) α_p=−0.008. The data points correspond to calculated values obtained from the relationship of σ_{mr} vs. *RQD* as $J_{fg}^{p}C_{hs} \rightarrow 0^{-}$ in Eq. (64). 5% error bars on theoretical lines are drawn to capture in-situ data for *RQD* in varied ranges of plasticity and damage.

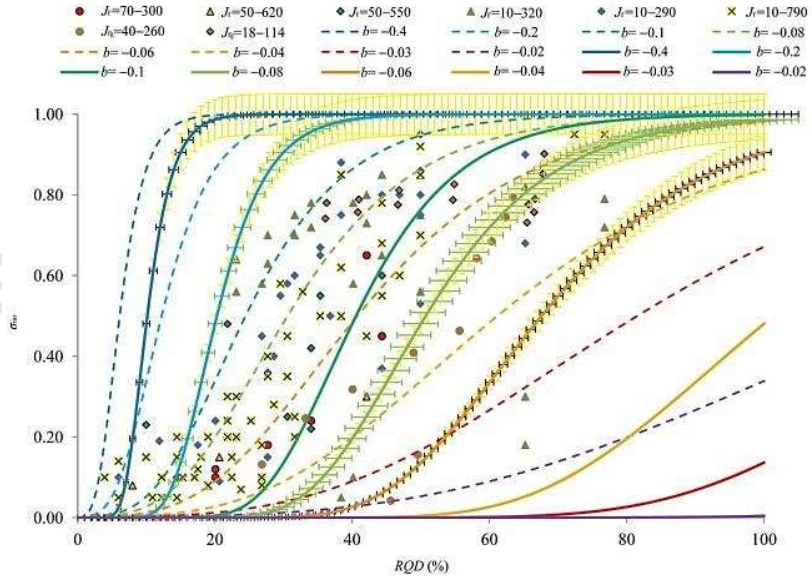

(e) α_p=−0.008. The data points correspond to calculated values obtained from the modified joint factor at upper bound of accumulated plastic strain. 5% error bars on theoretical lines are drawn to capture most of experimental data.

Fig. 17. Theoretical variation of strength ratio with *RQD* using the pressure and damage sensitive plastic parameter ζ=1, 5 and different α_p, implying their effects on varied levels of accumulated plastic strains identified by *b*-values. The effect of plasticity and damage is presented by the solid lines, and the effect of plasticity is shown by the dotted lines.

4. Steps for implementation of present technique

The following steps may be considered to implement the present technique:

(1) Identify important information to be included in bore log data sheet, namely depth of sample collection at requisite intervals; unit weight; overburden pressure; joint number; inclination of joints and orientation parameter; joint condition; the maximum, minimum and mean thickness of gouge; density of gouge; frictional properties; water pressure and *RQD*. Additional parameters for inputs of RMR, GSI, and *Q*-system may also be considered.

(2) Evaluate the values of J_{fg}, α_p, C_h, C_{hs}, and $<C_{hs}>$ in the spread sheet using Eqs. (10) and (11), (13), (15), (61) and (62), respectively. An example to calculate modulus and strength ratio using joint parameters evaluated from in-situ data of *RQD* is shown in Tables 12 and 13, respectively.

(3) Consider Eqs. (36), (38)–(40), inputs of J_{fg}, confining pressure and *n* to obtain a value of α_p.

(4) Evaluate the overburden and confining pressure, and consider C_h according to the values of α_p.

(5) Draw a plot between the modified joint factor and *RQD* to find out the parameter *b* (Eq. (21)).

(6) According to the values of α_p and *b*, find out the value of σ_{mr} from *RQD* (for example Fig. 17a–c).

(7) Estimate values of C_{hs} (Fig. 11) for an appropriate value of $<\eta_{hs}>$ and pressure.

(8) Operate C_{hs} at an appropriate pressure upon *RQD* to get σ_{mr} at any in-situ hardening and softening as well damage consideration shown in Fig. 17d and e, respectively.

(9) Obtain the index of progressive failure as per Eqs. (67) and (68) for the entire length of scan line of *RQD*.

5. Scope of application of the present model

The plastic parameter captures the available data set of strength ratio obtained from *RQD* and laboratory testing using the present technique. The strength criterion used herein provided a data set in normalized form for the application of this technique. The relations described above should be judiciously applied with the following reasons:

(1) The strength criterion cited in the paper is essentially empirical and the constants associated with various relationships (shown in Tables 4 and 5) provide an approximate interpretation of strength. The empirical strength criteria, namely, MC-criterion, HB-criterion, and JC-criterion, were initially proposed with idealization and they were extended later to rock masses.

(2) The strength of rock masses depends upon intact rock strength, joint parameters (represented by the modified joint factor), plastic volume change and damage characteristics.

(3) The range of strength ratio is essentially from 0 to 1. The strength ratio of 1 represents the strength of intact rocks. Occurrences of joints, decreasing size, and damage increases the modified joint factor, which is observed in a range of 1000–0. The zero value of modified joint factor may correspond to the strength of intact rock.

(4) In-situ characterization of rock masses is carried out by borehole-log-data (to provide the value of modified joint factor) and *RQD*. *RQD* is observed in a range of 0–100. The zero value of *RQD* is associated with heavily jointed rock masses. There exists an exponential relation between the modified joint factor and *RQD* based upon the in-situ data characterized by a fitting parameter *b* (Fig. 8).

(5) The plastic volume change characteristics consist of dominant hardening at relatively lower pressures and softening as a dominant process at higher pressures.

(6) This work applies concepts of progressive stiffness and degradation using a pressure and damage sensitive plastic parameter. The process used for the development of the present criterion is one of pure trial-and-error and of numerical implementation.

(7) The hardening first increases with isotropic pressure and then softening and damage appear as an effect of increasing isotropic pressure. The process from hardening to softening is continuous. As a result, the plastic parameter can be used to show the critical point between hardening and softening. Hence, the plastic parameter beyond the peak hardening is a value approaching the peak softening with plastic volume changes, shear and damage.

(8) The volume change of rock mass has a nonlinear relation with the strength. The laboratory estimated values of plastic and damage parameter can be extended for in-situ evaluation of strength and accumulated plastic strains adjusted for the laboratory and field data. The precise predictions of strength of rock masses depend upon an appropriate choice of plastic and joint damage parameters. As a result, there can be several possible combinations of rock mass parameters, namely, *b*, C_{hs}, α_p and ζ corresponding to a particular *RQD* which may provide the same strength ratio.

(9) Similar to the current trends in modeling, the present work intends to arrive at an appropriate level of plasticity and damage based upon selection of joint parameters. The purpose of this technique is to provide a framework to obtain a plastic parameter isolating damage in relation to strength and *RQD* and to find it using a simple numerical tool. An index of progressive failure can be obtained from the in-situ observations of *RQD*.

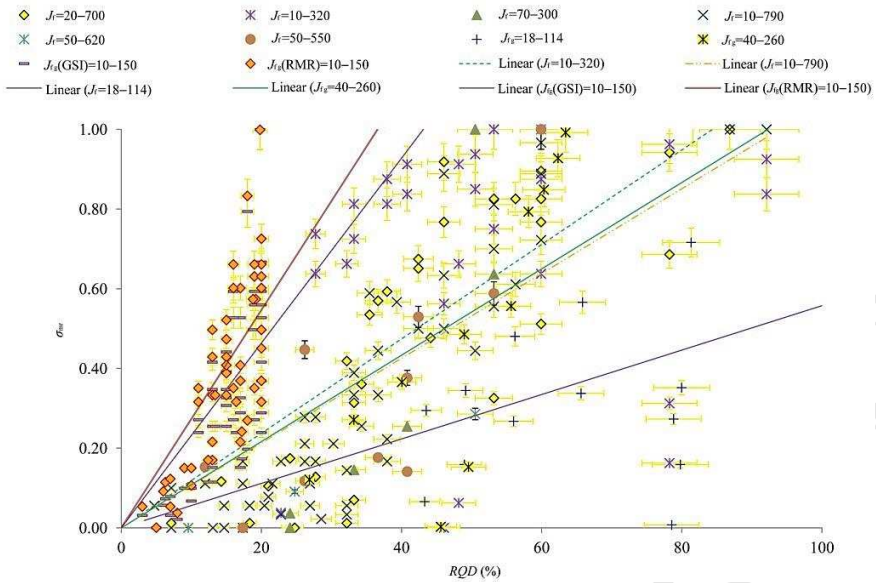

Fig. 18. Index of progressive failure obtained from in-situ tests and laboratory data of strength ratio vs. modified joint factor. *RQD* is obtained from the modified joint factor vs. *RQD* relationship at the maximum accumulated plastic strain with and without gouge shown by solid and dotted lines, respectively, along with 5% error bars.

6. Conclusions

This paper is based upon the current trends in modeling which does not necessarily predict exact values of in-situ strength of rock masses but brings out a methodology for more rational estimates of strength of rock masses with the consideration of pressure and damage sensitive plasticity using results of laboratory and in-situ testing. It further presents an argument in favor of wholeness in the behavior of rock masses such that the strength ratio drops below the one as the damage and plasticity are introduced into the mass material as an effect of induced pressure. The trends in strength criterion and rock mass characterisation techniques (RMR, GSI and Q-system) may not essentially capture altogether the contraction, dilation and damage sensitivities of joints, fractures and micro-crack network with reference to in-situ and laboratory estimates so well as the present proposal.

The relationships between intrinsic joint parameters and the isotropic pressure provide inputs for a numerical technique to incorporate these effects into the strength ratio. The results of the present work show that variability between laboratory testing and in-situ testing results is essentially due to the plasticity, damage and the accompanying changes in the joint parameters characterized by accumulated plastic strains. This technique considers the effect of a damage-sensitive plastic parameter on strength by initial and end conditions of the parameter of readily estimated modified joint factor and well recognized *RQD* for rock masses. The published data relating the modulus ratio with *RQD* and the strength ratio with the modified joint factor provide a scope for validation of present proposal and to obtain strength ratio. The recognition of intrinsic joint characteristics in relation to the pressure and damage sensitive plastic parameter provides a resolution to the multiplicity in interpreting the in-situ strength of rock masses.

Conflict of interest

The author would like to affirm that there is no known conflict of interest associated with this publication, as there was no significant funding for this work from any sponsoring agency, which could influence the finding of this study.

Acknowledgments

The author is thankful to several data sources, meaningful inputs from coworkers and editors for their suggestions in improving this paper.

Notations

A_b	Empirical constant which takes a value 3 for axi-symmetrical and 5 for plane strain case as per Bolton (1986)
δA	Parameter associated with changes in Helmholtz free energy density
a, b	Fitting parameters for experimental data of *RQD* and modified joint factor
a_γ, $a_{\gamma m}$, d, d_m, d_{mr}	Fitting constants and exponents for experimental data of strength and modulus of rocks and rock type masses
a_{HB}, m_b, and s	Empirical rock constants as per the generalized HB-criterion
C, C', C_s, C_{ij}, C'_{ij}, C''_{ij}	Plastic parameters
C_h, C_{hs}, $<C_{hs}>$	Variants of plastic parameter
$<\eta>$	Signum function which takes a value ±1
$<\eta_{hs}>$	Joint damage parameter
c'_a, c_g	Modification factor for joint number and joint factor, respectively
α_p	Observed parameter depending upon pressure and joint characteristic dependent softening
E_t, E_m	Modulus of intact rock and rock mass, respectively
F	Flow function
I_r	Relative dilatancy index

$\ddot{I}$, $\hat{I}$	Limit values for variation of softening parameters such that $\ddot{I} > C_{hs} > \hat{I}$
i	Potential for change in isotropic pressure with plastic volumetric strain
j	Potential for change in plastic shear strain with shear stresses
J_t, J_{dj}, J_w	Factors for joint thickness, depth, ground water condition
J_f , J_{fg}	Joint factor and modified joint factors respectively
J^h_{fg}, J^p_{fg}	Modified joint factors in hardening and softening range, respectively
J^{pd}_{fg}	Modified joint factor due to plasticity and damage
J_n	Number of joints in the direction of loading per unit length
L_{na}	Reference length =1 m
M and B	Empirical rock parameters depending upon compressive strength as per the JC-criterion
χ, χ_b, χ_m	Empirical rock constants in JC-criterion
n_β	Joint orientation parameter depending upon inclination of the joint plane (β) with respect to the direction of loading
p and δp	Mean effective confining pressure and its change, respectively
p_i	Initial mean confining pressure
q and δq	Shear stress and its change, respectively
r	Reference joint strength parameter
RMR, Q, GSI, MC, JC, HB	Rock mass rating, Q-system, Geological strength index, MC-criterion, JC-criterion and HB-criterion, respectively
R_D	Relative density of gouge
RQD	Rock quality designation
λ and C	Empirical parameters for dilatancy of joints
ε^h_r , ε^h_m , ε^h_{mr}	Hardening strains of intact rock, rock mass and hardening strain ratio
ε^p_{mr}	Plastic strain ratio of rock mass and intact rock
ε^p_v , ε^p_s	Plastic volumetric strain and plastic shear strain, respectively
η^h_r , η^h_m , η^h_{mr}	Stress multiplication factors for hardening of intact rock, rock mass, and rock mass stress ratio to reach full plastic state
ζ	Damage sensitive plastic multiplier
σ_1, σ_2, σ_3	Principal stresses in the intact rock
σ_{1m}, σ_{2m}, σ_{3m}	Principal stresses in the rock mass
σ_{1N}, σ_{3N}	Principal stress ratios used in the JC-criterion, $\sigma_{1N}=\sigma_{1m}/\sigma_t$ and $\sigma_{3N}=\sigma_{3m}/\sigma_t$
σ_t , σ_m	Uniaxial compressive strength of intact rock and rock mass, respectively
σ_a	Reference stress, σ_a=1 kPa
σ_{mr}, E_{mr}	Strength ratio and modulus ratio, resepectively
Λ_i, Λ_j	$\Lambda_i = \delta p / \delta \varepsilon^p_v$ and $\Lambda_j = \delta \varepsilon^p_s / \delta q$

References

ACI Committee 318. Building code requirements for structural concrete (ACI 318M-95) and commentary (ACI 318RM-95). Farmington Hills, USA: American Concrete Institute, 1995.

Akai K, Adachi T, Nishi K. Elasto-plastic behavior of soft sedimentary rock (porous tuff). Proceedings of the Japan Society of Civil Engineers 1978; (271): 83–95.

Al-Ajmi AM, Zimmerman RW. Relation between the Mogi and the Coulomb failure criteria. International Journal of Rock Mechanics And Mining Sciences 2005; 42(3): 431–9.

Aldrich MJ. Pore pressure effects on Berea sandstone subjected to experimental deformation. Geological Society of America Bulletin 1969; 80(8): 1577–86.

Arioglu N, Girgin Z, Arioglu E. Evaluation of ratio between splitting tensile strength and compressive strength for concretes up to 120 MPa and its application in strength criterion. ACI Materials Journal 2006; 103(1): 18–24.

Arora VK, Trivedi A. Effect of Kaolin gouge on strength of jointed rocks. In: Rock Slopes: Proceedings of the Asian Regional Symposium 1992, New Delhi. CRC Press, 1992. pp. 21–5.

Arora VK. Strength and deformation behavior of jointed rocks. PhD Thesis. Delhi, India: Indian Institute of Technology, 1987.

Barton N. Deformation phenomena in jointed rock. Geotechnique, 1986; 36(2): 147–67.

Barton N. Shear strength criteria for rock, rock joints, rockfill and rock masses: Problems and some solutions. Journal of Rock Mechanics and Geotechnical Engineering 2013; 5(4): 249–61.

Barton N. Some new *Q*-value correlations to assist in site characterization and tunnel design. International Journal of Rock Mechanics and Mining Sciences 2002; 39(2): 185–216.

Besuelle P, Desrues J, Raynaud S. Experimental characterization of the localisation phenomenon inside a Vosges sandstone in a triaxial cell. International Journal of Rock Mechanics and Mining Sciences 2000; 37(8): 1223–37.

Bieniawski ZT. Determining rock mass deformability: Experience from case histories. International Journal of Rock Mechanics and Mining Sciences and Geomechanics Abstracts 1978; 15(5): 237–47.

Billam J. Some aspects of the behaviour of granular material at high pressures. In: Parry RHG editor. Stress-strain Behaviour of Soils. London: G T Foulis & Co. Ltd., 1972. pp. 69–80

Bolton MD. The strength and dilatancy of sands. Geotechnique 1986; 36(1): 65–78.

Bortolotti L. First cracking load of concrete subjected to direct tension. ACI Materials Journal 1991; 88(1): 70–3.

Bortolotti L. Influence of concrete tensile ductility on compressive strength of confined columns. Journal of Materials in Civil Engineering 1994; 6(4): 542–63.

Brook N. Estimating the triaxial strength of rock. International Journal of Rock Mechanics and Mining Sciences and Geomechanics Abstracts 1979; 16(4): 261–4.

Brown ET, Trollope DH. Strength of models of jointed rock. Journal of the Soil Mechanics and Foundations Division, ASCE 1970; 96(SM2): 685–704.

Brown ET. Strength of models of rock with intermittent joints. Journal of the Soil Mechanics and Foundations Division, ASCE 1970; 96(6): 1935–49.

Carpinteri A, Cornetti P, Puzzi S. Size effect upon grained materials tensile strength: The increase of the statistical dispersion at the smaller scales. Theoretical and Applied Fracture Mechanics 2005; 44(2): 192–9.

Castellanza R, Nova R. Oedometric tests on artificially weathered carbonatic soft rocks. Journal of Geotechnical and Geoenvironmental Engineering 2004; 130(7): 728–39.

CEB-FIP Model Code. Comité Euro-International du Béton, Information Bulletin No. 213-214. 1990. doi: 10.1680/ceb-fipmc1990.35430)(URL: http://www.icevirtuallibrary.com/content/book/100121.

Chun BS, Ryu WR, Sagong M, Do JN. Indirect estimation of the rock deformation modulus based on polynomial and multiple regression analyses of the RMR system. International Journal of Rock Mechanics and Mining Sciences 2009; 46(3): 649–58.

Coon RF, Merritt AH. Predicting in situ modulus of deformation using rock quality indices. In: Determination of the in situ Modulus of Deformation of Rock. Philadelphia, USA: American Society for Testing and Materials (ASTM), 1970. pp. 154–173.

de Buhan P, Fréard J, Garnier D, Maghous S. Failure properties of fractured rock masses as anisotropic homogenized media. Journal of Engineering Mechanics 2002; 128(8): 869–75.

de Jong G. Rowe's stress dilatancy relation based on friction. Geotechnique 1976; 26(3): 527–34

Deere DU, Deere DW. The rock quality designation (RQD) index in practice. In: Rock Classification Systems for Engineering Purposes, ASTM-STP 984. Philadelphia, USA: ASTM, 1988. pp. 91–101.

Deere DU, Hendron AJ, Patton FD, Cording EJ. Design of surface and near surface construction in rock. In: Fairhurst C editor. Failure and Breakage of Rock, 8th Symposium on Rock Mechanics. American Institute of Mining, Metallurgical and Petroleum Engineers, 1967. pp. 237–302.

Desai CS. Constitutive modeling of materials and contacts using the disturbed state concept: Part 1–Background and analysis. Computers and Structures 2015a; 146: 214–33.

Desai CS. Constitutive modeling of materials and contacts using the disturbed state concept: Part 2–Validations at specimen and boundary value problem levels. Computers and Structures 2015b; 146: 234–51.

Drucker DC, Prager W. Soil mechanics and plastic analysis or limit design. Quarterly of Applied Mathematics 1952; 10(2): 157–65.

Drucker DC. A definition of stable inelastic material. Journal of Applied Mechanics 1959; 26: 101–6.

Ebisu S, Aydan O, Komura S, Kawamoto T. Comparative study on various rock mass characterization methods for surface structures. In: Hudson JA editor. ISRM Symposium: EUROCK'92, Rock Characterization. London, UK: Thomas Telford Ltd., 1992. pp. 203–8.

Eid HT. A technique for estimating permeability of a randomly fractured rock mass. Acta Geotechnica 2007; 2(2): 97–102.

Einstein HH, Hirschfeld RC. Model studies on mechanics of jointed rock. Journal of the Soil Mechanics and Foundations Division, ASCE 1973; 99(3): 229–48.

Förster S, Plantenberg T. From self-organizing polymers to nanohybrid and biomaterials. Angewandte Chemie International Edition 2002; 41(5): 688–714.

Grenon M, Hadjigeorgiou J. Evaluating discontinuity network characterization tools through mining case studies. In: Soil Rock America 2003 (Vol. 1), Boston. 2003. pp. 137–42.

Herrmann HJ, Kertész J, de Arcangelis L. Fractal shapes of deterministic cracks. Europhysics Letters 1989; 10(2): 147–52.

Herrmann HJ, Roux S. Statistical models for the fracture of disordered media. Amsterdam, Netherlands: North-Holland. 1990.

Hirai H, Satake M. Proposal of a yield function and description of plastic behavior of soft rocks. Proceedings of the Japan Society of Civil Engineering 1982; (320): 159–64.

Hoek E. Strength of jointed rock masses. Geotechnique 1983; 33(3): 187–223.

Hoek E, Brown ET. Empirical strength criterion for rock masses. Journal of Geotechnical Engineering 1980; 106(9): 1013–35.

Hoek E, Brown ET. Practical estimates of rock mass strength. International Journal of Rock Mechanics and Mining Sciences 1997; 34(8): 1165–86.

Hoek E, Diederichs MS. Empirical estimation of rock mass modulus. International Journal of Rock Mechanics and Mining Sciences 2006; 43(2): 203–15.

Hoek E, Martin CD. Fracture initiation and propagation in intact rock–A review. Journal of Rock Mechanics and Geotechnical Engineering 2014; 6(4): 287–300.

Horne MR. The behaviour of an assembly of rotund, rigid cohesionless particles, Parts I and II. Proceedings of the Royal Society of London. Series A, Mathematical and Physical Sciences 1965; 286: 62–97.

Horpibulsuk S, Miura N, Bergado DT. Undrained shear behavior of cement admixed clay at high water content. Journal of Geotechnical and Geoenvironmental Engineering 2004; 130(10): 1096–105.

Innocenzi P, Malfatti L, Falcaro P. Water droplets to nanotechnology: A journey through self-assembly. Cambridge, UK: Royal Society of Chemistry, 2013.

Isik NS, Doyuran V, Ulusay R. Assessment of deformation modulus of weak rock masses from pressuremeter tests and seismic surveys. Bulletin of Engineering Geology and the Environment 2008; 67(3): 293–304.

Jain NK. Effect of cemented fill on strength of jointed specimen. MTech Thesis Delhi, India: Department of Civil Engineering, Delhi University, 2011.

Johnston I, Chiu H. Strength of weathered Melbourne mudstone. Journal of Geotechnical Engineering 1984;110(7): 875–98.

Johnston I. Strength of intact geomechanical materials. Journal of Geotechnical Engineering 1985; 111(6): 730–49.

Kalamaras GS, Bieniawski ZT. A rock strength concept for coal seams incorporating the effect of time. In: Proceedings of the 8th International Congress on Rock Mechanics (Vol. 1), Tokyo, Japan. Rotterdam and Brookfield: A.A. Balkema, 1995. pp. 295–302.

Labrie D, Plouffe M, Haevey A, Major C. Distress blast testing at Sigma mine: Experimentation and results. Div. Rep. No. MMSL 97-143E. Ottawa, Canada: Mining and Mineral Sciences Laboratories, 1997.

Labuz J, Zang A. Mohr–Coulomb failure criterion. Rock Mechanics and Rock Engineering 2012; 45(6): 975–9.

Lama RD, Vutukuri VS. Handbook on mechanical properties of rocks. Clausthal-zellerfieL, Germany: Trans. Tech. Publications, 1978.

Li G, Liu Y, Dano C, Hicher P. Grading-dependent behavior of granular materials: From discrete to continuous modeling. Journal of Engineering Mechanics 2015; 141(6): 04014172.

Lisjak A, Grasselli G. A review of discrete modeling techniques for fracturing processes in discontinuous rock masses. Journal of Rock Mechanics and Geotechnical Engineering 2014; 6(4): 301–14

Luding S. Towards dense, realistic granular media in 2D. Nonlinearity 2009; *22*(12): R101–R146.

Martin CD, Kaiser PK, McCreath DR. Hoek-Brown parameters for predicting the depth of brittle failure around tunnels. Canadian Geotechnical Journal 1999; 36(1): 136–51.

McClintock FA, Irwin GR. Plasticity aspects of fracture mechanics. In: Fracture Toughness Testing and Its Applications. Philadelphia, USA: ASTM, 1965. pp. 84–113.

McLamore R, Gray KE. The mechanical behavior of anisotropic sedimentary rocks. Journal of Engineering for Industry 1967; 89(1): 62–73.

Nicholls K. Discussion on 'Measurement of total core recovery; dealing with core loss and gain'. Quarterly Journal of Engineering Geology and Hydrogeology 2012; 45(3): 391.

Nicholson GA, Bieniawski ZT. A nonlinear deformation modulus based on rock mass classification. International Journal of Mining and Geological Engineering 1990; 8(3): 181–202.

Noorian-Bidgoli M. Strength and deformability of fractured rocks. PhD Thesis. Stockholm, Sweden: Royal Institute of Technology (KTH), 2014.

Ojha S, Trivedi A. Shear strength parameters for silty-sand using relative compaction. Electronic Journal of Geotechnical Engineering 2013; 18: 81–99.

Palchik V, Hatzor YH. The influence of porosity on tensile and compressive strength of porous chalks. Rock Mechanics and Rock Engineering 2004; 37(4): 331–41.

Palmstorm A. Measurements of and correlations between block size and rock quality designation (RQD). Tunnelling and Underground Space Technology 2005; 20(4): 362–77.

Palmstrom A. Characterizing rock masses by the RMi for use in practical rock engineering: Part 1: The development of the Rock Mass index (RMi). Tunnelling and Underground Space Technology 1996; 11(2): 175–88.

Perras MA, Diederichs MS. A review of the tensile strength of rock: Concepts and testing. Geotechnical and Geological Engineering 2014; 32(2): 525–46.

Priest SD, Hudson J. Discontinuity spacing in rock. International Journal of Rock Mechanics and Mining Sciences and Geomechanics Abstracts 1976; 13: 135–48.

Ramamurthy T, Arora VK. Strength prediction for jointed rocks in confined and unconfined states. International Journal of Rock Mechanics and Mining Sciences and Geomechanics Abstracts 1994; 31(1): 9–22.

Ramamurthy T. A geo-engineering classification for rocks and rock masses. International Journal of Rock Mechanics and Mining Sciences 2004; 41(1): 89–101.

Roscoe KH, Schofield A, Wroth CP. On the yielding of soils. Geotechnique 1958; 8(1): 22–53.

Rowe PW. The relation between shear strength of sands in triaxial compression, plane strain and direct shear. Geotechnique 1969; 19(1): 75–86.

Rowe PW. The stress dilatancy relation for static equilibrium of an assembly of particles in contact. Proceedings of the Royal Society of London. Series A, Mathematical and Physical Sciences 1962; 269: 500–27.

Roy N. Engineering behavior of rock masses through study of jointed models. PhD Thesis. New Delhi, India: Indian Institute of Technology Delhi, 1993.

Santarelli FJ. Theoretical and experimental investigation of the stability of the axisymmetric wellbore. PhD Thesis. London: Imperial College, 1987.

Schofield A, Wroth P. Critical state soil mechanics. London: McGraw-Hill, 1968.

Sen T, Tiddy GJ, Casci JL, Anderson MW. One-pot synthesis of hierarchically ordered porous−silica materials with three orders of length scale. Angewandte Chemie 2003;115(38): 4797–801.

Sen Z, Eissa EA. Volumetric rock quality designation. Journal of Geotechnical Engineering 1991; 117(9):1331–46.

Sen Z. RQD models and fracture spacing. Journal of Geotechnical Engineering 1984; 110(2): 203–16.

Serafim JL, Pereira JP. Consideration of the geomechanical classification of Bieniawski. In: Proceedings of International Symposium on Engineering Geology and Underground Construction, Lisbon, Portugal. 1983. pp. 33–44.

Setunge S, Attard MM, Darvall PP. Ultimate strength of confined very high-strength concretes. ACI Structural Journal 1993; 90(6): 632–41.

Shield RT, Ziegler H. On Prager's hardening rule. Zeitschrift für angewandte Mathematik und Physik ZAMP, 1958; 9(3): 260–76.

Singh K, Singh D, Ranjith P. Simulating flow through fractures in a rock mass using analog material. International Journal of Geomechanics, 2014; 14(1): 8–19.

Singh M, Rao K. Bearing capacity of shallow foundations in anisotropic non-Hoek–Brown rock masses. Journal of Geotechnical and Geoenvironmental Engineering 2005; 131(8): 1014–23.

Singh M. Engineering behaviour of jointed model materials. PhD Thesis. New Delhi, India: Indian Institute of Technology Delhi, 1997.

Sonmez H, Tuncay E, Gokceoglu C. Models to predict the uniaxial compressive strength and the modulus of elasticity for Ankara Agglomerate. International Journal of Rock Mechanics and Mining Sciences 2004; 41(5): 717–29.

Spitzig WA, Richmond O. The effect of pressure on the flow stress of metals. Acta Metallurgica 1984; 32(3): 457–63.

Stoughton TB, Yoon JW. A pressure-sensitive yield criterion under a non-associated flow rule for sheet metal forming. International Journal of Plasticity 2004; 20(4–5): 705–31.

Swanson SR, Brown WS. An observation of loading path independence of fracture in rock. International Journal of Rock Mechanics and Mining Sciences and Geomechanics Abstracts 1971; 8(3): 277–81.

Taylor DW. Fundamentals of soil mechanics. New York: Wiley, 1948.

Terzaghi K. Rock defects and loads on tunnel supports. In: Proctor RV, White TL editors. Rock Tunneling with Steel Supports. Youngstown, USA: Commercial Shearing and Stamping Company, 1946. pp. 5–153.

Trivedi A, Arora VK. Discussion of bearing capacity of shallow foundations in anisotropic non-Hoek–Brown rock masses. Journal of Geotechnical and Geoenvironmental Engineering 2007; 133(2): 238–40.

Trivedi A, Banik T, Sukumar T, Kumar N, Jain A, Kumar A, Tewatia SK. Discussion: Consolidation of clayey gouge amid permeating rock masses. Environmental Geotechnics 2014. http://dx.doi.org/10.1680/envgeo.14.00038.

Trivedi A, Banik T, Sukumar T, Kumar N, Jain A, Kumar A. Consolidation of clayey gouge amid permeating rock masses. Environmental Geotechnics 2015;2: 137 – 154. doi: 10.1680/envgeo.13.00043.

Trivedi A, Sud VK. Ultimate bearing capacity of footings on coal ash. Granular Matter 2005; 7(4): 203–12.

Trivedi A. Effect of gouge on the strength of jointed rocks. MTech Thesis. Kurukshetra, India: Regional Engineering College, 1990.

Trivedi A. Engineering behavior of ash fills. In: Tiwari A, Shukla SK editors. Advanced Carbon Materials and Technology. Wiley-Scrivener, 2013b. pp. 419–74.

Trivedi A. Estimating in situ deformation of rock masses using a hardening parameter and RQD. International Journal of Geomechanics 2013a; 13(4): 348–64.

Trivedi A. Strength and dilatancy of jointed rocks with granular fill. Acta Geotechnica 2010; 5(1): 15–31.

Valentine S, Norbury D. Measurement of total core recovery; dealing with core loss and gain. Quarterly Journal of Engineering Geology and Hydrogeology, 2011; 44(3): 397–403.

Valentine S, Norbury D. Reply to discussion on 'Measurement of total core recovery; dealing with core loss and gain'. Quarterly Journal of Engineering Geology and Hydrogeology 2012; 45(3): 392.

Vatsala A, Nova R, Murthy BRS. Elastoplastic model for cemented soils. Journal of Geotechnical and Geoenvironmental Engineering 2001; 127(8): 679–87.

Vermeer PA, de Borst R. Non-associated plasticity for soils, concrete and rock. HERON 1984; 29 (3). http://repository.tudelft.nl/view/ir/uuid%3A4ee188ab-8ce0-4df3-adf5-9010ebfaabf0/

Vesic AS, Clough GW. Behavior of granular materials under high stresses. Journal of Soil Mechanics and Foundations Division, ASCE 1968; 94(SM3): 661–8.

Villeneuve M, Diederichs MS, Kaiser PK. Effects of grain scale heterogeneity on rock strength and the chipping process. International Journal of Geomechanics 2012; 12(6): 632–47.

Vukovic N. Comparison of laboratory and field modulus of elasticity of rocks. MS Thesis. Montreal, Canada: McGill University, 1998.

Walton G, Diederichs MS. A new model for the dilation of brittle rocks based on laboratory compression test data with separate treatment of dilatancy mobilization and decay. Geotechnical and Geological Engineering 2015; 33(3): 661–79.

Xiao Y, Liu H, Chen Y, Jiang J. Strength and deformation of rockfill material based on large-scale triaxial compression tests. II: Influence of particle breakage. Journal of Geotechnical and Geoenvironmental Engineering 2014; 140(12). doi:10.1061/(ASCE)GT.1943-5606.0001177.

Yaji RK. Shear strength and deformation of jointed rocks. PhD Thesis. New Delhi, India: Indian Institute of Technology, 1984.

Yang K. Analysis of laterally loaded drilled shafts in rock. PhD Thesis. Akron, USA: University of Akron, 2006.

Yapı Merkezi Inc.. Investigation of the failure criteria for concrete in triaxial compression, and determination of its material properties such as angle of internal friction, cohesion without making any experiments. Report No. YM/ARGE/96-12, 1996.

Yu HS. Plasticity and geotechnics. New York: Springer, 2006.

Yuan SC, Harrison J. An empirical dilatancy index for the dilatant deformation of rock. International Journal of Rock Mechanics and Mining Sciences 2004; 41(4): 679–86.

Zapperi S, Vespignani A, Stanley HE. Plasticity and avalanche behaviour in microfracturing phenomena. Nature 1997; 388(6643): 658–60.

Zhang L, Einstein HH. Using RQD to estimate the deformation modulus of rock masses. International Journal of Rock Mechanics and Mining Sciences 2004; 41(2): 337–41.

Zhang L. Estimating the strength of jointed rock masses. Rock Mechanics and Rock Engineering 2009; 43(4): 391–402.

Zhang L. Method for estimating the deformability of heavily jointed rock. Journal of Geotechnical and Geoenvironmental Engineering 2010; 136(9): 1242–50.

Zhao XG, Cai M, Wang J, Li PF, Ma LK. Objective determination of crack initiation stress of brittle rocks under compression using AE measurement. Rock Mechanics and Rock Engineering, 2015. doi: 10.1007/s00603-014-0703-9.

.

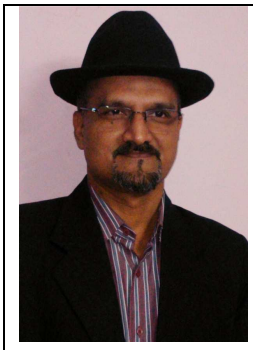

A. Trivedi presently serves as a Professor of Civil Engineering and Dean of Industrial Research and Development at Delhi Technological University, Delhi, India. His previous affiliations include Professor of Civil Engineering and Dean, Faculty of Technology at University of Delhi, Dean of Continuing Education at Delhi College of Engineering, Head of the Department of Civil, Mechanical and Electrical Engineering at University of Delhi, Head of the Department of Civil Engineering at Delhi Technological University, Delhi, India. He obtained his Bachelor and Master degrees from REC (now NIT), Kurukshetra and PhD from TIET, (now Thapar University), Patiala, India. He has more than fifty research papers, as lead author in the reputed journals, conferences and symposia. He is a fellow of Indian Association of Structural Engineers and an active member of several professional societies namely, ASCE, ISRMTT, ISTE, and IGS, Delhi. He has supervised a number of prestigious consultancy and research projects. He has guided more than fifty Master's and PhD candidates for the award of degrees at Thapar University, Patiala, University of Delhi and Delhi Technological University, Delhi, India. He also has a couple of patents and PCTs to his credit. His current interests include mechanics of fractured masses, hydraulic flow amid cemented and un-cemented ash fills, liquefaction of soils, and bio-cemented soils and rocks. He likes playing tennis, participates in the community activities of Yoga, and ontological studies.

IOSR Journal of Electrical and Electronics Engineering (IOSR-JEEE)
e-ISSN: 2278-1676,p-ISSN: 2320-3331, Volume 10, Issue 4 Ver. III (July – Aug. 2015), PP 98-104
www.iosrjournals.org

Constant Torque Operation of Wound Rotor Induction Motor using feedback mechanism in a Rectifier Fed Induction Motor Drive

[1]Anmol Aggarwal, [2]JN Rai, [3]Maulik Kandpal
[1,2,3]*Department of Electrical Engineering, Delhi Technological University (Formerly Delhi College of Engineering)*

Abstract: *This paper sets forth a technique to operate wound rotor induction motor in maximum torque region, using a feedback mechanism using rotor speed and slip.Static rotor resistance control has been used to vary the rotor resistance. The AC output voltage of motor is rectified by a diode bridge and is fed to a parallel combination of IGBT and external resistance. Effective value of rotor resistance is varied by varying the duty cycle of IGBT. Simulation models has been prepared in MATLAB in which a constant maximum torque is generated from standstill(s=1) to* $s_{Tmax}(=0.415)$.

Keywords: *Wound rotor induction motor,diode, IGBT, rotor speed, slip, MATLAB*

I. Introduction

Wound rotor induction motor is of pivotal importance when high staring torque is required and when the driven load requires precise speed control. The doubly-fed induction generator (DFIG) used in onshore wind turbines and motor generator set (MG Set) widely employ wound rotor induction motor. In past, liquid resistance starters (LRS) have been used to control the external resistance of rotor circuit for big induction machines but its setup requires large space .This problem can be easily rectified by employing in power electronic devices like chopper circuit and diode bridge which are compact.

In a wound rotor induction motor at the time of starting the entire external resistance is added to the rotor circuit and as the rotor speeds up, the external resistance is varied in steps so that motor torque tends to remain maximum during accelerating period. Finally, under normal operation the external resistance is fully cut off and the slip rings are short circuited.[1, 2, 4]

II. Models

In past pulse generator has been used to achieve varying rotor external resistance. The Wound Rotor Induction Rotor employing pulse generator is shown in Figure 1for such model

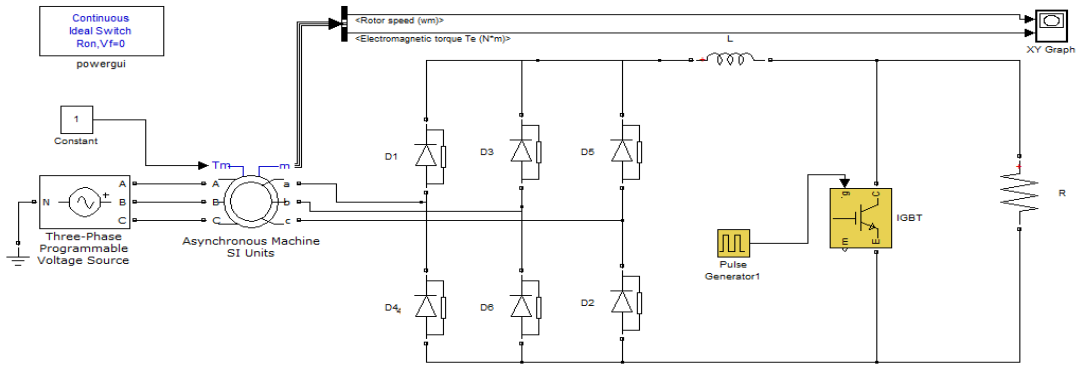

Figure 1: Wound Rotor Induction Motor employing pulse generator

In this model the rectified ac voltage of motor is fed to a parallel combination of resistance R and IGBT. Pulse Generator has been employed to trigger the IGBT.As no feedback mechanism has been employed the duty cycle has to be varied manually to get the desired results thus this model holds very less practical significance.

III. Proposed Models And Implementation

This article discusses about two models which have been simulated in MATLAB to maintain constant maximum torque for motor.

1. Application of feedback mechanism to vary duty ratio using no inductor (Figure 2).

2. Application of feedback mechanism to vary duty ratio using inductor as a filtering device (Figure 3).

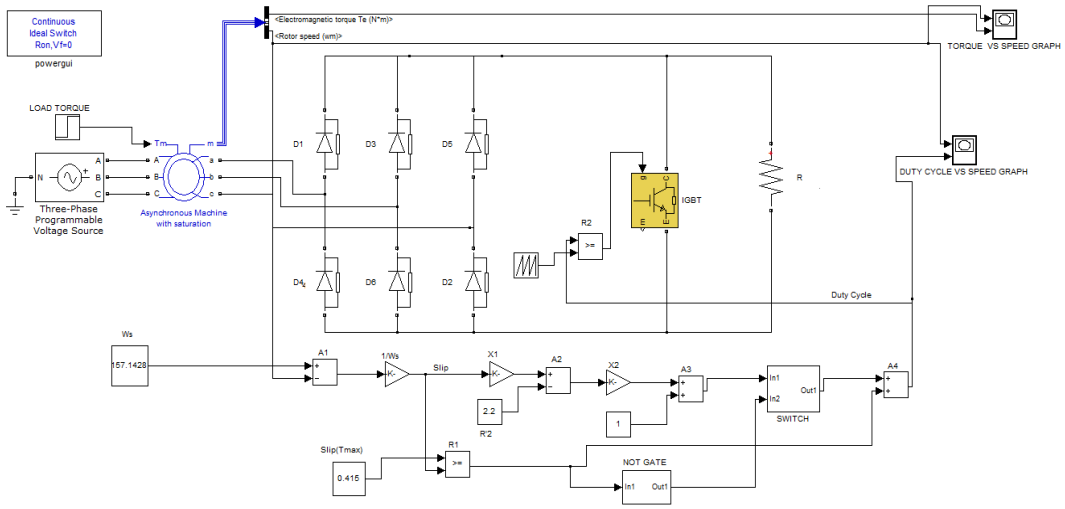

Figure 2:Model 1 for constant torque operation of wound rotor employing feedback control

This method employs in two feedback mechanism of rotor speed and slip to maintain a constant torque upto s_{Tmax} of wound rotor induction motor .The feedback mechanism has been prepared using following equations [1]:

$$s_m = \frac{R_r'}{\sqrt{R_s^2 + (X_s + X_r')^2}} \qquad (1)$$

With an external resistance whose stator referred equivalent resistance is Re

$$s_m = \frac{R_e + R_r'}{\sqrt{R_s^2 + (X_s + X_r')^2}} \qquad (2)$$

$$R_e = 0.5R(1-\delta)a^2 \qquad (3)$$

For maximum torque to occur at standstill i.e. s=1,δ=0 and
$R_e = 0.5Ra^2 (4)$

Where

s_m	Slip	Rr'	Rotor resistance referred to stator side
X_s	Stator Reactance	X_r'	Rotor reactance referred to stator side
R_s	Stator resistance	δ	Duty Cycle
A	Stator to rotor turns ratio	R_e	Stator referred external resistance

In feedback mechanism rotor speed is fed to the negative terminal of add block A1and rotor synchronous speed i.e. 157.14 rad/sec is fed to the positive terminal from constant Ws block toadd block A1.The output of add block A1 gives us the difference of the rotor speed and synchronous speed. The difference in speed is multiplied by a gain which has value same as reciprocal of synchronous speed (1/Ws) which gives us the slip of the motor. The slip value is multiplied by gain of X1 block whose value is $\sqrt{R_s^2 + (X_s + X_r')^2}$ and it gives us the value of effective rotor resistance i.e. $R_e + R_r$'. The output of X1 block is fed to positive terminal of add block A2. R'2 blockcontaining value of Rr' is fed to the negative terminal of add A2 block. The output of add A2 block gives us the value of external rotor resistance referred to stator side i.e. $R_e = 0.5R(1-\delta)a^2$ .R_e is fed to X2 block whose value is equal to negative of reciprocal of $0.5Ra^2$i.e. $(-1*1/0.5Ra^2)$.At this point it's imperative to understand that how the value of R i.e. external resistance introduced into rotor circuit is calculated. We have designed our model in such a way that the breakdown torque is produced from standstill. Hence for maximum torque to occur at standstill when s_m=1 and δ=0 following equation holds .Motor parameters mentioned in appendix have been substituted in the equations:

Using equation (2) we have,

$$1 = \frac{R_e + 2.2}{\sqrt{1.46^2 + (2.56 + 2.55)^2}}$$

R_e =3.11ohms

Using equation (3) we have,

$3.11 = 0.5R1.33^2$

R=3.505ohms

The output of X2 block is fed to positive terminal of add block A3 and a constant value to 1 is fed to another positive terminal of add block A3. The output of add block A3 gives us the value of δ i.e. duty cycle. The output of add block is fed to Inp 1 of SWITCH subsytem.

At this point we would like to re-emphasize that our calculations are valid only for machine running at maximum torque. Thus once the condition of δ=1 has been reached there would be no effect of external rotor resistance . The boundary condition for slip has been calculated using equation (2).

At boundary condition value of external resistance Re is zero as δ=1

$$s_m = \frac{2.2 + 0}{\sqrt{1.46^2 + (2.56 + 2.55)^2}}$$

$s_m = 0.415$

The constant value 0.415 fed to the relational operator R1 which is the value of slip at which value of duty cycle becomes one and there is no effect of external resistance. The relational operator R1 compares the constant value 0.415 with the rotor slip fed to other terminal of relational operator R1. When external resistance is in picture output of relational operator is low because 0.415 would be less than value of calculated slip , but once duty cycle, i.e. δ=1 is reached slip decreases below 0.415 and output of relational operator R1 turns high. The output of relational operator R1 is further fed to In1 of NOT GATEsubsystem.

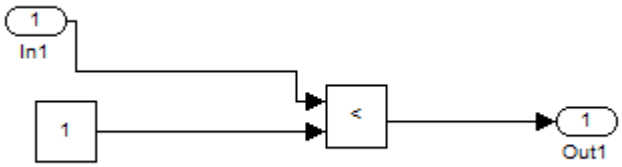

Figure 3:NOT GATE Subsystem

In NOT GATEsubsystem In1 is the output of the relational operator R1. When output of relational operator R1is high output of NOT GATE subsystem becomes 0.The output (Out1) of NOT GATE subsystem is fed to second input terminal In2 of SWITCH block subsystem.

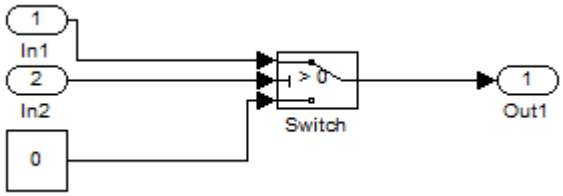

Figure 4:SWITCH block subsystem

If input to second terminal of SWITCH subsystem is high it means that switch would operate with terminal 1 configuration related to In1. The output of switch,which would be duty cycle δ in this case is fed to add block A4. A second input from relational operator R1 is fed to other positive terminal of add block A4. In this particular case the value of input from relational operator would be zero. Thus the output of add block A4 would be duty cycle which is further fed to 1stterminal of Relational Operator R2. The other terminal of relational operator is fed with a saw tooth pulse generated with the help of repeating sequence block which will produce repeated pulses of the duty cycle. Whenever value of terminal 1 would be greater than terminal 2 a gate pulse would be given to IGBT which will turn the power semiconductor device into action.

On the other hand if input to second terminal of SWITCH subsystem is low it means that switch would operate with terminal 3 configuration. The output of switch in this case would be 0 i.e. fed from a constant block .The output of switch is further fed to add block A4. A second input from relational operator R1 is fed in other positive terminal of add block A4. In this particular case the value of this signal would be 1. Thus the output of add block A4 would be 1 which is further fed to 1st terminal of Relational Operator R2. The other terminal of relational operator R2 is fed with a saw tooth pulse generated with the help of repeating sequence block. In this case the output of relational operator would be set at 1.The same is desired because at last we want the value of external rotor resistance being realized by the circuit to reduce to zero so that motor can operate with maximum efficiency for a given load.

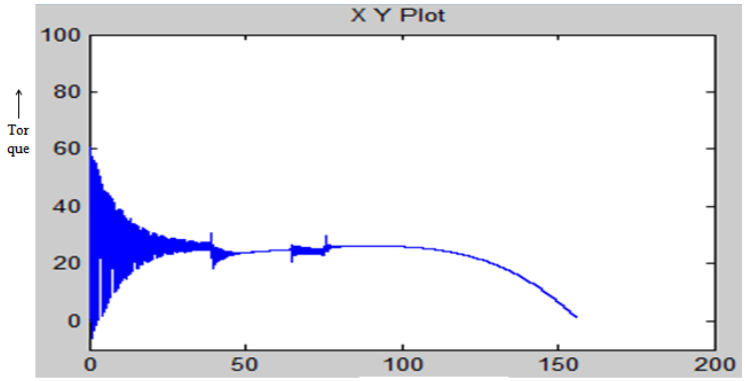

Figure 5:Torque V/S Rotor Speed

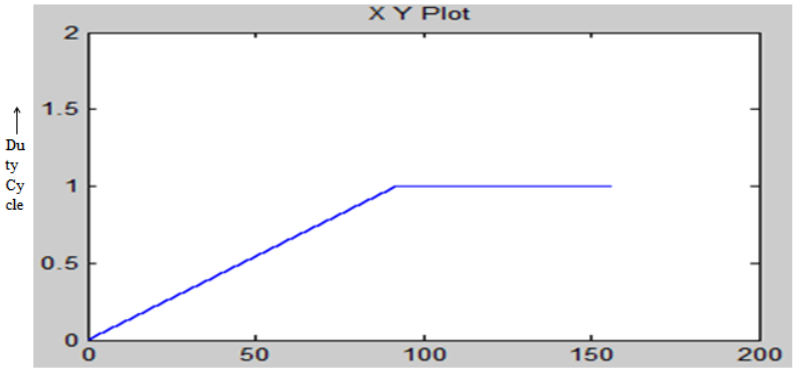

Figure 6: Duty Cycle V/S Speed

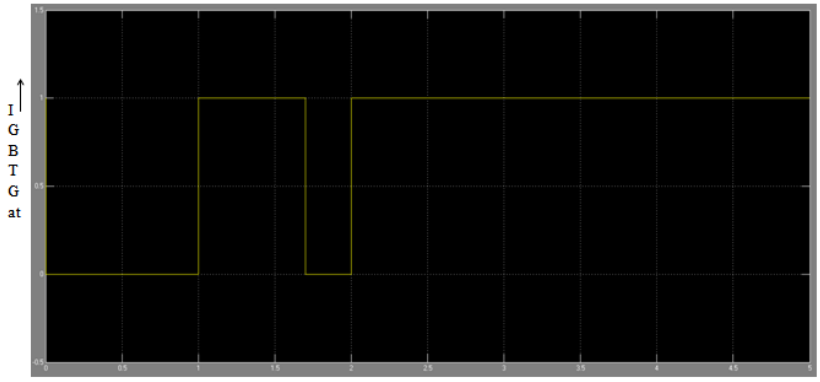

Figure 7:IGBT Gate Pulses

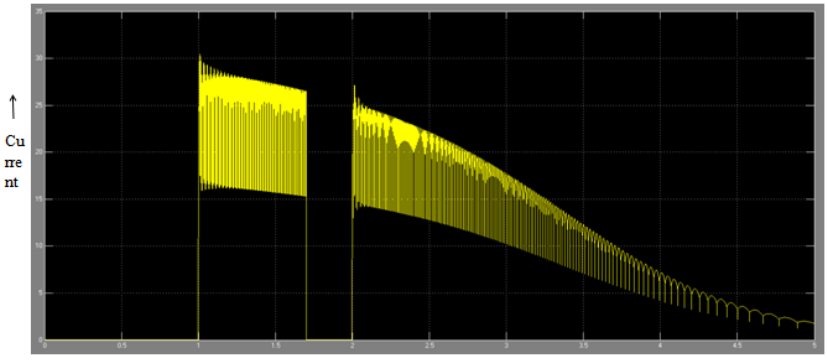

Figure 8:Current flowing in IGBT

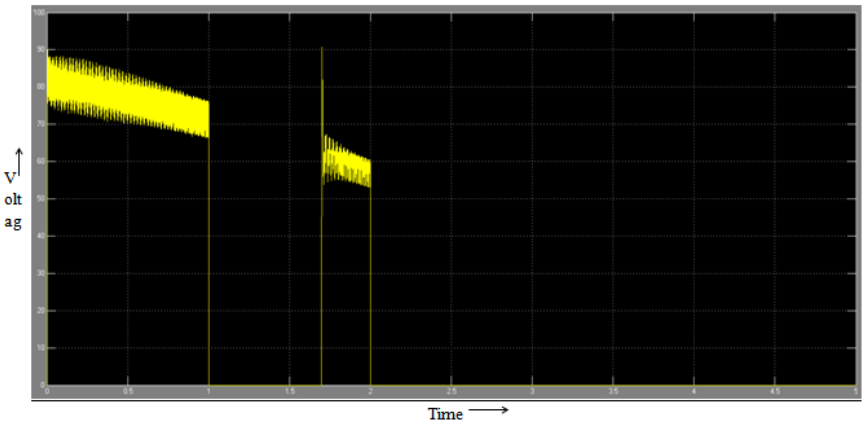

Figure 9:Voltage across IGBT

Model 2:Application of feedback mechanism to vary duty ratio using inductor as a filtering device.

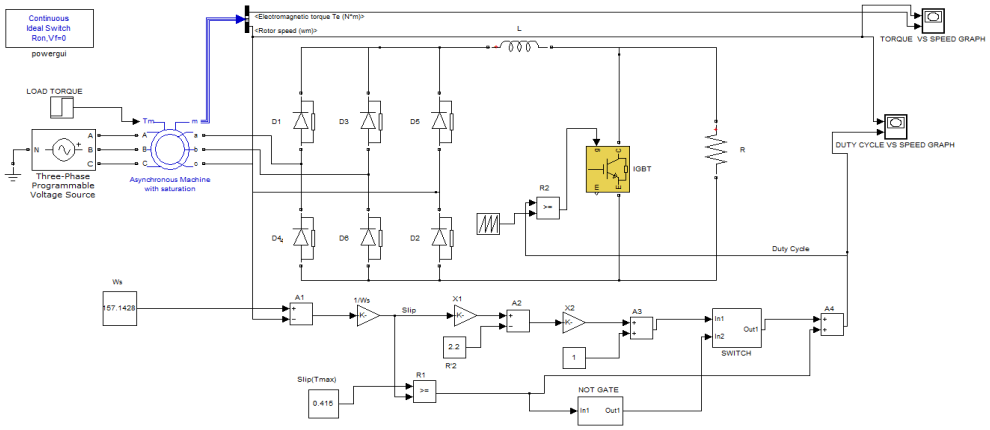

Figure 5: Model 2 for constant torque operationof wound rotor employing feedback control and inductor for rectification

The working of this model is similar to the model discussed above, only difference being that an inductor L has been used in the secondary rotor circuit for filtering purpose.

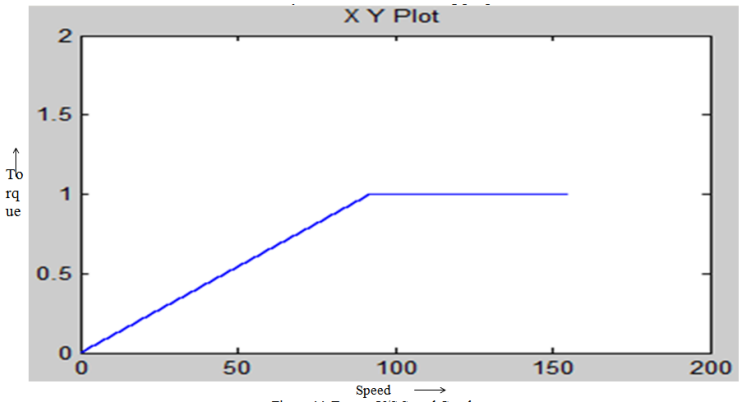

Figure 11:Torque V/S Speed Graph

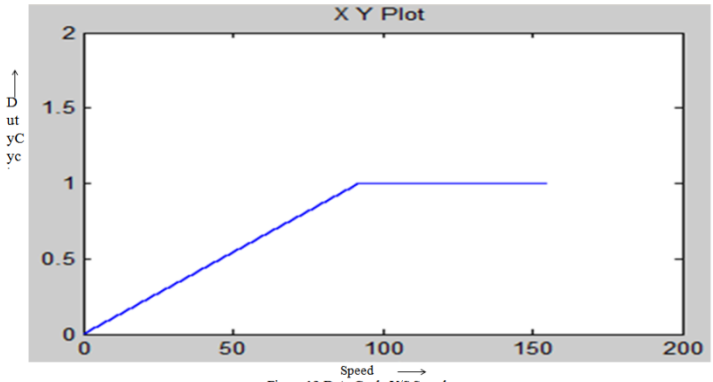

Figure 12:Duty Cycle V/S Speed

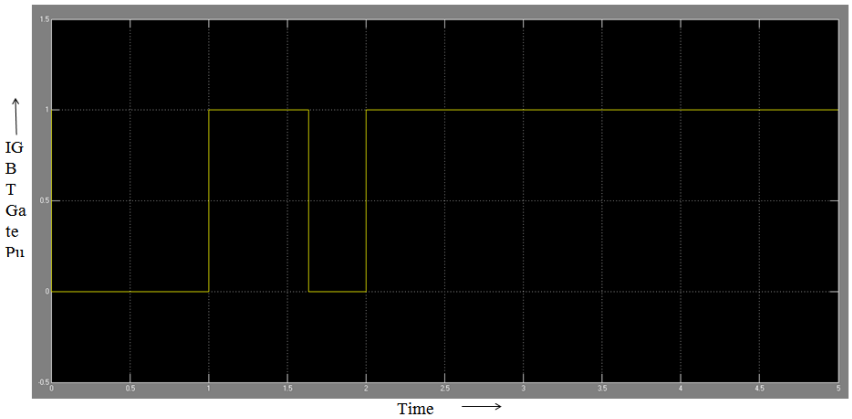

Figure 13: IGBT Gate Pulses

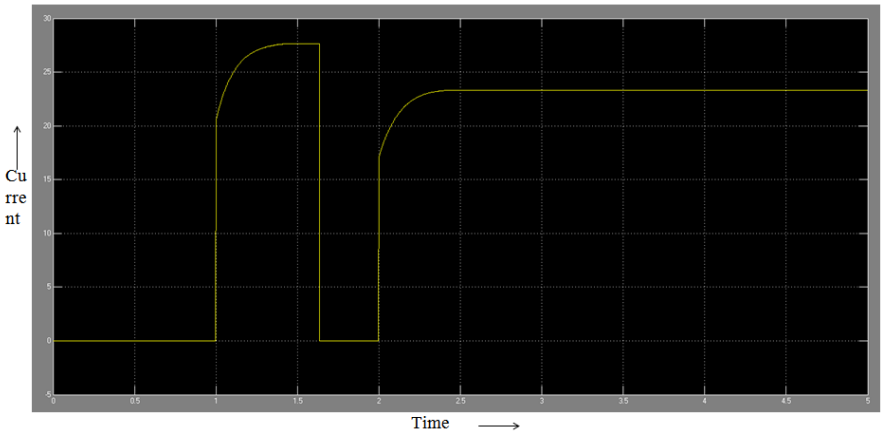

Figure 14: Current flowing through IGBT

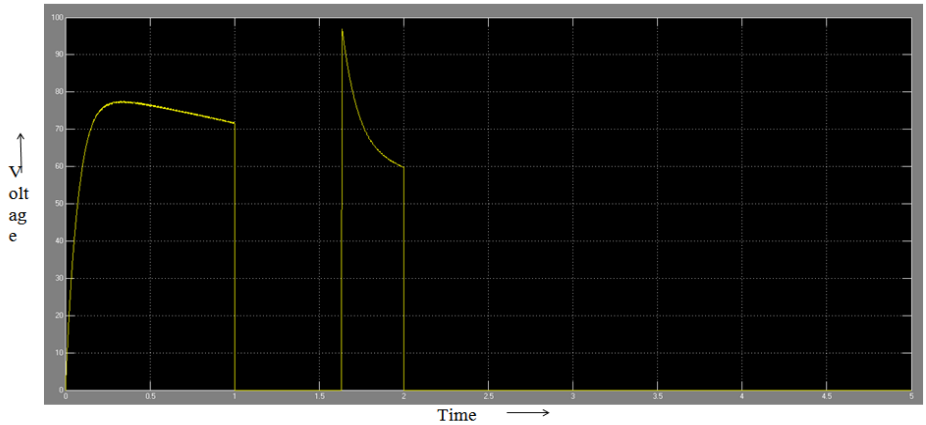

Figure 15: Voltage across IGBT

IV. Conclusion

An automatic controller to run the wound rotor induction motor at maximum torque from standstill slip(s=1) to slip (s_{Tmax}=0.415) has been successfully simulated using two circuits with help of MATLAB.The first model(Figure 2) and second model (Figure 3) employs a feedback mechanism to maintain maximum torque of motor.The second model uses an inductor in the secondary rotor circuit which acts a rectifier and reduces the harmonic distortions in torque curve which were prevalent in the first model.The graph between duty cycle and motor speed has been successfully plotted and observed to be linear which reaffirm that the motor has been operating at maximum torque.

Appendix-A

Specifications of the Wound Rotor Induction Motor [3]
V_L= 240 V
I_L= 5.72 A
Pole pairs= 2
Frequency= 50 Hz
P_{out}= 2.40 HP,Δ-Δ connection
R_s= 1.46 ohms
X_s= 2.56 ohms
X_m= 92 ohms
a=1.33
R_r'= 2.2 ohms
$X_{r'}$= 2.55 ohms

References

[1] Gopal K. Dubey, "Fundamentals of Electrical Drives", Narosa Publishing House Pvt. Ltd., 2001
[2] PS Bimbra, "Electrical Machinery", Khanna Publishers, 2010
[3] Control of Wound Rotor Induction Motor Using Thyristors in the Secondary Circuits,IEEE TRANSACTIONS ON INDUSTRY APPLICATIONS, VOL. 32, NO. 2, MARCWAPRIL 1996
[4] Comparative Study of Speed Control of Induction Motor Using PI and Fuzzy Logic Controller, Anmol Aggarwal, J. N. Rai, Maulik Kandpal, IOSR Journal of Electrical and Electronics Engineering (IOSR-JEEE) e-ISSN: 2278-1676,p-ISSN: 2320-3331, Volume 10, Issue 2 Ver. I (Mar – Apr. 2015), PP 43-52

International Journal of Scientific & Engineering Research, Volume 6, Issue 7, June-2015
ISSN 2229-5518

Convex Functions & Optimization

Aashray Yadav

Abstract - My research paper is based on the recent work in interior-point methods, specifically those methods that keep track of both the primal and dual optimization variables (hence primal-dual methods). These methods are special because they are numerically stable under a wide range of conditions, so they should work well for many different types of constrained optimization problems.However, you can always find a constrained optimization problem that is difficult enough to break these methods.

Keywords - Introduction, Types of Optimization, Graphical Minima, Convex function, Convex vs. Non-convex, Functions, Convex Hull, Test for convexity and Concavity, Convex Region, Solving Techniques, Some common convex OP's, LP Visualization, Quadratic Programming, QP Visualization, Interior Point Method,CVX:Convex Optimization, Building Convex Functions, Verifying Convexity Remarks , References

---

1.Introduction

Optimization is the mathematical discipline which is concerned with finding the maxima and minima of functions, possibly subject to constraints. It helps in various field such as Architecture, Nutrition, Electrical circuits, Economics , Transportation,etc.

2.Types of Optimization

a)A real function of n variables

$$f(\chi_1,\chi_2,\ldots,\chi_n)$$

with or without constrains

$$\min\ f(x,y)=x^2+2y^2$$

b)Unconstrained optimization

c) Optimization with constraints

$$\min\ f(x,y)=x^2+2y^2$$
$$x>0$$
OR
$$\min\ f(x,y)=x^2+2y^2$$
$$-2<x<5, y\geq 1$$
OR
$$\min\ f(x,y)=x^2+2y^2$$
$$x+y=2$$

3.Graphical Minima

a)To find the minimum of the function

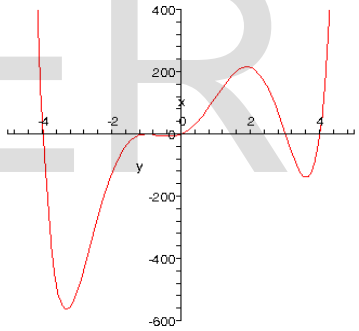

What is special about a local max or a local min of a function **f** (x)?

at local max or local min **f**'(x)=0
f"(x) > 0 if local min
f"(x) < 0 if local max

Aashray Yadav is pursuing Bachelor degree in Software engineering at Delhi Technological University, India

4.Convex Function

a)Definition

The weighted mean of function evaluated at any two points is greater than or equal to the function evaluated at the weighted mean of the two points

$$f_i(\alpha x + \beta y) \leq \alpha f_i(x) + \beta f_i(y)$$

$$\text{if } \alpha + \beta = 1,\ \alpha \geq 0,\ \beta \geq 0$$

b)Procedure

a)Pick any two points x, y and evaluate along the function, f(x), f(y)
b)Draw the line passing through the two points f(x) and f(y)
c)Convex if function evaluated on any point along the line between x and y is below the line between f(x) and f(y)

c)Graph

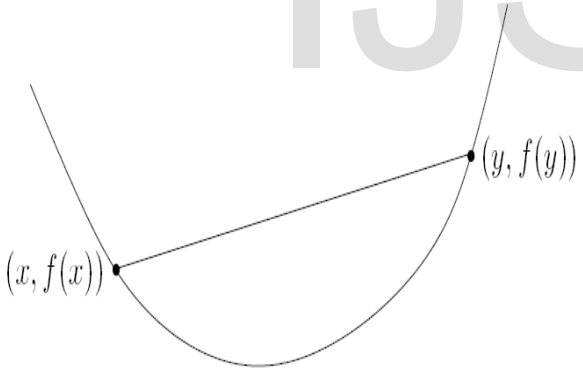

d)Examples

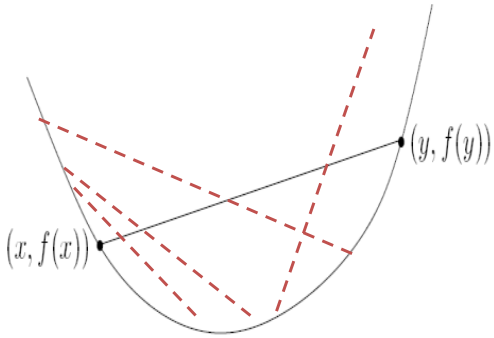

Convex

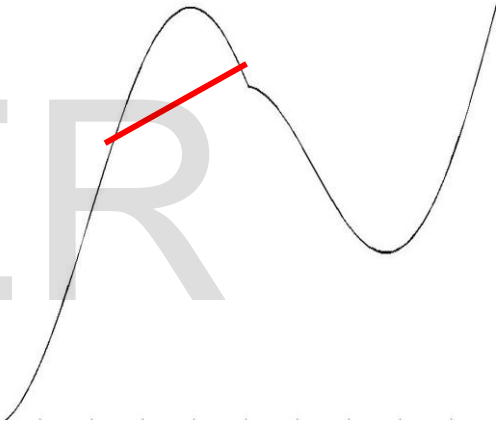

Not Convex

5.Local Optima is Global (simple proof)

proof: suppose x is locally optimal and y is optimal with $f_0(y) < f_0(x)$

x locally optimal means there is an $R > 0$ such that

$$z \text{ feasible}, \quad \|z - x\|_2 \leq R \implies f_0(z) \geq f_0(x)$$

consider $z = \theta y + (1-\theta)x$ with $\theta = R/(2\|y - x\|_2)$

- $\|y - x\|_2 > R$, so $0 < \theta < 1/2$
- z is a convex combination of two feasible points, hence also feasible
- $\|z - x\|_2 = R/2$ and

$$f_0(z) \leq \theta f_0(x) + (1-\theta) f_0(y) < f_0(x)$$

which contradicts our assumption that x is locally optimal

6. Convex vs. Non-convex

Convex

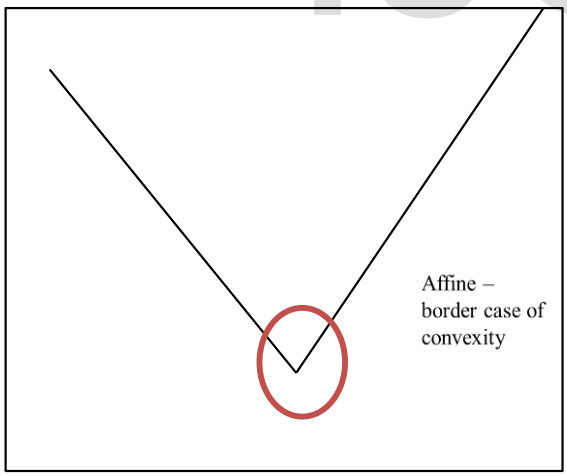

Not Convex

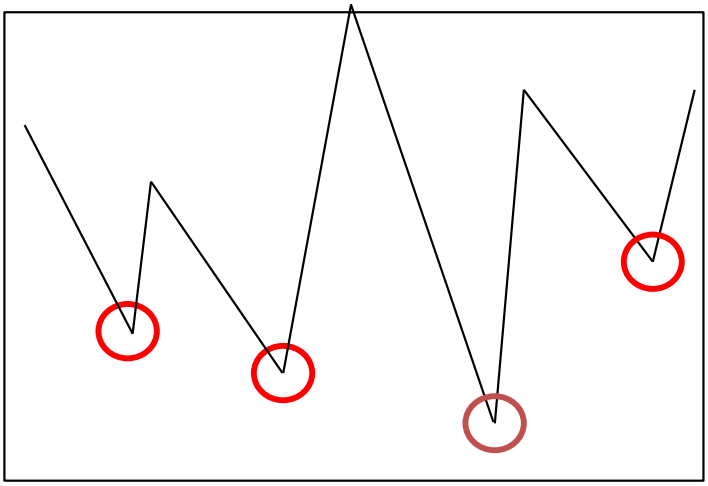

7. Functions

Convex

A function is called convex (strictly convex) if $\geq$ is replaced by $\leq$(<).

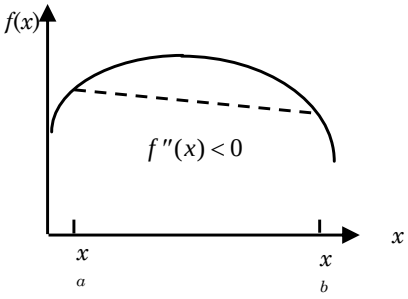

Concave

A function is called *concave* over a given region *R* if:

$$f(\theta \mathbf{x}_a + (1-\theta)\mathbf{x}_b) \geq \theta f(\mathbf{x}_a) + (1-\theta) f(\mathbf{x}_b)$$

where: $\mathbf{x}_a, \mathbf{x}_b \in R$, and $0 \leq \theta \leq 1$.

The function is *strictly concave* if $\geq$ is replaced by >.

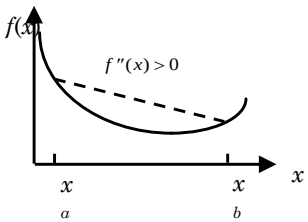

8.Convex Hull

A set C is **convex** if every point on the line segment connecting *x* and *y* is in *C*.

The **convex hull** for a set of points X is the minimal convex set containing X.

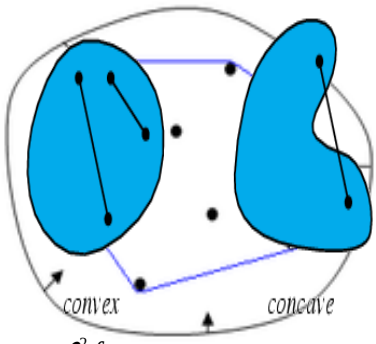

If $f''(x)=\frac{\partial^2 f}{\partial x^2}\le 0$ then $f(x)$ is concave.

If $f''(x)=\frac{\partial^2 f}{\partial x^2}\ge 0$ then $f(x)$ is convex.

For a *multivariate function f*(**x**) the conditions are:-

$f(\mathbf{x})$	**h(x) Hessian Matrix**
Strictly convex	+ve def
convex	+ve semi def
concave	-ve semi def
strictly concave	-ve def

9.Test for Convexity and Concavity

H is -ve def (-ve semi def) iff

$$\mathbf{x}^T\mathbf{H}\mathbf{x}>0 \ (\ge 0), \quad \forall \mathbf{x}\ne \mathbf{0}.$$

$$\mathbf{x}^T\mathbf{H}\mathbf{x}<0 \ (\le 0), \quad \forall \mathbf{x}\ne \mathbf{0}.$$

Convenient tests: **H**(**x**) is strictly convex (+ve def) (convex) (+ve semi def)) if:

1. all eigenvalues of **H**(**x**) are $>0 \ (\ge 0)$
or 2. all principal determinants of **H**(**x**) are $>0 \ \ (\ge 0)$

Example:

$$f(x)=2x_1^2-3x_1x_2+2x_2^2$$

$$\frac{\partial f(\mathbf{x})}{\partial x_1}=4x_1-3x_2 \quad \frac{\partial^2 f(\mathbf{x})}{\partial x_1^2}=4 \quad \frac{\partial^2 f(\mathbf{x})}{\partial x_1\partial x_2}=-3$$

$$\frac{\partial f(\mathbf{x})}{\partial x_2}=-3x_1+4x_2 \quad \frac{\partial^2 f(\mathbf{x})}{\partial x_2^2}=4$$

$$\therefore \mathbf{H}(\mathbf{x})=\begin{bmatrix}4 & -3\\ -3 & 4\end{bmatrix}, \quad \Delta_1=4, \quad \Delta_2=\begin{vmatrix}4 & -3\\ -3 & 4\end{vmatrix}=7$$

eigenvalues: $|\lambda\mathbf{I}_2-\mathbf{H}|=\begin{vmatrix}\lambda-4 & 3\\ 3 & \lambda-4\end{vmatrix}=\lambda^2-8\lambda+7=0$

$\Rightarrow \lambda_1=1, \ \lambda_2=7$. Hence, $f(\mathbf{x})$ is strictly convex.

10.Convex Region

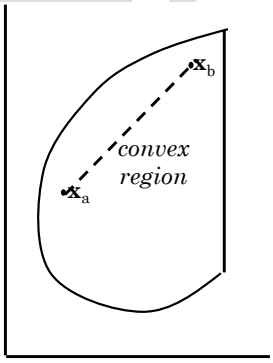

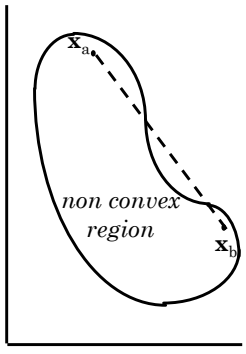

A convex set of points exist if for any two points, $\mathbf{x}_a$ and $\mathbf{x}_b$, in a region, all points:

$$\mathbf{x}=\mu\mathbf{x}_a+(1-\mu)\mathbf{x}_b, \quad 0\le\mu\le 1$$

on the straight line joining $\mathbf{x}_a$ and $\mathbf{x}_b$ are in the set.
If a region is completely bounded by concave functions then the functions form a convex region.

11.Solving Techniques

Can use definition (prove holds) to prove
If function restricted to any line is convex, function is convex
If 2X differentiable, show hessian >= 0
Often easier to:
Convert to a known convex OP
E.g. QP, LP, SOCP, SDP, often of a more general form
Combine known convex functions (building blocks) using operations that preserve convexity
Similar idea to building kernels

12. Some common convex OPs

Of particular interest for this book and chapter:
linear programming (LP) and *quadratic programming (QP)*
LP: affine objective function, affine constraints

$$\begin{array}{ll}\text{minimize} & c^T x + d \\ \text{subject to} & Gx \preceq h \\ & Ax = b\end{array}$$

-e.g. LP SVM, portfolio management

13.LP Visualization

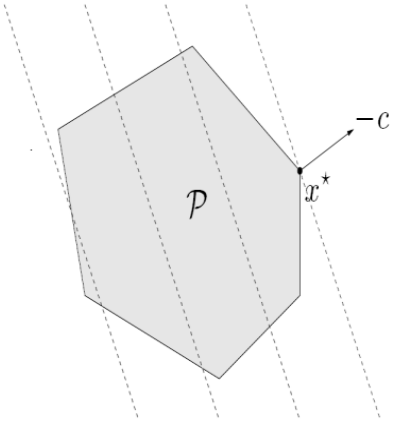

Note: constraints form *feasible set*
-for LP, polyhedra

14.Quadratic Program

➨QP: Quadratic objective, affine constraints

➨LP is special case
➨Many SVM problems result in QP, regression
➨If constraint functions quadratic, then Quadratically Constrained Quadratic Program (QCQP)

$$\begin{array}{ll}\text{minimize} & (1/2)x^T Px + q^T x + r \\ \text{subject to} & Gx \preceq h \\ & Ax = b\end{array}$$

15.QP Visualization

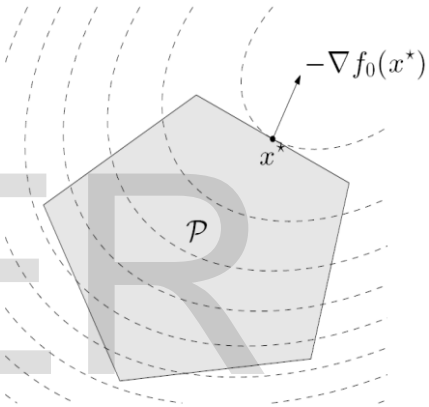

16.Interior Point Method

➨Solve a series of equality constrained problems with Newton's method
➨Approximate constraints with log-barrier (approx. of indicator)

$$\begin{array}{ll}\text{minimize} & f_0(x) + \sum_{i=1}^m I_-(f_i(x)) \\ \text{subject to} & Ax = b,\end{array}$$

$$I_-(u) = \begin{cases} 0 & u \leq 0 \\ \infty & u > 0 \end{cases}$$

$$\begin{array}{ll}\text{minimize} & f_0(x) - (1/t)\sum_{i=1}^m \log(-f_i(x)) \\ \text{subject to} & Ax = b\end{array}$$

As t gets larger, approximation becomes better

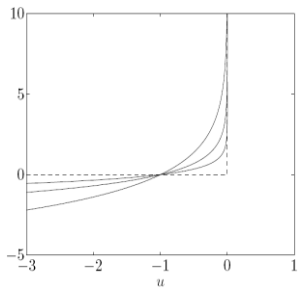

17.CVX: Convex Optimization

a)Introduction

CVX is a Matlab toolbox
Allows you to flexibly express convex optimization problems
Translates these to a general form and uses efficient solver (SOCP, SDP, or a series of these)

All you have to do is design the convex optimization problem
Plug into CVX, a first version of algorithm implemented
More specialized solver may be necessary for some applications

b)CVX - Examples

I)

```
Quadratic program: given H, f, A, and b
cvx_begin
variable  x(n)
            minimize (x'*H*x + f'*x)
subject to
             A*x  >= b
cvx_end
```

II)

```
SVM-type formulation with L1 norm
cvx_begin
  variable w(p)
  variable b(1)
  variable e(n)
  expression by(n)
  by = train_label.*b;
  minimize( w'*(L + I)*w + C*sum(e)  +
l1_lambda*norm(w,1) )
  subject to
                    X*w + by >= a - e;
                    e >= ec;
cvx_end
```

18.Building Convex Functions

From simple convex functions to complex: some *operations that preserve complexity*
Nonnegative weighted sum
Composition with affine function
Pointwise maximum and supremum
Composition
Minimization
Perspective (g(x,t) = tf(x/t))

19.Verifying Convexity Remarks

➨For more detail and expansion, consult the referenced text, *Convex Optimization*
➨Geometric Programs also convex, can be handled with a series of SDPs (skipped details here)
➨CVX converts the problem either to SOCP or SDM (or a series of) and uses efficient solver

20.References

a) Convex Optimization – Boyd and Vandenberghe
b) Tokhomirov, V. M. "The Evolution of Methods of Convex Optimization." *Amer. Math. Monthly* 103, 65 - 71 , 1996.
c) Convex Optimization Theory-Mathworld,Wolfram
d)Matlab-www.mathworks.com/matlab

Cross-Lingual Sentiment Analysis using modified BRAE

Sarthak Jain
Department of Computer Engineering
Delhi Technological University
DL, India
successar@gmail.com

Shashank Batra
Department of Computer Engineering
Indian Institute of technology, Delhi
DL, India
shashankg@gmail.com

Abstract

Cross-Lingual Learning provides a mechanism to adapt NLP tools available for label rich languages to achieve similar tasks for label-scarce languages. An efficient cross-lingual tool significantly reduces the cost and effort required to manually annotate data. In this paper, we use the Recursive Autoencoder architecture to develop a Cross Lingual Sentiment Analysis (CLSA) tool using sentence aligned corpora between a pair of resource rich (English) and resource poor (Hindi) language. The system is based on the assumption that semantic similarity between different phrases also implies sentiment similarity in majority of sentences. The resulting system is then analyzed on a newly developed Movie Reviews Dataset in Hindi with labels given on a rating scale and compare performance of our system against existing systems. It is shown that our approach significantly outperforms state of the art systems for Sentiment Analysis, especially when labeled data is scarce.

1 Introduction

Sentiment Analysis is a NLP task that deals with extraction of opinion from a piece of text on a topic. This is used by a large number of advertising and media companies to get a sense of public opinion from their reviews. The ever increasing user generated content has always been motivation for sentiment analysis research, but majority of work has been done for English Language. However, in recent years, there has been emergence of increasing amount of text in Hindi on electronic sources but NLP Frameworks to process this data is sadly miniscule. A major cause for this is the lack of annotated datasets in Indian Languages.

One solution is to create cross lingual tools between a resource rich and resource poor language that exploit large amounts of unlabeled data and sentence aligned corpora that are widely available on web through bilingual newspapers, magazines, etc. Many different approaches have been identified to perform Cross Lingual Tasks but they depend on the presence of MT-System or Bilingual Dictionaries between the source and target language.

In this paper, we use Bilingually Constrained Recursive Auto-encoder (BRAE) given by (Zhang et al., 2014) to perform Cross Lingual sentiment analysis. Major Contributions of this paper are as follows: First, We develop a new Rating scale based Movie Review Dataset for Hindi. Second, a general framework to perform Cross Lingual Classification tasks is developed by modifying the architecture and training procedure for BRAE model. This model exploits the fact that phrases in two languages, that share same semantic meaning, can be used to learn language independent semantic vector representations. These embeddings can further be fine-tuned using labeled dataset in English to capture enough class information regarding Resource poor language. We train the resultant framework on English-Hindi Language pair and evaluate it against state of the art SA systems on existing and newly developed dataset.

2 Related Work

2.1 Sentiment Analysis in Hindi

In recent years, there have been emergence of works on Sentiment Analysis (both monolingual and cross-lingual) for Hindi. (Joshi et al., 2010) provided a comparative analysis of Unigram based In-language, MT based Cross Lingual and WordNet based Sentiment classifier, achieving highest accuracy of 78.14%. (Mittal et al., 2013) described a system based on Hindi SentiWordNet for assign-

Proceedings of the 2015 Conference on Empirical Methods in Natural Language Processing, pages 159–168,
Lisbon, Portugal, 17-21 September 2015.

ing positive/negative polarity to movie reviews. In this approach, overall semantic orientation of the review document was determined by aggregating the polarity values of the words in the document assigned using the WordNet. They also included explicit rules for handling Negation and Discourse relations during preprocessing in their model to achieve better accuracies.

For Languages where labeled data is not present, approaches based on cross-lingual sentiment analysis are used. Usually, such methods need intermediary machine translation system (Wan et al., 2011; Brooke et al., 2009) or a bilingual dictionary (Ghorbel and Jacot, 2011; Lu et al., 2011) to bridge the language gap. Given the subtle and different ways in which sentiments can be expressed and the cultural diversity amongst different languages, an MT system has to be of a superior quality to perform well(Balamurali et al., 2012).

(Balamurali et al., 2012) present an alternative approach to Cross Lingual Sentiment Analysis (CLSA) using WordNet senses as features for supervised sentiment classification. A document in Resource Poor Language was tested for polarity through a classifier trained on sense marked and polarity labeled corpora in Resource rich language. The crux of the idea was to use the linked WordNets of two languages to bridge the language gap.

Recently, (Popat et al., 2013) describes a Cross Lingual Clustering based SA System. In this approach, features were generated using syntagmatic property based word clusters created from unlabeled monolingual corpora, thereby eliminating the need for Bilingual Dictionaries. These features were then used to train a linear SVM to predict positive or negative polarity on a tourism review dataset.

2.2 Autoencoders in NLP Tasks

Autoencoders are neural networks that learn a low dimensional vector representation of fixed-size inputs such as image segments or bag-of-word representations of documents. They can be used to efficiently learn feature encodings that are useful for classification. The Autoencoders were first applied in a recursive setting by Pollack (1990) in recursive auto-associative memories (RAAMs). However, RAAMs needed fixed recursive data structures to learn vector representations, whereas RAE given by (Socher et al., 2011) builds recursive data structure using a greedy algorithm. The RAE can be pre-trained with an unsupervised algorithm and then fine-tuned according to the label of the phrase, such as the syntactic category in parsing(Socher et al., 2013), the polarity in sentiment analysis, etc. The learned structures are not necessarily syntactically accurate but can capture more of the semantic information in the word vectors.

3 BRAE Framework

(Zhang et al., 2014) used the RAE along with a Bilingually Constrained Model to simultaneously learn phrase embeddings for two languages in semantic vector space. The core idea behind BRAE is that a phrase and its correct translation should share the same semantic meaning. Thus, they can supervise each other to learn their semantic phrase embeddings. Similarly, non-translation pairs should have different semantic meanings, and this information can also be used to guide learning semantic phrase embeddings. In this method, a standard recursive autoencoder (RAE) pre-trains the phrase embedding with an unsupervised algorithm by greedily minimizing the reconstruction error (Socher et al., 2011), while the bilingually-constrained model learns to finetune the phrase embedding by minimizing the semantic distance between translation equivalents and maximizing the semantic distance between non-translation pairs.

In this section, We will briefly present the structure and training algorithm for BRAE model. After that, we show how this model can be adapted to perform CLSA.

3.1 Recursive Auto-encoder Framework

In this model, each word w_k in the vocabulary V of given language corresponds to a vector $x_k \in \mathbb{R}^n$ and stacked into a single word embedding matrix $L \in \mathbb{R}^{n \times |V|}$. This matrix is learned using DNN (Collobert and Weston, 2008; Mikolov et al., 2013) and serves as input to further stages of RAE.

Using this matrix, a phrase $(w_1 w_2 \dots w_m)$ is first projected into a list of vectors $(x_1, x_2, \dots x_m)$. The RAE learns the vector representation of the phrase by combining two children vectors recursively in a bottom-up manner. For two children $c_1 = x_1, c_2 = x_2$, the auto-encoder computes the parent vector y_1:

$$y_1 = f(W^{(1)}[c_1; c_2] + b^{(1)}); y_1 \in \mathbb{R}^n \quad (1)$$

To assess how well the parent vector represents its children, the auto-encoder reconstructs the chil-

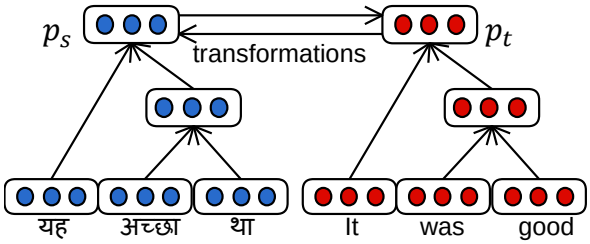

Figure 1: An illustration of BRAE structure

dren :

$$[c_1'; c_2'] = W^{(2)}p + b^{(2)} \quad (2)$$

and tries to minimize the reconstruction error (Euclidean Distance) $E_{rec}([c_1; c_2])$ between the inputs $[c_1; c_2]$ and their reconstructions $[c_1'; c_2']$.

Given y_1, Eq.1 is used again to compute y_2 by setting the children to be $[c_1; c_2] = [y_1; x_3]$. The same auto-encoder is re-used until the vector of the whole phrase is generated. For unsupervised phrase embedding, the sum of reconstruction errors at each node in binary tree y is minimized:

$$E_{rec}(x; \theta) = \arg\min_{y \in A(x)} \sum_{k \in y} E_{rec}([c_1; c_2]_k) \quad (3)$$

Where $A(x)$ denotes all the possible binary trees that can be built from inputs x. A greedy algorithm is used to generate the optimal binary tree y^*. The parameters $\theta^{rec} = (\theta^{(1)}, \theta^{(2)})$ are optimized over all the phrases in the training data. For further details, please refer (Socher et al., 2011)

3.2 Semantic Error

The BRAE model jointly learns two RAEs for source language L_S and target language L_T. Each RAE learn semantic vector representation p_s and p_t of phrases s and t respectively in translation-equivalent phrase pair (s, t) in bilingual corpora (shown in Fig.1). The transformation between the two is defined by:

$$p_t' = f(W_s^t p_s + b_s^t), p_s' = f(W_t^s p_t + b_t^s) \quad (4)$$

where $\theta_s^t = (W_s^t, b_s^t), \theta_t^s = (W_t^s, b_t^s)$ are new parameters introduced.

The semantic error between learned vector representations p_s and p_t is calculated as :

$$E_{sem}(s, t; \theta) = E_{sem}^*(t|s; \theta_t^s) + E_{sem}^*(s|t; \theta_s^t) \quad (5)$$

where $E_{sem}^*(s|t; \theta_t^s)$ is the semantic distance of p_s given p_t and vice versa. To calculate it, we first calculate Euclidean distance between original p_t and transformation p_t' as $D_{sem}(s|t, \theta_s^t) = \frac{1}{2}\|p_t - p_t'\|^2$. The max-semantic-margin distance between them is then defined as

$$E_{sem}^*(s|t, \theta_s^t) = max\{0, D_{sem}(s|t, \theta_s^t) - D_{sem}(s|t', \theta_s^t) + 1\} \quad (6)$$

where we simultaneously minimize the distance between translation pairs and maximized between non-translation pairs. Here t' in non-translation pair (s, t') is obtained by replacing the words in t with randomly chosen target language words. We calculate the $E_{sem}^*(t|s; \theta_t^s)$ in similar manner.

3.3 BRAE Objective Function

Thus, for the phrase pair (s, t), the joint error becomes:

$$\begin{aligned} E(s, t, \theta) &= E(s|t, \theta) + E(t|s, \theta) \\ E(s|t, \theta) &= \alpha E_{rec}(s; \theta_s^{rec}) + (1 - \alpha) E_{sem}^*(s|t, \theta_s^t)) \\ E(t|s, \theta) &= \alpha E_{rec}(t; \theta_t^{rec}) + (1 - \alpha) E_{sem}^*(t|s, \theta_t^s)) \end{aligned} \quad (7)$$

The hyper-parameter α weighs the reconstruction and semantic errors. The above equation indicates that the Parameter sets $\theta_t = (\theta_t^s, \theta_t^{rec})$ and $\theta_s = (\theta_s^t, \theta_s^{rec})$ on each side respectively can be optimized independently as long as the phrase representation of other side is given to compute semantic error.

The final BRAE objective over the phrase pairs training set (S, T) becomes:

$$J_{BRAE} = \frac{1}{N} \sum_{(s,t) \in (S,T)} E(s, t; \theta) + \frac{\lambda_{BRAE}}{2} \|\theta\|^2 \quad (8)$$

3.4 Unsupervised Training of BRAE

The word embedding matrices L_s and L_t are pre-trained using unlabeled monolingual data with Word2Vec toolkit (Mikolov et al., 2013). All other parameters are initialized randomly. We use SGD algorithm for parameter optimization. For full gradient calculations for each parameter set, please see (Zhang et al., 2014).

1. RAE Training Phase: Apply RAE Framework (Sec. 3.1) to pre-train the source and target phrase representations p_s and p_t respectively by optimizing θ_s^{rec} and θ_t^{rec} using unlabeled monolingual datasets.

2. Cross-Training Phase: Use target-side phrase representation p_t to update the source-side

parameters θ_s and obtain source-side phrase representation p'_s, and vice-versa for p_s. Calculate the joint error over the bilingual training corpus. On reaching a local minima or predefined no. of iterations (30 in our case), terminate this phase, otherwise set $p_s = p'_s$, $p_t = p'_t$, and repeat.

4 Adapting Model for Classifying Sentiments

At the end of previous Training procedure, we obtain high quality phrase embeddings in both source and target language and transformation function between them. We now extend that model to perform cross lingual supervised tasks, specifically CLSA.

To achieve this, we need to modify the learned semantic phrase embeddings such that they can capture information about sentiment. Since we only use monolingual labeled datasets from this point onwards, the supervised learning phases will occur independently for each RAE as we do not have any "phrase pairs" now. Thus, the new semantic vector space generated for word and phrase embeddings may no longer be in sync with their corresponding transformations.

We propose following modifications to the system to deal with this problem. Let L_S and L_T represent Resource rich and Resource poor language respectively in above model.

Modifications in architecture: We first include a softmax (σ) layer on top of each parent node in RAE for L_S to predict a K-dimensional multinomial distribution over the set of output classes defined by the task (e.g : polarity, Ratings).

$$d(p; \theta^{ce}) = \sigma(W^{ce} p) \tag{9}$$

Given this layer, we calculate cross entropy error $E_{ce}(p_k, t, W_{ce})$ generated for node p_k in binary tree, where t is target multinomial distribution or one-hot binary vector for target label. We use this layer to capture and predict actual sentiment information about the data in both L_S and L_T (described in next section). We show a node in modified architecture in Fig.2.

Penalty for Movement in Semantic Vector space: During subsequent training phases, we include the euclidean norm of the difference between the original and new phrase embeddings as penalty in reconstruction error at each node of the tree.

$$E^*_{rec}([c_1; c_2]; \theta) = E_{rec}([c_1; c_2]; \theta) + \frac{\lambda_p}{2} \|p - p^*\|^2 \tag{10}$$

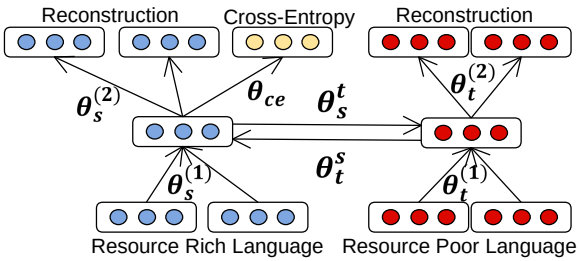

Figure 2: An illustration of BRAE segment with Cross Entropy layer

Here p is the phrase representation we get during forward propagation of current training iteration and p^* is the representation we get if we apply the parameters obtained at the end of the Cross training phase to children $[c_1; c_2]$ of that node. The reason to do this is twofold.

First, during supervised training, the error will back propagate through RAEs for both languages affecting their respective weights matrices and word embeddings. This will modify the semantic representation of phrases captured during previous phases of training procedure and adversely affect the transformations derived from them. Therefore we need to include some procedure such that the transformation information learned during Cross-training phase is not lost.

Secondly, we observe that the information about the semantic similarity of a word or phrase also implies sentiment similarity between the two. That is when dealing with bilingual data, words or phrases that appear near each other in semantic space typically represent common sentiment information and we want our model to create a decision boundary around these vectors instead of modifying them too much.

Disconnecting the RAEs: We fix the transformation weights between the two RAEs, i.e. in subsequent training steps the transformation weights(θ^t_s, θ^s_t) are not modified but rather pass the back propagated error as it is to previous layers. We observed that on optimizing the objective along with the penalty term, the transformation weights are preserved between new semantic/sentiment vector spaces, resulting in slightly degraded performance, but were still able to preserve enough information about the semantic structure of two languages.Also, it reinforced the penalty imposed on the movement of phrase embeddings in semantic vector space.On the other hand, if the weights were allowed to be updated,

the accuracies were affected severely as information learned during previous phases was lost and the weights were not been able to capture enough information about the modified phrase embeddings and generalize well on test phrases not encountered in labeled training set of Resource Scarce Language.

4.1 Supervised Training Phases

We now explain supervised training procedure using only monolingual labeled data for each language. These training phases occur at the end of BRAE training. In each training phase, we use SGD algorithm to perform parameter optimization.

4.1.1 Phase I : Resource Rich language

In this phase, we only modify the parameters of RAE_{L_S}, i.e. θ_s^{rec} and θ_{ce} by optimizing following objective over (sentence, label) pairs (x, t) in its labeled corpus.

$$J_S = \frac{1}{N} \sum_{(x,t)} E(x, t; \theta) + \frac{\lambda_S}{2} \|\theta\|^2 \qquad (11)$$

where $E(x, t; \theta)$ is the sum over the errors obtained at each node of the tree that is constructed by the greedy RAE:

$$E(x, t; \theta) = \sum_{k \in RAE_{L_S}(x)} \kappa E^*_{rec}([c_1; c_2]_k; \theta_s) + (1 - \kappa) E_{ce}(p_k, t; \theta_{ce}) \qquad (12)$$

To compute this gradient, we first greedily construct all trees and then derivatives for these trees are computed efficiently via back-propagation through structure (Goller and Kuchler, 1996). The gradient for our new reconstruction function (Eq. 10) w.r.t to p at a given node is calculated as

$$\frac{\partial E^*_{rec}}{\partial p} = \frac{\partial E_{rec}}{\partial p} + \lambda_p (p - p^*) \qquad (13)$$

The first term $\frac{\partial E_{rec}}{\partial p}$ is calculated as in standard RAE model. The partial derivative in above equation is used to compute parameter gradients in standard back-propagation algorithm.

4.1.2 Phase II : Resource Poor Language

In this phase, we modify the parameters of RAE_{L_T} and θ_{ce} by optimizing Objective J_T over (sentence, label) pairs (x, t) in labeled corpus for L_T (much smaller than that for L_S). The equation for J_T is similar to Eq.11 and Eq.12 but with θ_t and η as parameters instead of θ_s and κ respectively.

Since cross-entropy layer is only associated with L_S, we need to traverse the transformation parameters to obtain sentiment distribution for each node (green path in Fig.2). That is, we first transform p_t to source side phrase p'_s and then apply the cross entropy weights to it.

$$d(p_t, \theta_{ce}) = \sigma(W^{ce}.f(W^t_s p_t + b^t_s)) \qquad (14)$$

We use the similar back-propagation through structure approach for gradient calculation in Phase I. During back propagation, 1) we do not update the transformation weights, 2) we transfer error signals during back-propagation from Cross-entropy layer to $\theta_t^{(1)}$ as if the transformation was an additional layer in the network.

4.1.3 Predicting overall sentiment

To predict overall sentiment associated with the sentence in L_T, we use the phrase embeddings p_t of the top layer of the RAE_{L_T} and it transformation p'_s. Together, we train a softmax regression classifier on concatenation of these two vector using weight matrix $W \in \mathbb{R}^{K \times 2n}$

5 Experimental Work

We perform experiments on two kind of sentiment analysis systems : (1) that gives +ve/-ve polarity to each review and (2) assigns ratings in range 1 - 4 to each review.

5.1 External Datasets Used

For pre-training the word embeddings and RAE Training, we used HindMonoCorp 0.5(Bojar et al., 2014) with 44.49M sentences (787M Tokens) and English Gigaword Corpus.

For Cross Training, we used the bilingual sentence-aligned data from HindEnCorp[1] (Bojar et al., 2014) with 273.9k sentence pairs (3.76M English, 3.88M Hindi Tokens). This dataset contains sentence pair obtained from Bilingual New Articles, Wikipedia entries, Automated Translations, etc. Training and Validation division is 70% and 30% for all above datasets.

In Supervised Phase I, we used IMDB11 dataset available at *http://ai.stanford.edu/~amaas/data/sentiment/* and first used by (Maas et al., 2011) for +ve/-ve

[1] http://ufal.mff.cuni.cz/hindencorp

system containing 25000 +ve and 25000 -ve movie reviews.

For 4-ratings system, we use Rotten Tomatoes Review dataset (scale dataset v1.0) found at *http://www.cs.cornell.edu/People/pabo/movie-review-data*. The dataset is divided into four author-specific corpora, containing 1770, 902, 1307, and 1027 documents and each document has accompanying 4-Ratings ({0, 1, 2, 3}) label.

5.2 Rating Based Hindi Movie Review (RHMR) Dataset

We crawled the Hindi Movie Reviews Website[2] to obtain 2945 movie reviews. Each Movie Review on this site is assigned rating in range 1 to 4 by at least three reviewers. We first discard reviews that whose sum of pairwise difference of ratings is greater than two. The final rating for each review is calculated by taking the average of the ratings and rounding up to nearest integer. The fraction of Reviews obtained in ratings 1-4 are [0.20, 0.25, 0.35, 0.20] respectively. Average length of reviews is 84 words. For +ve/-ve polarity based system, we group the reviews with ratings {1, 2} as negative and {3, 4} as positive.

5.3 Experimental Settings

We used following Baselines for Sentiment Analysis in Hindi :

Majority class: Assign the most frequent class in the training set (Rating:3 / Polarity:+ve)

Bag-of-words: Softmax regression on Binary Bag-of-words

We also compare our system with state of the art Monolingual and Cross Lingual System for Sentiment Analysis in Hindi as described by (Popat et al., 2013) using the same experimental setup. The best systems in each category given by them are as below:

WordNet Based: Using Hindi-SentiWordNet[3], each word in a review was mapped to corresponding synset identifiers. These identifiers were used as features for creating sentiment classifiers based on Binary/Multiclass SVM trained on bag of words representation using libSVM library.

Cross Lingual (XL) Clustering Based: Here, joint clustering was performed on unlabeled bilingual corpora which maximizes the joint likelihood of monolingual and cross-lingual factors.. For details, please refer the work of (Popat et al., 2013). Each word in a review was then mapped to its cluster identifier and used as features in an SVM.

Our approaches

Basic RAE: We use the Semi-Supervised RAE based classification where we first trained a standard RAE using Hindi monolingual corpora, then applied supervised training procedure as described in (Socher et al., 2011). This approach doesn't use bilingual corpora, but is dependent on amount of labeled data in Hindi.

BRAE-U: We neither include penalty term, nor fix the transformations weights in our proposed system.

BRAE-P: We only include the penalty term but allow the transformation weights to be modified in proposed system.

BRAE-F: We add the penalty term and fix the transformation weights during back propagation in proposed system.

5.4 Experimental Setup

We combined the text data from all English Datasets (English Gigaword + HindEnCorp English Portion + IBMD11 + Scale Dataset) described above to train the word embeddings using Word2Vec toolkit and RAE. Similarly, we combined text data from all Hindi Datasets (HindMonoCorp + HindiEnCorp Hindi Portion + RHMR) to train word embeddings and RAE for Hindi.

We used MOSES Toolkit (Koehn et al., 2007) to obtain high quality bilingual phrase pairs from HindEnCorp to train our BRAE model. After removing the duplicates, 364.3k bilingual phrase pairs were obtained with lengths ranging from 1-6, since bigger phrases reduced the performance of the system in terms of Joint Error of BRAE model.

We randomly split our RHMR dataset into 10 segments and report the average of 10-fold cross validation accuracies for each setting for both Ratings and Polarity classifiers.

We also report 5-fold cross validation accuracy on Standard Movie Reviews Dataset (hereby referred as SMRD) given by (Joshi et al., 2010) which contains 125 +ve and 125 -ve reviews in Hindi. The dataset can be obtained at http://www.cfilt.iitb.ac.in/Resources.html.

Since this project is about reducing dependence on annotated datasets, we experiment on how accuracy varies with labeled training dataset (RHMR) size. To perform this, we train our model

[2]http://hindi.webdunia.com/bollywood-movie-review/

[3]http://www.cfilt.iitb.ac.in/

in 10% increments (150 examples) of training set size (each class sampled in proportion of original set). For each size, we sample the data 10 times with replacement and trained the model. For each sample, we calculated 10-fold cross validation accuracy as described above. Final accuracy for each size was calculated by averaging the accuracies obtained on all 10 samples. Similar kind of evaluation is done for all other Baselines explored.

In subsequent section, the word 'significant' implies that the results were statistically significant ($p < 0.05$) with paired T-test

5.5 BRAE Hyper Parameters

We empirically set the learning rate as 0.05. The word vector dimension was selected as 80 from set $[40, 60, 80, 100, 120]$ using Cross Validation. We used joint error of BRAE model to select α as 0.2 from range $[0.05, 0.5]$ in steps of 0.05. Also, λ_L was set as 0.001 for DNN trained for word embedding and λ_{BRAE} as 0.0001.

For semi-supervised phases , we used 5-fold cross validation on training set to select κ and η in range $[0.0, 1.0]$ in steps of 0.05 with optimal value obtained at $\kappa = 0.2$ and $\eta = 0.35$. Parameter λ_p was selected as 0.01 , λ_S as 0.1 and λ_T as 0.04 after selection in range $[0.0, 1.0]$ in steps of 0.01.

5.6 Results

Dataset	**RHMR**		**SMRD**
Classifier	**Ratings**	**Polarity**	**Polarity**
Majority class	35.19	51.83	52.34
Bag-of-Words	51.98	62.52	68.47
WordNet based	55.47	67.29	75.5
XL Clustering	72.34	84.46	84.71
Basic RAE	75.53	79.31	81.06
BRAE-U	76.01	82.66	84.83
BRAE-P	79.70	84.85	87.00
BRAE-F	81.22	90.50	90.21

Table 1: Accuracies obtained for various Experimental Settings. Model are trained on complete labeled training datasets

Table 1 present the results obtained for both ratings based and polarity classifier on RHMR and MRD Dataset. Our model gives significantly better performance for ratings based classification than any other baseline system currently used for SA in Hindi. The margin of accuracy obtained against next best classifier is about 8%. Also, for +ve/-ve polarity classifier, the accuracy showed an improvement of 6% over next highest baseline.

$A \downarrow / P \rightarrow$	P-1	P-2	P-3	P-4
A-1	83.19	15.28	1.53	0.00
A-2	12.23	82.20	5.57	0.00
A-3	0.00	9.03	81.26	9.71
A-4	0.00	1.87	19.69	78.44
F1-score	0.83	0.78	0.82	0.80

Table 2: Confusion Matrix for Ratings by BRAE-F, **Across**: Predicted Rating, **Downward:** Actual Rating

In Table 2, we calculate the confusion matrix for our model(BRAE-F) for the 4-Ratings case. Value in a cell (A_i, P_j) represents the percentage of examples in actual rating class i that are predicted as rating j. We also show the F1 score calculated for each individual rating class. It clearly shows that our model has low variation in F1-scores and thereby its performance among various rating classes.

In Fig. 3, we show the variation in accuracy of the classifiers with amount of sentiment labeled Training data used. We note that our approach consistently outperforms the explored baselines at all dataset sizes. Also, our model was able to attain accuracy comparable to other baselines at about 50% less labeled data showing its strength in exploiting the unlabeled resources.

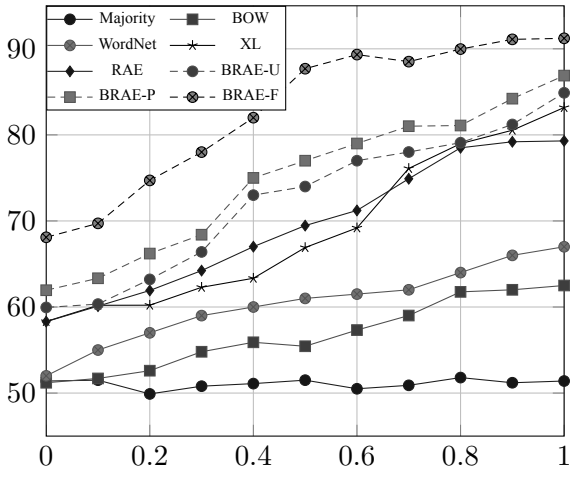

Figure 3: Variation of Accuracy (+ve/-ve Polarity) with Size of labeled Dataset(Hindi), **x-axis:** Fraction of Dataset Used, **y-axis:** %age Accuracy Obtained

We also experiment with variation of accuracies

New Word/Phrase	Similar Words/Phrases	Sentiment label
depressing निराशाजनक	gloomy उदास discouraging निराशात्मक	Rating : 1 Polarity : -ve
was painful दर्दनाक था	was difficult कठिन था was bad खराब था	Rating : 2 Polarity : -ve
should be awarded सम्मानित किया जाना चाहिए	was appreciated सराहना की गई will get accolades वाहवाही मिलना चाहिए	Rating : 4 Polarity : +ve
public won't come लोग नहीं आएगा	no one will come कोई नहीं आएगा viewers won't come दर्शक नहीं आएगा	Rating : 1 Polarity : -ve

Table 3: Semantically similar phrases obtained for new phrases and their assigned label

with amount of Unlabeled Bilingual Training Data used for Cross Lingual models explored. Again we increase size of bilingual dataset in 10% increments and calculate the accuracy as described previously. In Fig. 4, we observed that performance of the proposed approach steadily increases with amount of data added, yet even at about 50000 (20%) phrase pairs, our model produces remarkable gains in accuracy.

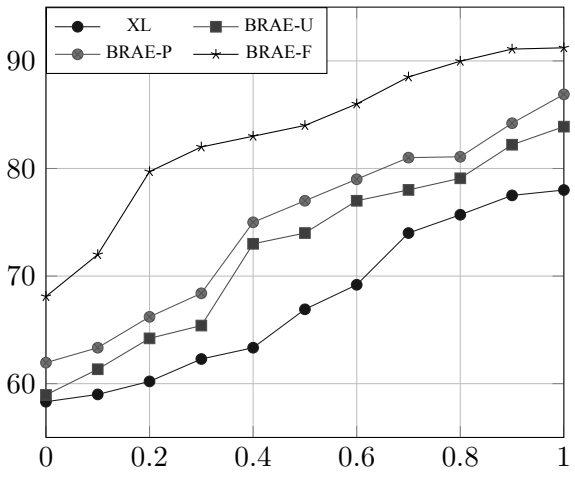

Figure 4: Variation of Accuracy (+ve/-ve polarity) with Size of Unlabeled Bilingual Corpora, **x-axis:** Fraction of Training Data Used, **y-axis:** %age Accuracy Obtained

We also observed that the model which restricts modification to transformation weights during supervised phase II does better than the one which allows the modification at all dataset sizes. This result appears to be counterintuitive to normal operation of neural network based models, but supports our hypothesis as explained in previous sections.

5.7 Performance and Error Analysis

Analysis on the test results showed that the major advantage given by our model occurs due to presence of unknown words (i.e.words not present in labeled dataset) in test data. Since we restricted the movement in semantic vector space, our model was able to infer the sentiment for a unknown word/phrase by comparing it with semantically similar words/phrases. In Table 3, we extracted the Top-2 semantically similar phrases in training set for small new phrases and sentiment labeled assigned to them by our model (the phrases are manually translated from Hindi for reader's understanding). As we can see, our model was able to extract grammatically correct phrases with similar semantic nature as given phrase and assign correct sentiment label to it.

Secondly, We found that our model was able to correctly infer word sense for polysemous words that adversely affected the quality of sentiment classifiers in our baselines. This eliminates the need for manually constructed fine grained lexical resource like WordNets and development of automated annotation resources. For example, to a phrase like *"Her acting of a schizophrenic mother made our hearts **weep**"*, the baselines classifiers assigned negative polarity due to presence of words like 'weep', yet our model was correctly able to predict positive polarity and assigned it a rating of 3.

Error Analysis of test results showed that errors made by our model can be classified in two major categories :

1) A review may only give description of the object in question (in our case , the description of the film) without actually presenting any individual sentiments about it or it may express conflicting sentiments about two different aspects about the same object. This presents difficulty in assign-

ing a single polarity/rating to the review.

2) Presence of subtle contextual references affected the quality of predictions made by our classifier. For example, sentence like *"His poor acting generally destroys a movie, but this time it didn't"* got a rating of 2 due to presence of phrase with negative sense (here the phrase doesn't have ambiguous sense), yet the actual sentiment expressed is positive due to temporal dependence and generalization. Also, *"This movie made his last one looked good"* makes a reference to entities external to the review, which again forces our model to make wrong prediction of rating 3.

Analyzing these aspects and making correct predictions on such examples needs further work.

6 Conclusion and Future Work

This study focused on developing a Cross Lingual Supervised Classifier based on Bilingually Constrained Recursive Autoencoder. To achieve this, our model first learns phrase embeddings for two languages using Standard RAE, then fine tune these embeddings using Cross Training procedure. After imposing certain restrictions on these embeddings, we perform supervised training using labeled sentiment corpora in English and a much smaller one in Hindi to get the final classifier.

The experimental work showed that our model was remarkably effective for classification of Movie Reviews in Hindi on a rating scale and predicting polarity using least amount of data to achieve same accuracy as other systems explored. Moreover it reduces the need for MT System or lexical resources like Linked WordNets since the performance is not degraded too much even when we lack large quantity of labeled data.

In Future, we hope to 1) extend this system to learn phrase representations among multiple languages simultaneously, 2) apply this framework to other cross Lingual Tasks such as Paraphrase detection, Question Answering, Aspect Based Opinion Mining etc and 3) Learning different weight matrices at different nodes to capture complex relations between words and phrases.

References

Balamurali, Aditya Joshi, and Pushpak Bhattacharyya. 2012. Cross-lingual sentiment analysis for Indian languages using linked wordnets. In *Proceedings of COLING 2012: Posters*, pages 73--82. The COLING 2012 Organizing Committee.

Ondřej Bojar, Vojtěch Diatka, Pavel Rychlý, Pavel Straňák, Vít Suchomel, Aleš Tamchyna, and Daniel Zeman. 2014. HindEnCorp - Hindi-English and Hindi-only Corpus for Machine Translation. In *Proceedings of the Ninth International Conference on Language Resources and Evaluation (LREC'14)*. European Language Resources Association (ELRA).

Julian Brooke, Milan Tofiloski, and Maite Taboada. 2009. Cross-linguistic sentiment analysis: From english to spanish. In *RANLP*, pages 50--54.

Ronan Collobert and Jason Weston. 2008. A unified architecture for natural language processing: Deep neural networks with multitask learning. In *Proceedings of the 25th international conference on Machine learning*, pages 160--167. ACM.

Hatem Ghorbel and David Jacot. 2011. Further experiments in sentiment analysis of french movie reviews. In *Advances in Intelligent Web Mastering--3*, pages 19--28. Springer.

Christoph Goller and Andreas Kuchler. 1996. Learning task-dependent distributed representations by backpropagation through structure. In *Neural Networks, 1996., IEEE International Conference on*, volume 1, pages 347--352. IEEE.

Aditya Joshi, AR Balamurali, and Pushpak Bhattacharyya. 2010. A fall-back strategy for sentiment analysis in hindi: a case study. *Proceedings of the 8th ICON*.

Philipp Koehn, Hieu Hoang, Alexandra Birch, Chris Callison-Burch, Marcello Federico, Nicola Bertoldi, Brooke Cowan, Wade Shen, Christine Moran, Richard Zens, et al. 2007. Moses: Open source toolkit for statistical machine translation. In *Proceedings of the 45th annual meeting of the ACL on interactive poster and demonstration sessions*, pages 177--180. Association for Computational Linguistics.

Bin Lu, Chenhao Tan, Claire Cardie, and Benjamin K Tsou. 2011. Joint bilingual sentiment classification with unlabeled parallel corpora. In *Proceedings of the 49th Annual Meeting of the Association for Computational Linguistics: Human Language Technologies-Volume 1*, pages 320--330. Association for Computational Linguistics.

Andrew L. Maas, Raymond E. Daly, Peter T. Pham, Dan Huang, Andrew Y. Ng, and Christopher Potts. 2011. Learning word vectors for sentiment analysis. In *Proceedings of the 49th Annual Meeting of the Association for Computational Linguistics: Human Language Technologies*, pages 142--150. Association for Computational Linguistics.

Tomas Mikolov, Ilya Sutskever, Kai Chen, Greg S Corrado, and Jeff Dean. 2013. Distributed representations of words and phrases and their compositionality. In *Advances in Neural Information Processing Systems*, pages 3111--3119.

Namita Mittal, Basant Agarwal, Garvit Chouhan, Nitin Bania, and Prateek Pareek. 2013. Sentiment analysis of hindi review based on negation and discourse relation. In *proceedings of International Joint Conference on Natural Language Processing*, pages 45--50.

Kashyap Popat, Balamurali A.R, Pushpak Bhattacharyya, and Gholamreza Haffari. 2013. The haves and the have-nots: Leveraging unlabelled corpora for sentiment analysis. In *Proceedings of the 51st Annual Meeting of the Association for Computational Linguistics (Volume 1: Long Papers)*, pages 412--422. Association for Computational Linguistics.

Richard Socher, Jeffrey Pennington, Eric H Huang, Andrew Y Ng, and Christopher D Manning. 2011. Semi-supervised recursive autoencoders for predicting sentiment distributions. In *Proceedings of the Conference on Empirical Methods in Natural Language Processing*, pages 151--161. Association for Computational Linguistics.

Richard Socher, John Bauer, Christopher D Manning, and Andrew Y Ng. 2013. Parsing with compositional vector grammars. In *In Proceedings of the ACL conference*. Citeseer.

Chang Wan, Rong Pan, and Jiefei Li. 2011. Bi-weighting domain adaptation for cross-language text classification. In *IJCAI Proceedings-International Joint Conference on Artificial Intelligence*, volume 22, page 1535.

Jiajun Zhang, Shujie Liu, Mu Li, Ming Zhou, and Chengqing Zong. 2014. Bilingually-constrained phrase embeddings for machine translation. In *Proceedings of the 52nd Annual Meeting of the Association for Computational Linguistics (Volume 1: Long Papers)*, pages 111--121. Association for Computational Linguistics.

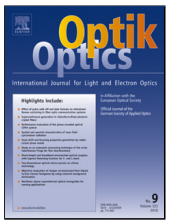

Title: Design and analysis of photonic crystal biperiodic waveguide structure based optofluidic-gas sensor

Author: Ajeet Kumar Than Singh Saini Ravindra Kumar Sinha

PII: S0030-4026(15)01226-7
DOI: http://dx.doi.org/doi:10.1016/j.ijleo.2015.09.157
Reference: IJLEO 56362

To appear in:

Received date: 24-10-2014
Accepted date: 9-9-2015

Please cite this article as: A. Kumar, T.S. Saini, R.K. Sinha, Design and analysis of photonic crystal biperiodic waveguide structure based optofluidic-gas sensor, *Optik - International Journal for Light and Electron Optics* (2015), http://dx.doi.org/10.1016/j.ijleo.2015.09.157

Design and analysis of photonic crystal biperiodic waveguide structure based optofluidic-gas sensor

Ajeet Kumar*, Than Singh Saini and Ravindra Kumar Sinha

Department of Applied Physics, Delhi Technological University, Delhi 110 442, India

E-mail: ajeetdph@gmail.com

ABSTRACT

We present a photonic crystal (PhC) biperiodic waveguide (BPW) structure for both gas and fluid sensing based on modulation of refractive index (RI) of supercavities. The proposed structure has been designed by creating a BPW in silicon (Si) substrate with triangular array of air holes. This BPW structure consists of an array of supercavities and only the resonant wavelength is allowed to pass through the waveguide while the rest of the wavelengths are reflected by the structure. The principle of sensing is based on the shift of the resonance wavelength of supercavities when infiltrated by any liquid or gas. The transmission spectra of sensor have been analyzed numerically by finite difference time domain (FDTD) method. The proposed design can be utilized as a gas sensor or fluid sensor by selectively filling the holes of supercavities. For gas sensing application, the sensitivity of the sensor has been found to be 610 nm per refractive index unit (RIU) with minimum detection limit of 0.0001 RIU. Sensitivity of 300 nm/RIU with wider RI detection range of 1.0-1.5 is obtained when the structure is used as a fluid sensor.

Keywords: Photonic crystal, biperiodic waveguide, gas sensor, fluid sensor

1. Introduction

In the recent years, refractive index (RI) based optical micro sensors have gained a high degree of interest because of their application in detection of wide range of physical parameters like humidity, temperature, pressure and force [1-4] as well as chemical and biological parameters [5-7]. Refractive index based sensors can be realized using directional couplers [8], Mach-Zender interferometers [9], micro-rings [10] and photonic crystals (PhCs). Among all the devices, PhCs have provided a new platform for the realization of RI optical sensor due to fabrication of low loss waveguides along with high-Q resonant cavities [11-12]. Various RI sensors based on waveguide [13-16], waveguide along with cavity [17-18] and resonant cavities [19-25] have been demonstrated theoretically and experimentally. Although structures employed with resonant cavity in waveguide offer wide measurement range of RI, they have less coupling efficiency from waveguide to cavity which reduces their transmission efficiency [22]. PhC waveguide based optofluidic RI sensors have higher transmission efficiency but they have relatively less sensitivity [15-16]. On the other hand, high Q-cavities based RI gas sensors offer high sensitivity, low detection limit and faster response but with low detection range [26]. All the aforementioned PhC structures can either be used as liquid sensor or a gas sensor, however, no PhC structure proposed which provides platform for both gas and liquid sensing with higher sensitivity.

In this paper, we have proposed a photonic crystal based biperiodic waveguide (BPW) structure for RI sensing. In our proposed structure, radii of the holes just adjacent to the waveguide have been changed in such a manner that they form an array of supercavities along the waveguide while one supercavity consists of three holes on both sides of the waveguide with radius of central hole modulated. The structure consists of two different lattice constants thus forming a BPW structure.

The design consists of triangular array of holes in silicon (Si) substrate as the PBG arises from periodically patterned dielectric lattice Si PhCs and can be utilized for relatively low-loss waveguiding [27] and microcavities with quality factor (Q) as high as 10^6 [28-29], which is advantageous for both gas and fluid sensing.

Initially, RI of all the holes of supercavities has been changed to study the response of structure while in the latter part, RI of only the bigger holes has been changed. In the former case, sensitivity of the structure has been found to be 610 nm/RIU(refractive index unit) with minimum detection limit of order of 10^{-4} and detection range from 1-1.002 while in the latter case sensitivity of 300 nm/RIU has been achieved with wider detection range from 1-1.5 and minimum detection limit of 10^{-3}. The proposed structure can be used for both gas sensing (all the holes of supercavities have been infiltrated) and fluid sensing (bigger holes of supercavities have been filled).

2. Sensor Design

The structure of the proposed sensor consists of one waveguide in two dimensional (2D) PhC with triangular lattice of circular air holes having periodicity *a*, as depicted in Fig.1. The triangular PhC is practically important because it offers large transverse electric (TE) bandgap and can be integrated along with other optoelectonic devices [30]. The waveguide has been formed by removing one row of air holes along the Γ-K direction. The radii of the holes just next to waveguide have been modulated at alternate positions in order to form array of supercavities while one supercavity possess three holes with central hole radius modulated, as shown in Fig.2. The proposed design for sensor consists of the array of supercavites having different periodicity a' = 856 nm, as shown in Fig. 3 and thus creating a biperiodic structure.

The structure consists of finite array of 17×15 air holes with silicon (n = 3.5) as background material due to its strong potential in the fields of integrated optics and optical sensing [31-34].

The structure has two different size of holes of radii, R_1 = 0.35*a and R_2 = 0.4*a with lattice constant, a = 428 nm. The radius, R_2 has been changed in order to get resonant mode in the structure. The light has been coupled at one end of the waveguide and the transmission spectrum has been observed at the other end of waveguide.

3. Simulation and Results

Numerical analysis has been done using finite difference time domain method (FDTD). Initially computation has been done to calculate resonant mode of supercavity inside the structure. The size of the green hole has been changed to get the resonant mode, as shown in Fig. 2. The calculated results show that the resonant mode has been found for R_2 = 0.4*a, as shown in Fig. 4. The resonance wavelength of the supercavity has been found to be λ =1550 nm. In order to form array of supercavities along the whole waveguide, holes at alternate position have been modified to R_2 = 0.4*a. The calculated transmission spectrum for the BPW structure has been found to have Lorentzian response with maximum transmission of 91.74%, as shown in Fig. 5.

It has been found that the BPW structure only allows the resonance wavelength to pass through the waveguide and reflects the remaining wavelengths. The field distribution for the sensor at resonance wavelength of 1550 nm is shown in Fig. 6. The principle involved in RI sensing is based upon the shift of the resonant wavelength of supercavities. Supercavities can be used as a local sensor which when infiltrated with gases or liquids of different RI observe change in their optical properties.

Two schemes have been employed to carry out simulation and analysis of the structure. In the first scheme, RI of all the holes of supercavities has been changed while in second case, RI of holes at alternate position has been changed.

3.1 All holes of supercavities have been filled

The resonance wavelength of the mode supported by cavity depends upon the local RI in the vicinity of cavity and geometric parameters of structure. When all the holes of supercavities have been filled with an analyte, there is change in local RI of the supercavity which shifts the resonance wavelength. The magnitude of the wavelength shift divided by change in RI gives the sensitivity of the device. The shift in resonance wavelength satisfies

$$\Delta\lambda = \lambda_o \frac{\Delta n}{n_o} \qquad (1)$$

where Δn is the change in RI of supercavities, n is the initial RI of supercavities, λ is the initial resonance wavelength and $\Delta\lambda$ is the shift in resonance wavelength when n changes to n+Δn. The FDTD simulation results show that when the device is operated at resonance wavelength of λ = 1550 nm, the resonance wavelength shifts about 0.061 nm for Δn = 0.0001 (as shown in Fig. 7) and hence the device has sensititvity, S=610nm/RIU, rendering it suitable for gas sensing. As the full width at half maxima of transmission spectra obtained for BPW structure, as shown in Fig. 5 is around 30 pm, the structure has been able to detect even the smallest change in RI of the order of 10^{-4} leading to high sensitivity of the structure. In Fig.8, the resonance wavelength shift $\Delta\lambda = \lambda(n)-\lambda(\text{air})$ is plotted as a function of ambient RI, and the shift is 61 pm for $\Delta n = 10^{-4}$ with detection limit of 1.002.

3.2 Only bigger holes of supercavities have been filled

In the second scheme, instead of filling all the holes of supercavities only bigger air holes have been infiltrated with an analyte. In this case also, there is change in local RI of the supercavities which shifts the resonance wavelength. The precise simulation results have shown that the sensitivity has been decreased dramatically. In this case, resonance wavelength shifts upto 0.3 nm

for Δn = 0.001, as shown in Fig. 9 with wider measurement range of RI 1.0-1.5. So the sensor's sensitivity is S=300nm/RIU.

In PhC waveguide sensor based on dispersive properties of waveguide, for obtaining larger sensitivity, filling fraction of the holes filled with the analyte must be larger. But in this case, by merely filling bigger holes, sensitivity of 300 nm/RIU has been achieved, which in turn means requirement of lesser volume of analyte over conventional waveguides. Also, structures with supercavities are more sensitive to RI changes and when these supercavities are arranged to form a complete waveguide, there is no coupling loss from waveguide to cavity thus offering wider measurement range of RI sensing. Figure 10 depicts the resonance wavelength shift $\Delta\lambda = \lambda(n)-\lambda(air)$ is plotted as a function of ambient RI, and the shift is 0.3 nm for $\Delta n = 10^{-3}$ with measurement range from 1.0 - 1.5.

4. Conclusions

We have presented a PhC based BPW structure which provides platform for both gas and fluid sensing. The structure has been implemented by changing the periodicity of holes just next to waveguide and introducing an array of supercavities along the whole waveguide. The transmission spectrum of BPW structure obtained using FDTD method shows that the structure allows only resonant wavelength of supercavity to pass through the waveguide and rest of the wavelengths are reflected. Thus, a Lorentzian response has been obtained for the waveguide instead of the dispersion curve obtained for conventional waveguides. The BPW structure offers several advantages over conventional waveguides or microcavity structures. The BPW structure offers high sensitivity and wider measurement range for RI sensing. By selective infiltration of holes of supercavity, the same structure can be used either as a gas sensor or a fluid sensor. Another advantage of this structure is that the structure is operated at resonance wavelength of 1550 nm and thus the device can be integrated with other optoelectronic devices used in

broadband optical communication. For gas sensing applications, BPW structure offers sensitivity of 610 nm/RIU with minimum detection limit of the order of 10^{-4}. As an optofluidic sensor, the same structure offers sensitivity of 300 nm/RIU along with wider measurement range of RI from 1.0 - 1.5 and minimum detection limit of 0.001.

References

1. H Y Fu, H Y Tam, L Shao, X Dong, P A Wai, C, Lu and S K Khijwania, "Pressure sensor realized with polarization maintaining photonic crystal fiber-based Sagnac interferometer, *Appl. Opt*. 47 (2008) 2835-2839.
2. W J Bock, J Chen, T Eftimov, and W Urbanczyk, A photonic crystal fiber sensor for pressure measurements, *IEEE Trans. Instrum. Meas.,* 55 (2006) 1119-1123.
3. X Dong, H Y Tam, and P Shum, Temperature-insensitive strain sensor with polarization-maintaining photonic crystal fiber based Sagnac interferometer, *Appl. Phys. Lett.*, 90 (2007) 151113 -151115.
4. T Stomeo, M Grande, A Qualtieri, A Passaseo, A Salhi, D Biallo, and F Prudenzano, Fabrication of force sensors based on two-dimensional photonic crystal technology, *Micro. Eng.*, 84 (2007) 1450 -1453.
5. T Hasek, R Wilk, H Kurt, D Citrin, and M Koch *Proc. Int. Conf. on Teraherz Electonic.*, (2006) 239.
6. N Skivesen, A Têtu, M Kristensen, J Kjems, L H Frandsen, and P I Borel, Photonic-crystal waveguide biosensor, *Opt. Express*, 15 (2007) 3169 – 3176.
7. I D Block, L Chan, and T Cunningham, Photonic crystal optical biosensor incorporating structured low-index porous dielectric, *Sensors and Actuators B: Chemical,* 120 (2006) 187-193.
8. B J Luff, B J Larris, and J S Wilkinson, Integrated-optical directional coupler biosensor, *Opt. Lett*. 21 (1996) 618-620.

9. R G Heideman, R P Kooyman, and Greve, Performance of a highly sensitive optical waveguide Mach-Zehnder interferometer immunosensor, *Sensors and Actuators B: Chemical*, 10 (1993) 209-217.
10. K D Vos, I Bartolozzi, E Schacht, P Bienstman and R Baets, Silicon-on-insulator microring resonator for sensitive and label-free biosensing, *Opt. Express*, 15 (2007) 7610- 7615.
11. J D Joannopoulos, R D Meade, and J N Winn, Photonic Crystals: Molding The Flow of Light, Princeton University Press, 1995, Princeton, NJ
12. Y Akahane, T Asano, B S Song, and S Noda, High-Q photonic nanocavity in a two-dimensional photonic crystal, *Nature*, 425 (2003) 944–947.
13. S Xiao and N A Mortenson, Proposal of highly sensitive optofluidic sensors based on dispersive photonic crystal waveguides, *J. Opt. A, Pure Appl. Opt*., 9 (2007) 463–467.
14. S Xiao and N A Mortensen, Highly dispersive photonic band-gap-edge optofluidic biosensors, *J. Eur. Opt. Soc. Rapid Publ.* 1 (2006) 06026.
15. Shruti, R K Sinha and R Bhattacharya, Photonic crystal slab waveguide-based infiltrated liquid sensors: design and analysis, *J. of Nanophotonics*, 5 (2011) 053505.
16. H S Dutta and S Pal, Design of a highly sensitive photonic crystal waveguide platform for refractive index based biosensing, *Opt. Quant. Electron.*, 45 (2013) 907-917.
17. X Wang, Z Xu, N Lu, J Zhu, and G Jin, Ultracompact refractive index sensor based on microcavity in the sandwiched photonic crystal waveguide structure, *Opt. Commu.* 281 (2008) 1725-1731.
18. X Wang, N Lu, Q Tan and G Jin, Investigation of biosensor built with photonic crystal microcavity ,*Chin. Opt. Lett.* 12 (2008) 925-927.
19. U Bog, C L Smith, M W Lee, S Tomljenovic-Hanic, C Grillet, C Monat, L O'Faolain, C Karnutsch, T F Krauss, R C McPhedran, and B J Eggleton, High Q microfluidic cavities in silicon-based two-dimensional photonic crystal structures, *Opt. Lett*., 33 (2008) 2206–2208.

20. S Tomljenovic-Hanic, C M de Sterke, and. M J Steel, Design of high-Q cavities in photonic crystal slab heterostructures by air-holes infiltration, *Opt. Express,* 14 (2006) 12451–12456.

21. P Domachuk, H C Nguyen, B J Eggleton, M Straub, and M Gu, Microfluidic tunable photonic band-gap device , *Appl. Phys. Lett.*, 84 (2004) 1838–1840.

22. D F Dorfner, T Hürlimann, T Zabel, L H Frandsen and G Abstreiter, Silicon photonic crystal nanostructures for refractive index sensing , *Appl. Phys. Lett.* 93 (2008) 181103.

23. T Sünner, T Stichel, S H Kwon, T W Schlereth and S Höfling, Photonic crystal cavity based gas sensor , *Appl. Phys. Lett.* 92 (2008) 261112.

24. J Jágerská, H Zhang, Z Diao, N L Thomas and R Houdré, Refractive index sensing with an air-slot photonic crystal nanocavity, *Opt. Lett*, 35 (2010) 2523 – 2525.

25. J Dahdah, N Courjal and F I Baida, Analysis of a photonic crystal cavity based on absorbent layer for sensing applications *J. Opt. Soc. Am. B*, 27 (2010) 305-310.

26. A Benz, C Deutsch, M Brandstetter, A M Andrews, P Klang, H Detz., W Schrenk., G Strasser and K Unterrainer, Terahertz Active Photonic Crystals for Condensed Gas Sensing, *Sensors*, 11 (2011) 6003-6014.

27. S Y Lin, E Chow, V Hietala, P R Villeneuve and J D Joannopoulos, Experimental demonstration of guiding and bending of electromagnetic waves in a photonic crystal , *Science*, 282 (1998) 274-276.

28. B Song, S Noda, T Asano, and Y Akahane, Ultra-high-Q photonic double-heterostructure nanocavity , *Nat. Mater*, 4 (2005) 207–210.

29. T Asano, B S Song, and S Noda, Analysis of the experimental Q factors (~ 1 million) of photonic crystal nanocavities, O*pt. Express*, 14 (2006) 1996–2002.

30. C Jamois, R Wehrspohn, J Schilling, F Muller, R Hillebrand, W Hergert, Silicon-based photonic crystal slabs: two concepts , IEEE *Journal of Quantum Electronics*, 38 (2002) 805-810.

31. T Krauss and R De La Rue, Photonic crystal in the optical regime-past, present and future, *Prog. Quantum Electron.,* 23 (1999) 51–96.

32. I M White and X Fan, On the performance quantification of resonant refractive index sensors, *Opt. Express*, 16 (2008) 1020–1028.

33. N Mortensen, S Xiao, and J Pedersen, Liquid-infiltrated photonic crystals: enhanced light-matter interactions for lab-on-a-chip applications, *Microfluid. Nanofluid.*, 4 (2008) 117–127.

34. D Dorfner, T Zabel, T Hürlimann, N Hauke, L Frandsen, U Rant, G Abstreiter, and J Finley, Photonic crystal nanostructures for optical biosensing applications, *Biosens. Bioelectron.,* 24 (2009) 3688–3692.

Figure Captions:

Fig. 1 Layout of the proposed structure for RI and gas sensing. The structure consists of an array of supercavity (as shown in inset)

Fig. 2 Supercavity which has been formed by changing the radius of one hole.

Fig. 3 Array of supercavities with different periodicity which lead to the formation of biperiodic structure.

Fig. 4 Computed mode profile of the supercavity for R_2=0.4**a* at which the resonance wavelength of the supercavity matches with the peak value of Lorentzian response obtained for waveguide.

Fig. 5 Transmission spectra obtained for biperiodic structure.

Fig. 6 The magnetic field distribution for biperiodic sensor at resonance wavelength of 1550 nm.

Fig. 7 Normalized transmission spectra of the sensor with five different refractive indices of supercavities.

Fig. 8 Resonant wavelength shift $\Delta\lambda$ plotted as a function of ambient index *n*.

Fig. 9 Normalized transmission spectra for the sensor with five different refractive indices ranging from n = 1.446 to n = 1.450 in 0.001 increments.

Fig. 10 Relation of resonant wavelength and ambient refractive index *n*.

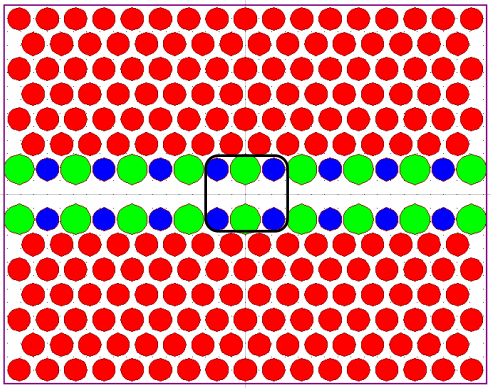

Figure. 1

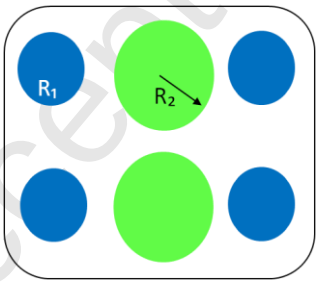

Figure. 2

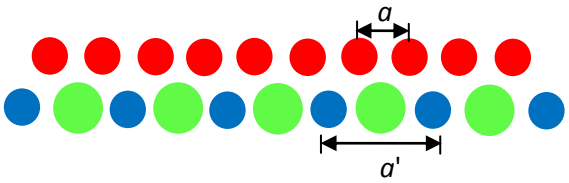

Figure. 3

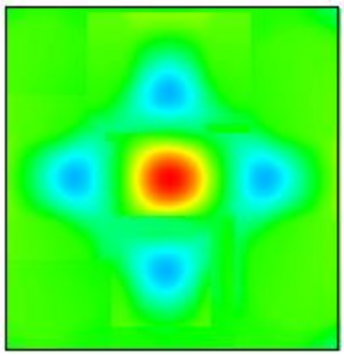

Figure. 4

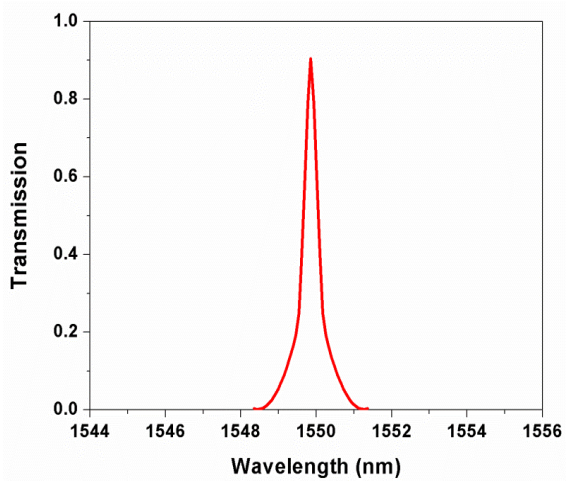

Figure. 5

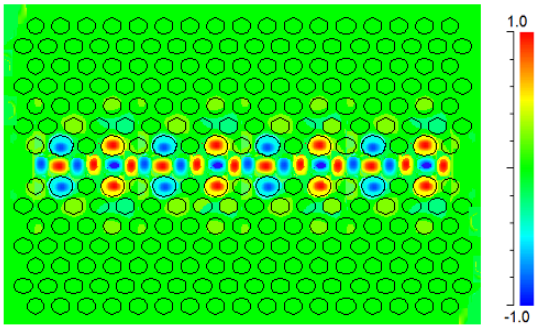

Figure. 6

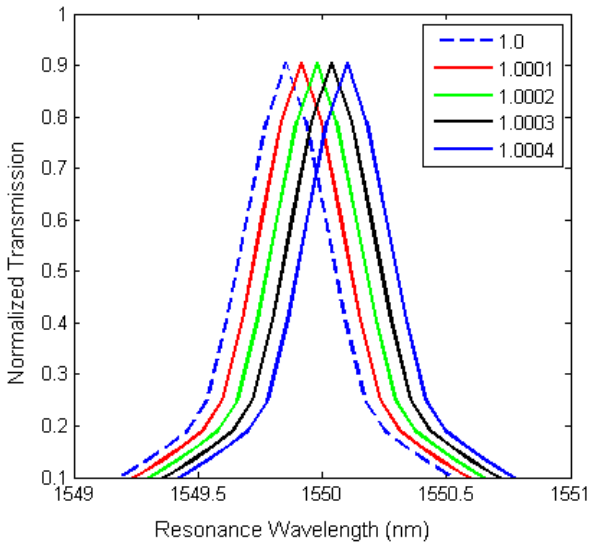

Figure. 7

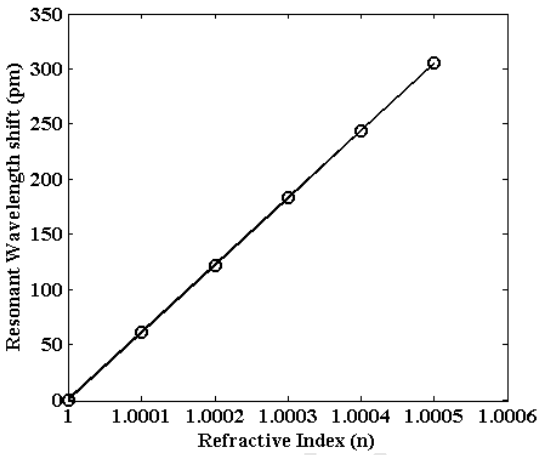

Figure. 8

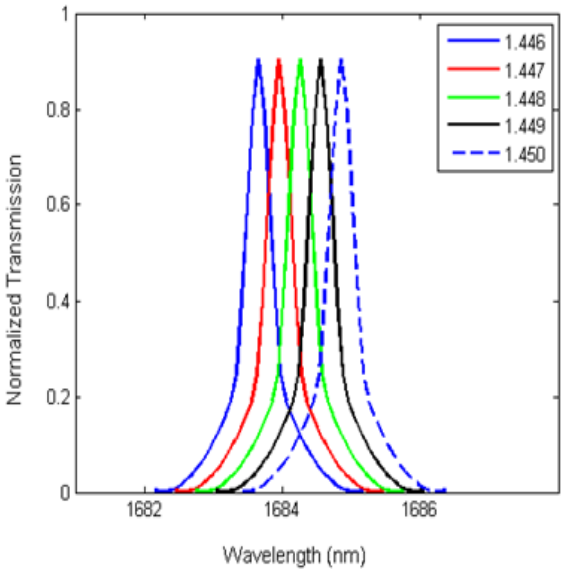

Figure. 9

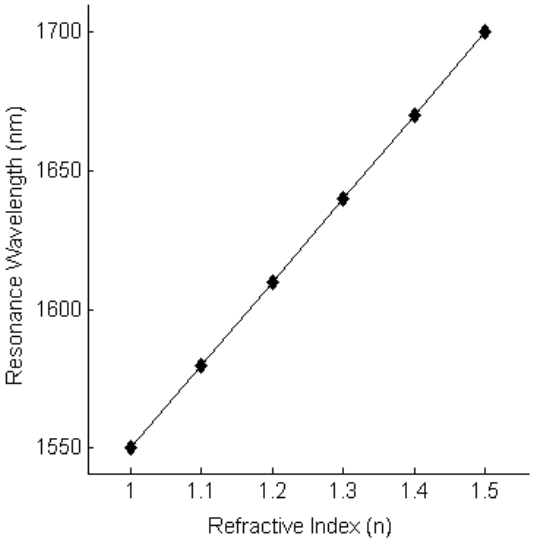

Figure. 10

Available online at www.sciencedirect.com

ScienceDirect

materialstoday: PROCEEDINGS

Materials Today: Proceedings 2 (2015) 3327 – 3341

4th International Conference on Materials Processing and Characterization

Design and Development of hybrid electrochemical and centrifugal force assisted abrasive flow machining

Rahul Vaishya[a], R.S. Walia[b], P. Kalra[c]

[a]Research scholar of Production Engineering , PEC University of Technology. Chandigarh
[b]Associate Prof, Mechanical Engg Deptt. Delhi Technological University, Delhi
[c]Professor, Deptt. of Production Engineering, PEC University of Technology, Chandigarh

Abstract

Abrasive flow machining is a nontraditional polishing process to polish metallic components using a semi-liquid paste, and with which complicated or miniaturized parts requiring high surface finish can be economically produced. To explore the possibility of a novel way of integrating AFM with electro-chemical machining with the objective to enhance its efficiency and quality of finish surface this study was undertaken. The newly design and developed solution is formed as electrochemical and centrifugal force assisted abrasive flow machining process (EC2A2FM)for various range of parameters. The effects of EC2A2FM process parameters, such as, Voltage, Salt molal concentration, RPM etc.and constant parameter such as number of cycles, extrusion pressure on material removal have been investigated. Taguchi method based experimental design was applied to optimize the hybrid AFM process parameter for better material removal. Analysis of variance (ANOVA)was applied to identify the significant parameters for maximum material removal. The analysis of results showed that there was enhanced material removal in EC2A2FM as compared to the other hybrid AFM process, as well as the operating pressure was allows 6 N/mm2.This small operating extrusion pressure was very much important as far as fragile components has to prevent from damageand retain their geometrical tolerances ,this seems to be the contributing factor for the increase in material removal and % improvement in surface roughness.

Selection and peer-review under responsibility of the conference committee members of the 4th International conference on Materials Processing and Characterization.

Keywords: Abrasive flow machining (AFM),material removal (MR), Electro chemical Aided Centrifugal forceassisted abrasive flow machining (EC^2A^2FM),ANOVA, Hybrid

Selection and peer-review under responsibility of the conference committee members of the 4th International conference on Materials Processing and Characterization.
doi:10.1016/j.matpr.2015.07.158

1. Introduction

Abrasive Flow Machining (AFM) is a nontraditional machining technique. In 1960's the Extrude Hone Corporation, USA developed Abrasive flow machining (AFM) as a method to deburr and polish difficult to reach surfaces and edges by flowable abrasive laden media (polymer) having some special rheological properties. Under the title " Method of honing by extruding " Mc Carty patented this process in 1970.The media (containing polymer and abrasive particles) is extruded under pressure through or across the surface to be machined[4,5]. The media behaves like a flexible cutting tool and provide a good surface finish.Rhoades [1-3] concluded that depth of cut firstly depends upon grain size of abrasive, relative hardness and extrusion pressure from the studies of basic principle of AFM. Przylenk [6] explain that more grains come in contact with the wall and Material removal(MR) increases in case of small bore diameter of workpiece. The velocity of media is increased then abrasion is increased and on increasing the pressure and viscosity of media the material removal rate (MRR) increased [7,8]. The limitations of process of AFM are low material removal rate, longer cycle time and requirement of large number of cycles to arrive at a finish level for the hard alloys. Scratches and large bumps cannot be removed due to lesser material removal [18] equally from all surfaces.Walia et al.(2004)developed the new hybrid process by introducing the centrifugal force in the extruding media to gain more material removal and high surface finish and reported that centrifugal force increase the material removal[9-13], It leads to the development of CFAAFM. [14, 15] Further optimized the no. of parameters of CFAAFM (centrifugal force assisted abrasive flow machining process) Like no. of cycles, shape and rotational speed of CFG rod to achieve polish surfaces. In CFAAFM process high machining rate result in faster cutting and lesser no. of cycles that are required to achieve high material removal.To improve the capabilities of conventional AFM process a centrifugal force is apply to the abrasive particles in the media to make a hybrid process. The modified setup is called CFAAFM (centrifugal force assisted abrasive flow machining. By using RSM (response surface methodology) the effect of parameters on the performance of the process studied. The relationships were found out between material removal and percentage improvement in surface finish of cylindrical components. It was observed that the combination of larger grain size and high speed of CFG rod gives higher material removal [19].Dabrowski et al.(2006) experimented with combination of electro-chemical machining (ECM) with abrasive flow machining (AFM) and developed electrochemical aided AFM(ECAFM) by using polymer electrolytes for the finishing of flat work-pieces only and concluded that material removal gets increased with the electrochemical aid, so electrochemically assisted abrasive flow machining (ECAFM) is possible using polymeric electrolytes[16,17].The material removal increased with the increase in applied Voltage [18].The performance of any machining process is measured in terms of material removal and surface quality produced. Conventional processes such as grinding, honing, lapping, buffing and super finishing have been in used in many years for material removal and finishing; however the uses of all these processes are limited to a restricted shape and geometry of work piece. Abrasive flow machining (AFM) is a widely used as non-conventional machining process to achieve high material removal and good surface quality [24]. The ability of abrasive media used in AFM to reach inaccessible areas to finish inner surfaces makes this more effective than other advanced machining processes[26,27]. This process has found application in many areas like aerospace, automobile, medical instruments, finishing of industrial valves, mould and die making and semiconductor equipments etc. The AFM setup carried two vertically opposite cylinders and in between these cylinders a fixture is placed. The abrasive media moves back and forth through the restricted passage in the fixture. The abrasive particles in the media consist of cutting edge with different orientations, which helps in material removal. Different types of abrasive grains like silicon carbide, aluminum oxide, boron carbide and diamond powder are used. To enhance the Hybrid AFM performance for MR either workpiece was rotated[29] or a mechanism was provided by attaching a D.C motor which provides rotational motion to the tooling rod inside the work piece. When the media was extruded, the rotating tool applied centrifugal force on media in result of the more abrasive particles comes in the contact of the inner surface(normal to the axis) of workpiece with high velocity as a result MR increased[25].S. Singh and Shan also reported that when work-piece was processed by magnetic field assisted AFM; the media viscosity interacted with magnetic flux density while affecting material removal as well as surface roughness. The effect of magnetic field has been shown to be dominant for low viscosity media [30].

2. Setup of hybrid EC2A2FM process

2.1. EC^2A^2FM process

An experimental setup was designed and constructed to further enhancement of material removal.The process was clubbed withelectro-chemical machining, CFGAFM with primary AFM process. This developed process is termed as EC^2A^2FM as shown in figure 1.

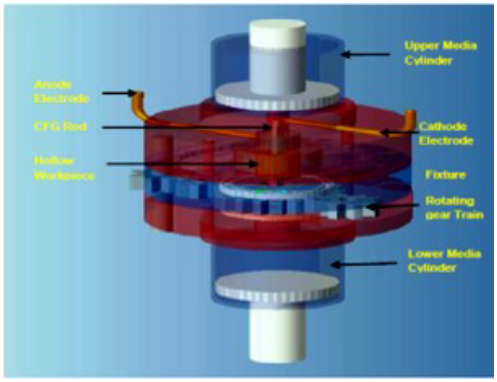

Figure 1 Schematic diagram of hybrid electrochemical and centrifugal force assisted AFM process

In this process, the pressure was intentionally kept low i.e. 6 N/mm^2in view of thin components. The experiment carried out successfully. The effects of five main EC^2A^2FM process parameters and their associated interactions on the quality characteristics were investigated at three levels. Taguchi parametric design methodology was adopted and the experimentation had been planned using standard L_{27} OA. The dominant process parameters were found to be voltage, molal concentration.The selected parameters were optimized. Few constant parameters like number of cycles, media flow volume, polymer gel ratio and the important one was operating pressure 6N/mm^2 which was less in comparison of all those processes investigated before.An electrolyte solution KI handles charge transfer in the working gap. The resulting electron current releases metal ions from the work piece.

2.2. Experimental Setup for EC^2A^2FM

The hybrid EC^2A^2FM process setup has been developed on the basic platform of an existing AFM setup in the Modern Manufacturing Laboratory of Production Engineering Department at PEC University of Technology, Chandigarh, India [21] as shown in figure 3(a) and (b). The AFM cutting action part is achieved due to the back and forth extrusion of the electrolyte-abrasives laden media through the gap between the CFG rod and anode work-piece. This extrusion is controlled by a hydraulic system already developed for the basic AFM setup as shown in figure 3(b). A combination of one upward and downward stroke completes a cycle of AFM process. To achieve the electrolytic machining along with the abrasives cutting action, the necessary nylon fixture has been developed shown in figure2(a). The modified nylon fixture was made in three parts and axially holds a cylindrical rod of copper inside the tightly held hollow cylindrical work-piece with the help of necessary retainers and fasteners as shown in fig 2(a). The axial CFG rod was supported at the two ends by two copper retainers in such a way that there was no hindrance in the media flow/sealing. In the nylon fixture, two copper electrodes were fitted in such a way that one electrode (cathode) was in contact with the axial copper rod through one of the rod retainers and was connected to the negative terminal of the DC power supply. The other electrode (anode) was in contact with the firmly seated work-piece and is connecting it to the positive terminal of the DC Power supply. A DC power supply Scientechas shown in figure2(b) with voltage range 0-30 V has been used to supply the DC current to the electrodes. For the present study, the suitable electrolytic salts-abrasives laden polymeric media was made by adding KI salt (a weak alkali) and Al_2O_3 (as abrasives) to a blend of a silicon based polymer (polyborosiloxane) and hydrocarbon gel. To measure the conductivity of media ELICO CM 180 conductivity meter was used. The conductivity of media was 0.15 S/cm. As the electrolytic salts-abrasives laden medium passes through the annular space between the stationary

CFG rod and work-piece under a DC potential, both electrolytic machining and abrasion due to the abrasives cutting action takes place.

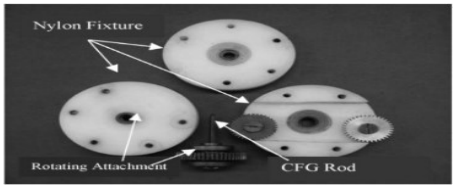

Figure 2(a) Nylon Fixture and CFG Rod; (b) DC Supply

Figure 3(a) Setup for EC^2A^2FM;

2.3. Mechanism of Metal Removal in EC^2A^2FM Process

EC^2A^2FM is a hybrid process, which is the combination of ECM, rod mechanism and AFM. It is suitable for finishing the through holes or cavities having prismatic surfaces. Dabrowski et al.(2006) mentioned that the electro-chemical aided AFM for fine surface finishing for flat surfaces only achieves more material removal [16, 17]. The main application of AFM hit upon the finishing of internal contours so the developed EC^2A^2FM process was deal with such types of finishing requirements. In ECM process anodic dissolution of material is getting in concurrence with the action of abrasion of work piece material due to cutting action of the abrasives while the electrolyte abrasives laden media is being extruded back and forth through the gap between the prismatic CFG rod and the internal surface of anode work-piece. The enhanced machining takes place due to the additional electrolytic dissolution of the material at the anodic work-piece along with the abrasion of materials through the abrasives cutting action. Due to the electrochemical machining attack the surface becomes soft as any oxide layer/ hard surface eroded [20] and the surface is more susceptible to abrasion.

2.4. Chemical reactions at anode and cathode in EC^2A^2FM

Electrochemical Machining (ECM) is an electrochemical anodic dissolution process in which low voltage and a direct current with high density is passed between a workpiece and a preshaped tool (the cathode). At the anode (workpiece surface), metaldivide into metallic ions due to the depleting reaction, and thus the shape of tool is copied into the workpiece. The electrolyte was forced to poured through the inter-electrode gap with high velocity, greater than 5 m/s, to intensify the mass/charge transfer through the sub layer near anode and heat and gas bubbles generated in the gap to remove the sludge(dissolution products e.g. hydroxide of metal). In this process, to maintain a small gap between the anode and cathode the cathode(tool) approaches towards the workpiece. When a potential difference wasused across the electrodes, many reactions take place at the anode and cathode.

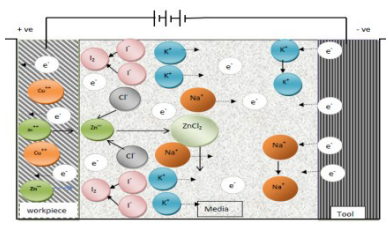

Figure 4 A Schematic representations of electrochemical reactions in EC^2A^2FM

A yellow Brass (65% Cu, 35% Zn, 156 BHN hardness) has been selected as workpiece material for the present investigation. It acts as an anode and when the current applied to it, ionization of zinc (Zn) takes place as shown in figure 4.

$Zn \rightarrow Zn^{++} + 2e^-$

While copper present in the alloy remains until all the zinc depleted from work piece internal cylindrical surface. This was due to the place of copper is at lower position than of zinc in the standard electrochemical series .After depletion of all zinc the ionization of copper (Cu) in the workpiece acts as an anode takes place i.e.

$Cu \rightarrow Cu^{++} + 2e^-$

Hydrogen is a reference point in the electrochemical series. In the electrochemical series the elements that are lower in series get discharged (lose their charge to become neutral) more easily than the ones above them. Hence tendency to deplete Zn^{++} ion is more than that of Cu^{++} ion from the anode material.The electrolytes present in media are sodium chloride (NaCl) and potassium iodide (KI) does not react with each other, only mixing of ions. NaCl is composed of Na^+ ions and Cl^- ions. KI is composed of K^+ ions and I^- ions. In this mixture all the ions are spectator ions (those do not undergo a chemical reaction when mixed together with other compounds. Electrolytes NaCl and KI tend to remain completely ionized in the media to the nearby area of anode to their neutral form.The dissociation reaction of electrolytes sodium chloride (NaCl) and potassium iodide (KI) are shown in the reaction as follows.

$NaCl \rightarrow Na^+ + Cl^-$

$KI \rightarrow K^+ + I^-$

As a result of ionization negatively charged Cl^- and I^- migrate towards anode and positively charged cations Na^+ and K^+ migrate towards cathode. The continuous flow of ions/electron in media was responsible for the flow of current. Since discharge potential of I^- ion is lower than that of Cl^-ion, I^- ions are discharged at anode while Cl^- ions remains in solution.The reactions areas follows.

At anode

$Zn \rightarrow Zn^{++} + 2e-$

$2I^- \rightarrow I_2(g) + 2e^-$

At cathode

$Na^+ + e \rightarrow Na + 496$ KJ/mole

$K^+ + e \rightarrow K + 496$ KJ/mole

The outcomes of these electrochemical reactions was that the zinc ion (Zn^{++}) combine with chloride ions (Cl^-) to make zinc chloride $ZnCl_2$

$Zn^{++} + 2Cl^- \rightarrow ZnCl_2$

In practice ZnI_2 and $ZnCl_2$ would form and get precipitated in the form of sludge. In this manner it can be noted that the work piece gets gradually machined and gets precipitated as the sludge. As the material removal takes place due to atomic level dissociation, the machined surface was of excellent surface finish and stress free. For keeping constant concentration of electrolyte it may be necessary to add more electrolytes (i.e. sodium chloride (NaCl) and potassium iodide (KI)).Addition of KI and NaCl to the abrasive media pastes consisting of threetypesincreased conducting of abrasive media manifold. The following constituents of media wereused for present study.

2.5. Experimental details

The outcome of various associated machining parameters on material removal (MR) was investigated for EC^2A^2FM process.

2.5.1. Process parameters

The selected process parameters and their range are specified in table 1 and other constant parameters are shown in table 2.

Table 1 Process parameters value at different level

Symbol	Parameters	Unit	Level1	Level2	Level3
A	Voltage	Volt	0	15	25
B	Molal concentration	molal	0.75	1.0	1.25
C	Diameter of CFG rod	mm	3.2	4.2	5.2
D	Rotational speed of CFG rod	RPM	0	25	50
E	Abrasive grit size number	micron	60(250)	100(150)	200(75)

Table 2 Constant process parameters and their value

S.N.	Process Parameters	Range/material	Unit
1	No. of cycle	10	NA
2	Extrusion pressure	6	N/mm^2
3	Shape of CFG rod	Square	NA
4	Abrasive material	Al_2O_3	NA
5	Reduction ratio	0.984	NA
6	Media flow volume	300	cm^3
7	Initial surface Ra	3.25-3.75	µm
8	Media flow volume	290	cm^3
9	Fixture material	Cast Nylon 6	NA
10	Polymer gel ratio	1:1	% by weight
11	Temp. of media	30±2	°C
12	Reduction ratio	0.95	NA
13	Work piece material	Brass	NA

2.5.2. Work piece

Work-piece was a hollow cylindrical piece made up of yellow Brass (65% Cu, 35% Zinc, 156 BHN hardness) andhad been selected based on literature review [11 and 13], past optimization of the developed basic AFM setup [21] andpilot experimentation [22-23] (refer Figure 5). The internal cylindrical surface of the test specimen to be finishedwas prepared by drilling operation followed by boring to the required size by machining at a set of constant boringparameters like speed of spindle, depth of cut and longitudinal feed. From a big lot of specimens, the test specimenswere selected so that the bore size and initial roughness of the bore was in a very narrow range so as to eliminateany effect of size variation and/or initial roughness (3.25-3.75 micron) of the work-piece.

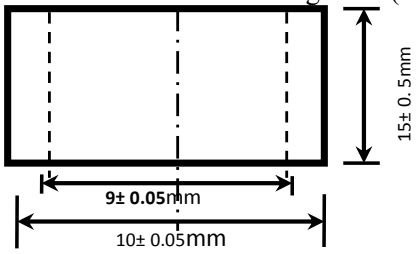

Figure 5 Work-piece dimensions

2.5.3. Designof Experiments

The scheme of experiments forthe setting of various parameters was as given in the Table3. R1, R2, R3 represents response value for three repetitions of each trial.The effects of five key EC^2A^2FM process parameters of Voltage (A), Salt Molal Concentration (B), Diameter ofCFG rod (C), Speed of CFG rod in RPM (D) and Abrasives Grain Size (E) and three prospective two-factorinteractions, i.e. Voltage and Salt Molal Concentration (AXB), Voltageand Diameter of CFG rod (AXC) andVoltage and Speed of CFG rod (AXD) on the response parameter of material removal (MR)were investigated. The design of experiment was according to Taguchi's standard $L_{27}(3^{13})$ orthogonal array.The total degrees of freedom related with the five parameters at three levels each (with three twofactorinteractions was 22 [5×(3-1)+3(2×2)=22], which was less than 26 (total degrees of freedom of L_{27}OA). The L_{27}orthogonal array has 13 columns and 27 rows, thus, five machining parameters were allotted to the columnsafter indentify the interacting columns using the linear graph for the standard L_{27} OA [22] leaving 12th and 13thcolumns empty (refer Table 3). The orthogonality preserved, even if one or more columns of the array remainempty.

Table 3Taguchi L_{27} OA with Experimental Results of material removal as a response output parameters

S.N.	A	B	Ax B	Ax B	C	Ax C	Ax C	D	Ax D	Ax D	E	e	R1	R2	R3	Avg. Response	S/N Larger(db)
1	1	1	1	1	1	1	1	1	1	1	1	1	3.75	3.88	3.83	3.82	11.63
2	1	1	1	1	2	2	2	2	2	2	2	2	4.32	4.05	4.26	4.21	12.47
3	1	1	1	1	3	3	3	3	3	3	3	3	2.11	2.13	1.72	1.98	5.83
4	1	2	2	2	1	1	1	2	2	2	3	3	8.52	8.33	8.44	8.43	18.51
5	1	2	2	2	2	2	2	3	3	3	1	1	4.22	4.84	4.12	4.39	12.79
6	1	2	2	2	3	3	3	1	1	1	2	2	3.21	3.91	3.31	3.47	10.72
7	1	3	3	3	1	1	1	3	3	3	2	2	8.12	8.12	9.12	8.45	18.50
8	1	3	3	3	2	2	2	1	1	1	3	3	6.52	7.21	6.81	6.84	16.68
9	1	3	3	3	3	3	3	2	2	2	1	1	5.91	6.41	6.33	6.21	15.85
10	2	1	2	3	1	2	3	1	2	3	1	2	14.92	14.32	14.01	14.41	23.16
11	2	1	2	3	2	3	1	2	3	1	2	3	15.6	15.41	13.88	14.96	23.46
12	2	1	2	3	3	1	2	3	1	2	3	1	12.8	13.12	15.88	13.93	22.76

13	2	2	3	1	1	2	3	2	3	1	3	1	16.58	17.54	16.8	16.97	24.58
14	2	2	3	1	2	3	1	3	1	2	1	2	18.74	19.62	18.94	19.1	25.61
15	2	2	3	1	3	1	2	1	2	3	2	3	15.87	16.52	15.91	16.1	24.13
16	2	3	1	2	1	2	3	3	1	2	2	3	16.45	16.7	16.1	16.41	24.30
16	2	3	1	2	2	3	1	1	2	3	3	1	15.9	14.31	14.4	14.87	23.41
18	2	3	1	2	3	1	2	2	3	1	1	2	20.36	19.75	20.19	20.1	26.06
19	3	1	3	2	1	3	2	1	3	2	1	3	21.12	20.9	21.4	21.14	26.50
20	3	1	3	2	2	1	3	2	1	3	2	1	19.21	18.91	19.4	19.17	25.65
21	3	1	3	2	3	2	1	3	2	1	3	2	18.5	18.13	18.7	18.44	25.31
22	3	2	1	3	1	3	2	2	1	3	3	2	26.5	26.9	27.1	26.83	28.57
23	3	2	1	3	2	1	3	3	2	1	1	3	27.57	27.02	26.71	27.1	28.65
24	3	2	1	3	3	2	1	1	3	2	2	1	29.56	29.06	29.42	29.34	29.35
25	3	3	2	1	1	3	2	3	2	1	2	1	21.5	20.7	24.88	22.36	26.90
26	3	3	2	1	2	1	3	1	3	2	3	2	30.65	29.92	29.73	30.1	29.56
27	3	3	2	1	3	2	1	2	1	3	1	3	32.59	31.83	32.15	32.19	30.15

3. Experimental Analysis

For experimental analysis, L_{27} orthogonal array based on Taguchi methodology was adopted. Each parameter was studied at three levels. As MR is higher the better type quality characteristics the S/N ratio was calculated for this type as: $\left(S/N\right)_{HB} = -10\log(MSD_{HB})$

$$MSD_{HB} = \frac{1}{R}\sum_{j=1}^{R}(1/y_j^2)\sum \quad (1)$$

where

R = Number of repetitions, y = response value

Where yj, j= 1, 2 .., R are the response values under the trial conditions repeated R times. The S/N ratio, which is a summary statistic measuring the sensitivity of the performance characteristic in a controlled manner to noise factors, is calculated based on data from all replications of a trial condition and a high value of S/N ratio signifies a higher signal effect as compared to the random effects.

3.1. Analysis of Variance

Analysis of variance (ANOVA), F-Test was performed. These test values indicated the significant EC^2A^2FM parameters which affect MR. Tables 4 and 5, represent the ANOVA results for the output response MR based on raw data and S/N ratio data respectively The analysis of variance (ANOVA) of raw data and S/N Ratio data were performed to identify the significant parameters and to quantify their effect on the response characteristic.From the ANOVA based on raw data, it was observed that all the selected parameters/parametricinteractions significantly affect the mean of MR, except the rod diameter 'C' was insignificant. From the ANOVA based on raw data, it was observed that the parameter Voltage (A), Salt Molal Concentration (B), RPM of CFG rod (D) were significant while parameter Diameter of CFG rod (C) and abrasive grain size (E) are insignificant. The two interactions, Voltage and Salt Molal Concentration (AXB)and Voltage and CFG rod diameter (AxC)are significant in both raw datatable 4 and S/N ratio table 5 but only one interactionVoltage and RPM (AxD) is significant for raw data in table 4 but insignificantfor S/N ratio in table 5.

According to the raw data, Voltage (A, 86.09%) has the maximum percentage contribution towards the MR followed by Salt molal Concentration (B, 6.57%), interaction of Voltage and Diameter of CFG Rod (AxC, 1.44%), interaction of Voltage and Salt Molal Concentration (AxB, 2.10%) and RPM (D, 0.77%).

According to the S/N ratio data, Voltage (A, 84.95%) has the maximum percentage contribution towards the MR followed by Salt molal Concentration (B, 6.31%), interaction of Voltage and Diameter of CFG Rod (AxC, 3.22%), interaction of Voltage and Salt Molal Concentration (B, 2.24%) and RPM (D, 1.09%).

Table 4ANOVA calculations(raw data, material removal)

Source	SS	DOF	V	P- value	F-Value	F-critical
A	5351.95	2	2675.98	86.09	2105.05*	3.15
B	408.25	2	204.13	6.57	160.58*	3.15
C	1.49	2	0.75	0.02	0.59	3.15
D	47.68	2	23.84	0.77	18.75*	3.15
E	34.65	2	17.33	0.56	13.63*	3.15
AxB	130.73	4	32.68	2.10	17.66*	2.52
AxC	89.80	4	22.45	1.44	15.46*	2.52
AxD	78.59	4	19.65	1.26	15.46*	2.52
Error	73.73	58	1.27	1.19		
Total	6216.91	80		100.00		

* Significant at 95 % confidence level, F Critical = F (0.05, 2, 58) = 3.15, F (0.05, 4, 58) = 2.52, SS – sum of squares
DOF – degree of freedom, V – variance, SS' – pure sum of squares, P%- is the percentage contribution of a treatment.

Table 5 ANOVA CALCUALTIONS (S/N Ratio Data, material removal)

Source	SS	DOF	V	P- value	F-Value	F-critical
A	974.93	2	487.47	84.95	585.91*	6.94
B	72.43	2	36.22	6.31	43.53*	6.94
C	8.95	2	4.48	0.78	5.38	6.94
D	12.51	2	6.26	1.09	7.52*	6.94
E	1.89	2	0.95	0.17	1.14	6.94
AxB	25.70	4	6.43	2.24	7.72*	6.39
AxC	36.98	4	9.25	3.22	11.11*	6.39
AxD	10.85	4	2.71	0.95	3.26	6.39
Error	3.32	4	0.83	0.29		

Total	1147.58	26	100.00

* Significant at 95 % confidence level, F Critical = F (0.05, 2, 4) = 6.94, F (0.05, 4, 4) = 6.39, SS – sum of squares
DOF – degree of freedom, V – variance, SS' – pure sum of squares, P%- is the percentage contribution of a treatment.

3.2. Parametric analysis(Effect on material removal)

3.2.1. Main effects

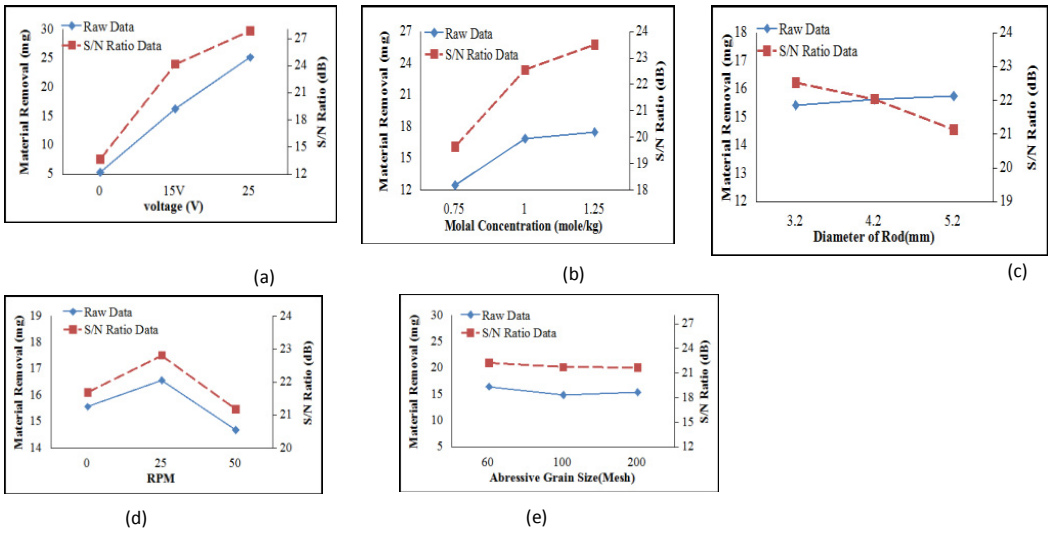

Figure 6(a) main effects for material removal in mg (raw data, S/N ratio);(b) effect of Voltage on MR; (c) effect of Molal concentration on MR; (d) effect of CFG rod diameter on MR; (d) effect of RPM on MR; (e) effect of abrasive grain size on MR

For the selected range of Voltage potential the main effect of the parameter Voltage figure6 (a) shows that the material removal (MR) increases when the increase in the applied Voltage (V). The enhanced machining takes place due to the additional electrolytic dissolution of the material at the anodic work-piece along with the abrasion of materials due to the abrasives micro cutting action. Increase in Voltage increases the inter-electrode gap current density, hence more material removal. With the electrochemical machining attack the surface becomes soft like any oxide layers and now the soft surface was more susceptible to abrasion due to the abrasives cutting action [32-33].The main effect of parameter salt molal concentration(B) figure 6(b) shows that MR increases with the increasing salt molal concentration. This observation corroborates the fact that the electrolytic action was one of the reasons behind the increased MR. As the concentration of salts increased the enhanced electro-chemical dissolution of material was observed at the anode work-piece due to moreionic interactions with the work surface result in more flow of current and hence more electrolytic attack on the hard surface along with more precipitation of the work material atoms on the surface. Thus softersurface generated which was subsequently abraded by the abrasives micro cutting action. So the increasing concentration of salt into the media results in more machining but a higher concentration may detrimentally affect the work surface quality as if the current density is too high, it may cause the formation of heat-affected zones, and it finally results in improper surface finish, more pitting [32], 2008)on the surface and generation of a surface with low accuracy [31].The effect of Rod diameter (C) on MR is plotted in figure6(c). It is observed that for the selected diameter range, the CFG rod diameter was not-significant in affecting the MR.The effect of theRPM of CFG rod (D) on MR is plotted in 6(d). The effect of abrasive grain size (E) on MR is plotted in figure6(e). It was observed that the combination of larger grain size and high speed of CFG rod gives higher material removal [19]. As the speed of CFG rod increased the more material was removed with the larger abrasive grain but the MR was less with the fine abrasive grains.

3.2.2. Effects of Interactions

The effects of three two-factor interactions, i.e. voltage and salt molal concentration (AxB), voltage and diameter of CFG rod (AxC) and voltage and RPM of CFG rod (AxD) on the response parameter of material removal (MR) are plotted by calculating average values of response characteristics for respective two-factor interaction at different level combinations.

Table 6 Parameters of raw data and S/N ratio data (A,B,C,D,and E)

	A1	A2	A3	B1	B2	B3	C1	C2	C3	D1	D2	D3	E1	E2	E3
Raw data	5.13	16.31	25.18	12.45	16.86	17.50	15.42	15.63	15.75	15.56	16.56	14.68	16.49	14.94	15.37
S/N Ratio	13.66	24.16	27.85	19.64	22.54	23.49	22.52	22.03	21.13	21.68	22.81	21.18	22.27	21.72	21.69

Table 7Interaction of Voltage and Salt molal Concentration (AxB)

Salt Molal Concentration at different Levels	B1		B2		B3	
Level of Voltage	Raw Data	S/N Ratio	Raw Data	S/N Ratio	Raw Data	S/N Ratio
A1	3.33	9.98	5.43	14.01	7.17	17.01
A2	14.43	23.13	17.39	24.77	17.12	24.59
A3	19.58	25.82	27.76	28.86	28.21	28.87

Table 8 interaction of Voltage and Diameter of CFG rod (AxC)

Diameter of CFG rod at different Levels	C1		C2		C3	
Level of Voltage	Raw Data	S/N Ratio	Raw Data	S/N Ratio	Raw Data	S/N Ratio
A1	6.9011	16.2187	5.15	13.9848	3.8933	10.8050
A2	15.9355	24.0196	16.3111	24.1654	16.7111	24.3190
A3	23.4444	27.3274	25.4577	27.9595	26.66	28.2727

Table 9 interaction of Voltage and RPM of CFG rod(AxD)

RPM at different Levels	D1		D2		D3	
Level of Voltage	Raw Data	S/N Ratio	Raw Data	S/N Ratio	Raw Data	S/N Ratio
A1	4.7144	13.0178	6.2855	15.6151	4.9444	12.3755
A2	15.1288	23.5722	17.3455	24.7046	16.4833	24.2271
A3	26.8622	28.4734	26.0655	28.1260	22.6344	26.9602

The increase in MR due to the increasing CFG rod size was steep from the rod diameter size (3.2-5.2mm) and then onwards there was relatively less increase in MR. This could be explained by the fact that with the very high reduction ratio, some critical higher media pressure in the working zone lead to lesser MR as the same abrasives (which were near to the surface) keep on abrading and lesser number of new abrasive particles are in action [10, 13].It was observed that the two-factor interaction of Voltage and RPM (AxD) was significant based on ANOVA (raw data) table 4 and was not-significant based on ANOVA (S/N ratio data) table 5. Based on the raw data analysis too it was the least significant parameter affecting the MR as shown in figure 7(c).

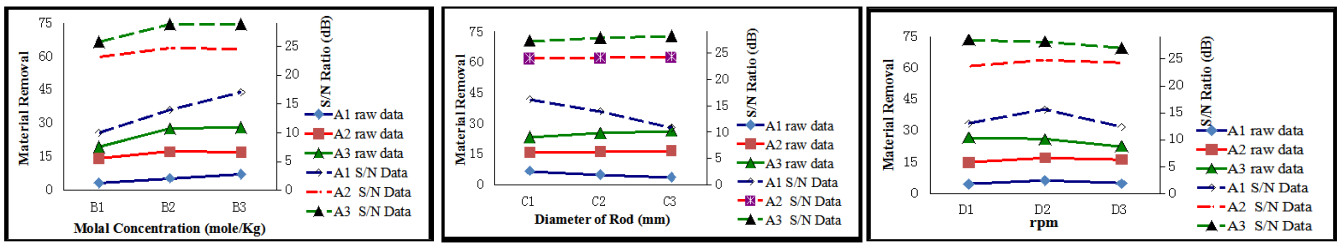

Figure 7 (a) Interaction plots for Voltage and Molal concentration (A x B); (b) Interaction plots for Voltage and diameter of rod (A x C) 7(c) Interaction plots for Voltage and RPM (A x D)

3.3. Optimal Material Removal

Material removal (MR) is the "higher-the-better" type of quality characteristic. Therefore, higher values of MR are considered to be optimal. The optimum levels of the significant parameters have been selected based on the Taguchi method's S/N ratio analysis and the optimum levels of various factors/factor-interactions for the maximum MR are A_3, B_3, A_3B_3, A_3C_3, and D2.

3.4. Estimation of optimal Material removal

The optimum values of the response characteristic MR along with their respective confidence intervals have been predicted using the Taguchi approach based on S/N ratio[22].

Predicted Optimal MR:

The mean at the optimal MR (optimal value of the response characteristic) was estimated as:

$$MR = A_3B_3 + A_3C_3 - A_3 - C_3 + D_2 \quad (2)$$

A_3B_3 =Average value of MR for the interaction of Voltage (third level) and molal concentration (Thirdlevel) parameters= 28.2166 mg (refer Table7)

A_3C_3=Average value of MR for the interaction of Voltage (third level) and Diameter of CFG rod (Third level) parameters = 26.66 mg (refer Table8)

A_3= Average value of MR at the third level of Voltageparameter= 25.18 mg (Table6)

C_3= Average value of MR at the third level of Diameter of CFG rod parameter= 15.75 mg (Table 6)

D_2 = Average value of MR at the second level of RPM parameter = 16.56 mg(table 6)

Substituting these values in the equation (2), MR = 30.44 mg

The confidence interval of confirmation experiments (CI_{CE}) and of population (CI_{POP}) is calculated by using the following equations:

$$CI_{CE} = \sqrt{F_\alpha (1, f_e) V_e [(1/n_{eff}) + (1/R)]} \quad (3)$$

$$CI_{POP} = \sqrt{((F_\alpha (1, f_e) V_e)/n_{eff})} \quad (4)$$

Where$F\alpha(1, fe)$ = The F-ratio at the confidence level of (1-α) against DOF 1 and error DOF fe = 4[Standard Tabulated F-ratio value, 22]

fe = error DOF = 58 (Table 4)

N = Total number of result = 81 (treatment = 27, repetition = 3)

R = Sample size for confirmation experiments = 3

Ve = Error variance = 1.27 (Table 4)

ηeff = Effective number of replications

neff = N / (1 + (DOF associated in the estimate of mean response)) = 7.36 (5)

So, CICE = ± 1.54

And CIPOP = ± 0.83

The 95% confirmation interval of predicted optimal range(confirmation run of three experiments)

Mean MR - CICE < MR < MR + CICE

29.15< MR <32.03

The 95% confirmation interval of the predicted mean was:

Mean MR – CIPOP < MR < MR + CIPOP

29.66 < MR < 31.32

3.5. Confirmation of Experimentation

Three confirmation experiments were conducted at the optimum setting of the process parameters. The Voltage(A) set at the third level, Salt molal concentration(B) set at the third level, Diameter of CFG rod (C) set at first level, rotational speed of CFG rod RPM (D) set at 2nd level and Abrasive grain size(E) at first level.The average material removal was 29.84 mg

With 1st Trial MR = 29.30 mg

With 2nd Trial MR = 31.69 mg
With 3rd Trial MR = 28.63 mg

3.6. SEM Micrographs and Discussion

The influence of presence of electro-chemical dissolution and abrasion on the inner surface of the hollowcylindrical work-piece in the EC^2A^2FM process was evident from the set of representative SEM micrographs (corresponding to various experiments of L_{27} OA as per Table 3) as shown in Figure 8. The micrograph in the figure 8(a) is corresponding to the initial condition of workpiece in which heavy boring tool marks observed. Figure 8(b) SEM image shows light boring tool marks after finishing using AFM with the combination of CFG rotating at 25 RPM and without aid of ECM. This was as per the second run of table 3. In figure 8(c) shows the deep crater as a result of ECM aidand the spotted profile on the machined surface observed corresponding to the experiment number 19 (voltage and molal concentration at level 3) according to table 3. It was due to ECM action the more material has been removed from the ridge. It denoted the electrolytic dissolution of the material from the surface [17]. In the case of electrochemically aided CFAAFM process both centrifugal force and axial force act simultaneously on the abrasive particles, and they impose at an angle on the work surface with the resultant force as shown in figure 8(d) corresponding to the experiment number 16 (RPM and Rod diameter at its level 3 and level 2 respectively) according to table 3. With increased amount of energy available for breaking the atomic bonds and for generating new surface as a result of removal of atoms, more material is removed within the given cycle time [24].In figure 8(e) all machining actions observed rigorously which can be controlled after measuring the Ra value and the material removal trends shown in the graphs and finally depending upon the requirement of Ra/MR parameters of the process selected.In the SEM image 8(f) is related to the confirmation experiment, finished at the optimum process parameters (R_a – 0.72µ) for the maximum MR. Almost all the traces of loosely held material and initial surface defects have been finished and the remaining ECM craters marks are very shallow.

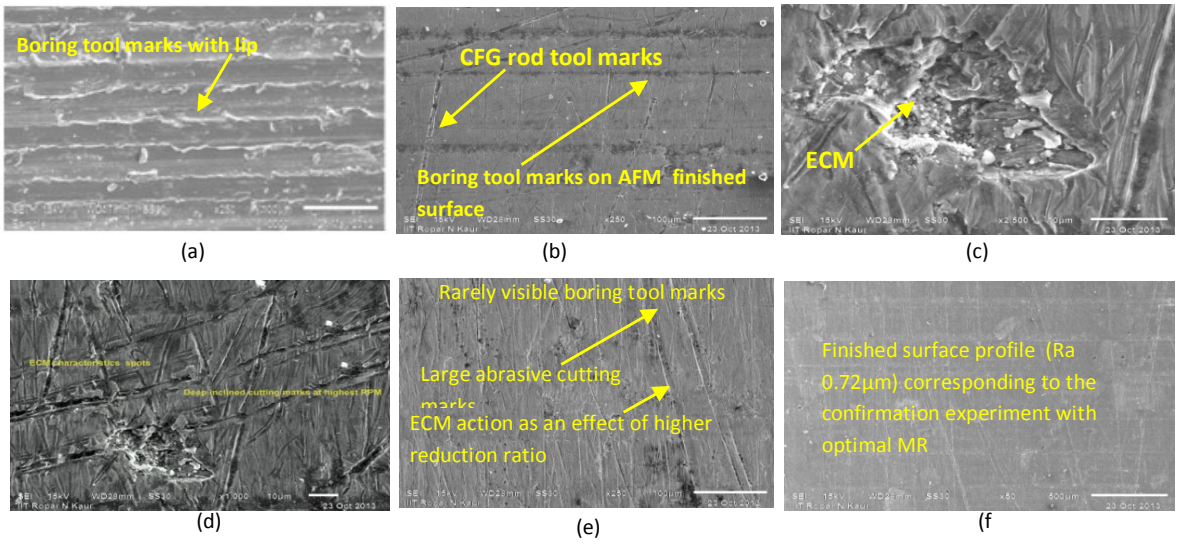

Figure 8 (a) Unfinished work-piece(x250); (b) finishing using AFM and rotating CFG rod without ECM(x250); (c) AFM finish with ECM(x 2500); (d) AFM finish with ECM and rotating CFG rod(x 1000); (e) (x1500); (f) optimal surface

4. Conclusions

The important conclusions from this paper can be summarized as follows:

- It is possible to enhance the productivity of AFM by improved fixturing. With the introduction of rotating CFG rod and ECM, as much as 70–80% reduction in machining time has been obtained even at less extrusion pressure and obtained surface finish in the range of 0.5-0.6 Ra, This small extrusion pressure in the hybrid AFM process can prevents damage of fragile or delicate components.
- Further enhancement in Material Removal can be expected with higher resultant pressure; however, the magnitudes of axial force and centrifugal force need to be optimized.
- The various contribution of ECM supported parameters was less but significant. It can be enhanced by using strong electrolytes such as cyanide based.In the electrolytic abrasive laden media, use of cyanide based salts is hazardous for nature due to its poisonous nature and requires a very firmly controlled environment.
- The various parameters used in EC^2A^2FM process like Voltage, salt molal concentration, RPM and abrasive grain size significantly influence the response parameter of MR and require to be selected close to the optimal setting for the combination of machine and work piece.
- The developed EC^2A^2FM is effective in increasing the material removal (MR) in AFM finishing of internal surface s of the cylindrical brass work-pieces.
- The predicted optimal range for MR was CIPOP: $29.66<MR < 31.32$; while the 95% confidence interval of the predicted mean for MR was CICE: $29.15< MR< 32.03$.

References

[1] L. J. Rhoades, Abrasive flow machining with not-so-silly putty. Met Finish, 1987, pp.27-29.
[2] L. J. Rhoades, Abrasive Flow Machining. Manufacturing Engineering, 1988,pp. 75-78.
[3] L. J. Rhoades, Abrasive flow machining: a case study. Journal of Materials Processing Technology, Volume 28, 1991, pp. 107-116.
[4] L. J. Rhoades, Abrasive flow machining and its use. Proc. Non-Traditional Machining Conference, Cincinnati, OH, 1985, pp. 111-120.
[5] H. S. Shan, Advanced manufacturing methods, Tata McGraw-Hill, New Delhi,2005.
[6] K. Przyklenk, Abrasive flow machining - a process for surface finishing and deburring of work pieces with a complicated shape by means of abrasive laden media. Advances in Non Traditional Manufacturing, PED, ASME, Volume 22, 1986, pp. 101-110.
[7] W. B.Perry, Abrasive flow machining: principles and practices. Proceeding Non Traditional Machining Conference, Cincinnati,Ohio, 1985,pp. 121-128.
[8] R. E. Williams, andK. P. Rajurkar, Stochastic modeling and analysis of abrasive flow machining. Transactions of ASME, Journal of Engineering for Industry, Volume 114, 1992, pp. 74-81.
[9] R.S. Walia, Development and investigations in centrifugal force assisted abrasive flow machining process, s.l.: Ph.D. Thesis, IIT, Roorkee, 2006.
[10] R. S. Walia, H.S. Shan and P. Kumar, Parametric optimization of centrifugal force-assisted abrasive flow machining (CFAAFM) by the Taguchi method. Materials and Manufacturing Processes, volume 21(4),2006,pp. 375-382.
[11] R. S. Walia, H.S. Shan and P. Kumar, Determining dynamically active abrasive particles in the media used in centrifugal force assisted abrasive flow machining process. International Journal of Advanced Manufacturing Technology, Volume 38, 2008,pp. 1157-1164.
[12] R. S. Walia, H.S. Shan and P. Kumar, Morphology and integrity of surfaced finished by centrifugal force assisted abrasive flow machining. International Journal of Advanced Manufacturing Technology, Volume 39, 2008, pp. 1171-1179.
[13] R. S. Walia., H.S. Shanand P. Kumar, Enhancing AFM process productivity through improved fixturing. International Journal of Advanced Manufacturing Technology, Volume 44, 2009,pp. 700-709.
[14] R. Singh and R. S. Walia, Study the effects of centrifugal force on abrasive flow machining process. International Journal of Research in Mechanical Engineering and Technology,volume 2(1), 2012,pp. 34-39.
[15] R. Singh, R. S. Walia andN. M. Suri, Study of parametric effect on surface roughness improvement for hybrid centrifugal force assisted abrasive flow machining process. International Journal of Latest Research in Science and Technology, volume 1(3), 2012, pp. 198-201.
[16] L. Dabrowski, M. Marciniak and T. Szewczyk, Analysis of abrasive flow machining with an electrochemical process aid. Proc. IMechE Part B: J. Engineering Manufacture, Volume 220, 2006, pp. 397-403.
[17] L. Dabrowski, M. Marciniak, W. Wieczarek, and A. Zygmunt,Advancement of Abrasive Flow Machining Using an Anodic Solution. Journal of New Materials for Electrochemical Systems, Volume 9, 2006 ,pp. 439-445.
[18] T. R. Loveless, K. P. Rajurkar, andR. E.Williams, A study of the effect of abrasive flow machining on various machining surfaces. Journal of Material Processing Technology, Volume 47, 1994,pp. 133-151.
[19] K. M. Reddy, A.K.Sharma and P. Kumar, Some aspects of centrifugal force assisted abrasive flow machining of 2014 Al alloy. Proc. IMechE Part B: J. Engineering Manufacture, Volume 222, 2008, pp.773-783
[20] A.K Dubey, H.S. Shan and N.K. Jain, Analysis of surface roughness and out-of-roundness in the electrochemical honing of internal cylinders, Int. J. Adv. Manuf. Technol. Volume 38, 2008, pp.491-500.
[21] B.S. Brar, R.S. Walia, V.P. Singh and M. Singh, Development of a robust abrasive flow machining process setup, Int. J. of Surface Engineering and Materials Technol. (IJSEMT). Volume1(1), 2011, pp. 17-23.

[22] B.S. Brar, R.S. Walia and V.P. Singh, Electro chemical machining in the aid of abrasive flow machining process", Int. J. of Surface Engineering and Materials Technol. Volume 2(1), 2012, pp. 5-9.
[23] B.S. Brar, R.S. Walia and V.P. Singh, Electro chemical aid to abrasive flow machining process: harnessed for improved surface finishing, Proc. of Int. Conf. on AFTMME, PTU, Kapurthala, Punjab, India, 2012, pp. 527-532.
[24] R. S. Walia., H.S. Shan and P. Kumar, Abrasive flow machining with additionally centrifugal force applied to media. Machining Science Technology volume 10, 2006, pp. 341-354.
[25] R. S. Walia and Ramandeep singh,Study the effect of centrifugal force on abrasive flow machining process, International Journal of research in mechanica engineering and tecnology volume 2, issue April.2012, pp. 34-39
[26] V.K. Jain, and A.G. Adsul, Experimental investigations into abrasive flow machining (AFM). International Journal of Machine Tools and Manufacture, Volume 40, 2000, pp. 1003-1021.
[27] V. K.Jain, C. Ranganatha and K. Muralidhar, Evaluation of rheological propertied of media for AFM. Machining Science and Technology, volume 5(2), 2001,pp. 151-170.
[28] V.K. Jain,Advance machining processes. New Delhi: Allied Publishers Pvt. Ltd.,2002.
[29] Mamilla Ravi Sankar, V.K. Jain and J. Ramkumar, Experimental investigations into rotating workpiece Abrasive flow finishing, Wear, Volume 267, (1-4), 2009, pp. 43-51
[30] S. Singh and H. S. Shan, Development of magneto abrasive flow machining process, International Journal of Machine Tools and Manufacture, Volume 42, 2002,pp. 953-959.
[31] B. Bhattacharyya, and J. Munda,Experimental investigation on the influence of electrochemical machining parameters on machining rate and accuracy in micromachining domain, International Journal of Machine Tools and Manufacture vol 43,2003, pp. 1301–1310.
[32] El-Taweel T.A.,Modelling and analysis of hybrid electrochemical turningmagnetic abrasive finishing of 6061 Al/Al2O3 composite, Int J Adv Manuf Technol, Volume 37, 2008,pp.705–714
[33] R.S. Walia, H.S. Shan and P. Kumar, Finite element analysis of media used in the centrifugal force assisted abrasive flow machining process, Proceeding the institute of mechanical engineering , Part B, Journal of engineering Manufacture, volume 222, 2006,pp. 1775-1785.

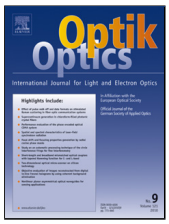

Title: Design and Simulation of "I" shaped Split Ring Resonator metamaterial at optical communication window around 1.55 μm

Author: Kamal Kishor Monu Nath Baitha R.K. Sinha

PII: S0030-4026(15)00847-5
DOI: http://dx.doi.org/doi:10.1016/j.ijleo.2015.08.086
Reference: IJLEO 56010

To appear in:

Received date: 1-8-2014
Accepted date: 19-8-2015

Please cite this article as: K. Kishor, M.N. Baitha, R.K. Sinha, Design and Simulation of "I" shaped Split Ring Resonator metamaterial at optical communication window around 1.55<ce:hsp sp=ö.25j>rmmum, *Optik - International Journal for Light and Electron Optics* (2015), http://dx.doi.org/10.1016/j.ijleo.2015.08.086

Design and Simulation of "I" shaped Split Ring Resonator metamaterial at optical communication window around 1.55 µm

Kamal Kishor, Monu Nath Baitha and R. K. Sinha*

TIFAC-Centre of Relevance & Excellence in Fiber Optics & Optical Communications,

Applied Physics Department, Delhi Technological University, (Formerly Delhi College of Engineering),

Bawana Road, Delhi 110 042, India

**Corresponding author: dr_rk_sinha@yahoo.com*

Tel.: +91 11 27871017; fax: +91 11 27871023

In this paper, we report design and simulation of "I" shaped split ring resonator (SRR) metamaterial. The prime focus of this manuscript is to a design of a split ring resonance (SRR) based planar metamaterial to achieve the negative refraction in optical communication window. The propagation characteristics in terms of reflection and transmission spectrum of the reported structure are obtained using finite differential time domain (FDTD) method. In this paper all the key electromagnetic parameters i.e. such as permittivity (ε), permeability (µ), refractive index (n) etc have been obtained from the simulation from propagation characteristics for the reported structure. It is observed and reported that the electromagnetic parameters (such as permittivity (ε) and permeability (µ)) as well as the refractive index for the reported structure is negative in broad optical communication windows around of 1.55µm.

Key words: *Metamaterials; Left-handed materials; Nanostructure*

INTRODUCTION

In 1968, Viktor G. Veselogo predicted the unusual electromagnetic properties of the left-handed metamaterials (LHMs) having negative permittivity and permeability simultaneously at the same operating frequency for which the electromagnetic wave shows anomalous behaviour, i.e. phase and group velocity would be in opposite direction [1]. It was a challenging task to design a structure which shows electric permittivity and magnetic permeability simultaneously negative for the desired frequency range with uncommon electromagnetic properties. With the practical realization of metamaterials by Smith *et al,* 2000, [7] using split ring resonators (SRRs) this challenge was solved after a long 30 years even after its mathematical solution and understanding.

The design and development of metamaterials using artificial structures is prime focus of the researchers in the recent past as it has uncommon applications such as negative refraction, reverse Doppler Effect, flat lens, Cloaking etc [1-17]. In the recent past, negative refraction has been demonstrated using different structure; like Ω- shaped, circular, U-shaped, S-shaped, V-shaped asymmetric- type split ring structures to name a few for various applications such as antenna and optical sensing [18-24]. In almost all cases, SRRs are fabricated as periodic arrays of metallic structures with a dimension smaller than the wavelength of radiation so the collective oscillations of conducting electrons in these metallic structures (known as localised surface Plasmon) determine the overall electromagnetic response of the entire material [25-31]. Metamaterials have characteristic dimensions of the order of the operating wavelength, with fabrication accuracies better than 10 nm. Now, due to this fabrication limit, metamaterial advantage is not being exploited in optical regime as much, as it is well explored and exploited in microwave regime. Following these issues, alternative approaches to design and development of new materials and their structures, exhibiting negative refraction have attracted much more attention of researchers [32-41]. A new planar metamaterials structure are being tailored to obtain the negative refractive index property in high frequency regime to overcome this difficulty in the fabrication of the conventional metamaterials (with the structures consisting a combination of split-ring resonator and metal wire) [42-43]. These new planar metamaterials structures are well suited for most applications in terms of feasibilities of design and fabrication [43-44] in the optical frequency regime. They have also advantage in easy excitation and easy matching with conventional planar circuits.

The prime focus of this manuscript is to design of a split ring resonance (SRR) based planar metamaterial to achieve the negative refraction in optical communication window. In this paper, we report design and simulation of "I" shaped split ring resonator (SRR) metamaterial, which is showing negative refraction in the optical communication window around wavelength of 1.5 μm. The proposed SRR's based metamaterial consisting of a periodic arrays of gold split ring resonators (SRR) deposited on silicon substrate, with a minimum feature size of 100 nm. The

propagation characteristics in terms of reflection and transmission spectrum of the reported structure are obtained using finite differential time domain (FDTD) method. In this paper all the key electromagnetic parameters i.e. such as permittivity (ε), permeability (μ), refractive index (n) etc have been obtained from the simulation data obtained for propagation characteristics for the reported structure. It is observed and reported that the electromagnetic parameters (such as permittivity (ε) and permeability (μ)) as well as the refractive index for the reported structure is negative in broad optical communication window of 1.4μm to 1.6μm. The reported structure provides a way to build the device such as sensors, cloaking device etc. in the range of optical frequency using the property of negative refraction within very small characteristics size. This achievement opens the way to advance metamaterial technology in optical frequency range for the design of nano scale optical devices.

GEOMETRY AND DESIGN OF THE STRUCTURE

Two dimensional, array of 12 x 8 was formed to simulate the proposed planar metamaterial structure which looks like the English capital alphabet letter "I" shaped made up on a 1.5 micron thick silicon substrate, gold strip of 0.6 micron thickness is used to form the proposed structure having the width 0.1 micron of gold strip. Figure 1 shows the 12x8 array as well as geometry and dimensions of the elementary cell of the proposed planar metamaterial.

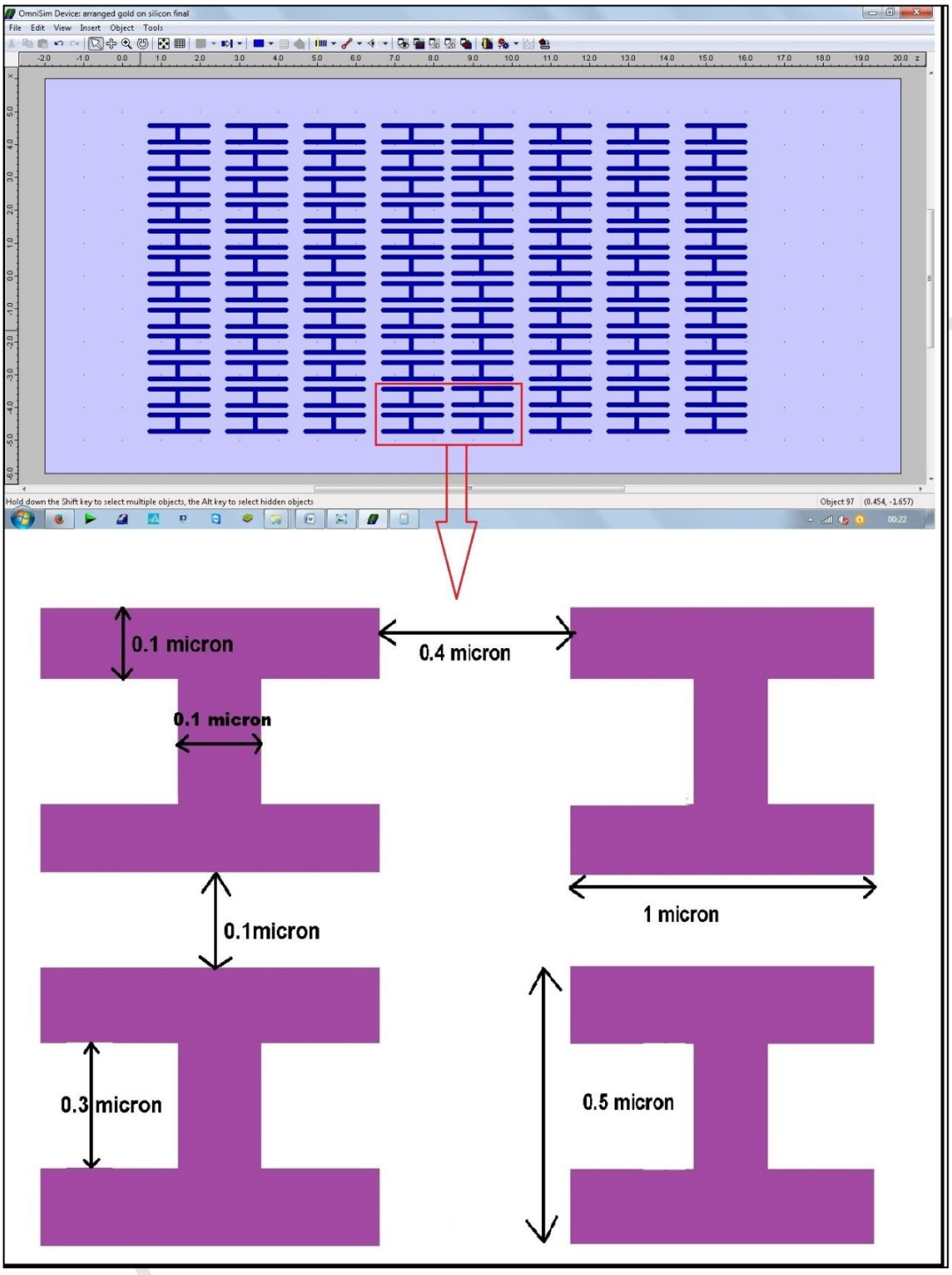

Fig.1 Two dimensional 12x8 arrays of I shaped structure and their dimensions.

Modeling and Simulation

The modeling and simulation of the reported "I" shape planar metamterial structure is performed by using finite-differential-time-domain method (FDTD) of omnisim simulation package from Photon Design, UK. To describe the complex dielectric constant of the gold layer we used the

Drude model. The modeled structures are simulated in terms of reflection and transmission spectra as a function of wavelength.

RESULT AND DISCUSSION

Fig 2 showing the transmittance and reflectance resonance response for the proposed "I" structure with respect to the wavelength. It is observed that proposed structure with above mentioned dimension produced very much significant resonance response at wavelength range around 1.4 μm to 1.6 μm i.e. optical communication frequency range.

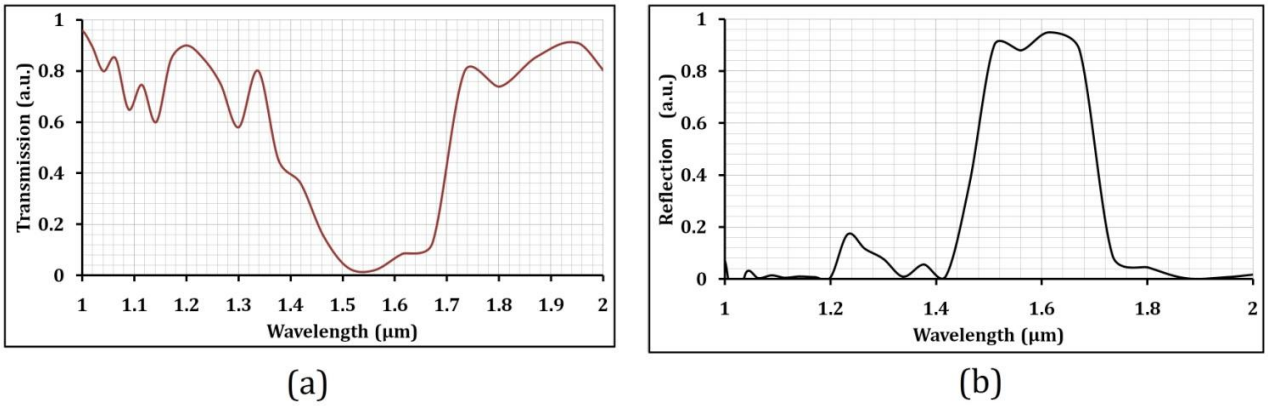

Fig. 2 – Transmission and Reflection characteristics of the structure

To exploit the amazing electromagnetic properties of the proposed structure it is required to characterization of proposed metamaterial structure in terms of its electromagnetic parameters such as real and imaginary value of electrical permittivity, magnetic permeability, refractive index and impedance etc. There are several methods in the recent past for evaluating the electromagnetic parameters and characterization of metamaterials (45-54). In the presence several method, we used the Yosuke et al. calculation method [54] to obtained the electromagnetic parameters by using the obtained data of transmittance and refractive coefficient of the proposed structure. The Yosuke et al. calculation method has the following formulas which are used for the purpose.

$$z^2=\frac{T'^2-(1+R')^2}{T'^2-(1-R')^2} \quad ..(1)$$

$$n=\frac{c}{i\omega d}\ln\left[\frac{(1+z)R'}{(1-z)T'}+\frac{1}{T'}\right] \quad ..(2)$$

$$T'=Te^{\left(\frac{i\omega d}{c}\right)} \quad ..(3)$$

$$R'=-R \quad ..(4)$$

$$\varepsilon=\frac{n}{z} \quad ..(5)$$

$$\mu=nz \quad ..(6)$$

Where T = Transmission coefficient, R = Reflection coefficient, d = effective thickness of the gold layer, c = velocity of light in vacuum, $\omega=2\pi/\lambda$, z= impedance, n=refractive index, ε=electric permittivity, μ= magnetic permeability.

The calculated result of the magnetic permeability of the proposed "I" structure with respect to the wavelength is shown in fig. 3a. Fig. 3b showing the calculated result of the electric permittivity of the proposed "I" structure with respect to the wavelength. Theses result gives the negative value of the parameters for the desired optical wavelength range of 1.4 μm to 1.6 μm. In fig. 3c the impedance variation w.r.t. the wavelength for the structure is shown. And finally the calculated value of refractive index for the structure w.r.t. wavelength is shown in fig. 3d. Like other electromagnetic properties e.g. electric permittivity, magnetic permeability also refractive index is also showing the negative value for the same wavelength range with very good resonance response.

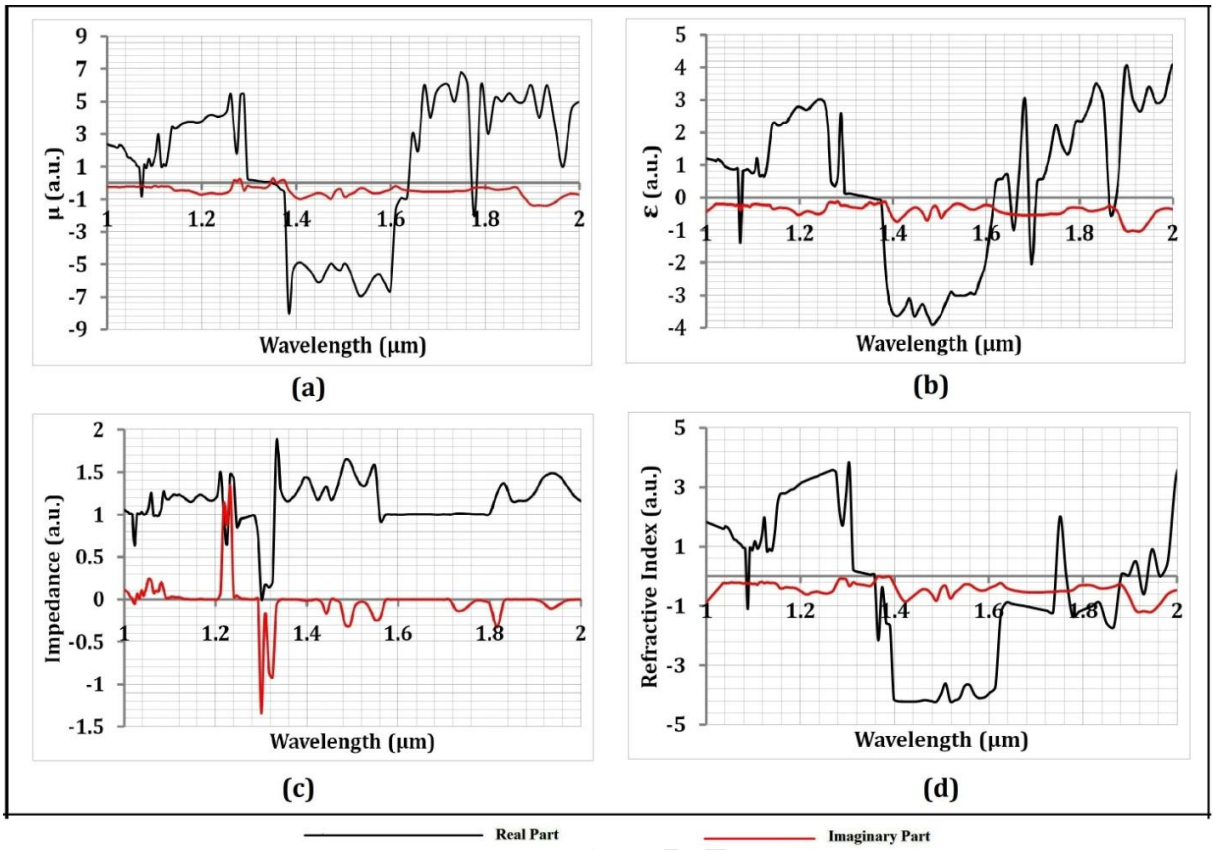

FIG. 3 Variation of Electromagnetic parameter (electric permittivity, magnetic permeability, impedance and refractive index) with respect to wavelength for the proposed structure.

CONCLUSION

A "I" shaped planar metamaterial structure and geometry is proposed and investigated for its electromagnetic parameters. In this work we studied the electromagnetic behavior of the proposed structure by numerical simulation method which is done by using omnisim finite-differential-time-domain method (FDTD) simulation package of Photon Design, UK. The transmission and reflection spectrum showing the resonance response in the wavelength range of 1.4 μm to 1.6 μm. Furthermore, the calculated spectrum of the electromagnetic properties such as negative refractive index, electric permittivity, and magnetic pemeability is found to be negative in the wavelength range of 1.4 μm to 1.6 μm. These obtained results open the window for the integrated application of the metamaterial in optical communication window. Thus, the reported structure put a significant mark in the design and development of metamaterials based devices in optical communication window.

ACKNOWLEDGMENT

The authors gratefully acknowledge the financial support provided by ‘‘TIFAC-Center of Relevance and Excellence in Fiber Optics and Optical communications at Delhi Technological University, Delhi (Formerly Delhi College of Engineering, Delhi)’’ through ‘‘Mission Reach’’ program of Technology, Vision-2020, Government of India. One of the authors, Mr. Kamal Kishor would also like to acknowledge Photon Design Ltd., UK for providing the Omnisim, FDTD simulation tool and for helpful and critical discussions on this research work.

Reference

1. V. G. Veselago, The electrodynamics of substances with simultaneously negative values of permittivity and permeability, Sov. Phys. Usp. 10 (1968) 509–514.
2. J. B. Pendry, Negative refraction makes a perfect lens, Physical Review Letters 85 (2000) 3966–3969.
3. R. A. Shelby, D. R. Smith, S. C. Nemat-Nasser, and S. Schultz, Microwave transmission through a two dimensional, isotropic, left-handed metamaterial, Applied Physics Letters 78 (2001) 489–491.
4. R. A. Shelby, D. R. Smith, and S. Schultz, Experimental verification of a negative index of refraction, Science 292 (2001) 77–79.
5. J. B. Pendry, A. J. Holden, D. J. Robbins, and W. J. Steward, Low frequency plasmons in thin-wire structures, Journal of Physics: Condensed Matter 10 (1998) 4785–4809.
6. J. B. Pendry, A. J. Holden, D. J. Robbins, and W. J. Steward, Magnetism from conductors and enhanced nonlinear phenomena, IEEE Transactions on Microwave Theory and Techniques 47 (1999) 2075–2084.
7. D.R. Smith, W. J. Padilla, D.C. Vier, S.C. Nemat-Nasser, and S. Schultz, Composite medium with simultaneously negative permeability and permittivity, Phys.rev. Lett. 84 (2000) 4184–4187.
8. S.Anantha Ramakrishna, Physics of negative refractive index materials, Reports on Progress in Physics 68 (2005) 449–521.
9. Jason Valentine, Jensen Li, Thomas Zentgraf, Guy Bartal and Xiang Zhang, An optical cloak made of dielectrics, Nature Materials 8 (2009) 568–571.
10. J. B. Pendry, D. Schurig, and D. R. Smith, Controlling electromagnetic fields, Science 312 (2006) 1780–1782.
11. D. Schurig, J. J. Mock, B. J. Justice, S. A. Cummer, J. B. Pendry, A. F. Starr, and D. R. Smith, Metamaterial electromagnetic cloak at microwave frequencies, Science 314 (2006) 977–980.
12. N. Engheta, W. Z. Richard, Metamaterials: physics and engineering explorations, Wiley & Sons. pp. xv, Chapter 1, Chapter 2. ISBN 978-0-471-76102-0 (2006).
13. S. Zouhdi, S. Ari, P. V. Alexey, Metamaterials and Plasmonics: Fundamentals, Modelling, Applications, New York: Springer-Verlag. pp. 3–10, Chap. 3, 106. ISBN 978-1-4020-9406-4 (2008-12).
14. Hou-Tong Chen, Willie J. Padilla, J. M. O. Zide, A. C. Gossard, A. J. Taylor and R. D. Averitt, Active terahertz metamaterial devices, Nature 444 (2006) 597–600.
15. V. G. Veselago, Formulating Fermat’s principle for light travelling in negative refraction material, Physics-Uspekhi 45 (2002) 1097–1099.
16. I.V. Lindell, S.A. Tretyakov, K.I.Nikoskinen, and S. Ilvonen, BW-media with negative parameter, capable of supporting backward waves, Microwave Opt. Tech. Lett. 31 (2001) 129–133.
17. R. W. Ziolkowski and E. Heynman, Wave propagation in media having negative permeability and permittivity, Phys. Rev. E 64 (2001) 056625-1-15.
18. B. Lahiri, A. Z. Khokhar, R. M. De La Rue, S. G. McMeekin, and N. P. Johnson, Asymmetric split ring resonators for optical sensing of organic materials, Optics Express 17 (2009) 1107–1115.
19. V. A. Fedetov, M. Rose, S. L. Prosvirnin, N. Papasimakis, and N. I. Zheludev, Sharp trapped-mode resonances in planar metamaterials with a broken structural symmetry, Phys. Rev. Lett. 99 (2007) 147401-1-4.

20. M. S. Rill, C. Plet, M. Thiel, I. Staude, G. V. Freymann, S. Linden, and M. Wegener, Photonic metamaterials by direct laser writing and silver chemical vapour deposition, Nat. Maters. 7 (2008) 543–546.
21. Kamal Kishor and R.K.Sinha, "Design of Planar Metamaterial Optical Resonator" International Conference on Fiber Optics and Photonics, doi–10.1364/PHOTONICS, 2012.M3B.5, OSA (2012).
22. Ranjan Singh, Carsten Rockstuhl, Christoph Menzel, Todd P. Meyrath, Mingxia He, Harald Giessen, Falk Lederer, and Weili Zhang, Spiral-type terahertz antennas and the manifestation of the Mushiake principle, Optics Express 17 (2009) 9971–9980.
23. Kamal Kishor, Monu Nath Baitha, R. K. Sinha, and Basudev Lahiri, Tunable negative refractive index metamaterial from V-shaped SRR structure: fabrication and characterization, Journal of Optical Society of America B (JOSA B) 7 (2014) 1410-1414.
24. G. Dolling, M. Wegener, C. M. Soukoulis, and S. Linden, Negative-index metamaterial at 780 nm wavelength, Opt. Lett. 32 (2007) 53–55.
25. C. Rockstuhl, F. Lederer, C. Etrich, T. Zentgraf, J. Kuhl, and H. Giessen, On the reinterpretation of resonances in split ring resonators at normal incidence, Opt. Express, 14 (2006) 8827–8836.
26. J. Zhou, T. Koschny, M. Kafesaki, E. N. Economu, J. B. Pendry, and C. M. Soukoulis, Saturation of the Magnetic Response of Split-Ring Resonators at Optical Frequencies, Phys. Rev. Lett. 95 (2005) 23902-1–4.
27. M. W. Klein, C. Enkrich, M. Wegener, C. M. Soukoulis, and S. Linden, Single-slit split-ring resonators at optical frequencies: limits of size scaling Opt. Lett. 31 (2006) 1259–1261.
28. S. Tretyakov, On geometrical scaling of split ring and double-bar resonators at optical frequencies, Metamaterials (Amst.) 1 (2007) 40–43.
29. B. Lahiri, S. G. McMeekin, A. Z. Khokhar, R. M. De La Rue and N. P. Johnson, Impact of titanium adhesion layers on the response of arrays of metallic split-ring resonators (SRRs), Optics Express 18 (2010) 3210–3218.
30. W. C. Chen, J. J. Mock, D. R. Smith, T. Akalin, and W. J. Padilla, Controlling gigahertz and terahertz surface electromagnetic waves with metamaterial resonators, Phys. Rev. X 1 (2011) 021016-1–6.
31. B. Lahiri, G. Holland, V. Aksyuk, and A. Centrone, Nanoscale imaging of plasmonic hot spots and dark modes with the photothermal-induced resonance technique, Nanoletters 13 (2013) 3218–3224.
32. J Yao, Z Liu, Y Liu, Y Wang, C Sun, G Bartal, AM Stacy, X Zhang, Optical negative refraction in bulk metamaterials of nanowires, Science **321** (2008) 930.
33. C. Yan, Q.Wang, S. Zhuo, Y. Cui, High-transmission negative refraction of discrete rod resonators confined in a metal waveguide at visible wavelengths, Opt. Express **16** 13818 (2008) 13818-13823.
34. H.K. Yuan, U.K. Chettiar, W. Cai, A.V. Kildishev, A. Boltasseva, V.P. Drachev, V.M. Shalaev, A negative permeability material at red light, Opt. Express **15** (2008) 1076-1083.
35. V.M. Shalaev,W.S. Cai, U.K. Chettiar, H.K. Yuan, A.K. Sarychev, V.P. Drachev, A.V. Kildishev, Negative index of refraction in optical metamaterials, Opt. Lett. **30**, (2005) 3356-3358.
36. S. Zhang, W.J. Fan, P.C. Panoiu, K.J. Malloy, R.M. Osgood, S. R. J. Brueck, Experimental Demonstration of Near-Infrared Negative-Index Metamaterials, Phys.Rev. Lett. **95** 137404 (2005) 137404-1-4.
37. G. Dolling, C. Enkrich, M. Wegener, C.M. Soukoulis, S. Linden, Simultaneous Negative Phase and Group Velocity of Light in a Metamaterial, Science **312**, 892 (2006) 892-894.
38. G. Dolling, M.Wegener, C.M. Soukoulis, S. Linden, Negative-index metamaterial at 780nm wavelength, Opt. Lett. **32**, (2007) 53-55.
39. H. Chen, L. Ran, J. Huangfu, X. Zhang, K. Chen, T.M. Grzegorczyk, J.A. Kong, Left-handed materials composed of only S-shaped resonators, Phys. Rev. E 70, (2004) 057605-1-4.
40. U. Algredo-Badillo, P. Halevi, Negative refraction and focusing in magnetically coupled loaded transmission lines, J. Appl. Phys. **102** (2007) 086104.
41. D. Kwon, D.H. Werner, A.V. Kildishev, V.M. Shalaev, Near-infrared metamaterials with dual-band negative-index characteristics, Opt. Express **15** (2007) 1647-1652.
42. Marques R., Martel J., Mesa F., and Medina F., Left-handed-media simulation and transmission of EM waves in subwavelength split-ring-resonator loaded metallic waveguides, Phys.Rev. Lett. 89 (2002) 183901-1-4.
43. R. W. Ziolkowski, Design, fabrication, and testing of double negative metamaterials," IEEE Transactions on Antennas and Propagation, 51, (2003) 1516-1529.

44. E. Ekmekci, G. Turhan-Sayan, Comparative investigation of resonance characteristics and electrical size of the double-sided SRR, BC-SRR and conventional SRR type metamaterial for varying substrate parameters, Progress In Electromagnetics Research B 12 (2009) 35-62.

45. S. Linden, C. Enkrich, M. Wegener, J. Zhou, T. Koschny,C. M. Soukoulis, Magnetic response of metamaterials at 100 terahertz, Science 306 (2004) 1351-1353.

46. A. M. Nicolson and G. F. Ross, Measurement of the intrinsic properties of material by time-domain techniques, IEEE Trans. Instrum. Meas. IM-19, (1970) 377-382.

47. D. R. Smith, S. Schultz, P. Markos, and C. M. Soukoulis, Determination of effective permittivity and permeability of metamaterials from reflection and transmission coefficients, Phys. Rev. B 65 (2002) 195104-1-5.

48. M. Iwanaga, Effective optical constants in stratified metal-dielectric metamaterial, Opt. Lett. 32 (2007) 1314–1316.

49. P. Markos and C. M. Soukoulis, Transmission properties and effective electromagnetic parameters of double negative metamaterials, Opt. Express 11 (2003) 649–661.

50. E. Saenzz, P. M. T. Ikonen, R. Gonzalo, and S. A. Tretyakov, On the definition of effective permittivity and permeability for thin composite layers, J. Appl. Phys. 101 (2007) 114910.

51. T. Koschny, P. Markos, D. R. Smith, and C. M. Soukoulis, Resonant and antiresonant frequency dependence of the effective parameters of metamaterials, Phys. Rev. E 68 (2003) 065602-1-4.

52. Ricardo A. Depine, and Akhlesh Lakhtakia, Comment I on Resonant and antiresonant frequency dependence of the effective parameters of metamaterials, Phys. Rev. E 70 (2004) 048601.

53. A. L. Efros, Comment II on Resonant and antiresonant frequency dependence of the effective parameters of metamaterials, Phys. Rev. E 70 (2004) 048602-1-2.

54. Yosuke Minowa, Takashi Fujii, Masaya Nagai, Tetsuyuki Ochiai Kazuaki Sakoda, Kazuyuki Hirao, and Koichiro Tanaka, Evaluation of effective electric permittivity and magnetic permeability in metamaterial slabs by terahertz time-domain spectroscopy, OPTICS EXPRESS 16 (2008) 4785–4796.

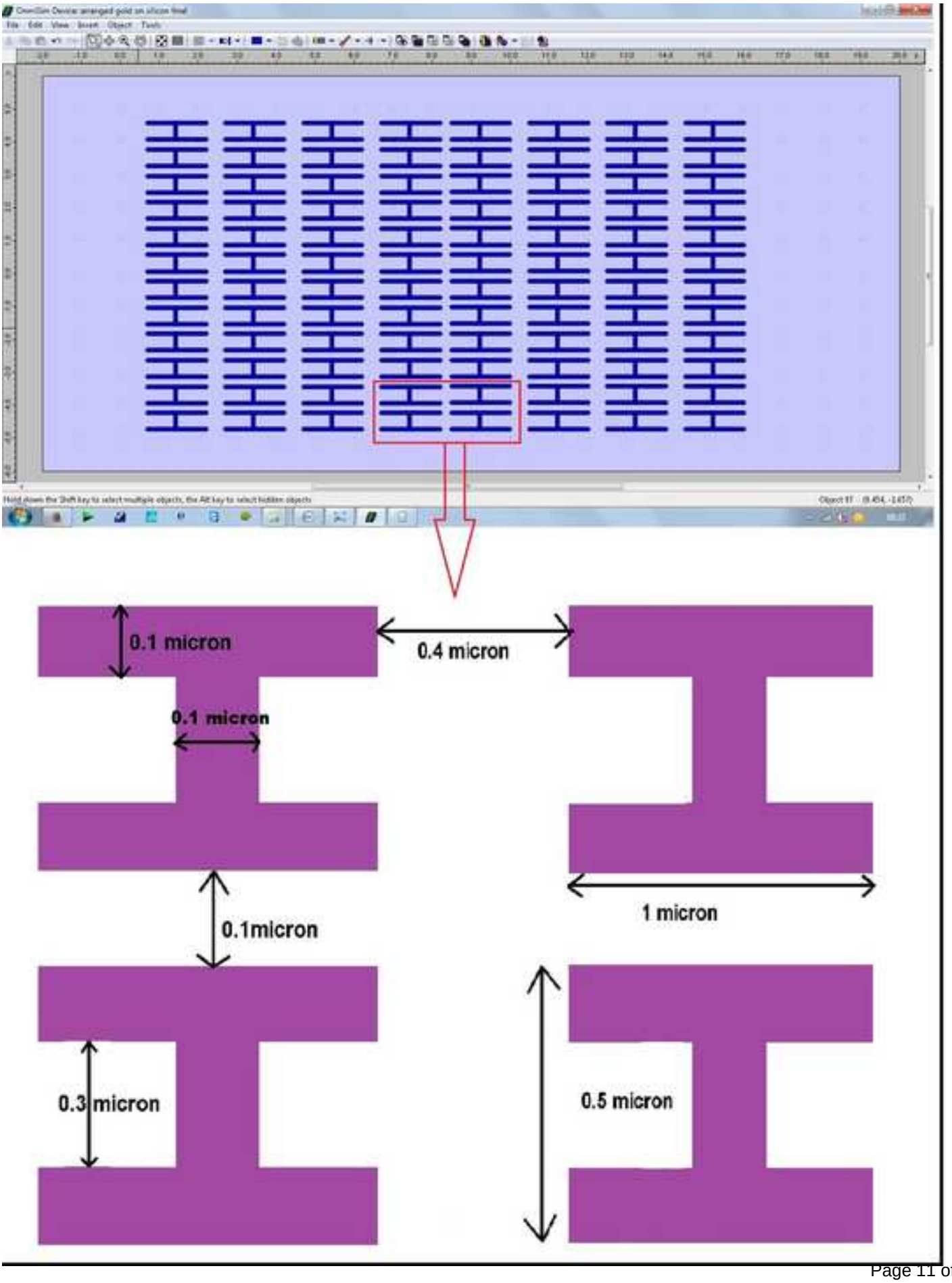

Figure 2

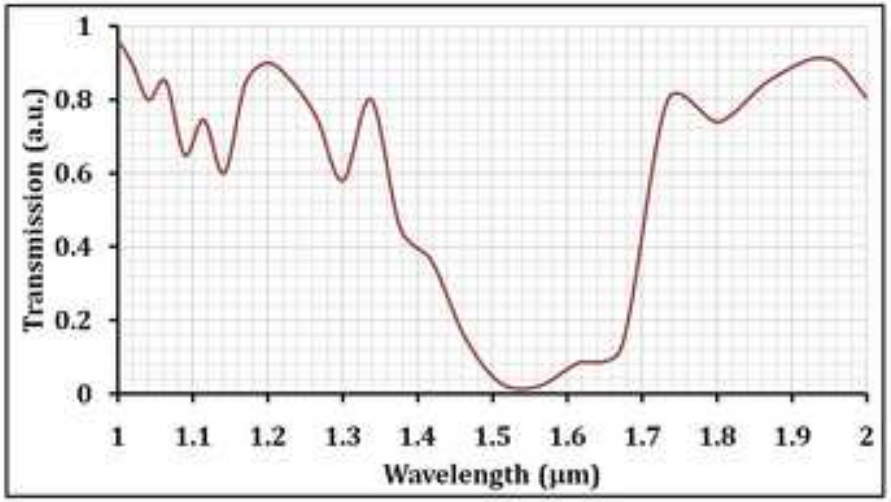

(a)

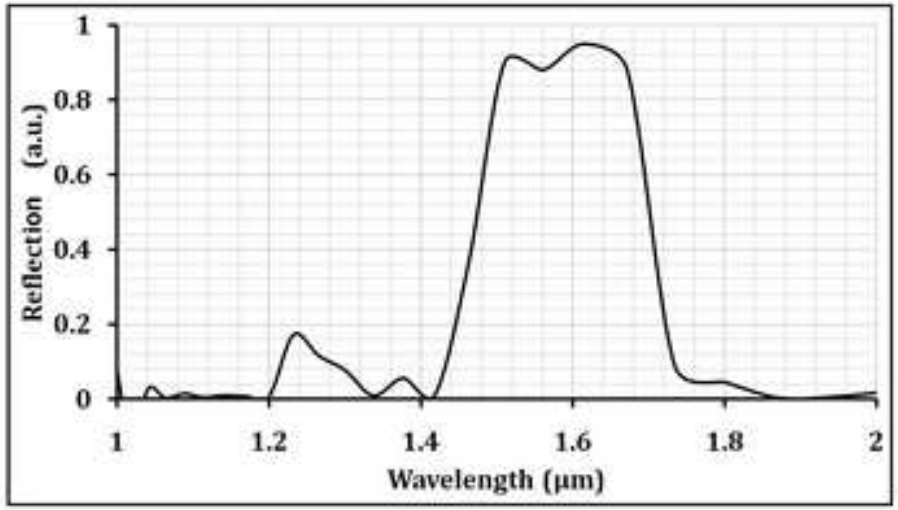

(b)

Figure 3

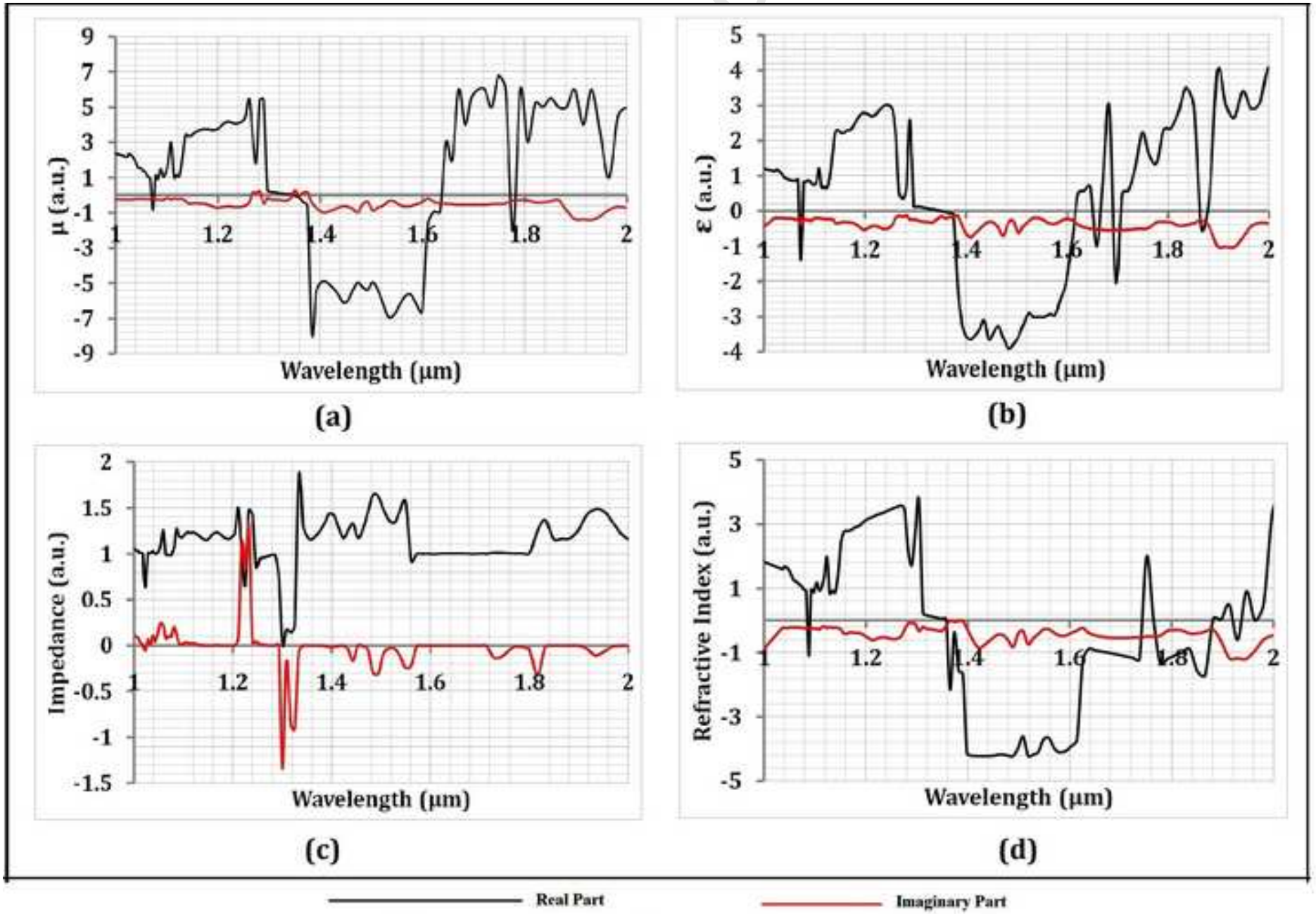
μ (a.u.)
Wavelength (μm)
(a)
ε (a.u.)
Wavelength (μm)
(b)
Impedance (a.u.)
Wavelength (μm)
(c)
Refractive Index (a.u.)
Wavelength (μm)
(d)
Real Part
Imaginary Part

Journal of Multidisciplinary Engineering Science and Technology (JMEST)
ISSN: 3159-0040
Vol. 2 Issue 8, August - 2015

Effect Of Chloride Environment On PPC Concrete Made Using Fly Ash And Pond Ash

Anamika Soni
Department of Civil Engineering
SHIATS
anamikasoni30@gmail.com

Vikas Srivastava, V. C. Agarwal
Department of Civil Engineering
SHIATS
Allahabad, India

***Abstract*—This paper presents the results of an experimental investigation carried out to explore the possibility of using fly ash and pond ash in concrete exposed in chloride environment. Specimens were cast and tested to determine their compressive strength replacing 10 percentage Portland Pozzolana Cement with fly ash and 15 percentage fine aggregate with pond ash individually. Specimens were cured in normal tap water as well as aggressive 5 percentage chloride solution up to 150 days. Test result showed that by addition of fly ash and ponded as partial replacement of PPC and fine aggregate respectively, improved compressive strength can be achieved as compared to referral conventional concrete both in tap water as well as in chloride environment at all the ages**

Keywords—Fly ash, pond ash, compressive strength, chloride effect.

I. INTRODUCTION

The history of using cement for making concrete is quite old. It is a binder which is used for the setting of other materials strength together for making concrete. The strength and durability of concrete is frequently experienced. It can be easily prepared from the readily available materials and its durability is quite remarkable. Hence it is widely used in construction field. Due to rapid advancement and increasing population, the demand of cement is increasing day by day. However there is emission of approximately same amount of CO_2 gas while production of cement. To meet this huge requirement and to control the emission of harmful gases, uses of several recycled products such as fly ash, pond ash etc have been initiated. Fly ash is the residual part left after combustion of coal in thermal power plants consisting of very fine particles, which are obtained and is collected by precipitators in dry form and possess good pozzolanic properties. Fly ash forms up to 3/4th of the total ash. Fly ash concrete has ability to moderate early setting time. Fly ash concrete is less permeable, has appreciable durability and is much economical and less susceptible than conventional concrete. Pond ash is the residue consisting of coarser particles and is obtained from the combustion of coal in large thermal power plants. Pond ash is composed of clustered ash particles which are too heavier, so they can't be carried along with flue gases and gets deposited at the bottom of the furnace. Pond ash forms up to 1/4th part of the total ash. It possess minimal or very little pozzolanic properties.

This study presents the performance of concrete in which cement was partially replaced by fly ash and fine aggregate was replaced partially by ponded ash individually. Addition of fly ash and pond ash was suitably done knowing the optimum content of replacement in the process of making concrete. The effect of chloride environment on PPC concrete using fly ash and pond ash was observed.

Mukherjee et al (2012) carried out an experimental investigation to study the physical and mechanical property of high volume fly ash cement paste. Ordinary Portland cement was replaced by 20, 30, 40, 50, 60 and 70 % class F fly ash (by weight) at w/b ratio of 0.30. Bulk density is reported to decrease with fly ash increment in the mixture. Apparent porosity and water absorption value increased with replacement of cement by fly ash. Results confirm the decrease in compressive strength at 3, 7 and 28 day with fly ash addition and it is more prominent in case of more than 30% fly ash content mixes. Mukherjee et al (2013) reported that the zero slump concrete shows higher compressive strength compare to workable concrete with super plasticizer up to 60% replacement with fly ash. The strength gain with time is higher compared to the OPC concrete at all replacement level of cement by fly ash and the optimum strength gain was noted at 70% replacement at 28 days. Kumar investigated the effect of addition of pond ash on the workability of concrete for 20, 40, 60 and 80% replacement of fine aggregate with ponded ash and with extra cement and water added to restore workability. (Ranganath et al), in their study on pond ash has shown that particles below 45um have a positive influence on the strength of cement concrete at 10% and 20% replacement of cement and concluded that pond ash contains both reactive small particles and non-reactive or poorly reactive large particles.

Horsakulthai and Paopongpaiboon (2013) reported that 7,28 and 90 days test results of chloride ion permeability of concrete by replacing 20, 40 and 60% of the cement content with coarse fly ash and found that in order to reduce the chloride ion permeability, 40% is the optimum replacement level of the cement. Siddqique et al (2003) studied the effects of furnace ponded ash on workability, compressive strength and chloride penetration of concrete were. The natural sand was replaced with furnace pond ash by 30, 50, 70 and 100% by mass at fixed free w/c ratio of 0.45

and 0.55 and cement content of 383kg/m^3. The result showed increase in workability of concrete and decreased compressive strength was observed. However the chloride transport coefficient decreased with the increase of replacement level up to 50%, beyond which it increases.

II. MATERIALS AND METHODOLOGY

A. Cement −

In this investigation, Birla Gold Portland Pozzolana cement was used, which is obtained from single batches and the test conducted on the cement are tabulated in table.1

Table1. *Properties of Cement*

Standard Consistency	31%
Initial Setting Time	240 minutes
Final Setting Time	315 minutes
7 days Compressive Strength	33 N/mm^2
28 days Compressive Strength	44 N/mm^2
Specific Gravity	2.72

B. Coarse aggregate −

Graded coarse aggregate from local available quarry of two different sizes were used in this investigation, one fraction was passing through 20mm sieve and another fraction was passing through 10mm sieve. The specific gravity of coarse aggregate was 2.66 for both fractions. The properties of coarse aggregate are given in table 2.

Table2. *Properties of Coarse Aggregate*

Fineness Modulus of 10 mm Aggregate	6.9
Fineness Modulus of 20 mm Aggregate	7.7
Water Absorption	0.8
Specific Gravity	2.6

C. Fine aggregate −

Local available river sand was used as fine aggregate, which was sieved for removing deleterious materials and over size particles. The properties of fine aggregate are given in table 3.

Table.3 *Physical properties of fine aggregate*

Specific gravity	2.2
Fineness modulus	2.84
Moisture content	2.2

D. Fly ash −

In the present study, the fly ash obtained from the NTPC, Tanda, U.P was used. The physical and chemical properties are shown in table 4

Table.4 *Properties of fly ash*

Color	Grey
% Passing	76 %
Size of particle	0.002-0.30 mm
Maximum dry density	1.183 g/cc
Optimum moisture content	22 %
Specific gravity	2.02 at 27^{0}c
Plastic limit	Non plastic
Classification	Class C and class F

E. Pond ash −

Pond ash obtained from NTPC, Tanda, U.P was used in this investigation. The specific gravity of ponded ash was found 1.65 and fineness modulus was 2.76.

F. Concrete −

The concrete mix design was done in accordance with IS 10262(1982). The cement content used in the mix design is taken as 380 kg/m^3 which satisfies minimum requirement of 300 kg/m^3 in order to avoid the balling affect. Good stone aggregate and Natural River sand of Zone-II were used as coarse and fine aggregate respectively. Maximum size of coarse aggregate was 20mm. A sieve analysis conforming to IS 383-1970 was carried out for both the fine and coarse aggregates. Potable water is used for mixing and curing. The water cement ratio (w/c) used was 0.42.

M 25 grade of concrete was used in this investigation and fine aggregate was kept as 50% of the total volume of aggregate. Slump test was done to check the workability of concrete

78 control specimens (78 cubes) of 100x100x100mm were casted to determine the compressive strength at 7, 28, 90 and 150 days interval respectively.

The resulting mix proportion of cement, fine aggregate and coarse aggregate was taken as 1:1.53:3 with water cement ratio of 0.42 and the quantity of cement is 380 kg/m^3. Compressive strength of cubes has been determined as per IS 516-1959 at a loading rate of about 140 kg/cm^2/min (about 30 tones per minute) on 2000 tons AIMIL. Two dial gauges in diametrically opposite direction were used to measure the deflection. Compression testing machine shown in fig 3.

III. RESULT AND DISCUSSION

A. Workability−

The strength and durability of concrete very much depends upon the workability of concrete. To measure the workability of concrete, slump test was done. Slump test is very popular and simple and used to measure the consistency of freshly made concrete under the action of gravity. By performing slump test, it was observed that the workability of concrete decrease as replacement level increases. Hence a dose of super plasticizer was added suitably as per the requirement. KEM SUPLAST 101 S super plasticizer was used in this study. It was an aqueous solution of sulphonated naphthalene and manufactured by Chembond Chemicals.

The slump value of concrete at the optimum replacement of cement with fly ash and fine aggregate with ponded ash at a constant dose of super plasticizer (i.e. at 0.8% by weight of cement and fine aggregate individually) is shown in table 5 .

Fig.1 *Workability measured by slump test*

Table.5. *Workability of concrete*

Sample Designation	Replacement (%)	Dose of Super Plasticizer (%)	Slump Value(mm)
W0	0	0.8	45
W1	10(cement with fly ash)	0.8	30
W2	15(fine aggregate with pond ash)	0.8	20

B. Compressive Strength

Compressive strength of referral concrete as well as concrete made using fly ash and ponded ash as partial replacement of PPC and fine aggregate respectively (replaced individually), cured in tap water and chloride environment are given in table 6.

Table.6 *Compressive strength of specimens cured in tap water*

Sl. No	Specimen designation	Replacement level (%)	Compressive Strength (MPa)				Remark
			7 days	*28 days*	*90 days*	*150 days*	
1	A1	0%	22	33	36.1	38	Tap water
2	A2	10% fly ash	27.7	39.8	48.6	49.3	Tap water
3	A3	15% pond ash	24.4	38.1	42.1	43.3	Tap water
4	A4	0%	20.2	27	34.5	36.7	5% Cl
5	A5	10% fly ash	24.8	38.2	40.3	43.6	5% Cl
6	A6	15% pond ash	21.5	34.4	39.1	40.7	5% Cl

The results of the same are reproduced in graphical form in fig. 2 and 3 for visual observation.

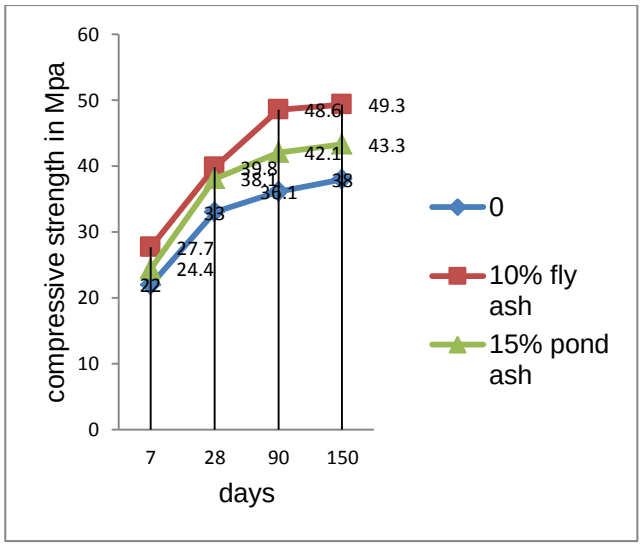

Tap water

Fig.2 *Compressive Strength of specimen cured in tap water*

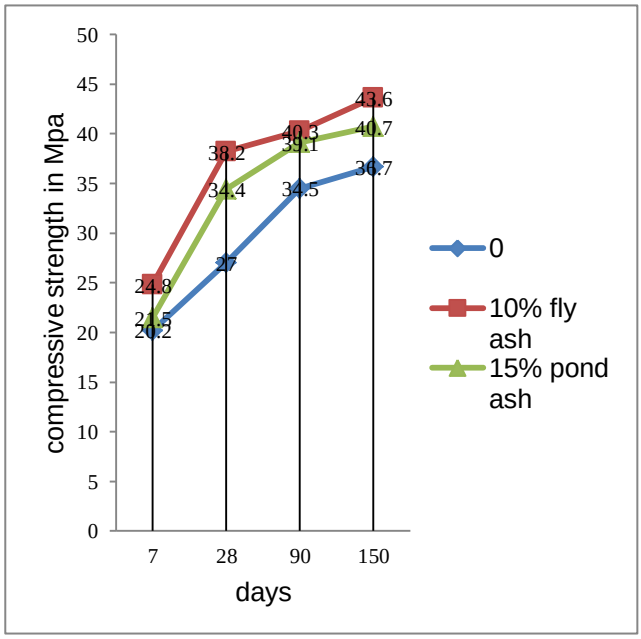

5% chloride

Fig.3 *Compressive Strength of specimen cured in 5% chloride solution.*

From table 6, it is seen that compressive strength of concrete made using fly ash and ponded ash as partial replacement of PPC and fine aggregate respectively (replaced individually) is substantially more than that of conventional concrete irrespective of curing period and curing environment.

The compressive strength of concrete made using 10% fly ash as partial replacement of PPC and cured in tap water is 25.9%, 20.6%, 34.6% and 29.7% more than that of referral conventional concrete at 7, 28, 90 and 150 days respectively. This increase in compressive strength may be due to pozzolanic action as well as filler action of fine particles of fly ash in concrete.

However, compressive strength of concrete made using 15% ponded ash as partial replacement of fine aggregate and cured in tap water is 10.9%, 15.5%, 16.6% and 13.9% more than that of referral conventional concrete at 7, 28, 90 and 150 days respectively.

The compressive strength of concrete made using 10% fly ash as partial replacement of PPC and cured in 5% chloride solution is 22.77%, 41.48%, 16.81% and 18.80% more than that of referral conventional concrete at 7, 28, 90 and 150 days respectively. However, compressive strength of concrete made .using 15% ponded ash as partial replacement of fine aggregate and cured in in 5% chloride solution is 6.4%, 27.4%, 13.33% and 10.9% % more than that of referral conventional concrete at 7, 28, 90 and 150 days respectively. This increase in compressive strength is due to increase in permeability as the percentage of replacement of PPC increases and hence contributes to the lesser chloride attack.

IV. CONCLUSION

From the above study following conclusions are drawn-

- By 10% replacement of Portland pozzolana cement (PPC) with fly ash compressive strength increases.
- At 15% replacement of fine aggregate with ponded ash compressive strength is more than the referral concrete.
- The workability of concrete specimen decreases with increase in replacement level of pozzolans due to the increase in water demand which can be maintained by increasing the dose of super plasticizer.
- Compressive strength of concrete cured in tap water and5% chloride solution increases as compared to referral conventional concrete at all ages.
- Compressive strength of concrete cured in 5% chloride solution decreases as compared to concrete cured in tap water at all the ages.

ACKNOWLEDGEMENT

I would like to express my gratitude to all the respected professors, faculty staff and my friends especially Mr .Vinit Kumar Singh, Mr. Mukesh Kumar and Mr. Sarfaraj Ahmed for their co-operation, support and guidance during entire investigation.

REFERENCES

[1] Alhozaimy, AP et al. 1 (1996), “Effects of curing conditions and age on chloride permeability of fly ash mortar”, ACI mater. J.93, pp87-95.

[2] Badur S. and Choudhary R., (2008) “Utilization of hazardous wastes and By-products as a green concrete material through s/s process: a review,” Advanced Study Cente Co. Ltd.Rev.Adv.Mater.Sci. 17, 42-61.

[3] Berndt M. L., (2009) “Properties of sustainable concrete containing fly ash, Slag and recycled concrete aggregate.” Construction and Building Materials Volume 23, Issue 7, Page no. 2606-2613.

[4] Cangialosi F., Intini G., Liberti L., Notarnicola M., and Di Canio F., (2010) “Activated Coal Fly Ash as Improved Mineral Addition in Cement and Concrete”. Second International Conference on Sustainable Construction Materials and Technologies.June 28 - June 30, ISBN 978-1-4507-1490-7.

[5] Ghafoori N., Cai Y., Ahmadi B., (1997) “Use of dry bottom ash as a fine aggregate in roller compacted concrete,” ACI Spec. Publ. (SP-171) 487– 507.February.

[6] Singh M, Siddique R. Effect of coal bottom ash as partial replacement of sand on the properties of concrete. Resour Conserv Recycl 2013; volume 72, pp20–32

[7] Horsakulthai and K. Paopongiboon, “Strenght, Chloride, Permeability and Corrosion of Coarse Fly Ash Concrete with Bagasse-Rice husk-Wood Ash Additive,” American journal of Applied Sciences, vol. 10, 2013

[8] Sushil kumar (1992) Use of fly ash as fine aggregate in concrete, M. E. Thesis, Civil Engineering, Delhi college of Engineering, University of Delhi, Delhi

[9] Ranganath R. V., B. Bhattacharjee, and S. Krishnamoorthy (1998) “Influence of size fraction of ponded ash on its pozzolanic activity”, Cement and Concrete Research, vol. 28 No. 5, May, pp749-761.

[10] IS1489: 1991, Specification for Portland Pozzolana Cement: part I - fly ash based (Third Revision) Bureau of Indian Standards, New Delhi, India.

[11] IS 383-1970, Specification for coarse and fine aggregates from natural sources for concrete (2nd revision) Bureau of Indian Standards, New Delhi, India.

[12] SP 23:1982, Indian standard hand book on concrete mixes (Amendment No. 1) Bureau of Indian Standards, New Delhi, India.

[13] IS 456:2000, Code of Practice for Plain and Reinforced Concrete, Bureau of Indian Standards, New Delhi.

[14] IS10262:1982, recommended Guidelines for concrete mix Design, Bureau of Indian Standards, New Delhi, India.

[15] IS 4032: 1968, Indian standard Method of chemical Analysis of Hydraulic Cement, Bureau of Indian Standards, New Delhi, India.

[16] Shaswata Mukherjee, Saroj Mandal, Adhikari.U.B , “Study on the physical and mechanical property of ordinary portland cement and fly ash paste” International Journal of Civil and Structural Engineering, Volume 2, No 3, 2012, pp731-736.

Far & Near in Water & Energy
News - Energy Section

SHRI TAPAN KUMAR BARAI TAKES OVER AS MEMBER (THERMAL), CENTRAL ELECTRICITY AUTHORITY

Born on 20th December, 1956, Shri Tapan Kumar Barai was graduated in B.Sc. Engineering (Electrical) in 1978 from Delhi College of Engineering, Kashmere Gate, Delhi. His service life commenced in November, 1979 when he joined Central Electricity Authority as Assistant Director. Since then, he has been working in CEA for last 35 years in various capacities, dealing with functions related to hydro power potential studies, hydro construction, monitoring, Financial and commercial appraisal of generation projects, Bid evaluation for Ultra Mega Power Projects, studies related to generation as well as retail tariff of electricity etc.

He was appointed as Secretary, CEA in August 2013 when he assisted the Chairperson, CEA in matters pertaining to administration & finance, expenditure control, Cadre Review/Service Rules, etc. including techno-economic appraisal and concurrence to H.E projects, and HRD.

Recently taken over as Member (Thermal) on 27th May, 2015, his main responsibility is to extend advice to Chairperson, CEA and the Central Government, State Utilities and other organization on matters relating to Thermal Power generation and its capacity addition, timely completion of thermal power projects under construction and R&M, thermal design and consultancy, thermal performance evaluation and climate change issues etc.

DR. SOMIT DASGUPTA TAKES OVER AS MEMBER (E&C), CENTRAL ELECTRICITY AUTHORITY

Dr. Somit Dasgupta is an officer from the Indian Economic Service of the 1984 batch and has had a long association with the power sector having worked for more than 15 years in various capacities in the Ministry of Power, Central Electricity Authority (CEA), the Delhi Electricity Regulatory Commission and also the Niti Aayog (formerly known as the Planning Commission). During his stint with the Government spanning over three decades, Dr. Dasgupta has also worked in other Ministries/Departments of the Government of India such as the National Building Organisation, Ministry of Urban Development, Ministry of Development of North Eastern Region and also the Department of Youth Affairs and Sports.

Dr. Dasgupta holds a Masters Degree in Economics from the Delhi School of Economics, Delhi University (1980-82) and had acquired his M. Phil. Degree on 'Economic Planning' from the University of Glasgow (1997-98). Dr. Dasgupta was awarded his Ph.D degree in the year 2013 from the Jawaharlal Nehru University and the subject of his dissertation was 'Power Sector Reforms in India'.

Dr. Dasgupta has served in the Board of the Nuclear Power Corporation of India (NPCIL) and the Bharatiya Nabhikiya Vidyut Nigam Ltd. (BHAVINI) for about a year with effect from June 2014. Before taking over as Member (E&C) in the CEA, Dr. Dasgupta was working in Niti Aayog as Adviser (Power & Coal) and was responsible for formulation of policy, development of long term plans, appraisal of Plan schemes, etc. He has also been actively involved in specific projects of the Planning Commission including the Indian Energy Security Scenario (IESS) 2047 which was launched in February, 2014.

RATTANINDIA SIGNS PACT, GETS TO DEVELOP SOLAR PROJECTS IN MP

Looking to augment solar power generation, Madhya Kshetra Vidyut Vitran Co (MPMKVVCL) has inked an agreement with RattanIndia Apna Solar to develop 5-MW grid-connected rooftop solar power projects in Madhya Pradesh. The power purchase agreement (PPA) and project implementation agreement (PIA) with MPMKVVCL was signed in Bhopal to develop 5-MW grid-connected rooftop solar power project in the state.

"It gives us immense pleasure to partner with the Madhya Pradesh government in its initiative to provide clean and affordable energy to people," Rajiv Rattan, Chairman, RattanIndia Group said after the signing of the agreement. Rattan India Apna Solar won the order through competitive bidding. This is one of the first rooftop solar projects tendered in the country and more are likely to come up very soon.

This rooftop solar power project will be executed on about 75 public buildings in cities of Bhopal, Indore and Jabalpur in Madhya Pradesh.

FLOOD FREQUENCY ANALYSIS OF RIVER KOSI, UTTARAKHAND, INDIA USING STATISTICAL APPROACH

Saurabh Sah[1], Jyothi Prasad[2]

[1]*M. Tech Student (Hydraulic Engineering) Dept. of Civil EngineeringG.B.P.U.A. &.T Pantnagar, Uttarakhand, India*
saurabhsah9933@gmail.com

[2]*Professor Dept. of Civil Engineering College of TechnologyG.B.P.U.A. &.T Pantnagar, Uttarakhand, India*
jptce@gbpuat-tech.ac.in

Abstract

In the present study, flood frequency analysis has been applied for river Kosi in Uttarakhand. The river Kosi is an important tributary of Ganga river system, which arising from Koshimool near Kausani, Almora district flows on the western side of the study area and to meet at Ramganga River. The annual flood series analysis has been carried out to estimate the flood quantiles at different return period at Kosi barrage site of river Kosi. The statistical approach provided a significant advantage of estimation of flood at any sites in the homogenous region with very less or no data. In the at –site analysis of annual flood series the Normal, Log normal, Pearson type III, Log Pearson type III, Gumbel and Log Gumbel distribution were applied using method of moments . From the analysis of different goodness of fit tests, it has been found that the Log Gumbel distribution with method of moment as parameters estimation found to be the best-fit distribution for Kosi River and other sites in the region. It is recommended that the regional parameters for Kosi Basin may be used only for primary estimation of flood and should be reviewed when more regional data available.

Keywords: *Flood Frequency Analysis, River Kosi, Annual Peak Flood discharge, Return Period, Goodness of fit Test*.

----------***----------

I. INTRODUCTION

Flood is one of the natural disasters which occur in India every year. Flood in India generally occur during the southwest monsoon season (June to October). Floods are generated by the random coincidence of several meteorological factors, but man's use of the river catchments also has an impact upon the severity and consequences of the events. The risk of floods is treated as a hazards if it has the of the specified hazard occurrence. An accurate estimation of flood at a site is frequently required for the safe and economic design of various river engineering works. For the purpose of design of small bridges, culverts etc. it is sufficient to estimates the maximum instantaneous discharge the structure has to pass during its economic life period. One way of estimates the flood of specific recurrence interval is by performing flood frequency analysis of the recorded annual peak discharge over number of the years at the site under consideration. Generally in frequency analysis, an appropriate statistical distribution function is used to fit past available records and then inferences are made about the future likely flows.

II. STUDY AREA AND DATA COLLECTION

River Kosi is one of the major rivers of Kumaon region of Uttarakhand. It is an important tributary of Ganga river system, which arising from Koshimool near Kausani, Almora district flows on the western side of the study area and to meet at Ramganga River. It is a sub basin of the Ganga River system. Geographically it is on the south east part of Nainital. It spreads from longitude 78° 07' to 80° 29' N and latitude 29° 16' E to 30° 05' E. Geographical extent of this catchment is 6753 km^2. For the study, annual peak discharge data of Kosi River at Kosi barrage Ramnagar from 1985-2014 (30 years flood data) were obtained from the measurements carried out by the Irrigation Department Ramnagar. The river is tributary of Ram Ganga River in Ganga river basin. Kosi River is the only available source of water for agricultural and industrial developments, in addition to fulfilling the needs of drinking water of the Ramnagar town and rural population of Bhabar area.

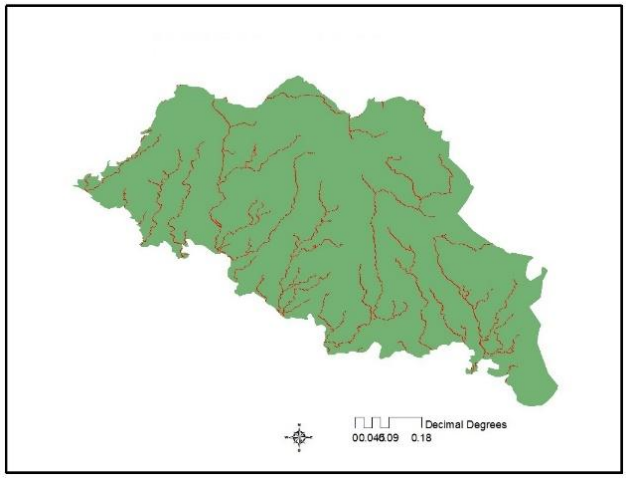

Figure- 1: Study Area

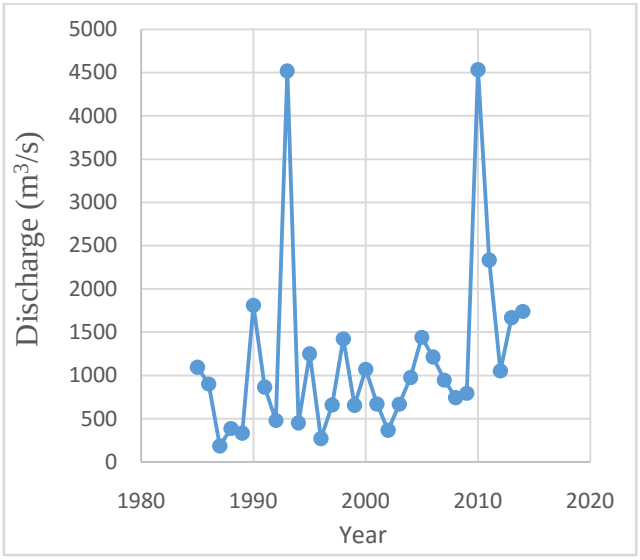

Figure- 2: Annual Peak discharge data at Kosi barrage (1985-2014)

III. METHODOLOGY

Method of Moments

The method of moments makes use of the fact that if all the moments of a distribution are known then everything about this distribution is known. For all the distribution in common usage four moments or fewer are sufficient all the oments. The method of moment's estimation is dependent on the assumption that the distribution of variate values in the sample is representative of the sample is representative of the population distribution. Given that the form of the distribution is known or assumed, the distribution which the sample follows is specified by its first two or three moments calculated from the data.

$$X_T = \mu + K_T\sigma \qquad (1)$$

In which,

X_T = the magnitude of flood at required return period T.

K_T = the frequency factor corresponding to T.

μ *and* σ = mean and standard deviation of the population.

Test of Goodness of Fit

The validity of probability distribution function proposed to fit the empirical frequency distribution of a given sample may be tested graphically or by analytical methods. The goodness fit measure involves identifying a distribution that fits the observed data. When computing the magnitudes of extreme events, such as flood flows, it is required that the probability distribution function be invertible, so that a given value of recurrence interval (T) and the corresponding value of frequency factor (K) can be determined. For plotting formula were adopted and compared to select the best flood frequency distribution that best fitted annual maximum flood flow of Kosi river catchment. A number of analytical tests have been proposed for testing the goodness of fit of proposed models. Three of these tests are presented. The Probability Density functions are used to fit the annual peak discharge series are shown in Table 1.

Table 1: Probability Density functions for selected

S.N	Distributions	f(x)
1	Normal	$f(X) = \frac{1}{\sigma\sqrt{2\pi}} exp\left[-\frac{1}{2}\left(\frac{X-\mu}{\sigma}\right)^2\right]$
2	Log Normal	$f(X) = \frac{1}{\sigma_y\sqrt{2\pi}} exp\left[-\frac{1}{2}\left(\frac{log_e(X)-\mu_y}{\sigma_y}\right)^2\right]$
3	Pearson Type III	$f(X) = \frac{(X-X_o)^{\gamma-1} e^{-(X-X_o)/\beta}}{\beta^{\gamma}(\gamma)}$
4	Log Pearson Type III	$f(X) = \frac{1}{\lvert\beta\rvert(\gamma).X}\left[\frac{log_e X - y_o}{\beta}\right]^{\gamma-1} exp\left[-\frac{log_e X - y_o}{\beta}\right]$
5	Gumbel	$f(X) = \frac{1}{\alpha} exp\left[-\frac{X-U}{\alpha} - e - \frac{(X-U)}{\alpha}\right]$
6	Log Gumbel	$f(X) = \frac{1}{\alpha}\left[1-k\left(\frac{X-\mu}{\alpha}\right)\right]^{\frac{1}{K}-1} e\left[1-K\left(\frac{X-\mu}{\alpha}\right)\right]^{\frac{1}{K}}$

Chi- Square Test

The chi- square goodness of fit test is one of the most commonly used tests for testing the goodness of fit of probability distribution functions to empirical frequency distribution.

$$C = \sum_{j=1}^{m} \frac{\left(N_j - NP_j\right)^2}{NP_j} \quad (2)$$

where,

N_J number of discharge lying in the Q domain for each class interval

N number of year

M number of classes

C is the Chi square

D-Index Test

In order to compare the relative fit of different distribution to hydrological data. The probability of exceedance of observation is estimated by Weibull plotting position formula.

$$P(X \geq x) = \frac{m}{(N+1)} \quad (3)$$

where,

P is the probability of exceedance
m is the rank of the flood values arranged in the descending order of magnitude, and N is the number of observations.

$$D - Index = \frac{1}{X_{av}} - \sum_{i=1}^{6} ABS\left(X_{i,}observed - X_{i,}computed\right) \quad (4)$$

Kolmogorov-Smirnov Test

This is a distribution free test widely used in statistical hydrology. It is based on the maximum difference between the cumulative distributions Fe(y) and the cumulative probability distribution being fitted $F_y(y;\theta')$.

$$D = \sum_{i=0}^{N} \left(F_e(y) - F_y;(y_i, \theta')\right) \quad (5)$$

The goodness of fit test of the selected probability model to the empirical distribution is accepted if:

$$D \leq d_\alpha(N) \quad (6)$$

where, $d_\alpha(N)$ is the Kolmogorov-Smirnov statistic corresponding to the sample size N and confidence level $y = (1-\alpha)$.

IV. RESULT AND DISCUSSION

The computated Statistical parameters are shown in Table 2, The probability distribution method is carried out to determine the predicted discharge for the return period of 10, 25, 50, 100, 200, 500, 1000 in years are shown in Table 3.

Table 2. Computation of Statistical parameter

Parameter	Original series	Log transformed series
Mean	1185.13	6.80
Standard Deviation	1039.75	0.73
Coefficient of Variation	0.87	0.10
Skewness Coefficient	2.35	0.17
Kurtosis Coefficient	8.97	3.55

Table 3: Estimation of T-Year Flood and its Standard Error of Kosi River

Return Period	Computed Discharge (m^3/s)	Standard Error (m^3/s)	95% Significances Level	
			Upper Confidence Level (m^3/s)	Lower Confidence Level (m^3/s)
NORMAL DISTRIBUTION				
10	2502	254	3022	1982
25	3527	357	4255	2799
50	4317	446	5229	3406
100	5113	541	6219	4008
200	5919	640	7225	4612
500	6991	773	8569	5413
1000	10816	876	12603	9029
LOG NORMAL DISTRIBUTION				
10	2339	429	3216	1463
25	3425	755	4966	1884
50	4389	1085	6604	2174
100	5506	1503	8573	2438
200	6794	2023	10922	2666
500	8798	2897	14703	2882
1000	10573	3723	18170	2976
PEARSON TYPE III DISTRIBUTION				
10	2502	510	3544	1460
25	3527	898	5360	1694
50	4317	1132	6582	2052
100	5116	1334	7839	2394
200	5922	1614	9215	2628
500	6994	1946	10965	3022
1000	7809	2272	12352	3267
LOG PEARSON TYPE III DISTRIBUTION				
10	2351	479	3309	1392
25	3425	950	5364	1485
50	4389	1243	6925	1853
100	5506	1575	8721	2291
200	6794	2017	10910	2678
500	8798	2407	13710	3895
1000	10573	3055	16807	4339
GUMBEL DISTRIBUTION				
10	2541	396	3350	1733
25	3310	534	4400	2220
50	3880	651	5209	2551
100	4446	744	5966	2926
200	5010	850	6745	3275
500	5754	990	7775	3733
1000	6316	1097	8555	4078
LOG GUMBEL DISTRIBUTION				
10	2362	396	3170	1553
25	4077	534	5167	2987
50	6114	629	7399	4829
100	9140	744	10660	7621
200	13648	850	15383	11912
500	23149	990	25710	21127
1000	34517	1097	36755	32278

Test of Goodness of Fit Test

Tests of Goodness fit namely Chi squared test, K-S test and D-index test have been applied to the chosen probability distributions for Kosi river stations are presented as summary in Table 4. Form this table it has been observed that Kosi River stations log normal and log Gumbel are fitted from both K-S test and D-index test.

The D-index fitness tests applied for the river stations are tested for model efficiency, Root mean square error (RMSE) and D-index (fit in the top six values) for different distributions.

It has been found that from the Table 4 for river Kosi, Log Gumbel distribution having Model efficiency 96.24 % and root mean square error 90.38 %.

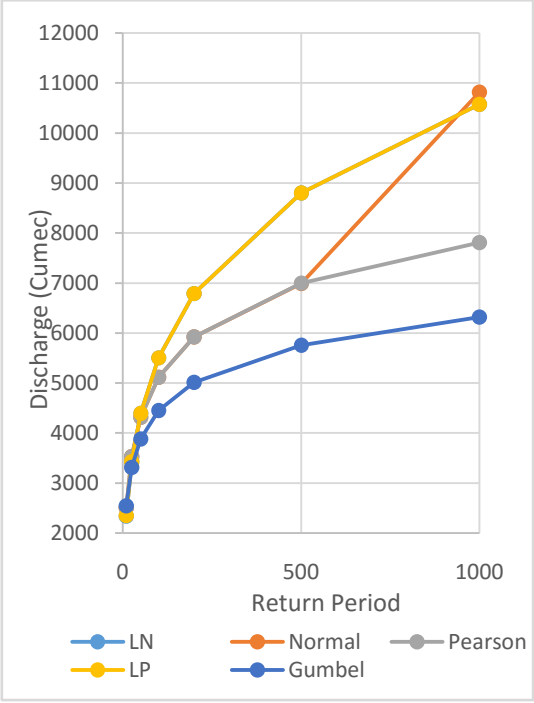

Figure -3 discharge vs. return period

Table 4: Model efficiency, RMSE for D-index of different distributions for Kosi River.

S.No.	Distribution	Model Efficiency (%)	RMSE	D-index
1	Normal	90.21	133.84	4.62
2	Log Normal	91.37	118.43	3.09
3	Pearson Type III	92.23	127.62	3.81
4	Log Pearson Type III	91.98	117.43	3.25
5	Gumbel	92.61	121.14	3.43
6	Log Gumbel	96.24	90.38	1.63

Coefficient of Determination

From trend line equation, Coefficient of determination (R^2) values obtained from the Figure 3 are given in Table 5. The value (R^2) shows that a pattern of the scattered and narrow. It has been found that Log Gumbel distribution having maximum (R^2) value is 0.9662. Hence for predicting expected flow in the Kosi Rivers Log Gumbel is the best suitable distribution.

Table 5: Coefficient of Determination

Coefficient of Determination (R^2)						
River	Distribution					
	Normal	Log Normal	Pearson Type III	Log Pearson Type III	Gumbel	Log Gumbel
Kosi	0.9339	0.8510	0.7553	0.8515	0.7444	0.9662

V. CONCLUSION

- In this study six distributions are considered and worked out the flood quantiles for different return period like 1000, 500, 200, 100, 75, 50, 25 and 10 years, here it is assumed that all the distributions are fittings for Kosi River.
- Tests of Goodness fit namely Chi squared test, K-S test and D-index test applied to the chosen probability distributions, it shows that Log normal and Log Gumbel distributions are fitted for both K-S test and D-index tests. However from the most of literature review recommends the use Log Gumbel distribution for estimation of flood quantities.
- Hence Log Gumbel distribution is the best distributions for predicting floods in Kosi River.

REFERENCES

[1] Dalrymple T. (1960), "Flood frequency methods", U. S. Geol. Surv. Water supply pap, 1543A, U.S. Govt. Printing office, Washington, D.C., 11 – 51.

[2] Jyothi Prasad(1994) unpublished M.E (Hydrology) thesis submitted to "Regional flood frequency Analysis for Central India to Department of Hydrology, University of Roorkee.

[3] Mukherjee. M. K. Model of Peak Discharge (Qp) & Return Period (T) of river Subernarekha, India. International Journal of Current Research. Vol-4. Issue 04. PP-164, April, 2012.

[4] P V Parameshwaran, J P Singh, Jyothi Prasad, H J Shiva Prasad "Flood Frequency Studies of Upper Godavari Basins in Maharashtra"- at National Workshop collaboration held at Delhi College of Engineering, Delhi during October 8-9, 1999.

Available online at www.sciencedirect.com

ScienceDirect

materialstoday: PROCEEDINGS

Materials Today: Proceedings 2 (2015) 3100 – 3106

4th International Conference on Materials Processing and Characterization

Jeans made out of plastics

Navendu Sharma, Amish, Manisha Meena,Saurabh Agrawal*

Production and Industrial Engineering Department, Delhi Technological University, New Delhi 110042, India

Abstract

In India the recycling of household waste especially plastic creates an enormous logistics problem. The negative effects of plastics are detrimental for the ecosystem and thus the government has laid out new regulations to ensure the proper recycle of waste. The plastic problem falls into the field of reverse logistics since we can process it to produce profitable goods. The objective of the case study was to analyse the opportunities generated by the reverse logistics of the plastic wastes, and their impact in environmental sense. We hereby studied one of the measures to recycle the waste of plastic bottles and produce jeans from it. As of now no previous case study has been done on this process, thus the process of converting plastic bottles to jeans is summarised in this case study.

Selection and peer-review under responsibility of the conference committee members of the 4th International conference on Materials Processing and Characterization.

Keywords: Reverse logistics; plastic waste; recycle.

1. Introduction

Due to plastics' relatively low cost, ease of manufacturing, versatility, and imperviousness to water, plastics are used in an enormous and expanding range of products. Products that constitute plastics are paperclips, window frames, flooring, food packaging, drinking straws, car bumpers and bottles, from carbonated drinks bottles to detergent bottles, to name a few. But with enormous uses, there also comes life-threatening hazards with use of plastics. Increasing presence of micro-plastics in the marine food chain along with toxics that accumulate in plastics, depletion of ozone layer due to use of CFC's in extrusion of polystyrene, incineration of plastics increases carbon emission.

* Corresponding author. Tel.: +91-813-077-1554; fax: +0-000-000-0000 .
E-mail address: navendusharma04@gmail.com

Selection and peer-review under responsibility of the conference committee members of the 4th International conference on Materials Processing and Characterization.
doi:10.1016/j.matpr.2015.07.261

As the negative effects of plastics are harmful for the ecosystem, government and industries have to come up with innovative ideas to tackle this out. One of the solutions that industries have come up with is the collection, recycling and reuse of products and materials. In the recent past, the growth of environmental concern has given the term reuse a new meaning (Dekker, 2006 [1]; Neumayer, 2003 [2]). This development to reuse and recycle products is not only because of the government policies but the industries see a better economic advantage in this. In this context, reverse logistics is an important issue.

Reverse logistics is defined as the process of planning, implementing and controlling the backward flows of raw materials, in process inventory, packaging and finished goods, from a manufacturing, distribution or use point to a point of recovery or point of proper disposal. Reverse logistics refers to the logistic management skills and activities involved in reducing, managing and recycle of waste from packaging to products. Reverse logistics has become an important source of opportunity for companies to improve visibility and profitability and lower costs across supply chain. Therefore, environmental issues are also increasing awareness of the importance of reverse logistics. Reverse logistics treats these materials as valuable industrial nutrients rather than trash [3]. Most research on reverse logistics is focused on automobiles, metal scraps, sales packaging material, and waste paper recycling (Stock, 1992 [4]; Kopicki et al., 1993 [5]; Flapper, 1996 [6]; Kumar and Putnam, 2008 [7]; Pilar et al., 2004 [8]). There has been research on reverse logistics in the apparel industry (Tibben-Lembke and Rogers, 2002 [9]; Svensson, 2007 [10]) but none of these study the Indian context. In recent years waste management has received increasing focus and attention, mainly due to the growing amount of waste produced, the lack of waste disposal sites and environmental protection. Due to the harmful environmental effects of waste disposal the emphasis has been increasingly inclined towards recycling.

Recycling is a process to change waste materials into new products to prevent waste of potentially useful materials, reduce the consumption of fresh raw materials, reduce energy usage, reduce air pollution and water pollution by reducing the need for conventional waste disposal, and lower the greenhouse gas emissions as compared to plastic production. One of the practical applications of reverse logistics in recycling of plastic waste is making jeans. This study is focussed on the conversion of plastic waste to jeans manufacturing. This is the first time when a case study of recycling plastic and manufacturing of jeans has been done.

This paper is organized as follows. In Section 2 we give the literature review of the papers that were studied to make this case study, and then described in detail is the research methodology in Section 3. Section 4 is the case study in which we have given the company profile [3.1] followed by [4.2] which include process of manufacturing jeans from plastic bottles. [4.3] has some discussions we had with the people associated with the company and in [0] we have listed some of the critical issues that were identified during our case study. Finally, Section 5 contains some concluding remarks.

2. Literature Review

Profound study of existing research papers written on reverse logistics and recycling have been done before undertaking this case study and have been stated in this section . No previous case study has been done on this topic.

Reverse logistics is defined as the process of planning, implementing and controlling the inbound flow and storage of secondary goods and related information opposite to the traditional supply chain directions for the purpose of recovering value and proper disposal [11]. The Reverse Logistics Association (2009) refers to the term reverse logistics “as all activity associated with a product/service after the point of sale, the ultimate goal to optimize or make more efficient aftermarket activity, thus saving money and environmental resources” [12]. Kroon et al. (1995) [13] have written about the returnable containers an application of reverse logistics. Fargher and Smith (1996) [14] and Kumar et al. (2008) have researched cases where the recovery of used product is economically more attractive than its disposal. Kwok Hung Lau and Y. Wang [15] have written a research paper on reverse logistics and discussed its application in the electronic industry in china. R. Tibben et al. (2002) [16] have written a brief and an excellent research paper explaining the difference between forward and reverse logistics. V. Ravi and R. Shankar (2005) [17] have written an article to analyse the interaction among the major barriers, which hinder or prevent the application of reverse logistics in automobile industries. Eltayeb et al. have explored that taking back products and packaging, business organizations can generate benefits to the environment, in the form of reduced waste and better

resource utilization, in addition to economic benefits and cost reductions to the organizations [18].

Recycling is one of the most important processes as it helps us to remove waste which has a huge negative impact on the natural environment. In this scenario, different drivers like government regulations have forced companies to take environmental initiatives in their supply chain operations [19]. Many researches have been done on recycling and lately it has been one of the most researched processes. A.I. Barros et al. (1998) [20] have written a case study on sand recycling from construction waste. F. Azadivar et al. (2011) [21] have written a paper on the decision rules for recycling returned products. According to (UNEP, 2004 [22]), life cycle thinking implies that organizations are responsible for environmental damages caused throughout the product chain [23]

Plastic waste:
According to Times of India [24] the total plastic waste which is collected and recycled in India is estimated to be 9205 tonnes per day and 6137 tonnes remain uncollected and littered. Delhi itself is producing 689.5 tonnes a day. As 40% of the plastic waste is not recycled, the daily addition to untreated plastic in Delhi is estimated at 275.6 tonnes. This waste is a source of continuing pollution as plastic is non-bio-degradable and poisons the environment for decades.

Plastics play an important role in almost every aspect of our lives. Plastics are used to manufacture everyday products such as beverage containers, toys, and furniture. They find use in durable (appliances, furniture) and nondurable (diapers, trash bags, utensils). 42% of India's consumption of plastics is used in packaging. The widespread use of plastics demands proper end of life management. Plastics make up almost 13% of the municipal solid waste stream. The largest amount of plastics is found in containers and packaging, 32million tons of plastic waste were generated in 2012. The United States generated almost 14 million tons of plastics as containers and packaging. The recycling rate for different types of plastic varies greatly, resulting in an overall recycling rate of 9%, or 2.8millions in 2012. India generates 5.6million metric tons of plastic waste annually, according to a report by Central Pollution Control Board (CPCB). We are sitting on a plastic bomb. In India alone, over a million people (known as rag pickers) find livelihood opportunities in waste collection and recycling through well-organized systems (Toxics Link, 2001).[25]

Fortunately, the world has come to a situation in which society feels that a change in attitude towards the environment is an absolute necessity. And in context of serving the society, the big denim brand, XYZ Ltd., has taken a step forward.

3. Research Methodology:

In total ten brief interviews were conducted with the people associated with the company telephonically. Questions of interview consisted of various issues faced and the overall process of converting plastic to jeans. To maintain consistency throughout the interviews the same procedure was used for each interview. Firstly to each interviewee a short introduction was given. The interviewee was told about the topic of our case study. Then we asked them to tell us the whole process of manufacturing jeans from plastic briefly. Then questions were asked about the end product and how it is different from other jeans. At the end we asked them about the key issues that they were or are facing and these issues were noted down.

4. Case Study:

4.1 Company profile:

With total assets of $4.57billion, XYZ Ltd is serving worldwide with its products, mainly are jeans and jackets. And now they are turning waste (plastic) into fashion. Bottles that would otherwise make presence in degrading landfills or would have been incinerated are now being used in jeans manufacturing. Company is using about 8-12 oz. bottles for production of per pair of jeans. A lot of research and development was done on the innovation of these denims- from the design to new fibre-spinning techniques to sourcing waste plastic. Plastic bottles and food trays are collected from municipal sites, cleaned, sorted, crushed into flakes and made into a polyester fibre. This is blended with cotton fibre, which is finally woven with traditional cotton yarn to create the denim. Since the fashion industry

is highly wasteful, these type of denims made of plastic bottles are found to be quite appealing for customers. Reverse logistics of plastic wastes especially of plastic bottles is gaining momentum as many brands are now entering this segment. The process of conversion of plastic bottles to jeans is summarised below:

4.2 Process:

Here we are going to discuss the process of transforming plastic waste to jeans in the manufacturing plant of xyz ltd. Consumers always leave a small of liquid in the bottle when we throw it away. Shredding removes this unwanted liquid so that the liquid does not affect quality of plastic and does affect our final product. The plastic is then sent for sorting. Sorting is a process that separates the clear plastic from coloured ones. White clothes or materials that can be dyed are made out of clear plastic and thus it's valuable. After this the material heads to the bath where the caps and labels are removed. The plastic of the caps of the bottles are much lighter in weight and thus it floats over the water bath and thus can be easily removed by the worker. Then the material heads for a second bath which is of caustic soda. One has to be really careful around this bath as caustic soda is highly corrosive for skin but is very efficient in removing labels.

After this all that is left is clear plastic shreds, but it is wet and has to be dried before further processing. Thus these clear plastic shreds head for the ovens. In these ovens this clear plastic is mixed deliberately with some light coloured plastic as it helps in producing white cloth that we need. This mixture remains inside the rotating drum ovens for about 10 hours after which the dried material is collected. The dried material is then sent to the extruder. An extruder is hollow cylindrical shaped with a solid screw rotating inside it. The plastic moves in between the cylindrical walls and the solid screw. Thus high temperatures are obtained because of friction around 270 degrees Celsius. Thus the plastic melts (as its melting point is around 235 degrees Celsius) and flows through the extruder. This molten plastic is then forced to pass through a sieve in thus it takes a form of thread and then these threads are collected.

But these threads are not strong enough yet to make the cloth material. So the threads are stretched several times while being heated. During this stretching the fibres bond together more strongly thus increasing the overall strength of the threads. After this these threads are torn apart to fluff form just like the cotton bale. This fluffy material is the baled and sent for further processing.

After all this the bonded fibres are brushed together in such a manner that they all lie in similar direction adding to the strength. This process is known as carding. After carding the threads are then collected on bobbins and from these bobbins the threads go to the loam where the transformation of threads to cloth takes place. This cloth is then used for making jeans through the regular processes of cutting and stitching. Thus the transformation of plastic bottles to jeans is thus completed.

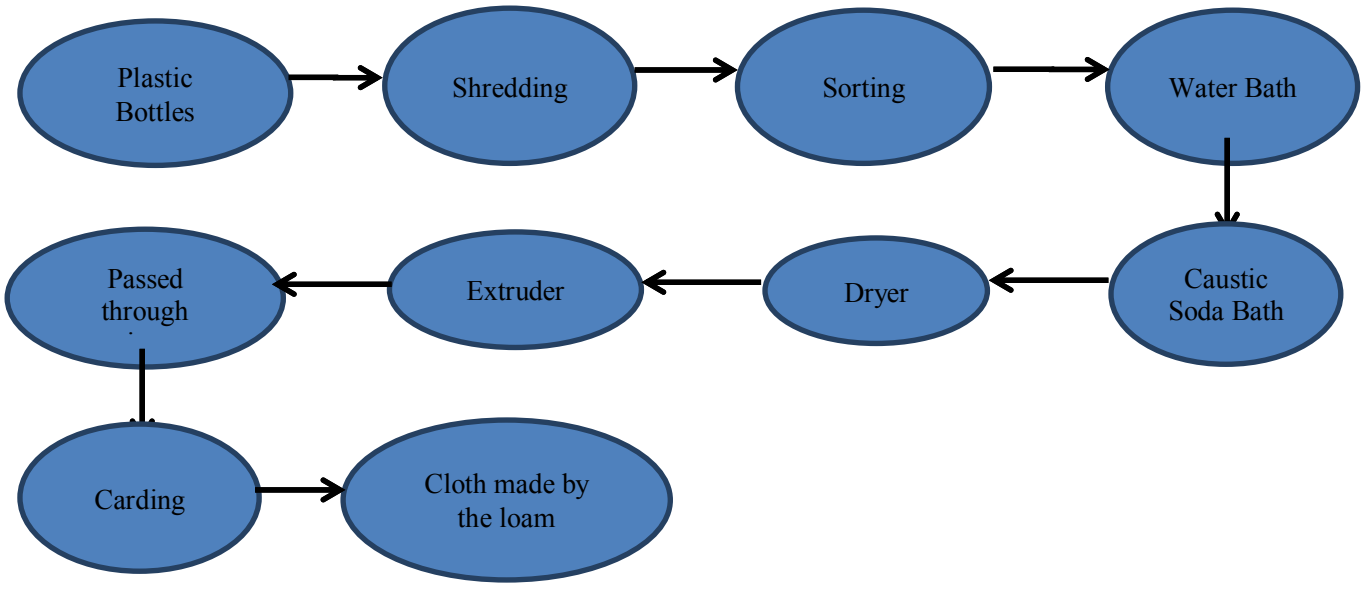

Fig.1. The current process used by xyz ltd to make jeans out of plastic

4.3 Discussion:

We had some queries during our study and we had them cleared by the people who have been working on this project for quite a while.

How do you get people to think differently about their waste i.e. to recycle it? As these jeans are made up from plastic does that has any effect on the looks of it? What are your specific targets for reducing waste through jeans? What was the idea behind starting up with such kind of production? How do you propose to market your product? As these jeans are made up of plastic it can be a concern that these will melt when ironed? Cost of one denim? What message are you trying to convey to the society through your product?
The experts answered these queries quite elaborately. If consumers get aware of the fact that the plastic they throw out on a regular bases can be used up by us to make something valuable they would surely be more inclined to recycle it and help us out. Look and feel seems to be no different to traditional cloth material you can be sure of that. Although the colour of the inner side of the jeans varies according to the type of plastic used in weave. Our target is to better ourselves year after year by using more recycled materials, alternate fibres and less water. Moreover it feels nice that we are contribution in the global waste reduction through it. We all as a team decided to take up something that was trash and make it into something that was both valuable and viable. The end goal is to get people to think a little bit different and help us recycle waste. We definitely assure that this will not be the case. We have it tried and tested. We have tried to make it reasonable for our consumers and price ranges from Rs.4000-6500. Mass media has grown immensely, and with a product like ours I don't think there will be any need for publicity as we are the first ones to introduce such kind of product in the market. Moreover people nowadays are well aware of the waste problems faced by the world so they would surely like to be a part of something which helps to resolve the issue. We are trying to improve the world and influence others to do the same. If we succeed in doing so we'll be more than satisfied.

4.4 Critical issues:

The key issues identified which are challenging in the manufacturing of plastic jeans are:

Complex marketing: It's difficult to convince people to pay a little extra for what they term as garbage or waste to them. Proper marketing strategy have to be set up to make the customer aware of the hazards and the make them realise that they are a part of something big. Even the forecasting is difficult.

Production issues: New Machinery has to be installed as some additional processes have to be done which further increase the cost but it can be recovered over a period of time.

Sorting and quality of plastic available: The plastic quality greatly varies over a wide range. Separating low quality plastic from the required standard quality plastic is thus an important but also a challenging task to do.

Inventory management of raw materials: Additional space has to be made available as we need to store plastic bottles thus adding up the inventory cost.
Processing issues: New processes have to be studied and applied such that an efficient and fast network chain may be set up.

Pricing issues: The price of the jeans may vary from place to place because of the quality of plastic we may get. The people of an economic country like India are highly sensitive to the price of a product. So the product can't be overpriced if it has to stay afloat in the Indian market.

Material handling too much: with the increase of processes the material handling also increases thus it has to be organised else it becomes troublesome.

Collection of raw material: There is no standard way to collect and transport raw material so different methods are applied at different places adding to the cost and trouble.

5. Conclusion

This case study has given an application of reverse logistics by recycling plastic waste in jeans manufacturing and.

In India, the process stated in the case study has already been operating successfully in a couple of regions for a couple of years. But the success of this process all over India that is on a larger scale is still to be proved. Lack of awareness of reverse logistics practices in developing countries like India is a very significant barrier. The key problems faced by the manufacturers have been identified and listed.

It is important to note that even though the use of plastic bottles might seem to be environmentally sound, companies will consider economic as well as logistic implications beforehand as a large sum of capital is stuck in the purchasing of raw material (plastic bottles). From this point of view, it is disadvantageous that the cost of jeans made by plastics is somewhat higher than that of normal jeans. However, this might change if large number of organisations comes forward and compete to bring the cost more close to the normal jeans by improvisation and research. Then it would be feasible to reduce the cost.
However, this is a small price a company has to pay to contribute towards "cleaner and greener environment", as the need of the hour is "sustainable development". Moreover, there are many subsidies or monetary aids are provided by government to organisation that practice eco-friendly manufacturing.

References:

1. Dekker, R. (2006), Focus on Recovery of Value, Rotterdam School of Economics, Erasmus University, Rotterdam.
2. Neumayer, E. (2003), Weak versus Strong Sustainability: Exploring the Limits of Two Opposing Paradigms, 2nd rev. ed., Edward Elgar, Cheltenham.
3. Krikke, H. (1998), "Recovery strategies and reverse logistic network design", Thesis, University of Twente, Enschede.
4. Stock, J.R. (1992), Reverse Logistics, Council of Logistics Management, Oak Brook, IL.
5. Kopicki, R.J., Berg, M.J., Legg, L., Dasappa, V. and Maggioni, C. (1993), Reuse and Recycling: Reverse Logistics Opportunities, Council of Logistics Management, Oak Brook, IL.
6. Flapper, S.D.P. (1996), "Logistic aspects of reuse: an overview", Proceedings of the First International Working Seminar on Reuse, Eindhoven, The Netherlands, pp. 109-18.
7. Kumar, S. and Putnam, V. (2008), "Cradle to cradle: reverse logistics strategies and opportunities across three industry sectors", International Journal of Production Economics, Vol. 115 No. 2, pp. 305-15.
8. Pilar, L.G.T., Dı´az, B.A. and Artiba, H. (2004), "Environmental and reverse logistics policies in European bottling and packaging firms", International Journal of Production Economics, Vol. 88 No. 1, pp. 95-104.
9. Tibben-Lembke, R.S. and Rogers,D.S. (2002), "Differences between forward and reverse logistics in a retail environment", Supply Chain Management: An International Journal, Vol. 7 No. 5, pp. 271-82.
10. Svensson, G. (2007), "Aspects of sustainable supply chain management (SSCM): conceptual framework and empirical example", Supply Chain Management: An International Journal, Vol. 12 No. 4, pp. 262-6.
11. Fleischmann, M. (2001). Quantitative models for reverse logistics. Lecture Notes in Economics and Mathematical Systems, 501.
12. Reverse Logistics Association (2009), "What is reverse logistics?", available at: www.reverselogisticstrends.com/reverse-logistics.php
13. Leo Kroon and Gaby Vrijens Erasmus University, Rotterdam, the Netherlands International Journal of Physical Distribution & Logistics Management, Vol. 25 No. 2, 1995, pp. 56-68.
14. Fargher, H.E. and Smith, R.A. (1996), "Method and system for production planning"
15. Kwok Hung Lau and Yiming Wang "Reverse logistics in the electronic industry of China" Supply Chain

Management: An International Journal Volume 14 · Number 6 · 2009 · 447–465.

16. Ronald S. Tibben, Lembke Dale S. Rogers, (2002),"Differences between forward and reverse logistics in a retail environment", Supply Chain Management: An International Journal, Vol. 7 Iss 5 pp. 271 -282.

17. Ravi V, Shankar R. Analysis of interactions among the barriers of reverse logistics Technological Forecasting and Social Change 2005;72(8):1011–29.

18. T. K. Eltayeb, S. Zailani, and T. Ramayah, "Green supply chain initiatives among certified Companies in Malaysia and environmental sustainability: Investigating the outcomes", Resources, Conservation and Recycling, vol. 55, no. 5, 2011, pp. 495-506.

19. Zhu, Q., Sarkis, J. Lai, K.H., 2007.Green supply chain management: pressures, practices and performance within the Chinese automobile industry. Journal of Cleaner Production 15(11–12), 1041–1052.

20. A.I. Barros et al. / European Journal of Operational Research 110 (1998) 199-214.

21. Farhad Azadivar & Sharon Ordoobadi (2012): Decision rules for recycling returned products, International Journal of Sustainable Engineering, 5:3, 208-219.

22. UNEP, 2004. Why take a lifecycle approach? UNEP Publications: 7. 92-807-24500-9. www.unep.fr/shared/publications/pdf/DTIx0585xPA-WhyLifeCycleEN.pdf

23. Lee, S., 2008. Drivers for the participation of small and medium-sized suppliers in green supply chain initiatives. Supply Chain Management: an International Journal 13(3), 185–198.

24. Times of India Link: http://timesofindia.indiatimes.com/home/environment/pollution/Plastic-waste-time-bomb-ticking-for-India-SC-says/articleshow/19370833.cms

25. Toxics Link, 2001. Rethinking waste management in India, Toxics Link Article, Published in Toxics Link: 20/04/2001 link: http://www.toxicslink.org/art-view.php?id¼9

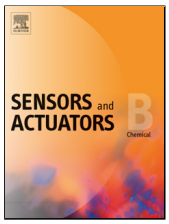

Title: Label-Free Piezoelectric Immunosensor Decorated With Gold Nanoparticles: Kinetic Analysis and Biosensing Application

Author: Ruchika Chauhan Jay Singh Pratima R. Solanki T. Manaka M. Iwamoto T. Basu B.D. Malhotra

PII: S0925-4005(15)30294-X
DOI: http://dx.doi.org/doi:10.1016/j.snb.2015.08.117
Reference: SNB 18972

To appear in: *Sensors and Actuators B*

Received date: 30-6-2015
Revised date: 14-8-2015
Accepted date: 28-8-2015

Please cite this article as: R. Chauhan, J. Singh, P.R. Solanki, T. Manaka, M. Iwamoto, T. Basu, B.D. Malhotra, Label-Free Piezoelectric Immunosensor Decorated With Gold Nanoparticles: Kinetic Analysis and Biosensing Application, *Sensors and Actuators B: Chemical* (2015), http://dx.doi.org/10.1016/j.snb.2015.08.117

Label-Free Piezoelectric Immunosensor Decorated With Gold Nanoparticles: Kinetic Analysis and Biosensing Application

Ruchika Chauhan,[1a] Jay Singh,[2b] Pratima R. Solanki,[3c] T.Manaka,[4d] M.Iwamoto,[5d] T. Basu[6a]* and B.D. Malhotra[7e]

[a]*Amity Institute of Nanotechnology, Amity University Uttar Pradesh, NOIDA India*
[b]*Department of Applied Chemistry & Polymer Technology, Delhi Technological University, Shahbad Daulatpur, Main Bawana Road, Delhi 110042, India*
[c]*Special Centre for Nanoscience, Jawaharlal Nehru University, New Delhi, India*
[d]*Department of Physical Electronics, Tokyo Institute of Technology, Japan*
[e] *Department of Biotechnology, Delhi Technological University, Shahbad Daulatpur, Main Bawana Road, Delhi 110042, India*

Email addresses: [1]ruchikachauhan@hotmail.com, [2]jaimnnit@gmail.com, [3]pratimarsolanki@gmail.com, [4]manaka.t.aa@m.titech.ac.jp; [5]iwamoto.m.ac@m.titech.ac.jp; [6]basu002@yahoo.com, [7]bansi.malhotra@gmail.com.

Abstract

A label-free electrochemical quartz crystal microbalance (EQCM) based immunosensor using self-assembled monolayers of hexandithiol (HDT), cysteamine and 3D gold nanoparticles (AuNPs) was fabricated and utilized for aflatoxin B1 (AFB1, food mycotoxin) detection. The morphology, bonding and optimized experimental conditions of fabricated electrode and immunoelectrode were investigated by scanning electron microscopy (SEM), atomic force microscopy (AFM), Fourier transform infrared spectroscopy (FT-IR) and electrochemical quartz crystal microbalance cyclic voltammetry (EQCM-CV) techniques. This novel Cys/AuNPs/HDT/Au platform was utilized for covalent immobilization of aAFB1. The two linear ranges are observed under optimized experimental conditions i.e 0.008 $ngmL^{-1}$ to 0.3 $ngmL^{-1}$ and 1ng mL^{-1} to 10 ng mL^{-1} that can be used to estimate AFB1 with high sensitivity of 30.96 x 10^{-4} A ng^{-1}mL cm^{-2} and low detection limit of 8 $pgmL^{-1}$ using EQCM-CV. The label free AFB1 detection in noncompetitive mode with high sensitivity and wide linear range is assigned to the confirmation of antibodies and networking of 3D AuNPs on self assembled HDT monolayer. Attempts have also been made to utilize the immnuno sensor for detection of AFB1 in spiked corn flakes samples for validating the observed results.

Keywords: Piezoelectric Immunosensor; Aflatoxin B1; Self-assembled monolayers SAM, AuNPs.

*Corresponding Author; Email address: basu002@yahoo.com

Introduction

Aflatoxin B1 (AFB1) is a carcinogenic mycotoxin produced as a secondary metabolite by *Aspergillus flavus* and *Aspergillus parasiticus* that readily grow on crops such as cereals, nuts, dried fruits, and beans [1-6]. It is highly resistant in nature and cannot be decomposed or broken down even at high temperature. AFB1 occurs in trace amount ranging from ppb level to microgram in per gram of contaminated food stuffs. The European Community Legislation has established 2 µg of AFB1 as the maximum amount permitted per kg (2ppb) [7]. There is an urgent need for detection of AFB1 in a given food stuff to avoid contamination. Although the conventional methods (TLC, HPLC) are sensitive and have low detection limit. However, they are laborious, time consuming, expensive and require skilled personnel. Thus, in order to obtain faster, cost-effective and user friendly technique, immunosensors have been considered as a viable option for the detection of AFB1. Among the various immunosensors, piezoelectric quartz crystal microbalance and electrochemical technique are found to be the most useful tools [8]. They offer higher sensitivity, specificity, selectivity, simplicity and real time monitoring as compared to the existing techniques like surface plasmon resonance and molecular fluoroscence [9-11]. However, it has been projected that the electrochemical detection system based on QCM (EQCM) electrode may perhaps yield higher sensitivity, wider detection range, fast response time and lower detection limit for AFB1 quantification as compared to the QCM frequency measurement under identical conditions by monitoring mass and conductivity simultaneously [12]. Moreover, EQCM provides multiple piezoelectric information concurrently in an electrochemical process, including the electron motional conductivity and the resonant frequency.

The reliability of an immunosensor depends on the orientation and accessibility of the antibodies and interaction process (antibody-antigen interaction) on the probe surface [13, 14]. However, self assembled monolayer (SAM) with a tail functional group may provide a molecularly oriented layer to orient the antibodies over the crystal surface in a manner that could perhaps be reproducible, stable, and selective to the corresponding antigen [15]. AFB1, being a small molecule, cannot be presently determined without labeling and the competitive mode [16-19]. The major challenges facing the competitive system are the requirement of multi steps and chemicals wherein the use of the label may influence the actual immuno-interaction either positively or negatively. In a previous study, we observed that the 4-amino thiophenol SAM terminated with the NH_2 group on gold coated quartz crystal has helped to orient antibodies towards AFB1 and facilitated the label-free detection of AFB1 with EQCM technique with the LOD of 0.08ngmL^{-1}. The SAM modified metal nanoparticles provide large surface area for biomolecule immobilization, fast electron transfer rate and fine tuneability. The metal nanoparticles film has also been used as an interface for electron transfer of redox-active protein and the electrode [20, 21]. Among various nanomaterials, AuNPs have attracted much attention due to their large specific surface area, biocompatibility and highly tunable property [22-24]. Additionally, AuNPs provide more freedom to biomolecules to orient the conformations more favorable for direct electron transfer, to the active sites of conducting electrode [25]. Liu et al. have reported HDT-AuNPs modified surface for tyrosinase biosensor using physical adsorption of enzyme over AuNPs and obtained high response rate, sensitivity, and fabrication simplicity [26]. The physical adsorption of biomolecule over the electrode provides limited stability of biomolecules. Morel et.al. demonstrated that the SAM of HDT functionalized with 3D AuNPs and mercaptoundecanoic acid, can be covalently linked with IgG [27]. The disadvantage of this design is that the Fc portion of antibody is exposed towards AFB1 which hinders the

accessibility of aAFB1 towards AFB1. Therefore, in the present investigation a SAM layer of HDT, followed by 3D AuNPs layer was deposited on the QCM electrode. The dithiol has an advantage of absorbing AuNPs through Au-S linkage to provide a 3D net work. The 3D AuNPs layer was further functionalized with cysteamine to link with aAFB1 through the Fc portion that may orient the Fab part towards AFB1 for label-free real time monitoring of AFB1 using EQCM cyclic voltammetry (EQCM-CV) as a measuring tool in the non-competitive format. During the fabrication process, each layer was washed thoroughly prior to addition of the next layer to remove the non-bonded material. Thus fabricated BSA/aAFB1/Cys/AuNPs/HDT/Au immunoelectrode offers a detection limit of 8pg/ml which is attributed to unique orientation of AuNPs coated HDT SAM layer obtained by the EQCM measuring technique.

2 Experimental Methods

2.1. Chemicals and Reagents

Monoclonal anti-aflatoxin B1 (aAFB1) antibody, aflatoxin B1 (AFB1), bovin serum albumin (BSA), HDT, cysteamine, aurochloric acid ($HAuCl_4$), tri sodium citrate, *N*-ethyl-*N*-(3-dimethylaminopropyl) carbodiimide (EDC), and *N*-hydroxysuccinimide (NHS) were procured from Sigma-Aldrich. All other chemicals were of analytical grade and were used without further purification. The de-ionized water (18MΩ cm) was used for the preparation of buffer solutions. The gold coated (6.7 mm dia) quartz resonator (AT cut quartz crystal, 13.7 mm dia, 6MHz) was procured from Autolab, Netherlands. The thickness of Au coating was 1000 A°. The oscillation frequency of AT cut quartz crystal was 6MHz (Autolab Manual).

Solutions Preparation

Anti-AFB1antibody (1 $mgmL^{-1}$) solution was prepared in 50 mM phosphate buffer {(PB), pH 7.4} and a 0.15M NaN_3 was used as a preservative. The AFB1 solution was prepared in PB (50 mM, pH 7.4) with 10% methanol and stored at -20 °C. A solution of BSA (1 $mgmL^{-1}$) was prepared in PB (50 mM, pH 7.0) and used as the blocking agent for nonspecific binding sites.

2.3 Preparation of cereal samples

The extracts of cereal samples (corn flakes) were spiked with various concentration of AFB1 solution. Cornflakes samples were crushed to powder using a hand-held blender. 2g of powdered cereals were added to methanol: water (7:3, v/v) solution on a sonication bath for 45 min. Extract was centrifuged for 7 min at 5000 rpm to remove the solids. The supernatants were collected and allowed to evaporate to dryness under nitrogen at room temperature (34°C). The residues were re-suspended in 5 mL PBS and filtered through 0.45 µm cut-off Whatman nylon membranes [28]. Finally, the extract was spiked with the different concentration of 0.05, 2 and 5 $ngmL^{-1}$ of AFB1.The BSA/aAFB1/Cys/AuNPs/HDT/Au was dipped in a cell containing spiked extract and incubated for 35 min.

2.4 Pretreatment of quartz crystals

The quartz crystals were immersed in 1M NaOH for 5 min and 1M HCl for 2 min in sequence after which the freshly prepared piranha solution (1:3 (30% v/v) H_2O_2–H_2SO_4) was dropped on the gold surface for 2 min, with special care to avoid contamination of the electrode leads. The crystals were rinsed with deionized water followed by ethanol and dried under stream of nitrogen at each pretreatment and then the initial resonance frequency (F_0) was recorded. After the cleaning procedure, the crystal was ready for surface modification and the antibody immobilization.

2.5 Synthesis of Gold Nanoparticles (AuNPs)

AuNPs suspension was synthesized by reduction of chloroauric solution ($HAuCl_4$) with sodium citrate. Briefly, 10 mL of 0.01% $HAuCl_4$ solution was heated to boil with gentle stirring, followed by the drop wise addition of 1% trisodium citrate solution till the color of the solution changed from yellow to red. The boiling was continued for an additional 10 min.

Then, the solution was cooled with continuous stirring until it attained room temperature (25 °C) and stored at 4°C. The resulting solution was characterized by UV-Vis spectroscopy. For AuNPs, the characteristic absorption peak was obtained approximately at 522 nm (data not shown).

2.6 Preparation of AuNPs/HDT/Au coated Quartz Crystal electrode

The piezoelectric immunosensing electrode was fabricated for label-free detection of AFB1 using AuNPs decorated SAM of hexanedithiols on gold electrode to bind the aAFB1. The desired quartz crystal was treated with various concentrations (0.5 to 4 mM) of HDT solution in ethanol for 12h to 24 h at room temperature (25°C). The HDT concentration was optimized with EQCM-CV and corresponding changes in frequency were observed (data not shown). However, it was found that 4 mM concentration of HDT for 16 h was adequate to prepare self assembled HDT layer on Au electrode (HDT/Au). The unbound HDT molecules were washed with ethanol followed by rinsing with water from HDT/Au electrode, as confirmed by EQCM-CV and frequency measurements. The HDT/Au electrode was covered with 10 µL of AuNPs solution for 4 h to obtain the AuNPs/HDT/Au electrode. The AuNPs/HDT/Au electrode was further immersed in 4 mM aqueous solution of cysteamine (Cys) overnight to functionalize AuNPs to prepare the AuNPs/HDT/Au electrode. All the electrodes were washed with the desired solvent and dried under nitrogen stream. The deposition of each layer was monitored by frequency change as well as by EQCM- CV.

2.7 Fabrication of aAFB1/ Cys/AuNPs/HDT/Au immunosensor

The optimized concentration of 40 μgmL^{-1} of aAFB1 antibody was used for fabrication of the aAFB1/Cys/AuNPs/HDT/Au immunoelectrode as determined as in our recent work. Firstly, aAFB1 antibody was activated with 0.2M EDC and 0.05M NHS for about 2 h. Then, 10 µL of activated aAFB1 antibody solution was spread over Cys/AuNPs/HDT/Au electrode and incubated overnight at 4 °C for the amide bond formation between aAFB1 and cysteamine. The covalent immobilization through EDC/NHS provides a linker less immobilization of antibodies with minimum cross reactions [29-32]. The non-specific sites of fabricated aAFB1/Cys/AuNPs/HDT/Au immunosensor were blocked by BSA ($1mgmL^{-1}$). These fabricated BSA/aAFB1/Cys/AuNPs/HDT/Au immunoelectrodes were utilized for AFB1 detection using EQCM-CV techniques. At each stage of the deposition, the bioelectrode was washed with PBS buffer pH 7.0 and monitored by frequency change and electrochemical studies with EQCM-CV.

2.8 Instrumentation

The resonant frequency of quartz crystal and electrochemical studies were monitored by Autolab Potentiostat/Galvanostat Model AUT83945 (PGSTAT302N). The CV studies were carried out in a three electrode cell using BSA/aAFB1/Cys/AuNPs/HDT/Au as the working electrode, gold wire (Au) as the auxiliary electrode, and saturated Ag/AgCl as the reference electrode in PBS, (50 mM, pH 7.4, 0.9% NaCl) containing 5 mM $[Fe(CN)_6]^{3-/4-}$ as a redox mediator. The structural and morphological characterization of HDT/Au, AuNPs/HDT/Au, Cys/AuNPs/HDT/Au, *a*AFB1/Cys/AuNPs/HDT/Au, BSA/*a*AFB1/Cys/AuNPs/HDT/Au, and AFB1/BSA/*a*AFB1/Cys/AuNPs/HDT/Au bioelectrodes were carried out by scanning electron microscopy from ZEISS Model EVO-18 surface topography are studied by atomic force microscope (Park Systems XE-70), Raman spectra from Varian-FT Raman spectrometer Series II, and Fourier Transform Infrared Spectrometer from Perkin-Elmer, Model 2000 was employed for the FT-IR studies.

2.9. AFB1 detection

The detection of AFB1 was carried out by electrochemical quartz crystal microbalance cyclic voltammetry (EQCM-CV) analysis. The resonant frequency and electrochemical cyclic voltammetry (EQCM-CV) studies of BSA/aAFB1/Cys/AuNPs/HDT/Au electrodes were carried out in PBS buffer under optimized

experimental conditions. The EQCM-CV studies were conducted in a three electrode cell (Fig.1) using a modified quartz crystal as the working electrode, gold wire (Au) as the counter electrode, and saturated Ag/AgCl as the reference electrode in phosphate buffer saline (PBS, 50 mM, pH 7.4, 0.9% NaCl) containing 5 mM $[Fe(CN)_6]^{3-/4-}$ as a redox species. All experiments were performed in triplicate and the experimental temperature was controlled at 25℃.

2.10. Preparation of spiked cereal extract

Cereal samples (corn-flakes) were crushed to powder using a hand-held blender and extract with mathanol. The details of extraction procedure of corn flakes sample were described in our previous study [33]. Finally, the extract was spiked with the concentrations of 0.05, 2 and 5 ng mL^{-1} of AFB1.

2.11. Shelf life or Stability of BSA/aAFB1/Cys/AuNPs/HDT/Au immunoelectrode

The stability of immunoelectrodes was monitored at a regular interval of 5 days. 30 sets of BSA/aAFB1/Cys/AuNPs/HDT/Au immunoelectrodes were prepared and stored at 4℃. The response studies of the three electrodes (BSA/aAFB1/Cys/AuNPs/HDT/Au) were investigated after 5 days via EQCM-CV in PBS (50mM, pH 7.4, 0.9% NaCl) in presence of 2 $ngmL^{-1}$ standard AFB1 solutions and average was noted. After 5 days, the response of another three set of BSA/aAFB1/Cys/AuNPs/HDT/Au electrodes were measured.

3. Results and discussion

3.1. Characterization of the Immunoelectrode

3.1.1 EQCM-CV of Immunelectrode

Fig. 2A shows the change in frequency of QCM (*ΔF*) after the SAM deposition of HDT on the bare gold crystal surface obtained using EQCM at a scan rate of 100 mV/s in the potential range of − 0.2 to 0.8 V. The cleaned bare quartz crystal was taken as a reference. The change in the frequency of oscillation (Δf) is sensitive to the change in mass deposited on the crystal surface (Δm) meaning that any variation in mass of the electrode or thickness of the deposited material will proportionally change the frequency at which the crystal oscillates. The relationship between Δf and Δm is given by the Sauerbrey equation (1):

$$\Delta f = -C_f . \Delta m \quad \ldots\ldots\ldots\ldots\ldots\ldots\ldots\ldots (1)$$

Where;

Δf is the change in frequency (Hz), C_f is the sensitivity factor of the crystal (0.0815 Hz·ng-1·cm-2 for a 6 MHz at 20 °C) and Δm is the change in mass per unit area (g·cm-2). The changes in mass deposition and number of atoms/molecules present at each layer of fabrication have been calculated using the above Sauerbrey equation (Table 1). The frequency change of 8.9 Hz is observed upon HDT deposition, which corresponds to 4.3×10^{14} number of molecules present onto the gold surface and the mass change (Δm) is found to be 109.2 ng/cm^2 (Table 1). The observed frequency change (*ΔF*) of 10.16 Hz for the AuNPs deposition corresponds to 124.66 ng/cm^2 (9.4 x 10^{14} atoms). On functionalization of AuNPs/HDT/Au electrode with cysteamine the frequency change of 12.7 Hz occurs, which corresponds to the $8.2x10^{14}$ no. of atoms. The immobilization of activated monoclonal anti aflatoxin antibodies (aAFB1) on Cys/AuNPs/HDT/Au electrode results in the frequency change corresponding to 269.49×10^{10} molecules (Table1) [Fig, 2A (d, e)]. The successive increase in mass and changes in the number of atoms/molecules confirms the formation of immunobioelectrode.

Fig.2B shows CV of a bare Au electrode (curve a), HDT/Au electrode (curve b), AuNPs/HDT/Au electrode (curve c), Cys/AuNPs/HDT/Au electrode (curve d), aAFB1/Cys/AuNPs/HDT/Au (curve e) and BSA/aAFB1/Cys/AuNPs/HDT/Au immuno electrode (curve f) in PBS, 50 mM, pH 7.4, 0.9% NaCl containing 5 mM $[Fe(CN)_6]^{3-/4-}$ at a scan rate of 100 mV/s in the potential range of − 0.2 to 0.8 V. As compared with CV of the bare gold electrode (curve a), the magnitude of anodic peak current (4.85 $x10^{-4}$ A) decreases indicating formation of the insulating self assembled HDT thiol monolayer on the QCM

electrode. The deposition of AuNPs on HDT/Au leads to an increase in peak current to 6.1 x 10^{-4} A (curve c) since absorbed AuNPs layer acts as a conducting wire or electron-conducting tunnel [34]. The cysteamine functionalized electrode surface (Cys/AuNPs/HDT/Au) shows decrease ($4.07x10^{-4}$) in amplitude of response current (response (curve d) due to insulating nature of cysteamine.

The peak current increases to 6.3 x 10^{-4} A for the aAFB1/Cys/AuNPs/HDT/Au immuno bioelectrode due to presence of the polar groups such as carboxyl and amine moieties in the aAFB1antibody (curve e). We have observed an increase in the magnitude of current of 6.9 x 10^{-4} A for the BSA/aAFB1/Cys/AuNPs/HDT/Au after immobilization of BSA indicating enhanced electron-transfer introduced upon assembly of BSA layer (curve f).

The CV of BSA/aAFB1/Cys/AuNPs/HDT/Au immuno electrode (Fig. 2C) as a function of scan rate from 20 to 100 mV s^{-1} was investigated. It can be seen that the magnitudes of cathodic (*Ipc*) and anodic (*Ipa*) peak current increase linearly with square root of the scan rate (Fig. 2C: inset), revealing that electrochemical reaction is a diffusion-controlled process [11] The slopes and intercepts are given by the following Eq. (2-3):

$Ipa = -2.51 \times 10^{-4}$ (A) + 7.125×10^{-4} (A^2 mV^{-1} s) ½ * [scan rate (mV s -1)] ½ Eq. (2)

$Ica = 1.521 \times 10^{-4}$ (A) – 0.0017 (A^2 mV^{-1} s) ½ * [scan rate (mV s -1)] ½ Eq. (3)

The anodic (*Epa*) and cathodic (*Epc*) peak potentials are shifted as scan rate increases. The difference between anodic and cathodic peak potential (ΔE) increases with scan rate with value of linear regression coefficient as 0.9933. This indicates facile charge transfer kinetics in the range, 20 – 100 mV/s scan rate. These results (Fig. 2D, and inset) reveal that the AuNPs/HDT/Au electrode can be used for the immobilization of aAFB1, providing sufficient accessibility to electrons, to shuttle between the antibodies and the electrode. The value of diffusion co-efficient (D) of the redox species from the electrolyte to the BSA/aAFB1/Cys/AuNPs/HDT/Au immuno electrode was calculated using the Randles–Sevcik equation [35].

$Ip = (2.69 \times 10^5)\, n^{3/2} A D^{1/2} C \nu^{1/2}$ Eq. (4)

where Ip is the peak current of the immuno electrode (*Ipa* anodic and *Ipc* cathodic), n is the number of electrons involved or electron stoichiometry (1), A is the surface area of the immuno electrode (0.28 cm^2), D is the diffusion co-efficient, C is the concentration of the redox species (5 mM $[Fe(CN)_6]^{3-/4-}$) and ν is the scan rate (100 mV s^{-1}). The D value is obtained as 2.375 x 10^{-3} cm^2 s^{-1}. The surface concentration of the BSA/aAFB1/Cys/AuNPs/HDT/Au immuno electrode can be estimated from the plot of current versus potential (CV) using the Brown-Anson model [36], via the following equation.

$Ip = n^2F^2gA\nu/4RT$ Eq. (5)

where n is the number of electrons transferred (1), F is the Faraday constant (96485 C mol^{-1}), g is the surface concentration of the corresponding electrode (mol cm^{-2}), A is the surface area of the electrode (0.28 cm^2), ν is the scan rate (100mVs^{-1}), R is the gas constant (8.314 J $mol^{-1}K^{-1}$) and T is room temperature (25℃). The surface concentration of aAFB1/Cys/AuNPs/HDT/Au (2.55 x10^{-8} mol cm^{-2}) is lower than that of the BSA/aAFB1/Cys/AuNPs/HDT/Au bioelectrode (2.64 x 10^{-8}mol cm^{-2}) electrode surface, while higher than Cys/AuNPs/HDT/Au (1.67x 10^{-8} mol cm^{-2}) electrode. The value of the heterogeneous electron transfer rate constant (Ks) obtained for the BSA/aAFB1/Cys/AuNPs/HDT/Au immuno electrode was calculated from the Lavrion model [37];

$Ks = mnF\nu/RT$ Eq. (6)

where m is the peak-to-peak separation (0.23 V), F is the Faraday constant (96 485 C mol^{-1}), ν is the scan rate (100 mV s^{-1}), n is the number of transferred electrons (1), R is the gas constant (8.314 J $mol^{-1}K^{-1}$) and T is room temperature (25 ℃). The value of Ks is found to be 0.895 s^{-1}, which indicates fast electron transfer between the immobilized antibodies and electrode due to the presence of AuNPs.

3.1.2. Scanning Electron Microscopy (SEM) Studies

The surface morphology of HDT/Au electrode, AuNPs/HDT/Au, Cys/AuNPs/HDT/Au electrode, aAFB1/Cys/AuNPs/HDT/Au and BSA/aAFB1/Cys/AuNPs/HDT/Au immuno electrode was investigated by scanning electron microscopy [Fig 3A (a) and (b)]. Image 2A shows the uniformly distributed spherical AuNPs of average diameter 60.23±5.3nm on HDT/Au electrode whereas the inset (i) and (ii) indicate uniformly deposited self assembled HDT monolayer on (HDT/Au) QCM crystal and cysteamine functionalized AuNPs particles (AuNPs/HDT/Au), respectively. The rough and dense surface morphology seen in image 2A (b) reflects the immobilization of aAFB1 on Cys/AuNPs/HDT/Au electrode. The change in surface as indicated by Fig 3A (b): inset (i) confirm immobilization of BSA to avoid non-specific binding and inset (ii) reveals binding of the AFB1 on the BSA/aAFB1/Cys/AuNPs/HDT/Au immuno electrode.

3.1.3. Atomic force microscopy (AFM) studies

AFM measurements of dried surfaces were conducted in the non-contact mode. A topographic image was taken on 1μm×1μm surface. In order to compare the topology of each surface, surface roughness (*R*a) and root mean square roughness (*R*q) were estimated from the AFM images [38]. Fig.3B exhibits surface morphology of the bare Au (image a), AuNPs/HDT/Au (image b), Cys/AuNPs/HDT/Au (image c), aAFB1/Cys/AuNPs/HDT/Au (image d) and AFB1/BSA/aAFB1/Cys/AuNPs/HDT/Au (image e) bioelectrode. The *R*a and *R*q values of bare gold are found to be as 0.90 nm and 1.14 nm, respectively. The bare gold electrode shows surface roughness due to the nucleation generated during the nucleation stage [39]. The surface roughness of bare Au and HDT/SAM electrode was almost similar (Ra= 0.99 nm and Rq= 1.19 nm) (data not shown), revealing a highly ordered and densely packed self assembled layer of HDT layer on QCM electrodes. The values of *R*a and *R*q for the AuNPs/HDT/Au electrode are found to be 1.23 nm and 2.15 nm, respectively. The surface topology of Cys/AuNPs/HDT/Au electrode (QCM crystal) changes with the considerable increase values of Ra and Rq of 2.17 nm and 3.73 nm, it reveals that cysteamine is oriented on the embedded AuNPs via self assembling. Due to immobilization of monoclonal aAFB1 immobilized on the Cys/AuNPs/HDT/Au electrode surface, Ra and Rq are found 2.36 nm and 3.76 nm, respectively. The topological image of each layer reflects ordered successive assembly of HDT, AuNPs and cysteamine. The average surface roughness and root mean square roughness of aAFB1/Cys/AuNPs/HDT/Au immuno electrode increase due to the configuration change and the presence of paratope on antibody, indicating immobilization of aAFB1 (antibody) on the Cys/AuNPs/HDT/Au electrode. On interaction with the antigen, the *R*a and *R*q values decrease to 1.41 nm and 2.29 nm indicating that surface becomes less rough due to the interaction of the antigen with the paratope at antibody. These results confirm the intraction of antigen with antibody.

3.1.4. Raman and FT-IR studies

The Raman spectra of HDT/Au, AuNPs/HDT/Au, Cys/AuNPs/HDT/Au and aAFB1/Cys/AuNPs/HDT/Au electrodes are shown in Fig. 4A. The intense band seen at 680cm^{-1} (S-Au stretching) and the absence of band at 2586 cm^{-1} (S-H stretching) in Raman spectra of HDT/Au electrode (Fig. 4A (a)) confirm the formation of S-Au bond. The inset in Fig. 4A a shows the spectra obtained for the HDT solution (spectra a). On grafting of the

AuNPs, the Raman signal is found to be enhanced due to the surface enhanced Raman spectroscopy (SERS) effect [40,41]. The Raman spectra of AuNPs/HDT/Au surface, (Fig. 4A (b) reveals the presence of characteristic two intense bands at 1023 and 1245 cm^{-1}, corresponding to the C–O vibration of citrates indicating presence of the ligands stabilizing the nanoparticles. The Raman spectrum of cysteamine functionalized Cys/AuNPs/HDT/Au electrode surface shows one additional band at 3252cm^{-1} for N-H vibration of -NH_2 group indicating presence of the cysteamine. The, characteristic bands found peratining to C=O and N-H at 1686 and 1545 cm^{-1} in the Raman spectra (Fig. 4A (d) of the aAFB1 of the immobilized surface reveals the formation of the amide bond between – COOH of aAFB1 and -NH_2 of cysteamine.

Fig.4B (a-d) shows FT-IR spectra of the HDT/Au, AuNPs/HDT/Au, Cys/AuNPs/HDT/Au and aAFB1/Cys/AuNPs/HDT/Au immunoelectrodes between 500-3500 cm^{-1}. The band at 754 cm^{-1} (Fig 4B (a) indicates the presence of a covalent Au-S bond on HDT/Au electrode. On grafting of AuNPs on the surface of HDT/Au electrode, the bands seen at 1107 and 1297 cm^{-1} in the FT-IR spectrum of AuNPs/HDT/Au electrode (curve b) due to the stretching and bending of C-O and band at 1668 cm^{-1} due to the stretching of C=O of citrate ion confirms presence of the AuNPs. When AuNPs/HDT/Au surface is functionalized with cysteamine, an additional peak is found at 3427 cm^{-1} corresponds to the N-H stretching of NH_2 group present at cysteamine (Fig. 4B(c)). After immobilization of aAFB1 on Cys/AuNPs/HDT/Au electrode surface, an amide I at 1608 cm^{-1} corresponding to carbonyl C=O stretching vibration, amide II band at 1527 cm^{-1} due to the coupled C-N stretching and NH bending mode indicate successful immobilization of aAFB1 (Fig. 4B(d). The NH_2 groups of cysteamine bind with COOH group of (fragment crystallisable (Fc)) aAFB1 forming amide linkage on the Cys/AuNPs/HDT/Au surface [15]. However, on immobilization of BSA on aAFB1/Cys/AuNPs/HDT/Au immuno electrode, the bands remain unchanged due to BSA (data not shown).

3.5 Operational parameters *BSA/aAFB1/Cys/AuNPs/HDT/Au immunosensor*

The operational parameters of the bioelectrode were investigated with variation of the concentration of antibody (aAFB1), operating pH and the incubation time for aAFB1 antibody and AFB1 interaction over the electrode. The response studies of the immuno bioelectrode were carried out at optimized pH 7.4. At this pH, maximum interaction between antigen and antibody takes place. It is observed that after 35 min of incubation, optimum change in current occurs. Thus 35 min of incubation time at pH 7.4 PBS was used for the entire experiments. All these parameters are described in our previous work [12].

The AuNPs/HDT/Au electrode surface was also studied with various concentration of AFB1 to determine surface activity of the matrix. It illustrates that the fabricated AuNPs/HDT/Au QCM electrode does not show any significant recognition towards AFB1 (See supplementary file Fig. S1 and S2).

3.6. Response studies o*f the immunosensor*

The response study of BSA/*a*AFB1/Cys/AuNPs/HDT/Au immuno electrode was investigated using EQCM-CV in PBS containing $[Fe(CN)_6]^{-3/-4}$ from - 0.2V to 0.8V at 100 mV/s scan rate as a function of AFB1 toxin concentration (0.008 $ngmL^{-1}$ to 10ng mL^{-1}). It is found that magnitude of the current decreases after increasing the concentration of AFB1 over the BSA/*a*AFB1/Cys/AuNPs/HDT/Au immuno electrode. This may perhaps be due to hindrance in electron transfer to the electrode after the adsorption of AFB1 onto the BSA/*a*AFB1/Cys/AuNPs/HDT/Au immuno electrode. Interestingly, two calibration curves are observed, one for lower concentration (0.008 $ngmL^{-1}$ to 0.3 $ngmL^{-1}$) and another for higher concentration (1 $ngmL^{-1}$ to 10 $ngmL^{-1}$). The Fig. 5A: Inset shows the calibration plot obtained between anodic peak current and AFB1 concentration for two different ranges. The corresponding linear relation follows the following equations:

I (A) = (6.243 x 10^{-4}A $ng^{-1}mL^{-1}$) -8.67 x10^{-4} $A^{-1}ng^{-1}mL^{-1}$) [AFB1] $ngmL^{-1}$ with a regression coefficient of ca. 0.9823, ... Eq (7)
I (A) = (3.858 x 10^{-4}A/ng/mL) -3.54 x10^{-5} $A^{-1}ng^{-1}mL^{-1}$) [AFB1] $ngmL^{-1}$ with a regression coefficient of ca. 0.9912 respectively. .....Eq (8)
The sensitivity of immunosensor is 30.96 x10^{-4} A $ng^{-1}mLcm^{-2}$ and detection limit of 8 pg mL^{-1} is obtained from the calibration curve. The association constant (K_a) with EQCM-CV obtained as 7x10^{-2} $ngmL^{-1}$ is calculated using a Lineweaver-Burke plot. The high value of *Ka* indicates high affinity of AFB1 towards BSA/aAFB1/Cys/AuNPs/HDT/Au immuno sensor. It can be noted that the conformational changes of antibodies affect the interaction with AFB1. The high K_a value indicates strong interaction of AFB1 with BSA/aAFB1/Cys/AuNPs/HDT/Au immuno sensor surface due to favorable orientation of aAFB1 on the modified surface of QCM electrode. Moreover, the current response of the BSA/aAFB1/Cys/AuNPs/HDT/Au immuno electrode was determined at different frequencies as a function of different concentration of AFB1. The extent of change in frequency is found to increase on addition of AFB1. This can be attributed to the formation of AFB1–aAFB1 complex. The calibration plot (Inset: Fig 5B) shows a linear relationship between 0.008 ng mL^{-1} to 0.3 $ngmL^{-1}$ and 1 $ngmL^{-1}$ to 10$ngmL^{-1}$. Two regression equations with the two ranges are given as follows:
ΔF (Hz) = 30.67 + (98.53) [AFB1] $ngmL^{-1}$ regression coefficient 0.990, and..... Eq. (9)
ΔF (Hz) = 33.99 + (27.89) [AFB1] $ngmL^{-1}$ regression coefficient 0.986, respectively Eq. (10)
This corresponds to the sensitivity of 351.89 Hz $ng^{-1}mL\ cm^{-2}$ for AFB1. The positive slope of the linear equation is due to change in the frequency plotted instead of absolute frequency (Eq 9 and 10). The high sensitivity, wide linear range and low detection limit (8 pg mL^{-1}) can be ascribed to the molecularly oriented HDT film, chemi-absorption of AuNPs with the thiol group of HDT and functionalization of AuNPs with cysteamine to bind covalently with COOH group of antibody and electrochemical detection of immuno interaction through EQCM technique. In this study, AuNPs are sandwiched between the two SAM layers hexane dithiol and cysteamine layer. The AuNPs over the dithiol layer are uniformaly distributed providing a enhanced area and higher sensitivity to the electrode. The final surface layer comprises of cysteamine having NH_2 group as an active functional group which can bind with antibodies only through COOH group of Fc portion. These results confirm the orientation of the antibodies. It appears that the multilayer molecularly oriented electrode is perhaps responsible for the observed LOD upto 8 $pgmL^{-1}$.
Fig.6 shows the stepwise fabrication of the BSA/aAFB1/Cys/AuNPs/HDT/Au immuno sensor along with the biochemical interaction between AFB1 and aAFB1 on the Cys/AuNPs/HDT/Au electrode surface. The high sensitivity, LOD value and linear range of the response current on the immuno sensor can be attributed to enhanced surface area with high electron transfer rate offered by AuNPs embedded molecularly oriented SAM of HDT on Au electrode, covalent binding via cysteamine with the Fc part of aAFB1 through amide linkage to offer an oriented layer of aAFB1 to interact efficiently with AFB1 [15].

Table 2 represents characteristics of the BSA/aAFB1/Cys/AuNPs/HDT/Au immuno sensor along with those reported in literature. From the literature it is observed that the fabricated AFB1 sensing platform is competitive, labeled and is a multi antibody based system, while the developed immuno sensor is simple, label free, highly sensitive, and offers low LOD and wide linear range [8,13, 18, 42, 43]. There are mainly three factors that perhaps contribute to the enhanced sensitivity, LOD and linear range of the fabricated immunoelectrode (BSA/aAFB1/Cys/AuNPs/HDT/Au immuno). These are (i) orientation of the antibodies: the advantage of SAM layer is to provide molecularly oriented layer that finally governs the orientation of covalently linked aAFB1 so that these can access the AFB1 through the Fab part [29] (ii) enhanced surface area and high conductivity: The presence of

3D AuNPs between the HDT SAM layer and cysteamine increases surface area and loading of aAFB1 as well as makes a direct contact between aAFB1 and electrode due to decrease of interfacial resistance [24, 26]. (iii) higher sensitivity of EQCM [12,33] is due to the miniaturized electrode.

3.7. Real sample testing with BSA/aAFB1/Cys/AuNPs/HDT/Au immunosensor

Corn flakes samples followed by an extraction procedure with a methanolic solution of potassium bicarbonate were used as a real sample. Evaporation to dryness and final reconstitution in PBS buffer were necessary to avoid inhibition of the antibody-antigen binding caused by methanol. The extract of the samples were spiked with three different concentrations of AFB1 (0.05, 2 and 5ngmL^{-1}) to examine applicability of the proposed probe. The EQCM-CV of BSA/aAFB1/Cys/AuNPs/HDT/Au immunosensor, examined with the cornflakes extract in PBS, reflects the minimum interference. Variation of the peak current in blank and the cornflakes extract shown in Fig.7 (bar 1, 2) occurs within 5%. It indicates that the BSA/aAFB1/Cys/AuNPs/HDT/Au immunosensor shows its specificity towards the AFB1, not inflated with other constituents present in the cornflakes sample. However, the response of the BSA/aAFB1/Cys/AuNPs/HDT/Au immunosensor changes when the cornflakes sample contains AFB1 and magnitude of the anodic peak further decreases as the AFB1 concentration increases in the cornflakes sample. The results were obtained in triplicate of experiments sets with the extracted solution in PBS within 3-5% variations reveal that the developed immunosensor is highly specific to AFB1.

3.8. Reproducibility and Regeneration of Immunoelectrode

The reproducibility of BSA/aAFB1/Cys/AuNPs/HDT/Au immunosensor was investigated under optimized experimental conditions at 5 ngmL^{-1} of AFB1. The average current response of three parallel experiments is obtained as 2.07x10^{-4} A, and the relative standard deviation (R.S.D.) is 1.19x10^{-5}. The immunosensor can be regenerated by 0.1 molL^{-1} glycine-HCl buffer solution at pH 2.3 for 10 min, followed by washing with PBS 3-4 times to desorbs. The regenerated immunosensor was investigated at a concentration 5 ngmL^{-1}. The current response of BSA/aAFB1/Cys/AuNPs/HDT/Au immunosensor reveals that it can be used for 6-8 times with 8-10% loss of activity. After the 6th cycle a marked decline (35-40%) is noticed. The loss in activity is perhaps due to denaturation of the antibodies. The regeneration was performed in triplicate of experimental sets at 25℃. After six detection cycles the used quartz crystals were rinsed with piranha solution to remove all the unutilized molecules present on absorbed on the gold surface of crystal.

3.9. Shelf life of BSA/aAFB1/Cys/AuNPs/HDT/Au electrode

The shelf lives of the electrodes were studied at a regular interval of 5 days. Fig. 8 shows the result with error bars of the three set of experiments. The immuno electrode retains its activity up to 20 days with 5-9 % decrease in activity. After 20 days, the immunoelectrode response decreases to 18-22%. This can be attributed to degradation of aAFB1 activity. The stability of the electrode depends on activity of the biomolecule and the materials (HDT SAM layer and AuNPs) used for fabrication. Among these, if any one of loses stability, response current is affected. Here, stability refers to the integrated stability of the bioelectrode. To investigate it further, we studied stability of the Cys/AuNPs/HDT/Au electrode. It was found that these Cys/AuNPs/HDT/Au electrodes were stable more than 45 days at 4 ^{0} C. For longer device-life, the bioreceptors can be replaced with the advanced synthetic receptors like aptamers, molecular imprinted polymer (MIP) and mimotopes etc.

Conclusions

A label free immunosensor based on complex self assembled monolayer consisting of HDT, decorated with cysteamine functionalized AuNPs on PQC has been developed to detect AFB1 toxin in the non-competitive environment using EQCM-CV tool. This immunosensor (BSA/aAFB1/Cys/AuNPs/HDT/Au) exhibits two linear detection ranges: one for lower

concentration from 0.008 ngmL^{-1} to 0.3 ngmL^{-1} and another for the higher concentration from 1ngmL^{-1} to 10 ngmL^{-1}, 8 pgmL^{-1} of LOD, high association constant (K_a) of 7x10^{-2} ngmL^{-1} and a sensitivity of 30.96 x10^{-4} A ng^{-1}mL cm^{-2}. This electrochemical piezoelectric immunosensor is found to be highly promising for detection of AFB1 in real samples. The immunosensor offers high sensitivity, low value of LOD, broad linear range and high association constant in a direct and label free environment as compared to the reported values in the literature. The high efficiency of the immuno sensor lies in well ordered self assembled monolayer of HDT, decorated with cysteamine functionalized AuNPs. The cysteamine has been found to work as a linker to bind covalently with -Fc part of aAFB1 through amine group to avoid aggregation. Furthermore, this approach can be used to develop the sensor for other food mycotoxins such as OTA, OTB, fumonisins and zearalenone etc. And efforts should be made to simplify the fabrication process of the sensing device for speedy commercialization.

Acknowledgements
We thank Dr. Ashok Kumar Chauhan (Founder President, Amity University Uttar Pradesh) for providing the facilities. We also thank to Dr. (Mrs) Balwinder Shukla, Vice chancellor Amity University Uttar Pradesh and Prof. L.M. Bhardwaj, Director, AINT. Author J.S. acknowledges the Department of Science & Technology, Govt of India for awarding the DST-INSPIRE Fellowship [IFA-13 CH-105] 2013.

References:

D.M. Parkin, F. Bray, J. Ferlay, P. Pisani, Estimating the world cancer burden : Globocan 2000, International Journal of Cancer, 94, (2001), 153-156.
J.W. Bennett, M. Klich, Mycotoxins, Clinical microbiology reviews, 16 (2003) 497-516.
D.L. Eaton, J. D. Groopman, The Toxicology of Aflatoxins; Academic Press: New York (1994).
S. J. Daly, G.J. Keating, P.P. Dillon, B.M. Manning, R.O. Kennedy, H. A. Lee, M. R. A. Morgan, Development of Surface Plasmon Resonance-Based Immunoassay for Aflatoxin B1. Journal of Agricultural and Food Chemistry, 48(2011) 5097-5104.
M.O. Moss, Risk assessment for aflatoxins in foodstuffs, International Biodeterioration & Biodegradation, 50 (2002) 137-142.
International Agency for Research on Cancer, IARC, Monograph on the Evaluation of Carcinogenic Risk to Humans IARC Lyon 56(1993) 489-521.
E. Anklam, J. Saroka, A. Boenke, Acceptance of analytical methods for implementation of EU legislation with a focus on mycotoxins.Food Control 13 (2002) 173.
L. Wang, X.-X. Gan Biomolecule-functionalized magnetic nanoparticles for flow-through quartz crystal microbalance immunoassay of aflatoxin B1 Bioprocess and Biosystem Engineering, 32 (2009) 109 –116.
J. Singh, P. Kalita, M.K. Singh, B.D. Malhotra, Nanostructured nickel oxide-chitosan film for application to cholesterol sensor, Applied Physics Letters, 98 (2011) 4493-4503.
C. Singh, S. Srivastava, M.A. Ali, T.K. Gupta, G. Sumana, A. Srivastava, R.B. Mathur, B.D. Malhotra, Carboxylated multiwalled carbon nanotubes based biosensor for aflatoxin detection, Sensors and Actuators B: Chemical, 185 (2013) 258-264.
S. Srivastava, V. Kumar, M.A. Ali, P.R. Solanki, A. Srivastava, G. Sumana, P.S. Saxena, A.G. Joshi, B.D. Malhotra, Electrophoretically deposited reduced graphene oxide platform for food toxin detection, Nanoscale, 5 (2013) 3043-3051.
R. Chauhan, P.R.Solanki, J.Singh, I. Mukherjee, T. Basu, B.D. Malhotra, A novel electrochemical piezoelectric labelfree immunosensor for aflatoxin B1 detection in groundnut. Food Control, 52 (2015) 60-70.

X. Jin, X. Jin, X. Liu, L. Chen, J. Jiang, G. Shen, R. Yu, Biocatalyzed deposition amplification for detection of aflatoxin B1 based on quartz crystal microbalance, Analytica Chimica Acta, 645 (2009) 92-97.
S. Sadhasivam, J.-C. Chen, S. Savitha, F.-H. Lin, Y.-Y. Yang, C.-H. Lee, A real time detection of the ovarian tumor associated antigen 1 (OVTA 1) in human serum by quartz crystal microbalance immobilized with anti-OVTA 1 polyclonal chicken IgY antibodies, Materials Science and Engineering: C, 32 (2012) 2073-2078.
P.R. Solanki, A. Kaushik, T. Manaka, M.K. Pandey, M. Iwamoto, V.V. Agrawal, B.D. Malhotra, Self-assembled monolayer based impedimetric platform for food borne mycotoxin detection, Nanoscale, 2 (2010) 2811-2817.
K. Spinella, L. Mosiello, G. Palleschi, F. Vitali, Development of a QCM Biosensor to the Detection of Aflatoxin B1, Open Journal of Applied Biosensor, 2 (2013) 112-119.
J.H.O. Owino, O.A. Arotiba, N. Hendricks, E.A. Songa, N. Jahed, T.T. Waryo, R. F. Ngece, P. G.L. Baker, E. I. Iwuoha Electrochemical immunosensor based on polythionine/Gold nanoparticles for the determination of aflatoxinB1. Sensors, 8(2008) 8262-8274.
J.Y. Liao, Construction of nanogold hollow balls with dendritic surface as immobilized affinity support for protein adsorption, Colloids and Surfaces B: Biointerfaces, 57 (2007) 75-80.
L. Masoomi, O. Sadeghi, M.H. Banitaba, A. Shahrjerdi, S.S.H. Davarani, A non-enzymatic nanomagnetic electro-immunosensor for determination of Aflatoxin B1 as a model antigen, Sensors and Actuators B: Chemical, 177 (2013) 1122-1127.
J. Zhao, R.W. Henkens, J. Stonehuerner, J.P. O'Daly, A.L. Crumbliss, Direct electron transfer at horseradish peroxidase—colloidal gold modified electrodes, *Journal of Electroanalytical Chemistry*, 327 (1992) 109-119.
M. Horisberger, Colloidal gold as a tool in molecular biology, *Trends in Biochemical Sciences*, 8 (1983) 395-397.
S. Xu, X. Han, A novel method to construct a third-generation biosensor: self-assembling gold nanoparticles on thiol-functionalized poly(styrene-co-acrylic acid) nanospheres, *Biosensors and Bioelectronics*, 19 (2004) 1117-1120.
S. Liu, D. Leech, H. Ju, Application of Colloidal Gold in Protein Immobilization, Electron Transfer, and Biosensing, *Analytical Letters*, 36 (2003) 1-19.
J. C. Vidal & P. Duato & L. Bonel & J. R. Castillo, Use of polyclonal antibodies to ochratoxin A with a quartz–crystal microbalance for developing real-time mycotoxin piezoelectric immunosensors, Analytical and Bioanalytical Chemistry, 394 (2009) 575–582.
S. Liu, D. Leech, H. Ju, Application of Colloidal Gold in Protein Immobilization, Electron Transfer, and Biosensing, *Analytical Letters*, 36, (2003), 1-19.
S.-Q. Liu, H.-X. Ju, Renewable reagentless hydrogen peroxide sensor based on direct electron transfer of horseradish peroxidase immobilized on colloidal gold-modified electrode, *Analytical Biochemistry*, 307, (2002), 110-116.
A.L. Morel, R.M. Volmant, C. Methivier, J.M. Krafft, S. Boujday, C.M. Pradier, Optimized immobilization of gold nanoparticles on planar surfaces through alkyldithiols and their use to build 3D biosensors, *Colloids and surfaces. B, Biointerfaces*, 81, (2010), 304-312.
B. Prieto-Simon, M. Campas, J.L. Marty, T. Noguer, Novel highly-performing immunosensor-based strategy for ochratoxin A detection in wine samples, Biosensors & bioelectronics, 23 (2008) 995-1002.
Z. Matharu, A. J. Bandodkar, G. Sumana, P. R. Solanki, E. M. I. Mala Ekanayake, K. Kaneto, V.Gupta, and B. D. Malhotra, Low Density Lipoprotein Detection Based on Antibody Immobilized Self-Assembled Monolayer: Investigations of Kinetic and Thermodynamic Properties, Journal of Physical Chemistry B, 113, (2009), 14405–14412.

S. Srivastava, V. Kumar, M.A. Ali, P.R. Solanki, A. Srivastava, G.Sumana, P.S.Saxena, A.G. Joshi, and B.D. Malhotra, Electrophoretically deposited reduced graphene oxide platform for food toxin detection. Nanoscale 5, (2013), 3043-3051.
J. Wang, Y. Cao, Y. Xu, G. Li, Colorimetric multiplexed immunoassay for sequential detection of tumor markers, Biosensors and Bioelectronics, 25 (2009) 532-536.
M. A. Bangar, D. J. Shirale, W. Chen, N. V. Myung, A. Mulchandani, Single Conducting Polymer Nanowire Chemiresistive Label-Free Immunosensor for Cancer Biomarker, Analytical Chemistry, 81, (2009), 2168–2175.
R. Chauhan, J. Singh, P.R. Solanki, T. Basu, R. O'Kennedy, B.D. Malhotra, Electrochemical piezoelectric reusable immunosensor for aflatoxin B1 detection, *Biochemical Engineering Journal*, 103, (2015), 103-113.
J. Zhao, R.W. Henkens, J. Stonehuerner, J.P. O'Daly, A.L. Crumbliss, Direct electron transfer at horseradish peroxidase—colloidal gold modified electrodes, Journal of Electroanalytical Chemistry, 327 (1992) 109-119.
J. Singh, M. Srivastava, P. Kalita, B.D. Malhotra, A novel ternary NiFe2O4/CuO/FeO-chitosan nanocomposite as a cholesterol biosensor, Process Biochemistry, 47 (2012) 2189-2198.
P. Kalita, J. Singh, M. Kumar Singh, P.R. Solanki, G. Sumana, B.D. Malhotra, Ring like self assembled Ni nanoparticles based biosensor for food toxin detection, Applied Physics Letters, 100 (2012) 093702-093705.
J. Singh, P. Kalita, M.K. Singh, B.D. Malhotra, Nanostructured nickel oxide-chitosan film for application to cholesterol sensor, Applied Physics Letters, 98 (2011) 123702-123703.
Y.M. Bae, B.-K. Oh, W. Lee, W.H. Lee, J.-W. Choi, Study on orientation of immunoglobulin G on protein G layer, Biosensors and Bioelectronics, 21 (2005) 103-110.
M. Hegner, P. Wagner, G. Semenza, Ultralarge atomically flat template-stripped Au surfaces for scanning probe microscopy, Surface Science, 291 (1993) 39-46M.
M. Moskovits, Surface-enhanced Raman spectroscopy: a brief retrospective, Journal of Raman Spectroscopy, 36 (2005) 485-496.
Z.Q. Tian, Surface-enhanced Raman spectroscopy: advancements and applications, Journal of Raman Spectroscopy, 36 (2005) 466-470.
X. Jin, X. Jin, L. Chen, J. Jiang, G. Shen, and R. Yu, Piezoelectric immunosensor with gold nanoparticles enhanced competitive immunoreaction technique for quantification of aflatoxin B1. Biosensors and Bioelectronics, 24, (2009), 2580-2585.

Authors Biography

Mrs. Ruchika Chauhan is a PhD scholar, perusing her PhD in Nanotechnology from Amity Institute of Nanotechnology, Amity University Uttar Pradesh. She received her M.phil. in Chemistry from Dr. Bhim Rao Ambedkar University, Agra, Uttar Pradesh in 2007. She did her masters in organic chemistry from Kumaun University Nainital, Uttarakhand in 2005. She has published 10 national and international researcher papers. Her research area is nano materials and Biosensors.

Dr. Jay Singh has been working as an Assistant Professor under the DST Inspire Faculty program in the Department of Applied Chemistry & Polymer Technology, Delhi Technological University, Delhi since 2013. He received his PhD degree in Polymer science from Motilal Nehru National Institute of Technology in 2010. He obtained his MSc and BSc degrees from Allahabad University, Uttar Pradesh, India. Presently, he is working on the synthesis of various nanomaterials, polymer modification, nanocomposites formation and

their application in nanobiosensors, tissue engineering, drug delivery, and food packaging. He has published 46 research papers and is actively engaged in the research and development of nanomaterials based biosensors for clinical applications. His main research attention is development of wearable sensor for personalizes health care.

Dr. Pratima R. Solanki obtained her MSc and PhD degrees in bioscience from Maharishi Dayanand University, Rohtak, India, in 1995 and 2000. She worked at Biomedical Instrumentation Section, National Physical Laboratory, Council of Scientific Industrial Research, New Delhi. She now works at Special centre for Nanosciences, Jawaharlal Nehru University, New Delhi, India. She has published around 100 papers, has filed 3 patents. She is actively engaged in the research and development of biosensors for healthcare and environmental monitoring

Dr T. Manaka is presently Associate Professor in Department of Physics Electronics, at Tokyo Institute of Technology, Tokyo, Japan. His research area is Organic Material Electronics, Molecular Electronics, Electrical Insulation and Dielectrics Engineering, and Dielectrics Physics. He has published more than 90 papers in various repute journals,
Dr. Mitsumasa Iwamoto is a Professsor in Department of Physical Electronics, Tokyo Institute of Technology, Tokyo, Japan. His research area is Organic Material Electronics, Molecular Electronics, Electrical Insulation and Dielectrics Engineering, and Dielectrics Physics. He has published several papers in various repute journals.

Prof. Tinku Basu is Dy. Director in Amity Institute of Nanotechnology. She did her Ph.D from IIT, Kharagpur in the year 1993. She has done her Post DOC in National Physical Laboratory, Pusa in Delhi. She has got 33 National and International Publications and she have attended more than 50 National and International Conferences. She has filed 6 complete patents. Dr. Basu has been awarded as a Visiting Researcher from Global Center of Excellence Programme from Japan Government in 2011 and 2014. She has written a book on Text Book of Engineering Chemistry. She has reviewed 2 books. Her area of teaching is Polymer Science and Technology, Functionalization of Nano Materials, Industrial Application of Nano Materials Molecular Nanotechnology, Biosensors, Nano Materials in Theruptic and diagnosis.

Prof. B. D. Malhotra received his Ph.D. degree from the University of Delhi, Delhi, India in 1980. He has published more than 250 papers in peer-reviewed journals, filed 10 patents, and edited/co-edited books on biosensors and polymer electronics. After his stint as Chief Scientist and Head of the DST Centre on Biomolecular Electronics at the biosensors and polymer electronics. After his stint as Chief Scientist and Head of the DST Centre on Biomolecular Electronics at the National Physical Laboratory, New Delhi, India, he moved to the Delhi Technological University (DTU), India and is currently He has nearly 30 years of research experience in the field of biomolecular electronics and has guided 24 Ph.D. students to date. His current activities include biosensors, nanobiomaterials, conducting polymers, and ordered molecular assemblies including Langmuir−Blodgett films and self-assembled monolayers among others. Dr. Malhotra is a Fellow of the Indian National Science Academy

(INSA), the National Academy of Sciences, India (NASI), and an Academician of the Asia-Pacific Academy of Materials (APAM).

Figure caption

Figure 1: Shows the Autolab work station EQCM assembly with three electrode system.
Figure 2 A) Change in frequency of the Au coated 6MHz AT-cut quartz crystal (a) HDT/Au, (b) AuNPs/HDT/Au (c) AuNPs/HDT/Au, (d) aAFB1/AuNPs/HDT/Au (e) BSA/aAFB1/AuNPs/HDT/Au immunoelectrode and inset shows the bar diagram of the corresponding electrodes. B) EQCM-CV of: (a) bare Au, (b) HDT/Au, (c) AuNPs/HDT/Au (d) AuNPs/HDT/Au (e) aAFB1/AuNPs/HDT/Au (f) BSA/AuNPs/HDT/Au electrodes. C) CV of the BSA/aAFB1/AuNPs/HDT/Au immunoelectrode and D) CV of the AuNPs/HDT/Au with scan rate from 20 to 100 mV s^{-1}. Inset shows the variation of the magnitude of current vs square root of scan rate (20–100 mV s^{-1}) measured in the potential range of -0.2 V to 0.8 V.
Figure 3 A) SEM image of surface morphology of (a) AuNP/HDT/Au and (b) aAFB1/AuNPs/HDT/Au. 2A (a): (i) Inset shows surface morphology of (HDT/Au) and (ii) AuNPs/HDT/Au), 2A(b): (i) Inset shows surface morphology of BSA/aAFB1/AuNPs/HDT/Au and (ii) AFB1/BSA/aAFB1/AuNPs/HDT/Au electrodes. B) AFM images of surface topography and roughness analysis of (a) bare Au, (b) AuNPs/HDT/Au, (c) AuNPs/HDT/Au (d) aAFB1/AuNPs/HDT/Au and (e) AFB1/BSA/aAFB1/AuNPs/HDT/Au electrodes.
Figure 4 A) Raman spectra, B) FT-IR spectra of (a) HDT/Au (b) AuNPs/HDT/Au (c) AuNPs/HDT/Au and (d) aAFB1/AuNP/HDT/Au electrode. Inset: Raman spectrum of HDT solution.
Figure 5 A) Cyclic voltammogram (Response) B) Frequency Change (Response) of the BSA/aAFB1/AuNPs/HDT/Au immunoelectrode as a function of AFB1 using EQCM-CV in PBS containing $[Fe(CN)_6]^{-3/-4}$ (concentration 0.008 ng/ml to 10ng/ml). Inset: Calibration curve obtained between the magnitude of current (A) versus AFB1 concentration (ng mL^{-1}).
Figure 6: Schematic diagram of fabrication of immunoelectrode antigen and antibody interaction,
Figure 7: Bar chart of frequency change obtained for corn flakes sample on addition of different concentrations of AFB1.
Figure 8: Self life study of immunoelectrode with 2 ngmL^{-1} concentration of AFB1.

Graphical Abstract

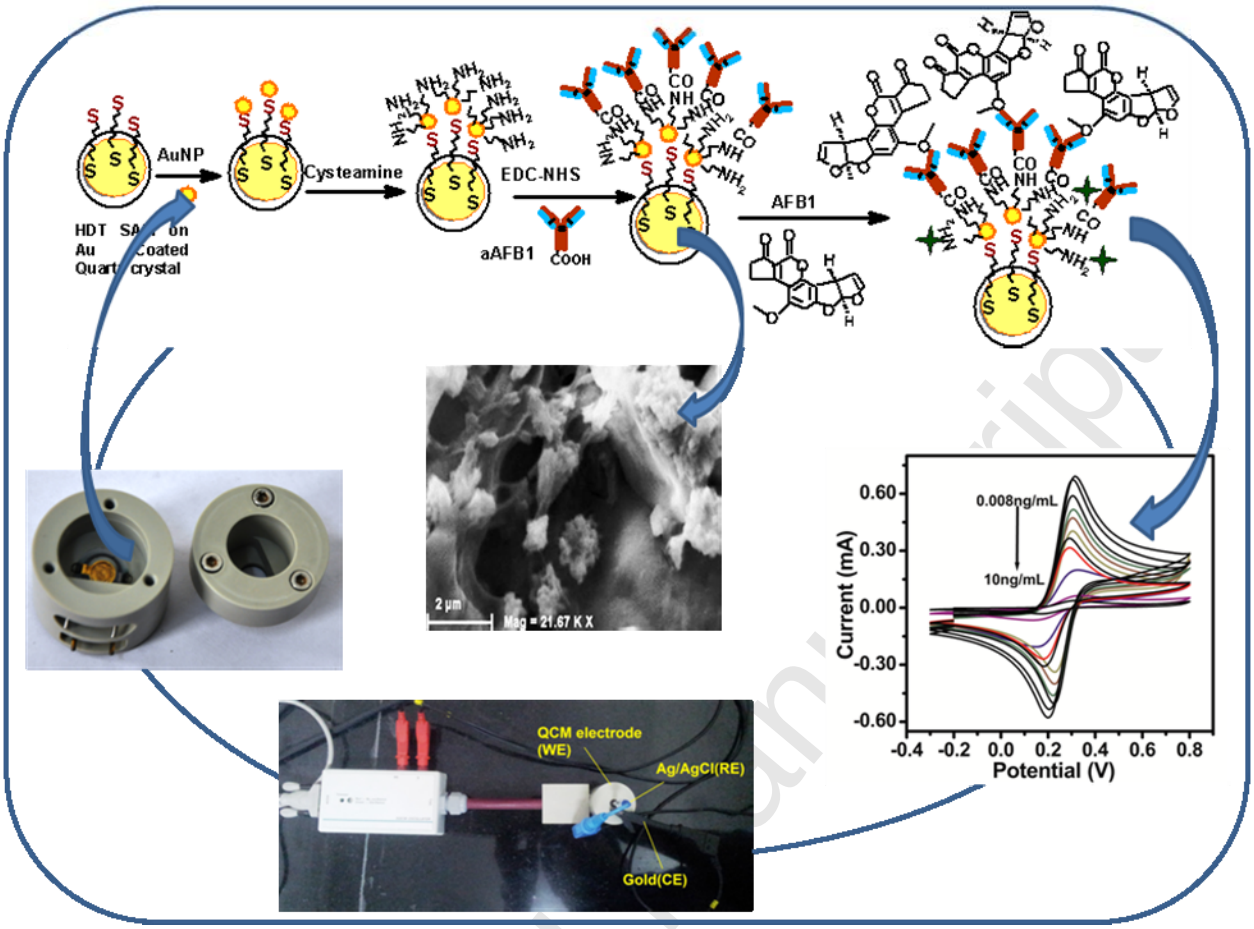

A label free electrochemical quartz crystal microbalance (EQCM) based immunosensor using self-assembled monolayers of hexandithiol (HDT) and gold nanoparticles (AuNP) was fabricated and utilized for aflatoxin B1(AFB1, food mycotoxin) detection. The label free AFB1 detection in noncompetitive mode with high sensitivity and wide linear range may be attributed to novel electrochemical quartz crystal microbalance (EQCM-CV) technique, confirmation of antibodies and networking of 3D AuNPs on self assembled HDT monolayer. Attempts are also made to utilize the immnuno sensor for detection of AFB1 in spiked corn flakes samples for validating the finding results.

Highlights

SAM of HDT, AuNPs and cysteamine fabricated using QCM electrode.
EQCM measurement technique utilized for biosensing.
Non-competitive mode with high sensitivity and wide linear range for AFB1 detection
The immunoelectrode includes linear range as 0.008 - 10 ngmL^{-1}, LOD as 8 pgmL^{-1}
Immune sensor used for detection of AFB1 in spiked corn flakes samples

Table 1: Frequency change (Δf) and mass deposition upon surface modification and no of atoms present over the electrode and bioelectrode.

S.No.	Electrode/Bioelectrode	Frequency Change (Δf) in Hz	Mass Change (Δm)in ng/cm^2	No. of atoms/ molecules
1	HDT/Au	8.9	109.2	4.3x10^{14}

2	AuNPs/ HDT/Au	10.16	124.66	$9.4x10^{14}$
3	AuNPs/ HDT/Au	12.7	155.82	$8.2x10^{14}$
4	aAFB1/AuNPs/HDT/Au	54.7	671.16	$269.49\ x10^{10}$
5	BSA/aAFB1/AuNPs/HDT/Au	66.8	819.63	$7475x10^{9}$

Table 2: Characteristics of the BSA/aAFB1/AuNP/HDT/Au bioelectrode along with those reported in the literature for aflatoxin B1 detection, with their important parameters

Bioelectrode	Detection Method (Direct/Indirect)	sensitivity	Detection limit ($ngmL^{-1}$)	Detection range ($ngmL^{-1}$)	Stability (days)	Ref.
aAFB1/DSP /Au	QCM	-	0.5	0.5-10		16
Fe_3O_4/SiO_2/aAFB1/BSA	QCM	$20.39Hz/ngmL^{-1}$	0.3	0.3–7.0	13	8
aAFB1/BSA-AFB1/MPA/Au	QCM, indirect HRP	$33.13\ Hz/ngmL^{-1}$	0.01	0.01–10.0	-	13
aAFB1/BSA-AFB1/MPA/Au	QCM indirect labeled Secondary Ab with AuNP	$32.5\ Hz/ngmL^{-1}$	0.01	0.01–10.0	-	42
Nano-size gold hollow balls (NGB)	QCM	-	0.05	0.6-12.5	-	18
BSA/aAFB1/AuNP/HDT/Au	EQCM-CV	$3096\ \mu A\ ng^{-1}mLcm^{-2}$	0.008	0.008-10	28	Present work

DSP - 3,3'-Dithiodipropionic-acid-di-N-hydroxysuccinimide ester
MPA – Merczpto propanoic Acid

Figures:

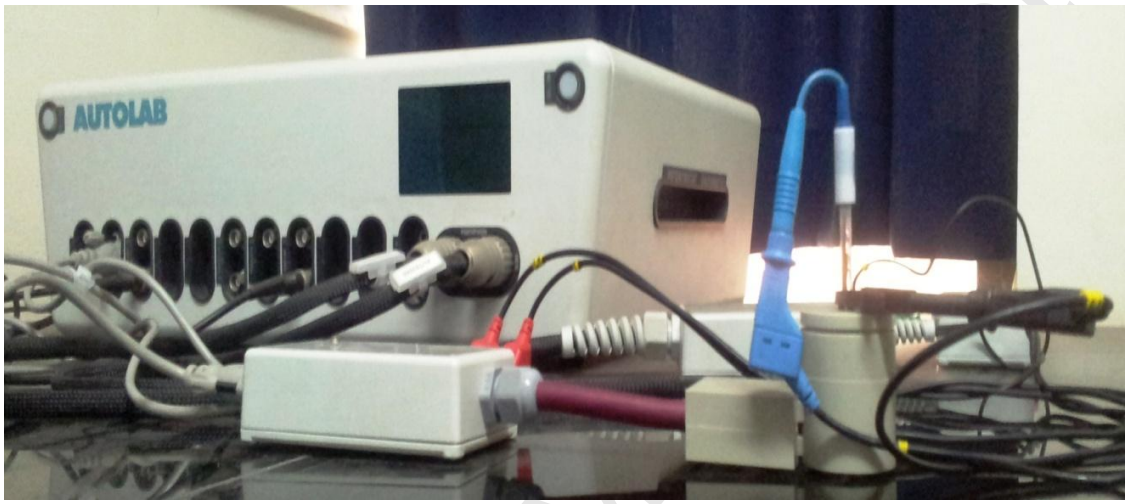

Figure 1

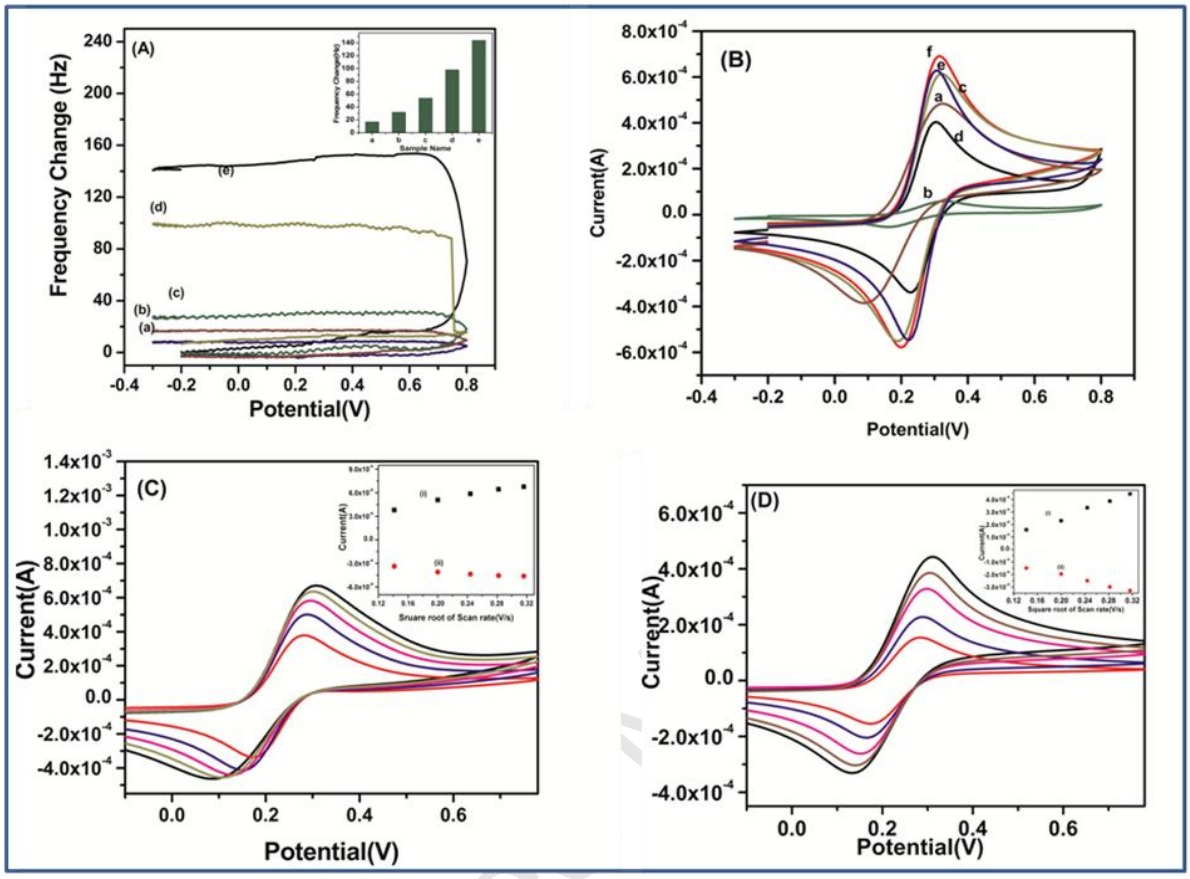

Figure 2

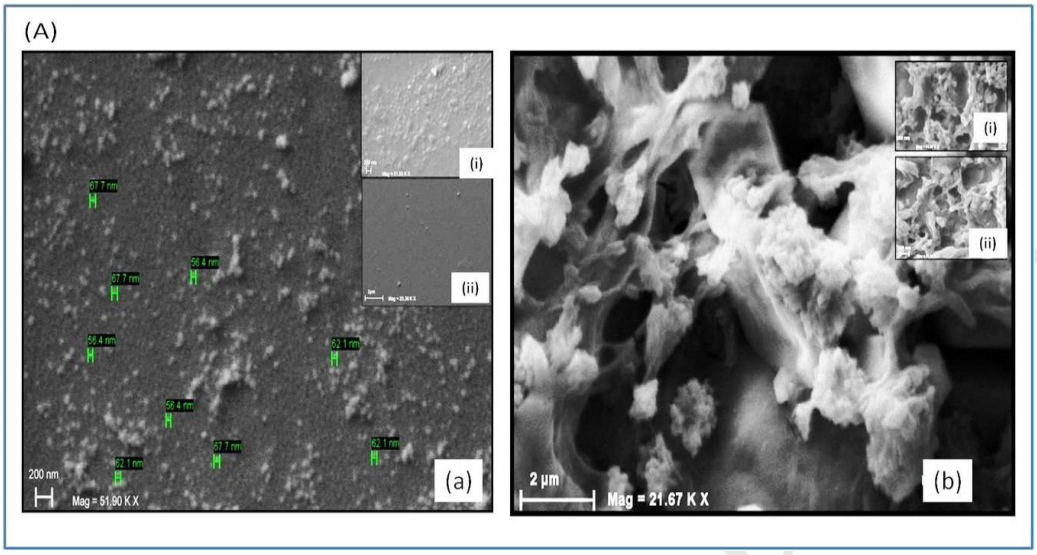

Figure 3A

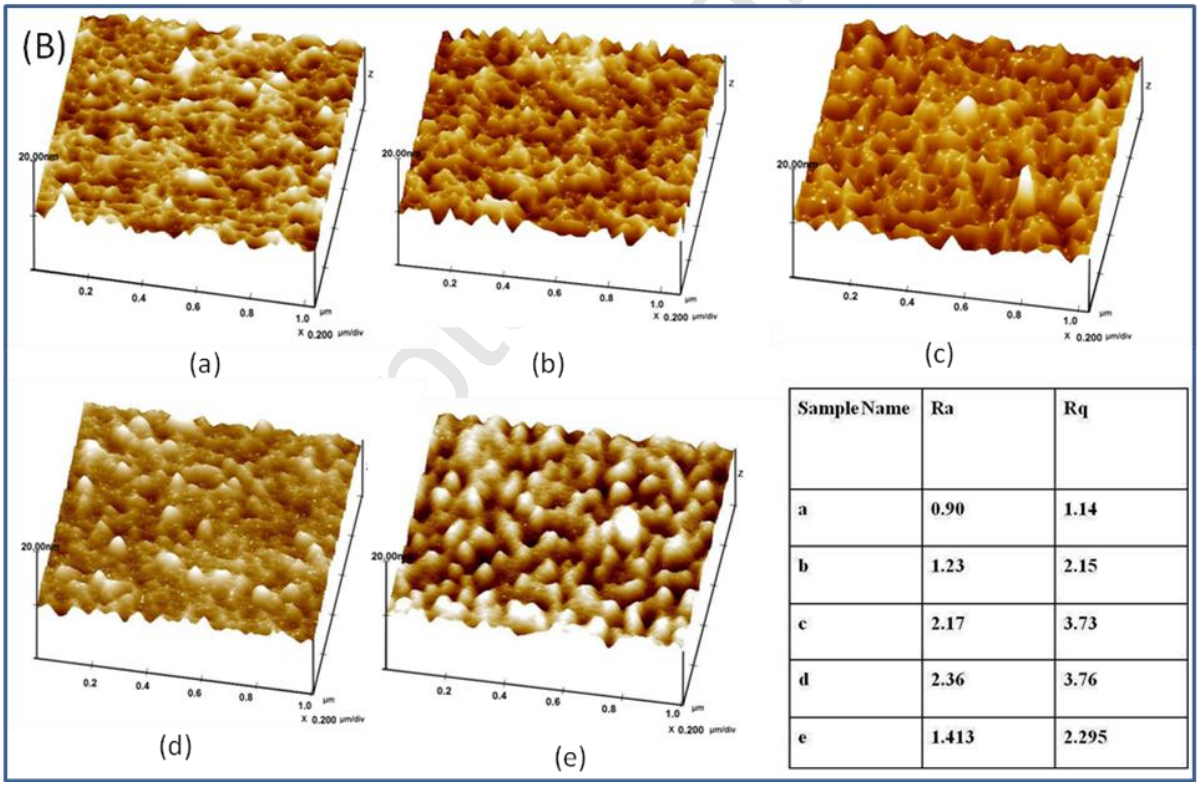

Sample Name	Ra	Rq
a	0.90	1.14
b	1.23	2.15
c	2.17	3.73
d	2.36	3.76
e	1.413	2.295

Figure 3B

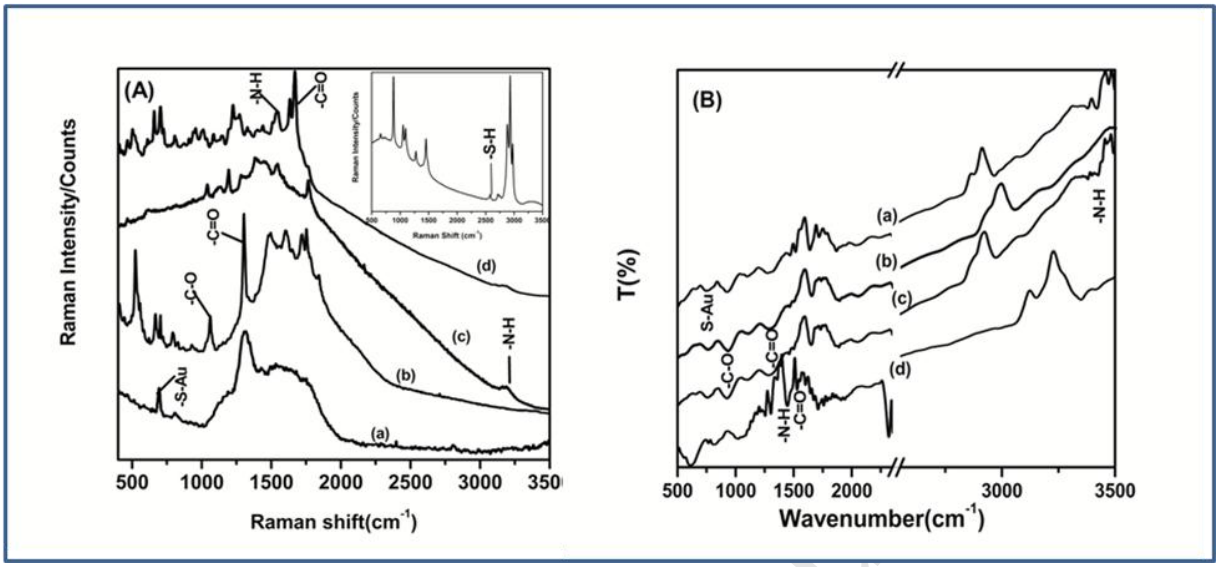

Figure 4

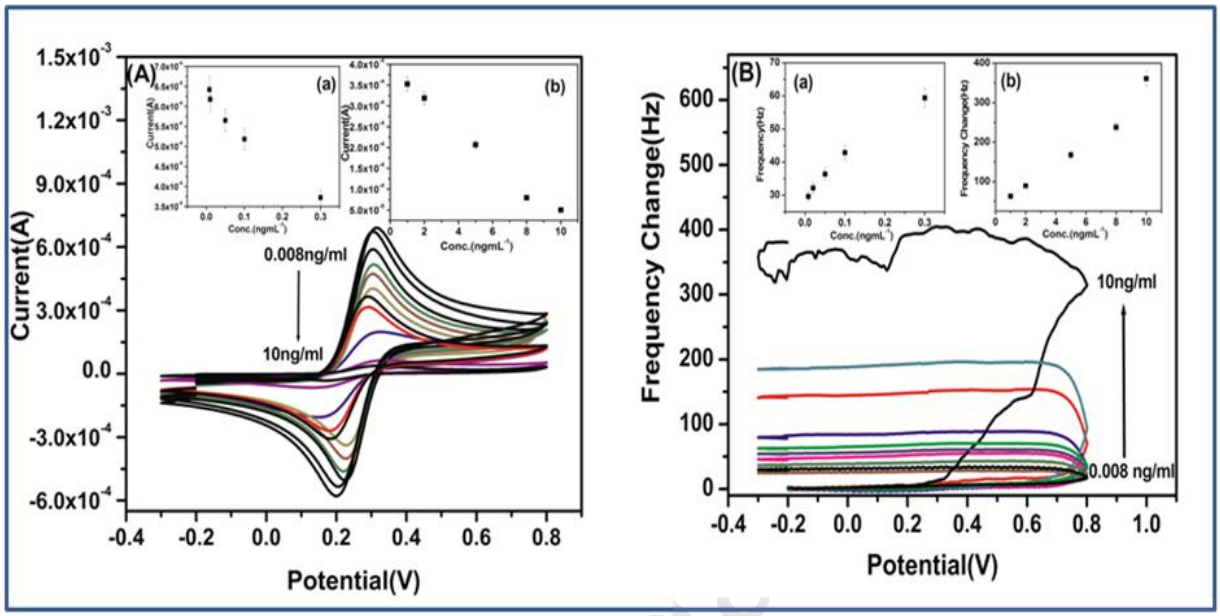

Figure 5

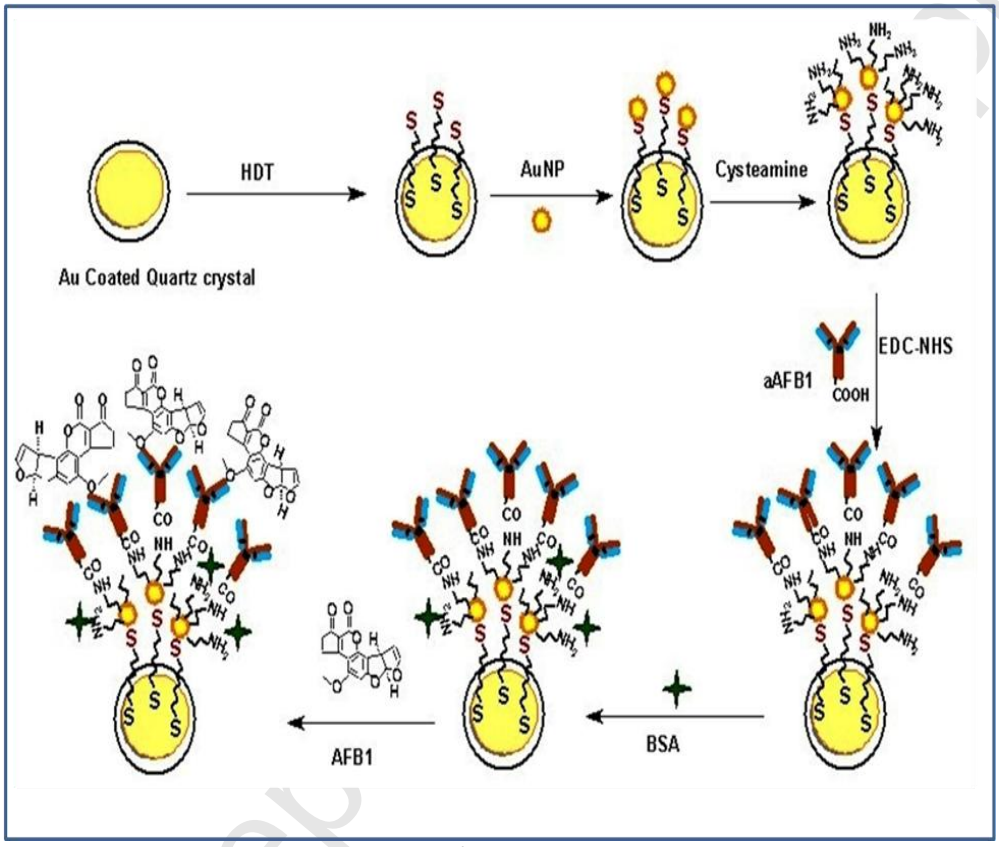

Figure 6

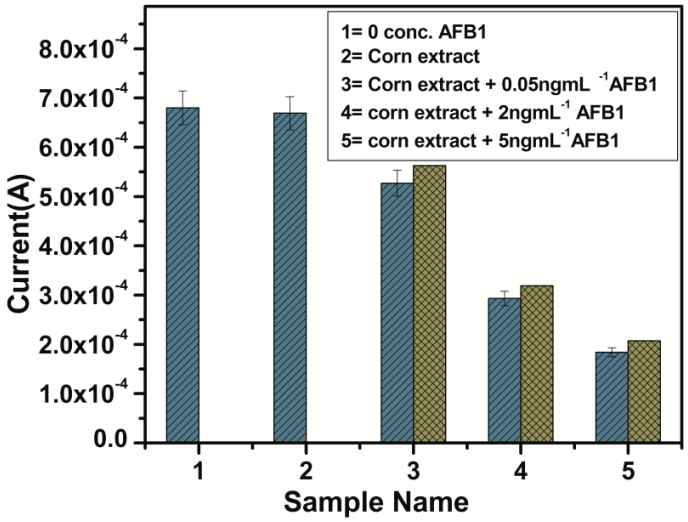

Figure 7

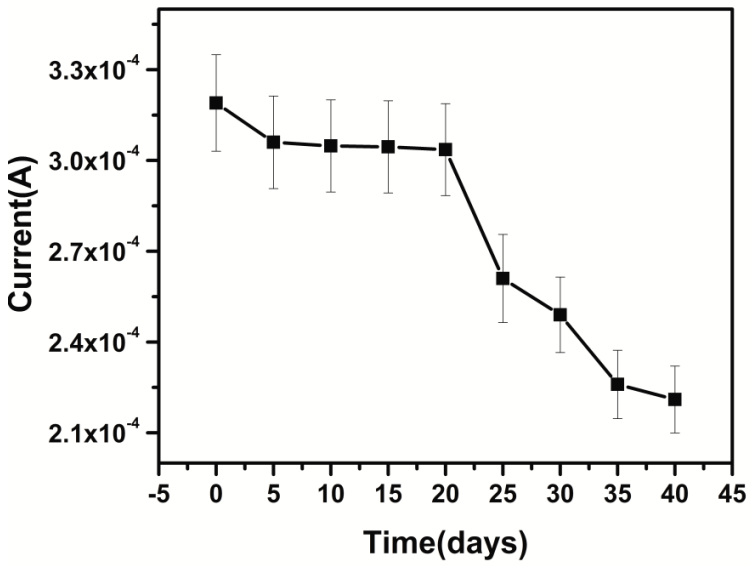

Figure 8

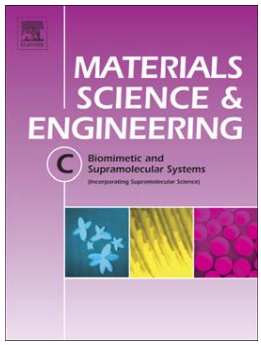

Nanostructured SnO_2 encapsulated guar-gum hybrid nanocomposites for electrocatalytic determination of hydrazine

Priya Malik, Manish Srivastava, Ranjana Verma, Manish Kumar, D. Kumar, Jay Singh

PII: S0928-4931(15)30292-7
DOI: doi: 10.1016/j.msec.2015.08.035
Reference: MSC 5676

To appear in: *Materials Science & Engineering C*

Received date: 30 June 2015
Revised date: 11 August 2015
Accepted date: 22 August 2015

Please cite this article as: Priya Malik, Manish Srivastava, Ranjana Verma, Manish Kumar, D. Kumar, Jay Singh, Nanostructured SnO_2 encapsulated guar-gum hybrid nanocomposites for electrocatalytic determination of hydrazine, *Materials Science & Engineering C* (2015), doi: 10.1016/j.msec.2015.08.035

Nanostructured SnO_2 encapsulated guar-gum hybrid nanocomposites for electrocatalytic determination of hydrazine

Priya Malik[1], Manish Srivastava[2], Ranjana Verma[3], Manish Kumar[1], D. Kumar[1*], Jay Singh[1*]

[1]*Department of Applied Chemistry & Polymer Technology, Delhi Technological University, Shahbad Daulatpur, Main Bawana Road, Delhi 110042, India*

[2]*Department of Physics & Astrophysics, University of Delhi, Delhi 110007, India*

[3]*Solar Energy Material Laboratory, Department of Energy, Tezpur University, Tezpur, Assam 784 028, India*

*Corresponding authors Addresses: E-mail addresses: jay_singh143@yahoo.co.in (J. Singh), and dkumar@dce.ac.in (D. Kumar).

Abstract

The present article deals with synthesis of sol-gel derived tin dioxide (SnO_2) nanoparticles encapsulated in to guar gum (GG) biopolymer as the organic-inorganic hybrid materials for the determination of hydrazine. The organic-inorganic hybrid combines the perfunctory strength offered by the inorganic SnO_2 nanoparticles with flexible binding sites provided by the organic polymer (GG) solution by the ultrasonication. The phase identification, crystalline size, surface morphology and optical properties of prepared SnO_2 and SnO_2-GG nanocomposites has been investigated through FT-IR, XRD, SEM, AFM, TEM, UV-Vis, and PL techniques. The colloidal solution of SnO_2 and GG is electrophoretically deposited (EPD) onto the indium tin-oxide (ITO) glass substrate and studied for the electrooxidation of hydrazine. Under the optimized experimental conditions, the linearity between the current response and the hydrazine concentration has been obtained in the range of 2-22 mM, with a low detection limit of 2.76 mM and a high sensitivity of 5.72 μAcm^{-2}. Based on the linear increase in amperometric current, a sensitive hydrazine electrochemical sensor is constructed. The proposed SnO_2-GG/ITO electrode shows a good response time (35 s), reproducibility, and long-term stability. The obtained results suggest that SnO_2-GG nanocomposites electrode provides a favorable sensing platform for the electrochemical studies. In addition, the cyclic voltammetry (CV) studies are used to evaluate the kinetic parameters.

Key Words: Guar-gum, SnO_2, nanoparticles, hydrazine, electrochemical studies

1. Introduction

Development of various non-enzymatic electrochemical sensors using innovatively designed electrocatalytic materials of optimum efficiency has gained a great deal of interest in recent years [1-3]. Over the last few decades, nanosctructured metal oxide and polymer based organic-inorganic hybrids materials has evolved greatly [4-6], and lead to the construction and improvement of many electrochemical sensors **[**7.10]. Numerous electrochemical sensors have been developed based on the electrocatalytic properties of nanostructured materials such as Au, Pt, and TiO_2, SnO_2, by incorporating in different organic and inorganic matrices [11-14]. Among them, SnO_2 as a n-type semiconductor with direct band gap of 3.6 eV has paid much attention because of its applications in different fields such as designing of transparent conducting electrode [15], gas sensors [16], solar cells [17], and catalyst [18]. Several methods have been introduced to synthesize various types of nano/microstructures SnO_2, including size controllable, template free, hydrothermal, sonochemical, facile one-pot and sol-gel methods [19-23]. Biopolymers have number of attractive features and therefore, these materials are gaining interest to design the multifunctional materials [24-27]. These features include biocompatibility, nontoxicity, biodegradability, adjustable hydrophobic/hydrophilic nature, as well as metal ion chelating ability [28]. Biopolymer, such as GG is a natural polysaccharide consisting of galactose and mannose units [29]. Because of its unique properties such as strong hydrogen bonding, film forming ability, excellent thickening, emulsion and stabilizing agent, it has gained popularity for the development of advanced materials [30]. In addition, GG is soluble in hot and cold water, having high viscosity over a broad range of pH which is compatible with a variety of inorganic and organic substances. Organic-inorganic hybrid nanostructures can provide an efficient and effective electrochemical sensing platform which gives superior response to the

analytes in aqueous solution. It is expected that the inorganic component (SnO_2) provides good charge transfer ability, large surface area, high catalytic activity and high adsorption ability. On the other hand, organic polymer matrix (GG) is advantageous due to good film forming ability, fascinating electron transfer ability, large surface area and biocompatibility. Exploiting the properties of SnO_2 and GG, the (SnO_2-GG) hybrid nanocomposites based electrode having tunable mechanical, thermal, electrical and optical properties can be prepared with a low production cost which can be further used for the construction of an electrochemical device.

Hydrazine and its derivatives have wide range of applications such as pharmaceutical intermediates, antioxidants, blowing agents, pesticides, plant-growth regulators and corrosion inhibitors [31]. However, hydrazine is toxic and can be carcinogenic. Therefore, it has adverse effect on health such as brain damage, DNA damage, and creation of blood abnormalities and irreversible deterioration of nervous system [32,33]. In order to resolve the above mentioned issues, development of a catalyst that can oxidize hydrazine at high rate is required [34-36]. In this context, efforts have been made towards the development of different types of electrocatalysts, based on nanostructure materials such as, Au nanoparticles supported on a TiO_2 nanotube matrix [37], metal electrodes [38], titanium supported Ag/Ti electrode [39], Ni-Pd nanoparticles [40], carbon supported metalloporphyrin [41], indium [42], and Pd/poly anilline nanocomposites [43].

In the present study, we report results of the studies related to the sol-gel derived SnO_2 nanoparticles encapsulated in to GG to prepare the SnO_2-GG nanocomposites. The hybrid film comprising of SnO_2 and GG has been fabricated onto indium tin oxide (ITO) glass electrode via solution casting method and which was further utilize as the electro catalyst for determination of hydrazine.

2. Experimental

2.1 Materials

Stannous chloride ($SnCl_2.2H_2O$) was purchased from Qualigens. Hydrochloric acid (HCl), sodium phosphate monobasic (NaH_2PO_4), sodium phosphate dibasic (Na_2HPO_4), potassium ferrocyanide $K_4[Fe(CN)_6]$, potassium ferricyanide $K_3[Fe(CN)_6]$, sodium chloride (NaCl), acetone (CH_3COCH_3) and cetyl-trimethyl ammonium bromide (CTAB) ($C_{19}H_{42}BrN$) were procured from CDH, New Delhi. Ammonia solution (NH_3) (25%), hydrogen peroxide (H_2O_2) (30%) and ethanol (C_2H_6O) were purchased from Thomas Baker. GG powder was obtained from Dabur India Ltd. (viscosity 5000 cps). 1% solution of GG was prepared by blending with 1% polyvinylalcohol solution. The pre-cleaned hydrolyzed indium-tin-oxide (ITO) coated glass sheet of resistance 15 W/cm were used as the substrate for the deposition of synthesized materials and used as the working electrode. All other chemicals were of analytical grade and used without further purification. The stock solutions of hydrazine (2-22 mM) were freshly prepared in phosphate buffer (5 mM, pH 7.0).

2.2 ***Synthesis of SnO_2 nanoparticles***

SnO_2 nanoparticles were prepared via sol-gel method. In this method, firstly, 0.2 M $SnCl_2.2H_2O$ solution was prepared in double de-ionized water with continuous stirring to get a uniform solution. Next, an aqueous solution of ammonia (25%) was added drop wise into the above solution with steady stirring for 2 h, until pH of the solution was reached to ~12, resulting white precipitate. Subsequently, 2 mL of 0.3 M CTAB solution (as surfactant) was added in to above prepared solution and stirring was continued for next 5 h. The solution was then placed in a hot water bath at 50-60 °C for 2 h till the foam gets separated and the solution became transparent.

Afterwards, the obtained solution was quenched by dipping the solution in to a cold water bath. The resulting mixture was filtered and washed several times with double distilled water and ethanol till neutral pH was achieved. After that, obtained material was dried in oven at 70-80 °C and further calcined at 400 °C for 6 h. The resulting dried sample was crushed to obtain the final product.

2.3. Electrophoretic deposition of SnO_2 /ITO film

Electrophoretic deposition (EPD) was carried out by using DC battery (BioRad, Model 200/0.2). A uniform colloidal suspension of SnO_2 nanoparticles was prepared by dispersing 50 mg SnO_2 nanoparticles in 5 mL double deionized water through the vigorous stirring using ultrasonicatior for 1 h prior to EPD. A platinum foil (1 cm × 2 cm) and a hydrolyzed ITO-coated glass plate were used as anode and cathode, respectively. The two electrodes were parallely placed to each other with a separation of 1 cm, and dipped in to the colloidal suspension SnO_2 nanoparticles. The optimum condition for EPD to obtain a uniform, thin and homogeneous SnO_2 films onto the ITO coated glass surface (0.25 cm^2) was found to be 40 mV for 30 s. After that the prepared SnO_2/ITO electrode was removed from the suspension and washed with double de-ionized water to remove any unbound particles.

2.4. Fabrication of SnO_2 -GG/ITO nanocomposite film

30 mg of SnO_2 nanoparticles were dispersed into 5 mL of GG solution with vigorous sonication for 2 h to get a viscous GG solution with uniformly dispersed SnO_2 nanoparticles. The hybrid thin films were synthesized by uniformly spreading freshly prepared 10 μL solution of SnO_2-GG onto a hydrolyzed ITO-coated glass surface (0.25 cm^2) and dried for 12 h at room temperature in

a controlled environment followed by washing with de-ionized water to remove any unbound particles.

2.5.Characterization

The crystallite size and phase identification of SnO_2 nanoparticles was investigated using X-ray diffraction (XRD) pattern, using Bruker D8 Advance Diffractometer, equipped with Ni-filtered and Cu Kα radiation, operated at 30 kV and 35 mA. Fourier transform infrared spectra (FT-IR) spectra of electrodes have been recorded using Thermoscientific Nicolet 380. The UV-visible spectroscopic studies have been carried out using UV/VIS/NIR spectrometer (Perkin Elmer, Lambda 950). The photoluminescence (PL) spectroscopy studies have been done using Fluorolog 3 spectrophotometer (Horiba). Scanning electron microscope (SEM) and energy dispersive X-ray (EDX) analysis were carried out on HITACHI, (Model No. S-3700N). Transmission electron microscope (TEM) analysis was done through the FEI Tecnai S Twin. For TEM analysis a colloidal solution of nanoparticles was placed on a carbon coated copper grid followed by drying. The surface morphological studies of SnO_2/ITO and SnO_2-GG/ITO electrode have been done through atomic force microscope (AFM) (Park Systems, XE 100). The cyclic voltammetry (CV) and differential pulse voltammetry (DPV) studies have been done using an Autolab Potentiostat/Galvanostat (Metrohm). The electrochemical measurements have been conducted on a three-electrode system using SnO_2-GG /ITO as the working electrode, a platinum (Pt) wire as the counter electrode, and saturated Ag/AgCl as a reference electrode, in a phosphate buffer saline (PBS, 50 mM, pH 7.0, 0.9% NaCl) containing 5 mM $[Fe(CN)_6]^{3-/4-}$ as a mediator.

3. Results and discussion

3.1. XRD analysis

Fig. 1 shows XRD pattern of GG, bare SnO_2 and SnO_2-GG nanocomposites. The XRD pattern of GG shows two broad peaks centered at ~ 20^0 and 40^0 suggest the amorphous structure because of the polymeric nature [44]. In (Fig. 1 b) ten peaks are indexed to (110), (101), (200), (211), (220), (002), (310), (112), (301) and (321) planes [JCPDS No. 41-1445], attributed to rutile phase of SnO_2 with tetragonal structure [45]. No peak corresponding to any impure phase is detected. In the XRD pattern, shown in Fig. 1 c, diffraction peaks corresponding to SnO_2 phase and GG can be clearly seen. These observations confirm the formation of SnO_2-GG nanocomposites. It is also observed that the diffraction peaks of SnO_2 phase are considerably broadened suggesting very small crystallite size. The crystallite size of SnO_2 and SnO_2-GG nanocomposites have been calculated using the Scherrer formula (Eq^n-i) and found to be 10 and 12 nm, respectively.

$D = 0.9\lambda / (\beta\cos\theta)$, ----------(i)

Where D is the crystallite size, λ is the X-ray wavelength (1.5406 Å), β is the full width at half maximum of the diffraction peak and θ is the Bragg diffraction angle.

.

3.2. TEM analysis

The particles size and shape of the SnO_2-GG nanocomposites has been probed through TEM and results are shown in Fig. 2. The TEM micrograph reveals that most of the particles are nearly spherical in shape. A quantitative analysis about the size of the nanoparticles has also been done through the histogram fitted by lorentzian function and the average size of the particles is calculated to be ~ 11 nm which is well agreement the result of XRD.

3.3. FT-IR

The FT-IR spectra of GG, SnO_2 and SnO_2-GG are shown in Fig 3. In [Fig 3(a)] absorption band at 3430 and 1640 cm^{-1} are ascribed to stretching and bending vibration of –OH, respectively. Further, peaks at 2930 and 1430 cm^{-1} are associated with the –CH bending vibration. The peak at 1020 cm^{-1} is attributed to stretching vibration of C-OH bond. Similarly, Fig 3 (b) shows a broad band at 3430 and 1640 cm^{-1} due to the stretching and bending vibrations because of the O-H groups or water molecules absorbed at the surface of SnO_2. A peak observed at 661 cm^{-1} can be assigned to Sn-O stretching mode in SnO_2 crystal. As shown in [Fig 3(c)], the FT-IR spectra exhibit collective peaks, observed in GG and bare SnO_2 which suggests the formation of SnO_2-GG nanocomposites [46].

3.4. UV-Vis

Fig 4A shows UV-Vis absorption spectra of GG, SnO_2 and GG-SnO_2 nanocomposites. It can be seen that all the spectra show high absorption below 250 nm and a peak ~ 290 nm. Further, we have calculated the energy band gap by Tauc plot as shown in Fig. 4 (b). The direct band gap has been calculated by plotting the graph of $[(\alpha h\nu)^2$ vs. $h\nu]$. Here α, ν and h are absorption coefficient, frequency of the incident rays and plank constant respectively. The extrapolation of the linear part to the energy axis yields energy band gaps of 3.28 and 3.30 eV for SnO_2 and GG-SnO_2 nanocomposites [Fig.4C & 4D] respectively [47].

3.5. Photoluminescence spectra

Fig. 4B shows PL spectra of GG, SnO_2 nanoparticles and SnO_2-GG nanocomposites. The PL spectrums of GG were obtained by exciting the sample using 280 nm whereas SnO_2 nanoparticles and SnO_2-GG nanocomposites were excited using 400 nm laser source. It can be seen that the PL spectra of GG exhibit a peak at ~ 438 nm. The emission maximum ~ 463 nm is

obtained for SnO_2 nanoparticle is attributed to the contribution of oxygen vacancies and defect in the SnO_2 crystal. In addition, the energy of emission and excitation both are lower than the calculated band gap of SnO_2 (~ E_g= 3.5eV), and therefore it is expected that emission may be due to the indirect recombination of a conduction electron in the 4p band of Sn and a hole in the 2p valence band of O. These observations are in agreement with earlier studies [48,49]. In case of the SnO_2-GG nanocomposites, PL spectrum shows both the peak corresponds to SnO_2 and GG with the emission maximum ~ 436 and 470 nm respectively. The p-π conjugated side chain can make the emission maximum of SnO_2-GG nanocomposites red shift. The above results support successful grafting of SnO_2 nanoparticles in to the polymeric matrix of GG.

3.6. ***AFM analysis***

AFM studies were carried out to investigate the surface properties for GG/ITO, SnO_2/ITO and SnO_2-GG/ITO electrodes and results are shown in Fig 5 (a-f).The morphology of SnO_2/ITO electrode exhibits uniformly distributed SnO_2 nanoparticles on the surface of ITO; with root mean square roughness (R_q) = 1.03 nm, average roughness (R_a) = 0 .883 nm and maximum profile peak height = 9.12 nm. It can be seen that nanoparticles on ITO surface are uniformly distributed and comprised spherical shape. The 3D surface morphology of GG/ITO electrode shows homogeneous and porous structural elements. The 2D and 3D morphology of SnO_2-GG/ITO nanocomposites film shows that nanoparticles were incorporated in to the GG layer having root mean square roughness (R_q) = 9.892 nm, average roughness (R_a) = 7.34 nm and maximum profile peak height = 27.70 nm.

3.7. SEM analysis

The surface morphology of SnO_2 nanoparticles and SnO_2-GG nanocomposites were investigated through SEM. Fig. 6(a) shows the SEM micrograph of GG powder whereas Fig. 6(b) shows

SEM micrographs of GG film. GG particles appear to have coarse structure and irregularly shaped. GG film shows homogeneous with relatively smooth, mesoporous and crack-free surface. Fig. 6 (c) shows that SnO_2 nanoparticles are uniformly distributed and consist of grain size 20-50 nm, however, upto some extent agglomeration can also be seen Fig. 6(d) shows the SEM micrograph of SnO_2-GG nanocomposites which shows spherical nanoporous morphology uniformly embedded in the porous GG matrix with minimum aggregation. It appears that GG may acts as a bridge between the individual SnO_2-nanoparticles.

3.8. EDX analysis

The chemical compositions of the synthesized products were examined through EDX and results are shown in Fig 7. The EDS analysis of EPD deposited SnO_2 nanoparticles (Fig.7b), exhibited peaks corresponding to Sn and O elements only, whereas no additional peaks could be detected, which suggest that the as-prepared prepared SnO_2 nanoparticles are free from impurities that arises from the starting precursors. In case of SnO_2 nanoparticles, the atomic % of Sn and O elements are found to be 83.47 and 16.53 atom %, respectively. The EDX analysis of GG (Fig. 7a) indicates 83.69 and 16.31 atom % of C and O. On the other hand in case of SnO_2-GG nanocomposites (Fig 7c), the atomic % of Sn, O and C are found to be 18.52, 67.48 and 14.00 %, respectively.

4. Electrochemical studies

*4.1. **CV and DPV studies***

The electrochemical behavior of bare ITO, GG/ITO, SnO_2/ITO and SnO_2-GG/ITO electrode are investigated in PBS (5 mM, pH 7.0, 0.9% NaCl) containing $[Fe(CN)_6]^{3-/4-}$ (5 mM) at a scan rate of 50 mV/s (Fig 8A). The cyclic voltamograms (CV) of the bare ITO (curve a) exhibits

electrochemical characteristics with a couple of redox peaks corresponding to $[Fe(CN)_6]^{3-/4-}$ mediator, and shows an oxidation peak current (I_{pa}) of 0.27 mA. After the modification of ITO with GG, the I_{pa} value is enhanced to 0.30 mA (curve b). The peak current of the SnO_2/ITO electrode (curve c) (I_{pa}) 0.47 mA is higher than those of GG/ITO and bare ITO, which can be ascribed to relatively better conductivity and large surface area of the SnO_2 nanoparticles. However, in case of SnO_2-GG/ITO electrode, the peak current is increased up to 0.51 mA (curve d), indicating the superior electro catalytic behavior compared to GG/ITO and SnO_2/ITO electrode. Further, the SnO_2-GG/ITO electrode shows oxidation peak potential (E_{pa}) and reduction peak potential (E_{pc}) located at 0.39 and 0.041 V, respectively [50]. The results of differential pulse voltammetric (DPV) studies reveal similar the behavior of SnO_2/ITO, GG/ITO and SnO2-GG/ITO electrodes and support the CV measurements (Fig 8 B).

4.2. Effect of scan rate

To investigate the interfacial kinetics of the SnO_2-GG/ITO electrode, CV studies have been conducted as a function of scan rate, varying from 10 to 100 mVs^{-1} (Fig 8C). It can be seen that the magnitudes of both anodic (I_{pa}) and cathodic (I_{pc}) peak currents increase linearly with square root of scan rate ($v^{1/2}$) (Fig 8D). In addition, with increasing scan rate the oxidation peak shifts towards more positive potential whereas reduction peak shifts towards the more negative potential, suggesting the redox process is quasi-reversible.

4.3.Kinetic studies

The value of electron transfer coefficient (α), for n number of electrons has been calculated from two straight lines with a slope value equal to $2.3RT/(1 - \alpha)nF$ for the anodic peak and $2.3RT/\alpha nF$ for the cathodic peak, using the Laviron's equations [51]. The electron transfer

coefficient (α) for the SnO_2-GG/ITO electrode has been calculated to be 0.913966 V for anodic peak and 0.0790355 V for cathodic peak.

The change in value of the charge transfer rate constant (K_s) of the electrode due to surface modification has been calculated by the following Eq (ii)

$$K_s = mnF\ \nu/RT \qquad \text{…….. (ii)}$$

where m is the peak-to-peak separation (V), F is the Faraday constant (96485 C mol^{-1}), ν is the scan rate (30 mV s^{-1}), n is the number of transferred electrons (1), R is the gas constant (8.314 J mol^{-1} K^{-1}) and T is the room temperature (25 °C).

The K_s value of the SnO_2/ITO electrode and the SnO_2-GG/ITO electrode has been calculated to be 1.312313 and 0.68682 s^{-1} respectively. The increased K_s value at the surface of the SnO_2/ITO electrode clearly indicates that both the electronic structure and surface physicochemistry of the SnO_2 nanoparticles contribute to increased electron transfer arising from high catalytic behavior of SnO_2 nanoparticles.

The anodic (E_{pa}) and cathodic (E_{pc}) peak potentials and shift in peak potential ($\Delta E_p = E_{pa} - E_{pc}$) exhibit a linear relationship (Fig 8D) with scan rate. These results reveal that the chemical reaction at the electrode is a diffusion controlled process. The diffusion coefficient value (D) for diffusion of $[Fe(CN)_6]^{3-/4-}$ from electrolyte solution to the corresponding electrode surface has been calculated using the Randles–Sevcik Eq (iii) [51].

$$I_p = (2.69 \times 10^5)\, n^{3/2} A D^{1/2} C\, v^{1/2} \qquad \text{……..……..……. (iii)}$$

where I_p is the peak current of the corresponding electrode [I_{pa} (anodic peak current) & I_{pc} (cathodic peak current)], n is the number of electrons involved or electron stoichiometry (1), A is

the surface area of the electrode (0.25 cm^2), *D* is the diffusion coefficient, *C* is the surface concentration in mol (5 mM) and ν is the scan rate (50 mV/s). The value of D for the SnO_2-GG/ITO electrode is calculated to be 4.31 x 10^3 cm^2s^{-1}.

The surface concentration of the electrodes has been estimated using the Brown−Anson model following the Eq (iv).

$$I_p = n^2F^2I^*AV/4RT \quad \text{……..…….. (iv)}$$

where *n* is the number of electrons transferred (1), *F* is the Faraday constant (96485 C/mol), *I** is the surface concentration of the corresponding electrode (mol cm^{-2}), *A* is the surface area of the electrode (0.25 cm^2), *V* is the scan rate (30 mV/s), *R* is the gas constant (8.314 J mol^{-1} K^{-1}), and T is the room temperature. The surface concentration of SnO_2-GG/ITO (4.32603 × 10^{-8} mol cm^{-2}) is found to be higher than that of SnO_2/ITO (4.08095 × 10^{-8} mol cm^{-2}) electrode.

4.4.Optimization of pH

The effect of solution pH (5.7 to 8.0) on the electrochemical behavior of the SnO_2-GG/ITO electrode is measured by the CV technique in PBS (5 mM, 0.9% NaCl) containing $Fe(CN)_6]^{3-/4-}$ (5 mM) at scan rate 50 mV/s (Fig. 9). It can be seen that the oxidation peak current increases from pH, 5.7 to 7.0 and after that on increasing the pH value the E_{pa} value decreases. The highest magnitude of current is observed at pH 7.0. In is concluded that the limited electron transfer between the medium and electrode may lead to decrease in the $E_{pa,}$ over the pH 7.0). These changes in the peak current may arise due to a decrease in concentration of the positively charged moieties (Sn^{2+}) present at the matrix as the pH of PBS approaches its isoelectric point (IEP); which may result in decreased interaction between redox ions $[Fe(CN)_6]^{3-}$

$^{/4-}$ and the SnO_2/ITO surface. Thus, pH, 7 is selected as the optimum value for further CV measurements.

4.5. Electro-oxidation studies of hydrazine

The effect of hydrazine concentration on the CV response of SnO_2-GG/ITO electrode has been investigated in presence of 5 mM phosphate buffer (PBS, pH = 7.0, 0.9% NaCl) containing $[Fe(CN)_6]^{3-/4-}$ at a scan rate of 50 mV/s. Fig 10A shows CV of the SnO_2-GG/ITO electrode as a function of hydrazine concentration varying from 2-22 mM. It is seen that on increasing the concentration of hydrazine, the anodic peak current increases. Further, it is observed that the oxidation current of hydrazine first rises and then reaches a maximum value at ~ 0.52 V.

The overall reaction for the oxidation of hydrazine can be written as follows (Eq v):

$$N_2H_4 + 4OH^- \rightarrow N_2 + 4H_2O + 4\,e^- \quad \text{……..…….. (v)}$$

This catalytic peak current has a linear relationship with the concentration of hydrazine in the range of 2-22 mM (Fig 10B). A linear calibration is obtained, with a coefficient of 0.9892, demonstrating the good relationship between the concentration of hydrazine and oxidation current. The detection limit, linearity and sensitivity have been estimated to be 2.769 mM, 2-22 mM and 5.72 μAcm^{-2}, respectively. The detection limit was calculated by using formula of 3 sb/S, where, sb and S denoted the standard deviation of background current and the slope of the calibration plot, respectively. From the above results, it can be concluded that the electro-oxidation of hydrazine at SnO_2-GG/ITO electrode can be used for quantitative determination of hydrazine in a given samples, and it may have a potential application in the electrochemical sensing devices. For the determination of response time of SnO_2-GG/ITO nanocomposites electrode, we have measured the electrochemical current response from 2 to 40 s. We found that

the magnitude of current increases initially and achieves maximum value at 35 s. After 35 s the value of current starts decreasing, indicating that 35 s is the response time for SnO_2-GG/ITO nanocomposites electrode. The reproducibility of SnO_2-GG/ITO electrode was monitored using CV technique at similar condition. For this study, we have observed the change in the magnitude of oxidation current of SnO_2-GG/ITO electrode in presence of hydrazine (8 mM). The results indicated that (data not shown) good reproducibility as is evidenced by the low standard deviations found as 1.9 % indicating good precision. **Table 1** Shows the electro-analytical parameters for electrocatalytic oxidation of hydrazine at different electrodes materials [36, 52-55].

5. Conclusion

In the present work SnO_2-GG nanocomposites were prepared by incorporating SnO_2 nanoparticles into GG. The SnO_2-GG nanocomposites was characterized by several techniques and studied towards the electro oxidation of hydrazine. The electrooxidation behavior of SnO_2-GG/ITO electrode showed optimal response (35 s), good sensitivity (5.72 μAcm^{-2}), linearity (2-22 mM), low detection limit (2.769 mM), good reproducibility and long term stability. The wide detection range and high sensitivity may be ascribed to the amplification of current response due to the presence of SnO_2 nanoparticles in GG matrix which offered facile electron transfer ability between the electrolyte and the surface of SnO_2-GG/ITO electrode. The findings of present studies proposed a promising platform for the application of SnO_2-GG nanocomposites for rapid and a simple quantitative determination of hydrazine in pharmaceutical and clinical samples.

Acknowledgments

We thank Prof. P. Kumar, Vice chancellor, Delhi Technological University, Delhi, India for providing necessary facilities for research work. Author J.S. acknowledges the Department of

Science & Technology, Govt of India for awarding the DST-INSPIRE Fellowship [IFA-13 CH-105] 2013. Author M.S. acknowledges the Department of Science & Technology, Govt of India for awarding the DST-INSPIRE Fellowship [IFA-13 MS-02] 2014

References

1. M. Baghayeri, M. Namadchian, H.K. Maleh, H. Beitollahi, Determination of nifedipine using nanostructured electrochemical sensor based on simple synthesis of Ag nanoparticles at the surface of glassy carbon electrode: Application to the analysis of some real samples J. Electroanal. Chem. 697 (2013) 53-59.
2. M. Baghayeri, M. Namadchian, Fabrication of a nanostructured luteolin biosensor for simultaneous determination of levodopa in the presence of acetaminophen and tyramine: Application to the analysis of some real samples, Electrochim. Acta. 108 (2013) 22-31.
3. M. Baghayeri, B. Maleki, R. Zarghani, Voltammetric behavior of tiopronin on carbon paste electrode modified with nanocrystalline Fe 50 Ni 50 alloys, Mater. Sci. Eng. C 44 (2014) 175-182.
4. M. Baghayeri, H. Veisi, Fabrication of a facile electrochemical biosensor for hydrogen peroxide using efficient catalysis of hemoglobin on the porous Pd@Fe_3O_4-MWCNT nanocomposite, Biosens. Bioelectron. 74 (2015) 190-198.
5. M. Baghayeri, E.N. Zare, M.M. Lakouraj, Monitoring of hydrogen peroxide using a glassy carbon electrode modified with hemoglobin and a polypyrrole-based nanocomposite, Microchim. Acta. 182 (2015) 771-779.
6. M. Baghayeri, Glucose sensing by a glassy carbon electrode modified with glucose oxidase and a magnetic polymeric nanocomposite, RSC Adv. 5 (2015) 18267-18274.

7. Y. Cheng, B. Feng, X. Yang, P. Yang, Y. Ding, Y. Chen and J. Fei, Electrochemical biosensing platform based on carboxymethyl cellulose functionalized reduced graphene oxide and hemoglobin hybrid nanocomposite film, Sens. Actuators, B 182 (2013) 288-293.
8. A. Chen and S. Chatterjee, Nanomaterials based electrochemical sensors for biomedical applications, Chem. Soc. Rev. 42 (2013) 5425-5438.
9. B. Rafiee and A. R. Fakhari, Electrocatalytic oxidation and determination of insulin at nickel oxide nanoparticles-multiwalled carbon nanotube modified screen printed electrode, Biosens. Bioelectron. 46 (2013) 130-5.
10. J. Singh, A. Roychoudhury, M. Srivastava, V. Chaudhary, R. Prasanna, D. W. Lee, S. H. Lee and B. D. Malhotra, Highly efficient bienzyme functionalized biocompatible nanostructured nickel ferrite–chitosan nanocomposite platform for biomedical application, J. Phys. Chem. C 117 (2013) 8491-8502.
11. Y. Zhang, L. Zhang, W. Liu, M. Zhao and H. Chen, Facile synthesis of SnO_2-Pt/carbon nanotubes nanocatalyst with high electrocatalytic performance for methanol oxidation, Indian J. Chem 51A (2012) 549-553.
12. W. Chen, D. Ny and S. Chen, SnO_2–Au hybrid nanoparticles as effective catalysts for oxygen electroreduction in alkaline media, J. Power Sources 195 (2010) 412-418.
13. A. Martyla, M. Kopczyk, P. Marciniak and R. Przekop, One-pot method of synthesis of Pt/SnO_2 system and its electrocatalytic activity, Chem Cent. J 8 (2014) 49.
14. A. A. Ansari, A. Kaushik, P. R. Solanki and B. D. Malhotra**,** Electrochemical cholesterol sensor based on tin oxide-chitosan nanobiocomposite film, Electroanal. 21 (2009) 965–972.

15. J. Zhu, Z. Lu, S. T. Aruna, D. Aurbach and A. Gedanken, Sonochemical synthesis of SnO_2 nanoparticles and their preliminary study as Li insertion electrodes, Chem. Mater. 12 (2000) 2557-2566.

16. A. Kumar, A. C. Pandey and R. Prakash, Electro-oxidation of formic acid using polyindole-SnO_2 nanocomposite, Catal. Sci. Technol. 2 (2012) 2533-2538.

17. N. Kudo, Y. Shimazaki, H. Ohkita, M. Ohoka and S. Ito, Organic–inorganic hybrid solar cells based on conducting polymer and SnO_2 nanoparticles chemically modified with a fullerene derivative, Sol. Energy Mater. Sol. Cells 91 (2007) 1243-1247.

18. W.W. Wang, Y.J. Zhu and L.X. Yang, ZnO–SnO_2 hollow spheres and hierarchical nanosheets: hydrothermal preparation, formation mechanism, and photocatalytic properties, Adv. Funct. Mater. 17 (2007) 59-64.

19. R. D. Cakan, Y-S. Hu, M. Antonietti, J. Maier and M-M. Titirici, Facile one-pot synthesis of mesoporous SnO_2 microspheres via nanoparticles assembly and lithium storage properties, Chem. Mater. 20 (2008) 1227-1229.

20. F. Gu , S. F. Wang , M. K. Lü , G. J. Zhou , D. Xu and D. R. Yuan, Photoluminescence properties of SnO_2 nanoparticles synthesized by sol-gel method., J. Phys. Chem. B 108 (2004) 8119–8123.

21. H. C. Chiu and C. S. Yeh, Hydrothermal synthesis of SnO_2 nanoparticles and their gas-sensing of alcohol, J. Phys. Chem. C 111 (2007) 7256–7259.

22. X. W. Lou, Y. Wang, C. Yuan, J. Y. Lee, and L. A. Archer, Template-free synthesis of SnO_2 hollow nanostructures with high lithium storage capacity, Advanc. Mater. 18 (2006) 2325-2329.

23. L. Jiang, G. Sun, Z. Zhou, S. Sun, Q. Wang, S. Yan, H. Li, J. Tian, J. Guo, B. Zhou and Q. Xin, Size-controllable synthesis of monodispersed SnO_2 nanoparticles and application in electrocatalysts, J. Phys. Chem. B 109 (2005) 8774–8778.

24. M. Baghayeri, E.N. Zare, M.M. Lakouraj, A simple hydrogen peroxide biosensor based on a novel electro-magnetic poly (p-phenylenediamine)@ Fe_3O_4 nanocomposite, Biosens. Bioelectron. 55 (2014) 259-265.

25. M. Baghayeri, E.N. Zare, M.M. Lakouraj, Novel superparamagnetic PFu@ Fe_3O_4 conductive nanocomposite as a suitable host for hemoglobin immobilization, Sens. Actuators, B 202 (2014) 1200-1208.

26. M. Baghayeri, E.N. Zare, M. Namadchian, Direct electrochemistry and electrocatalysis of hemoglobin immobilized on biocompatible poly(styrene-alternative-maleic acid)/functionalized multi-wall carbon nanotubes blends, Sens. Actuators, B 188 (2013) 227-234.

27. M. Baghayeri, E.N. Zare, R. Hasanzadeh, Facile synthesis of PSMA-g-3ABA/MWCNTs nanocomposite as a substrate for hemoglobin immobilization: Application to catalysis of H_2O_2, Mater. Sci. Eng. C 39 (2014) 213-220.

28. H. Wu, C. Wu, Q. He, X. Liao and B. Shi, Collagen fiber with surface-grafted polyphenol as a novel support for Pd (0) nanoparticles: Synthesis, characterization and catalytic application, Mater. Sci. Eng. C 30 (2010) 770–776.

29. X. Wan, Y. Li, X. Wang, S. Chen and X. Gu, Synthesis of cationic guar gum-graft-polyacrylamide at low temperature and its flocculating properties, Euro. Polym. J. 43 (2007) 3655-3661.

30. R. G. Auddy, Md F. Abdullah, S. Das, P. Roy, S. Datta and A. Mukherjee, New Guar Biopolymer Silver Nanocomposites for Wound Healing Applications, BioMed Res. Internat. 2013 (2013) 8.
31. E. F. Rothgery, In Kirk-Othmer Encyclo. Chem. Tech., John Wiley & Sons, Inc.: 2000.
32. J. W. Mo, B. Ogorevc, X. Zhang and B. Pihlar, Cobalt and Copper Hexacyanoferrate Modified Carbon Fiber Microelectrode as an All-Solid Potentiometric Microsensor for Hydrazine, Electroanal. 12 (2000) 48.
33. S. Amlathe and V. K. Gupta, Spectrophotometric determination of trace amounts of hydrazine in polluted water, Analyst 113 (1988) 1481.
34. N. Maleki, A. Safavi, E. Fariami and F. Tajabadi, Palladium nanoparticle decorated carbon ionic liquid electrode for highly efficient electrocatalytic oxidation and determination of hydrazine, Anal. Chim. Acta. 611 (2008) 151-5.
35. U. P. Azad, V. Ganesan, Determination of hydrazine by polyNi (II) complex modified electrodes with a wide linear calibration range, Electrochim. Acta. 56 (2011) 5766.
36. P. K. Rastogi, V. Ganesan, S. Krishnamoorthi, Palladium nanoparticles decorated gaur gum based hybrid material for electrocatalytic hydrazine determination, Electrochim. Acta. 125 (2014) 593-600.
37. M. Hosseini, M. M. Momeni, M. Faraji, Electro-oxidation of hydrazine on gold nanoparticles supported on TiO_2 nanotube matrix as a new high active electrode, J. Mol. Catal A Chem. 335 (2011) 199–204.
38. K. Asazawa, K. Yamada, H. Tanaka, M. Taniguchi, K. Oguro, Electrochemical oxidation of hydrazine and its derivatives on the surface of metal electrodes in alkaline media, J. Pow. Sourc. 191 (2009) 362-365.

39. Q. Yi, L. Li, W. Yu, Z. Zhou, G. Xu, A novel titanium-supported Ag/Ti electrode for the electro-oxidation of hydrazine, J. Mol. Catal A Chem. 295 (2008) 34-38.

40. S. K. Singh, Y. Iizuka, Q. Xu, Nickel-palladium nanoparticle catalyzed hydrogen generation from hydrous hydrazine for chemical hydrogen storage, Int. J. Hydrogen Energy. 36 (2011) 11794-11801.

41. S. I. Yamazaki, T. Ioroi, K. Tanimoto, K. Yasuda, K. Asazawa, S. Yamaguchi, H. Tanaka, Electrochemical oxidation of hydrazine derivatives by carbon-supported metalloporphyrins, J. Pow. Sourc. 204 (2012) 79-84.

42. Y. B. Jang, T. H. Kim, M. H. Sun, J. Lee, S. J. Cho, Preparation of iridium catalyst and its catalytic activity over hydrazine hydrate decomposition for hydrogen production and storage, Catal. Today 146 (2009) 196–201.

43. S. Ivanov, U. Lange, V. Tsakova, V. M. Mirsky, Electrocatalytically active nanocomposite from palladium nanoparticles and polyaniline: oxidation of hydrazine, Sens. Actuators B-Chem. 150 (2010) 271-278.

44. R. S. Soumya, V. P. Vineetha, P. L. Reshma and K. G. Raghu, Preparation and characterization of selenium incorporated guar gum nanoparticle and its interaction with H9c2 cells, PLoS One 8 (2013) e74411.

45. C. Xu, J. Sun and L. Gao, Controllable synthesis of monodisperse ultrathin SnO_2 nanorods on nitrogen-doped graphene and its ultrahigh lithium storage properties, Nanoscale 4 (2012) 5425-5430.

46. S. P. Mondal, S. K. Ray, J. Ravichandran and I. Manna, Temperature dependent growth and optical properties of SnO_2 nanowires and nanobelts, Bull. Mater. Sci. 33 (2010) 357–364.

47. M. Srivastava, A. K. Das, P. Khanra, Md. E. Uddin, N. H. Kim and J. H. Lee, Characterizations of in situ grown ceria nanoparticles on reduced graphene oxide as a catalyst for the electrooxidation of hydrazine, J. Mater. Chem. A 1 (2013) 9792–9801.

48. Y. Li, W. Yin, R. Deng, R. Chen, J. Chen, Q. Yan, B. Yao, H. Sun, Su-Huai Wei and Tom Wu, Realizing a SnO2-based ultraviolet light-emitting diode via breaking the dipole-forbidden rule, NPG Asia Mater. 4 (2012) e30.

49. R. K. Mishra, Ajay Kushwaha, P. P. Sahay, Influence of Cu doping on the structural, photoluminescence and formaldehyde sensing properties of SnO_2 nanoparticles, RSC Adv. 4 (2014) 3904-3912.

50. J. Singh, A. Roychoudhury, M. Srivastava, P. R. Solanki, D. W. Lee, S. H. Lee and B. D. Malhotra, A dual enzyme functionalized nanostructured thulium oxide based interface for biomedical application, Nanoscale 6 (2014) 1195-1208

51. J. Singh, A. Roychoudhury, M. Srivastava, P. R. Solanki, D. W. Lee, S. H. and B. D. Malhotra, Bienzyme-functionalized monodispersed biocompatible cuprous oxide/chitosan nanocomposite platform for biomedical application, J. Phys. Chem. B 117 (2013) 141−152.

52. J. Panchompoo, L. Aldous, C. Downing, A. Crossley, R.G. Compton, Facile synthesis of Pd nanoparticle modified carbon black for electroanalysis: application to the detection of hydrazine, Electroanalysis, 23 (2011) 1568-1578.

53. D. Jayasri, S.S. Narayanan, Amperometric determination of hydrazine at manganese hexacyanoferrate modified graphite–wax composite electrode, J. Hazard. Mater. 144 (2007) 348-354.

54. R. Kumar, D. Rana, A. Umar, P. Sharma, S. Chauhan, M.S. Chauhan, Iron-doped ZnO nanoparticles as potential scaffold for hydrazine chemical sensor, Sensor Lett. 12 (2014) 1273-1278.

55. B. Sljukic, C. E. Banks, A. Crossley, R. G. Compton, Iron(III) oxide graphite composite electrodes: Application to the electroanalytical detection of hydrazine and hydrogen peroxide, Electroanalysis 18 (2006) 1757.

Figure Captions

Fig. 1 X-ray diffraction patterns of (a) GG, (b) SnO_2 nanoparticles and (c) SnO_2-GG hybrid.

Fig. 2 (a-b) TEM micrographs of SnO_2 nanoparticles and inset shows corresponding histograms.

Fig. 3 FT-IR spectra of (a) GG, (b) SnO_2 nanoparticles and (c) SnO_2-GG hybrid.

Fig. 4 (A) UV-Vis absorption spectrum and (B) Photoluminescence spectra of (a) GG, (b) SnO_2 nanoparticles and (c) SnO_2-GG hybrid. (C) Tauc plot $(\alpha h\nu)^2$ vs $(h\nu)$ for SnO_2 and (D) SnO_2-GG hybrid.

Fig. 5 AFM analysis of (a) GG in 2D, (b) 3D, (c) SnO_2 nanoparticles in 2D, (d) 3D, (e) SnO_2-GG hybrid in 2D and (f) 3D.

Fig. 6 SEM micrograph of (a) GG powder, (b) GG film, (c) SnO_2 nanoparticles (d) SnO_2-GG hybrid nanocomposites

Fig. 7 EDX analysis of (a) GG, (b) SnO_2 nanoparticles and (c) SnO_2-GG hybrid.

Fig. 8 (A) Cyclic voltammogram (B) differential pulse voltammetric of (a) bare ITO electrode, (b) GG/ITO electrode, (c) SnO_2/ITO electrode and (d) SnO_2-GG/ITO electrode (C) CV curve of the SnO_2-GG/ITO electrode at different scan rate 10 -100 mV/s (pH = 7) at 25 ^{0}C.(D) The magnitude of the current vs. potential difference as a function of square root of scan rate (10–100 mV/s).

Fig. 9 (A) CV studies of the SnO_2-GG/ITO electrode as a function of pH ranging from 5.7 to 8.0 in phosphate buffer containing $[Fe(CN)_6]^{3-/4-}$. Inset shows current response of SnO_2-GG/ITO electrode as a function of pH.

Fig.10 (A) Electrochemical response of the SnO_2-GG/ITO electrode with respect to hydrazine concentration (2-22 mM) in PBS (5 mM, 7.0 pH, 0.9% NaCl) containing $[Fe(CN)_6]^{3-/4-}$ at a scan rate of 50 mV/s (B) Calibration curve of the SnO_2-GG/ITO electrode and the variation of current as a function of hydrazine concentration (2-22 mM) in PBS (5 mM, 7.0 pH, 0.9% NaCl) containing $[Fe(CN)_6]^{3-/4-}$ at a scan rate of 50 mV/s.

Fig 1

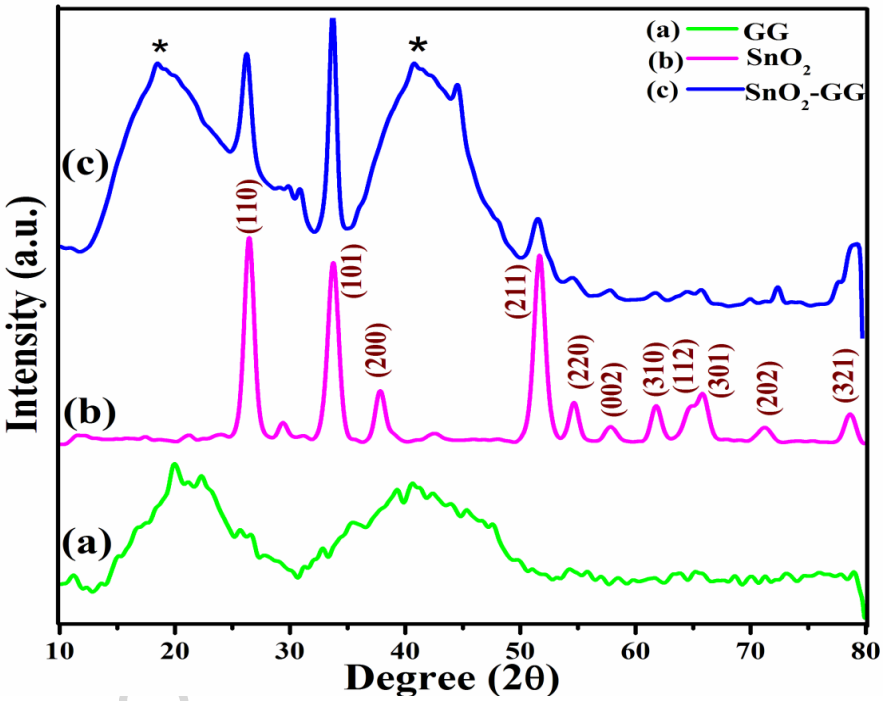

Fig. 2

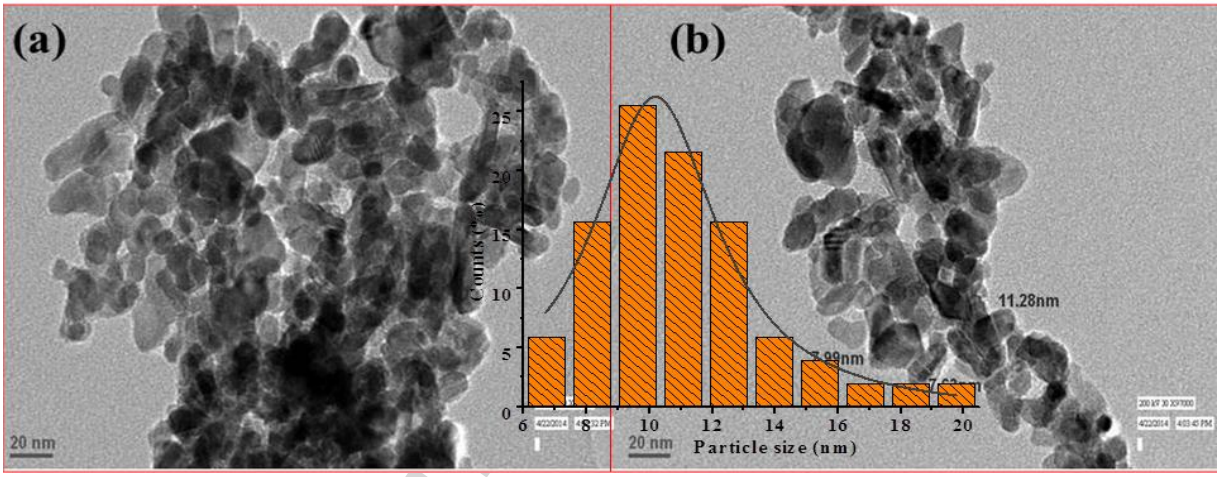

Fig. 3

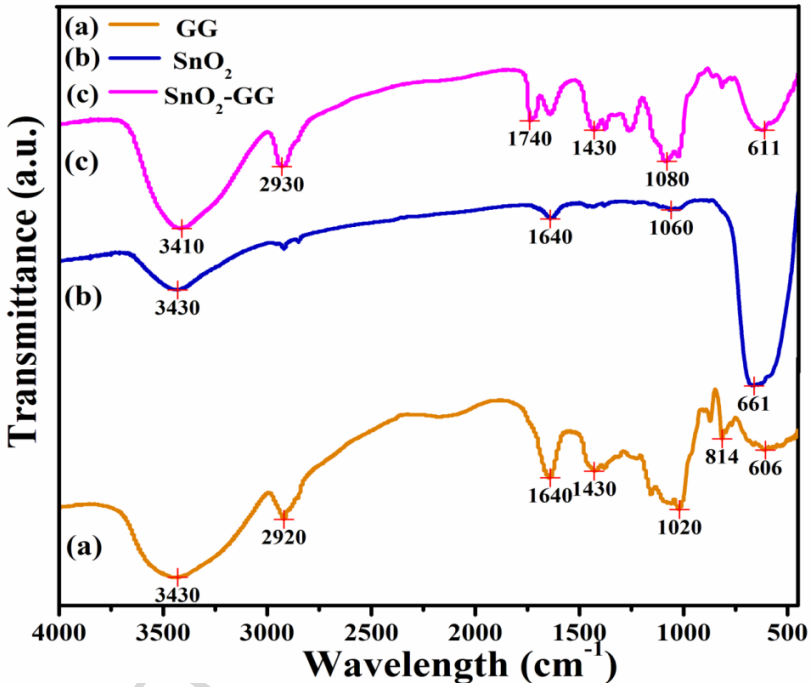

Fig 4.

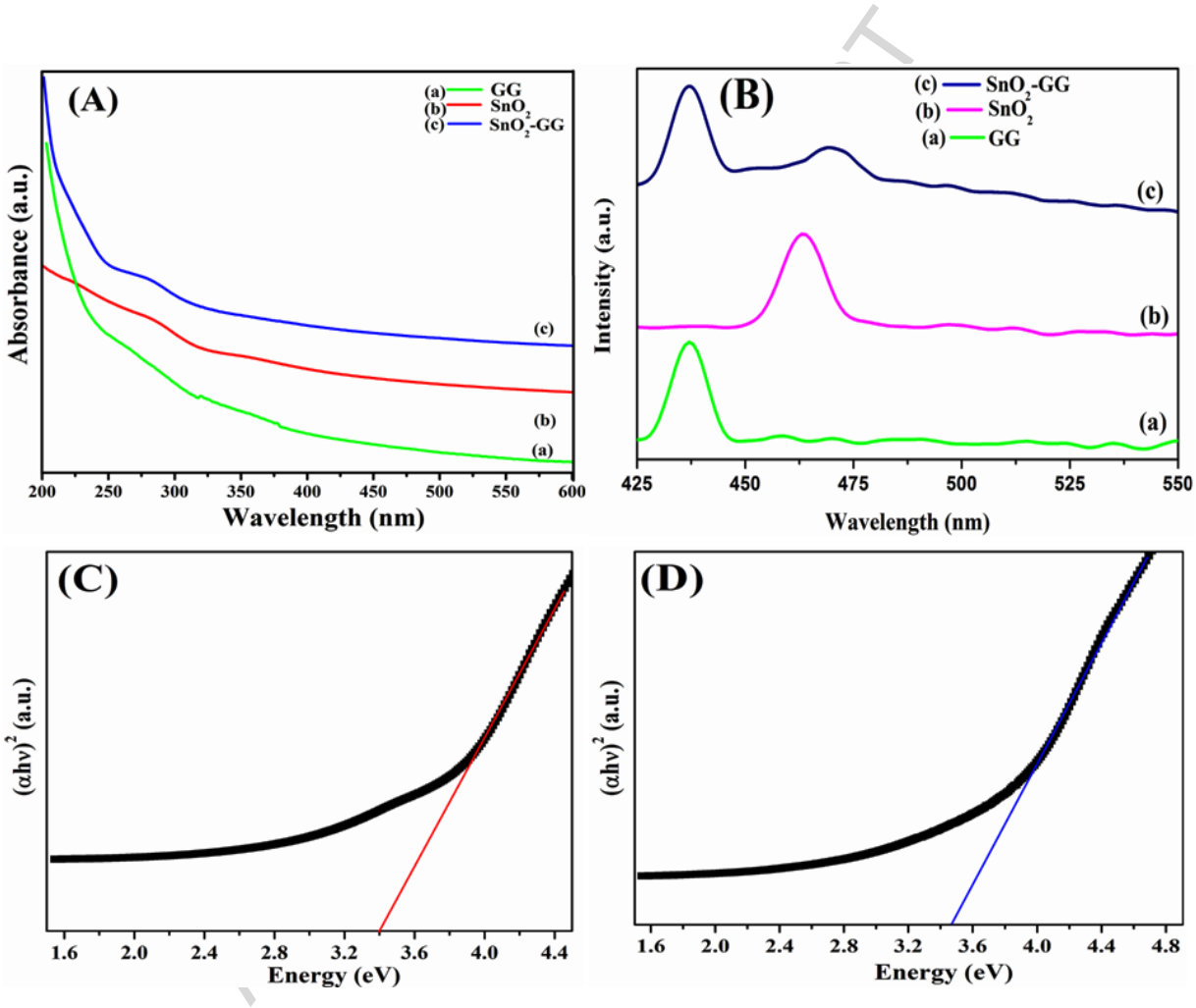

Fig. 5

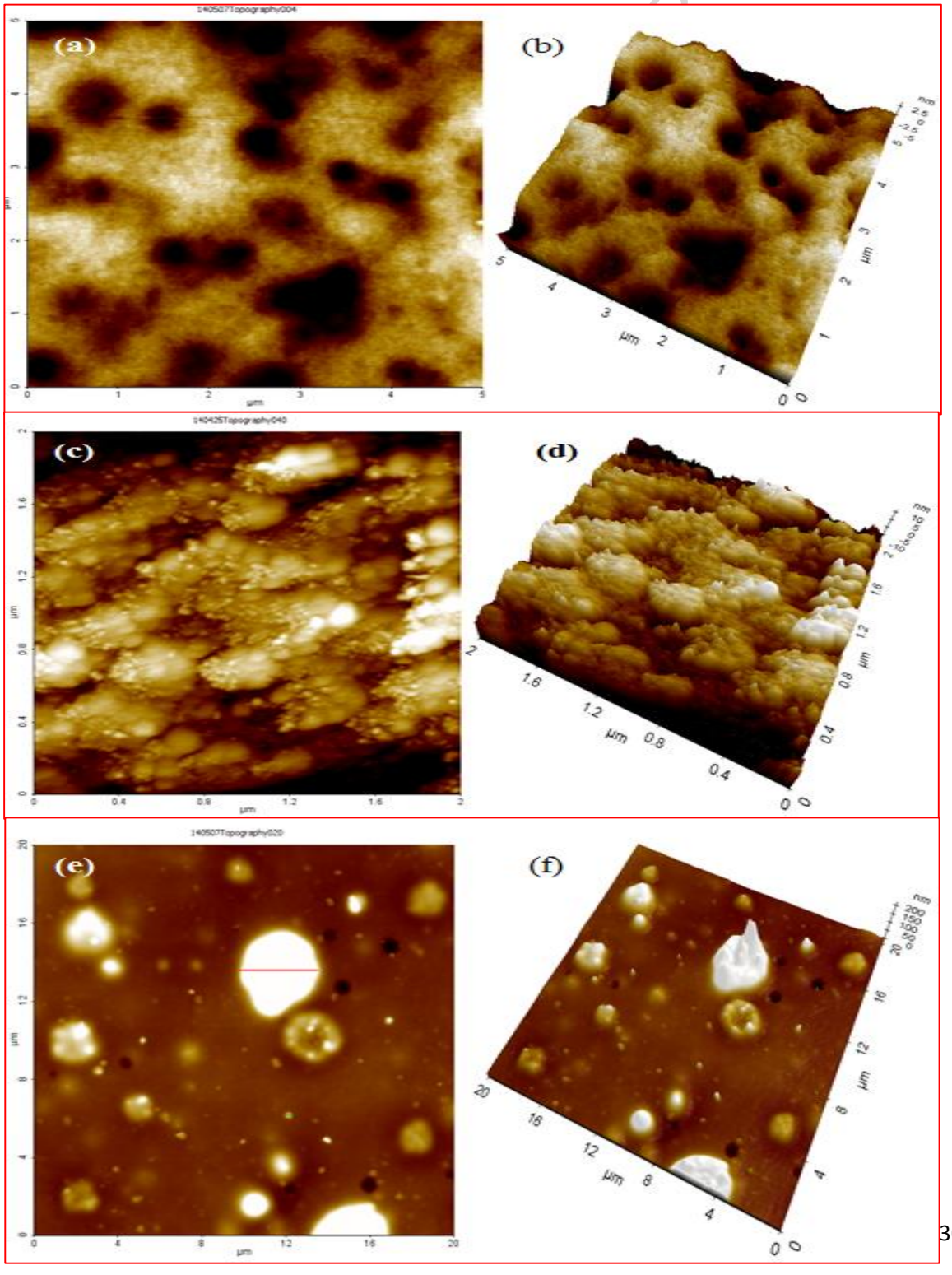

Fig. 6

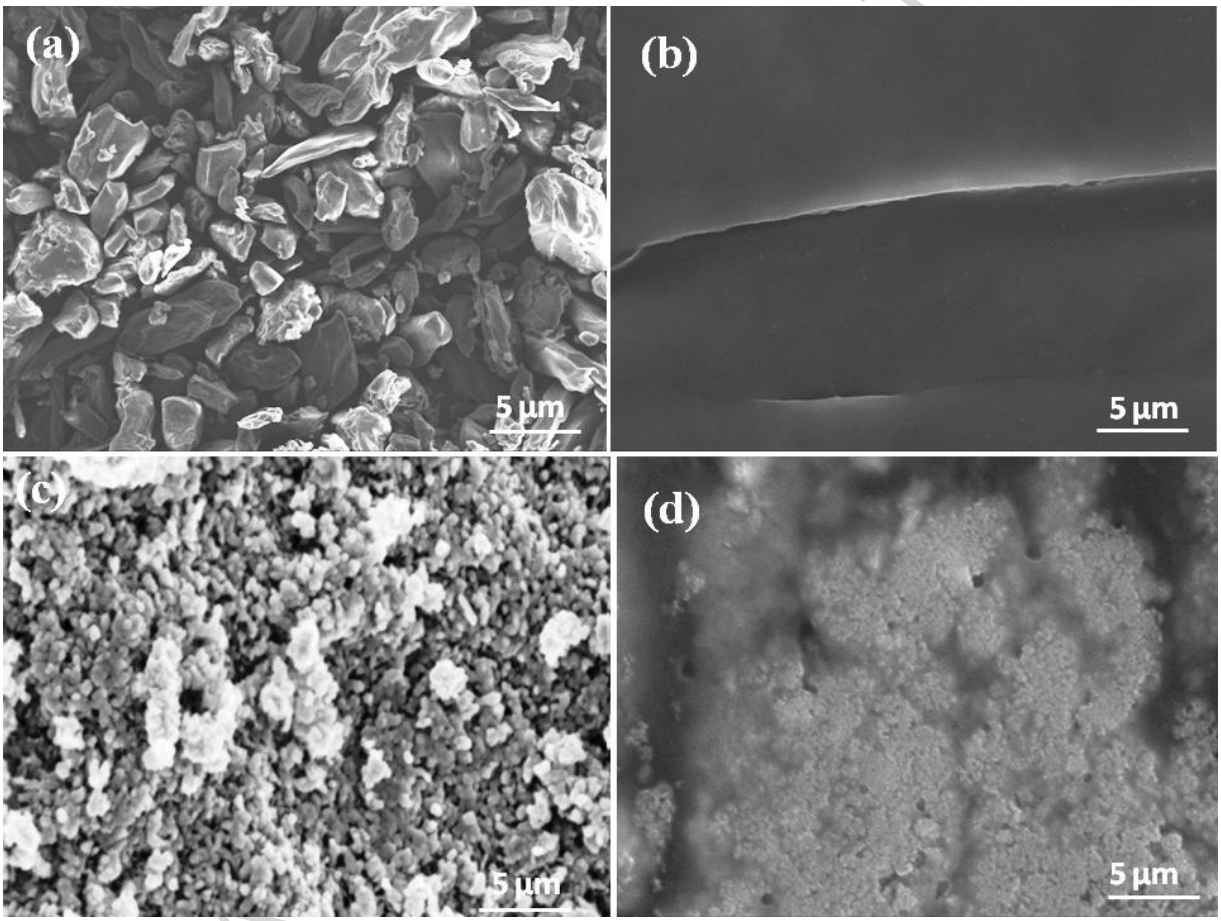

Fig. 7

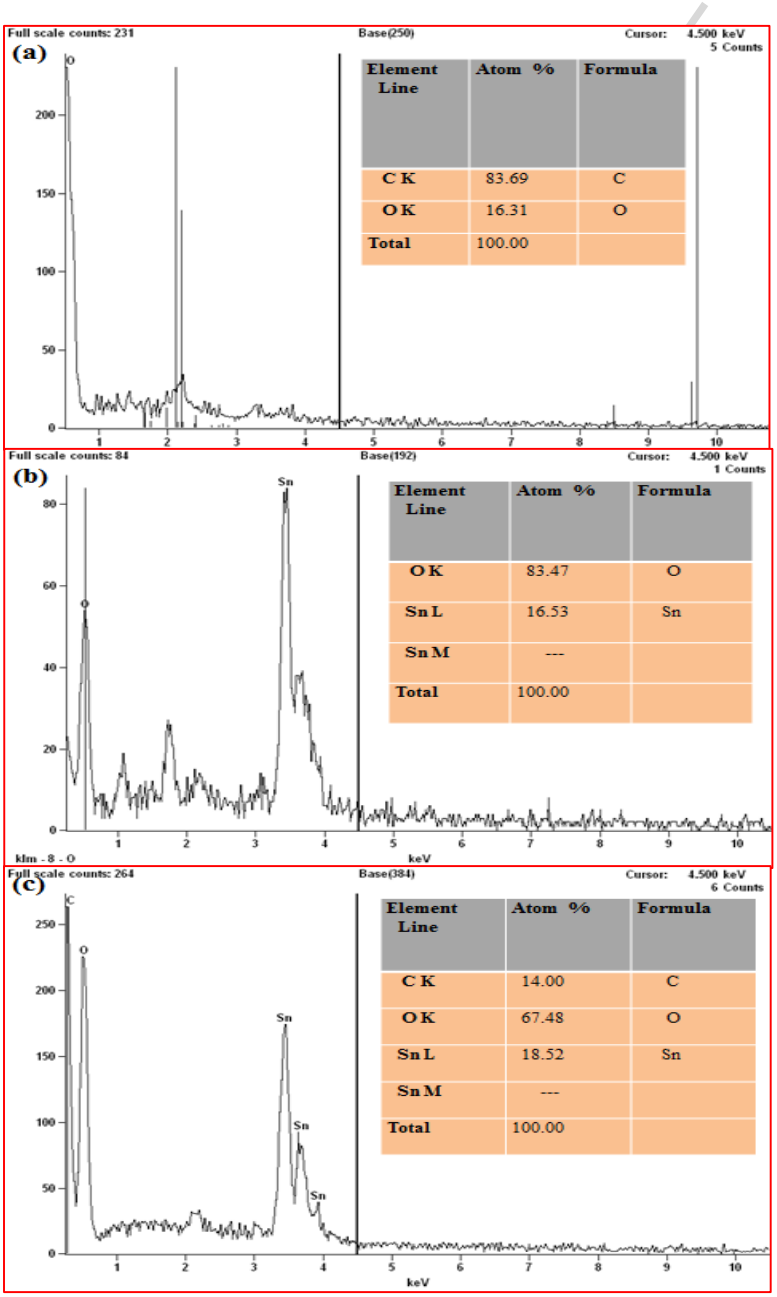

Fig. 8

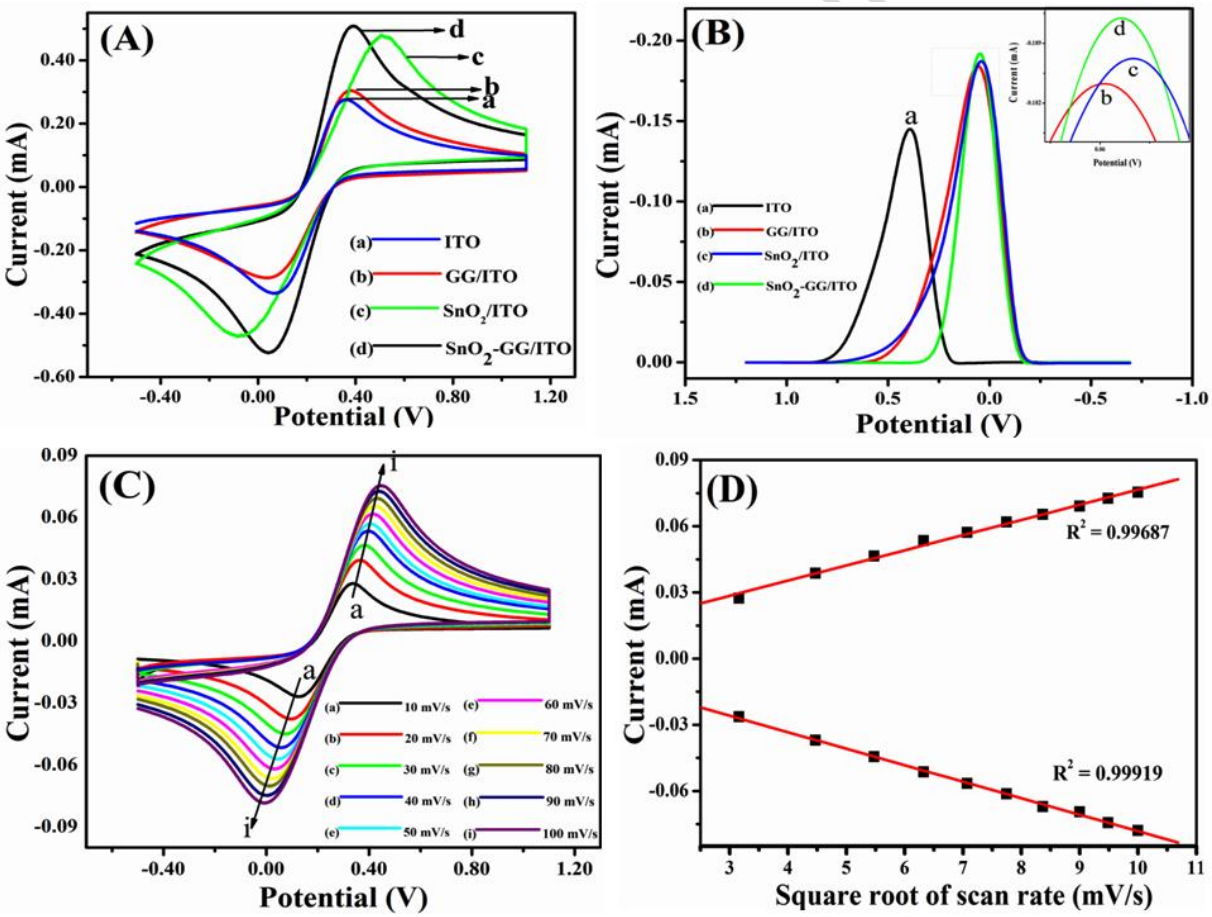

Fig. 9

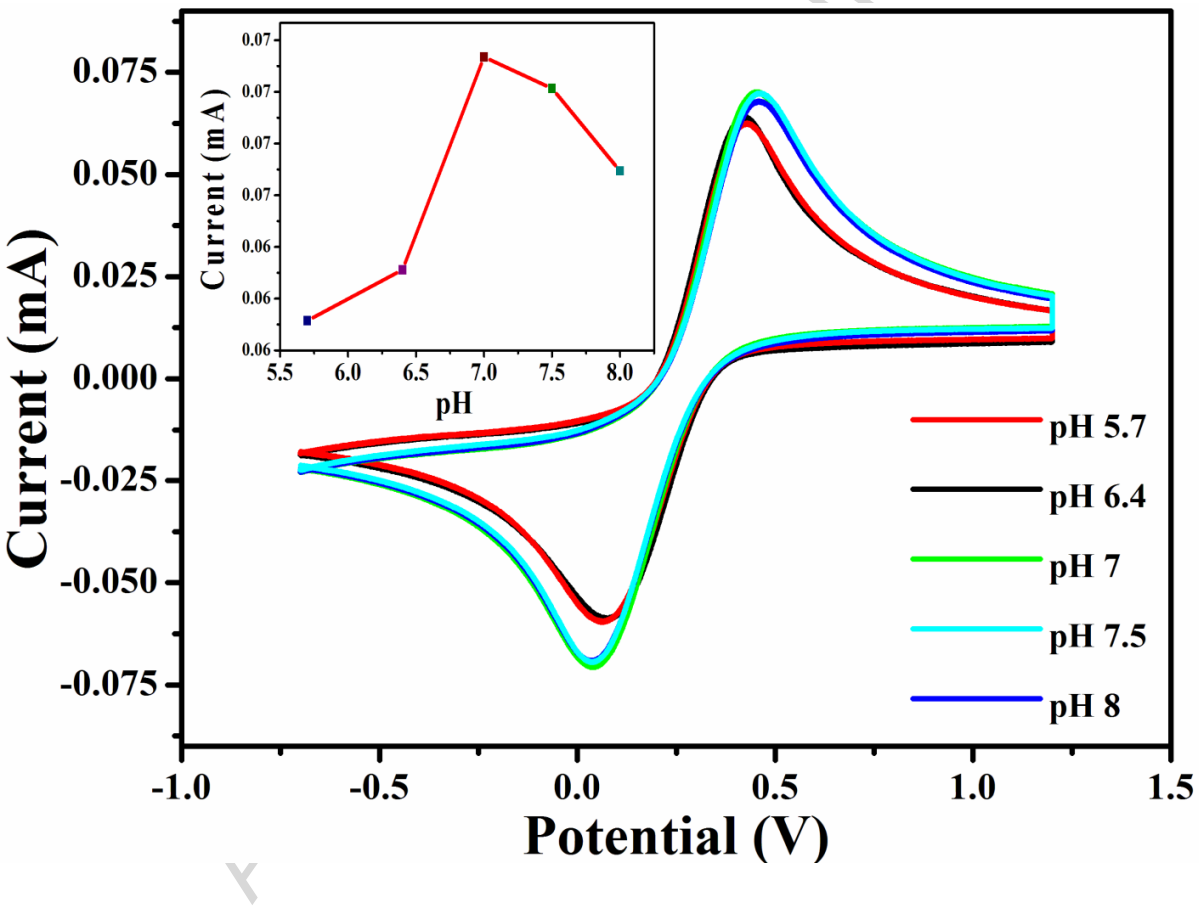

Fig. 10

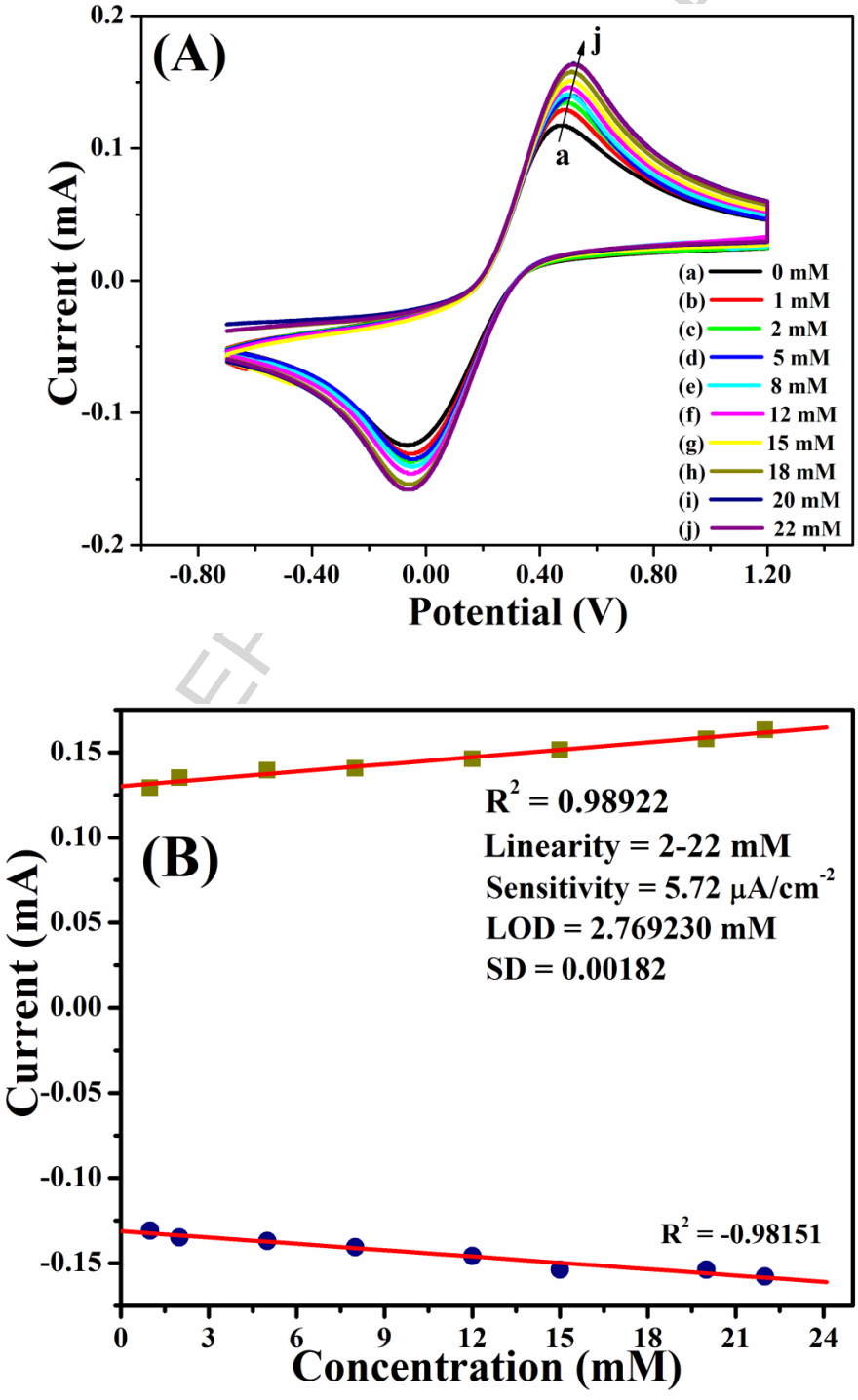

Table 1. Shows the electro-analytical parameters for electrocatalytic oxidation of hydrazine at different electrodes materials.

Methods	Electrode	pH, Medium	Sensitivity (μA/cm^2 μM)	Linear range (mmol dm^{-3})	Detection limit (mmol dm^{-3})	Response time (s)	References (Year)
CV	Pd-GG-g-PAM-silica modified GCE	7.0, PBS	-	0.05 - 0.6 0.6 - 180.0	4.1 x10^{-3}	-	[36]
CV	Pd NPs modified CB	9.0, PBS	-	0.005 - 0.5 0.5 - 10 10 - 50	8.8 x 10^{-3}	-	[52[
Amperometry	MnHCF modified graphite–wax composite electrode	7.0, PBS	-	0.0333 - 8.18	6.65 x 10^{-3}	-	[53]
CV	Fe-doped ZnO nanoparticle electrode	-	39.36	-	0.01 x 10^{-3}	~10	[54]
Amperometry	Fe_2O_3 modified carbon powder epoxy composite electrode	7.4, PBS	-	1-8	1.18 x 10^{-3}	~60	[55]
CV	SnO2 -GG/ITO	7.0, PBS	5.72	2 - 22	2.76	~34	Present work

Graphical Abstract

Synthesis of sol-gel derived tin dioxide (SnO_2) nanoparticles grafted in to gaur gum (GG) organic-inorganic hybrid nanocomposite for determination of hydrazine (HZ). Under optimized experimental conditions, SnO_2-GG/ITO electrode shows, linearity 2-22 mM, and detection limit 2.769 mM with high sensitivity of 5.72 μAcm^{-2}. The results clearly suggest that SnO_2-GG nanocomposite electrode provides an attractive matrix for impregnation of metal-oxide nanoparticles and an improved sensing platform for the electrochemical studies.

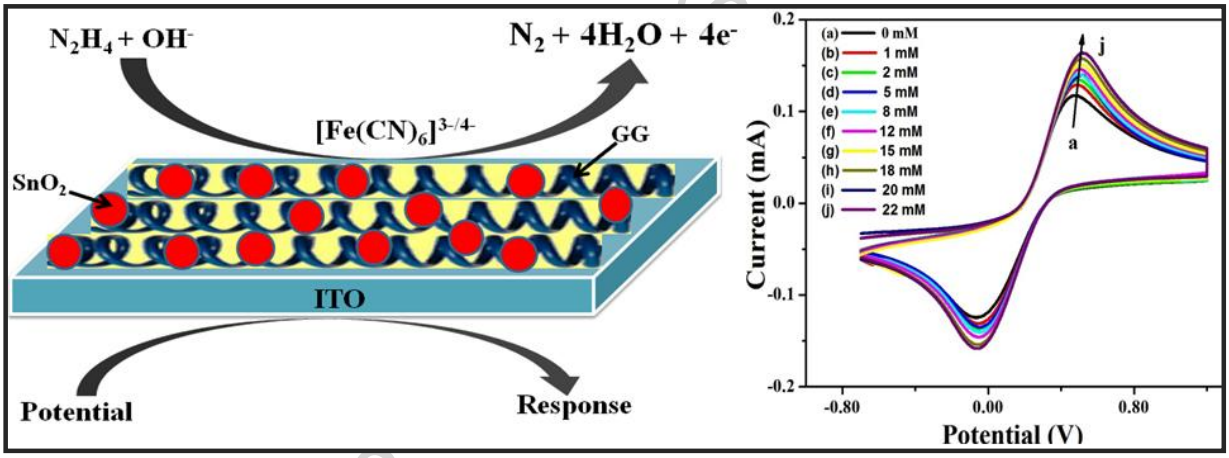

Highlights

- Sol-gel derived SnO_2 nanoparticles encapsulated into gaur gum matrix
- Utilizes organic-inorganic hybrid nanocomposite for determination of hydrazine
- Cyclic voltammetry studies were used to evaluate kinetic parameters
- SnO_2-Guar gum nanocomposite an attractive matrix for the electrochemical studies

www.combinatorics.ir

Transactions on Combinatorics
ISSN (print): 2251-8657, ISSN (on-line): 2251-8665
Vol. x No. x (201x), pp. xx-xx.

www.ui.ac.ir

ON •-LICT SIGNED GRAPHS $L_{\bullet_c}(S)$ AND •-LINE SIGNED GRAPHS $L_\bullet(S)$

MUKTI ACHARYA, RASHMI JAIN* AND SANGITA KANSAL

Communicated by Tommy R. Jensen

Abstract. A *signed graph* (or, in short, *sigraph*) $S = (S^u, \sigma)$ consists of an underlying graph $S^u := G = (V, E)$ and a function $\sigma : E(S^u) \longrightarrow \{+, -\}$, called the signature of S. A *marking* of S is a function $\mu : V(S) \longrightarrow \{+, -\}$. The *canonical marking* of a signed graph S, denoted μ_σ, is given as

$$\mu_\sigma(v) := \prod_{vw \in E(S)} \sigma(vw).$$

The *line graph* of a graph G, denoted $L(G)$, is the graph in which edges of G are represented as vertices, two of these vertices are adjacent if the corresponding edges are adjacent in G. There are three notions of a *line signed graph* of a signed graph $S = (S^u, \sigma)$ in the literature, viz., $L(S)$, $L_\times(S)$ and $L_\bullet(S)$, all of which have $L(S^u)$ as their underlying graph; only the rule to assign signs to the edges of $L(S^u)$ differ. Every edge ee' in $L(S)$ is negative whenever both the adjacent edges e and e' in S are negative, an edge ee' in $L_\times(S)$ has the product $\sigma(e)\sigma(e')$ as its sign and an edge ee' in $L_\bullet(S)$ has $\mu_\sigma(v)$ as its sign, where $v \in V(S)$ is a common vertex of edges e and e'.

The line-cut graph (or, in short, *lict graph*) of a graph $G = (V, E)$, denoted by $L_c(G)$, is the graph with vertex set $E(G) \cup C(G)$, where $C(G)$ is the set of cut-vertices of G, in which two vertices are adjacent if and only if they correspond to adjacent edges of G or one vertex corresponds to an edge e of G and the other vertex corresponds to a cut-vertex c of G such that e is incident with c.

In this paper, we introduce *dot-lict signed graph* (or •*-lict signed graph*) $L_{\bullet_c}(S)$, which has $L_c(S^u)$ as its underlying graph. Every edge uv in $L_{\bullet_c}(S)$ has the sign $\mu_\sigma(p)$, if $u, v \in E(S)$ and $p \in V(S)$ is a common vertex of these edges, and it has the sign $\mu_\sigma(v)$, if $u \in E(S)$ and $v \in C(S)$. we characterize signed graphs on K_p, $p \geq 2$, on cycle C_n and on $K_{m,n}$ which are •-lict signed graphs or •-line signed graphs, characterize signed graphs S so that $L_{\bullet_c}(S)$ and $L_\bullet(S)$ are balanced. We also establish the characterization of signed graphs S for which $S \sim L_{\bullet_c}(S)$, $S \sim L_\bullet(S)$, $\eta(S) \sim L_{\bullet_c}(S)$ and $\eta(S) \sim L_\bullet(S)$, here $\eta(S)$ is negation of S and $\sim$ stands for switching equivalence.

MSC(2010): Primary: 05C22; Secondary: 05C75.

Keywords: Signed graph, Balance, Switching, •-line signed graph, •-lict signed graph.

Received: 20 September 2013, Accepted: 2 February 2015.

*Corresponding author.

1. Introduction

For graph theory terminology in general we refer the reader to [6]. All graphs considered here are simple, connected, and finite. Let $V(G)$, $E(G)$ and $C(G)$ respectively denote the vertex set, the edge set and the cut-vertex set of a graph G.

A *signed graph* is an ordered pair $S = (S^u, \sigma)$, where $S^u := G = (V, E)$ is a graph called the underlying graph of S and $\sigma : E(S^u) \longrightarrow \{+, -\}$ is a function, called the *signature* of S. In general terms, we say that the edges are *signed* by σ. In a pictorial representation of a signed graph S, its positive edges are shown as bold line segments ('Jorden curves' drawn on the plane) and negative edges as broken line segments as shown in Figure 1. $E^+(S) = \{e \in E(S^u) : \sigma(e) = +\}$ and $E^-(S) = \{e \in E(S^u) : \sigma(e) = -\}$. The elements of $E^+(S)$ ($E^-(S)$) are called *positive* (*negative*) *edges* of S and the set $E(S) = E^+(S) \cup E^-(S)$ is called the edge set of S.

A signed graph in which all the edges are positive, we regard as *all-positive signed graph* (*all-negative signed graph* is defined similarly). A signed graph is said to be *homogeneous* if it is either all-positive or all-negative and *heterogeneous* otherwise. By $d(v)$, we denote degree of $v \in V(S)$, $d(v) = d^+(v) + d^-(v)$, where $d^+(v)$ ($d^-(v)$) denote the positive (negative) degree of v.

A *marking* of S is a function $\mu : V(S) \longrightarrow \{+, -\}$. Sampathkumar introduced the idea of marking the vertices with signs derived from the edges signs in [10], which is $\mu_\sigma : V(S) \longrightarrow \{+, -\}$ given as

$$\mu_\sigma(v) := \prod_{vw \in E(S)} \sigma(vw).$$

This marking is called canonical marking. In this paper, a vertex $v \in V(S)$ of $d^-(v)$ even or $\mu_\sigma(v) = +$ is called *positive vertex* (*negative vertex* is defined similarly).

Lemma 1.1 (**Sampathkumar** [10])**.** *In any canonically marked signed graph there are an even number of vertices marked negative.*

A cycle in a signed graph is said to be positive (negative) if the product of the signs of its edges is positive (negative); that is, it contains an even (odd) number of negative edges. A signed graph is said to be *balanced*, if every cycle in it is positive [7].

Lemma 1.2 (**Zaslavsky** [14])**.** *A signed graph in which every chordless cycle is positive, is balanced.*

A cycle in a signed graph is said to be *consistent* with respect to marking μ if it contains an even number of negative vertices and a signed graph is said to be consistent with respect to marking μ if every cycle in it is consistent [11]. Similarly, a cycle of a signed graph is called *canonically consistent (or $\mathcal{C}$-consistent)* if it contains an even number of negative vertices and a signed graph is said to be

$\mathcal{C}$-consistent if every cycle in it is $\mathcal{C}$-consistent.

Signed graphs S_1 and S_2 are said to be *isomorphic*, written as $S_1 \cong S_2$, if there is a graph isomorphism $f : S_1^u \to S_2^u$ that preserves edge signs.

One of the important operations on signed graphs involves changing signs of their edges. The *negation* of a signed graph S, denoted by $\eta(S)$, is obtained by negating the sign of every edge of S, i.e., by changing the sign of every edge to its opposite [8].

The idea of *switching* of a signed graph was introduced in connection with structural analysis of marking μ of a signed graph S in [1, 13]. Switching of S with respect to a marking μ is the operation of changing the sign of every edge of S to its opposite whenever its end vertices are of opposite signs. The signed graph obtained in this way is denoted by $\mathbb{S}_\mu(S)$ and is called *μ-switched* signed graph or just switched signed graph.

Further, a signed graph $S_1 = (S_1^u, \sigma)$ *switches* to a signed graph $S_2 = (S_2^u, \sigma')$ (or that S_1 and S_2 are *switching equivalent*) written as $S_1 \sim S_2$ whenever there exists a marking μ of S_1 such that $\mathbb{S}_\mu(S_1) \cong S_2$. Since the definition of switching does not change the underlying graphs of the respective signed graphs, $S_1 \sim S_2$ implies that $S_1^u \cong S_2^u$.

Signed graphs S_1 and S_2 are said to be *weakly isomorphic* (see [12]) or *cycle isomorphic* (see [13]) if there is a graph isomorphism $f : S_1^u \to S_2^u$ that preserves cycle signs. The following result is well known:

Theorem 1.3 (**Zaslavsky** [13])**.** *Two signed graphs S_1 and S_2 with the same underlying graph are switching equivalent if and only if they are cycle isomorphic.*

2. •-line signed graph and •-lict signed graph

The *line graph* of a graph G, denoted $L(G)$, is the graph in which edges of G are represented as vertices, two of these vertices are adjacent if the corresponding edges are adjacent in G (*c.f.:*[6], *chapter 8*). The following theorem is the well-known characterization of line graphs.

Theorem 2.1. [6] *The following statements are equivalent:*

- **(1)** *G is a line graph.*
- **(2)** *The lines of G can be partitioned into complete subgraphs in such a way that no point lies in more than two of these subgraphs.*

Theorem 2.2 (**Harary** [6])**.** *For a connected graph G, $G \cong L(G)$ if and only if G is a cycle.*

There are three notions of a *signed line graph* of a signed graph $S = (S^u, \sigma)$ in the literature, viz., $L(S)$, $L_\times(S)$ and $L_\bullet(S)$, all of which have $L(S^u)$ as their underlying graph; only the rule to assign

signs to the edges of $L(S^u)$ differ. Every edge ee' in $L(S)$ is negative whenever both the adjacent edges e and e' in S are negative [5], an edge ee' in $L_\times(S)$ has the product $\sigma(e)\sigma(e')$ as its sign [4] and an edge ee' in $L_\bullet(S)$ has $\mu_\sigma(v)$ as its sign, where $v \in V(S)$ is a common vertex of edges e and e' [3]. Note that for a graph G, $L(G) \cong L_\times(G) \cong L_\bullet(G)$ as G is an all-positive signed graph. For an all-negative signed graph S in which every vertex is positive, $L_\times(S) \cong L_\bullet(S)$ and are all-positive.

Figure 1 illustrates a signed graph and its line, $\times$-line and $\bullet$-line signed graphs.

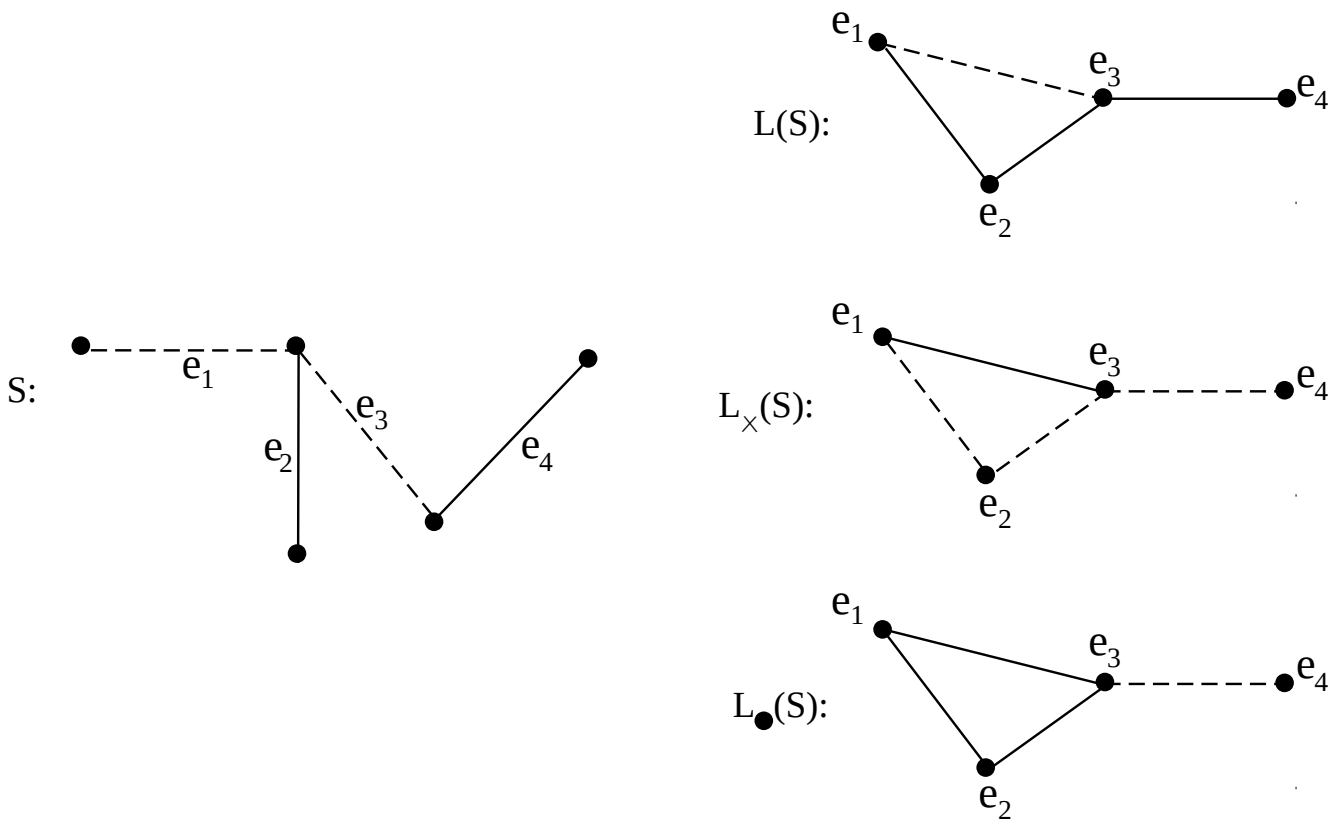

FIGURE 1. A signed graph S and its $L(S)$, $L_\times(S)$ and $L_\bullet(S)$

A signed graph S is said to be a line ($\times$-line or $\bullet$-line) signed graph if there exists a signed graph T whose line ($\times$-line or $\bullet$-line) signed graph $L(T)$ ($L_\times(T)$ or $L_\bullet(T)$) is isomorphic to S; and this signed graph T is called the line ($\times$-line or $\bullet$-line) root of S.

Kulli and Muddebihal [9] introduced the idea of a line-cut graph:

Definition 2.3. *The line-cut graph $L_c(G)$ (also known as the lict graph) of a graph $G = (V, E)$ is a graph having vertex set $E(G) \cup C(G)$, in which two vertices are adjacent if and only if they correspond to adjacent edges of G or one vertex corresponds to an edge e of G and the other vertex corresponds*

to a cut-vertex c of G such that e is incident with c in G; that is, $L_c(G)$ is the intersection graph $\Omega(E(G) \cup C(G))$. Clearly, $L_c(G) \cong L(G)$ if $C(G) = \phi$.

A graph G is said to be a lict graph if there exists a graph H whose lict graph $L_c(H)$ is isomorphic to G.

A *clique* of a graph is its maximal complete subgraph. The following theorem gives the characterization of lict graphs.

Theorem 2.4 (**Acharya et al.** [2])**.** *The following statements are equivalent:*

(1) *$G = (V, E)$ is a lict graph.*

(2) *The edges of G can be partitioned into cliques in such a way that no vertex lies in more than two of these cliques and for each clique G',*

(i) *if each vertex of G' lies in two cliques of the partition, then $G - E(G')$ is connected; and*

(ii) *if each vertex of G' lies in two cliques of the partition except exactly one vertex (say v) of G' then $G - E(G') - v$ is disconnected. G does not contain a pendant vertex.*

Theorem 2.5 (**Kulli and Muddebihal** [9])**.** *For a connected graph G, $G \cong L_c(G)$ if and only if G is a cycle.*

In this paper, we introduce $\bullet$-lict signed graph $L_{\bullet_c}(S)$ as follows:

Definition 2.6. *The dot-lict signed graph (or $\bullet$-lict signed graph) of a signed graph $S = (S^u, \sigma)$, is a signed graph $L_{\bullet c}(S) = (L_c(S^u), \sigma')$, where for every edge uv of $L_c(S^u)$*

$$\sigma'(uv) = \begin{cases} \mu_\sigma(p) & \text{if } u, v \in E(S) \text{ and } p \in V(S) \text{ is a common vertex of these edges;} \\ \mu_\sigma(v) & \text{if } u \in E(S) \text{ and } v \in C(S) \end{cases}$$

Figure 2 illustrates a signed graph and its $\bullet$-lict signed graph.

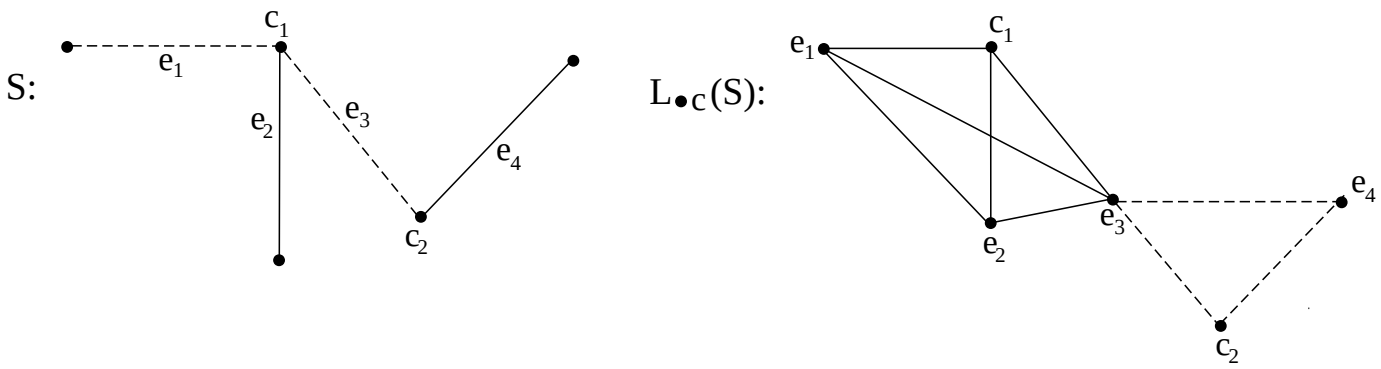

FIGURE 2. A signed graph S and its $\bullet$-lict signed graph $L_{\bullet c}(S)$

Note that for a graph G, $L_c(G) \cong L_{\bullet c}(G)$ as G is an all-positive signed graph. For a signed graph S

in which every non-pendant vertex is positive, $L_{\bullet c}(S) \cong L_c(S^u)$.

A signed graph S is said to be a $\bullet$-lict signed graph if there exists a signed graph T whose $\bullet$-lict signed graph $L_{\bullet c}(T)$ is isomorphic to S; and this signed graph T is called the $\bullet$-lict root of S.

3. Main Results

Theorem 3.1. *A signed graph $S = (S^u, \sigma)$, on a complete graph $S^u := K_p$, $p \geq 3$, is a $\bullet$-lict signed graph if and only if S is homogeneous or a triangle having two negative edges.*

Proof. Necessity:
Let $S = (S^u, \sigma)$, on a complete graph K_p, $p \geq 3$, be a $\bullet$-lict signed graph. Therefore, $S \cong L_{\bullet c}(T)$ for some signed graph $T = (T^u, \sigma')$. This implies that $S^u \cong L_{\bullet c}(T^u)$, i.e., $K_p \cong L_c(T^u)$. By the definition of lict graph it is clear that

$$T^u = \begin{cases} K_3 \text{ or } K_{1,2} & \text{if p=3;} \\ K_{1,p-1} & \text{if } p \geq 4. \end{cases}$$

- If $T^u := K_3$, then for homogeneous T on T^u, S is all-positive triangle and for heterogeneous T, S is a triangle having two negative edges, as shown in Figure 3.

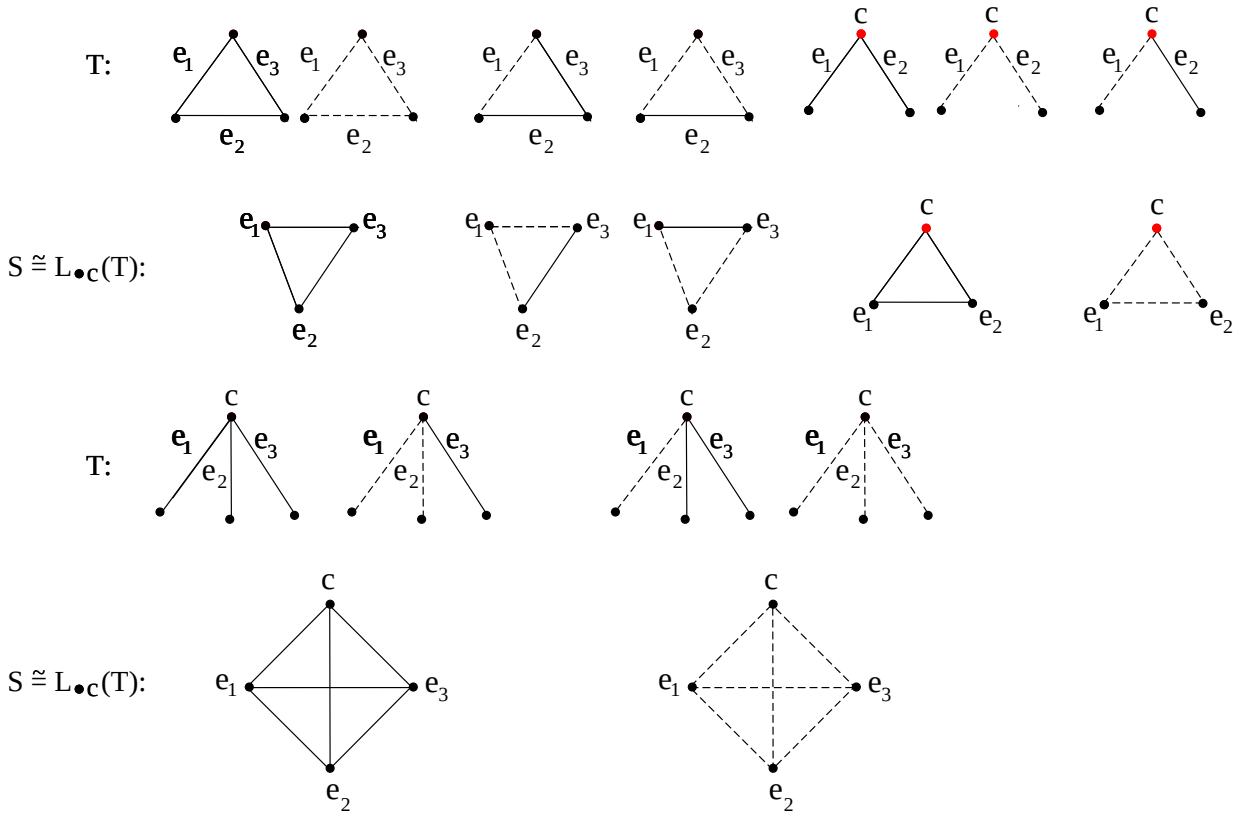

FIGURE 3. Signed graphs S and T such that $S \cong L_{\bullet c}(T)$

- If $T^u := K_{1,p-1}$, $p \geq 3$, then since non-pendant vertex is positive or negative, S is homogeneous. Thus, the necessity follows.

Sufficiency:
Suppose conditions hold. We give the construction of a signed graph T whose $\bullet$-lict signed graph is S. Let $\mathcal{P}(S) = \{S_1, S_2, ..., S_n\}$ be the partition of $E(S)$ into homogeneous cliques. The vertices of T^u correspond to the set $\mathcal{P}(S)$ together with the set U of vertices of S belonging only one of the homogeneous cliques S_i leaving one such vertex for each S_i. Thus $V(T^u) = \mathcal{P}(S) \cup U$, two of these vertices are adjacent whenever they have a nonempty intersection in S. Now, assign '+' ('-') sign to each non-pendant vertex $S_i \in V(T^u)$ if it corresponds to an all-positive (all-negative) S_i in S and take signature of T in such a way that signs assigned to vertices of T^u are preserved under canonical marking of T. For this signed graph T, $S \cong L_{\bullet c}(T)$; that is, S is a $\bullet$-lict signed graph. This completes the proof. □

Figure 4 illustrates construction of a signed graph T such that $S \cong L_{\bullet c}(T)$ for a signed graph S that satisfies sufficiency condition of Theorem 3.1. Note that T need not be unique.

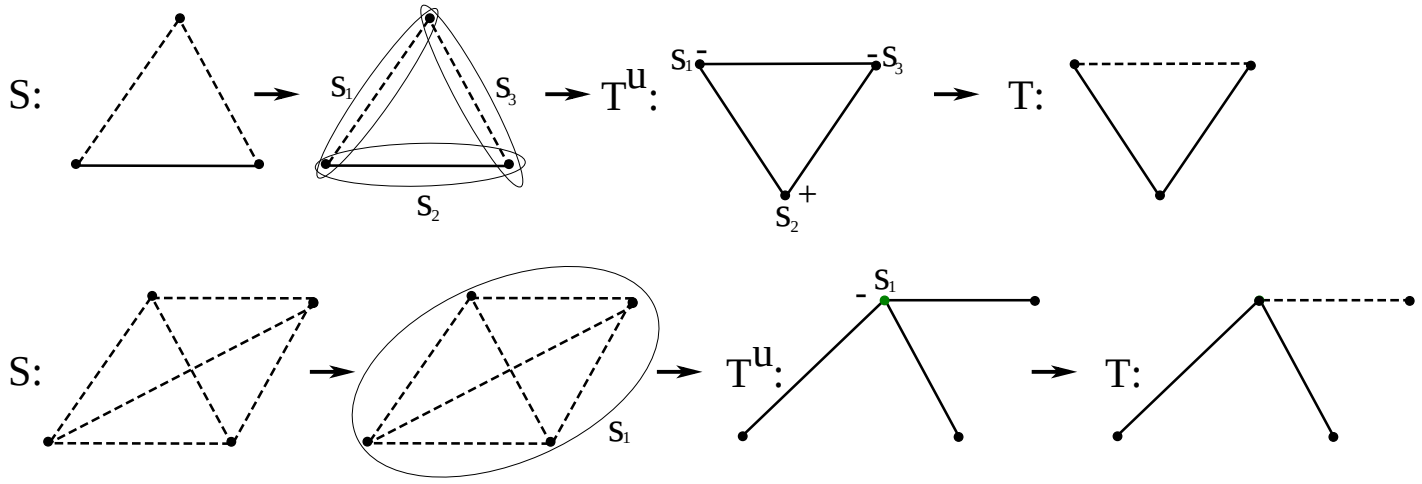

FIGURE 4. The construction of signed graph T from S such that $S \cong L_{\bullet c}(T)$

Theorem 3.2. *A signed graph $S = (S^u, \sigma)$, on a complete graph $S^u := K_p$, $p \geq 2$, is a $\bullet$-line signed graph if and only if S is homogeneous or a triangle having two negative edges.*

Proof. Necessity:
Let $S = (S^u, \sigma)$, on a complete graph K_p, $p \geq 2$, be a $\bullet$-line signed graph. Therefore, $S \cong L_{\bullet}(T)$ for some signed graph $T = (T^u, \sigma')$. This implies that $S^u \cong L_{\bullet}(T^u)$, i.e., $K_p \cong L(T^u)$. Clearly,

$$T^u = \begin{cases} K_3 \text{ or } K_{1,3} & \text{if p=3;} \\ K_{1,p} & \text{if } p = 2 \text{ or } p \geq 4. \end{cases}$$

- If $T^u := K_3$, then for homogeneous T on T^u, S is all-positive triangle and for heterogeneous T, S is a triangle having two negative edges, as shown in Figure 5.
- If $T^u := K_{1,p}$, $p \geq 2$, then since non-pendant vertex is positive or negative, S is homogeneous. Thus, the necessity follows.

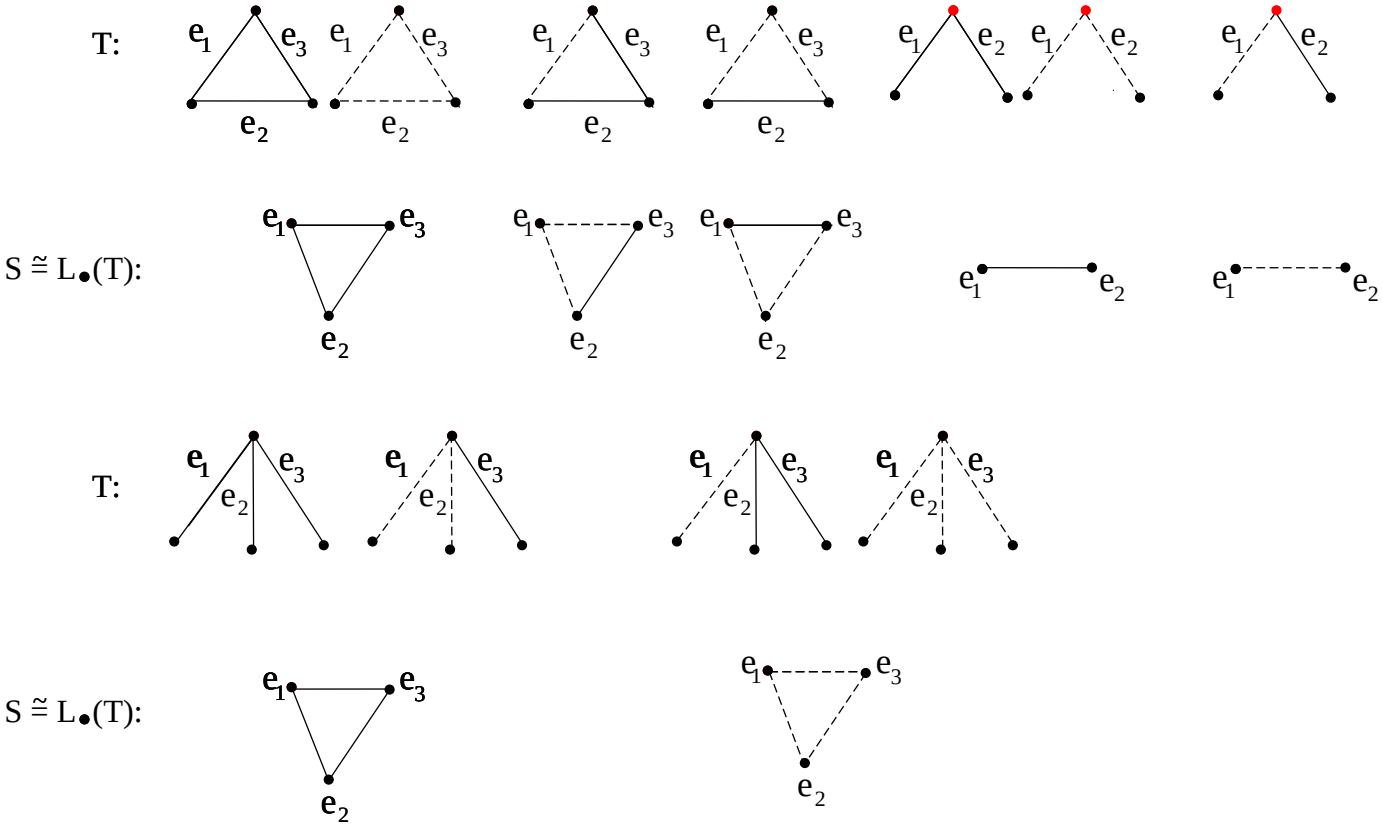

FIGURE 5. Signed graph T such that $S \cong L_\bullet(T)$

Sufficiency:

Suppose conditions hold. We give the construction of a signed graph T whose $\bullet$-line signed graph is S. Let $\mathcal{P}(S) = \{S_1, S_2, ..., S_n\}$ be the partition of $E(S)$ into homogeneous complete subgraphs. The vertices of T^u correspond to the set $\mathcal{P}(S)$ together with the set U of vertices of S belonging only one of the homogeneous complete subgraphs S_i. Thus $V(T^u) = \mathcal{P}(S) \cup U$, two of these vertices are adjacent whenever they have a nonempty intersection. Now, assign '+' ('-') sign to each non-pendant vertex $S_i \in V(T^u)$ if it corresponds to an all-positive (all-negative) S_i in S and take signature of T in such a way that signs assigned to vertices of T^u are preserved under canonical marking of T. For this signed graph T, $S \cong L_\bullet(T)$; that is, S is a $\bullet$-line signed graph. This completes the proof. □

Figure 6 illustrates construction of a signed graph T such that $S \cong L_\bullet(T)$ for a signed graph S that satisfies sufficiency condition of Theorem 3.2.

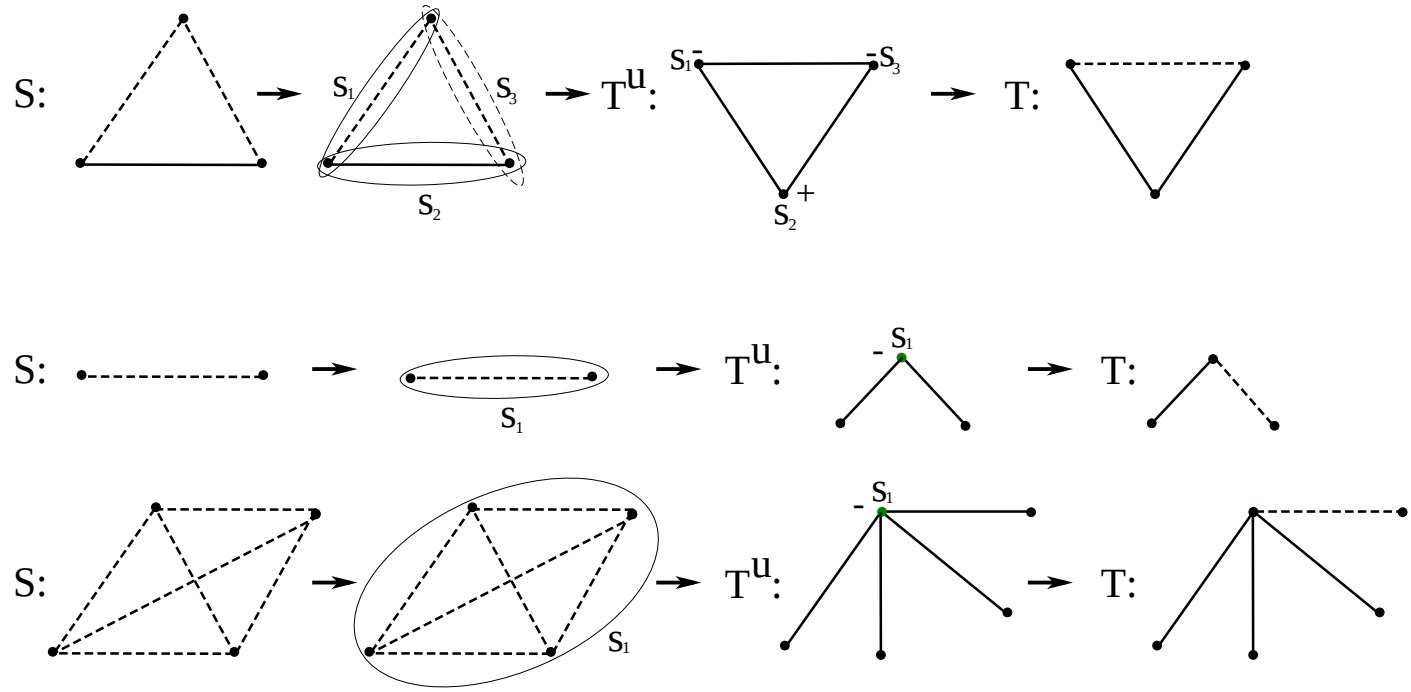

FIGURE 6. The construction of signed graph T from S such that $S \cong L_{\bullet}(T)$

Theorem 3.3. *A signed graph $S = (S^u, \sigma)$, on a cycle $S^u := C_n$, is $\bullet$-lict signed graph if and only if S is an all-negative triangle or a positive cycle.*

Proof. Necessity:
Let $S = (S^u, \sigma)$, on cycle C_n, be a $\bullet$-lict signed graph. Therefore, $S \cong L_{\bullet c}(T)$ for some signed graph $T = (T^u, \sigma')$. This implies that $S^u \cong L_{\bullet c}(T^u)$, i.e., $C_n \cong L_c(T^u)$. By the definition of lict graph it is clear that

$$T^u = \begin{cases} C_3 \text{ or } K_{1,2} & \text{if n=3;} \\ C_n & \text{if } n \geq 4. \end{cases}$$

- If $T^u := K_{1,2}$, then for T on T^u containing one negative edge, S is an all-negative triangle, as shown in Figure 3 and for other $T's$, S is a positive triangle.
- If $T^u := C_n$, then by the definition of $L_{\bullet c}(T)$, $|E^-(L_{\bullet c}(T))|$ = the number of negative vertices in T. By Lemma 1.1, in any canonically marked signed graph there are an even number of vertices marked negative. Hence $|E^-(L_{\bullet c}(T))|$ = even, i.e., S is a positive cycle.
  Thus the necessity follows.

Sufficiency:
Suppose conditions hold. We give the construction of a signed graph T by the procedure as discussed in the sufficiency of Theorem 3.1. For this signed graph T, $S \cong L_{\bullet c}(T)$; that is, S is a $\bullet$-lict signed graph. This completes the proof. □

Figure 7 illustrates construction of a signed graph T such that $S \cong L_{\bullet c}(T)$ for a signed graph S that satisfies sufficiency condition of Theorem 3.3.

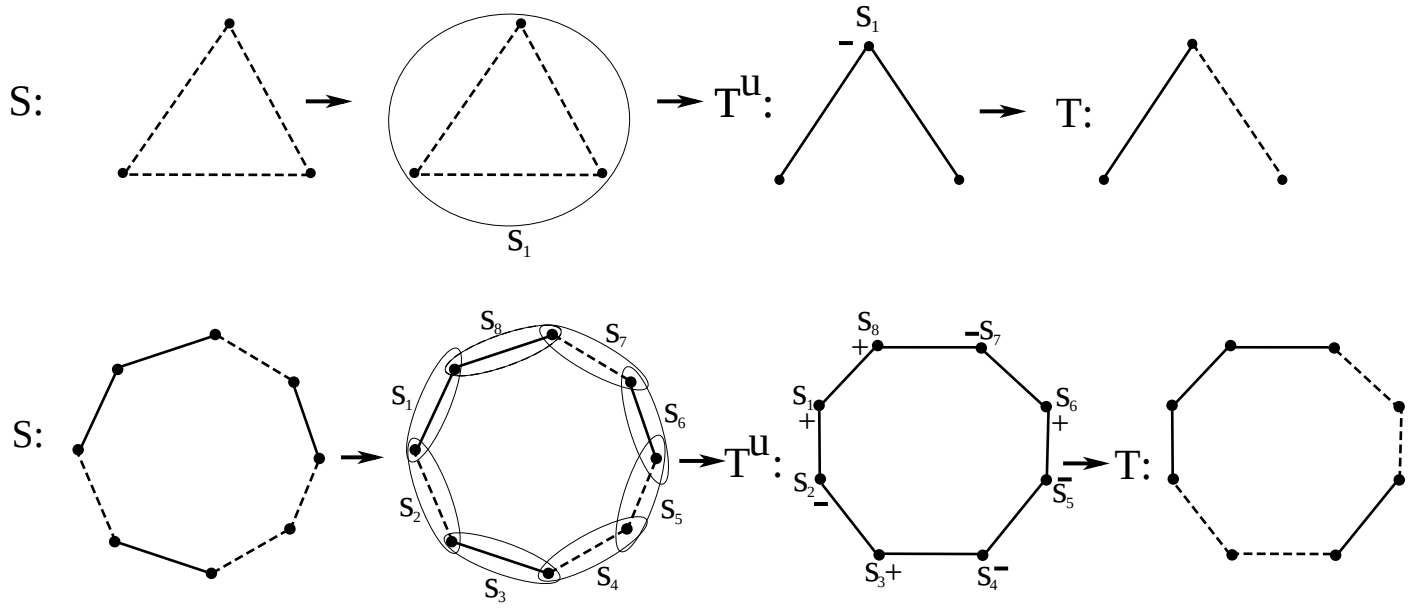

FIGURE 7. The construction of signed graph T from S such that $S \cong L_{\bullet c}(T)$

Corollary 3.4. *A signed graph $S = (S^u, \sigma)$, on a cycle $S^u := C_n$, is $\bullet$-line signed graph if and only if S is an all-negative triangle or a positive cycle.*

Proposition 3.5. *For a signed graph S on cycle C_n, $L_{\bullet c}(S) \cong L_{\bullet}(S)$ is a positive cycle.*

Proof. For a signed graph S on cycle C_n, $L_{\bullet c}(S) \cong L_{\bullet}(S)$, since $C(S) = \phi$. By the definition of $L_{\bullet c}(S)$, $|E^-(L_{\bullet c}(S))|$ = the number of negative vertices in S. By Lemma 1.1, in any canonically marked signed graph there are an even number of vertices marked negative. Hence $|E^-(L_{\bullet c}(S))|$ = even, i.e., $L_{\bullet c}(S)$ is a positive cycle. □

Theorem 3.6. *A signed graph $S = (S^u, \sigma)$ on a complete bipartite graph $S^u := K_{m,n}$, is a $\bullet$-lict signed graph if and only if S is a positive cycle of order 4.*

Proof. Necessity:
Let $S = (S^u, \sigma)$, on a complete bipartite graph $K_{m,n}$ be a $\bullet$-lict signed graph. Therefore, $S \cong L_{\bullet c}(T)$ for some signed graph T. This implies that $S^u \cong L_{\bullet c}(T^u)$ or $K_{m,n} \cong L_c(T^u)$, i.e., $K_{m,n}$ is a lict graph.

Let v be a cut-vertex of T^u then clearly $d(v) \geq 2$ and by the definition of lict graph, the edges incident with cut-vertex v in T^u induce a complete subgraph $K_{d(v)+1}$, i.e., K_p, $p \geq 3$ in $S^u := K_{m,n}$. Since a complete bipartite graph does not contain any odd cycle, K_p, $p \geq 3$ can not be a subgraph of $K_{m,n}$. Hence, $C(T^u) = \phi$. Therefore $K_{m,n}$ is also a line graph. Since $K_{1,3}$ is a forbidden induced subgraph of a line graph, $m \leq 2$ and $n \leq 2$. Furthermore by Theorem 2.4, a lict graph does not contain

a pendant vertex, $K_{m,n} \ncong K_{1,1}$ and $K_{1,2}$. Thus $K_{m,n} \cong C_4$ and by Theorem 3.3, S is a positive cycle of order 4.

Sufficiency:

Suppose S is a positive cycle of order 4 then by Theorem 3.3, S is a $\bullet$-lict signed graph. This completes the proof. □

Corollary 3.7. *A signed graph $S = (S^u, \sigma)$ on a complete bipartite graph $S^u := K_{m,n}$, is a $\bullet$-line signed graph if and only if S is any one of the following:*

- **(i)** *any signed graph on $K_{1,1}$ or $K_{1,2}$*
- **(ii)** *a positive cycle of order 4.*

Theorem 3.8. *For a signed graph S, $L_{\bullet c}(S)$ is balanced if and only if the following conditions hold in S:*

- **(i)** *S is $\mathcal{C}$-consistent and;*
- **(ii)** *each vertex v of $d(v) \geq 3$ and cut-vertex of degree 2 are positive vertices.*

Proof. Necessity:

Suppose for a signed graph S, $L_{\bullet c}(S)$ is balanced, i.e., every cycle in $L_{\bullet c}(S)$ is a positive cycle. By the definition of $L_{\bullet c}(S)$, a cycle Z in S induces a cycle Z' in $L_{\bullet c}(S)$ and $|E^-(Z')|$ = the number of negative vertices in Z. Since Z' is a positive cycle, every cycle Z in S contains an even number of negative vertices; that is, S is $\mathcal{C}$-consistent.

Next, we prove the necessity of condition **(ii)** by contrapositive:

Assume that a vertex $v \in V(S)$ which is of degree≥ 3 or a cut-vertex of degree 2, is a negative vertex, i.e., $d^-(v)$ is odd or $\mu_\sigma(v) = -$. Then by the definition of $L_{\bullet c}(S)$, the edges incident with v will induce an all-negative complete subsignedgraph of order ≥ 3 in $L_{\bullet c}(S)$ that makes $L_{\bullet c}(S)$ unbalanced. Thus, the necessity of **(ii)** follows.

Sufficiency:

A cycle in $L_{\bullet c}(S)$ is induced due to a cycle or a cut-vertex of degree 2 or a vertex of degree≥ 3 or their combinations in S. Suppose conditions **(i)** and **(ii)** hold in S then every chordless cycle in $L_{\bullet c}(S)$ will be positive. By Lemma 1.2, a signed graph in which every chordless cycle is positive, is balanced. Hence $L_{\bullet c}(S)$ is balanced. This completes the proof. □

Corollary 3.9. *$L_\bullet(S)$ is balanced if and only if the following conditions hold in signed graph S:*

- **(i)** *S is $\mathcal{C}$-consistent and;*
- **(ii)** *each vertex v of $d(v) \geq 3$ is a positive vertex.*

Theorem 3.10. *For a signed graph S, $S \sim L_{\bullet c}(S)$ if and only if S is a positive cycle.*

Proof. Suppose for a signed graph S, $S \sim L_{\bullet c}(S)$. This implies that $S^u \cong L_{\bullet c}(S^u)$, i.e., $S^u \cong L_c(S^u)$. By Theorem 2.5, S^u is a cycle and by Proposition 3.5, $L_{\bullet c}(S)$ is a positive cycle. By Theorem 1.3,

two signed graphs S_1 and S_2 with the same underlying graph are switching equivalent if and only if they are cycle isomorphic. Hence S is a positive cycle.

Conversely, Suppose S is a positive cycle then by Proposition 3.5, $L_{\bullet c}(S)$ is also a positive cycle. Hence by Theorem 1.3, $S \sim L_{\bullet c}(S)$, as shown in Figure 8. Thus the result follows. □

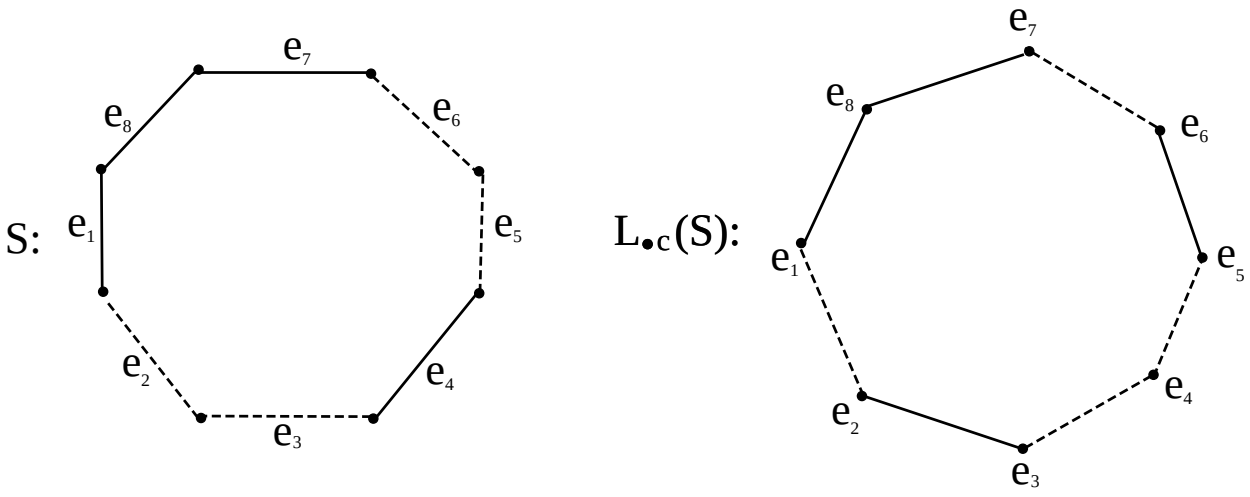

FIGURE 8. A signed graph S such that $S \sim L_{\bullet c}(S)$

Proposition 3.11. *For a signed graph S, $S \sim L_{\bullet}(S)$ if and only if S is a positive cycle.*

Theorem 3.12. *For a signed graph S, $\eta(S) \sim L_{\bullet c}(S)$ if and only if S is a positive even cycle or a negative odd cycle.*

Proof. Necessity:
Suppose for a signed graph S, $\eta(S) \sim L_{\bullet c}(S)$. This implies that $S^u \cong L_{\bullet c}(S^u)$, i.e., $S^u \cong L_c(S^u)$. By Theorem 2.5, S^u is a cycle and by Proposition 3.5, $L_{\bullet c}(S)$ is a positive cycle. By Theorem 1.3, two signed graphs S_1 and S_2 with the same underlying graph are switching equivalent if and only if they are cycle isomorphic. Hence $\eta(S)$ is also a positive cycle; that is, S is a positive even cycle or a negative odd cycle.

Sufficiency:
Suppose S is a positive even cycle or a negative odd cycle. Then clearly $\eta(S)$ is a positive cycle, as shown in Figure 9 and by Proposition 3.5, $L_{\bullet c}(S)$ is a also positive cycle. Hence, by Theorem 1.3, $\eta(S) \sim L_{\bullet c}(S)$. This completes the proof. □

Proposition 3.13. *For a signed graph S, $\eta(S) \sim L_{\bullet}(S)$ if and only if S is a positive even cycle or a negative odd cycle.*

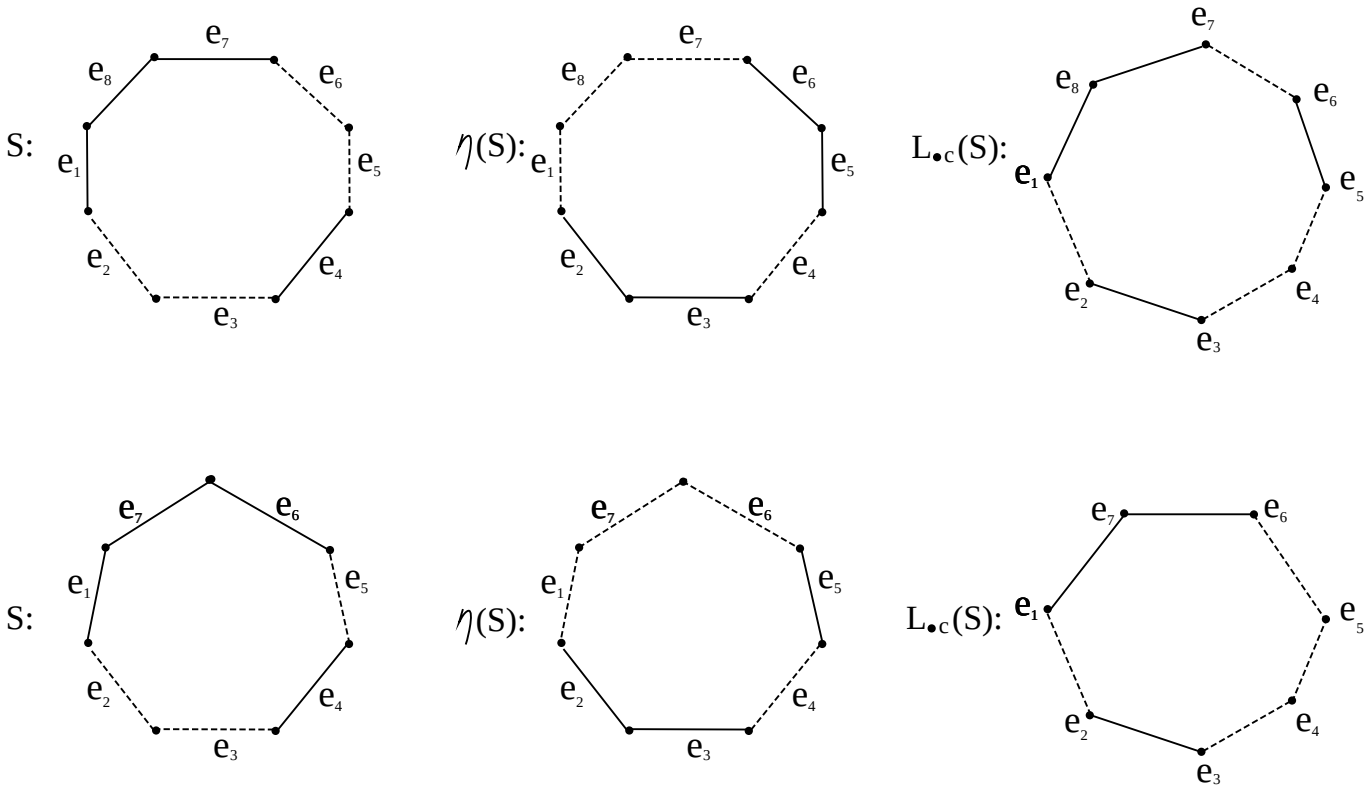

FIGURE 9. A signed graph S such that $\eta(S) \sim L_{\bullet c}(S)$

Acknowledgments

The authors are thankful to the referee for his valuable comments that enabled them to produce a much simpler version of the original manuscript and authors express their gratitude to Dr B. D. Acharya who always nurtured but could not witness the same. The corresponding author is thankful to the University Grants Commission (UGC), Govt. of India, for granting her research fellowship.

REFERENCES

[1] R. P. Abelson and M. J. Rosenberg, Symoblic psychologic : A model of attitudinal cognition, *Behav. Sci.*, **3** (1958) 1-13.

[2] M. Acharya, R. Jain and S. Kansal, Characterization of line-cut graphs, *Graph Theory Notes of New York*, **LXVI** (2014) 43-46.

[3] B.D. Acharya, Signed Intersection Graphs, *J. Discrete Math. Sci. and Cryptogr.*, **13** no. 6 (2010) 553-569.

[4] M. Acharya, ×-Line signed graphs, *J. Combin. Math. and Combin. Comp.*, **69** (2009) 103-111.

[5] M. Behzad and G.T. Chartrand, Line coloring of signed graphs, *Element der Mathematik*, **24** (1969) 49-52.

[6] F. Harary, *Graph Theory*, Addison-Wesley Publ. Comp., Massachusetts, Reading, 1969.

[7] F. Harary, On the notion of balance of a signed graph, *Mich. Math. J.*, **2** (1953) 143-146.

[8] F. Harary, Structural duality, *Behav. sci.*, **2** no. 4 (1957) 255-265.

[9] V.R. Kulli and M.H. Muddebihal, The lict graph and litact graph of a graph, *J. of Analysis and Comput.*, **2** no. 1 (2006) 33-43.

[10] E. Sampathkumar, Point-signed and line-signed graphs, *Nat. Acad. Sci. Letters*, **7** no. 3 (1984) 91-93.

[11] D. Sinha, *New frontiers in the theory of signed graphs*, Ph.D. Thesis, University of Delhi, India, 2005.

[12] T. Sozánsky, Enumeration of weak isomorphism classes of signed graphs, *J. Graph Theory*, **4** no. 2 (1980) 127-144.

[13] T. Zaslavsky, Signed graphs, *Discrete Appl. Math.*, **4** no. 1 (1982) 47-74.

[14] T. Zaslavsky, Signed analogs of bipartite graphs, *Discrete Appl. Math.*, **179** (1998) 205-216.

Mukti Acharya

House No. 22, 10th Cross, 5th Main MalleshPalya Bangaluru-560 075, India

Email: mukti1948@gmail.com

Rashmi Jain

Department of Applied Mathematics, Delhi Technological University, Delhi- 110 042, India

Email: rashmi2011f@gmail.com

Sangita Kansal

Department of Applied Mathematics, Delhi Technological University, Delhi- 110 042, India

Email: sangita_kansal15@rediffmail.com

Expert Systems With Applications xxx (2015) xxx–xxx

Contents lists available at ScienceDirect

Expert Systems With Applications

journal homepage: www.elsevier.com/locate/eswa

Opposition and dimensional based modified firefly algorithm

Q1 Om Prakash Verma, Deepti Aggarwal*, Tejna Patodi

Department of Information Technology, Delhi Technological University, Delhi, India

ARTICLE INFO

Keywords:
Firefly algorithm
Fitness function
Modified firefly algorithm
Opposition based learning
Optimization

ABSTRACT

This paper presents the modified Firefly Algorithm (FA) originally proposed by Yang.

Firefly Algorithm is based on the idealized behavior of the flashing characteristics of the fireflies. Though firefly is powerful in local search, it does not search well globally due to being trapped in local optimum. Due to this reason, the convergence is generally slow. The FA also doesn't give efficient solution in high dimensional problems. The proposed approach gives more efficient solution with reduced time complexity in comparison to original FA. Two modifications made are: (1) Opposition-based methodology is deployed where initialization of candidate solutions is done using opposition based learning to improve convergence rate of original FA, which includes initializing the opposite number of positions of each firefly. This also ensures efficient searching of the whole search space, (2) The dimensional-based approach is employed in which the position of each firefly is updated along different dimensions. This results in more optimal solution. This algorithm works for High Dimensionality problems, especially in terms of accuracy in finding the best optimal solution and in terms of fast convergence speed as well. Several complex multidimensional standard functions are employed for experimental verification. Experimental results include comparison with other Evolutionary algorithms which show that the Opposition and Dimensional based FA (ODFA) gives more accurate optimal solution with high convergence speed than the original FA and those achieved by existing methods.

1. Introduction

Optimization is the process of selecting the optimum solution from the set of alternative ones. We have to either maximize or minimize the objective function by calculating the value of function using several input values from the given range of values. Evolutionary algorithms are being widely used in optimization problems. Reproduction, mutation, crossover, recombination, etc., mechanisms are used in such algorithms. Population is formed by the candidate solutions of the given problem and in every generation evolution of the population takes place by applying above mentioned mechanisms. In this paper, for optimization process, FA is used which is a simple, effective and robust global optimization algorithm with few control parameters. FA outperforms many other optimization methods like GA, PSO etc. Yang had done several researches on FA like FA has been applied to solve nonlinear design problems (Yang, 2010a), the search strategy of FA has been combined with Levy flights to improve its efficiency (Yang, 2010b), and FA has also been extended to solve multi objective problems (Yang, 2013). FA has been used is several applications which include structural optimization (Gandomi, Yang, & Alavi, 2011), cross entropy threshold selection (Horng & Liou, 2011), traveling salesman problem (Jati & Suyanto, 2011), clustering (Senthilnath, Omkar, & Mani, 2011), image compression (Horng, 2012) etc.

FA, being the global optimization method is originated from fireflies swarm. It finds the optimal solution by movements and updations (Wang, Guo, Wang, & Wang, 2013). However, this strategy is based on randomness, so we might not always get the global optima. Also, when FA is applied for higher dimensions, some dimensions give results close to global optima and some dimensions give results away from global optima (Yang & He, 2013). On the other hand, we add a mutation to the fireflies, which includes opposition and Dimension based learning, which includes finding solutions in the opposite direction and multiple dimension. This increases the search space of finding the global optima (Ergezer, 2011; Wang, Li, Chen, & Qin, 2013).

The approach of opposition-based learning (OBL) was given by Tizhoosh (Tizhoosh, 2005a). Here, whole search space is searched efficiently by considering the corresponding opposite estimate simultaneously along with the estimate. So, the current estimate is searched in two directions and the search space is searched more efficiently. The opposition based optimization helps the solution to converge faster hence reduces the time complexity. The comparison between randomness and opposition based approach has been

* Corresponding author. Tel.: +919958664740.
E-mail addresses: opverma.dce@gmail.com (O.P. Verma), deepti.deeps.aggarwal18@gmail.com, deepti90_agg@yahoo.com (D. Aggarwal), patoditejna@gmail.com (T. Patodi).

http://dx.doi.org/10.1016/j.eswa.2015.08.054
0957-4174/

Begin

Let Fitness function be $f(x)$ *where* $x = (x_1, x_2, ..., x_D)$

Generate an initial population of fireflies x_i $(i = 1, 2, ...n)$

Light intensity I_i *at* x_i *is determined by* $f(x_i)$

Define the light absorption coefficient γ

While *(t <MaxGeneration)*

For $i = 1$ to n *all n fireflies*

For $j = 1$ to n *all n fireflies*

If $(I_j > I_i)$

Move firefly i *towards* j *in d-dimension*

End if

Attractiveness varies with distance r via $\beta_0 e^{-\gamma r^2}$

Evaluate new solutions and update light intensity

End for j

End for i

Rank the fireflies and find the current best

End while

Post process results and visualization

End

Fig. 1. Pseudo code of Firefly Algorithm.

done in Tizhoosh, Rahnamayan, and Salama, 2008, which proves that opposition based learning gives better results in less time. OBL has been applied in image segmentation (Tizhoosh & Sahba, 2007), management of water resources (Tizhoosh, Ponnambalam, & Mahootchi, 2007), learning in neural network (Tizhoosh, 2005b) etc. In this paper, OBL has been used at the time of population initialization. This gives the better approximation of the initial values of the particles and hence the solution converges faster.

There are situations, particularly for high dimensional data points, when one or fewer dimensions force a data point to be away from a given cluster. The odd parametric values of fewer dimensions, although apparently looks absurd, but in practice is apparent in real-world measurements. This paper proposes a solution to the above problem, by giving importance to each dimension to independently participate in global solution.

The major contribution of this paper in the field of Evolutionary Algorithms compared to other approaches would be a significantly less time complexity. Firefly algorithm has two inner loops when going through the population n, and one outer loop for number of generations G. So the complexity at the worst case is order of $n^2 * G$(represented as $O(n^2 * G)$). The time complexity is very high. The same applies to many other Evolutionary Algorithms (BFO, PSO, ACO etc.). But in modified firefly algorithm, for each iteration, we need to find the Gbest (global best firefly) whose complexity is $O(n * D)$ where D is the number of dimensions and then update each of the firefly using that Gbest firefly only, whose complexity is O(n), we do not need the comparison of each firefly with all other fireflies. Therefore the time complexity becomes $(O(G(n * D + n))) = O(G(n * D))$. Hence, the time complexity of modified algorithm is much lesser than original FA.

The rest paper is arranged in the following manner: Section 2 gives the overview of the Firefly algorithm. Section 3 reviews the OBL. Section 4 describes the proposed method. Section 5 shows the experimental results obtained through proposed algorithm and conclusions are given in section 6.

2. Firefly algorithm

This section reviews Firefly algorithm proposed by Yang in 2008 (Yang, 2008). FA consists of three idealized rules: (1) Regardless of its sex, each firefly will be attracted towards every other fireflies i.e. they are considered unisexual, (2) Attraction of one firefly towards another

Please cite this article as: O.P. Verma et al., Opposition and dimensional based modified firefly algorithm, Expert Systems With Applications (2015), http://dx.doi.org/10.1016/j.eswa.2015.08.054

is determined by the brightness so less bright firefly moves towards brighter firefly. The attractiveness and brightness are inversely proportional to distance, (3) the landscape of the fitness function determines the brightness of a firefly.

The pseudo code of FA is shown in Fig. 1.

The distance between any two Fireflies i and j whose positions are x_i and x_j is given by the Cartesian distance as follows:

$$r_{ij} = \sqrt{\sum_{m=1}^{D} (x_{i,m} - x_{j,m})^2} \tag{1}$$

where D is the number of dimensions.

The Firefly's attractiveness is given by:

$$\beta(r) = \beta_0 e^{-\gamma r^2} \tag{2}$$

At $r = 0$ attractiveness is β_0 and γ is the light absorption coefficient. The movement of the i_{th} Firefly towards more attractive j_{th} Firefly is calculated as:

$$x_i^{new} = x_i^{old} + \beta_0 e^{-\gamma r_{ij}^2}\left(x_i^{old} - x_j\right) + \alpha\left(rand - \frac{1}{2}\right) \tag{3}$$

Here, second term represents the attraction of one firefly towards another and the randomization in the movement of firefly is caused by the third term with α as randomization parameter. Rand is random number generator. x_i^{new} is the new position of the i_{th} firefly and x_i^{old} is the old position of i_{th} firefly. The parameter γ determines the attractiveness and hence the speed of convergence. In implementation, we can take $\beta_0 = 1$ and $\alpha \approx [0, 1]$. In this paper we have set $\gamma = 0.001$ however the results do not show much variation with change in value of γ.

3. Opposition-based learning (OBL)

This section reviews OBL introduced by Tizhoosh (Tizhoosh, 2006). The reinforcement learning based upon opposition based approach has been explained in Tizhoosh and Ventresca, 2006 (Tizhoosh, 2006). To get the optimum solution of a given problem we have to make some initial estimates. This estimate can be made by having some prior information about the solution or it can be completely random. In absence of prior information, convergence of solution depends upon the distance of the optimal solution from the random estimate. In worst case, if random guess is very much far away from the initial random guess than sometimes the solution could not be reached. The solution to this problem could be to look for solution in all directions or at least in the opposite direction. In the initialization step, along with the random guess of the solution x, the opposite of the x, $\tilde{x}$ should be considered simultaneously. This leads to searching of search space more thoroughly and increase in rate of convergence.

Opposite number—Suppose x is a real number which lies in the interval: $x \in [m, n]$. The opposite number of x is given by $\tilde{x}$ as follows:

$$\tilde{x} = m + n - x \tag{4}$$

In multidimensional space, the opposite number can be given as.

Let $x = (x_1, x_2, \ldots, x_D)$ be a point in D-dimensional space, where $x_1, x_2, \ldots, x_D \in R$ and $x_i \in [m_i, n_i]\ \forall i \in \{1, 2, \ldots, D\}$. The opposite point $\tilde{x}$ is defined by $\tilde{x}_1, \ldots, \tilde{x}_D$ in D-dimensional space where

$$\tilde{x}_i = m_i + n_i - x_i \quad i = 1, \ldots, D. \tag{5}$$

Opposition-based optimization — let $f(\cdot)$ be the fitness function, x be a candidate solution in D-dimensional space and $\tilde{x}$ be the opposite point of x. Replace point x with $\tilde{x}$ if $f(\tilde{x}) \geq f(x)$ else continue with x. Hence, the point and its corresponding opposite point are assessed simultaneously to determine the more appropriate point for the given problem.

4. The proposed algorithm

The original FA stuck in the local optima for high-dimensional problems as it doesn't consider every dimension of each firefly separately for finding the best solution due to which some dimensions move towards the better solution but some dimensions are moves away from the global solution therefore global optima is not reached. The proposed dimensional FA helps FA to not to stuck in the local optima as in this, in every generation global best solution is formed whose each dimension represents the best value of that dimension among all the fireflies and then position of all fireflies are updated according to the global best firefly. This leads to optimization of each dimension and hence we got the global optima.

Two major changes to the original FA are: (1) Opposition-based methodology is deployed where initialization of candidate solutions is done using opposition based learning to improve convergence rate of original FA, which includes initializing the opposite number of positions of each firefly. This also ensures efficient searching of the whole search space, (2) The dimensional-based approach is employed in which the position updation of each firefly is done along different dimensions.

The opposition based FA helps in initialization of the fireflies more efficiently so that fireflies converge faster and hence the time complexity is reduced. The proposed approach is explained as follows.

Let there are N-number of fireflies represented by $x = (x_1, x_2, \ldots, x_N)$ in D-dimensional space such that, i_{th} firefly, $x_i = (x_{i1}, x_{i2}, \ldots, x_{iD})$. Now we proposed the following modifications in the original FA:

A. In the proposed approach, at the time of initialization phase, OBL is employed in which the opposite number of the positions of each firefly is calculated. Let the population generated after calculating the opposite number is $\tilde{x}$. From x and $\tilde{x}$, the best N fireflies are selected. Steps are as follows:
   (1) Initialize the position of fireflies x randomly.
   (2) Generate N more fireflies by calculating the opposite population, $\tilde{x}$. This is done using the multi-dimensional opposite number of each firefly in the set x

   $$\tilde{x}_{ij} = a_j + b_j - x_{ij}, \text{ where } i = 1, 2, \ldots, N \text{ and } j = 1, 2, \ldots, D$$

   Where, x_{ij} and $\tilde{x}_{ij}$ represent j_{th} dimension of the i_{th} firefly of the population and the opposite-population, respectively.
   (3) Select the best N fireflies from $x \cup \tilde{x}$. These fireflies constitute the initial population.

```
For each dimension j , 1 to D
    For each firefly i , 1 to n
        Y = Gbestpos
        Y = x_ij
        If f(Y) > Gbest
            Gbest = f(Y)
            Gbestpos = Y
    End
End
```

Fig. 2. Pseudo code for Dimensional FA.

/* Opposition-Based population */
1. Generate initial population of fireflies $x = (x_1, x_2, ..., x_N)$ in the range $[m, n]$, such that $x_i = (x_{i1}, x_{i2}, ..., x_{iD})$
2. Generate opposite population, $\breve{x}_{ij} = m_j + n_j - x_{ij}$, $i \in [1, N]$ & $j \in [1, D]$
3. Select N fitted fireflies from the set $\{x, \tilde{x}_{ij}\}$ as initial population of fireflies, x.
/* End */
4. Optimization function given by, $f(x_i) = f(x_{i1}, x_{i2}, ..., x_{iD})$
5. Light intensity at x_i is equivalent to $f(x_i)$
6. Initialize the value of γ
7. Initialize Gbest as the best firefly from the initial fireflies position

/* Iterate till maximum number of generations*/
8. while (t <MaxGeneration)

/*update Gbest by Dimensional-Based approach*/
9. For each dimension $i = 1$ to D
10. For each firefly $j = 1$ to N
11. $Y :=$ Gbestpos
12. $Y := x(j, i)$
13. If $f(Y) >$ Gbest
14. Gbest $:= f(Y)$
15. Gbestpos $:= Y$
16. End
17. End
18. End
/* End of Dimensional-Based approach*/

19. For $i = 1$ to N
20. Move firefly i towards Gbest in D-dimension
21. Determine the distance between i^{th} firefly and Gbest by Euclidean distance:

$$R_{ij} = \sqrt{\sum_{m=1}^{d} \left(x_{i,m} - x_{j,m}\right)^2}$$

22. Determine Attractiveness which varies with distance r :

$$B(r) = \beta_0 e^{-\gamma r^2}$$

23. Move firefly i towards Gbest

$$x_i^{new} = x_i^{old} + \beta_0 e^{-\gamma r_{ij}^2} (x_i^{old} - Gbestpos) + \alpha(rand - \frac{1}{2})$$

24. end for i
25. end while
26. end

Fig. 3. Pseudo code of Dimensional Opposition based FA.

B. Each firefly in FA represents a candidate solution of the optimization problem. In original FA, the updation of the D-dimensional firefly takes place together which leads to some dimensions move towards the optimal solution and other dimensions move away from it. The deteriorated dimensions are neglected hence it becomes difficult to find the global optimum in high-dimensional problem. The time taken to reach every dimension at their optimum value is high so dimensional FA is introduced in which every dimension is updated separately. This is made possible by introducing the concept of Gbest in FA. Gbest represents the best firefly in the current generation. This Gbest is further improved by changing the value of one dimension at a time with the corresponding dimension value of other fireflies one by one and then if the fitness value improves, the Gbest is updated. Fig. 2 represents the pseudo code for dimensional FA. Gbestpos is the position of the Gbest. Y is the context vector used to represent the

Table 1
Experimental results (proposed approach vs original Firefly approach for lower dimensions).

Functions	Dimensions								
	Two-Dimension			Three-Dimension			Four-Dimension		
	Original $f(\cdot)$	Proposed $f(\cdot)$	K	Original $f(\cdot)$	Proposed $f(\cdot)$	K	Original $f(\cdot)$	Proposed $f(\cdot)$	K
Ackley	$2.08*10^{-2}$	$5.7119*10^{-5}$	1.1144	$2.125*10^{-2}$	$2.506*10^{-5}$	1.1428	$1.844*10^{-1}$	$6.421*10^{-5}$	0.9416
Rosenbrock	0	0	1.7189	0	0	2.67	0.1774	$4.156*10^{-3}$	3.175
De Jong	$2.79*10^{-6}$	$4.63*10^{-11}$	2.317	$3.307*10^{-5}$	$4.57*10^{-10}$	3.056	$1.198*10^{-4}$	$1.038*10^{-10}$	2.59
Griewank	0.1051	$4.124*10^{-11}$	1.509	0.1482	$7.7*10^{-11}$	1.125	0.1601	$1.065*10^{-10}$	1.273
Easom	−0.811	−1	3.335	NA	NA	NA	NA	NA	NA
Shubert	−186.73	−186.7309	2.928	NA	NA	NA	NA	NA	NA
Schwefel	$1.4*10^{-3}$	$2.58*10^{-5}$	1.564	0.04318	$3.818*10^{-5}$	2.86	0.056	$8.08*10^{-5}$	2.14
Rastrigin	$7.816*10^{-3}$	$6.928*10^{-9}$	1.32	$8.097*10^{-2}$	$7.414*10^{-7}$	1.51	$5.304*10^{-2}$	$4.316*10^{-6}$	1.86
Michalewicz	−1.37	−1.8013	0.946	−1.959	−2.7604	0.9029	−2.2667	−3.6571	0.7713
Beale	0	0	1.7189	0	0	2.67	0.056	$0.76*10^{-5}$	2.12
Matyas	0	0	2.34	0.1	0.0056	2.59	$1.35*10^{-5}$	$1.22*10^{-6}$	2.62

Table 2
Experimental results (proposed approach vs original firefly approach for higher dimensions).

Functions	Dimensions								
	10-Dimension			20-Dimension			30-Dimension		
	Original $f(\cdot)$	Proposed $f(\cdot)$	K	Original $f(\cdot)$	Proposed $f(\cdot)$	K	Original $f(\cdot)$	Proposed $f(\cdot)$	K
Ackley	1.4833	$7.1293*10^{-5}$	0.9155	2.9124	$8.7004*10^{-5}$	0.8736	3.2939	$1.8175*10^{-3}$	0.862
Rosenbrock	0.3478	0.0160	1.2005	0.8432	0.1184	0.998	0.86541	0.236	0.714
De Jong	$0.716*10^{-4}$	$1.349*10^{-11}$	1.986	$0.979*10^{-2}$	$2.9733*10^{-11}$	0.7576	$1.003*10^{-1}$	$1.2698*10^{-11}$	0.788
Griewank	0.1258	$0.1818*10^{-5}$	1.3986	0.5800	0.2349	1.2122	0.4277	0.365	0.929
Schwefel	0.232	$0.8756*10^{-4}$	1.455	0.455	$0.256*10^{-3}$	0.977	0.462	$0.158*10^{-1}$	0.860
Rastrigin	$5.732*10^{-2}$	$4.887*10^{-5}$	1.345	$9.877*10^{-1}$	$7.141*10^{-3}$	0.832	1.040	$9.229*10^{-1}$	0.815
Michalewicz	−1.12	−1.7533	0.898	−0.876	−1.432	0.856	−0.278	−1.212	0.783
Beale	0.13	0.1145	0.912	0.1	$0.0065*10^{-2}$	1.1	$9.35*10^{-4}$	$6.544*10^{-3}$	1.865
Matyas	0.0067	0.0009	1.243	0.0079	$0.06*10^{-3}$	1.55	$8.3*10^{-5}$	$8.45*10^{-6}$	2.112

vector formed by putting x_{ij} in the Gbestpos. Y is first initialized with the Gbestpos. The fitness of the firefly in dimension j is calculated by replacing the j_{th} component of Y by j_{th} of this firefly. Then, if $f(Y)$ is better than Gbest, Gbestpos is replaced with Y. Therefore, this method helps the firefly to contribute its merits in each dimension. This process is repeated for every dimension of every firefly in each generation. At the end of each generation, all the fireflies move towards the Gbest whereas in original firefly, the fitness value of each firefly is compared with all other fireflies and if the fitness value of that firefly is less than any other firefly, the firefly moves towards that better firefly. This concept of original firefly consumes time whereas in modified algorithm all fireflies move towards Gbest and no comparison is required. This helps in saving time.

C. ODFA is formed by using both the above modifications. Fig. 3 explains the pseudo code of ODFA. Lines 1–3 explain the generation of fireflies using OBL. Light intensity of a particular firefly x_i is equivalent to the value of the fitness function $f(x_i)$. Lines 9–18 explain the dimensional-based approach for updating the global best firefly using the context vector Y. In lines 19–24, the Euclidean distance is calculated between each firefly and best firefly. Each firefly is then move towards the Gbest. This process is repeated for maximum number of generations.

5. Experimental results

The experiments are performed on MATLAB, 2.50 GHz Intel i5 processor.

Test functions — a set of standard functions has been used for performance analysis of the proposed approach against original FA. In Appendix A, the definition of those functions with their global minimum values is enlisted.

Comparison strategy: The measure used in this paper for comparing the speed of FA and ODFA is execution time. Smaller execution time means higher convergence speed. In order to compare convergence speeds, a parameter speed rate is used given by

$$K = \frac{t_{FA}}{t_{ODFA}} \tag{6}$$

Where t_{FA} the execution is time for FA and t_{ODFA} is the execution time for ODFA. K > 1 signifies ODFA is faster.

Table 1 shows the value of fitness function $f(\cdot)$ obtained by modified algorithm as well as by the original FA for several standard functions with two, three and four dimensions. Table 2 shows the fitness function obtained by modified algorithm and original Firefly algorithm for higher dimensions i.e. 10, 20 and 30. Results show that the solutions obtained by the proposed approach for lower as well as higher dimensions are more accurate. The fitness value of Ackley function obtained through modified algorithm is approximately 1000 times better than the value obtained through the original FA. In the same manner, the fitness value of other functions obtained by proposed algorithm is also better than the original FA. The value of K is also mentioned in the table. The value of K is almost greater than 1 for every function which proves that the convergence speed of the proposed algorithm is higher than the original FA. Easom and Shubert function are 2-D functions so the values of these functions in 3-D and 4-D are not applicable and not shown in the table. Table 3 shows the comparison of proposed algorithm with other algorithms (**FA, BFO, PSO, ACO and DE**). The results show that proposed algorithm gives a better result than other algorithms and with much less time complexity for a particular dimension.

Parameters initialization: For all the experiments the parameters are initialized as follows: N = 50, MaxGeneration = 200, $\alpha = 0.2$, $\gamma = 0.001$ but in Schwefel's and Griewank's function, the search space is

Table 3
Experimental results (proposed approach vs other evolutionary algorithms for dimension = 10).

	FA	Proposed modified FA	BFO	PSO	ACO	DE
Ackley	1.4833	$7.1293*10^{-5}$	$2.69*10^{-2}$	$2.43*10^{-4}$	$3.22*10^{-4}$	$2.15*10^{-2}$
Rosenbrock	0.3478	0.0160	$1.53*10^{-4}$	$2.67*10^{-5}$	3.72	0
De Jong	$0.7166*10^{-4}$	$1.3494*10^{-11}$	$2.31*10^{-7}$	$3.98*10^{-8}$	$1.19*10^{-6}$	$3.487*10^{-5}$
Griewank	0.1258	$0.18188*10^{-5}$	$1.89*10^{-6}$	0.1986	$1.297*10^{-5}$	0.1367
Schwefel	0.232	$0.8756*10^{-4}$	−0.99	0.01529	$0.145*10^{-6}$	0.04678
Rastrigin	$5.732*10^{-2}$	$4.887*10^{-5}$	−186.7093	$7.326*10^{-6}$	$4.45*10^{-5}$	$9.097*10^{-2}$
Michalewicz	−1.12	−1.7533	$1.86*10^{-4}$	−2.0124	−2.667	−1.5

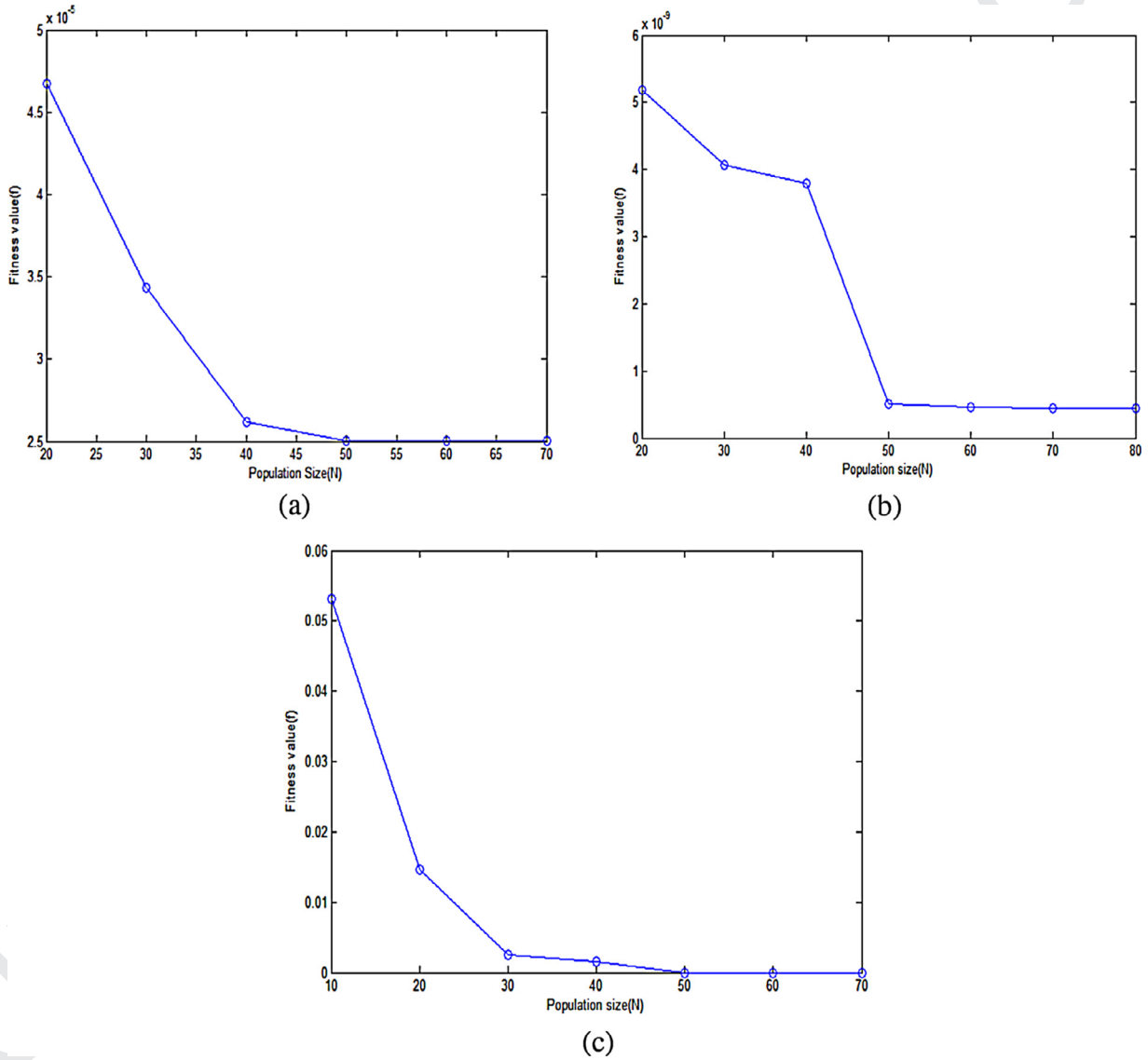

Fig. 4. Convergence of the proposed algorithm with change in population size (a) Ackley function, (b) De Jong function and (c) Rosenbrock function.

very large which lies in the range [−500,500] and [−600 600], respectively, so number of fireflies required is more to explore the whole search space therefore, N = 200 and MaxGeneration = 500 is taken for Schwefel's function. The fitness value of different functions with respect to the population size is plotted in Fig. 4 which shows that at N = 50 the functions attain their global optima. Fig. 5 shows the plot of the fitness value of different functions with respect to number of generations and it is clearly visible that at generations of 200, the functions converges faster towards their optima and the fitness value of different functions with respect to the value of alpha is plotted in Fig. 6. It can be seen that the fitness function converges very fast and attain their optimal value at the above mentioned values of the parameters.

6. Conclusions

This paper has described an improved variant of FA, i.e. Opposition and Dimensional based FA. This variant of FA employs opposition based learning which fastens the convergence rate and the Dimensional approach to obtain the global optima. The global optimum

Please cite this article as: O.P. Verma et al., Opposition and dimensional based modified firefly algorithm, Expert Systems With Applications (2015), http://dx.doi.org/10.1016/j.eswa.2015.08.054

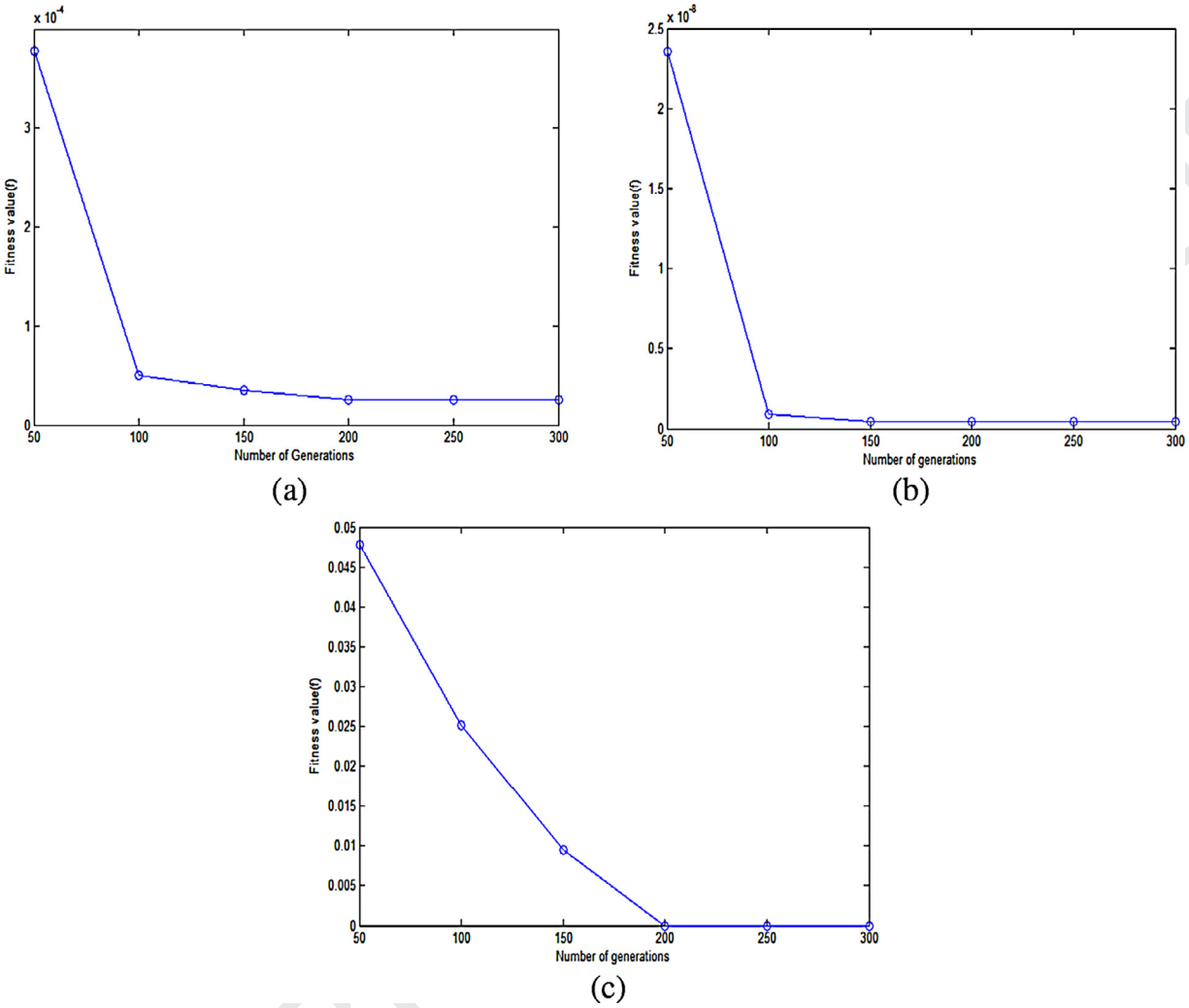

Fig. 5. Convergence of the proposed algorithm with change in Generations (a) Ackley function (b) De Jong function (c) Rosenbrock function.

is selected from the optimum solutions among all dimensions. The rate of convergence and time complexity reduces by opposition based Firefly. This hybrid variant of FA is employed for several benchmark images and they could demonstrate tremendous performance enhancement compared to several other popular contemporary methods, employed for the same images.

Although the number of iterations is more due to obtaining optima along each dimension and also due to opposition based learning the search space is more, still the time taken is much less than original FA due to decrease in random movement of fireflies. This is the main advantage of the proposed technique. The experimental section shows that for some dimensions, the other algorithms may prove better due to trade off in time space complexity, but on an overall basis, the results are more accurate in proposed method.

Also, when the proposed approach is compared to other Evolutionary algorithms, the results are more appropriate for the proposed approach for a particular dimension with lesser time complexity. This shows that the proposed approach is much better as compared to other techniques, proving the novelty of the approach.

An interesting future research motivation is to choose another recent optimization algorithm like PSO or ACO and achieve the most appropriate global optima with a further reduction in convergence time. Future works will also include application of this variant of FA color image enhancement and edge detection.

Appendix A

The functions used for verification of proposed algorithm

- Ackley function

$$f(x) = -ae^{-b\sqrt{\frac{1}{d}\sum_{i=1}^{d} x_i^2}} - e^{\frac{1}{d}\sum_{i=1}^{d}\cos(cx_i)} + a + e^1$$

Where, $a = 20$, $b = 0.2$ and $c = 2\pi$, $x_i \in [-32.768\ 32.768]$ for all $i = 1, \ldots, d$

Global minimum: $f(x) = 0$, at $x = (0, \ldots, 0)$

- Rosenbrock function

$$f(x) = \sum_{i=1}^{d-1} [100(x_{i+1} - x_i^2)^2 + (x_i - 1)^2]$$

Where, $x_i \in [-2.048, 2.048]$ for all $i = 1, \ldots, d$

Global minimum: $f(x) = 0$, at $x = (1, \ldots, 1)$

- De Jong function 1

$$f(x) = \sum_{i=1}^{d} x_i^2$$

Where, $x_i \in [-5.12, 5.12]$ for all $i = 1, \ldots, d$

Global minimum: $f(x) = 0$, at $x = (0, \ldots, 0)$

Please cite this article as: O.P. Verma et al., Opposition and dimensional based modified firefly algorithm, Expert Systems With Applications (2015), http://dx.doi.org/10.1016/j.eswa.2015.08.054

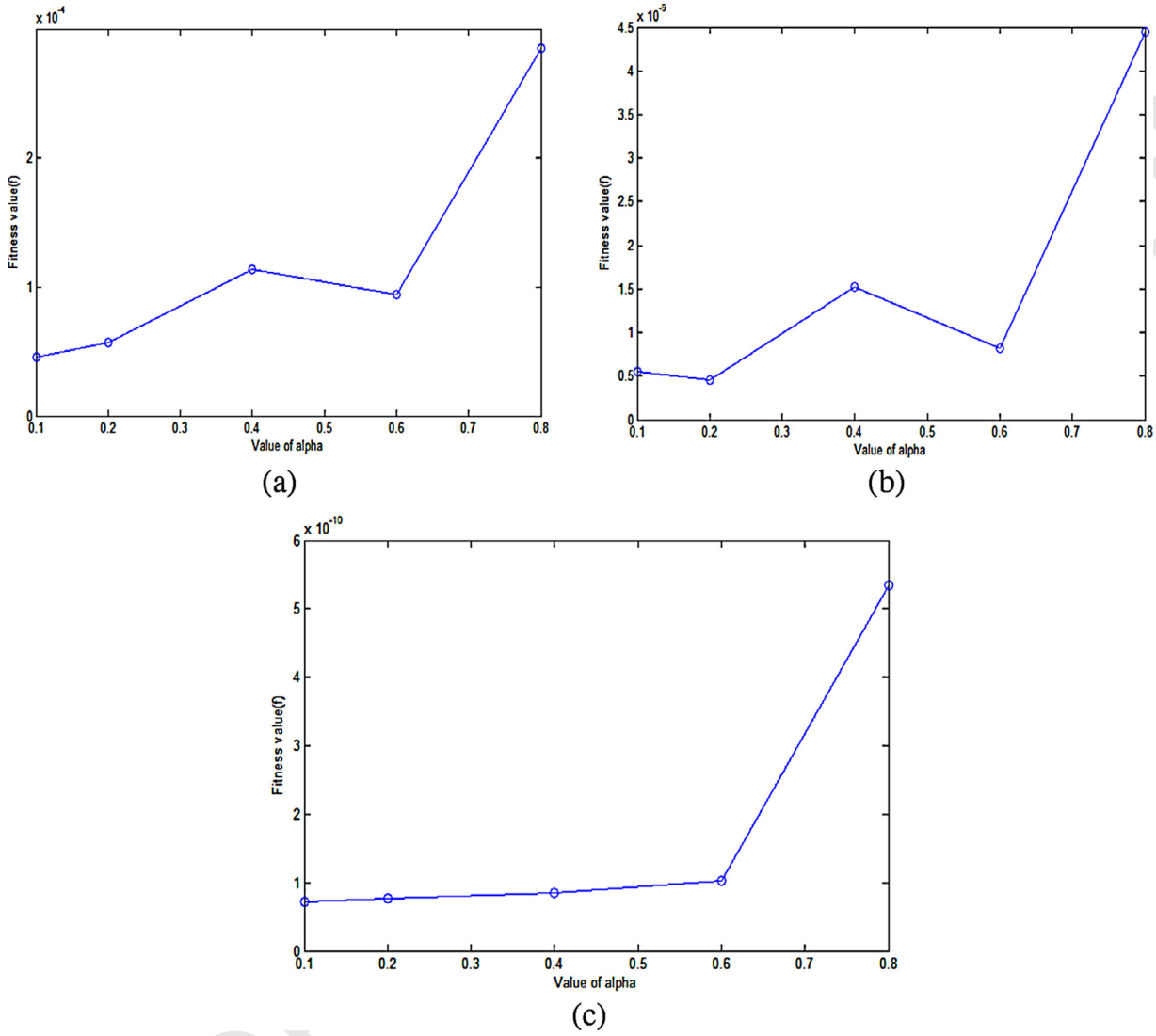

Fig. 6. Convergence of the proposed algorithm with change in value of alpha (a) Ackley function (b) De Jong function (c) Griewank function.

- Griewank function

$$f(x) = \sum_{i=1}^{d} \frac{x_i^2}{4000} - \prod_{i=1}^{d} \cos\left(\frac{x_i}{\sqrt{i}}\right) + 1$$

Where, $x_i \in [-600, 600]$ for all $i = 1, \ldots, d$
Global minimum: $f(x) = 0$, at $x = (0, \ldots, 0)$

- Easom function

$$f(x) = -\cos(x_1)\cos(x_2)\exp(-(x_1 - \pi)^2 - (x_2 - \pi)^2)$$

Where, $x_1 \in [-100, 100]$, $x_2 \in [-100, 100]$
Global minimum: $f(x) = -1$, at $x = (\pi, \pi)$

- Shubert function

$$f(x) = \left(\sum_{i=1}^{5} i\cos((i+1)x_1 + i)\right)\left(\sum_{i=1}^{5} i\cos((i+1)x_2 + i)\right)$$

Where, $x_1 \in [-10, 10]$, $x_2 \in [-10, 10]$
Global minimum: $f(x) = -186.7309$

- Schwefel function

$$f(x) = 418.9829d - \sum_{i=1}^{d} x_i \sin(\sqrt{|x_i|})$$

Where, $x_i \in [-500, 500]$ for all $i = 1, \ldots, d$
Global minimum: $f(x) = 0$, at $x = (1, \ldots, 1)$

- Rastrigin function

$$f(x) = 10d + \sum_{i=1}^{d} \left[x_i^2 - 10\cos(2\pi x_i)\right]$$

Where, $x_i \in [-5.12, 5.12]$ for all $i = 1, \ldots, d$
Global minimum: $f(x) = 0$, at $x = (0, \ldots, 0)$

- Michalewicz function

$$f(x) = -\sum_{i=1}^{d} \sin(x_i)\sin^{2m}\left(\frac{ix_i^2}{\pi}\right)$$

Where, m = 10, $x_i \in [0, \pi]$
Global minimum: At d = 2, $f(x) = -1.8013$, at $x = (2.20, 1.57)$

- Beale function

$$f(x) = (1.5 - x_1 + x_1x_2)^2 + (2.25 - x_1 + x_1{x_2}^2)^2 + (2.65 - x_1 + x_1{x_2}^2)^2$$

where $-4.5 \le xi \le 4.5$, i = 1, 2
The global minimum: x = (3, 0.5), f(x) = 0

Please cite this article as: O.P. Verma et al., Opposition and dimensional based modified firefly algorithm, Expert Systems With Applications (2015), http://dx.doi.org/10.1016/j.eswa.2015.08.054

- Matyas function

$$f(x) = 0.2G\left(x_1{}^2 + x_2{}^2\right) - 0.48x_1x_2$$

where $-10 \leq xi \leq 10$, i = 1, 2

The global minima: x = (0, 0), f(x) = 0.

References

Ergezer, M. (2011). Survey of oppositional algorithms. In *Proceedings of the 2011 14th International Conference on Computer and Information Technology (ICCIT)* (pp. 623–628).

Gandomi, A. H., Yang, X. S., & Alavi, A. H. (2011). Mixed variable structural optimization using firefly algorithm. *Computers & Structures, 89*(23–24), 2325–2336.

Horng, M.-H. (2012). Vector quantization using the firefly algorithm for image compression. *Expert Systems with Applications, 39*(1), 1078–1091.

Horng, M.-H., & Liou, R.-J. (2011). Multilevel minimum cross entropy threshold selection based on the firefly algorithm. *Expert Systems with Applications, 38*(12), 14805–14811.

Jati, K. G., & Suyanto (2011). Evolutionary discrete firefly algorithm for travelling salesman problem. *Adaptive and Intelligent Systems, 6943*, 393–403.

Senthilnath, J., Omkar, S. N., & Mani, V. (2011). Clustering using firefly algorithm: performance study. *Swarm and Evolutionary Computation, 1*(3), 164–171.

Tizhoosh, H. R., Rahnamayan, S., & Salama, M. M. A. (2008). Opposition versus randomness in soft computing techniques. *Applied Soft Computing, 8*(2), 906–918.

Tizhoosh, H. R., & Sahba, F. (2007). Application of opposition-based reinforcement learning in image segmentation. In *Proceedings of IEEE Symposium on Computational Intelligence in Image and Signal Processing, 2007. CIISP 2007* (pp. 246–251).

Tizhoosh, H. R., Ponnambalam, K., & Mahootchi, M. (2007). Opposition-based reinforcement learning in the management of water resources. In *Proceedings of IEEE Symposium on Approximate Dynamic Programming and Reinforcement Learning, 2007. ADPRL 2007* (pp. 217–224).

Tizhoosh, H. R. (2006). Opposition-based reinforcement learning. *J. Advanced Comput. Intell. Intelligent Inform., 10*(3), 578–585.

Tizhoosh, H. R., & Ventresca, M. (2006). Improving the convergence of backpropagation by opposite transfer functions. In *Proceedings of EEE World Congress Computational Intelligence* (pp. 9527–9534). Vancouver, BC, Canada.

Tizhoosh, H. R. (2005). Opposition-based learning: a new scheme for machine intelligence. In *Proceedings of International Conference on Computational Intelligence for Modelling, Control and Automation: 1* (pp. 695–701). Vienna, Austria.

Tizhoosh, H. R. (2005). Reinforcement learning based on actions and opposite actions. In *Proceedings of ICGST International Conference on Artificial Intelligence and Machine Learnin: 10* (pp. 578–585). Cairo, Egypt.

Wang, Gai-Ge, Guo, L., Wang, H., & Wang, D. (2013). An effective hybrid firefly algorithm with harmony search for global numerical optimization. *The Scientific World Journal* 125625.

Wang, G., Li, Y., Chen, H., & Qin, L. (2013). An ant colony optimization based dimension reduction method for high-dimensional datasets. *Journal of Bionic Engineering, 10*, 231–241.

Yang, X. S. (2013). Multi-objective firefly algorithm for continuous optimization. *Engineering with Computers, 29*(2), 175–184.

Yang, X. S. (2010). Firefly algorithm, stochastic test functions and design optimization. *Int. J. bio-inspired computation, 2*(2), 78–84.

Yang, X. S. (2010). Firefly algorithm, lévy Flights and global optimization. *Research and Development in Intelligent Systems, 26*, 209–218.

Yang, X. S. (2008). *Nature Inspired Metaheuristic Algorithm* (pp. 81–95). Luniver press.

Yang, X. S., & He, X. (2013). Firefly algorithm: recent advances and applications. *Int. J. Swarm Intelligence, 1*(1), 36–50.

International Journal of Research (IJR)
e-ISSN: 2348-6848, p- ISSN: 2348-795X Volume 2, Issue 08, August 2015
Available at http://internationaljournalofresearch.org

Production of Biodiesel from Crude Neem Oil Feedstock and the Effects of Various Parameters on the Yield of Biodiesel

Anand Prakash Mall
M.Tech (Thermal) Scholar, Delhi Technological University (DTU), New Delhi, India
Mb No: +919415879658: E-mail:anandwrites@gmail.com

ABSTRACT

Currently, most of the biodiesel is produced from the edible/refined type oil using methanol and alkaline catalyst. However, large amount of non-edible type oils and fats are available in our country. In this study, crude neem oil is used as alternative fuel for biodiesel production. The difficulty with alkaline transesterification of these oils has contained large amounts of free fatty acids (FFA). These free fatty acids quickly react with the alkaline catalyst to produce soaps that inhibit the separation of the ester and glycerin.

A two-step transesterification process is developed to convert the high FFA oils to its mono-esters. Using 100 ml of oil, the optimum combination of parameters for pretreatment were found to be 0.45 v/v methanol-oil-ratio, 0.5% v/v H_2SO_4 acid catalyst, 50˚C and 45 min reaction time. After pretreatment of neem oil, transesterification reaction was carried out with 4.5:1 methanol-to-oil molar ratio, 1% KOH as alkaline catalyst, 75 min reaction time and 50˚C reaction temperature to produce the fatty acid methyl ester. This two step process gave maximum average yield of 70±2%.

Key Words: Experimentation, Acid esterification; Alkaline transesterification; Neem Oil (Azadirachta indica); Neem Oil Methyl Ester (Biodiesel)

1. INTRODUCTION:

The use of alternative fuels instead of conventional fossil fuels is becoming increasingly significant due to decreasing petroleum reserves and increasing greenhouse gases, all of which lead to global warming, ozone depletion and political and health concerns (Fukuda et al., 2001). Plant oils have been used as alternative fuels for many years, since they are renewable and readily available. However, these oils cannot be used directly as fuel sources in diesel engines due to: (a) high viscosity which leads to poor fuel atomization during the injection process, (b) low volatility and (c) polymerization which results in deposit formation, incompletion combustion and poor emissions (Ma and Hanna, 1999). To overcome these disadvantages, oils can be converted into fatty acid methyl esters (FAME) which are also known as biodiesel. Biodiesel is an alternative fuel that is non-toxic, completely biodegradable and renewable and can be adapted easily without any modification to diesel engines.

Several processes have been developed for biodiesel production, such as pyrolysis, micro emulsification and transesterification. The chemical change of the products from the reactants caused by the thermal energy in the presence of air or nitrogen sparging is called a pyrolytic process. These products are similar to the petroleum-derived fuel. However, during the pyrolysis process, the removal of oxygen leads to reduce the environmental benefits (Ma and Hanna, 1999). The problem of the high viscosity of the substrates has been investigated using microemulsions with solvents (methanol, ethanol and 1-butanol) to meet the international standards of petroleum-derived fuels. However, an increase of lubricating oil viscosity, irregular injector needle sticking, incomplete combustion and heavy carbon deposits were reported in the laboratory screening endurance test. Therefore,

International Journal of Research (IJR)
e-ISSN: 2348-6848, p- ISSN: 2348-795X Volume 2, Issue 08, August 2015
Available at http://internationaljournalofresearch.org

transesterification process plays a vital role, in order to overcome these disadvantages.

The process of displacing alcohol from an ester to form another ester is called transesterification. Transesterification is the most simple and efficient method to produce biodiesel by using acids, alkalis, or enzymes as catalysts. Triglycerides with high free fatty acid and water contents are not essential for a biodiesel conversion process using an acid catalyst. However, the reaction rates are slower than those of the alkali catalytic process (Freedman et al., 1986). The alkali-catalysis transesterification process has been widely used in the biodiesel industry, because it gives a high yield of conversion of fatty acid methyl esters from triglycerides at low temperatures and pressures in a relatively short reaction time of 4-10 hours. However, it has several drawbacks including product separation, soap formation and negative environmental impacts such as greenhouse gas, CO, hydrocarbons, NOx and particles in exhaust emissions (Nielsen et al., 2008).

Neem is a tree in the family 'maliaceae' which grows various parts in Bangladesh. It's scientific name 'Azadirachtaindica'. The evergreen tree is large, reaching 12 to 18 meters in height with a girth of up to 1.8 to 2.4 meters. The seeds have 40% oil which has high potential for the production of biodiesel. It has a higher molecular weight, viscosity, density, and flash point than diesel fuel. Neem oil is generally light to dark brown, bitter and has a strong odor that is said to combine the odors of peanut and garlic [M.A. Fazal et al., 2011].

Neem comprises mainly of triglycerides and large amounts of triterpenoid compounds. It contains four significant saturated fatty acids, of which two are palmitic acid and two are stearic acid. It also contains polyunsaturated fatty acids such as oleic acid and linoleic acids [Muthu et al., 2010]

2. MATERIALS AND METHODOLOGY:

2(i) Materials

Crude neem oil was purchased from local market. The magnetic stirrer with hot plate was at DTU laboratory. Chemicals are used in transesterification process like Pottassium hydroxide pellet (88% purity), Methanol (99% purity), Concentrated sulphuric acid and Sodium hydroxide pellet (88% purity).

2(ii) Equipment

A round bottom conical flask is used as reactor for these experimental purposes. A magnetic stirrer with hot plate arrangement is used for heating the mixture in the flask. The mixture is stirred at the same speed for all test runs. The temperature range of 40–60˚C is maintained during this experiment and its monitored by thermometer. The separating funnel is used to separate the methanol-water mixture after acid pretreatment and the glycerol after transesterfication.Three set of trail runs are carried out for each combination of parameter.

2(iii) Methodology

The aim of this study is to improve the process for producing biodiesel from crude neem oil.

There are three processes such as

Oil filtration,

Acid esterification

and alkaline transesterification.

2(iii)(a) Oil filtration

Neem oil has higher moisture content and some other impurities. So, in order to remove the moisture and impurities from the neem oil it should be refined. The purification can be done by boiling oil with about 20% of water. The boiling should continue until no bubbles of water vapor anymore. After one hour the oil then becomes clear. This refined neem oil is taken as raw material for transesterification process.

2(iii)(b) Acid esterification

International Journal of Research (IJR)
e-ISSN: 2348-6848, p- ISSN: 2348-795X Volume 2, Issue 08, August 2015
Available at http://internationaljournalofresearch.org

100 ml of refined neem oil is poured into the flask and heated up to 60˚C. The 45% v/v methanol is added with the preheated neem oil and stirred for a few minutes. 0.5% of sulphuric acid is added with the mixture. Heating and stirring should continue about 45min at atmospheric pressure. After completion of this reaction, the mixture is poured into a separating funnel for separating the excess alcohol, impurities and sulphuric acid. The excess alcohol, sulphuric acid and impurities move to the top layer and it's discarded. The lower layer is separated for further processing of transesterified into methyl ester. This process reduces the acid value of crude neem oil to less than 1% of FFA.Viscosity reduction increases with increase in methanol-to-oil ratio.

2(iii)(c) Alkaline transesterification

After acid pretreatment the esterified oil is taken in flask and heated up to 60˚C. 1% of KOH is dissolved in 30% (6:1 M) methanol. The dissolved solution is poured into flask. The mixture is heated and stirred for 1hr.On completion of reaction, the mixture is poured into separating funnel over 12 hr.The glycerol and impurities are settled in lower layer and it's discarded. The impure biodiesel remain in upper layer. It contains some trace of catalyst, glycerol and methanol. The washing process can be done by the 3/4th of hot distilled water added with methyl ester and gently stirred. The upper layer is pure biodiesel and lower layer is drawn off.

3. RESULTS AND DISCUSSION:

3(i) Acid esterification:

3(i)(a) Effect of methanol-to-oil ratio

Two important parameter significantly affected the acid value. These are sulphuric acid concentration and methanol quantities. Molar ratio is defined as the ratio of number of moles of alcohol to number of moles of vegetable oil. Theoretically, transesterification reaction requires 3 moles of alcohol for each mole of oil. However, in practically molar ratio should be higher than stoichiometric ratio. By varying methanol proportion such as 0.35:1, 0.40:1,0.45:1, 0.50:1,0.55:1 methanol-to-oil ratio, among these 0.45:1 gave higher yied.The last two 0.50:1, 0.55:1 have only slight variation. In economic view 0.45:1 proportion is selected for reaction condition. The effect of methanol variation is shown in fig.3(i)(a) from the figure conversion efficiency is slightly increase up to 0.45:1 methanol-to-oil ratio. After that conversion efficiency is decreased with increase in methanol-to oil ratio because it leads to increasing the acid value. It has been determined that viscosity reduction increases with increase in methanol-to-oil ratio.

Methanol to Oil Ratio(v/v)	0.35	0.40	0.45	0.50	0.55
Conversion Efficiency (%)	77	84	95	90	87

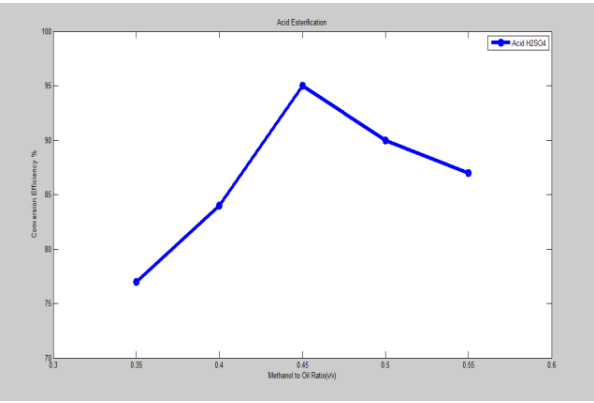

Fig.3(i)(a) Effect of Methanol-to-oil ratio on conversion efficiency

3(i)(b) Effect of acid catalyst amount

Amount of acid catalyst variation is affecting the conversion efficiency. By varying sulphuric acid proportion such as 0.30, 0.40, 0.50, 0.60 and

International Journal of Research (IJR)
e-ISSN: 2348-6848, p- ISSN: 2348-795X Volume 2, Issue 08, August 2015
Available at http://internationaljournalofresearch.org

0.70% v/v. Maximum conversion efficiency 95% is achieved in 0.5 % v/v H2SO4. Effect of acid catalyst variation is shown in fig. 3(i)(b) from the figure more than 0.5% v/v H2SO4, the product color is become black. Lower amount of sulphuric acid addition affects the final product yield.

Acid Catalyst % (v/v)	0.3	0.4	0.5	0.6	0.7
Conversion Efficiency (%)	67	72	95	82	77

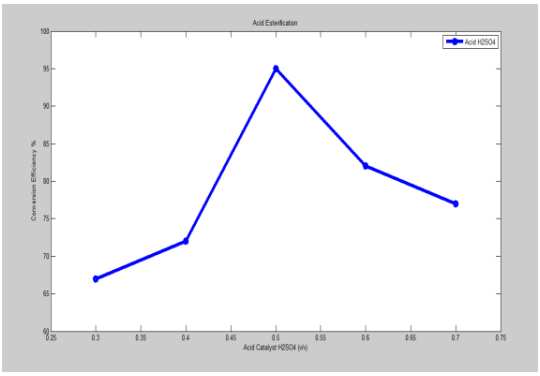

Fig.3(i)(b) Effect of acid catalyst amount on conversion efficiency

3(i) (c) Effect of reaction temperature

The conversion efficiency is very low at room temperature even after 2 hr reaction .If increase in temperature the conversion takes place at higher rate. The optimum temperature is achieved at 50˚C.At high reaction temperature; the methanol is lost because melting point of methanol is 65˚C.Above 50˚C product color become black.

3(ii) Alkaline transesterification:

3(ii)(a) Effect of methanol-to-oil ratio

Molar ratio is very important factor for transesterificatin reaction. Theoretically, transesterification reaction requires 3 moles of alcohol for each mole of oil. However, in practically molar ratio should be higher than stoichiometric ratio. The higher molar ratio is required for complete the reaction at higher rate. In lower molar ratio, it takes longer duration for complete the reaction. The effect of methanol-to-oil ratio on conversion efficiency is shown in fig.3(ii) (a) It has been seen that yield is slightly increase up to 4.5:1 methanol-to-oil molar ratio. The maximum methyl ester yield 69% is achieved at 4.5:1methanol to oil molar ratio. With further increase in methanol-to oil molar ratio the conversion efficiency is decreases.

Methanol to Oil Molar Ratio	3	4.5	6	7.5
Conversion Efficiency (%) with 1% NaOH	41	60	51	46
Conversion Efficiency (%) with 1% KOH	50	69	60	55

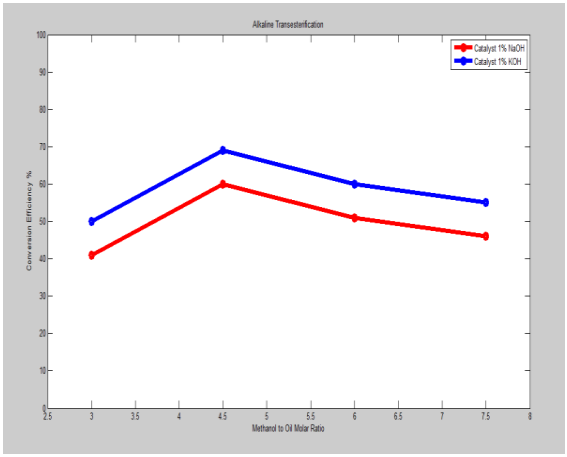

Fig.3(ii)(a) Effect of methanol on conversion efficiency

3(ii)(b) Effect of alkaline catalyst

The amount of catalyst variation is affecting the conversion efficiency. The catalyst proportion is varied from 0.75- 1.50% KOH. The effect of catalyst variation on conversion efficiency is shown in fig.3(ii)(b) From the figure yield is slightly increased up to 1% KOH and after that yield is decreased due to reverse reaction is take place (emulsion formation).The maximum yield is achieved of 70% at 1% KOH.

Alkaline Catalyst %(wt/wt)	0.75	1	1.25	1.5

International Journal of Research (IJR)
e-ISSN: 2348-6848, p- ISSN: 2348-795X Volume 2, Issue 08, August 2015
Available at http://internationaljournalofresearch.org

Conversion Efficiency(%) by NaOH	52	62	55	50
Conversion Efficiency(%) by KOH	62	70	65	60

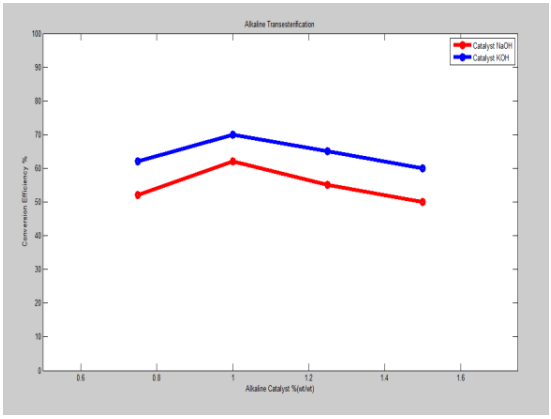

Fig.3(ii)(b) Effect of alkaline catalyst amount on conversion efficiency

3(ii)(c) Effect of reaction temperature

The reaction temperature has important role in alkaline-catalyst transesterification .At room temperature no significant yield is notified for even 2hr reaction. The yield is increased with increase in reaction temperature. The effect of temperature variation on conversion efficiency is shown in fig.3(ii)(c). By varying temperature in four different levels such as 45, 50, 55 and 60˚C among these 50˚C gave maximum methyl ester yield. If greater than 50˚C, chance for loss the methanol. The maximum ester efficiency 72% is achieved at 50˚C.

Reaction Temperature(°C)	45	50	55	60
Conversion Efficiency (%) with 1% NaOH	54	66	64	58
Conversion Efficiency (%) with 1% KOH	64	72	69	62

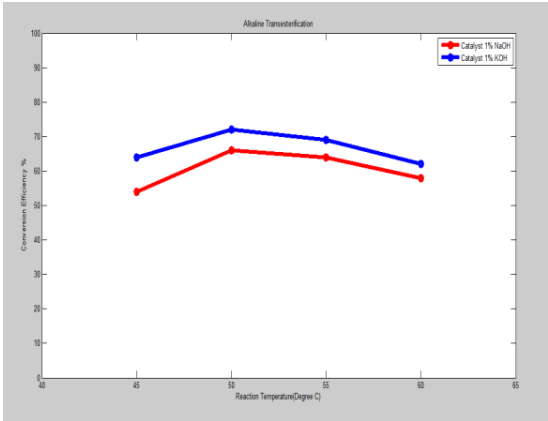

Fig.3(ii)(c) Effect of reaction temperature on conversion efficiency

3(ii) (d) Effect of reaction time

The conversion rate is increased with increase in reaction time. In this experiment, reaction time varying from 55-85 min. The effect of reaction time variation on the conversion efficiency is shown fig.3(ii)(d) from the figure yield was slightly increased up to 75min reaction time and after that yield is decreased. The maximum efficiency is achieved of 68% for 75min reaction time. From these experiments the optimum yield is obtained at 75min reaction.

Reaction Time(min)	55	65	75	85
Conversion Efficiency (%) with NaOH	48	52	58	49
Conversion Efficiency (%) with KOH	58	62	68	59

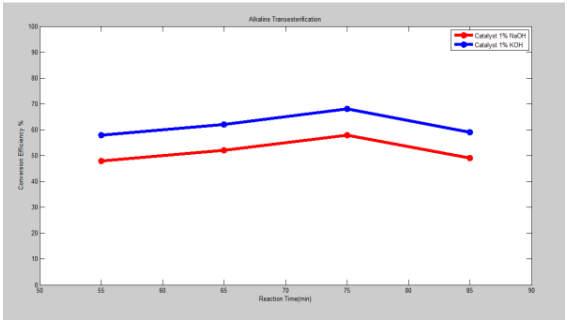

Fig.3(ii)(d) Effect of reaction time on conversion efficiency

International Journal of Research (IJR)
e-ISSN: 2348-6848, p- ISSN: 2348-795X Volume 2, Issue 08, August 2015
Available at http://internationaljournalofresearch.org

4. CONCLUSION

The high FFA (20%) content neem oil has been investigated for the biodiesel production. It has been found that the feedstock with high FFA its could not be transesterified with alkaline catalyst because the alkaline catalyst react with FFA to form soap. So in this study, two step processes was developed to convert FFA to its methyl ester. The first step is acid treatment it reduces the FFA content of oil to less than 1% using acid catalyzed (0.5 % v/v H_2SO_4) reaction with methanol (0.45 v/v) at 50˚C temperature and 45 min reaction time. After acid treatment alkaline transesterfication reaction was carried out at 1% w/w KOH, 4.5 methanols to oil molar ratio, 50˚C and 75 min reaction time. The maximum yield is 70±2%.The effect of molar ratio, catalyst; reaction temperature and reaction time are analyzed in each step process. Excess addition of sulphuric acid darkens the product and it leads to more production cost.

5. COST ANALYSIS:

Sl. No	Component	Cost (Rs.)
1	Sodium Hydroxide (Catalyst)	23/kg
2	Potassium hydroxide (Catalyst)	36/kg
3	Neem oil (Feedstock)	150/ litre
4	Methanol (Alcohol)	35/ litre
5	Glycerin (By product of Biodiesel)	75/ litre

Sl. No.	Component	Cost (Rs.)
1	Neem Oil – 100 ml	15
2	Two step transesterification Cost - 65 ml(45 ml + 20 ml) of Methanol [4.5 Methanol/Oil Molar Ratio]	2.275
3	Catalyst KOH 1.0 gm	0.036
4	Recovery (Glycerin 50 ml)	3.75
5	Total Cost (1 + 2 + 3 – 4)	17.311 – 3.75 = 13.561

Biodiesel production from 1 litre Neem Oil=0.70 Litre

So Cost of Biodiesel per litre = [(13.561 /100)*1000] / 0.70 = 193.73 Rs.

The cost of the biodiesel production can be minimized as possible to recover the used methanol. Recycling of methanol again and again in mass production and commercial use, the cost must be come to the lowest amount. Also the by-product such as glycerin and soap play an important role to minimize the cost.

6. KEY REFERENCES

[1.] Abebe K. Endalew, Yohannes Kiros, Rolando Zanzi. Heterogeneous catalysis for biodiesel production from Jatropha curcas oil (JCO). Energy 2011; Vol. 36: pp. 2693-2700.

[2.] Atul Dhar, Roblet Kevin, Avinash Kumar Agarwal. Production of biodiesel from high-FFA neem oil and its performance, emission and combustion characterization in a single cylinder DICI engine. Fuel Processing

Technology 2012; Vol. 97: pp. 118–129.

[3.] Ayhan Demirbas. Progress and recent trends in biodiesel fuels. Energy Conversion and Management 2009; Vol. 50: pp. 14 -34.

[4.] C. Martín , A. Moure , G. Martín ,E. Carrillo , H. Domínguez , J.C. Parajó. Fractional characterization of jatropha, neem, moringa, trisperma, castor and candlenut seeds as potential feedstocks for biodiesel production in Cuba. Biomass Bioenergy 2010; Vol. 34: pp. 533-538.

[5.] Deepak Tanwar, Ajayta, Dilip Sharma, Y. P. Mathur. Production and Characterization of Neem Oil Methyl Ester. International Journal of Engineering Research & Technology (IJERT) 2013; Vol. 2. : pp. 1896-1903.

[6.] Dennis Y.C. Leung, Xuan Wu, M.K.H. Leung. A review on biodiesel production using catalyzed transesterification. Applied Energy 2010; Vol. 87: pp. 1083-1095. .

[7.] E.F. Aransiola, E Betiku, DIO Ikhuomoregbe and TV Ojumu. Production of biodiesel from crude neem oil feedstock and its emissions from internal combustion engines. African Journal of Biotechnology 2012; Vol. 11: pp. 6178-6186

[8.] Freedman B, R. Butterfield and E. Pryde. Transesterification kinetics of soybean oil. Journal of the American oil Chemists Society 1986; Vol. 63: pp. 1375-1380.

[9.] Fukuda H., A. Kondo and H. Noda. Biodiesel fuel production by transesterification of oils. Journal of Bioscience and Bioengineering 2001; Vol. 92: pp. 405-416.

[10.] GT Jeong, HS Yang, DH Park. Optimization of transesterification of animal fat ester using response surface methodology. Bioresour. Technol 2009; Vol. 100: pp. 25-30.

[11.] H.N.Pandey. Development of a New Catalyst for Bio-diesel Production. Ist International Conference on New Frontiers in Biofuels, DTU January 18-19, 2010, New Delhi.

[12.] H Ibrahim, A. S. Ahmed, I.M. Bugaje, Dabo Mohammed, C. D. Ugwumma. Synthesis of Bulk Calcium Oxide (Cao) Catalyst and its Efficacy for Biodiesel Production. Journal of Energy Technologies and Policy 2013; Vol. 3. : pp. 14-16.

[13.] Jon Von Gerpen. Biodiesel processing and production. Fuel Process Technol 2005; Vol. 86: pp. 1097–1107.

[14.] J.M. Marchetti, A.F Errazu. Esterification of free fatty acids using sulfuric acid as catalyst in the presence of triglycerides. Biomass. Bioenerg. 2008; Vol. 32: pp. 892–895.

[15.] Juan Calero, Gema Cumplido, Diego Luna , Enrique D. Sancho, Carlos Luna , Alejandro Posadillo, Felipa M. Bautista , Antonio A. Romero and Cristóbal Verdugo-Escamilla, Production of a Biofuel that Keeps the Glycerol as a Monoglyceride by Using Supported KF as Heterogeneous Catalyst . Energies 2014; Vol. 7: pp. 3764-3780.

[16.] L.C. Meher, D. Vidya Sagar, S.N. Naik. Technical aspects of biodiesel production by transesterification – a review. Renew. Sustain. Energy 2006; Vol. 10: pp. 248-268.

[17.] Madhu Agarwal, Kailash Singh, Ushant Upadhyaya and S P Chaurasia, Potential vegetable oils of Indian origin as biodiesel feedstock – An experimental study. Journal of Scientific & Industrial Research 2012; Vol. 71: pp. 285-289.

[18.] Maryam Hassani, Ghasem D Najafpour, Maedeh Mohammadi and Mahmood Rabiee. Preparation, Characterization and Application of Zeolite-based Catalyst for Production of Biodiesel from Waste Cooking Oil. Journal of Scientific & Industrial Research 2014; Vol. 73: pp. 129-133.

[19.] M. A. Hanna, Loren Isom and John Campbell, Biodiesel; Current perspectives and future. Journal of Scientific & Industrial Research 2005; Vol. 64: pp. 854-857.

[20.] F. Ma, M. A. Hanna. Biodiesel production: a review. Bioresour Technol 1999; Vol. 70: pp. 1–15.

[21.] Md. Hasan Alia, Mohammad Mashud, Md. Rowsonozzaman Rubel, Rakibul Hossain Ahmad, Biodiesel from Neem oil as an alternative fuel for Diesel engine. Procedia Engineering 2013; Vol. 56: pp. 625 – 630.

[22.] M.A. Fazal, A.S.M.A. Haseeb and H.H. Masjuki. Biodiesel feasibility study: An evaluation of material compatibility; performance; emission and engine durability. Renew. Sustain. Engy Reviews 2011; Vol.15: pp. 1314-1324.

[23.] Module 5, Lecture 4. Design for Reliability and Quality. IIT, Bombay.

[24.] Muthu, V. SathyaSelvabala, T. K. Varathachary, D. Kirupha Selvaraj, J. Nandagopal and S. Subramanian. Synthesis of biodiesel from neem oil using sulfated zirconia via tranesterification. Brazilian Journal of chemical Engineering 2010; Vol. 27: pp. 601-608.

[25.] N.Satya Sree, V.Madhusudhan Rao, P.Vijetha. Production of Bio-Diesel From Soap Stock of Cotton Seed Oil By Using Ferric Sulphate Catalyst Via A Two Step Heterogeneous Catalysis: Characteristics of Bio-Diesel Produced. International Journal of Scientific & Technology Research 2014; Vol. 3. : pp. 141-144.

[26.] Nielsen P. M., J. Brask and Fjerbaek. Enzymatic biodiesel production: Technical and economical considerations. European Journal of Lipid Science 2008; Vol. 110: pp. 692-700.

[27.] Olugbenga Olufemi Awolu and Stephen Kolawole Layokun. Optimization of two-step transesterification production of biodiesel from neem (Azadirachta indica) oil. International Journal of Energy and Environmental Engineering 2013; Vol. 4. : pp. 1-9.

[28.] Padmarag Deshpande, Kavita Kulkarni, A.D.Kulkarni. Supercritical Fluid Technology in Biodiesel Production: A Review. Chemistry and Materials Research 2011; Vol. 1. : pp. 27-32.

[29.] Poonam Gera, S.K.Puri and M.K. Jha. Use of Basic Heterogeneous Catalysts for Biodiesel Production: A Review. Ist International Conference on New Frontiers in Biofuels, DTU January 18-19, 2010, New Delhi.

[30.] Suman Singh, P.K.Omre, Kirtiraj Gaikwad. Standardization of Process Parameters for Neem Oil & Determination of Properties for Using as a Fuel. International Journal of Engineering Research and General Science 2014; Vol. 2. : pp. 1-7.

[31.] Talebian-Kiakalaieh, N. A. S. Amin, A. Zarei, H. Jaliliannosrati. Biodiesel Production from High Free Fatty Acid Waste Cooking Oil by Solid Acid Catalyst. Proceedings of the 6th International Conference on Process Systems Engineering (PSE ASIA) 25 - 27 June 2013, Kuala Lumpur.

[32.] Vivek and A. K. Gupta. Biodiesel production from karanja oil. Journal of Scientific & Industrial Research 2004; Vol. 63: pp. 39-47.

[33.] V. Manieniyan, R.Senthilkumar and Dr. S. Sivaprakasam. Experimental Investigation on Optimized Biodiesel (Based on Various Catalysts) used in a Twin Cylinder Diesel Engine. Ist International Conference on New Frontiers in Biofuels, DTU January 18-19, 2010, New Delhi.

Solid State Ionics 280 (2015) 24–29

Contents lists available at ScienceDirect

Solid State Ionics

journal homepage: www.elsevier.com/locate/ssi

Role of oxygen anion diffusion in improved electrochemical performance of layered perovskite $LnBa_{1-y}Sr_yCo_{2-x}Fe_xO_{5+\delta}$ (Ln = Pr, Nd, Gd) electrodes

Uzma Anjum [a], Saumye Vashishtha [b], Nishant Sinha [c], M. Ali Haider [a,*]

[a] Department of Chemical Engineering, Indian Institute of Technology Delhi, New Delhi-110016, India
[b] Department of Applied Chemistry and Polymer Technology, Delhi Technological University, New Delhi-110042, India
[c] Dassault Systemes India Pvt. Ltd., Galleria Commercial Tower, Leela Palace, 23 Old Airport Road, Bangalore 560008, India

ARTICLE INFO

Article history:
Received 7 April 2015
Received in revised form 8 July 2015
Accepted 5 August 2015
Available online xxxx

Keywords:
Molecular dynamics
Double perovskite
Electrochemical performance
Oxygen diffusivity
Solid oxide fuel cells

ABSTRACT

Molecular dynamics simulations were utilized to calculate self-diffusion coefficients in double perovskite $LnBa_{1-y}Sr_yCo_{2-x}Fe_xO_{5+\delta}$ (Ln = Pr, Nd, Gd) electrodes. Anisotropic oxygen diffusion was observed in the *a–b* plane for all the studied structures. In order to assess the role of A-site and B-site dopants such as Sr and Fe, the diffusion coefficient of oxygen ion in $PrBaCo_2O_{5.5}$ was estimated and compared to $PrBa_{0.5}Sr_{0.5}Co_2O_{5.5}$ and $PrBaCo_{1.5}Fe_{0.5}O_{5.5}$. On doping with 50% Sr at A′-site, a 2.77 fold increase in diffusivity value was predicted at 873 K as compared to the undoped structure. Similar levels of increase in diffusivity values were observed with 25% Fe doping relative to $PrBaCo_2O_{5.5}$. On co-doping Sr and Fe, oxygen diffusion coefficient was observed to be of the highest value (1.18×10^{-7} cm^2 s^{-1}) at 873 K for $PrBa_{0.5}Sr_{0.5}Co_{1.5}Fe_{0.5}O_{5.5}$. Changing the A-site lanthanide cation from Pr to Gd and Nd, led to the reduction in diffusivity value in the order of $Pr^{3+} > Nd^{3+} > Gd^{3+}$. The calculated diffusivity was observed to be higher, wherever an improved electrochemical performance is reported, highlighting the important role of oxygen anion transport.

1. Introduction

The state of the art research in solid oxide fuel cells (SOFCs) is directed towards the development of technology for intermediate to low temperature (<973 K) operations [1]. Cathode materials at these operating temperatures are observed to show relatively higher polarization losses due to the sluggish oxygen reduction reaction [2]. Therefore, the development of novel cathode materials requires considerable attention. Simple perovskite materials showing high electronic conductivity ($La_{1-x}Sr_xMnO_{3-\delta}$, LSM) [3] or mixed ion-electron conductivity ($La_{1-x}Sr_xCo_{1-y}Fe_yO_{3-\delta}$, LSCF) [4] have been used in the past as cathode for SOFC. The oxygen ion diffusivity in these isotropic perovskite structures is reported to be of the order of ~10^{-16} cm^2 s^{-1} for LSM [5] and ~10^{-10} cm^2 s^{-1} for LSCF [6] at temperatures around 873 K. Recent studies have promulgated novel layered perovskite structured materials such as double perovskites ($LnBaCo_2O_{5+\delta}$, where Ln = La, Pr, Nd, Sm, Gd and $0<\delta<1$) for intermediate temperature SOFC (IT-SOFC) cathode [1]. The cation ordering in these perovskite units is repeated to form an $AA'B_2O_{5+\delta}$ type layered structure, where vacancies are aligned in the A-plane [7]. Owing to this, relatively higher diffusivity values of the order of ~10^{-9} cm^2 s^{-1} and 10^{-8} cm^2 s^{-1} for the anisotropic structure of $GdBaCo_2O_{5+\delta}$ (GBCO) [7] and $PrBaCo_2O_{5+\delta}$ (PBCO) [8] respectively, at around 873 K have been reported. Favorable oxygen transport in the bulk of the perovskite structure may translate to observed higher electrochemical performance of the SOFC, measured in terms of area specific resistance (ASR) or peak power density. For example a cell made up of the composite of LSM and yttria stabilized zirconia (YSZ) cathode was reported to show a peak power density of 0.11 W/cm^2 [9] measured at 873 K and a cell with a LSCF electrode was reported to show a peak power density of 0.346 W/cm^2 [10] at the same temperature. Compared to this, relatively higher peak power densities were reported at 873 K for the SOFC made up of layered perovskite electrodes such as GBCO (0.56 W/cm^2) [11], and PBCO (0.62 W/cm^2) [12].

Aliovalent dopants such as Sr at the A site have been observed to improve the diffusivity of the perovskite structured materials. For example on doping the A site by Sr in $LaCoO_{3-\delta}$ the diffusivity was observed to increase from ~10^{-10} cm^2 s^{-1} (at 1173 K) [13] to a value of ~10^{-8} cm^2 s^{-1} (at 973 K) [14]. High diffusivity may also lead to an overall improvement in the electrochemical performance, where the peak power density of a SOFC was reported to increase (0.302 to 0.73 W/cm^2 at 923 K) on increasing the Sr content (x = 0.2 to 0.4) of the electrode $La_{1-x}Sr_xCo_{0.2}Fe_{0.8}O_{3-\delta}$ [15,16]. The transition metal dopants at the B-site such as Fe are suggested to improve stability and electrode–electrolyte compatibility by reducing the thermal expansion coefficient mismatch [17]. The effect of Fe doping on oxygen diffusion

* Corresponding author. Tel.: +91 11 2659 1016; fax: +91 11 2658 2037.
E-mail address: haider@iitd.ac.in (M.A. Haider).

http://dx.doi.org/10.1016/j.ssi.2015.08.002
0167-2738/

coefficient is noteworthy, where slight or no improvement has been observed [14,18]. Interestingly, better electrochemical performance for the cells has been reported with these Fe doped electrodes [19].

Recent studies have tried co-doping the A and B-site on the PBCO by Sr and Fe respectively and have shown significant enhancement in the performance of $PrBa_{0.5}Sr_{0.5}Co_{1.5}Fe_{0.5}O_{5+\delta}$ (PBSCFO) to 2.2 W/cm^2 at 873 K [20]. The improved performance was assigned to facile oxygen anion transport via the formation of unique pore channels as predicted by the density functional theory (DFT) calculations. Similar enhanced performance in the co-doped structures of $GdBa_{0.5}Sr_{0.5}Co_{2-x}Fe_xO_{5+\delta}$ (GBSCFO) [21] and $NdBa_{0.5}Sr_{0.5}Co_{2-x}Fe_xO_{5+\delta}$(NBSCFO) [20] is reported as compared to GBCO [11] and $NdBaCo_2O_{5+\delta}$ (NBCO) [22], respectively. To our knowledge no study, experimental or theoretical, has attempted to measure the diffusivity in these co-doped double perovskite structures and to relate to its electrochemical performance.

In this work, a methodological approach is adopted to study the effect of Sr and Fe dopants on the diffusivity of double perovskite structured materials $LnBaCo_2O_{5+\delta}$ (Ln = Pr, Gd, Nd) by molecular dynamics (MD) simulations [23]. $PrBaCo_2O_{5.5}$ ($PBCO_{5.5}$) is chosen as an initial model which is further modified to include the effect of Sr and Fe doping on the estimated diffusivity. The diffusion coefficients of the co-doped structures (PBSCFO, NBSCFO and GBSCFO) are compared to establish the role of A-site cation on the bulk oxygen anion transport. MD simulations have been successfully utilized in the past to measure the diffusivity in GBCO [24], LSCF [25] and LSM [26], albeit at higher temperatures (>1273 K), where the reported structure may not be stable. Herein we estimate oxygen diffusion in a realistic temperature range corresponding to the SOFC operation. On changing the A-site cation and doping the A-site and B-site with Sr and Fe, the estimated diffusivity may provide an insight on its correlation with measured electrochemical performance.

2. Methodology

Molecular dynamics simulations were performed using the Forcite module of Material Studio 7.0 (Accelrys Inc.-San Diego, USA). Lattice parameters, space group and fractional coordinates of the electrode materials included in this study are given in Table S1 and S2. A supercell size of $4 \times 4 \times 2$ was chosen to study the process of oxygen diffusion. The literature is replete with studies reporting on values of oxygen diffusion coefficient for various perovskites [24]–[28], with different superstructure configurations. In this study, the choice of super-cell dimensions was based on the study of oxygen diffusion in GBCO using MD simulations [24]. The resulting layered perovskite supercell contained 304 atoms and 16 vacancies for a non-stoichiometry value of $\delta = 0.5$. In addition, simulations were conducted on both un-doped and co-doped PBCO structures with varying amounts of vacancies corresponding to a non-stoichiometry value of $\delta = 0$ and $\delta = 0.8$.

Long-range columbic interactions were computed using the Ewald summation under charge neutral conditions [27]. Short-range Pauli repulsion and van der Waals' interactions were computed using the Buckingham potentials [29] having a cut-off distance of 1.55 nm, with formal charges of +2, +3, +3, +3, +2, and −2 for Ba, Pr, Co, Fe, Sr, and O, respectively, Table S3. For vacancy concentrations of $\delta = 0.0$ and $\delta = 0.8$, in the layered undoped and co-doped PBCO it has to be noted that any change in the amount of oxygen vacancies, would invariably be accompanied by charge compensation leading to an increase in the value of formal charges or the number of cation vacancies. Even though the mixed values of valencies (Pr^{3+}/Pr^{4+} and Co^{3+}/Co^{4+}) are observed in the perovskite structure, limitations in MD simulations persisted for mixed valence systems due to the absence of reliable values of short-range interaction potentials denoting mixed valencies simultaneously. A vacancy concentration of $\delta = 0.5$ was therefore employed in the majority of simulations for the associated advantage of charge neutrality of resulting superstructure with the used values of formal charges of the elements. Moreover, previous MD simulations on ABO_3-type and layered perovskite structured materials employed a similar value of non-stoichiometry ($\delta = 0.5$), possibly due to similar limitations.

Prior to simulations, structures were geometrically optimized using an iterative process to find the minimum energy configuration until the energy and forces converged to a specified criteria of 42 J/mol and 21 J/mol/Å respectively. Consequently, systems were first equilibrated at temperature range of 873–1273 K using Isobaric–Isothermal (NPT) ensemble prior to final simulation run for a duration of 10 ps. A time step 1 fs was specified using Nosé–Hoover thermostat [30,31] with a Q ratio of 0.01 and Berendsen barostat [32], having a decay constant of 0.1 ps for achieving the desired control of temperature and pressure respectively. Another run using constant volume (NVT) ensemble was carried out for 10,000 time steps (10 ps) for calculation of lattice parameters. Using the specified set of potential parameters all the structures were able to retain the structural symmetry and observed lattice parameters were found to be in good agreement with experimentally reported values. Subsequently, the diffusion data was collected from mean square displacement (MSD) curves obtained in final simulation run of 100 ps using NVT ensemble (Nosé–Hoover Thermostat). With respect to the position of the ion, $r_i(t)$, compared to its initial position, $r_i(0)$, MSD is given by the following equation:

$$\langle r_i^2(t)\rangle = \frac{1}{N}\sum_{i-1}^{N}[r_i(t) - r_i(0)]^2.$$

The oxygen ion diffusivity (D) was estimated from the slope of the MSD curve fitted in the linear region (5 ps to 60 ps), given by the following equation [33].

$$\langle r_i^2(t)\rangle = 6Dt + B$$

Few reported studies on similar perovskite structured material (GBCO) tend to choose a relatively longer simulation time, which is of the order of 10^3 ps [24]. In order to ascertain the validity of the specified simulation time (100 ps) in the final run, the simulation time was extended to re-calculate the diffusivity. Fig. S1 reports the MSD versus time plot for oxygen diffusion in a simulation run of 600,000 time steps. No change in the estimated oxygen ion diffusivity ($D = 3 \times 10^{-8}$ cm^2 s^{-1}) at 873 K was observed as compared to the short duration simulations, Fig. S1. Furthermore, the choice of the ensemble and the simulation time is consistent with the previous MD simulation study on PBCO [28].

3. Results and discussion

Oxygen diffusion coefficient for $PBCO_{5.5}$ was determined from MSD curves for a temperature range of 873–1323 K (Fig. 1(a)). The estimated value of oxygen diffusion co-efficient was of the order of 3×10^{-8} cm^2 s^{-1}, at 873 K. The calculated value of diffusivity was observed to be in good agreement with the previously reported value of $PBCO_{5.5}$ from molecular dynamics simulations by Seymour et al. [28]. This value was found to be underestimated by an order of magnitude from the reported value of self-diffusion co-efficient by Kim et al. [34], in which self-diffusion co-efficient was indirectly calculated by relating it to the experimentally measured chemical diffusion coefficient (D_{chem}) and independent measurements of thermodynamic factor. However, it needs to be emphasized here that experimental studies have reported aberrantly high values of oxygen ion diffusion from isotopic exchange depth profiling (IEDP) measurements [34]. This was attributed to excessive permeation of tracer component owing to the presence of porosity in the ceramic samples [1]. Whereas, for electrical conductivity relaxation (ECR) experiments, the method employed to calculate the diffusivity has shown unreliability in simultaneous measurement of surface exchange and chemical diffusion coefficients for LSCF perovskite,

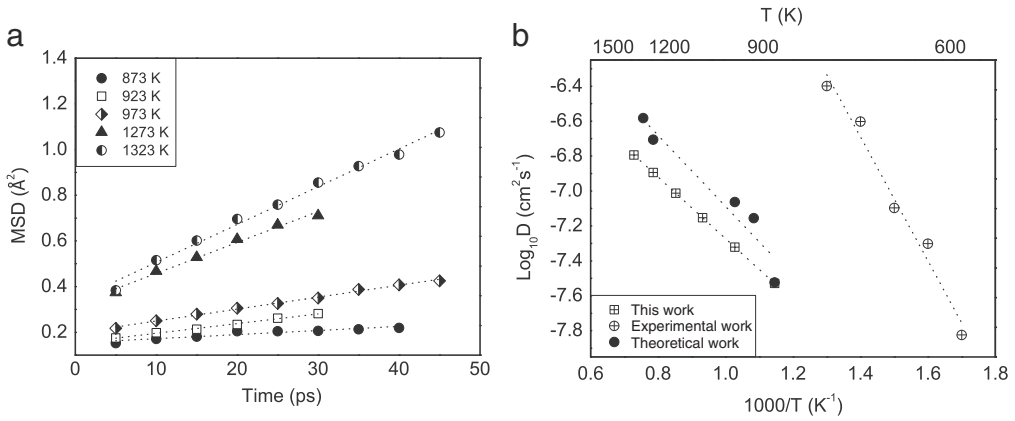

Fig. 1. a) MSD plots showing oxygen diffusion in the *a–b* plane of $PBCO_{5.5}$ and b) corresponding Arrhenius plots computed in this study and compared to the MD simulation [28] and experimental measurements [34] of self-diffusion co-efficient for a temperature range of 773–1323 K.

where the values of D_{chem} may also differ at any given temperature within an order of magnitude between the two experiments conducted under similar conditions [35]. This is likely due to the operations in co-limited regime of surface exchange and bulk diffusion in a realistic temperature range corresponding to IT-SOFC.

Furthermore, as pointed in the previous study, the inherent cation disorder and variation of oxygen non-stoichiometry with temperature may lead to disparate values [28]. The simulations here have utilized a fixed oxygen content ($\delta = 0.5$) over the entire temperature range, where no cation disordering was observed. In addition, the MD simulations showed a high anisotropic diffusion of oxygen atoms at all simulation temperatures. Diffusion was observed primarily in the *a–b* plane (Fig. S2), in full agreement with the experimental studies [8]. Moreover, the activation barrier for oxygen diffusion in $PBCO_{5.5}$ was estimated to be 38.6 kJ mol^{-1}, Fig. 1(b), which is comparable to the reported theoretical (33.8 kJ mol^{-1}) and experimental (46.3 kJ mol^{-1}) values as shown in, Table 1.

Vacancy concentrations in the perovskite and layered perovskite structures have significant impact on its diffusivity [4]. In order to access the role of oxygen vacancy concentrations, MSD simulations were performed in the excess ($\delta = 0.8$) and deficient ($\delta = 0$) non-stoichiometric structures of PBCO, Fig. S3. Structures having excess oxygen content ($\delta = 0.8$) were computed to show lower diffusion coefficient, $D = 8.66 \times 10^{-8}$ cm^2 s^{-1} at 1273 K. Interestingly on dropping the non-stoichiometry value to $\delta = 0$, no significant improvement in diffusivity was observed. Therefore, it can be hypothesized that high vacancy concentrations may lead to the disruption of preferential diffusion pathways in layered perovskites [36].

Strontium-doping at the A-site leads to an improvement in the measured diffusivity of commonly utilized perovskite materials for SOFC. MSD curves for Sr-doped PBCO i.e. $PrBa_{0.5}Sr_{0.5}Co_2O_{5.5}$ ($PBSCO_{5.5}$) are shown in Fig. 2(a). Doping with strontium ion led to an overall increase in oxygen diffusivity by 2.77 fold with an estimated value of 8.33×10^{-8} cm^2 s^{-1} at 873 K, Table 1. The anisotropic oxygen diffusion was retained in Sr containing samples and the oxygen diffusion was observed to be restricted in the Co—O and Pr—O planes. The simulation results showed an increase in the extent of vacancy disordering in the structure of $PBSCO_{5.5}$, in agreement with the experimentally observed trend at temperatures >373 K [37]. The observed vacancy order–disorder transition may lead to an increased diffusivity [38]. Consequently, the activation energy barrier reduced to a value of 28.9 kJ/mol as compared to the undoped $PBCO_{5.5}$. Park et al. have measured ASR of PBSCO electrode which showed better electrochemical performance (0.073–0.076 Ω cm^2) [39], as compared to PBCO (0.4 Ω cm^2) [12] at 873 K. While the authors have assigned improved performance on a possible phase transition from orthorhombic PBCO to tetragonal PBSCO, it remains unclear whether an improved diffusivity has a possible effect on it. Furthermore, PBCO in pure tetragonal phase has also been reported to show higher area specific resistance (0.15 Ω cm^2 at 873 K) as compared to PBSCO [34].

In order to understand the role of diffusivity in determining the electrochemical performance, B-site doping with Fe was attempted in double perovskite $PBCO_{5.5}$. Fig. 2(b) shows the time-averaged displacement of oxygen ions in $PrBaCo_{1.5}Fe_{0.5}O_{5.5}$ ($PBCFO_{5.5}$). The diffusion coefficient was estimated to be 8×10^{-8} cm^2 s^{-1} at 873 K, similar to $PBSCO_{5.5}$ and 2.67 times higher than $PBCO_{5.5}$. In contrast to $PBSCO_{5.5}$, no vacancy disordering was observed in $PBCFO_{5.5}$ structure. Fe doping leads to an increase in the unit cell volume of $PrBaCo_{1.5}Fe_{0.5}O_{5+\delta}$ (PBCFO) as compared to PBCO, Table S2. It can be envisaged that the structural expansion causes a decrease in the strength of the Co—O bond [40] and thus enhancing its diffusivity. The diffusion was fitted to the activation law $D = 2.686 \times 10^{-6}\exp(-24.1(kJ/mol)/k_bT)$, where the estimated activation energy was observed to be comparable to $PBSCO_{5.5}$ and lesser than $PBCO_{5.5}$, Fig. 2(d). The cell impedance spectra of a PBCFO electrode showed a reduced polarization resistance (0.11 Ω cm^2) as compared to PBCO measures at 873 K, Table 2. Thus

Table 1
Diffusion coefficient and activation energy calculated in this study by molecular dynamics (MD) and compared to the other MD simulation and electrical conductivity relaxation (ECR) measurements.

	Diffusion coefficient (cm^2 s^{-1})	Temperature (K)	Method	Activation energy (kJ/mol)	Reference
$PrBaCo_2O_{5.5}$	3.0×10^{-8}	873	MD	40.5	This work
$PrBaCo_2O_{5+\delta}$	2.96×10^{-8}	873	MD	33.8	[28]
$PrBaCo_2O_{5+\delta}$	3.6×10^{-7}	773	ECR	46.3	[34]
$PrBa_{0.5}Sr_{0.5}Co_2O_{5.5}$	8.33×10^{-8}	873	MD	28.9	This work
$PrBaCo_{1.5}Fe_{0.5}O_{5.5}$	8.0×10^{-8}	873	MD	24.1	This work
$PrBa_{0.5}Sr_{0.5}Co_{1.5}Fe_{0.5}O_{5.5}$	1.18×10^{-7}	873	MD	30.9	This work
$GdBa_{0.5}Sr_{0.5}Co_{1.5}Fe_{0.5}O_{5.5}$	3.0×10^{-8}	873	MD	34.7	This work
$NdBa_{0.5}Sr_{0.5}Co_{1.5}Fe_{0.5}O_{5.5}$	5.16×10^{-8}	873	MD	48.0	This work

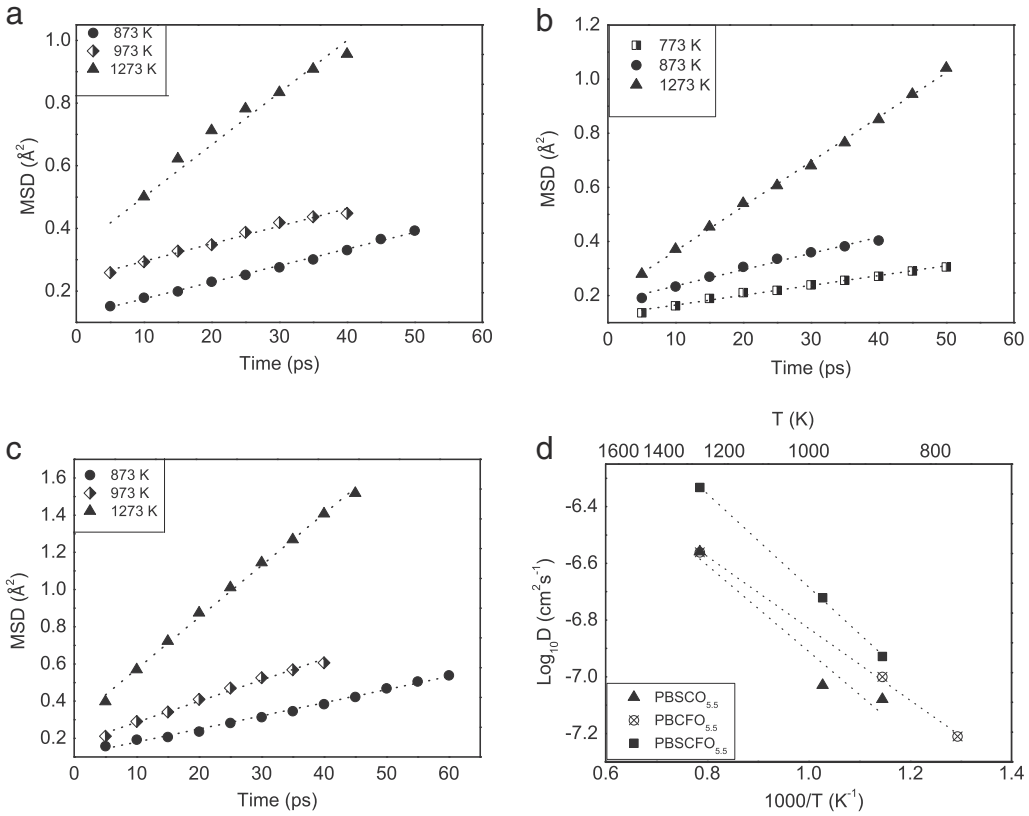

Fig. 2. MSD plots showing oxygen diffusion in the *a–b* plane of Sr and Fe doped structures a) $PBSCO_{5.5}$, b) $PBCFO_{5.5}$, c) $PBSCFO_{5.5}$ and d) corresponding Arrhenius plots for a temperature range of 773–1273 K.

Fe doping leads to an increase in oxygen anion diffusivity, which may be correlated to its improved electrochemical performance.

The results suggest that on co-doping Sr and Fe, high diffusivity values can be achieved in the intermediate temperature range. Mean square displacement curve for $PrBa_{0.5}Sr_{0.5}Co_{1.5}Fe_{0.5}O_{5.5}$ ($PBSCFO_{5.5}$) is shown in Fig. 2(c). Indeed, the diffusivity was estimated to be maximum (1.18×10^{-7} cm^2 s^{-1} at 873 K) amongst all the layered perovskite compounds studied, Table 1. The simulations showed a high degree of vacancy disordering, which was observed to be consistent with the Sr doped $PBSCO_{5.5}$ structure, and thus explaining the enhanced diffusivity. The effects of dopants on the inherent anisotropic nature of oxygen ion diffusion in these perovskites were analyzed. Interestingly, the introduction of dopant metal cation on A- and B-site had negligible effect on the oxygen diffusivity in the c-plane (Fig. S2 (a) and S2 (b)) and the oxygen diffusion was observed to be restricted to *a–b* plane. On changing the oxygen non-stoichiometry, the diffusivity was observed to be maximum for $\delta = 0.5$ as compared to other non-stoichiometric structures; $\delta = 0$ and 0.8, Fig. S4, indicating the disruption of proposed zig-zag pore channels for oxygen diffusion [20]. As suggested in the experimental study, a synergistic effect of co-doping Sr and Fe could be envisaged in high estimates of diffusion coefficient for $PBSCFO_{5.5}$. The diffusivities were fitted to an activation law $D = 8.58 \times 10^{-6}$ exp $(-30.9(kJ/mol)/k_bT)$, Fig. 2(d). While the diffusivity values for $PBSCFO_{5.5}$ were observed to be higher than $PBCFO_{5.5}$ in the intermediate temperature range (873–1073 K), the activation energy showed an opposite trend compared to $PBCFO_{5.5}$. We expect that slightly higher activation energy may lead to lower diffusivity of $PBSCFO_{5.5}$ compared to $PBCFO_{5.5}$ at high temperatures (>1273 K). The activation energy for oxygen ion diffusion compares well to the estimate of energy barrier ($E_a = 44.4$ kJ/mol) calculated by *ab-initio* DFT simulations [20]. Thus, the high diffusivity of $PBSCFO_{5.5}$ at 873 K can be correlated to the exceptionally high level of electrochemical performance reported for SOFC with a PBSCFO electrode at 873 K.

Changing the A-site cation from Pr to Nd and Gd has shown significant effect on the transport properties and electrochemical performance of the layered perovskites $LnBaCo_2O_{5+\delta}$ (Tables 1 and 2). The area specific resistance was reported to decrease in the order-$Pr^{3+} > Nd^{3+} > Gd^{3+}$ for the three electrodes PBCO, NBCO and GBCO, sharing similar oxygen diffusion mechanism, Table 2. Interestingly this same order of decreasing ASRs of the electrochemical cell on changing lanthanide cation was also observed in cells with co-doped PBSCFO, NBSCFO and GBSCFO electrodes, Table 2. We conducted molecular dynamics simulations in the co-doped $GdBa_{0.5}Sr_{0.5}Co_{1.5}Fe_{0.5}O_{5.5}$ ($GBSCFO_{5.5}$) and $NdBa_{0.5}Sr_{0.5}Co_{1.5}Fe_{0.5}O_{5.5}$ ($NBSCFO_{5.5}$) to investigate the possible link of cell performance with diffusivity. Fig. 3(a–c) shows the corresponding MSD and Arrhenius plots reporting the diffusion and activation energy. The measured diffusivity was observed to follow the order Pr^{3+} (1.18×10^{-7} cm^2 s^{-1}) > Nd^{3+} (5.16×10^{-8} cm^2 s^{-1}) > Gd^{3+} (3×10^{-8} cm^2 s^{-1}) at 873 K in these co-doped perovskites, Table 1. Furthermore, extent of size difference between A-site lanthanide cation and B-site (Ba^{2+}) followed the periodic trend, $Gd^{3+} > Nd^{3+} > Pr^{3+}$.

Table 2
Electrochemical performance of layered perovskites measured in terms of ASR of the electrode in a symmetric cell configuration at the reported temperature.

	ASR (Ω cm^2)	Temperature (K)	Reference
$GdBaCo_2O_{5+\delta}$	0.16	973	[52]
$NdBaCo_2O_{5+\delta}$	0.11	973	[22]
$PrBaCo_2O_{5+\delta}^{O}$	0.4	873	[12]
$PrBaCo_2O_{5+\delta}^{T}$	0.15	873	[34]
$PrBa_{0.5}Sr_{0.5}Co_2O_{5+\delta}$	0.07	873	[39]
$PrBaCo_{1.5}Fe_{0.5}O_{5+\delta}$	0.11	873	[20]
$PrBa_{0.5}Sr_{0.5}Co_{1.5}Fe_{0.5}O_{5+\delta}$	0.056	873	[20]
$NdBa_{0.5}Sr_{0.5}Co_{1.5}Fe_{0.5}O_{5+\delta}$	0.066	873	[20]
$GdBa_{0.5}Sr_{0.5}Co_{1.5}Fe_{0.5}O_{5+\delta}$	0.095	873	[21]

^{T}—tetragonal symmetry, ^{O}—orthorhombic symmetry.

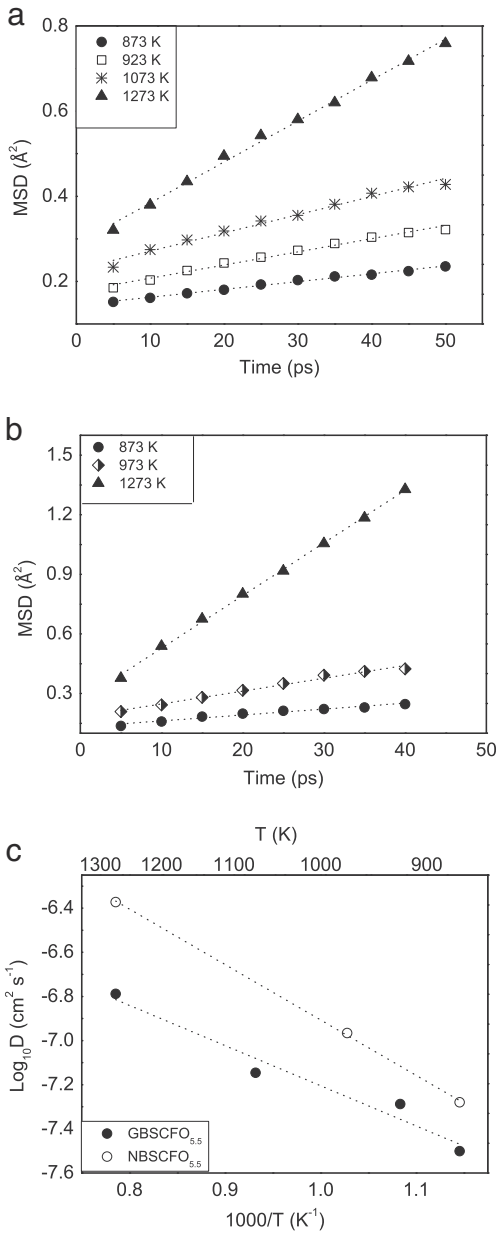

Fig. 3. MSD plots showing oxygen diffusion in the *a*–*b* plane of co-doped structures of a) $GBSCFO_{5.5}$, b) $NBSCFO_{5.5}$, and c) corresponding Arrhenius plot for a temperature range of 873–1273 K.

Consequently, the extent of lattice distortion would be maximum in Gd-containing perovskite relative to others with similar dopant levels [41]. This disruption of cation ordering in crystals led to the reduction in diffusivity as evident from the calculation, where diffusion co-efficient was observed to follow the reverse order $Pr^{3+} > Nd^{3+} > Gd^{3+}$. Thus the change in diffusion coefficient of the electrode material led to a corresponding change in the electrochemical performance of a SOFC.

A caution should be emphasized here that besides diffusivity, a number of factors such as the composition, thickness, method of synthesis, impurities, microstructure and other components of the cell play an important role in determining the overall electrochemical performance of the electrode and the cell. It was observed in several studies that on changing the method of synthesis and fabrication of the same electrode material, a different value of ASR and peak power density was measured. This could possibly be due to the change in the operating mechanism of the electrode vis-à-vis to surface exchange and/or bulk diffusion. For example, a number of studies have reported electrode performance to be dominated by surface exchange kinetics [42,43] where diffusivity has no control on measured ASR. The improved diffusion kinetics ($D = 1.41 \times 10^{-5}$ cm^2 s^{-1} at 973 K) of $SmBa_{0.6}Sr_{0.4}Co_2O_{5+\delta}$ [44] did not result in the reduction of its measured ASR (0.86 Ω cm^2 at 973 K) relative to PBCO. Similarly on changing other components of the cell such as the electrolyte a different value of the ASR is reported, likely due to the change in electrode–electrolyte interface. For example, on changing the electrolyte from YSZ to CGO ($Ce_{0.8}Gd_{0.2}O_{2-\delta}$), the ASR value of GBCO electrode was observed to decrease from about 100 Ω cm^2 [45] to about 0.53 Ω cm^2 [46] in the operating temperature range of an IT-SOFC. Similarly, electrode materials tested in the same geometry and conditions; however, with a different microstructure and grain size showed a change in ASR which is attributed to the grain boundary effect [47]. Furthermore, diffusion coefficient of the electrode could show disparate values when fabricated in a different configuration, which can be attributed to the operating mechanism, grain boundary and/or space charge-layer effects. For example oxygen diffusion coefficient of $La_2NiO_{4+\delta}$ was measured to be 2.09×10^{-8} cm^2 s^{-1} at 973 K for bulk samples synthesized by a modified citrate method [48]. In contrast for epitaxial thin-films of $La_2NiO_{4+\delta}$ fabricated by chemical vapor deposition, D_{chem} was measured to be 3.38×10^{-7} cm^2 s^{-1} at 973 K [49]. Similarly for BSCF perovskites, the values of diffusion coefficient were measured to differ for samples synthesized by modified EDTA-citrate process ($D_{chem} = 10^{-7}$ cm^2 s^{-1} at 873 K) [50] and sol–gel process ($D_{chem} = 10^{-5}$ cm^2 s^{-1} at 873 K) [51].

Consequently, it should be noted that oxygen diffusion coefficient of the electrode may not necessarily always be linked to the electrochemical performance. However, in cases where electrochemical process is likely to be limited by bulk oxygen anion transport, diffusivity plays an important role in determining the electrochemical performance.

4. Conclusion

Preferential oxygen diffusion in the Ln—O and Co—O plane was observed in double perovskite structured $LnBa_{1-y}Sr_yCo_{2-x}Fe_xO_{5+\delta}$ (Ln = Pr, Gd, Nd) electrodes. The diffusivity was enhanced on doping Sr at the A′-site and Fe at the B-site in $PBCO_{5.5}$ electrode. On altering the A-site cation, in co-doped structures the diffusion coefficient increases in the order $Gd^{3+} < Nd^{3+} < Pr^{3+}$. The diffusivity was observed to be maximum ($D = 1.18 \times 10^{-7}$ cm^2 s^{-1}) at 873 K in $PBSCFO_{5.5}$ which explains the high peak power density values reported for a SOFC fabricated with the same electrode. The trend in diffusivity values compares well with the measured electrochemical performance of the double perovskite electrodes. Therefore, wherever the electrode is dominated by bulk anion transport, diffusivity plays an important role in ascertaining its electrochemical performance.

For the double perovskite electrodes, molecular dynamics simulations can be successfully utilized in the calculation of diffusivity, with significant accuracy and at operating conditions of an IT-SOFC. Dopants having a direct impact on diffusivity of the layered perovskite structures such as Sr and Fe may be utilized in future for the design of novel electrodes.

Acknowledgment

Assistance from Dr. Manish Agarwal in setting up the calculations on high performance cluster is appreciated. The authors would like to acknowledge the financial support from the Department of Science and Technology, Government of India (SB/S3/CE/037/2014).

Appendix A. Supplementary data

Supplementary data to this article can be found online at http://dx.doi.org/10.1016/j.ssi.2015.08.002.

References

[1] A. Tarancón, M. Burriel, J. Santiso, S.J. Skinner, J.A. Kilner, J. Mater. Chem. 20 (19) (2010) 3799–3813.
[2] B. Steele, K.M. Hori, S. Uchino, Solid State Ionics 135 (1–4) (2000) 445–450.
[3] S.P. Jiang, J. Mater. Sci. 43 (21) (Oct. 2008) 6799–6833.
[4] S.B. Adler, Chem. Rev. 104 (10) (Oct. 2004) 4791–4843.
[5] R.a. De Souza, J.A. Kilner, J.F. Walker, Mater. Lett. 43 (1) (2000) 43–52.
[6] S.J. Benson, D. Waller, J.A. Kilner, J. Electrochem. Soc. 146 (4) (2000) 1305–1309.
[7] A. Tarancón, S.J. Skinner, R.J. Chater, F. Hernández-Ramírez, J.A. Kilner, J. Mater. Chem. 17 (30) (2007) 3175.
[8] M. Burriel, J. Peña-Martínez, R.J. Chater, S. Fearn, A.V. Berenov, S.J. Skinner, J.A. Kilner, Chem. Mater. 24 (2012) 613–621.
[9] T. Tsai, S.A. Barnett, Solid State Ionics 93 (3–4) (1997) 207–217.
[10] W. Zhou, Z. Shao, R. Ran, H. Gu, W. Jin, N. Xu, J. Am. Ceram. Soc. 91 (4) (2008) 1155–1162.
[11] Y. Lee, D.Y. Kim, G.M. Choi, Solid State Ionics 192 (1) (Jun. 2011) 527–530.
[12] D. Chen, R. Ran, K. Zhang, J. Wang, Z. Shao, J. Power Sources 188 (2009) 96–105.
[13] S. Yamauchi, T. Ishigaki, J. Mizusaki, K. Fueki, Solid State Ionics 9–10 (1983) 997–1000.
[14] a.V. Berenov, a. Atkinson, J.A. Kilner, E. Bucher, W. Sitte, Solid State Ionics 181 (17–18) (Jun. 2010) 819–826.
[15] M.A. Nath, A.S. Hameed, R. Chockalingam, S. Basu, A.K. Ganguli, Fuel Cells 13 (2) (2013) 270–278.
[16] H. Sumi, T. Yamaguchi, K. Hamamoto, T. Suzuki, Y. Fujishiro, J. Power Sources 226 (Mar. 2013) 354–358.
[17] X. Ding, C. Cui, X. Du, L. Guo, J. Alloys Compd. 475 (2009) 418–421.
[18] J.E. ten Elshof, M.H.R. Lankhorst, H.J.M. Bouwmeester, Solid State Ionics 99 (1–2) (1997) 15–22.
[19] A. Mai, V.A.C. Haanappel, S. Uhlenbruck, F. Tietz, D. Stover, Solid State Ionics 176 (15–16) (2005) 1341.
[20] J. Kim, J. Shin, H.Y. Jeong, Y. Choi, G. Kim, M. Liu, Sci. Rep. 3 (2013) (2013) 2426.
[21] J. Kim, A. Jun, J. Shin, G. Kim, J. Am. Ceram. Soc. 97 (2) (Feb. 2014) 651–656.
[22] J.H. Kim, J.T.S. Irvine, Int. J. Hydrog. Energy 7 (2012) 1–10.
[23] A. Chroneos, B. Yildiz, A. Tarancon, D. Parfitt, J.A. Kilner, A. Tarancón, Energy Environ. Sci. 4 (8) (2011) 2774–2789.
[24] J. Hermet, G. Geneste, G. Dezanneau, Appl. Phys. Lett. 97 (17) (2010) 174102.
[25] C.A.J. Fisher, Y. Iwamoto, M. Asanuma, T. Anyashiki, K. Yabuta, J. Eur. Ceram. Soc. 25 (13) (Aug. 2005) 3243–3248.
[26] M.S. Islam, M. Cherry, C.R.A. Catlow, J. Solid State Chem. 124 (1996) 230–237.
[27] P.P. Ewald, Ann. Phys. 369 (3) (1921) 253–287.
[28] I. Seymour, A. Tarancón, A. Chroneos, Solid State Ionics 216 (2012) 41–43.
[29] R.A. Buckingham, Proc. R. Soc. A Math. Phys. Eng. Sci. 168 (933) (Oct. 1938) 264–283.
[30] S. Nosé, J. Chem. Phys. 81 (1) (Jul. 1984) 511.
[31] W. Hoover, Phys. Rev. A 31 (3) (Mar. 1985) 1695–1697.
[32] H.J.C. Berendsen, J.P.M. Postma, W.F. van Gunsteren, A. DiNola, J.R. Haak, J. Chem. Phys. 81 (8) (Oct. 1984) 3684.
[33] J.M. Haile, Molecular Dynamics Simulation: Elementary Methods, John Wiley and Sons, New York, 1992.
[34] G. Kim, S. Wang, A.J. Jacobson, L. Reimus, P. Brodersen, C.A. Mims, J. Mater. Chem. (2007) 2500–2505.
[35] R.A. Cox-Galhotra, S. McIntosh, Solid State Ionics 181 (31–32) (2010) 1429–1436.
[36] Y. Hu, O. Hernandez, T. Broux, M. Bahout, J. Hermet, A. Ottochian, C. Ritter, G. Geneste, G. Dezanneau, J. Mater. Chem. 22 (36) (Aug. 2012) 18744.
[37] A.K. Azad, J.H. Kim, J.T.S. Irvine, J. Power Sources 196 (17) (2011) 7333–7337.
[38] B.C.H. Steele, Mater. Sci. Eng. B 13 (2) (Mar. 1992) 79–87.
[39] S. Park, S. Choi, J. Kim, J. Shin, G. Kim, ESC Electrochem. Lett. 1 (5) (2012) F29–F32.
[40] L. Zhao, J. Shen, B. He, F. Chen, C. Xia, Int. J. Hydrog. Energy 36 (5) (Mar. 2011) 3658–3665.
[41] M. Mogensen, D. Lybye, N. Bonanos, P. Hendriksen, F. Poulsen, Solid State Ionics 174 (1–4) (Oct. 2004) 279–286.
[42] Z.P. Shao, S.M. Haile, Nature 431 (7005) (2004) 170.
[43] A.C. Tomkiewicz, M. Meloni, S. McIntosh, Solid State Ionics 260 (2014) 55–59.
[44] A. Subardi, M.-H. Cheng, Y.-P. Fu, Int. J. Hydrog. Energy 39 (35) (Dec. 2014) 20783–20790.
[45] A. Tarancon, J. Penamartinez, D. Marrerolopez, A. Morata, J. Ruizmorales, P. Nunez, Solid State Ionics 179 (40) (Dec. 2008) 2372–2378.
[46] A. Chang, S.J. Skinner, J.A. Kilner, Solid State Ionics 177 (19–25) (Oct. 2006) 2009–2011.
[47] M.A. Haider, S. McIntosh, J. Electrochem. Soc. 158 (9) (2011) B1128.
[48] M. Burriel, G. Garcia, J. Santiso, J.A. Kilner, R.J. Chater, S.J. Skinner, J. Mater. Chem. 18 (4) (2008) 416–422.
[49] J.A. Kilner, S.j. Skinner, Solid State Ionics 135 (2000) 709–712.
[50] D. Chen, Z. Shao, Int. J. Hydrog. Energy 36 (11) (Jun. 2011) 6948–6956.
[51] S.M.H. Zongping Shao, Nature 431 (2004) 170–173.
[52] B. Lin, S. Zhang, L. Zhang, L. Bi, H. Ding, X. Liu, J. Gao, G. Meng, J. Power Sources 177 (2) (Mar. 2008) 330–333.

Available online at www.sciencedirect.com

ScienceDirect

materialstoday: PROCEEDINGS

Materials Today: Proceedings 2 (2015) 3446 – 3452

4th International Conference on Materials Processing and Characterization

Scuffing behaviour of EN31 steel under dry sliding condition using pin-on-disc machine

Paras Kumar[a]*, Harish Hirani[b], Atul Agrawal[c]

[a]*Assistant Professor, Mechanical Engineering Department, Delhi Technological University, Delhi-110042, India*

[b] *Professor, Mechanical Engineering Department, Hauzkhas, IIT Delhi -110016, India*

[c]*Associate Professor, Mechanical Engineering Department Delhi Technological University, Delhi-110042, India*

Abstract

The focus of the present study is to investigate the scuffing phenomenon of EN 31(Pin) against EN 19(Disc) steel under dry running condition using pin-on-disc machine. Coefficient of friction (COF) and pin wear are experimentally measured for different combination of loads (10N-70N) and rotational speeds (200 rpm-2000 rpm). The speed and load at which transition to scuffing occur are also examined. It is observed that the wear resistance increases with sliding velocity for lower load, while at higher load it increases initially and then becomes stable at higher speed. The COF increases with sliding velocity at lower loads and then becomes steady, while at higher loads, the COF first increases with increase in speed and then decreases considerably. This abrupt decrease in friction coefficient is due to intense heat generation between the disc and the pin and the experiment is stopped due to higher noise and vibration. Archard's wear model is also used to validate the wear of pin at different loads and speeds. Experimentally measured pin wear shows higher value probably due to decreases in material hardness with increase in interface temperature.

Selection and peer-review under responsibility of the conference committee members of the 4th International conference on Materials Processing and Characterization.

Keywords: Wear; Wear resistance; Coefficient of friction; Scuffing; sliding velocity; Archard's wear model

* Corresponding author. Tel.: +91-9560063121; fax: +91-11-27871023.
E-mail address: paraskum007@rediffmail.com

Selection and peer-review under responsibility of the conference committee members of the 4th International conference on Materials Processing and Characterization.
doi:10.1016/j.matpr.2015.07.320

1. Introduction

The different mechanical components like gear, cams, piston ring and bearing etc. are used in different machines or mechanisms and they operate under different operating and loading conditions with or without lubrication. When the two surfaces rub against each other, interface temperature increases. As the interface temperature increases with time, the contact materials soften and asperities get welded and sheared out due to motion. With the breaking of these weld connections, the material surface becomes rougher, and coefficient of friction increases which further increases the level of noise and vibration. This localized welding and shearing of connections is termed as scuffing.

Many research works have been reported in literature related to scuffing behaviour of materials. Shaw and Leavey [1] measured the coefficient of friction for various combinations of pure metals, and concluded that scuffing and adhesion depend on their "chemical affinity". The higher the affinity, the larger the coefficient of friction. Affinity is also connected with the mutual solubility of the metals; a larger solubility corresponds to a larger affinity. Accordingly, inter-diffusion processes can play a critical role in scuffing, and some researchers have proposed a diffusion-based hypothesis of scuffing. Ernst and Merchant [2] ascertained that the coefficient of friction is lower for pairs of metals that do not form solid solutions at ambient temperature. Coffin [3] confirmed that the ability of metals to create alloys is a quantitative criterion for the occurrence of local scuffing and surface damage. Parks [4] asserted that recrystallization precedes scuffing. He suggested that the recrystallization at ambient temperatures results from plastic deformation of the asperities. During that process, the crystal growth occurs, leading to junction formation between the two contacting bodies. Semenov [5] proposed a theory of scuffing in which scuffing occurs when the energy state of the atoms in the crystal lattice reaches some high level, called "energetic threshold of scuffing" for the given metal. An energy increase takes place as a result of the elastic and plastic deformation or an increase in temperature. Supposedly, metals become amorphous, metallic bonds form, and the physical interface disappears at the energetic threshold of scuffing. A comprehensive experimental investigation of scuffing was presented by Golego [6]. The effects of sliding speed, specific pressure, vibration, temperature, shape of the contacting bodies, sliding time, gaseous and fluid environments, solid lubricants, type of materials, surface treatment methods, and properties of oxide layers on scuffing were reported. In another review, Dyson [7] introduced the concept of 'friction power intensity' as a function of sliding speed. Hershberger et al. [8] suggested that the austenite formation was caused by scuffing, which formed due to a rapid austenitization process, mechanical dissolution of carbides, or diffusion less transformation. Scuffing mechanism based on adiabatic shear instability was recently proposed by Ajayi et al. [9]. Scuffing was predicted to occur when the rate of local thermal softening exceeded that of work hardening. Ajayi et al. [10] have further attempted to develop a scuffing mechanism of near-surface material with lubricated contact.

There are numerous applications, like gear, bearing, cam and follower etc., where both the interacting parts are made of the same or different grade of steel. When these parts are operating under dry or starved condition at higher load and rotational speed, scuffing is the common failure observation. The goal of the present study is to investigate the scuffing phenomenon of EN 31(Pin) against EN19 (Disc) steel under dry running condition using pin-on-disc machine. The variation of friction and pin wear with respect to various sliding speeds, and time duration of the test are studied. Archard's wear model is also used to validate the wear of pin at different loads and speeds. The speed and load at which transitions to scuffing occurred are also examined.

2. Experimental setup and parameters

Wear tests are conducted on a pin-on-disc machine. This machine is capable of providing wear data at different sliding speeds and loads with respect to time. An EN19 test disc of diameter 165 mm and thickness 7 mm is attached to a vertical motor shaft whose rotational speed continuously varied from 200 rpm to 2000 rpm. The EN31 steel pin of diameter 4 mm is tested against EN19 steel disc under dry sliding condition as shown in Fig.-1. A magnetic pick-up and digital display device are used for monitoring disc revolution. The load on the pin specimen is applied by dead weights supported at the end of a hinged horizontal beam. The vertical arm carrying the specimen is rigidly secured to the beam. The dead weight of the horizontal beam assembly is counter-balanced by a weight that is positioned at the end of the beam. The load varies from 10N–70 N in step of 20N and the wear track diameter is fixed at 90 mm. A spring-loaded linear voltage differential transducer (LVDT) is used to continuously monitor the

reduction in the length of the pin. The latter is related to the wear volume through a calibration process. The LVDT and strain gauge signals are recorded by a data acquisition system. The time duration for each test is set at 900 second during which the speed varies from 200 rpm to 2000 rpm and the data are recorded after an interval of 150 second.

Fig. 1. (a) EN19 steel disc (b) EN31 steel pin

3. Results and discussion

The complete measured and calculated data are summarized in Table-1. It is seen that the wear of pin increases with the increase in disc rotational speed for any value of load. The variation of coefficient of friction (COF) with time at different disc rotational speed and load are illustrated in Fig.2-4. The load on the pin is 10 N in Fig.-2 and it is noticed that as the rotational speed increases, the COF increases initially and becomes almost stable at higher rotational speed. The transition rotational speed is 1000 rpm when COF suddenly increases from 0.2 to 0.4. The sudden increase in COF is related to scuffing phenomenon. The scuffing is observed at a speed of 1000 rpm and 10 N load when the machine are operated for about 300 second.

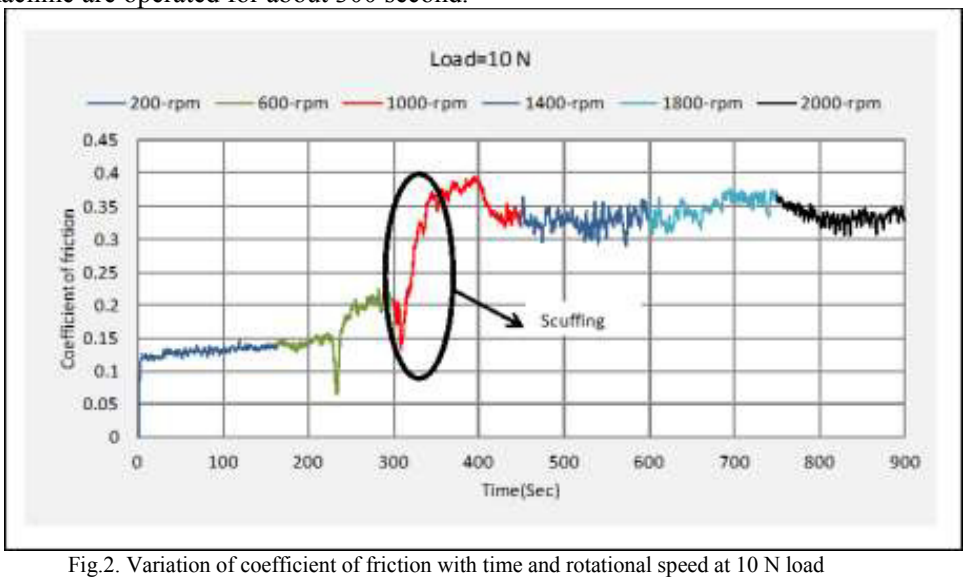

Fig.2. Variation of coefficient of friction with time and rotational speed at 10 N load

Table-1 Wear test results for 10, 30 and 70 N loads

Load (N)	Time (sec)	Speed (rpm)	Friction coefficient	Wear (μm)	Wear coefficient
10	150	200	0.1384	16.05	1.21 E-04
	300	600	0.1942	30.38	4.83 E-05
	450	1000	0.3588	29.74	1.97 E-05
	600	1400	0.3313	34.37	1.22 E-05
	750	1800	0.3568	40.99	9.09 E-06
	900	2000	0.3281	49.74	8.22 E-06
30	150	200	0.2096	15.55	4.04 E-05
	300	600	0.3079	81.21	4.66 E-05
	450	1000	0.3102	90.53	2.08 E-05
	600	1400	0.3077	127.04	1.64 E-05
	750	1800	0.2847	193.92	1.45 E-05
	900	2000	0.2957	232.09	1.28 E-05
70	100	200	0.3392	126.31	2.70 E-04
	200	400	0.3352	152.11	8.20 E-05
	300	600	0.3954	1859.16	4.37 E-04
	400	800	0.3850	3464.19	4.58 E-04
	500	1000	0.1968	4394.56	3.76 E-04
	600	1200	0.1962	4393.36	2.60 E-04

The variation of COF as shown in Fig.-3 is for 30 N load. The trend is almost the same as for 10 N load except the scuffing is observed at 600 rpm disc rotational speed. The COF increases with increase in speed and at 600 rpm, its value abruptly increases from 0.17 to 0.35 after 150 seconds.

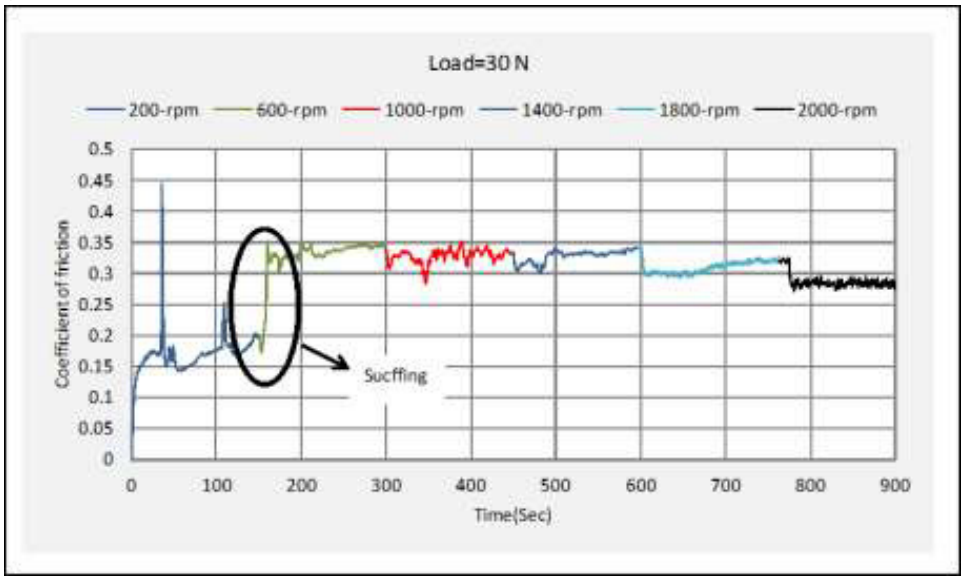

Fig.3. Variation of coefficient of friction with time and rotational speed at 30 N load

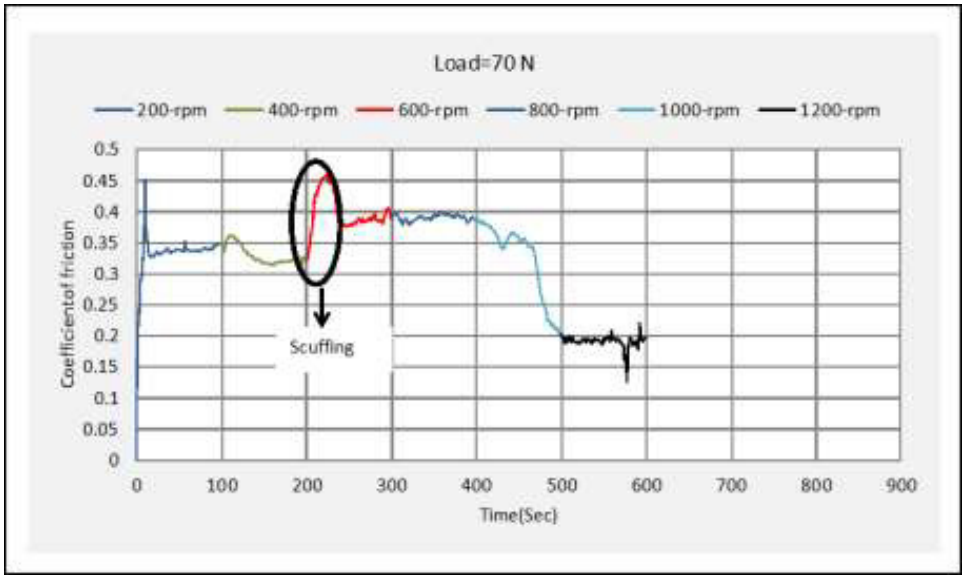

Fig. 4. Variation of coefficient of friction with time and rotational speed at 70 N load

Figure-4 shows variation of COF with time and speed at 70 N load. The COF remains almost steady up to 400 rpm and after that it shows a jump at 600 rpm. At higher rpm, around 1000, the COF suddenly drops from 0.4 to 0.2 and then remains stable up to 600 second. After 600 second, the test is stopped due to intense heat generation and noise. The probable reason for this drop is softening of material, i.e. drop in material strength at higher speed and load due to increased interface temperature.

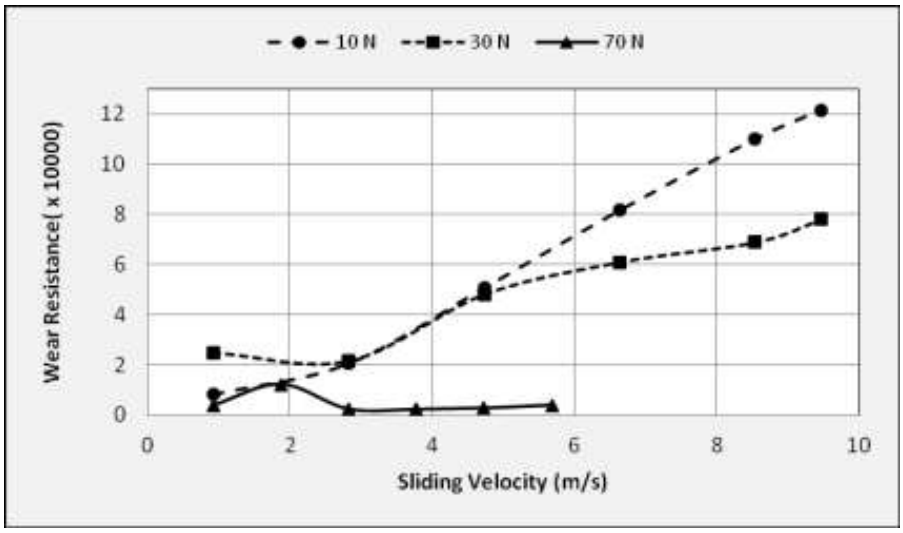

Fig. 5. Wear resistance at different loads and rotational speed

The variation of wear resistance with sliding velocity is plotted in Fig. 5. For lower load values of 10 and 30 N, the wear resistance increases with increase in sliding speed. The rate of increase is slower for higher loads as compared with smaller load. At higher speed, the difference in wear resistance between lower and higher loads is seen to be higher, e.g., at a sliding velocity of 8.5 m/s, the wear resistance at 30 N load is lower by 33% than that at 10 N load.

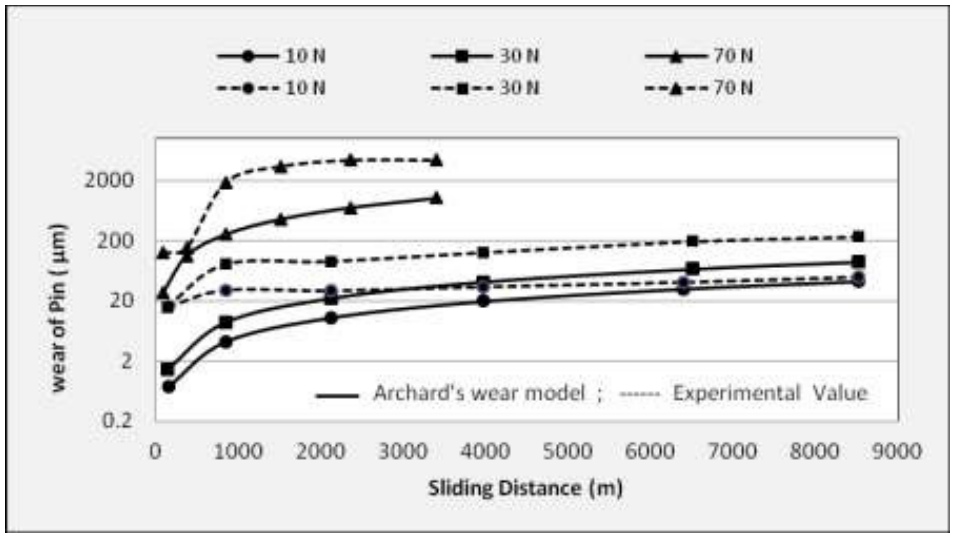

Fig.6. Variation of wear of pin with sliding distance

Archard's wear model is used to calculate the amount of sliding wear of pin. According to Archard, the amount of wear is dependent upon wear coefficient, contact pressure, sliding velocity, sliding duration and expressed as

$$Wear\ of\ pin\ (h) = K\ p\ v\ t \quad (1)$$

where K is the wear coefficient (mm^2/N), p is contact pressure (MPa), $(L = v\ t)$ is sliding distance (mm).

The wear of pin can also be expressed in terms of non –dimensional wear coefficient (k), hardness of softer material (H, N/mm^2), Load (W, Newton), area of contact (A, mm^2) and sliding distance (L, mm).

$$\text{Wear of pin (h)} = \left(\frac{\text{k}}{\text{H}}\right)\left(\frac{\text{W}}{\text{A}}\right)\ \text{(L)} \quad (2)$$

The wear of pin is calculated by Eq.-2, which is based on Archard's wear law, and plotted in Fig.-6 for different loads and sliding distances. With increase in sliding distance, the wear of pin increases at all the loads using Archard's wear model. The experimental plots have similar trends but with higher amount of pin wear. The deviation between experimental and model values is more for higher load and longer sliding distance. The probable reason for the deviation is decrease in value of material hardness with increase in interface temperature due to increased sliding distance.

4. Conclusions

Conclusions from the experimental results are:

- The friction coefficient increases slowly with sliding velocity at lower loads and becomes almost stable at higher speed. However at higher load, it shows stable behaviour for initial running and then decreases considerably at higher speed.
- The sudden increase in coefficient of friction is termed as scuffing. The transition speeds, at which scuffing phenomenon observed, are 1000 rpm, 600 rpm and 600 rpm at 10 N, 30N and 70 N load respectively.

- In general friction coefficient first increases, and then becomes steady. However, at higher load such as 70 N, it decreases abruptly at higher speed due to intense heat generation as the material loses strength with temperature.
- For lower load wear resistance increases with sliding velocity; while at higher load, wear resistance decreases with increase in speed. The rate of increase is slower for higher loads as compared with smaller load.
- Archard's wear model and experimental observation shows similar trends for pin wear, i.e. with increase in sliding distance, the wear of pin increases at all the loads. Experimental observation shows higher value probably due to decreases in material hardness with interface temperature.

References

[1] E. Shaw, E.W.L. Leavey, Friction of dry solids in vacuum, Philos. Mag. 10 (1930) 809–822.
[2] H. Ernst, M. Merchant, Chip formation, friction and high quality of machined surfaces, Surf. Treat. Met. Soc. Met. 29 (1941) 299.
[3] L.F. Coffin, A study of the sliding of metals, with particular reference to atmosphere, Lubr. Eng. 12 (1956) 50–59.
[4] J.M. Parks, Recrystallization welding, Weld. J. 32 (1953) 209–221.
[5] A.P. Semenov, Scuffing of Metal, Mashgiz, Moscow, 1958.
[6] N.L. Golego, Scuffing in machines and methods of its elimination, Tekhnika, Kiev (1965).
[7] A. Dyson, Scuffing–a review: part 1, Tribol. Int. 8 (1975) 77–87.
[8] J. Hershberger , O.O. Ajayi, J. Zhang, H. Yoonb, G.R. Fenske , Formation of austenite during scuffing failure of SAE 4340 steel, Wear 256 (2004) 159–167.
[9] O.O. Ajayi, J.G. Hersberger, J. Zhang, H. Yoon, G.R. Fenske, Microstructural evolution during scuffing of hardened 4340 steel – implication for scuffing mechanism, Tribol. Int. 38 (2005) 277–282.
[10] O.O. Ajayi, C. Lorenzo-Martin, R.A. Erck, G.R. Fenske, Scuffing mechanism of near-surface material during lubricated severe sliding contact, Wear 271 (2011) 1750– 1753.

Available online at www.sciencedirect.com

ScienceDirect

materialstoday: PROCEEDINGS

Materials Today: Proceedings 2 (2015) 2538 – 2547

4th International Conference on Materials Processing and Characterization

Selection of locations of collection centers for reverse logistics using GTMA

Sana Malik*, Aradhana Kumari, Saurabh Agrawal

Delhi Technological University, Shahbad Daulatpur, Rohini, New Delhi 110042

Abstract

The application of reverse logistics is gaining attention with the pressure from environmental and social necessities. An efficient management of return of products is a taxing task because of uncertainty involved. To reduce this, the returned products are collected into collection sites. Hence, for an efficient reverse supply chain, the location of collection sites must be appropriate in order to make it profitable for the organization. In this paper we discuss the Graph Theory and Matrix Approach (GTMA) to find the location of collection sites. A case study has been presented to illustrate the method.

Selection and peer-review under responsibility of the conference committee members of the 4th International conference on Materials Processing and Characterization.

Keywords: Reverse Logistics, Graph Theory and Matrix Approach, SSI, EOL, E-waste.

1. Introduction

In recent years, more and more attention to environmental protection and increase in environmental legislations has made the organization to recover and process the unused products or products which are at their end –of –life (EOL). In industrialized countries, waste reduction has become a prime concern. In view of depleted land and incineration capacities, efforts are made to re-integrate waste products into industrial production processes for further use. Several countries have enforced environmental legislation charging producers with responsibility for the whole life cycle of their products [1, 2, 3, and 4]. Reverse Logistics (RL) is the way to implement proper disposal of waste products in the industries. It is therefore, defined as the process of planning, implementation and operation of efficient, cost effective flow of materials and information from the point of consumption to the point of origin for the purpose of recapturing value, or proper disposal [5]. Recovery of products for remanufacturing, repair and recycling can create

* Corresponding author. Tel.: +0-000-000-0000 ; fax: +0-000-000-0000 .
E-mail address: sm.sanamalik.93@gmail.com

2214-7853
Selection and peer-review under responsibility of the conference committee members of the 4th International conference on Materials Processing and Characterization.
doi:10.1016/j.matpr.2015.07.199

profitable business opportunities [6]. Owing to RL's interdisciplinary approach; this area presents an opportunity for research.

Decisions related to reverse logistics are tricky as there is no uniformity or periodicity for the return of goods and forecasting is complex. Also, there is no set pattern for the condition of goods that have been given back. In this paper, a model for the determination of location of the collection sites for the recovery of returned product has been given which is the initial step towards the recovery of products. Appropriate location of collection sites reduces the uncertainty in amount of retuned products, thus improving the reverse logistics.

Graph Theory is a systematic and logical approach. The advanced theory of graphs are very well documented. Graph/Digraph model have proved to be useful for modelling and analysing various kinds of problems in numerous fields of Science and Technology. Hence, this approach has been used in this paper. This paper has been arranged section wise. First, a review of the literature has been presented. The GTMA approach has been explained and the method for creating a permanent function along with explanation about the suitability index is presented. Also, a case study of ABC Infosystems is included where the critical factors for the alternatives at three locations have been decided. Also, these matrices have been solved and indexes are given. The paper is concluded with the presentation of results along with the observations.

2. Literature review

Reverse Logistics is related to the operations involved in the movement of an article back from the user to the manufacturer. Reverse Logistics is basically related to the return of a product that has either reached its End of Life (EOL) or has been returned by the customer. According to Rogers and Tiben Lembke (1991)[7] , reverse logistics is the "planning, implementation and operation of efficient, cost effective flow of materials and information from the point of consumption to the point of origin of recapturing value or proper disposal." Kelle and Silver (1989) [8] described methods for the forecast of reusable containers. Santibanez-Gonzalez and Diabat (2013) [9] proposed improved Benders decomposition schemes for solving a remanufacturing supply chain design problem (RSCP). Gandhi and Aggarwal (1992) [10] have used di-graph and matrix approach for failure mode and effect analysis. Yadav et al. (2010) [11] used Graph Theoretic Approach for the selection of a power plant. Vidal, Infante, Pecas and Vilaca [12] used ANOVA method to identify the factors that affect tensile strength and other properties. An algebraic model to find best mechanical performance was made.

Tagaras and Zikopoulos (2008) [13] studied a supply chain consisting of a central remanufacturing facility and a number of collection sites (CS). The central facility procures returned items from the CS for remanufacturing and sale. Examination of the application of a sorting procedure that identifies the units those are suitable for remanufacturing before disassembly. Application of graph theory has been widely spread into various fields of science and technology. The collection sites are generally used for the collection of the returnable products. Other modes may also be there. We found that the location of collection centres was one field that was not explored into and hence had a lot of scope for new investigations and have hence tried to address the location of the collection centres for different regions using Graph Theoretic Approach (GTA) and with the help of Digraph Matrices.

Graph theoretic approach is a powerful decision making method which has been in use since 1736. Graph theory has served an important role in the modelling of systems, network analysis, functional representation, conceptual modelling, diagnosis, etc. In GTA, the relationship between different variables is represented in the form of a digraph (directional graph) and matrix. Their interdependence on each other as well as their individual contribution to the system is assigned numerical values and an overall index is calculated. This index is then used for the self-analysis of the system or the comparative analysis of two or more system to select the best alternative. There are some other techniques like Analytical Network Process (ANP) and Analytical Hierarchy Process (AHP), which are based on the similar idea of parametric interrelationship. However, AHP does not capture the interdependence of variables while ANP does not include the hierarchy among them .GTA has no such limitations (Raj et al., 2010) [14] and hence can be used in a variety of fields.

3. Graph Theory and Matrix Approach

Graph theory is a logical approach and is used to convert qualitative factors into quantitative values and mathematical modelling gives an edge to the proposed technique over conventional methods like flow charts, cause-effect diagrams, etc. This is a relatively new technique of decision-making method and offers a simple, easy, and convenient way for decision-making method and involves less computation. A "graph" consists of number of "nodes" and lines (with direction) called edges that connect them. A graph can be unidirectional, meaning that the distinction between the two

vertices associated with each edge is negligible, or its edges may be directed from one vertex to another. The matrix representation of graph is then used to analyse the model to derive the function and finally the numerical index to get the result.

3.1 Steps Involved

Step 1: Identify the appropriate attributes and the alternatives that are involved in the decision-making problem of finding the location of collection site. Obtain the values of attributes (Ai) and their relative importance (aij).

Step 2: After shortlisting the different locations of collection sites, develop an attribute digraph which contains all the identified attributes and their relative importance. The number of nodes in the digraph must be equal to the number of attributes considered above. The edges and their directions will be decided upon based on the interrelations among the attributes (aij).

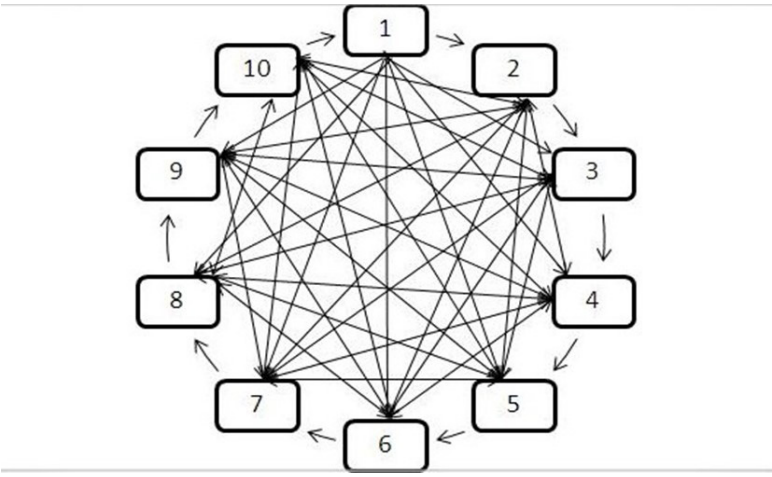

Figure 1: Attribute digraph showing interrelationship between ten attributes.

In the figure1, the digraph contains ten nodes which is equal to the number of attributes being considered in the model. The directed edge from 1 to 2 shows that attribute 1 has relative importance over attribute2, similarly directed edge for other attributes are made according to their relative importance.

Step 3: Develop the attributes matrix for the attributes digraph. This will be the M*M matrix with diagonal elements as Ai and off-diagonal elements as aij.

Step 4: Obtain the permanent function for the attributes matrix from per(j) equation.

Step 5: Substitute the values of Ai and aij, obtained in step 1, in Equation of per(j)above to evaluate the index for the short-listed alternatives.

Step 6: Arrange the alternatives in the descending order of the numerical index. The alternative having the highest value of index is the best choice for the location of collection centre.

Step 7: Take the final decision, keeping in mind the practical considerations and possible constraints likely to be experienced by the user are looked into during this stage. These include constraints such as: availability or assured supply, management constraints, political constraints, economic constraints, environmental constraints etc.

3.2 Matrix Representation of Digraph

Based on the digraph, a matrix is made. This will be the M*M matrix with diagonal elements as Di and off-diagonal elements as aij. The diagonal element Ai indicates the importance or contribution (also called as inheritance) of the ith parameter on the overall System index. The off-diagonal elements, aij's, indicate the relative Importance of one parameter over the other .In other words, they are an indicative of the parametric inter-dependencies.

In general, if there are M numbers of attributes, and there exists relative importance among all the attributes, then the attributes matrix, 'X' is written as:

Attributes 1 2 3 - - M

$$X=\begin{bmatrix} A1 & a12 & a13 & - & - & a1m \\ a21 & A2 & a23 & - & - & a2m \\ a22 & a32 & A3 & - & - & a3m \\ - & - & - & - & - & - \\ - & - & - & - & - & - \\ am1 & am2 & am3 & - & - & AM \end{bmatrix}$$

The permanent function of an MxM matrix is represented a given below (Rao, 2007) [15]:

per(j)=

$$\prod_{i=1}^{M} A_i$$

+

$$\sum_{i=1}^{M-1}\sum_{j=i+1}^{M} \dots\dots\dots \sum_{M=t+1}^{M} (a_{ij}a_{ji})A_kA_1A_mA_nA_o \dots\dots A_tA_M$$

.. .M≠ pus

+

$$\sum_{i=1}^{M-2}\sum_{j=i+1}^{M-1}\sum_{k=j+1}^{M} \dots \sum_{M=t+1}^{M} (a_{ij}a_{jk}a_{ki} + a_{ik}a_{kj}a_{ji})A_1A_mA_nA_0 \dots A_tA_M$$

k….M≠ pus

+

$$\sum_{i=1}^{M-3}\sum_{j=i+1}^{M}\sum_{k=i+2}^{M-1}\sum_{l=i+2}^{M} \dots \sum_{M=t+1}^{M} (a_{ij}a_{ji})(a_{kl}a_{lk})A_mA_nA_o \dots A_tA_M$$

k,l ….M≠ pus

+

$$\sum_{i=1}^{M-3}\sum_{j=i+1}^{M+1}\sum_{k=i+1}^{M}\sum_{l=i+1}^{M} \dots\dots \sum_{M=t+1}^{M} (a_{ij}a_{jk}a_{kl}a_{li} + a_{il}a_{lk}a_{kj}a_{ji})A_mA_nA_o\dots A_tA_M$$

k,l …M ≠ pus

+

$$\sum_{i=1}^{M-2}\sum_{j=i+1}^{M-1}\sum_{k=j+1}^{M}\sum_{l=1}^{M-1}\sum_{m=l+1}^{M} \dots \sum_{M=t+1}^{M} (a_{ij}a_{jk}a_{ki} + a_{ik}a_{kj}a_{ji})\ (a_{lm}a_{ml})A_nA_o \dots A_tA_M$$

+ k,l,m…..M≠ pus

$$\sum_{i=1}^{M-4}\sum_{j=i+1}^{M-1}\sum_{k=i+1}^{M}\sum_{l=i+1}^{M}\sum_{m=j+1}^{M} \dots \sum_{M=t+1}^{M} (a_{ij}a_{jk}a_{kl}a_{lm}a_{mi} + a_{im}a_{ml}a_{lk}a_{kj}a_{ji})A_nA_o \dots A_tA_M$$

+ k,l,m…..M≠ pus

$$\sum_{i=1}^{M-5}\sum_{j=i+1}^{M-1}\sum_{k=j+1}^{M}\sum_{l=1}^{M-2}\sum_{m=l+1}^{M-1}\sum_{n=m+1}^{M} \dots \sum_{M=t+1}^{M} (a_{ij}a_{jk}a_{ki} + a_{ik}a_{kj}a_{ji})(a_{lm}\ a_{mn}a_{nl} + a_{lm}a_{nm}a_{ml})A_o \dots A_tA_M$$

+ k,l,m,n…..M≠ pus

$$\sum_{i=1}^{M-5}\sum_{j=i+1}^{M}\sum_{k=i+1}^{M-3}\sum_{l=i+2}^{M}\sum_{m=k+1}^{M-1}\sum_{n=k+2}^{M} \dots \sum_{M=t+1}^{M} (a_{ij}a_{ji})(a_{kl}a_{lk})(a_{mn}a_{nm})A_o \dots\dots A_tA_M$$

+

k,l,m,n…..M≠ pus

$$\sum_{i=1}^{M-5}\sum_{j=i+1}^{M-1}\sum_{k=i+1}^{M}\sum_{l=i+1}^{M}\sum_{m=i+1}^{M}\sum_{n=j+1}^{M} \dots \sum_{M=t+1}^{M} a_{ij}a_{jk}a_{kl}a_{lm}a_{mn}a_{in} + a_{ni}a_{nm}a_{ml}a_{lk}a_{kj}a_{ji})A_o \dots A_tA_M$$

The expression has M+1 groups for an MxM matrix. Here pus means 'previously used subscripts. These represent attributes, their relative importance and values. The 1st one gives the measures of M criteria. There is no 2nd group. The 3rd subgroup has values of (M-2) attributes and 2-attribute relative importance loops. Every term of the 4th group gives a set of a 3- attribute relative importance loop, or its pair, and measures of (M-3) attributes. The 5th group contains 2 further groups. In the 1st group, there are a set of two 2-attribute relative importance loops and the values of (M-4) criteria. Every second sub-group's term is a set of pairs of 4-attribute relative importance loop or themselves and the values of (M-4) criteria. The 6th group has 2 sub-groups. The 1st group has a 3-criteria relative importance loop pairs and loops themselves and values of (M-5) criteria and 2-attribute relative importance loop. Every second sub-group's term is a set of pairs of 5-attribute relative importance loop or themselves. Also, it contains the values of (M-5) criteria. Other terms can be found. (Rao, 2007).

A permanent function from which the selection index is found out is thus obtained.

Table 1: Value of Attribute

Subjective measure of attribute	**Assigned value**
Exceptionally low	0.0
Extremely low	0.1
Very low	0.2
Low	0.3
Below average	0.4
Average	0.5
Above average	0.6
High	0.7
Very high	0.8
Extremely high	0.9
Exceptionally high	1.0

Table 2: Relative Importance of Attributes

Class description	**Relative importance**	
	aij	**aji = 1 - aij**
Two attributes are equally important	0.5	0.5
One attribute is slightly more important over the other	0.6	0.4
One attribute is strongly more important over the other	0.7	0.3
One attribute is very strongly important over the other	0.8	0.2
One attribute is extremely important over the other	0.9	0.1
One attribute is exceptionally more important over the other	1.0	0.0

4. Case Study

4.1 Company Profile

ABC Infosystems is an IT services with its headquarter in Gurgaon, Haryana. It offers a gamut of services from IT hardware to internet infrastructure solutions. ABC Infosystems products cover the entire spectrum of the information technology needs of its customers. ABC Infosystems products offerings include everything from enterprise level servers for mission critical applications to multimedia home computers. The company as a part of the business sells laptops, desktops and tablets apart from a myriad of other products and services.

Since it produces hardware to the consumers, after the products reach their end of life (EOL) stage, waste in the form of e-waste is generated. This e-waste includes electrical and electronic equipment and in order to minimize the hazardous impact of e-waste on the environment, the firm has recognized the need for the management, recycling and

recovery of e-waste. The company has already established 21 collection centres in India as a part of its campaign on reducing the carbon footprint in addition to other initiatives taken for the same. All the e-waste generated is recycled after separation of the recyclable waste from scrap and recycling is done by the manufacturer in the area. The company has even enabled the customers to put up an email request for collection of e-waste The company developed electronic waste take back initiatives in the year 2005-06. It has increased the collection of e-waste year on year for the last 7 years and its e-waste collection initiative includes other brands also. The company has collected more than 300 tonnes of e-waste in the last 7 years. ABC's e-waste policy begins from the very beginning of the manufacturing process. It designs its products in a way that they can easily be dismantled later on. The company believes it could benefit from the establishment of more collection centres. Considering that the company provides products and thus generates e-waste in the whole of India, it is in agreement with the general opinion that the numbers of collection centres are not enough.

In this paper, we have tried to set up three more collection centres for the company in 3 different Indian states (where the company does not already have collection centres) by calculating the SSI's (Site Suitability Index) of the alternatives for the location of the collection centre and comparing them. Three alternatives for the viable location have been taken and based upon ten important factors, their availabilities and relative importance, the most feasible location has been selected using GTA.

4.2 Selection Criteria

After discussion with the managers (e-waste) at Delhi branch, the following factors were identified as most critical to the setting up of a collection centre.

1. *OC: OPERATING COST: This cost involves the running cost of the collection site. The operating cost includes rent along with the cost involved in the day-to-day working of the centre.*
2. *PM: PROXIMITY TO THE MANUFACTURER: This involves the nearness to the manufacturer. Since this gets translated directly into the cost of transportation, it is also a critical factor.*
3. *C: PROXIMITY TO THE CUSTOMERS (RETURNING THE PRODUCT): Just as the proximity to the manufacturer is important, so is the proximity to the customer base.*
4. *F: FLEXIBILITY: Flexibility is the ability to increase (or decrease) the space requirement when needed. It incorporates the ability of the facility to be flexible to cater to higher needs, if necessary.*
5. *W: AVAILABILITY OF WATER: This was identified as crucial to the optimal working of any centre and hence was taken as an important measure.*
6. *L: AVAILABILITY OF SKILLED LABOUR: This factor incorporates the availability of managers, workers etc.).*
7. *LD: COST OF LAND: This involves the cost of land in case there is a need to buy the land for setting up of the collection centre or for further expansion.*
8. *T: TAXES (SPECIFIC TO THE AREA): The difference of taxes in this respect is regional. Some cities may have higher while others lower.*
9. *A: CUSTOMER AWARENESS AND WILLINGNESS TO RETURN THE PRODUCT: This is the willingness on the part of the customer to return the product in the particular area.*
10. *P: AVAILABILITY OF POWER: This involves the availability of electricity. It was identified to be extremely crucial to the decision.*

4.3 Selection of Alternatives

The company has an extensive number of users of its products in the Indian state of Punjab denoted by A. Hence, three important locations with respect to the setting up of a collection site were identified as Jallandhar (A1), Hoshiarpur (A2) and Patiala (A3) by talking with the company's e-waste chain manager in Delhi. For similar reasons, the company's e-waste chain manager presented the company's willingness to set up centres in the states of Goa (B) and Rajasthan (C). When asked about the three most viable alternatives, for Goa, these were identified as Panaji (B1), Margao (B2) and Siolim (B3) while for Rajasthan (C), these were identified as Ganganagar (C1), Jaipur (C2) and Kota (C3).

State A

For A1	OC	PM	C	F	W	L	LD	T	A	P
OC	0.2	0.8	0.8	0.6	0.5	0.7	0.9	0.5	0.4	0.5
PM	0.2	0.7	0.5	0.3	0.2	0.4	0.7	0.2	0.3	0.2
C	0.2	0.5	0.8	0.3	0.2	0.4	0.7	0.2	0.3	0.3
F	0.4	0.7	0.7	0.6	0.3	0.6	0.8	0.3	0.6	0.3
W	0.5	0.8	0.8	0.7	0.9	0.8	0.9	0.5	0.7	0.5
L	0.3	0.6	0.6	0.4	0.2	0.8	0.8	0.3	0.4	0.2
LD	0.1	0.3	0.3	0.2	0.1	0.2	0.2	0.1	0.4	0.1
T	0.5	0.8	0.8	0.7	0.5	0.7	0.9	0.3	0.2	0.4
A	0.6	0.7	0.7	0.4	0.3	0.6	0.6	0.8	0.7	0.3
P	0.5	0.8	0.7	0.7	0.5	0.8	0.9	0.6	0.7	0.9

SSI1– 1649.754292

For A2	OC	PM	C	F	W	L	LD	T	A	P
OC	0.2	0.8	0.8	0.6	0.5	0.7	0.9	0.5	0.4	0.5
PM	0.2	0.6	0.5	0.3	0.2	0.4	0.7	0.2	0.3	0.2
C	0.2	0.5	0.7	0.3	0.2	0.4	0.7	0.2	0.3	0.3
F	0.4	0.7	0.7	0.7	0.3	0.6	0.8	0.3	0.6	0.3
W	0.5	0.8	0.8	0.7	0.7	0.8	0.9	0.5	0.7	0.5
L	0.3	0.6	0.6	0.4	0.2	0.8	0.8	0.3	0.4	0.2
LD	0.1	0.3	0.3	0.2	0.1	0.2	0.3	0.1	0.4	0.1
T	0.5	0.8	0.8	0.7	0.5	0.7	0.9	0.4	0.2	0.4
A	0.6	0.7	0.7	0.4	0.3	0.6	0.6	0.8	0.5	0.3
P	0.5	0.8	0.7	0.7	0.5	0.8	0.9	0.6	0.7	0.7

SSI 2– 1508.332626

FOR A3	OC	PM	C	F	W	L	LD	T	A	P
OC	0.3	0.8	0.8	0.6	0.5	0.7	0.9	0.5	0.4	0.5
PM	0.2	0.5	0.5	0.3	0.2	0.4	0.7	0.2	0.3	0.2
C	0.2	0.5	0.6	0.3	0.2	0.4	0.7	0.2	0.3	0.3
F	0.4	0.7	0.7	0.7	0.3	0.6	0.8	0.3	0.6	0.3
W	0.5	0.8	0.8	0.7	0.7	0.8	0.9	0.5	0.7	0.5
L	0.3	0.6	0.6	0.4	0.2	0.6	0.8	0.3	0.4	0.2
LD	0.1	0.3	0.3	0.2	0.1	0.2	0.4	0.1	0.4	0.1
T	0.5	0.8	0.8	0.7	0.5	0.7	0.9	0.4	0.2	0.4
A	0.6	0.7	0.7	0.4	0.3	0.6	0.6	0.8	0.4	0.3
P	0.5	0.8	0.7	0.7	0.5	0.8	0.9	0.6	0.7	0.7

SSI3 – 1435.563380

STATE B

FOR B1	OC	PM	C	F	W	L	LD	T	A	P
OC	0.1	0.8	0.8	0.6	0.5	0.7	0.9	0.5	0.4	0.5
PM	0.2	0.9	0.5	0.3	0.2	0.4	0.7	0.2	0.3	0.2
C	0.2	0.5	0.9	0.3	0.2	0.4	0.7	0.2	0.3	0.3
F	0.4	0.7	0.7	0.5	0.3	0.6	0.8	0.3	0.6	0.3
W	0.5	0.8	0.8	0.7	0.8	0.8	0.9	0.5	0.7	0.5
L	0.3	0.6	0.6	0.4	0.2	0.7	0.8	0.3	0.4	0.2
LD	0.1	0.3	0.3	0.2	0.1	0.2	0.2	0.1	0.4	0.1
T	0.5	0.8	0.8	0.7	0.5	0.7	0.9	0.2	0.2	0.4
A	0.6	0.7	0.7	0.4	0.3	0.6	0.6	0.8	0.7	0.3
P	0.5	0.8	0.7	0.7	0.5	0.8	0.9	0.6	0.7	0.8

SSI4 – 1539.895504

FOR B2	OC	PM	C	F	W	L	LD	T	A	P
OC	0.3	0.8	0.8	0.6	0.5	0.7	0.9	0.5	0.4	0.5
PM	0.2	0.7	0.5	0.3	0.2	0.4	0.7	0.2	0.3	0.2
C	0.2	0.5	0.7	0.3	0.2	0.4	0.7	0.2	0.3	0.3
F	0.4	0.7	0.7	0.6	0.3	0.6	0.8	0.3	0.6	0.3
W	0.5	0.8	0.8	0.7	0.7	0.8	0.9	0.5	0.7	0.5
L	0.3	0.6	0.6	0.4	0.2	0.6	0.8	0.3	0.4	0.2
LD	0.1	0.3	0.3	0.2	0.1	0.2	0.4	0.1	0.4	0.1
T	0.5	0.8	0.8	0.7	0.5	0.7	0.9	0.3	0.2	0.4
A	0.6	0.7	0.7	0.4	0.3	0.6	0.6	0.8	0.5	0.3
P	0.5	0.8	0.7	0.7	0.5	0.8	0.9	0.6	0.7	0.8

SSI5 – 1529.145626

FOR B2	OC	PM	C	F	W	L	LD	T	A	P
OC	0.5	0.8	0.8	0.6	0.5	0.7	0.9	0.5	0.4	0.5
PM	0.2	0.6	0.5	0.3	0.2	0.4	0.7	0.2	0.3	0.2
C	0.2	0.5	0.5	0.3	0.2	0.4	0.7	0.2	0.3	0.3
F	0.4	0.7	0.7	0.8	0.3	0.6	0.8	0.3	0.6	0.3
W	0.5	0.8	0.8	0.7	0.6	0.8	0.9	0.5	0.7	0.5
L	0.3	0.6	0.6	0.4	0.2	0.6	0.8	0.3	0.4	0.2
LD	0.1	0.3	0.3	0.2	0.1	0.2	0.7	0.1	0.4	0.1
T	0.5	0.8	0.8	0.7	0.5	0.7	0.9	0.3	0.2	0.4
A	0.6	0.7	0.7	0.4	0.3	0.6	0.6	0.8	0.4	0.3
P	0.5	0.8	0.7	0.7	0.5	0.8	0.9	0.6	0.7	0.5

SSI6 – 1527.258881

STATE C

FOR C1	OC	PM	C	F	W	L	LD	T	A	P
OC	0.5	0.8	0.8	0.6	0.5	0.7	0.9	0.5	0.4	0.5
PM	0.2	0.6	0.5	0.3	0.2	0.4	0.7	0.2	0.3	0.2
C	0.2	0.5	0.6	0.3	0.2	0.4	0.7	0.2	0.3	0.3
F	0.4	0.7	0.7	0.7	0.3	0.6	0.8	0.3	0.6	0.3
W	0.5	0.8	0.8	0.7	0.4	0.8	0.9	0.5	0.7	0.5
L	0.3	0.6	0.6	0.4	0.2	0.7	0.8	0.3	0.4	0.2
LD	0.1	0.3	0.3	0.2	0.1	0.2	0.8	0.1	0.4	0.1
T	0.5	0.8	0.8	0.7	0.5	0.7	0.9	0.8	0.2	0.4
A	0.6	0.7	0.7	0.4	0.3	0.6	0.6	0.8	0.5	0.3
P	0.5	0.8	0.7	0.7	0.5	0.8	0.9	0.6	0.7	0.6

SSI7 – 1779.196734

FOR C2	OC	PM	C	F	W	L	LD	T	A	P
OC	0.3	0.8	0.8	0.6	0.5	0.7	0.9	0.5	0.4	0.5
PM	0.2	0.7	0.5	0.3	0.2	0.4	0.7	0.2	0.3	0.2
C	0.2	0.5	0.8	0.3	0.2	0.4	0.7	0.2	0.3	0.3
F	0.4	0.7	0.7	0.6	0.3	0.6	0.8	0.3	0.6	0.3
W	0.5	0.8	0.8	0.7	0.7	0.8	0.9	0.5	0.7	0.5
L	0.3	0.6	0.6	0.4	0.2	0.8	0.8	0.3	0.4	0.2
LD	0.1	0.3	0.3	0.2	0.1	0.2	0.6	0.1	0.4	0.1
T	0.5	0.8	0.8	0.7	0.5	0.7	0.9	0.3	0.2	0.4
A	0.6	0.7	0.7	0.4	0.3	0.6	0.6	0.8	0.8	0.3
P	0.5	0.8	0.7	0.7	0.5	0.8	0.9	0.6	0.7	0.7

SSI8 – 1781.438306

FOR C3	OC	PM	C	F	W	L	LD	T	A	P
OC	0.6	0.8	0.8	0.6	0.5	0.7	0.9	0.5	0.4	0.5
PM	0.2	0.6	0.5	0.3	0.2	0.4	0.7	0.2	0.3	0.2
C	0.2	0.5	0.9	0.3	0.2	0.4	0.7	0.2	0.3	0.3
F	0.4	0.7	0.7	0.6	0.3	0.6	0.8	0.3	0.6	0.3
W	0.5	0.8	0.8	0.7	0.5	0.8	0.9	0.5	0.7	0.5
L	0.3	0.6	0.6	0.4	0.2	0.6	0.8	0.3	0.4	0.2
LD	0.1	0.3	0.3	0.2	0.1	0.2	0.4	0.1	0.4	0.1
T	0.5	0.8	0.8	0.7	0.5	0.7	0.9	0.3	0.2	0.4
A	0.6	0.7	0.7	0.4	0.3	0.6	0.6	0.8	0.6	0.3
P	0.5	0.8	0.7	0.7	0.5	0.8	0.9	0.6	0.7	0.7

SSI9 – 1584.688565

5. Results and Conclusion

The graph theory and the digraph matrix approach is a method that involves lesser computation when compared with other decision making models and methods. Also, it is comparatively simple, easy and generic as it can be applied to a whole lot of situations by only altering the attributes/criteria and choosing suitable alternatives. In the paper, the need for the setting up of collection centres was realized. This was then translated into the desire to apply a suitable methodology for taking the decision for the location of the same. For this, it was seen that Graph Theoretic Approach served the purpose completely by taking important factors into consideration. Thus, the methodology was introduced and discussed. After this, the numerical expressions and the method to calculate the indexes and comparison were also discussed. Then this method was illustrated with the example of ABC info systems which makes an attempt to collect e-waste from the customers and recycle it when the products reach their End of Life (EOL). For this, after talking to the e-waste manager in Delhi, the various important factors (criteria) as well as locations along with alternatives were decided. Then, collectively, the matrixes for all the nine locations were made. These, may however vary as different decision makers may have varied opinions about what is more important ad by what measure. Consequently, the matrices were solved and the SSI's (Site Selection Index) for all were calculated. Then, from each state one out of the three alternatives was chosen to be the best site because of the highest value of the SSI. For Punjab, SSI1>SSI2>SSI3, hence A1 (Jallandhar) is the best place to set up a site. For Goa, SSI4>SSI5>SSI6, hence B1 (Panaji) would be the most important place to set up the collection centre. For Rajasthan, SSI8>SSI7>SSI9, hence, it would be best to set up a collection centre at C2 (Jaipur).

References:

[1] Boks C, Nilsson J, Masui K, Suzuki K, Rose C, Lee BH. "An International comparison of product end-of-life scenarios and legislation for consumer electronics". In: Proceedings of the IEEE International Symposium on Electronics and the Environment, Oak Brook, IL, 1998.
[2]Dutch Ministry of Housing. Spatial planning and the environment. http://www.minvrom.nl/environment/.
[3] European Commission. Directorate-general environment. http://europa.eu.int/comm/dgs/environment/index_-en.htm/.
[4] Thierry M. "An analysis of the impact of product recovery management on manufacturing companies". PhD thesis, Erasmus University Rotterdam, The Netherlands, 1997.
[5] Rogers DS, Tibben-Lembke RS. An examination of reverse logistics practices. Journal of Business Logistics 2001; 22:129-148.
[6] Giuntini R, Andel TJ. "Advance with reverse logistics". Transportation and Distribution Part I 1995; 36: 73-75.
[7] Ronald S. Tibben-Lembke, Dale S. Rogers, (2002) "Differences between forward and reverse logistics in a retail environment", Supply Chain Management: An International Journal, Vol. 7 Iss: 5, pp.271 – 282
[8] Kelle, P. and Silver, E.A. (1989a), "Forecasting the Returns of Reusable Containers", Journal of Operations Management, Vol.8, No.1, pp. 17-35
[9] EDR Santibanez-Gonzalez, A Diabat, Computers & Industrial Engineering 66 (4), 889-898
[10] Gandhi, OP & Agrawal, VP, "FMEA-A digraph and matrix approach", Journal of Reliability Engineering and System Safety, vol. 35, 1992, p.47-158
[11] Yadav, N. & Khan, IA & Grover, S., "Operational-based economics evaluation and selection of a power plant using graph theoretic approach, world academy of science", Engineering and Technology, vol. 63, 2010, p. 426-436
[12] Vidal, C , Infante, V, Peças, P, Vilaça P, "Application of Taguchi Method in the Optimization of Friction Stir Welding Parameters of an

Aeronautic Aluminium Alloy", Advanced Materials Manufacturing & Characterization Vol 3 Issue 1 (2013)

[13] Tagaras G. and C. Zikopoulos, "Optimal Location and Value of Timely Sorting of Used Items in a Remanufacturing Supply Chain with Multiple Collection Sites," International Journal of Production Economics, Vol. 115, No. 2, pp. 424-432, 2008.

[14] Raj, T. & Shankar, R. & Suhaib, M. & Khan, RA, "A graph-theoretic approach is evaluate the intensity of barriers in the implementation directory of FMSs", International Journal of Services and Operations Management, vol. 7, 1, 2010, p.24-52

[15] Rao, R.V. (2007). Decision making in the manufacturing environment: using graph theory and fuzzy multiple attribute decision making methods. London: Springer

[16] http://www.sciencedirect.com/science/article/pii/S2211812814004866

[17] http://www.emeraldinsight.com/doi/abs/10.1108/JAMR-02-2013-0013

Defence Science Journal, Vol. 65, No. 5, September 2015, pp. 418-422, DOI : 10.14429/dsj.65.8960

Sol Freeze Dry Nd:YAG Nanopowder Synthesis and Sinterability Studies

Rekha Mann*, Kiranmala Laishram, Sheikh Ashfaq Ahmed,
Khavangkhui Zimik, and Neelam Malhan

Laser Materials Division, Laser Science and Technology Centre, Delhi - 110 054, India
**E-mail: mann_rekha@lastec.drdo.in*

ABSTRACT

Citrate nitrate sol freeze dry synthesis of 2 atomic % neodymium ion doped Yttrium Aluminium Oxide (Nd:YAG) nanopowders was explored for the first time. Sol was prepared by dissolving nitrates of Al^{3+}, Y^{3+} and Nd^{3+} keeping molar ratio to be 5: 2.94: 0.06. Total metal ion to citric acid ratio was optimised at 1 is to 0.25. Sol was freeze dried at -80 °C for 48 h. Dried mass thus obtained was calcined at 1000 °C for 2 h to give phase pure Nd:YAG as characterised by FTIR and XRD. Particles were in the size range of 35 nm - 50 nm with close to spherical morphology as observed by TEM. Nanopowder was compacted and sintered at 1700 °C for 5 h under 10^{-6} mbar followed by hot isostatic press at 1750 °C for 4 h under 200 MPa, to give 71 per cent transmission at 1064 nm indicating synthesis of well sinterable Nd:YAG nanopowders.

Keywords: Freeze dry, Nd:YAG, transparent ceramic, vacuum sintering, HIP, Nd:YAG nanopowder, sinterability

1. INTRODUCTION

Nd:YAG laser ceramic has some important advantages over single crystals such as large size fabrication, possibility of producing multilayer ceramic structure and low cost production[1,2]. It is particularly useful for high temperature and high energy applications. When doped with rare earth ions (Nd^{3+}), it is the most widely explored and used solid state laser material till date[3,4]. Worldwide research for the synthesis of highly sinterable Nd:YAG nanopowder is going on tremendously exploring different types of methods for developing transparent ceramics. To name a few, Nd:YAG synthesis has been reported using methods like co-precipitation[5-7], sol-gel[8], spray drying[9], homogeneous precipitation[10], freeze drying[11,12], microwave assisted combustion[13], etc.

Freeze drying is a very good technique for synthesis of multi component compounds with an accurate control of stoichiometry with high surface area, since it involves sublimation for elimination of water from frozen solution containing cations in stoichiometric ratios[14]. Freezing the sol make cations mobility difficult and thus prevent cation segregation leading to high cation homogeneity. Since water is directly removed by sublimation during freeze drying solid bridge formation is prevented, leading to well dispersed powder formation[15]. Some reports are there in the literature for the synthesis of Nd:YAG by freeze drying starting from organo-metallic precursors[12] and carbonate precipitates[16] and fabrication of transparent ceramics.

In the present study freeze drying synthesis of Nd:YAG nanopowders from sol of simple metal nitrates with citric acid is reported for first time. Sinterability of these nanopowders was also explored and transparent ceramic with 71% transmission at 1064 nm was obtained. By citrate nitrate and other sol gel route YAG and Nd:YAG nanopowder synthesis has been reported[17-20] with no description of transmission value.

2. EXPERIMENT

Yttrium nitrate, $Y(NO_3)_3.6H_2O$ (99.9 per cent, Alfa Aesar), Aluminum nitrate, $Al(NO_3)_3.9H_2O$ (99.999 per cent, Alfa Aesar), Neodymium nitrate, $Nd(NO_3)_3.6H_2O$ (99.9 per cent purity Alfa Aesar) and Citric acid anhydrous (99.5+ per cent purity Alfa Aesar) were used as the starting materials. The metal nitrates were taken in the molar ratio of Nd^{+3}:Y^{3+}:Al^{3+} as 0.06: 2.94: 5 to give 2 atomic per cent neodymium ion doped Yttrium Aluminium Garnet ($Nd_{0.06}Y_{2.94}Al_5O_{12}$). Sol was prepared by dissolving metal nitrates along with citric acid, used as the complexing agent, keeping the metal nitrate to citrate ratio as 1: 0.25, in high purity water of resistivity >5 MΩ-cm purified by Millipore Elix 10 water purifier. Sol thus prepared was treated in two ways. A part of it was freeze dried at very low temperature of -80 °C for 48 h in freeze drier (Virtis pilot scale lyophilizer) and another part was dried in conventional oven at 80 °C - 110 °C for 40 h. Metal nitrates are often used as starting materials due to their high solubility and low decomposition temperature. But it is very difficult to freeze the nitrate sol[14]. Metal nitrate-citrate sol underwent freeze drying at -80 °C for 48 h compared to reported at -20 °C for 20 h for organmetallic sol. The freeze dried swollen solid mass and oven dried gel thus obtained were calcined at 1000 °C for 2 h to give Nd:YAG nanopowder. Calcination temperature has been optimised in previous work[21]. The whole process is illustrated in the flow chart.

Evolution of the crystalline phases was monitored by X-Ray Diffraction (XRD) on X'PERT PRO PANalytical PW 3050/60 Standard Resolution Goniometer, keeping 2θ range from 15° to 75°. The crystallite size was determined by using the well known Scherrer's equation. Particle size range and morphological studies were carried out on transmission electron microscope (TEM, 200 kV, JEOL TEM-2100) by preparing samples on copper grids. Both the powders were

Received 29 June 2015, revised 11 August 2015, online published 08 September 2015

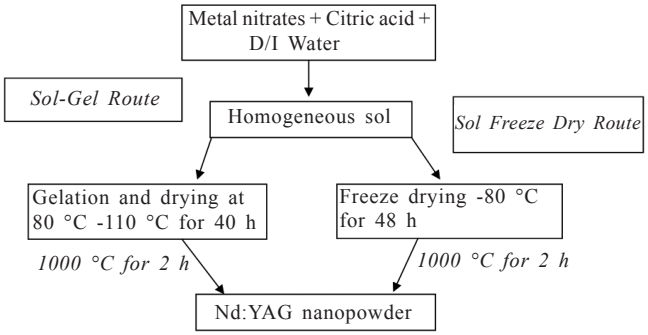

uniaxially pressed in a 13 mm diameter steel die lined with tungsten carbide at 34 MPa and isostatically pressed at 300 MPa. The green compacts were sintered at 1700 °C for 5 h under vacuum 1.1X10^{-6} mbar in a furnace with tungsten and molybdenum mesh heaters at 600 °C/h heating and cooling rates. Vacuum sintered pellets were then hot isostatically pressed at 1750 °C for 4 h at 200 MPa. The sintered specimen was analysed for retention of phase purity by XRD. Ceramics were post sintered at 1300 °C for 5 h, polished and gold coated to observe microstructure using scanning electron microscope (SEM) LEO-1430. Transmission studies of samples was done on Cary 5000 UV-VIS-NIR spectrophotometer.

The emission spectra of specimens were recorded using 808 nm 3 W diode laser as the excitation source and the emission was coupled to a monochromator (Acton SP2300) attached with an InGaAs detector. The spectral measurements were carried out at room temperature within the spectral region of 900 nm - 1200 nm with 0.1 nm resolution.

3. RESULTS AND DISCUSSION

The powders obtained by sol-gel (SG) route and freeze dry (FD) route after calcination at 1000 °C for 2 h were found to be highly crystalline and phase pure on peak indexing the XRD data with the standard JCPDS as shown in Fig. 1. The main peak is centered at 2θ = 33.35° and corresponds to a crystal plane with Miller indices of [420] characteristic of YAG[22].

Particle size was calculated using Scherrer's[23] Eqn (1).

$$t = \frac{0.9\lambda}{\cos\theta\sqrt{\beta_{sample}{}^2 + \beta_{inst}{}^2}} \quad (1)$$

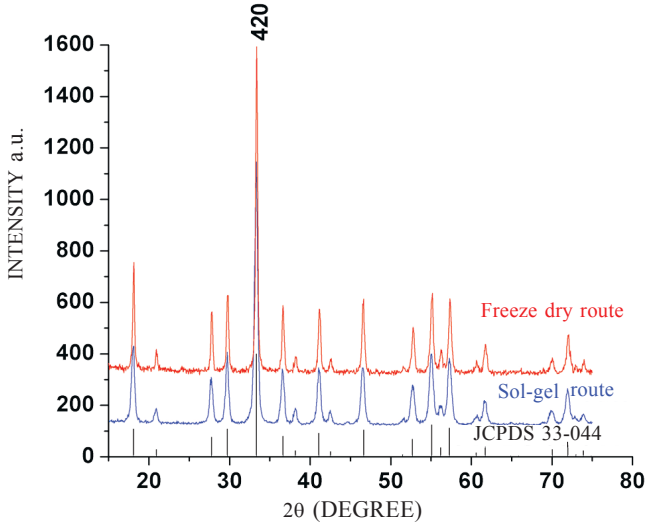

Figure 1. XRD of Nd:YAG nanopowder on calcination at 1000 °C for 2 h.

where t is the crystallite diameter, λ=1.54056Å, θ is the diffraction angle, β_{sample} is the FWHM of the diffraction peak and β_{inst} is characteristic of the instrument. The particle size calculated by applying Scherer's equation was found to be 30 nm. By TEM the particle size range was 35 nm - 50 nm in both the cases as shown in Fig. 2. The freeze dry route resulted into particles with close to spherical and very uniform morphology. This is a characteristic consequence of freeze dry synthesis due to the elimination of water by sublimation leading to uniform porous structure[14]. On the other hand sol-gel route synthesised nanopowder showed non uniform and polyhedral morphology as observed by TEM. After vacuum sintering at 1700 °C for 5 h under vacuum 1.1x10^{-6} mbar, opaque ceramics were obtained in both the cases with densities ~90-93%. The densities were determined by Archimedes principle using density kit of Mettler Toledo XS205DU. The sintered ceramics were hot isostatically pressed at 1750 °C for 4 h under 200 MPa Argon pressure and achieved 71% transmission at 1064 nm for freeze dried nanopowder compared to translucent ceramic from citrate nitrate sol-gel route as shown in Fig. 3. The green compacts were repeatedly sintered at different sintering schedules from 1600 °C to 1700 °C under vacuum (1.1 x 10^{-6} mbar) from 5 h to 10 h followed by Hot Isostatic Press treatment from 1650 °C to 1750 °C under 200 MPa for 2 h - 4 h. Finally heat treatment schedule mentioned above gave 71 per cent transmission at 1064 nm. Optimisation of sintering schedule is still underway to increase transmission from 71 per cent to 84 per cent, which is theoretical transmission[24].

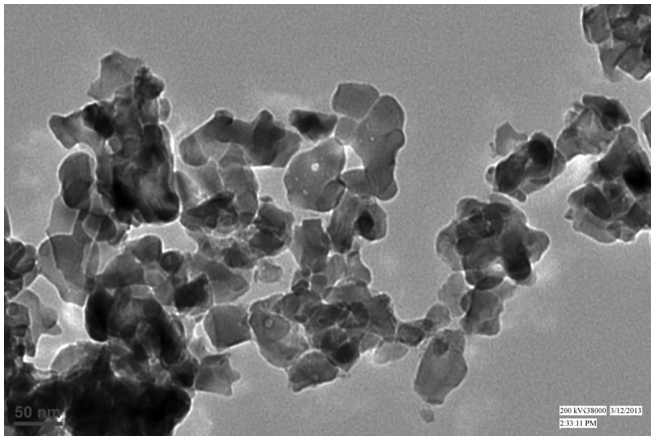

(a)

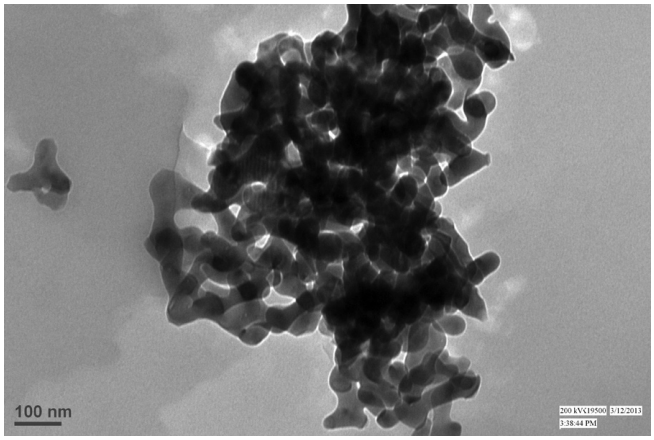

(b)

Figure 2. TEM of Nd:YAG nanopowders obtained by (a) Sol-Gel route and (b) Freeze dry route.

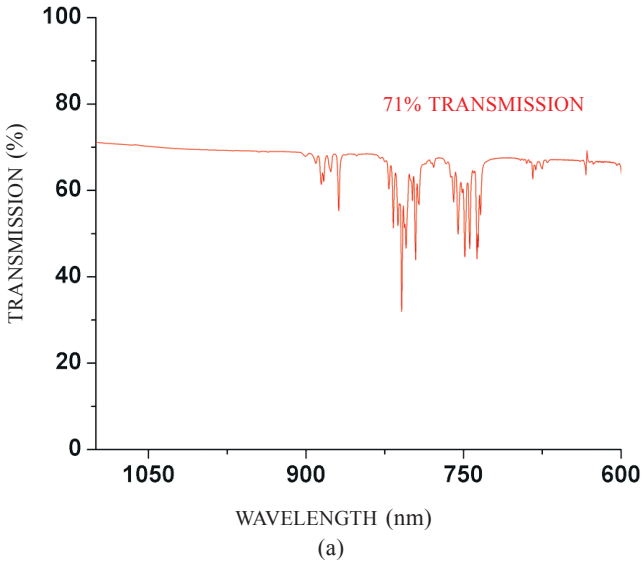

(a)

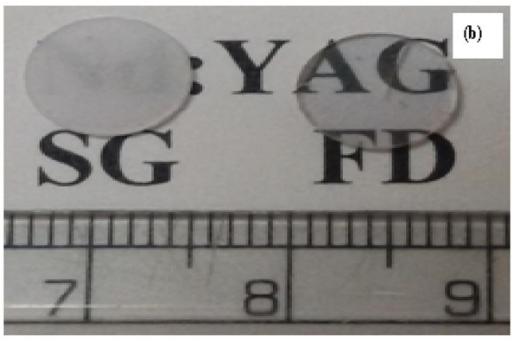

(b)

Figure 3. (a) Transmission of sintered ceramics and (b) actual photographs of samples.

SEM of the polished and gold coated surface of freeze dry route transparent ceramic as shown in Fig. 4 after annealing at 1300 °C for 5 h revealed grain size upto 15 µm - 20 µm. Phase purity has been retained as observed by XRD is as shown in Fig. 5. This indicated formation of highly sinterable Nd:YAG nanopowder from freeze dry route.

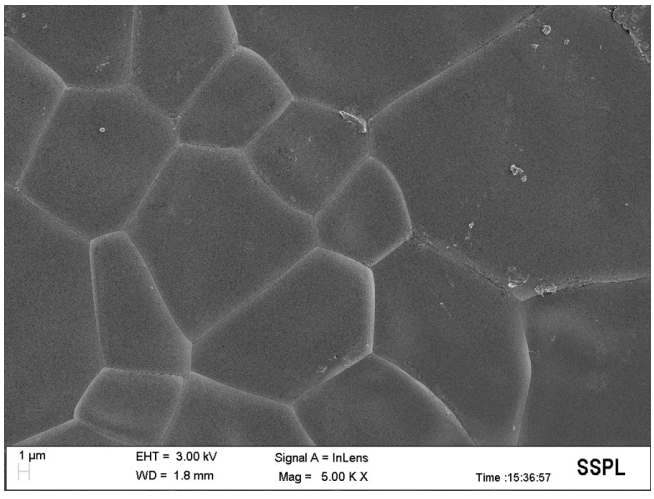

Figure 4. SEM of sintered ceramics of FD Route nanopowder.

Room temperature emission spectra of freeze dry route Nd:YAG transparent ceramic measured under 808 nm excitation as shown in Fig. 6, shows strongest flourescence emission of Nd^{3+} ions at 1064 nm corresponding to $^4F_{3/2} \rightarrow {}^4I_{11/2}$ transition.

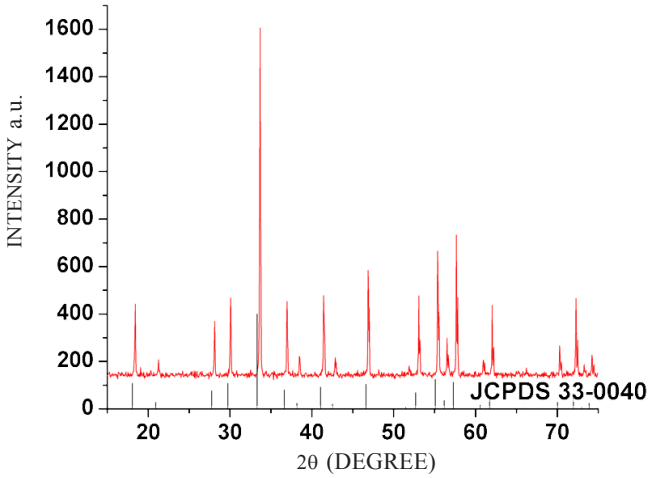

Figure 5. XRD of sintered ceramics of FD Route nanopowder.

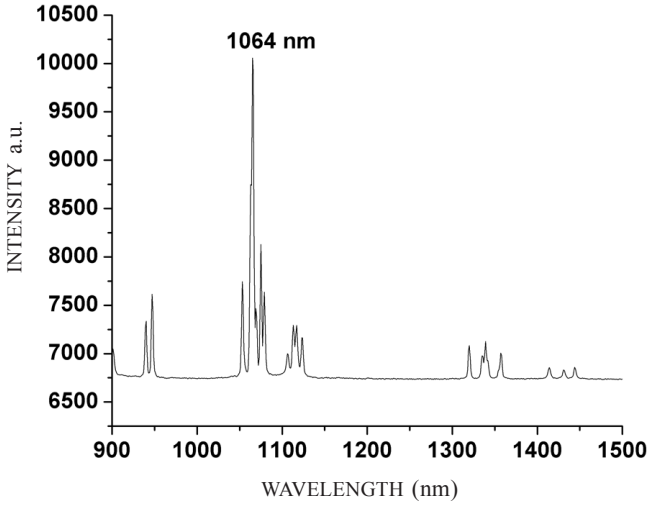

Figure 6. Emission spectra of Nd:YAG transparent ceramics from FD Route.

4. CONCLUSION

A very simple citrate nitrate sol freeze dry synthesis of Nd:YAG nanopowder was explored and compared with nitrate citrate sol-gel route leading to formation of uniform homogeneously uniform, non agglomerated Nd:YAG nanopowders in case of freeze dry route. Sintering at low temperature of 1700 °C for mere 5 h under vacuum 1.1×10^{-6} mbar followed by hot isostatic press at 1750 °C for 4 h under 200 MPa Argon pressure led to 71 per cent transmission at 1064 nm, indicating high sinterability of nanopowders from sol freeze dry route. Phase purity was retained from powder to ceramic all through the sintering process.

REFERENCES

1. Vatnik, S.M.; Osipov, V.V.; Vedin, I.A. & Kurbatov, P.F. Investigation of lasing characteristics of 1% Nd:YAG laser ceramics. *Quantum. Electron.*, 2013, **43**(3), 288-

290.
doi: 10.1070/qe2013v043n03abeh015135
2. Sanghera, J.; Kim, W.; Villalobos, G.; Shaw, B.; Baker, C.; Frantz, J.; Sadowksi, B. & Aggarwal, I. Ceramic laser materials. *Mater.,* 2012, **5**(2), 258-277.
doi: 10.3390/ma5020258
3. Sanghera, J.; Kim, W.; Villalobos, G.; Shaw, B.; Baker, C.; Frantz, J.; Sadowksi, B. & Aggarwal, I. Ceramic laser materials: Past and present. *Opt. Mat.*, 2013, **35**(4), 693-699.
doi: 10.1016/j.optmat.2012.04.021
4. Wen, L.; Sun, X.; Xiu, Z.; Chen, S. & Tsai, Chi-Tay. Synthesis of nanocrystalline yttria powder and fabrication of transparent YAG ceramics. *J. Eur. Ceram. Soc.*, 2004, **24**(9), 2681-2688.
doi: 10.1016/j.jeurceramsoc.2003.09.001
5. Li, J.; Chen, F.; Liu, W.; Zhang, W.; Wang, L.; Ba, X.; Zhu, Y.; Pan, Y. & Guo, J. Co-precipitation synthesis route to yttrium aluminum garnet (YAG) transparent ceramics. *J. Eur. Ceram. Soc.,* 2012, **32**(11), 2971-2979.
doi: 10.1016/j.jeurceramsoc.2012.02.040
6. Yagi, H.; Yanagitani, T.; Takaichi, K.; Ueda, K. & Kaminskii, A.A. Characterizations and laser performances of highly transparent Nd^{3+}:$Y_3Al_5O_{12}$ laser ceramics. *Opt. Mater.*, 2007, **29**(10), 1258-1262.
doi: 10.1016/j.optmat.2006.01.033
7. Li , J.; Chen, F.; Liu, W.B.; Zhang, W.X.; Wang, L.; Ba, X.W.; Zhu, Y.J.; Pan, Y.B. & Guo, J.K. Co-precipitation synthesis route to yttrium aluminum garnet (YAG) transparent ceramics. *J. Eur. Ceram. Soc*., 2012, **32**(11), 2971-2979.
doi: 10.1016/j.jeurceramsoc.2012.02.040
8. Zhydachevskii, Ya.; Syvorotka, I.I.; Vasylechko, L.; Sugak, D.; Borshchyshyn, I.D.; Luchechko, A.P.; Vakhula, Ya. I.; Ubizskii,S.B.; Vakiv, M.M. & Suchocki, A. Crystal structure and luminescent properties of nanocrystalline YAG and YAG:Nd synthesized by sol-gel method. *Opt. Mater*., 2012, **34**(12), 1984-1989.
doi: 10.1016/j.optmat.2011.12.023
9. Lopez, R.; Zarate, J.; Aguilar, E.A. & Munoz-Saldana, J. Preparation of neodymium doped yttrium aluminum garnet powders and fibres. *J. Rare Earths*, 2008, **26**(5), 670-673.
doi: 10.1016/S1002-0721(08)60159-3
10. Yaohui, Lv; Zhang, W.; Liu, H.; Sang,Y.; Qin, H.; Tan, J. & Tong, L. Synthesis of nano-sized and highly sinterable Nd:YAG powders by the urea homogeneous precipitation method. *Powder Technol.,* 2012, **217**, 140-147.
doi: 10.1016/j.powtec.2011.10.020
11. Zhou, Z.; Yang, F.; Chen, J.; Gao, X. & Lu, Y. An easy way to synthesize YAG nanoparticles for transparent ceramics via allegro vacuum freeze drying. *Adv. Mater. Res.,* 2013, **710**, 203-207.
doi: 10.4028/www.scientific.net/amr.710.203
12. Ravinovitch, Y.; Bogicevic, C.; Karolak, F.; Tetard, D. & Dammak, H. Freeze-dried nanometric neodymium-doped YAG powders for transparent ceramics. *J. Mater. Process. Technol.*, 2008, **199**(1-3), 314-320.
doi: 10.1016/j.jmatprotec.2007.08.022
13. Choudhary, R.; Laishram, K. & Gupta, R.K. Rapid synthesis of Nd:YAG nanopowder by microwave flash combustion. *Mater. Sci. Poland,* 2009, **27**(4/1), 1025-1031.
14. Tallon, C.; Moreno, R. & Nieto, M.I. Synthesis of γ-Al_2O_3 nanopowders by freeze drying. *Mater. Res. Bull.,* 2006, **41**(8), 1520-1529.
doi: 10.1016/j.materresbull.2006.01.021
15. Gong, H.; Zhang, J.; Tang, D-Y.; Xie, G-Q.; Huang, H. & Ma, J. Fabrication and laser performance of highly transparent Nd:YAG ceramics from well-dispersed Nd:Y_2O_3 nanopowders by freeze-drying. *J. Nanopart. Res.* 2011, **13**(9), 3853-3860.
doi: 10.1007/s11051-011-0336-9
16. Gong, H.; Tang, D.-Y.; Huang, H. & Ma, J. Agglomeration control of Nd:YAG nanoparticles via freeze drying for transparent Nd:YAG ceramics. *J. Am. Ceram. Soc.* 2009, **92**(4), 812-817.
doi: 10.1111/j.1551-2916.2009.02987.x
17. Costa, A.L.; Esposito, L.; Medri, V. & Bellosi, A. Synthesis of Nd:YAG material by citrate-nitate sol-gel combustion route. *Adv. Eng. Mater.,* 2007, **9**(4), 307-312**.**
doi: 10.1002/adem.200600264
18. Guo, K.; Chen, H-H.; Guo, X.; Yang, X-X.; Xu, F-F. & Zhao, J-T. Morphology investigation of yttrium aluminum garnet nanopowders prepared by sol-gel combustion method. *J. Alloys Compd*., 2010, **500**(1), 34-38.
doi: 10.1016/j.jallcom.2010.03.037
19. Zhydachevskii, Y.; Syvorotka, I.I.; Vasylexhko, L.; Sugak, D.; Borshchyshyn, I.D.; Luchechko, A.P.; Vakhula, Y.I.; Ubizskii, S.B.; Vakiv, M.M. & Suchocki, A. Crystal structure and luminescent properties of Nanocrystalline YAG and YAG:Nd synthesized by sol-gel method. *Opt. Mater*., 2012, **34**(12), 1984-1989.
doi: 10.1016/j.optmat.2011.12.023
20. Derbas, M.H. Asaad, I. & Kandeel, F. Synthesis and characterization of Nd:YAG nanopowder via polymer DTPA|metal chelated complexes. *Int. J. Chem. Technol. Res*., 2014-2015, **7**(4), 2090.
21. Devi, K.; Choudhary, R.; Satsangi, A.K. & Gupta, R.K. Sol-gel synthsis and characterization of Nanocrystalline yttrium aluminium garnet nanopowder. *Def. Sci. J.*, 2008, **58** (4), 545-549.
doi: 10.14429/dsj.58.1675
22. Vaidhyanathan, B. & Binner, J.G.P. Microwave assisted synthesis of nanocrystalline YAG. *J. Mater. Sci.,* 2006, **41**(18), 5954-5957.
doi: 10.1007/s10853-006-0260-z
23. Culity, B.D. & Stock, S.R. Elements of X-ray diffraction 2nd Edn, Addition-Wesley, MA. 1978
24. Kochawattana, S.; Stevenson, A.; Lee, S.-H.; Ramirez, M.; Gopalan, V.; Dummb, J.; Castillo, V. K.; Quarles, G.J. & Messing, G.L. Sintering and grain growth in SiO_2 doped Nd:YAG. *J. Eur. Ceram. Soc.,* 2008, **28**(7), 1527–1534.
doi: 10.1016/j.jeurceramsoc.2007.12.006

ACKNOWLEDGEMENTS

The authors wish to express their sincere thanks to Director, Laser Science and Technology Centre (LASTEC), Delhi, for his constant inspiration and encouragement. The authors also like to thank all the members of Laser Materials Division, LASTEC for their support and cooperation. The authors also like to thank Dr G. Vijaya Prakash, IIT Delhi for emission measurements.

CONTRIBUTORS

Dr (Mrs) Rekha Mann obtained her MSc and MPhil (Organic Chemistry) from Kurukshetra university, and PhD (Applied Chemistry) from Delhi College of Engineering, Delhi, in 2003. Presently she is working as Scientist 'E' at LASTEC, Delhi. Her areas of interest are : Nanomaterial synthesis and processing, laser materials (transparent ceramics & single crystals), organic synthesis, and polymer materials. She has published 26 research papers in the journals and conferences, and published 5 technical reports

Ms Kiranmala Laishram obtained her MSc (Physical Chemistry) from Manipur university in 2002. She is working as Scientist 'D' at Laser Science and Technology Centre (LASTEC), Delhi. Her areas of interest are: Material characterisation techniques, laser materials, and nonmaterial-synthesis and applications. She has published 24 research papers in the journals and conferences and 5 technical reports.

Mr Khavangkhui Zimik obtained his MSc (Physics) from Delhi University IN 1997. He is working as Scientist 'E' at Laser Science and Technology Centre (LASTEC), Delhi. His areas of interest are: laser materials (single crystals & ceramics). He has published 10 research papers in the journals and conferences.

Mr Sheikh Ashfaq Ahmed obtained his BE (Chemical Engineering) from Regional College of Engineering, Srinagar (J&K). He is working as Scientist 'D' at Laser Science and Technology Centre (LASTEC), Delhi. His areas of interest are: laser materials (single crystals & ceramics).

Ms Neelam Malhan obtained her MSc (Physical Chemistry) from university of Delhi and MTech from Indian Institute of Technology Delhi, in 1979. Presently she is working as Scientist 'G' at LASTEC, Delhi. Her areas of interest are : Development of high purity grade oxide materials and catalyst for laser applications, analytical techniques for material characterisation, nanomaterial synthesis, ceramic processing and sintering, polycrystalline laser ceramics Nd-doped YAG and Nd-doped yttria for SSL applications. She has published 22 research papers in journals and conferences.

TCAD Analysis of Small Signal Parameters and RF Performance of Heterogeneous Gate Dielectric-Gate All Around Tunnel FET

CONFERENCE PAPER · JUNE 2015

DOI: 10.13140/RG.2.1.3605.4883

3 AUTHORS, INCLUDING:

Jaya Madan
Delhi Technological University
3 PUBLICATIONS **0** CITATIONS
SEE PROFILE

Rishu Chaujar
Delhi Technological University
72 PUBLICATIONS **106** CITATIONS
SEE PROFILE

TCAD Analysis of Small Signal Parameters and RF Performance of Heterogeneous Gate Dielectric-Gate All Around Tunnel FET

J. Madan[*], R.S. Gupta[**] and R. Chaujar[*]

[*]Delhi Technological University, Bawana Road
Delhi-110042, India, jayamadan.2012@gmail.com, rishu.phy@dce.edu
[**]Maharaja Agrasen Institute of Technology, Rohini, Delhi, India, rsgupta1943@gmail.com

ABSTRACT

In this paper, the simulation study of the small signal parameters and RF performance of n-type heterogeneous gate dielectric gate all around tunnel FET (n-type-HD-GAA-TFET) is studied and is compared with n-GAA-TFET, in terms of parasitic capacitances, cut off frequency and maximum oscillation frequency. TFET has entirely different mechanism (different from MOSFET) of inversion layer formulation, so the effect of purposely applied hetero-gate dielectric (to enhance the ON current of TFET) is seen on parasitic capacitances. Cut off frequency is also studied for analyzing the switching speed of the device.

Keywords: band to band tunneling, hetero-gate dielectric, inversion layer, parasitic capaciatance, tunnel FET (TFET).

1 INTRODUCTION

Static and dynamic power dissipation of ICs are main hindrance in growing demands of smart phones and laptops, which require semiconductor devices with low standby power operation. As the conventional MOSFET has a thermodynamic limit of $60mVdec^{-1}$ at room temperature on subthreshold slope SS. So the device, which uses a new operation mechanism other than diffusion over a thermal barrier, came into existence. In this regard, TFET has emerged as a possible replacement candidate [1-2]. Due to its steeper subthreshold slope, lower OFF current, reduced power consumption, lower value of leakage current and negligible short channel effects, TFET have achieved a lot of attention in the recent years [3-5].

TFET uses band to band tunneling mechanism; the gate voltage controls the position of the energy bands, and thus controls the barrier width at the source channel junction (the tunneling junction). For N-type TFET, a positive gate bias lowers the energy band of the channel and for a gate voltage where the conduction band of the channel goes below the valence band of source, the tunneling of electrons from source to channel takes place which results in ON current. In the OFF state of TFET, the valence band of source is below the conduction band of channel, resulting in a large barrier width at the tunneling junction, which obstructs the tunneling of electrons and results into an OFF current of the order of approximately femto amperes [6-7].

Despite of its lower I_{OFF}, steeper SS and negligible short cannel effects, TFET suffers from very low ON state current which make it unsuitable for practical application. Many device architectures were proposed in order improve the ON current, such as band gap engineering (narrow bandgap materials III-V semiconductors), high-k dielectric materials, dual material gate, highly doped pocket geometry [8-9]. Another problem with TFET is its ambipolar conduction [10]. For lowering ambipolar current and simultaneously enhancing the I_{ON} hetero-gate dielectric (HD) TFET have been proposed [11]. In HD-TFET a high-K material located partially near the source side induces a local minimum of the conduction band at the source channel junction and hence reduces the tunneling barrier width and thus enhances the I_{ON} and the low-K dielectric present near the drain side suppresses the ambipolar current. Thus, in this work a HD-GAA-TFET with different high-k combinations and GAA-TFET with SiO_2 and HfO_2 as a gate dielectric are taken into consideration.

2 SIMULATION AND DEVICE DETAILS

All simulations have been performed using the ATLAS device simulator. The models activated during simulation are as follows: concentration and field dependent mobility model, Shockley-Read-Hall for carrier recombination, non-local band to band tunneling, band gap narrowing and Fermi Dirac statistics [12].

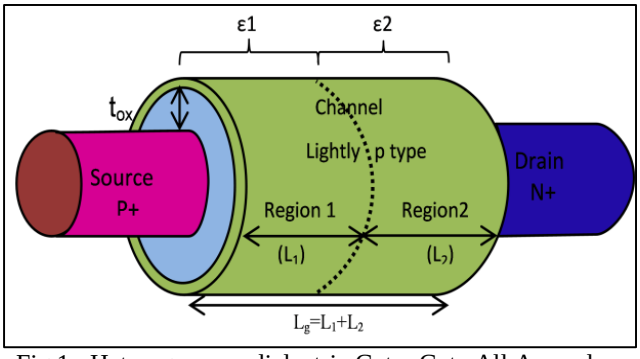

Fig 1: Heterogeneous dielectric Gate- Gate All Around-Tunnel MOSFET.

Fig. 1 shows the simulated structure of n-type HD-GAA-TFET. Table 1 shows Device Geometrical Parameters and the values used in the simulation.

Both the numerical methods Gummel (decoupled) together with Newton's (Fully coupled) has been incorporated to mathematically solve the carrier transport equation.

Parameter symbol	Technology parameter	Value
L	Channel Length	50nm
R	Channel radius	10nm
t_{ox}	Gate oxide thickness	3nm
N_s	Source doping (p^+)	$10^{20}cm^{-3}$
N_{ch}	Channel Doping lightly p type	$10^{17}cm^{-3}$
N_d	Drain doping (N^+)	$5\times10^{18}cm^{-3}$
Φ_m	Metal work function	4.5eV
L_1	Length of region 1	20nm
L_2	Length of region 2	30nm

Table 1: Device Geometrical Parameters and the values used in the Simulation.

All the simulation cases have different dielectric as shown in table 2. Case 1 and 2 is for GAA-TFET with different dielectric (SiO_2 and HfO_2). Case 3, 4 and 5 are of n-HD-GAA-TFET.

	Region 1	Region 2
	Dielectric Constant	
Case 1	3.9	3.9
Case 2	21	21
Case 3	7.5	3.9
Case 4	21	3.9
Case 5	29	3.9

Table: 2 All the Simulation cases.

3 RESULTS AND DISCUSSION

The dynamic performance influencing factors parasitic capacitances are studied for all the simulation cases shown in table 2. The partitioned of total gate capacitance C_{gg} in a TFET is entirely different from that of a MOSFET. This difference is mainly attributed to the difference in the inversion charge distribution. For a MOSFET, both source and drain regions are connected to the inversion layer (operating in linear region) and thus total gate capacitance is symmetrically apportioned between source and drain or (C_{gs} ~ C_{gd} ~ $C_{gg}/2$). But in case of TFET, only C_{gd} contributes a larger fraction of C_{gg} as compared to C_{gs}. For a constant drain bias, at the lower gate bias the inversion charge layer is formed near the drain end, with increase in gate bias the inversion layer extends towards the source side (unlike as in the case of MOSFET) [13].

All the capacitances are extracted by using small signal ac simulations at a constant frequency of 1MHz. The

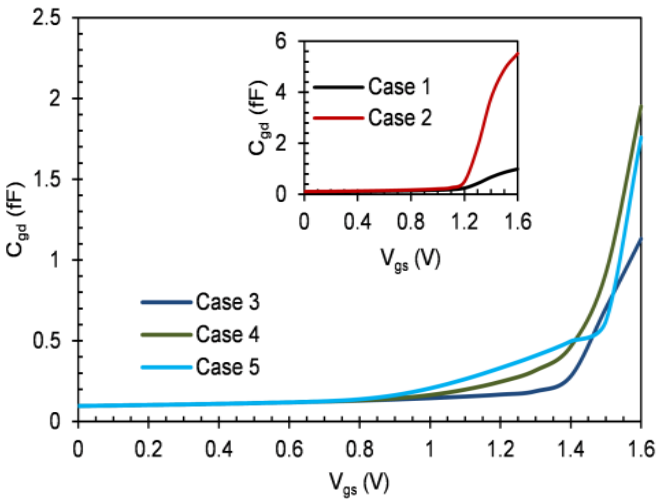

Fig. 2 Gate to drain capacitance as a function of gate bias for all the cases.

miller capacitance C_{gd} as a function of gate bias at a constant drain bias is shown in Fig. 2. As the gate bias is increased the inversion charges present underneath the gate dielectric increases resulting in enhanced gate drain capacitance. The miller capacitance accounts for the response time of the device. There is a reduction of approximately 1.2 times in miller capacitance with the implementation of hetero gate dielectric. Thus results in the reduction of the response time of the device.

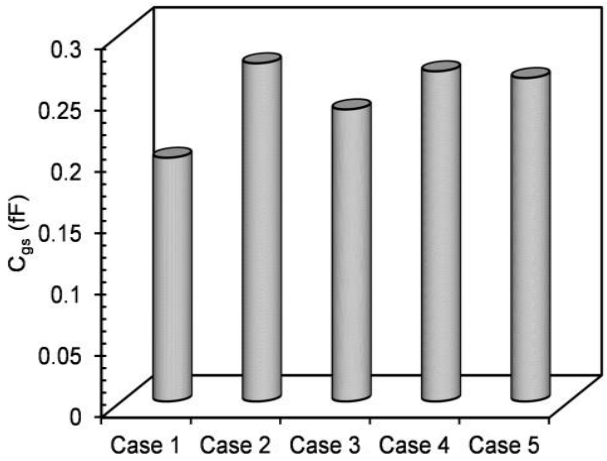

Fig. 3 Gate to source capacitance at V_{gs}=1.2 V and V_{ds}= 1.0V for all cases.

The gate to source capacitance C_{gs} is shown in Fig. 3 at V_{gs}=1.2 V and V_{ds}=1.0 V. As the inversion charges moves from drain to source side which results in lower value of gate to source capacitance as compared to gate to drain capacitance, or total gate capacitance is mainly contributed by C_{gd}. As evident from Fig. 2 and Fig. 3, the order of C_{gs} is very much lower than that of C_{gd}.

TechConnect Briefs 2015, TechConnect.org, ISBN 978-1-4987-4730-1

Fig. 4 shows the parasitic gate capacitance (total gate capacitance) C_{gg} with respect to gate voltage. Total gate capacitance interrelates to the active power dissipation ($C_{gg}V_{dd}^2f$). It is clear from the fig. 4 that C_{gg} is almost of the same order as that of C_{gd} which clearly shows that total gate capacitance is mainly contributed by gate drain capacitance. As evident from the figure that with the implementation of hetero-gate dielectric the C_{gg} has reduced drastically, which helps in reduction of active power dissipation [14-15].

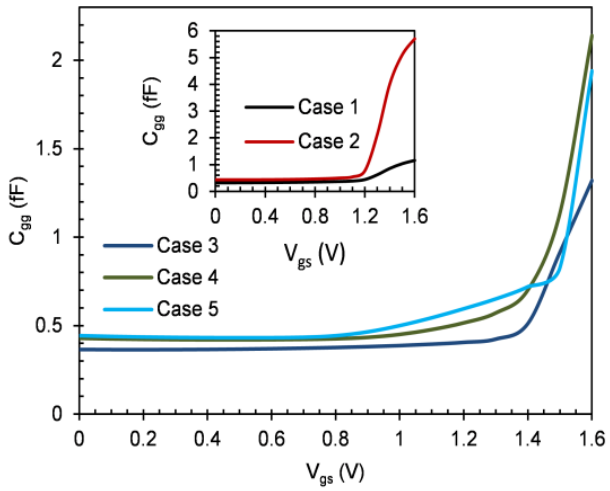

Fig. 4 Gate capacitance as a function of gate voltage for all the cases.

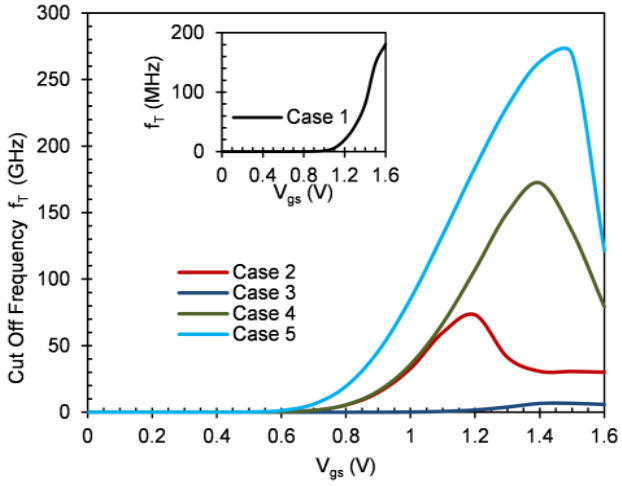

Fig.5 Cut off frequency as a function of gate voltage for all the cases.

Furthermore the Radio frequency figure of merit (RF-FOM) such as cut off frequency and maximum oscillation frequency of the device has been studied for all the cases. Fig. 5 shows the cut off frequency of the device with respect to gate bias variation. The cut off frequency f_T of the device is the frequency at which the short circuit current gain of the device falls to unity. The switching speed of the device depends on the cut off frequency. As clearly shown, the cut off frequency is enhanced by an order of 1.5 KHz in case 5 as compared to case 1 or with the application of Hetero dielectric the cut off frequency is enhanced tremendously, which results in higher switching speed of the device.

F_{max} is the highest frequency at which the power gain is unity. Fig. 6 shows the maximum oscillation frequency is enhanced to an order of 10^{10}Hz from 10^7Hz with the application of hetero gate dielectric [16, 17].

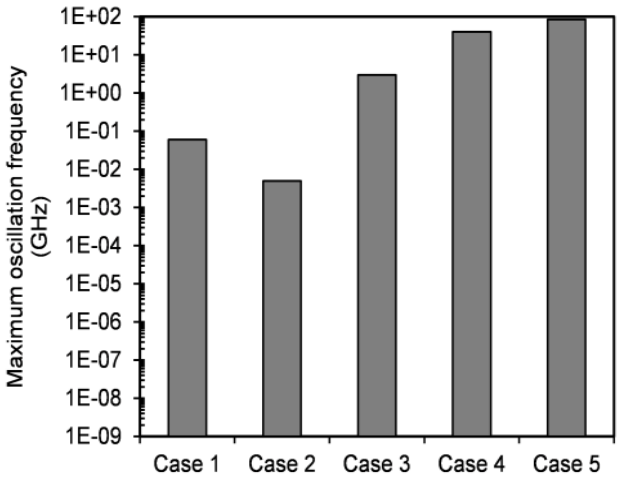

Fig. 6 Maximum oscillation frequency for all the cases.

4 CONCLUSION

In this work, the small signal parameters and RF performance of HD-GAA-TFET has been studied using TCAD device simulations. To study the impact of HD, various combinations of high-k has been studied. With the implementation of HD superior benefits of TFET are obtained. The parasitic capacitances are decreased and the cutoff frequency and the maximum oscillation frequency is manifold increased (better RF performance), which results in increase in switching speed. So the HD TFET can find applications in high-switching-speed electronics.

ACKNOWLEDGMENT

Authors would like to thank to Microelectronics Research Lab, Department of Engineering Physics Delhi Technological University to carry out this work. One of the authors (Jaya Madan) would like to thank University Grants Commission, Govt. of India, for providing the necessary financial assistance during the course of this research work.

REFERENCES

[1] Chakraborty S, Mallik A, Sarkar CK, Rao VR, " Impact of halo doping on the subthreshold

performance of deep-submicrometer CMOS devices and circuits for ultralow power analog/mixed-signal applications," IEEE Trans Electron Dev, 54(2), 241–8, 2007.
[2] Khatami Y, Banerjee K, "Steep Subthreshold slope n- and p-type tunnel-FET devices for low-power and energy-efficient digital circuits," IEEE Trans Electron Dev, 56(11), 2752–61, 2009.
[3] E. H. Toh, G. H. Wang, L. Chan, G. Y. Samudra, and C. Yeo, "Device physics and guiding principles for the design of double-gate tunneling field effect transistor with silicon-germanium source heterojunction", Appl. Phys. Lett., 91 (24) , 243505, 2007.
[4] W. Y. Choi, B. G. Park, J. D. Lee, and T. J. K. Liu, "Tunneling field-effect transistors (TFETs) with subthreshold swing (SS) less than 60 mV/dec", IEEE Electron Device Lett., 28(8), 743-45, 2007.
[5] V. Nagavarapu, R. Jhaveri, and J. C. S. Woo, "The Tunnel Source (PNPN) n MOSFET: A Novel High Performance Transistor," IEEE Trans. Electron Devices, 55(4), 1013-1019, 2008.
[6] A.M. Ionescu, H. Riel, "Tunnel field-effect transistors as energy-efficient electronic switches," Nature 479 (7373), 329–337, 2011.
[7] A. C. Seabaugh and Q. Zhang, "Low-voltage tunnel transistors for beyond CMOS logic," Proc. IEEE, 98(12), 2095–2110, 2010.
[8] Q.T. Zhao, J.M. Hartmann, S. Mantl, "An improved Si tunnel field effect transistor with a buried strained Si1-3Gex source," IEEE Electron Dev. Lett., 32 (11), 1480–1482, 2011.
[9] K. Ganapathi, S. Salahuddin, "Heterojunction vertical band-to-band tunneling transistors for steep subthreshold swing and high ON current," IEEE Electron Dev. Lett. 32 (5), 689–691, 2011.
[10] K. Boucart, and A. M. Ionescu, "Double-Gate Tunnel FET with High-κ Gate Dielectric", IEEE Trans. Electron Devices, 54(7), 1725– 1733, 2007.
[11] W.Y. Choi, and W. Lee, "Hetero-Gate-Dielectric Tunneling Field Effect Transistors," IEEE transactions on electron devices, 57(9), 2317-2319, 2010.
[12] ATLAS User's guide, SILVACO International, Version 5.14.0.R, 2010.
[13] Yue Yang, Xin Tong, Li-Tao Yang, Peng-Fei Guo, Lu Fan, and Yee-Chia Yeo, "Tunneling Field-Effect Transistor: Capacitance Components and Modeling," IEEE Electron Device letters, 31(7), 752-754, 2010.
[14] S. Cho, K. R. Kim, B.G. Park, and I. M. Kang, "RF performance and small-signal parameter extraction of junctionless silicon nanowire MOSFETs," IEEE Trans. Electron Devices, 58(5), 1388–1396, 2011.
[15] S. Cho, J.S. Lee, K.R. Kim, B.-G. Park, J.S. Harris Jr., I.M. Kang, Analyses on small-signal parameters and radio-frequency modeling of gate-all-around tunneling field-effect transistors, IEEE Trans. Electron Dev. 58 (12), 4164–4171, 2011.
[16] Mookerjea S, Krishnan R, Datta S, Narayanan V. "On enhanced miller capacitance effect in interband tunnel transistors". IEEE Electron Device Letters, 30(10), 1102–4, 2009.
[17] S. Mookerjea, R. Krishnan, S. Datta, and V. Narayanan, "Effective capacitance and drive current for tunnel FET (TFET) CV/I estimation," IEEE Trans. Electron Devices, 56(9), 2092–2098, 2009.

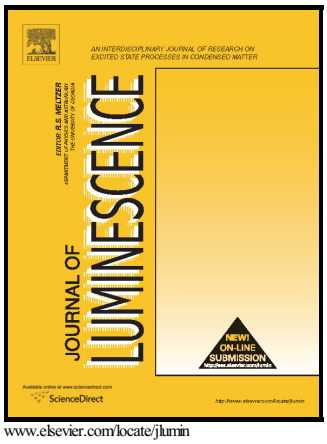

www.elsevier.com/locate/jlumin

White Light Emission and Color Tunability of Dysprosium doped Barium Silicate Glasses

Lokesh Mishra, Anchal Sharma, Amit K. Vishwakarma, Kaushal Jha, M. Jayasimhadri, B.V. Ratnam, Kiwan Jang, A.S. Rao, R.K. Sinha

PII: S0022-2313(15)00496-2
DOI: http://dx.doi.org/10.1016/j.jlumin.2015.08.063
Reference: LUMIN13569

To appear in: *Journal of Luminescence*

Received date: 21 April 2015
Revised date: 7 August 2015
Accepted date: 14 August 2015

Cite this article as: Lokesh Mishra, Anchal Sharma, Amit K. Vishwakarma, Kaushal Jha, M. Jayasimhadri, B.V. Ratnam, Kiwan Jang, A.S. Rao and R.K. Sinha, White Light Emission and Color Tunability of Dysprosium doped Barium Silicate Glasses, *Journal of Luminescence,* http://dx.doi.org/10.1016/j.jlumin.2015.08.063

White Light Emission and Color Tunability of Dysprosium doped Barium Silicate Glasses

Lokesh Mishra[1], Anchal Sharma[1], Amit K. Vishwakarma[1], Kaushal Jha[1], M. Jayasimhadri[1,*], B.V. Ratnam[2], Kiwan Jang[2], A.S. Rao[1], R.K. Sinha[1]

[1]Department of Applied Physics, Delhi Technological University, Delhi - 110042, India

[2]Department of Physics, Changwon National University, Changwon, Korea 641-773

Abstract

The present work elucidates the synthesis of Dy^{3+} doped barium silicate glasses, along with subsequent studies performed to evaluate its viability in solid state lighting applications. The synthesized photonic glasses were investigated via X-ray diffraction, scanning electron microscopy and fourier transform infrared spectroscopy. The photoluminescence properties were examined under ultraviolet (UV)/near UV (NUV) excitation. Photoluminescence spectrum exhibited characteristic emission bands at λ_{em}= 483 nm (blue) and λ_{em}= 576 nm (yellow) which are ascribed to the $^4F_{9/2} \rightarrow {}^6H_{15/2}$ and $^4F_{9/2} \rightarrow {}^6H_{13/2}$ transitions of Dy^{3+} ion, respectively. The chromaticity coordinates under excitation of λ_{ex}= 348 nm are (0.31, 0.34), which lies in the white region of CIE 1931 chromaticity diagram and are in excellent proximity with the standard equal energy white illuminant (0.333, 0.333). The calculated correlated color temperature and the yellow to blue (Y/B) ratio are found to be 6602 K and 1.12, respectively for the optimized sample. The synthesized photonic glass also offered the possibility of tuning the color as exemplified through the variation in CIE coordinates, correlated color temperature and the Y/B ratio. The results confirm the possibility of color tunability from the proposed glass and may be useful for various photonic device applications.

Keywords: Photoluminescence, Silicate glass, FT-IR, w-LEDs

---

*E- mail: jayaphysics@yahoo.com (M. Jayasimhadri); Tel.: +91 9013553360

1. Introduction

Solid State Lighting (SSL) based devices are predicted to play a crucial role in the coming years. They offer to save huge amounts of electrical energy and reduce carbon emissions by almost 28 million metric tons per year globally [1]. Apart from the significant roles in reducing energy consumption and being environment friendly, SSL based devices such as white LEDs (w-LEDs), liquid-crystal displays, full-color displays, traffic signals, automotive displays, cellular phone illumination etc., are seen to be a significant improvement over their predecessors especially in performance, durability, cost-effectiveness. Their innumerous applications have motivated researchers to improve upon their technology so as to continue achieving an ever-more color tunable and energy efficient luminescence. This has paved the way for development of w-LEDs, which have an edge over traditional lighting sources due to their compact size, higher reliability, shock resistance, interesting design possibilities, higher transparency and an extremely long lifetime [2].

Conventionally, there are two main approaches to produce w-LEDs. One of them is to use a blue emitting InGaN LED and yellow YAG: Ce^{3+} phosphor. Though this method of phosphor converted w-LEDs (pc w-LEDs) has advantages of low cost and high brightness, but various drawbacks like yellow/blue halo effect, poor color rendering index (with R_a = 70-80) and high CCT (~7750 K) have been observed [3]. Alternatively, the other approach of manufacturing w-LEDs makes use of RGB phosphors excited by a ultraviolet (UV) chip. This method has merits like higher CRI values, but suffers from low luminescent efficiency due to re-absorption of blue light [4]. Moreover in both of these approaches, phosphors are encapsulated in an epoxy resin, which holds the powder together in the w-LED package. This epoxy resin adds a lot of disadvantages such as the problems of cracking or delamination of epoxy encapsulations and yellowing of the epoxy, which heavily impacts the color output of the w-LEDs. Recently, silicone-based materials with high thermal resistance have been used for making an epoxy. They add problems like declining performance of w-LEDs and deviation from originally required shape due to thermal shrinking. Hence, the manufacturing process becomes difficult, lengthy and costly which decreases the manufacturing productivity of w-LEDs encapsulants [5].

Glasses doped with rare-earth ions are an alternative to pc w-LEDs due to their advantages like ease of manufacture, ease in forming any shape, lower production cost, higher thermal stability, and especially for epoxy resin free manufacturing process [2,6]. Barium borosilicate (BBS) glass system was chosen as the glass medium for the present study due to high chemical stability from silicates, high RE ion solubility from borates, low coefficient of thermal expansion, and impressive absorption of gamma & x-rays for application in radiation shielding glasses [7]. In addition, BBS glass matrix has lower phonon energy (less than 1100 cm^{-1}) which is much lower than that of visible light (14285 - 25000 cm^{-1}). Thus, its resultant effect on visible light emission is consequently negligible [8].

Trivalent dysprosium ion, with $4f^9$ electronic configuration, was chosen as the rare earth dopant in the barium silicate matrix. There are many advantages of using Dy^{3+} ion including potential applications in white light generation as a single phase white emitting source, mercury-free luminescence lamps, electron trapping materials and as light conversion materials when used along with a mixture of other rare earth ions [9-15]. Moreover, Dy^{3+} ion is one of the most preferred activator ions to be used for estimating the local environment inside the luminescent materials [12]. As explained later, the observed variations in the branching ratio of Dy^{3+} ion due to changes in the local structure allow dysprosium to work as a 'local field sensor' [13]. Dy^{3+} doped/co-doped glasses and phosphors have been extensively studied for various applications [4, 10-15]. However, to the best of our knowledge, white light generation from Dy^{3+} doped BBS glass system has not been reported so far.

In this paper, synthesis of Dy^{3+} doped BBS glasses and their structural and photoluminescent (PL) properties are presented. Subsequently discussions are included on X- Ray Diffraction (XRD), Scanning Electron Microscope (SEM), and Fourier Transform Infrared Spectroscopy (FTIR) studies, which describe the structural, morphological, and chemical nature of the as prepared glass. Further, photoluminescent properties are discussed with the help of excitation and emission spectra. Colorimetric parameters are calculated from the emission spectra which identify the applicability of the as prepared glass in various applications like SSL, electronics displays etc. Finally, the variation in these colorimetric parameters is studied and observed color tunability is explained.

2. Experimental details

Various glass samples were prepared using reagent grade high purity oxides: H_3BO_3, SiO_2, $BaCO_3$ and Dy_2O_3. The glass samples had the composition of 32 BaO - 23 B_2O_3 - (45-*x*) SiO_2- *x* Dy_2O_3 (where *x* = 0.0, 0.1, 0.5, 1.0, and 1.5). The samples were designated as BBS00, BBS01, BBS05, BBS10, and BBS15 in accordance with the *x* values. Reagent grade chemicals were thoroughly mixed with acetone in an agate mortar and placed in an alumina crucible. The mixture was heated for 45-60 min in an electric furnace at 1225 ^oC. This obtained melt was quenched by pouring onto a pre-heated brass mold and then annealed at 400 ^oC for 3 hours to release internal stresses. The as prepared transparent glass was then obtained by cooling the annealed glass to room temperature.

The amorphous structure of the glass was investigated on an X-ray diffractometer (Rigaku Corp., Model-Mini flex-II with Ni filtered Cu Kα radiation) in the 2θ range from 10 to 80°. Surface morphology was observed via SEM (Hitachi VP-SEM S-3700N) obtained at an accelerating voltage of 15 KV, with a magnification of 3700, at a working distance of 7.2 nm and an emission current of 116 µA. The nature of chemical bonds inside the glass matrix was investigated via FTIR spectra (Perkin Elmer's Frontier FTIR spectrometer) with an accuracy of ± 0.1%T. For the FTIR spectra sample pellets were prepared by mixing and grinding the glass powder and KBr (Sigma Aldrich, 99.99%) in the ratio 1:5. Finally, the mixture was compressed at 3 tons to obtain thin pellets, which were used for testing. The PL properties were measured by using Shimadzu's RF5301PC spectrofluorophotometer. The slit width for both the excitation and emission slits was fixed at 3 nm.

3. Results and discussion

3.1. Microstructure from XRD & SEM Characterization

The XRD pattern of the optimized BBS05 sample, presented in Fig. 1, clearly indicates the amorphous nature of the synthesized glass. The broad diffuse XRD pattern confirms the absence of any long range structural order in the as-obtained glass. The surface image of BBS05 sample was examined using SEM as shown in Fig. 2. The SEM image shows a homogenous glassy phase of the as-prepared glass sample. This is in consonance with the XRD pattern as seen in Fig. 1. Therefore, the

result presented in Figs. 1 & 2 characteristically confirms the amorphous nature in the synthesized glass.

3.2. Fourier Transform Infrared Spectroscopy (FTIR) Characterization

The transmittance spectra of BBS05 glass sample is shown in Fig. 3, which was recorded in the wave number range: 400 - 4000 cm^{-1}. The FTIR spectra of the investigated glass shows the following four prominent bands which are centered around (i) 3447.6 cm^{-1} (ii) 1384.5 cm^{-1} (iii) 1022.4 cm^{-1} and (iv) 452.9 cm^{-1}.

Firstly, absorption bands above 2500 cm^{-1} are ascribed to the presence of water groups [7]. Thus, the first broadband centered at 3447.6 cm^{-1} is ascribed to the symmetric stretching of the O-H bonds inside the glassy network [12, 16-18]. These O-H bond groups are found in existence at the sites of non bridging oxides (NBOs) [19]. NBOs are those oxygen atoms which do not take part in the network as former, but are modified due to the presence of a modifier cation, where they abruptly end the long repeating chain, hence leaving an oxygen atom vacant for participating in the O-H bond. The next three absorption bands can be attributed to chemical bonds of the constituent atoms.

The three absorption bands from 400 to 1500 cm^{-1} contains overlapping contributions from both borates and silicates as they form the glassy network. Kamitsos et. al. divided the infrared spectra of glassy borates into three regions which indicates the presence of borates as various arrangements of BO_3 and BO_4 units [20]. The next relatively sharp peak at 1384.5 cm^{-1} is due to the vibrational stretching of the B-O bonds in the BO_3 tetrahedral units. More specifically this peak can be attributed to the ring stretching vibrations of $B_3O_3(O^{-1})_3$ boroxol units [18], arrangements of BO_3 as diborates [20], and asymmetric stretching of NBOs of trigonal units of BO_3 [7, 17].

The next broad band lying in the region 800 cm^{-1} to 1200 cm^{-1} is made of up of a variety of contributions coming from the asymmetric stretching modes of silicates and the B-O bond vibrations of tetrahedral BO_4 units [20, 21]. For silicates, the possible configurations of existence in the glassy network are Q^3 species (1075 cm^{-1}), Q^2 species (1000 cm^{-1}), and Q^1 species (900 cm^{-1}). Along with these combinations, the broad band also contains contributions from the stretching vibrations of Si-O-Si bonds [22]. From borates, the contributions arise from the arrangement of BO_4 units in groups of

pentaborates (900 cm^{-1} and 1080 cm^{-1}), triborates (1000 cm^{-1}), and various other arrangements (871 cm^{-1}, 965 cm^{-1}, and 1060 cm^{-1}) [20], along with the stretching of the B-O-B bonds in the amorphous network [22]. The evidence of existence of borates and silicates in the as-obtained glass as chemical mixtures and not just physical mixtures is seen from the small shoulder of this band centered at 930 cm^{-1}. The absorption at 930 cm^{-1} was attributed to the B-O-Si bond by A. S. Tenney et.al. as early as in 1972 [18].

There is a small plateau as one proceeds towards the next band (400 cm^{-1} to 600 cm^{-1}). This small plateau is centered at 750 cm^{-1} and is ascribed to the bending motion of B-O-B (720 cm^{-1}) and O-Si-O in the quasi-lattices (810 cm^{-1}). Finally, the last band from 400 cm^{-1} to 600 cm^{-1} is almost entirely due to the rocking motion of Si-O-Si bridging oxygen which connects the various Q^n species of silicates. The center of the band at 452.9 cm^{-1} is therefore attributed to the bending of the Si-O-Si bonds in the borosilicate structure [17, 18, 22].

In the present matrix, one of the network formers, B_2O_3 exists as a two-dimensional BO_3 triangle. In glasses, an agglomerate of three BO_3 triangles forms the boroxol (B_3O_6) group, which further forms the irregular network. The addition of Ba^{2+} ions to this network (from BaO, which acts as a network modifier), results in a shift from 3-coordinated BO_3 to 4-coordinated BO_4 borons, with Ba^{2+} ions adjoining the BO_4 tetrahedron. Resultantly, the number of points of polyhedron linkage increases from three to four, which leads to an increase in stability [7, 23].

3.3. Luminescent properties

The PL excitation spectra of BBS glasses doped with different concentrations of Dy^{3+} ion is shown in Fig. 4. This spectra was measured while keeping the monitoring wavelength at λ_{em} = 575 nm, as it corresponded to the most intense peak in PL emission spectra (Fig. 5). In the excitation spectra, sharp peaks are observed due to the 4f - 4f transitions of Dy^{3+} ions, which are forbidden by the Laporte parity selection rule. They originate from the ground level ($^6H_{15/2}$) to higher excited levels. From the figure it is observed that the positions of the different excitation bands does not change with increasing Dy^{3+} ion concentration in various BBS00 – BBS15 glasses, but the relative intensity of individual peaks varies tremendously and is strongly dependent on the Dy^{3+} ion concentration. This

may be explained due to the simultaneous play of two different effects. Firstly, the screening effect of the electron clouds of the 5s and 5p orbitals shields the intra 4f transitions from any variation in the local crystal-field environment. This renders the electrons in the 4f orbitals relatively insensitive to the glassy matrix, hence the positions of the bands (or their energies, which is strongly correlated with the configuration of electrons in the 4f orbital) does not change with changing Dy^{3+} ion concentration. Secondly, as the concentration of Dy^{3+} ions is increased, the average Dy^{3+} - Dy^{3+} distance is decreased, which in turn increases the probability of non-radiative energy transfers between the activator ions through cross-relaxation beyond the critical distance. The excitation spectra exhibit six major bands centered at 325 nm ($^6H_{15/2} \rightarrow {}^6P_{3/2} + {}^4M_{17/2}$), 348 nm ($^6H_{15/2} \rightarrow {}^6P_{7/2}$), 363 nm ($^6H_{15/2} \rightarrow {}^6P_{5/2}$), 386 nm ($^6H_{15/2} \rightarrow {}^4I_{13/2} + {}^4K_{17/2}$), 423 nm ($^6H_{15/2} \rightarrow {}^4G_{11/2}$) and 453 nm ($^6H_{15/2} \rightarrow {}^4I_{15/2}$) [4, 11, 14-15]. The results confirm that the sample can be effectively excited from ultraviolet light (UV), near ultraviolet light (NUV) and blue light. It is well known that an ideal phosphor should show strong absorption band in the wavelength range from 350 nm to 410 nm, which matches with the emission of commercially available UV, NUV, and blue LED chips [4]. Thus, the above results establish that our glasses could be efficiently excited by using commercially available GAN based light sources, providing an additional support in favour of the BBS glasses.

PL emission spectra measured for BBS glasses by varying Dy^{3+} ion concentration under λ_{ex} = 348 nm, is shown in Fig. 5. Each spectrum consists of two dominant emission bands which are prominently characteristic of Dy^{3+} ions. The two bands, centered at λ_{em}= 483 nm (blue) and λ_{em}= 575 nm (yellow), originate, when the electrons make a radiative transition from the $^4F_{9/2}$ energy level to the lower lying levels (i.e. $^6H_{15/2}$ and $^6H_{13/2}$, respectively) [10]. The reasons for observing radiative transitions from $^4F_{9/2}$ level are three-fold. Firstly, the energy difference between energy states lying above $^4F_{9/2}$ level is very small, thus the $^4F_{9/2}$ level must be receiving many electrons via non-radiative relaxation and would be highly populated. Secondly, the energy separation between $^4F_{9/2}$ level and its lower lying level is quite large (approximately 7000 cm^{-1}) [12], and finally, as mentioned earlier, the phonon energy of the borosilicate amorphous matrix is almost 1100 cm^{-1}, which is not enough to induce a phonon mediated relaxation from the excited state. The $^4F_{9/2} \rightarrow {}^6H_{15/2}$ (blue) transition is a magnetic dipole allowed transition, hence its intensity does not depend on the local crystal field of the

constituent atoms in the glassy matrix. Whereas, the emission due to the transition $^4F_{9/2} \rightarrow {}^6H_{13/2}$ ($\Delta L = 2$, $\Delta J = 2$) is an electric dipole transition band. This transition is a hypersensitive transition wherein the influence of the host's local environment on this yellow emission band is much more pronounced [24**]**. Yang et.al. have described the hypersensitivity of this transition from the view point of Judd-Ofelt theory [8,15]. In addition, the predominance of the yellow emission in the PL spectrum firmly indicates that Dy^{3+} ions are located at low symmetry sites with no inversion center. Therefore the Y/B ratio for Dy^{3+} or even R/O ratio (Red/Orange) for Eu^{3+} (due to similar ionic radii) are used as effective tools to probe the structural nature of the luminescent glass [25, 26].

As the relative intensities of the yellow-blue emission are strongly dependent on the host lattice and Dy^{3+} ion concentration, it is possible to modify the yellow to blue ratio or the luminescence branching ratio. Branching ratio is an important parameter as it describes the chances of any transition to occur via stimulated emission [10]. The Y/B ratio for the optimized sample (BBS05) is 1.12, which is very close to the desired ratio of unity to obtain white light. The variation of Y/B ratio for BBS glass samples for different Dy^{3+} concentration is shown in Table 1. The reason for these slight variations in the Y/B ratio could be (a) that an addition of Dy^{3+} ions in the glass matrix has severe impact on the local field, which in turn affects the intensity of the hypersensitive emission at λ_{em} = 575 nm (yellow region). Moreover, it has been found that addition of modifiers such as Al_2O_3 or PbO can result in declusterization of Dy^{3+} ions. Such a declusterization occurring due to modification in the amorphous structure can significantly alter the transition intensities. This has been studied systematically for ions Dy^{3+}, Nd^{3+} and Yb^{3+} in various silicate based glass matrices [27, 28, 29]. The addition of such network modifiers results in de-polymerization of the repeating glassy matrix due to cleavage of Si-O-Si bonds. This leads to a change in the coordination of the cations in the vicinity of the RE ions resulting in the observed increase in the luminescence intensity.

The variation of PL intensity with varying Dy^{3+} ion concentration is shown in Fig. 6. The emission intensity enhanced rapidly with increasing Dy^{3+} ion concentration upto 0.5 mol%. After which, the emission intensity declined. The highest excitation and emission intensity was observed for BBS05 glass sample with a critical Dy^{3+} ion concentration of 0.5 mol%. Concentration quenching occurs when energy is transferred from one donor to another until the energy reaches a sink or an

acceptor in the amorphous matrix [15]. Further in a predictable manner, concentration quenching was observed at a low concentration, which is due to the fact that increasing Dy^{3+} ion concentration causes cross relaxation through various channels as explained later.

Fig. 7. shows a schematic energy-level diagram of Dy^{3+} in BBS glass. Once Dy^{3+} ions are in the excited state, these ions may relax to their ground state by means of radiative transitions or non-radiative transitions via the emission of photons and phonons, respectively. Vibrations of atoms or molecular groups constitutes phonons, which can mediate relaxation in the Dy^{3+} ions [30,31]. As seen in Fig. 7. the states above $^4F_{9/2}$ are closely spaced and relaxation occurs predominantly by non-radiative transitions. The large energy gap between $^4F_{9/2}$ and the lower level $^6F_{1/2}$ (more than 7000 cm^{-1}) decreases the probability of non-radiative relaxations, thereby resulting in radiative transitions. Thus, the low phonon energy of BBS glass plays a crucial role in the high yield of the visible bands **[**32]. Two of the prominent mechanisms which may be employed to explain concentration quenching as seen in Fig. 6. are Resonance Energy Transfer and Cross- Relaxations (among neighboring Dy^{3+} ions). Cross-Relaxation occurs when an excited Dy^{3+} ion loses part of its excitation energy to a nearby Dy^{3+} ion at the ground state and promoting it to some metastable state. In this way both of the participating Dy^{3+} ions enter into metastable states. Considering the energy match rule [13, 33], three cross-relaxation channels can be identified:

CRC1: $^4F_{9/2} + {}^6H_{15/2} \rightarrow ({}^6H_{9/2} + {}^6F_{11/2}) + {}^6F_{5/2}$

CRC2: $^4F_{9/2} + {}^6H_{15/2} \rightarrow ({}^6H_{7/2} + {}^6F_{9/2}) + {}^6F_{3/2}$

CRC3: $^4F_{9/2} + {}^6H_{15/2} \rightarrow {}^6F_{1/2} + ({}^6H_{9/2} + {}^6F_{11/2})$

3.4. Colorimetry of BBS glass samples

The color of any object (self luminous or reflecting) can be conveniently specified via a point, marked on a chromaticity diagram (popularly called a color map) through its color coordinates. These color coordinates are calculated from the PL emission spectra with the help of $\bar{x}(\lambda), \bar{y}(\lambda)$ and $z(\lambda)$ color matching functions defined in the CIE 1931 color space for a 2^o observer [34].

As the information specifying the color is stored in the ratio of the primary colors required and not in the specific amounts of each individual primary color, the number of dimensions used to uniquely specify a color can be reduced from three to two. This was done for the CIE 1931 XYZ

space, and the resultant CIE 1931 x-y chromatic diagram is the most commonly used tool in spectroscopy toady.

It is important to mention here, that even though usage of CIE 1931 chromaticity diagram is popular, it has been supplanted by other color spaces. MacAdam and others have already pointed out the inconsistencies and non-uniformity of the CIE 1931 chromaticity diagram [35, 36]. Briefly, the idea behind non uniformity is that an equal distance travelled on the chromaticity map does not correspond to equal difference in the perception of change in color. To overcome this, CIE has recommended the usage of CIE 1960 UCS (uniform color space), which has to its advantage that other important parameters (CCT, CRI etc) are defined in this space [34, 36]. To obtain the (u, v) coordinates, ones uses the following:

$$u = \frac{4x}{-2x+12y+3}$$

$$v = \frac{6y}{-2x+12y+3}$$

The calculated chromaticity coordinates (x,y) and (u,v) for different BBS samples under λ_{ex} = 348 nm are presented in Table 1. Various color points corresponding to different BBS samples excited by a variety of wavelengths in UV, NUV and blue light are marked in Fig.8, which shows the possibility of obtaining color tunability. The chromaticity coordinates calculated for BBS05 under λ_{ex} = 348 nm is (x=0.310, y=0.340), which lies very close to the CIE standard D65 illuminant (x= 0.31, y=0.33) and also standard equal energy white illuminant (x= 0.33, y=0.33). Hence, it is suggested that BBS05 glass under λ_{ex} = 348 nm excitation is very suitable for the generation of white light (average daylight illuminant) by using commercial BLUE/UV LED chip.

Further specification of white color may be reduced from two dimensions to just one, with the introduction of the Correlated Color Temperature (CCT). CCT is an extremely important tool, for they characterize a key feature about illuminants, which is, their role on our emotional state, mental well-being and visual acuity. Many research studies have concluded that cool white light (high CCT or high blue content) corresponds to an increase in visual acuity and concentration. Consequently, today, cool white lights are preferred as the lighting of choice in schools, offices, hospitals etc. While

on the other hand, a warmer light (low CCT) tends to be employed more prominently in houses, restaurants, hotels etc., where the warmer light invites a calm, relaxed and peaceful atmosphere [37, 38].

The CCT of various BBS glass samples was evaluated from the chromaticity coordinates using McCamy's relation [34], by first evaluating *n* as:

$$n = \frac{(x - 0.3320)}{(y - 0.1858)}$$

Then the CCT was evaluated as:

$$CCT = -437n^3 + 3601n^2 - 6861n + 5524.31$$

The results can be seen in Table 1. The CCT of optimized sample BBS05 under λ_{ex} = 348 nm is 6602 K corresponding to a cool white light and is close to the CCT of D65 illuminant, which is the current CIE recommendation for illuminants to represent average daylight [34].

Finally, Fig. 9 (a) and (b) shows the variation of the x and y-coordinates with increasing Dy^{3+} ion concentration and for four different excitation wavelengths λ_{ex} = 348 nm, λ_{ex} = 363 nm, λ_{ex} = 386 nm, and λ_{ex} = 453 nm. Fig. 9 (c) shows the variation of CCT and Fig. 9 (d) shows the variation of Y/B ratio with variation in Dy^{3+} concentration, under λ_{ex} = 348 nm. The common trend of these four curves i.e. first increasing and then decreasing or vice-versa, indicates that the underlying reason for these changes could be inter-related. This trend results from the variation of the hypersensitive yellow band emission as explained in preceding sections.

4. Conclusion

Dy^{3+} doped Barium Silicate glasses with good optical quality and transparency were successfully prepared. The glassy nature of the prepared glasses was confirmed from the XRD pattern and SEM images. The structural properties thoroughly investigated by using FTIR and confirmed the participation of both borates and silicates as glass-formers as chemical mixtures. Analysis of the excitation and emission spectra showed that the glasses can be efficiently excited from UV, NUV or blue light (325-473 nm) and the optimized sample BBS05 exhibits a cool white emission (CCT=

6602 K) with CIE 1931 coordinates (0.31, 0.34), which are in close proximity to that of standard white color coordinates. Variation in excitation wavelengths and Dy^{3+} ion concentration in the BBS samples brought a possibility to control the color and CCT of the white light emission. Hence, the presented Dy^{3+} doped BBS glasses are potentially usable in photonic applications, especially for white-LEDs, thereby contributing to both environmental as well as financial saving through its SSL applications.

Acknowledgments

The authors are grateful to DST-SERB, Govt. of India for the sanction of a research project (No. SB/FTP/PS-082/2014, dt. 02/03/2015)

References

[1] A. Bergh, G. Craford, A. Duggal and R. Haitz, Phys. Today, 54 (2001) 42-47.

[2] X. Y. Sun, S. M. Huan, X. S. Gong, Q. C. Gao, Z. P. Ye and C. Y. Cao, J Non-Cryst Solids, 356 (2010) 98-101.

[3] C.H. Chiu, C.H. Liu, S.B. Huang and T.M. Chen, J. Electrochem. Soc. 154 (2007) J181-J184.

[4] Z. Ci, Q. Sun, S. Qin, M. Sun, X. Jiang, X. Zhang and Y. Wang, Phys. Chem. Chem. Phys., 16 (2014) 11597-11602

[5] J.S. Kim, S.C. Yang, S.Y. Kwak, Y. Choi, K.W. Paik and B.S. Bae, J. Mater. Chem. 22 (2012) 7954–7960.

[6] C. Zhu, X. Liang, Y. Yang and G. Chen, J. Lumin. 130 (2010) 74.

[7] R. Kaur, S. Singh and O. P. Pandey, Phy Br 407 (2012) 4765.

[8] Q. Chen et. al., Appl. Phys. A 115 (2014) 1159.

[9] M. Jayasimhadri, L. R. Moorthy, R. V. S. S. N. Ravikumar, Opt. Mater., 29 (2007) 1321-1326.

[10] M. Jayasimhadri, K. Jang, H. S. Lee, B. Chen, S. S. Yi and J. H. Jeong, J. Appl. Phys. 106 (2009) 013105.

[11] W. A. Pisarski, L. Zur, T. Goryczka, M. Soltys and J. Pisarska, J. Alloys Compd. 587 (2014) 90 (2014).

[12] J. Pisarska, L. Zur and W. A. Pisarski, Phys. Status Solidi A 209 (2012) 1134-1140.

[13] Q. Su, J. Lin and B. Li, J. Alloys Compd. 225 (1995) 120-123.

[14] L. Marciniak, D. Hreniak and W. Strek, J. Mater. Chem. C, 2 (2014) 5704-5708.

[15] Z. Yang, H. Dong, X. Liang, C. Hou, L. Liu and F. Lu, Dalton Trans. 43 (2014) 11474-11477.

[16] C. Gautam, A. Kumar Yadav, V. K. Mishra and K. Vikram, Open Journal of Inorganic Non-metallic Materials 2 (2012) 47.

[17] A.K. Mandal, D. Agrawal and R. Sen, J. Non-Cryst. Solids 371–372 (2013) 41-46.

[18] A. S. Tenney and J. Wong, J. Chem. Phys. 56 (1972) 5516.

[19] C. Gautam, A. K. Yadav, and A. K. Singh, ISRN Ceramics 2012 (2012) 428-497.

[20] E. I. Kamitsos, A. P. Patsis, M. A. Karakassides and G. D. Chryssikos, J Non-Cryst Solids 126 (1990) 52-67.

[21] S. Feller et. al., J Non-Cryst Solids, 356 (2010) 304-313.

[22] C. Yusufali, R.J. Kshirsagar, Jagannath, R.K. Mishra, R.S. Dutta and G.K. Dey, J Non-Cryst Solids 366 (2013) 54-58.

[23] E. S. Lim, B. S. Kim, J. H. Lee, J. J. Kim, J. Eur. Cerm. Soc. 27 (2007) 825-829.

[24] MJS Nd Fluoro

[25] Q. Su, Z. Pei, L. Chi, H. Zhang, Z. Zhang and F. Zou, J. Alloys Compd. 192 (1993) 25-27.

[26] A. K. Vishwakarma, K. Jha, M. Jayasimhadri, A. S. Rao, K. Jang, B. Siviah, J. Alloys Compd. 622 (2015), 97-101

[27] M. S. Rao, V. Sudarsan, M. G. Brik, Y. Gandhi, K. Bhargavi, M. Piasecki, I. V. Kityk, N. Veeraiah, J. Alloys Compd. 575 (2013), 375-381

[28] M. S. Rao, V. Sudarsan, M. G. Brik, K. Bhargavi, C. S. Rao, Y. Gandhi, N. Veeraiah, Opt. Commun 298-299 (2013), 135-140

[29] M. S. Rao, C. S. Rao, B. V. Raghavaiah, G. S. Baskaran, V. Ravikumar, I. V. Kityk, N. Veeraiah, J. Mol. Struct. 1007 (2012), 185-190

[30] L. A. Riseberg, M. J. Weber, "Relaxation Phenomenon in Rare-Earth Luminescence" in: E. Wolf (Eds), "Progress in Optics XIV" Elsevier Ltd., North-Holland, 1977

[31] B. C. Jamalaiah, J. S. Kumar, A. M. Babu, L. R. Moorthy, K. Jang, H. S. Lee, M. Jayasimhadri, J. H. Jeong, H. Choi, J. Lumin. 129 (2009), 1023-1028

[32] S. Mahmuda, K. Swapna, A. S. Rao, M. Jayasimhadri, T. Sasikala, K. Pavani, L. R. Moorthy, J. Phys. Chem. Solids 74 (2013) 1308-1315

[33] S. Dutta, S. Som, S. K. Sharma, Dalton Trans. 42 (2013) 9654-9661

[34] N. Ohta, A. R. Robertson, "Colorimetry – Fundamental and Applications", John Wiley & Sons, Ltd., England, 2005.

[35] D. L. MacAdam, J. Opt. Soc. Am., 32 (1942) 247-274.

[36] J. Schanda, "CIE Colorimetry - Colorimetry: Understanding the CIE System", John Wiley & Sons, Inc., New Jersey, 2007.

[37] S. M. Berman, M. Navvab, M. J. Martin, J. Sheedy and W. Tithof, Lighting Res. Technol. 38 (2006) 41.

[38] I. T. Kim, A. S. Choi and J. W. Jeong, Building and Environment 57 (2012) 302.

Table. 1: Color Coordinates, CCT and Y/B ratio of various phosphors

Sample	Color Coordinates (x, y)	Color Coordinates (u, v)	CCT	Y/B ratio	References
STANDARD WHITE	(0.33, 0.33)	(0.21, 0.32)	5455	-	[25]
D65	(0.31, 0.33)	(0.19, 0.32)	6504	-	[25]
YAG + Blue chips	(0.29, 0.30)	(0.19, 0.32)	5610	-	[4]
BBS01 (under 348 nm)	(0.29, 0.33)	(0.19, 0.31)	7300	1.04	Present work
BBS05 (under 348 nm)	(0.31, 0.34)	(0.19, 0.32)	6602	1.12	Present work
BBS10 (under 348 nm)	(0.31, 0.34)	(0.19, 0.31)	6749	1.12	Present work
BBS15 (under 348 nm)	(0.30, 0.33)	(0.19, 0.31)	7274	1.13	Present work

Figure Captions:

Fig. 1: X-ray diffraction pattern of BBS05 glass powder.

Fig. 2: SEM image of BBS05 glass.

Fig. 3: FT-IR Spectrum of BBS05 Glass Sample

Fig. 4: Room temperature excitation Spectra of Dy^{3+} doped barium silicate glass at various concentrations with emission wavelength fixed at λ_{em} = 575 nm.

Fig. 5: Room temperature photoluminescence emission Spectra of Dy^{3+} doped barium silicate glasses at various concentrations with excitation wavelength fixed at λ_{ex} = 348 nm.

Fig. 6: Variation of emission intensity with increasing Dy^{3+} ion concentration.

Fig.7: Energy level diagram of Dy^{3+} in BBS glass.

Fig.8: Chromaticity Coordinates of Dy^{3+}: BBS glass samples on CIE 1931 color diagram for different excitation wavelengths and Dy^{3+} concentrations.

Fig.9: Plots of various colorimetric parameters against increasing Dy^{3+} ion concentration in various BBS samples: (a) variation in value of CIE 1931 chromaticity coordinate *x* (b) variation in value of CIE 1931 chromaticity coordinate *y* (c) variation in CCT and (d) variation in Y/B ratio with λ_{ex} = 348 nm for BBS05 sample.

Fig. 1.

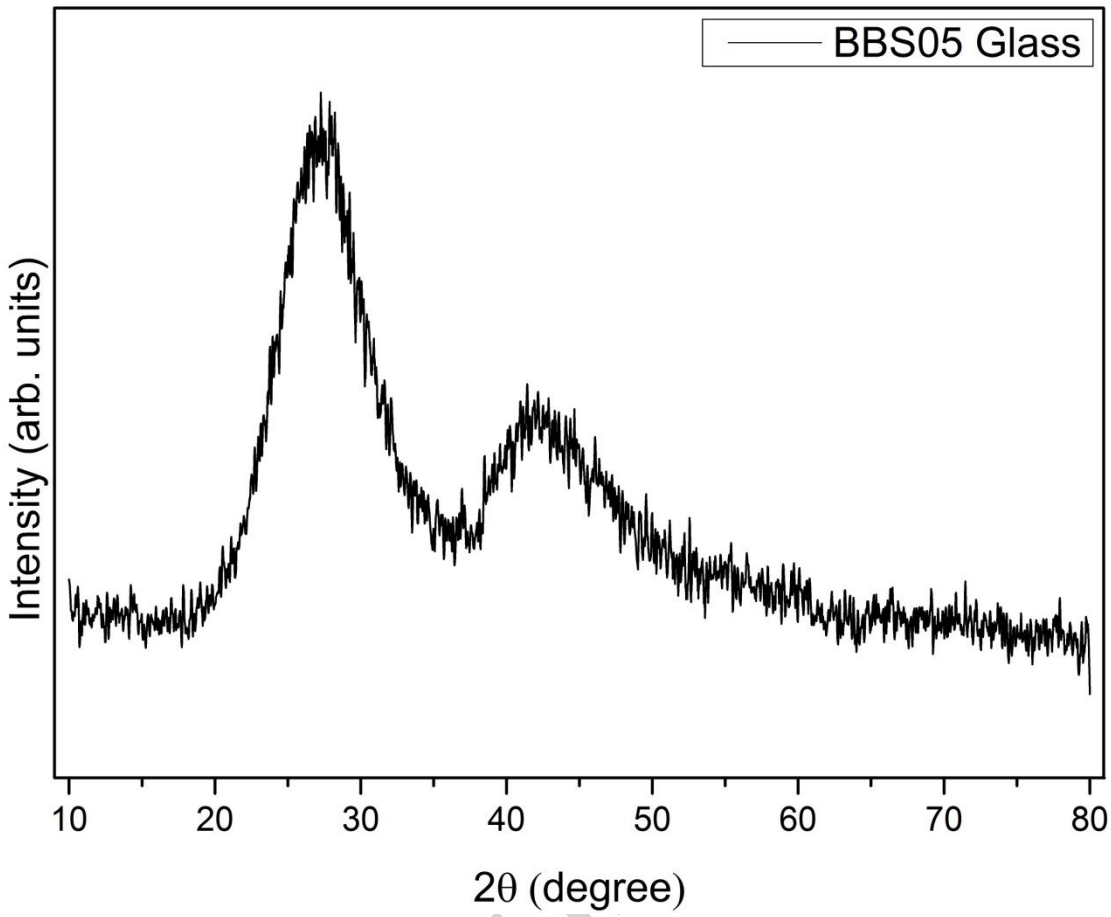

Fig. 2.

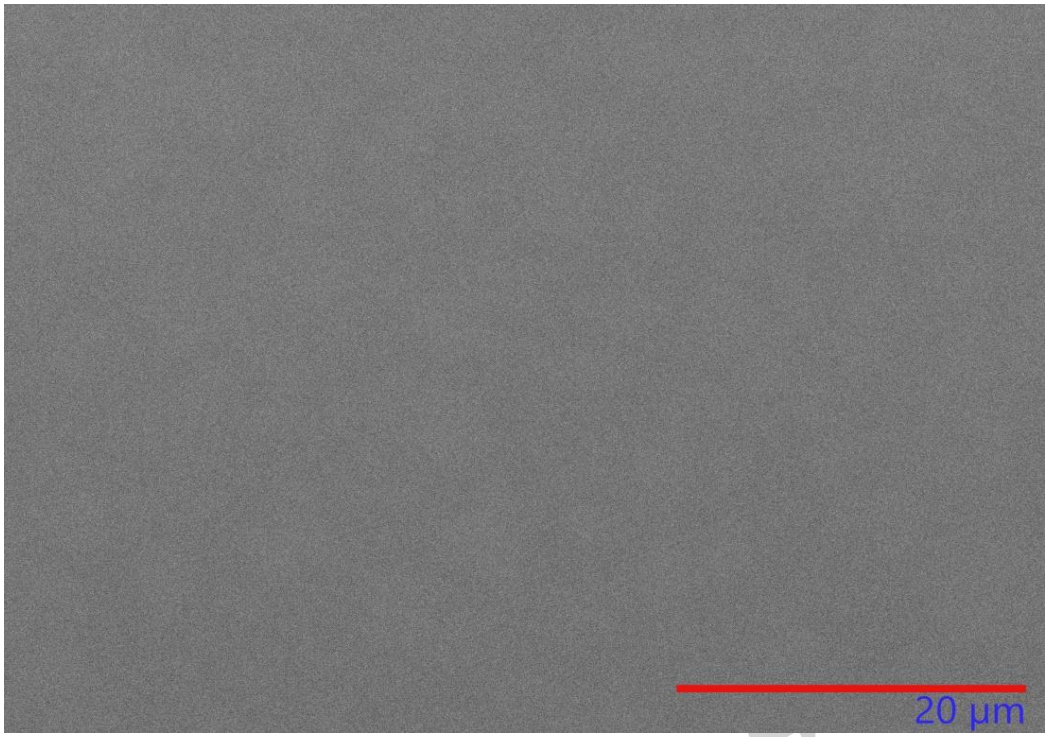

Fig. 3.

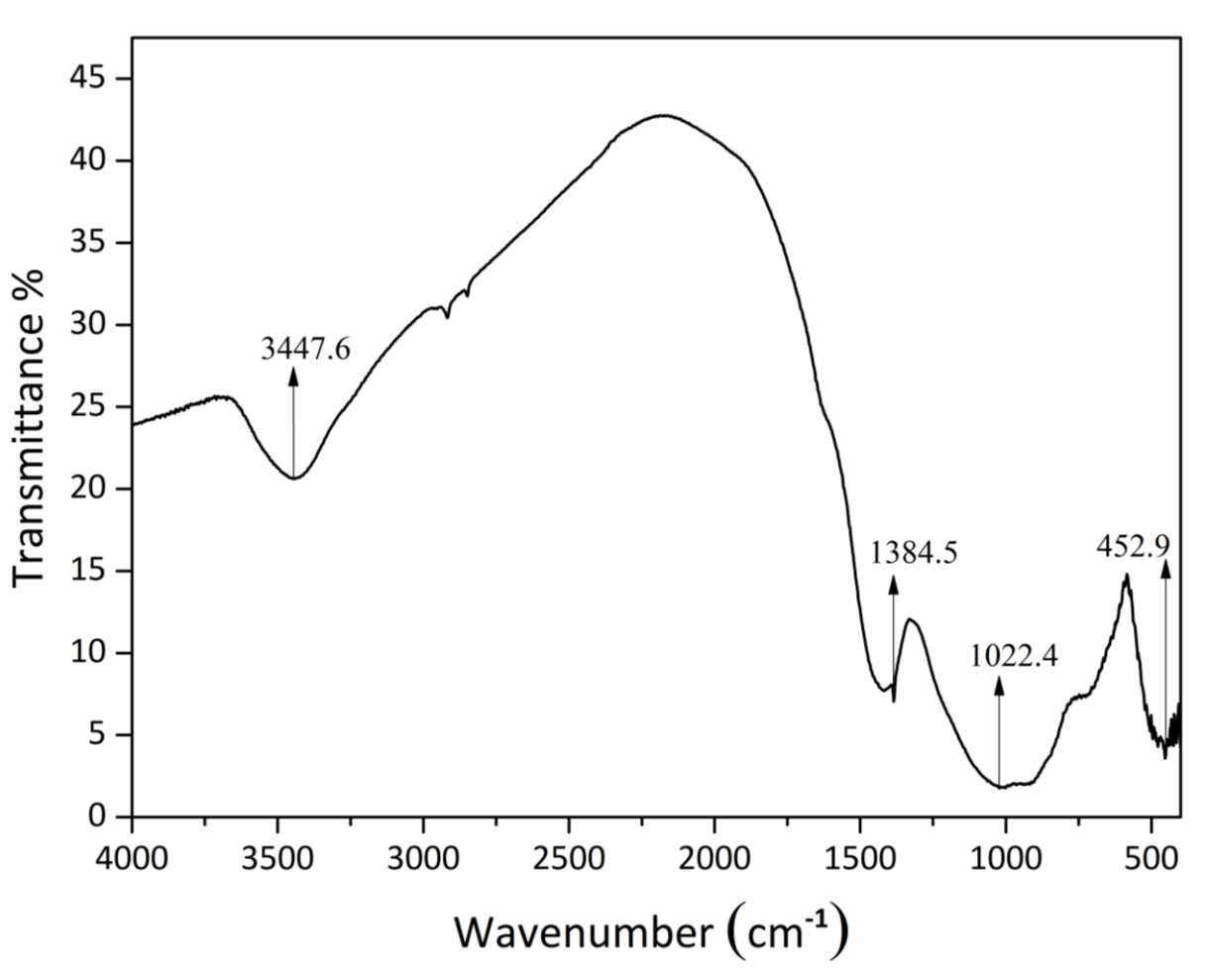

Fig. 4.

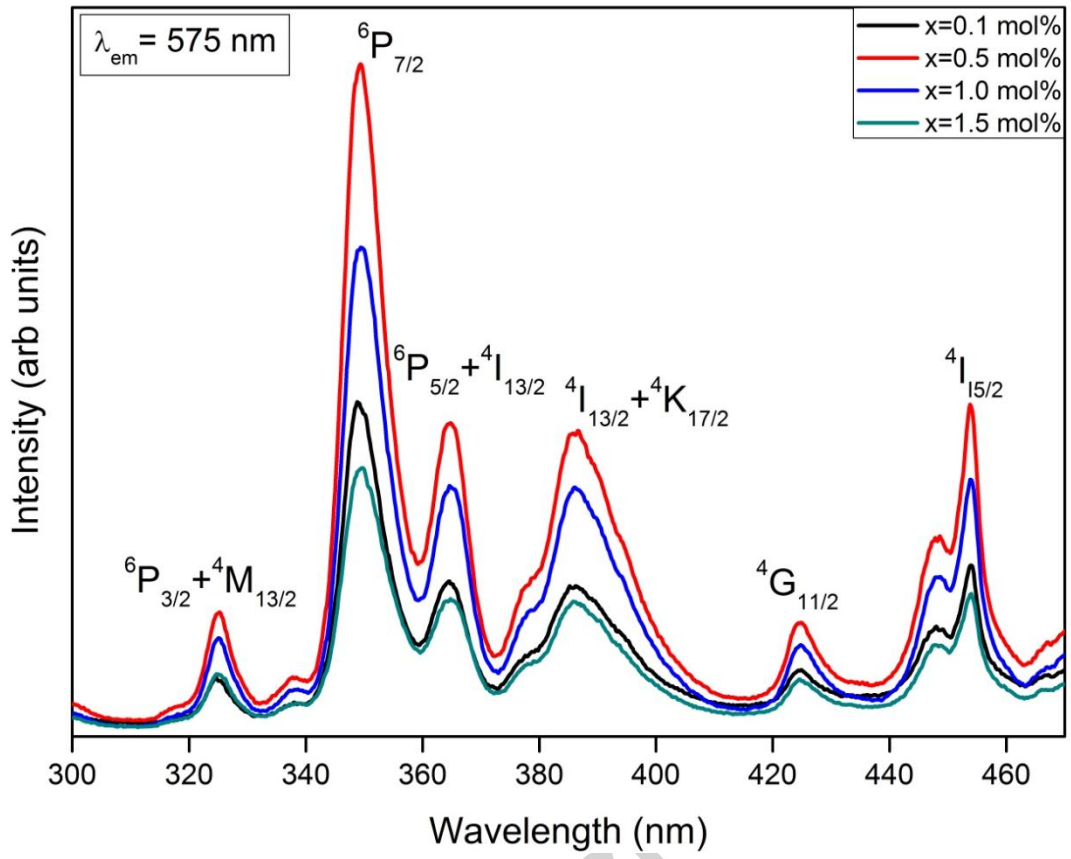

Fig. 5.

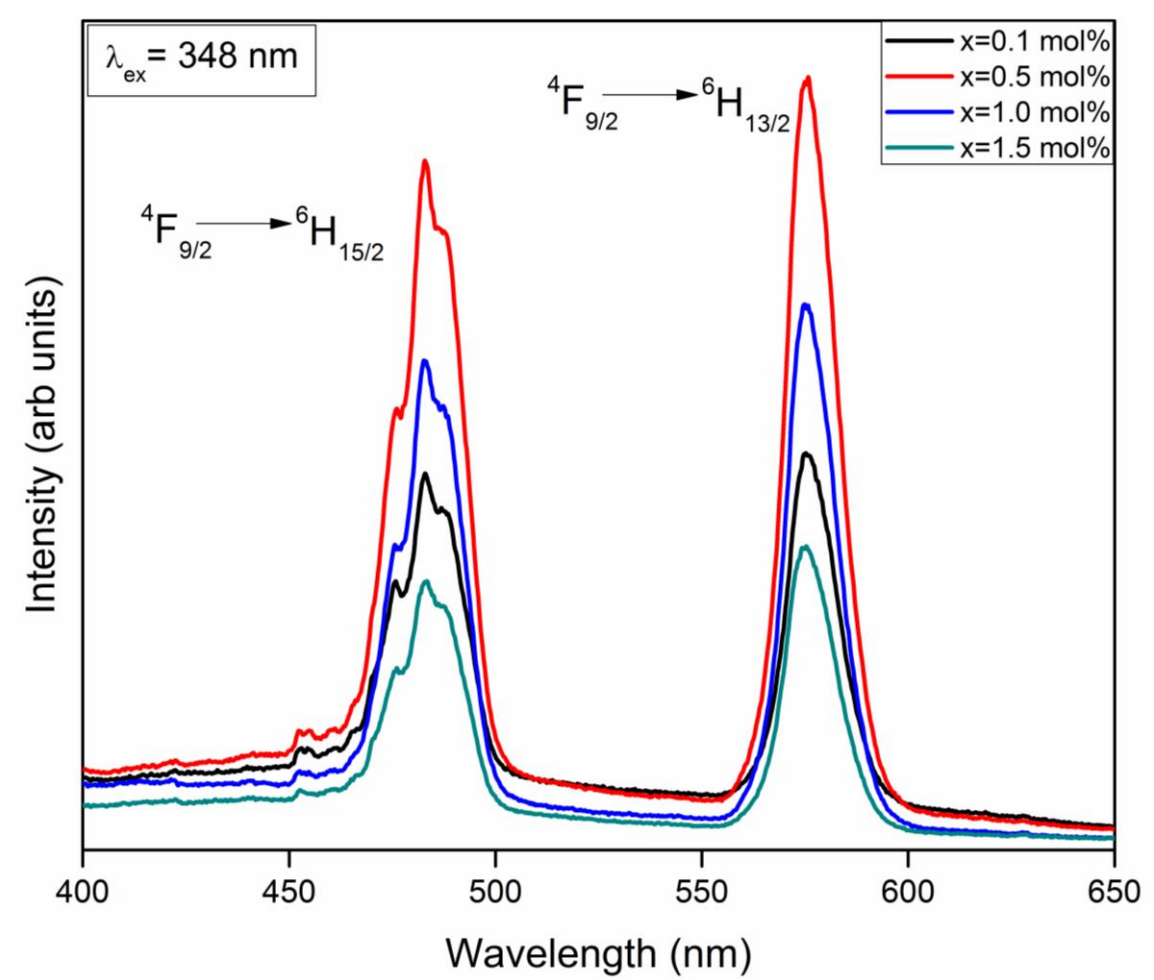

Fig. 6.

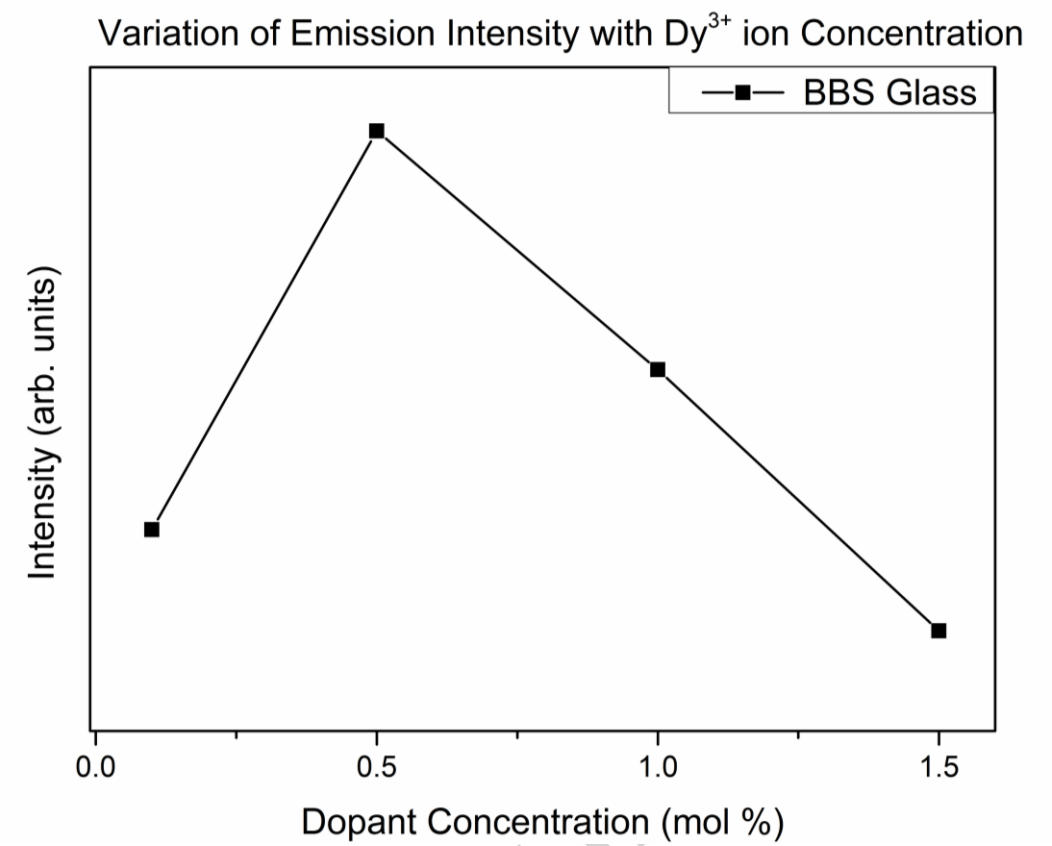

Fig.7.

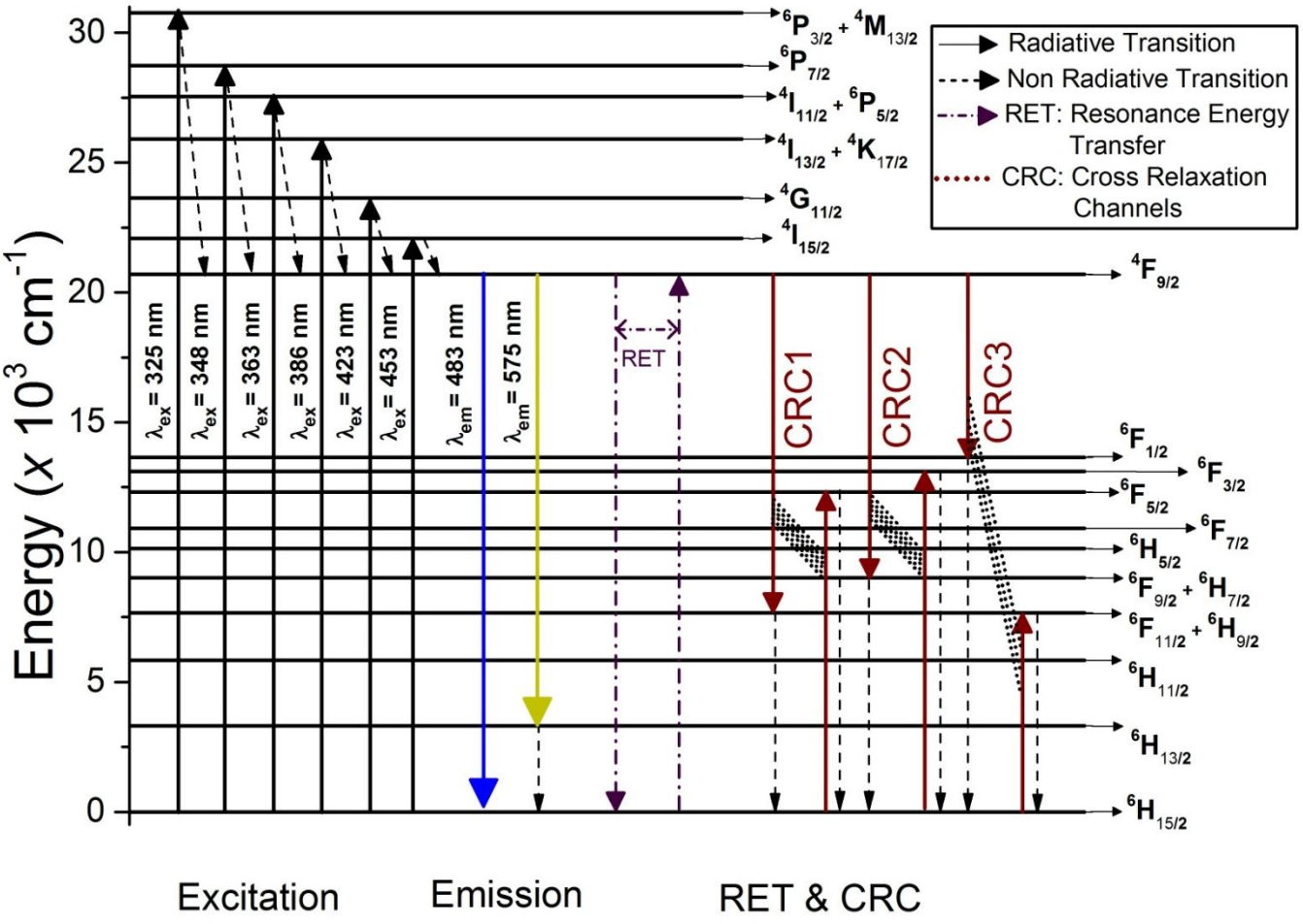

Fig. 8.

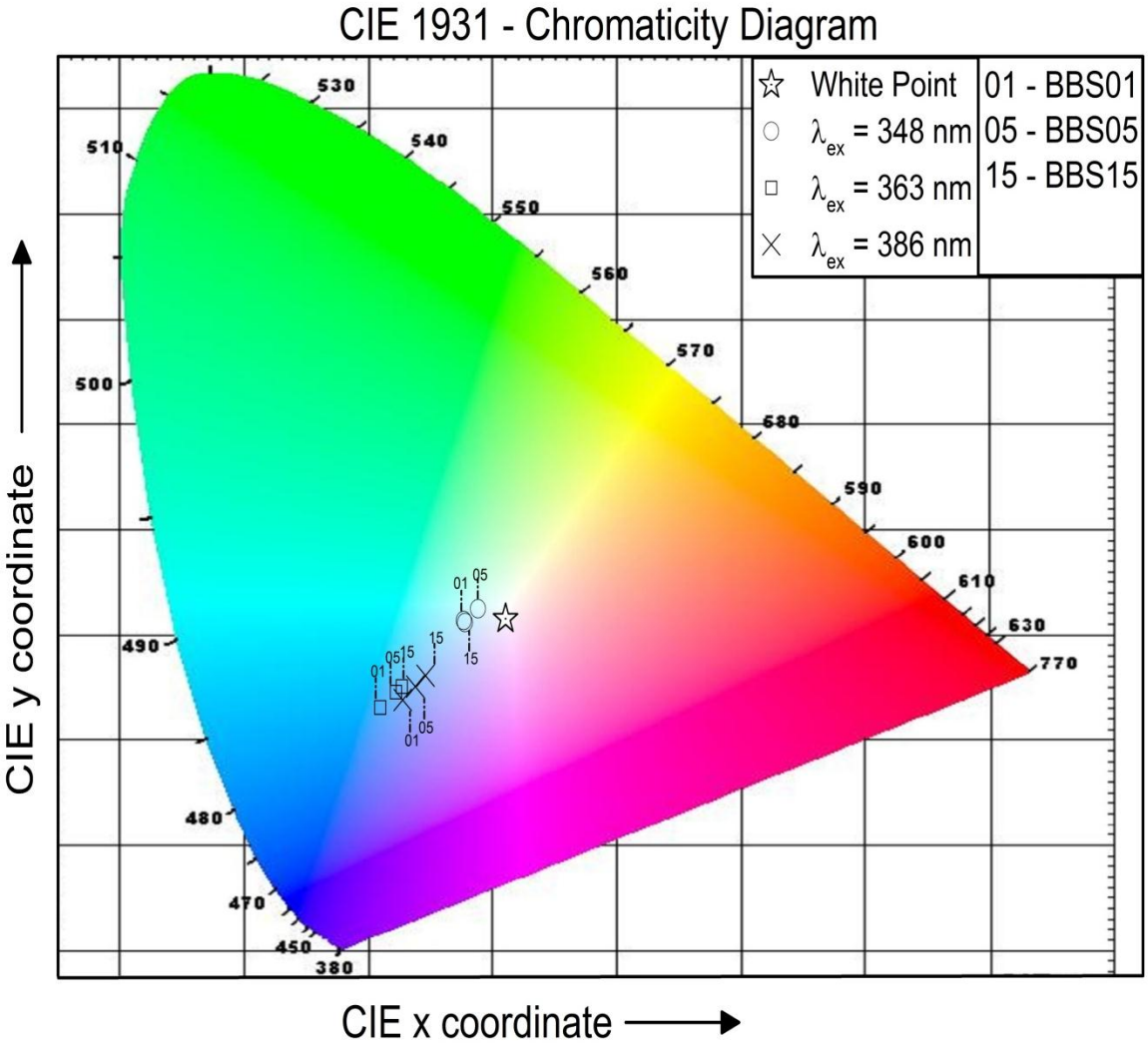
CIE 1931 - Chromaticity Diagram
White Point
λex = 348 nm
λex = 363 nm
λex = 386 nm
01 - BBS01
05 - BBS05
15 - BBS15
CIE y coordinate
CIE x coordinate
530
540
550
560
570
580
590
600
610
630
770
510
500
490
480
470
450
380

Fig. 9.

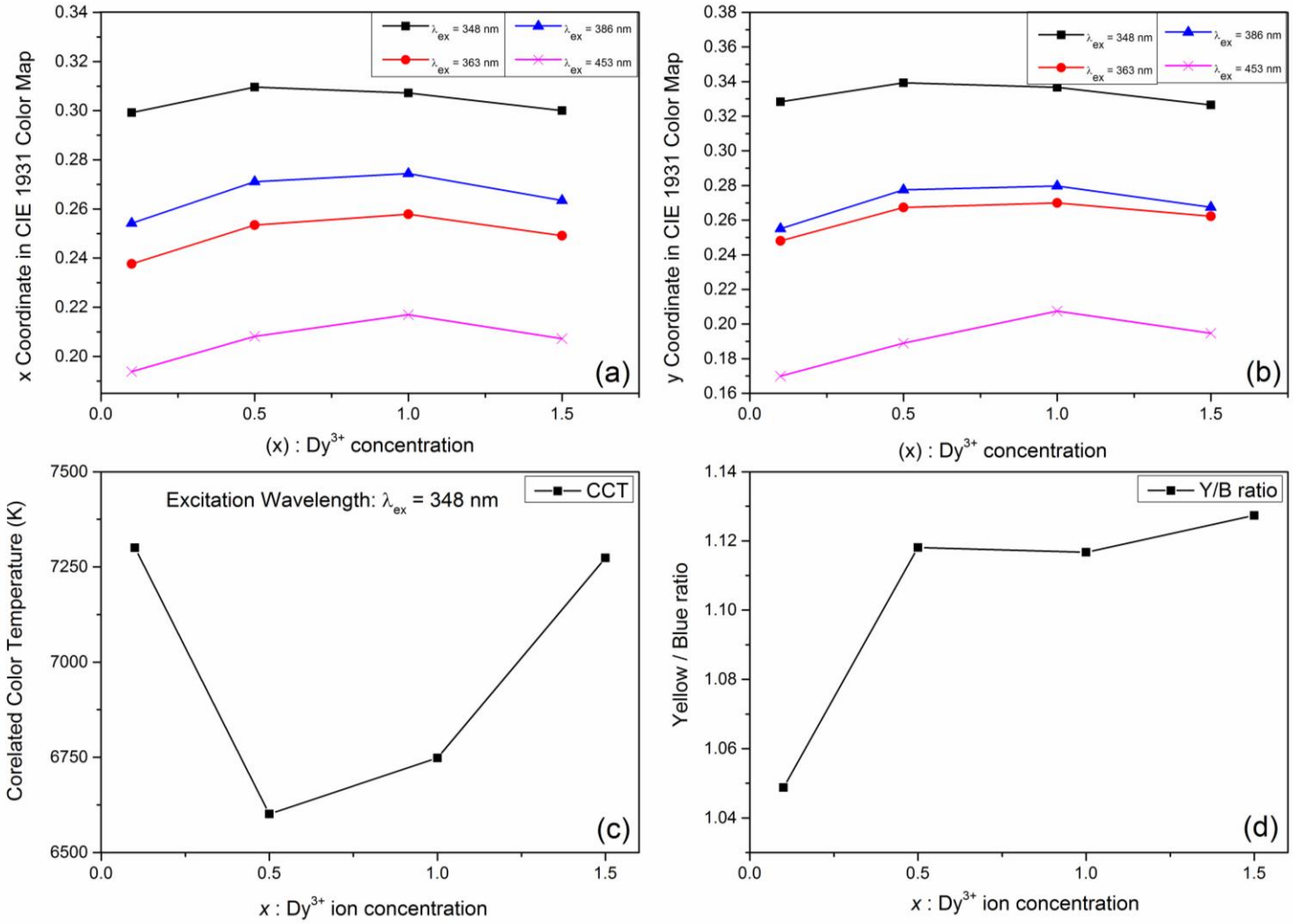

Highlights (for review)

(i) Successfully synthesized Dy^{3+} doped barium silicate glasses

(ii) Structural properties thoroughly discussed by using XRD and FT-IR

(iii) Photoluminescence and colorimetry properties have been investigated.

(iv) Y/B ratio and the reason for color tunability have successfully explained.

(v) CIE coordinates of Dy^{3+}:BBS glass confirms its suitability for w-LEDs/photonic devices.